云南师范大学可再生能源材料先进技术与制备教育部重点实验室

年　　报

2015

ANNUAL REPORT

Key Laboratory of Advanced Technique & Preparation for Renewable Energy Materials，Ministry of Education

Yunnan Normal University

目 录

实验室简介

云南师范大学可再生能源材料先进技术与制备教育部重点实验室（Key Laboratory of Advanced Technique & Preparation for Renewable Energy Materials, Ministry of Education, Yunnan Normal University）于 2004 年 5 月经国家教育部批准建设，2007 年 8 月实验室通过教育部验收，2008 年底正式挂牌运行。

实验室贯彻执行“创新、开放、流动、联合、竞争”的运行管理机制，紧紧围绕可再生能源材料先进技术与制备开展研究工作；下设光伏材料科学与工程、光热材料与利用工程、生物质能工程材料与利用、复合光功能材料与制备等四个研究方向，研究人员由固定人员和流动人员组成。

重点实验室的建设与发展将紧紧围绕“平台、项目和人才”这一主线，始终坚持资源共享、综合集成的发展理念，坚持与时俱进，整合科研资源，突出优势、特色和重点的发展思路。重点实验室将密切围绕国家中长期科学技术发展规划、可再生能源发展的国际前沿以及云南省科技发展的战略需要，致力于解决应用在能源、环境和节能减碳等领域的核心材料制备的关键技术问题，同时揭示和解决影响材料性能的主要基础科学问题；重点突破太阳能高效利用的关键材料和生物质能材料。

主要研究目标

近期目标：通过完善科研平台建设，使其能支撑可再生能源材料及其综合利用的基础研究和应用基础研究，为成为培养、凝聚和吸引优秀人才提供支撑平台，提升重点实验室承担重大科研项目的能力，产出高水平科研成果，培养高水平人才。

中长期目标：在可再生能源材料领域造就国内一流的科研队伍，综合实力达到国内领先水平，在某些研究领域达到国际先进水平，最终申报国家层次重点实验室或工程中心。在科研平台建好的 5 年内，争取在国家级重点或重大项目：国家 973 项目、国家自然科学基金重点或重大项目，国家自然科学基金委创新群体项目和国家重大专项等取得突破，发表 SCI 收录论文不少于 100 篇，申报国家发明专利超过 50 项，在新型太阳电池材料及器件、太阳能光热材料及高效综合利用、生物质能和光化学方向形成具有自主知识产权的核心技术。

主要研究方向

重点实验室主要依托云南师范大学太阳能研究所，同时物理与电子信息学院、化学化工学院和生命科学学院等相关技术和专业给予大力合作和支撑，紧紧围绕可再生能源材料先进技术与制备开展研究工作；下设光伏材料科学与工程、光热材料与利用工程、生物质能工程材料与利用、复合光功能材料与制备等四个研究方向。

主要研究内容

光伏科学与工程方向

- 半导体材料先进制备技术
- 染料敏化太阳电池先进制备技术
- 硅基薄膜材料及高效器件制备
- 铜锌锡硫硒材料及高效器件制备
- 光伏系统优化设计及智能电网技术

太阳能热利用工程方向

- 先进太阳能热转换系统理论与设计
- 新型选择性吸收涂层制备先进技术
- 太阳能跟踪聚焦技术
- 新型光伏光热综合系统设计

生物质能工程方向

- 生物质发酵产氢先进技术
- 生物污水处理先进技术
- 生物质制备液体燃料先进技术
- 先进沼气系统设计及应用

学术委员会

重点实验室学术委员会人员名单

姓名	职务	工作单位、职称
褚君浩	主任	中科院上海技术物理研究所研究员，中科院院士
苏君红	副主任	昆明物理研究所研究员，中国工程院院士
何伟全	副主任	云南师范大学，教授
朱剑豪	委员	香港城市大学首席教授，美国材料研究学会院士
陈立东	委员	中科院上海硅酸盐研究所,中科院百人计划和杰青获得者，高性能陶瓷与超微结构国家重点实验室主任
王如竹	委员	上海交通大学，教育部长江学者和杰青获得者
杨德仁	委员	浙江大学,教育部长江学者和杰青获得者,国家“973”项目首席科学家，硅材料国家重点实验室主任
沈辉	委员	中山大学，中科院百人计划
骆仲泱	委员	浙江大学,教育部长江学者和杰青获得者,国家“973”项目首席科学家，能源清洁利用国家重点实验室主任
佟金	委员	吉林大学，教育部长江学者和杰青获得者
李保明	委员	中国农业大学，教授
沈波	委员	北京大学,教育部长江学者和杰青获得者,国家“973”项目首席科学家
王文静	委员	中科院电工研究所，中科院百人计划
牛智川	委员	中科院半超导体研究所，中科院百人计划
傅文甫	委员	中科院理化所，中科院百人计划
李明	委员	云南师范大学，教授
杨培志	委员	云南师范大学，教授

Electrochimica Acta 182 (2015) 827–833

Contents lists available at ScienceDirect

Electrochimica Acta

journal homepage: www.elsevier.com/locate/electacta

Robust counter electrodes from nanoporous NiM (M = Pt, Pd) alloys for dye-sensitized solar cells

Peizhi Yang[a,*], Qunwei Tang[b,*]

[a] Key Laboratory of Advanced Technique & Preparation for Renewable Energy Materials, Ministry of Education, Yunnan Normal University, Kunming 650500, China

[b] Institute of Materials Science and Engineering, Ocean University of China, Qingdao 266100, China

ARTICLE INFO

Article history:
Received 25 August 2015
Received in revised form 30 September 2015
Accepted 3 October 2015
Available online xxx

Keywords:
Dye-sensitized solar cell
Counter electrode
Alloy electrocatalyst
Zinc oxide nanorod
Template synthesis

ABSTRACT

Alloys are a class of rising counter electrode (CE) electrocatalyst candidates for dye-sensitized solar cells (DSSCs). We present here the mild solution synthesis of NiM (M = Pt, Pd) alloys using zinc oxide nanorod templates and employment as CE electrocatalysts for liquid-junction DSSC applications. Due to the good matching of work functions to redox potential of I^-/I_3^- redox couples and reduced charge-transfer resistance at CE/electrolyte interface, the electrocatalytic activity of NiPt CE and therefore cell performances have been markedly enhanced, yielding a promising power conversion efficiency of 8.27% in the liquid-junction DSSC platform.

1. Introduction

Dye-sensitized solar cell (DSSC) [1,2], a photoelectrochemistry device converting solar energy into electricity, has triggered growing interests in both scientific and industrial aspects. The maximum power conversion efficiency of 13% [3] has been recorded by optimizing the three components of a typical DSSC platform such as dye-sensitized TiO_2 photoanode, a redox electrolyte, and a counter electrode (CE). One of the remaining problems on this architecture is high expense of preferred Pt CE [4]. By addressing this issue, many efforts have been made to develop cost-effective and efficient CE alternatives to Pt species. Up to now, carbonaceous materials [5,6], conductive polymers [7,8], metal sulfides [9], metal selenides [10,11], alloys [12,13], and hybrids [14] have been successfully created as CE electrocatalysts to catalyze I_3^- to I^- ions. However, there is not a CE can meet the required demands for cost-effectiveness, high electrocatalytic activity, good electron-conduction ability, and long-term stability. Alloys have been considered as promising electrocatalysts for energy conversion devices. In our previous reports, we have pioneerly developed Pt-free [15] and low-Pt [16] alloys as potential CEs in liquid-junction DSSC platforms. The electrochemical and therefore photovoltaic performances can be maximized by tuning the stoichiometries. A possible mechanism behind the enhanced performances is the good matching of CE work function to redox potential of liquid electrolyte, creation of gigantic active sites, and electronic structure redistribution.

Under the guide of above-mentioned concept for robust CEs, in the current work, we launch a strategy of preparing nanoporous NiM (M = Pt, Pd) alloy CEs using ZnO nanorods as templates. In details, the Ni layer is electrodeposited on outward surface of mild solution synthesized ZnO nanorod arrays, subsequently the galvanic displacement is applied on the ZnO nanorod supported Ni to form ZnO NiM (M = Pt, Pd) nanorods. After suffering chemical dissolution of ZnO, the resultant nanoporous NiM alloy CEs can be obtained for CE utilization. This rational design can not only maximize the active area for I_3^- adsorption and reduction, but minimize the dosage of precious metals. An impressive power conversion efficiency of 8.27% is determined on the liquid-junction DSSC platform with NiPt alloy CE.

2. Experimental

2.1. Preparation of ZnO nanorod arrays

Zinc nitrate hexahydrate [$Zn(NO_3)_2{\cdot}6H_2O$, 99%] and hexamethylenetetramine (HTMA, $C_6H_{12}N_4$, 99%) were used as reagents without further purification. The ZnO nanorods were synthesized using a mild solution process. Briefly, 2.9749 g of $Zn(NO_3)_2{\cdot}6H_2O$

* Corresponding authors. Fax: +86 871 5517313.
E-mail addresses: pzhyang@hotmail.com (P. Yang), tangqunwei@ouc.edu.cn (Q. Tang).

http://dx.doi.org/10.1016/j.electacta.2015.10.014
0013-4686/

and 1.4019 g of hexamethylene tetramine were dissolved in 100 mL of deionized water to make 100 mL aqueous solution. Subsequently, the freshly cleaned FTO glass substrates (12 Ω square^{-1}) were put face up in the above solution at 95 °C for 12 h. After cooling to the room temperature, the substrates were carefully rinsed with deionized water, dried in air, and subsequently calcined at 350 °C for 10 min.

2.2. Preparation of nanoporous NiM alloy CEs

The nanoporous NiM alloy CEs were prepared by electrodepositing metallic Ni on the surfaces of ZnO nanorods, followed by galvanic displacement and chemical dissolution of ZnO. In details, 0.6571 g of $NiSO_4{\cdot}6H_2O$ and 0.0267 g of NH_4Cl were dissolved in 50 mL of deionized water to form a homogeneous solution. The electrochemical deposition was performed in a three-electrode cell consisting of a Pt plate as a CE, an FTO substrate supported ZnO nanorods as a working electrode and an Ag/AgCl electrode as a reference electrode. The current density and deposition time were controlled at 0.25 mA cm^{-2} and 600 s, respectively. Subsequently, the FTO glass supported ZnO/Ni was immersed into 1 mmol L^{-1} of H_2PtCl_6 (or $PdCl_2$) aqueous solution for 15 min to realize the displacement reaction. Finally, the ZnO nanorods were removed by 2 mmol L^{-1} of H_2SO_4 aqueous solution to obtain the resultant nanoporous NiM alloy CEs.

2.3. Assembly of DSSCs and photovoltaic tests

The photoanodes were prepared by sensitizing FTO glass substrates supported TiO_2 film (~10 μm in thickness) with N719 (purchased from DYESOL LTD) ethanol solution for 24 h at room temperature. The details can be found in our previous reports [17]. Subsequently, the dye-sensitized TiO_2 photoanodes were combined with various CEs and hot-sealed by 60 μm-thickness Surlyn film. Before cell characterizations, the I^-/I_3^- redox electrolyte was injected into the interspace in vacuum atmosphere.

The photocurrent-voltage (J–V) curves of the DSSCs with an active area of 0.25 cm^2 were recorded under irradiation of a simulated solar light (Xe Lamp Oriel Sol3A^{TM}Class AAA Solar Simulators 94023A, USA) from a 100 W xenon arc lamp in ambient atmosphere. A mask was placed on the top surface of DSSC device. Each device was repeatedly measured at least ten times to control the results within experimental errors.

2.4. Electrochemical characterizations

The corresponding electrochemical performances were recorded on a conventional three-electrode CHI660E setup. The cyclic voltammetry (CV) curves were recorded in a supporting electrolyte consisting of 50 mmol L^{-1} of LiI, 10 mmol L^{-1} of I_2, and 500 mmol L^{-1} of $LiClO_4$ in acetonitrile. Electrochemical impedance spectroscopy (EIS) measurements for symmetric dummy cells were carried out in a frequency range of 1E-2 ~ 1E5 Hz and at an ac amplitude of 10 mV. Tafel polarization curves were also recorded on the same symmetric cells. All the electrochemical characterizations were performed at room temperature and atmosphere.

2.5. Other characterizations

The morphologies of the resultant NiM alloys were observed with a scanning electron microscope (SEM, SU8020) and a transmission electron microscopy (TEM, JEM2010, JEOL). Before TEM characterization, the NiM alloys were scraped from substrate to prepare a ~1 mg mL^{-1} ethanol solution. The work functions of various CEs were determined by a SKP RCH020 Kelvin probe combined with a gold tip (5.1 eV) as a reference electrode and the work function of the samples were calculated by the work function of reference electrode plus the relative values. The compositions of

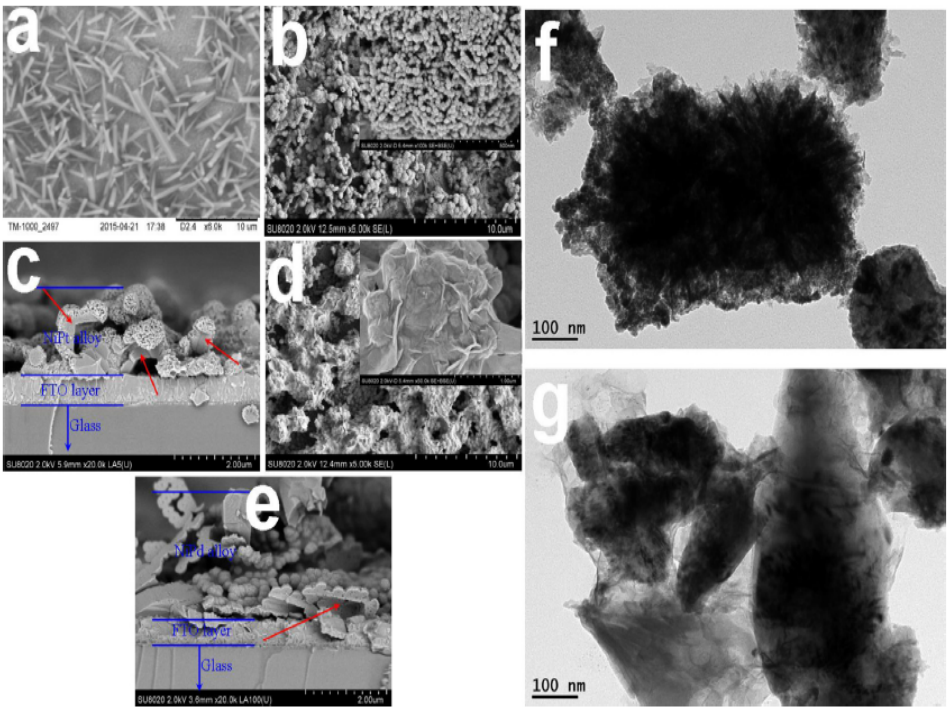

Fig. 1. SEM photographs of (a) ZnO nanorods, (b) top-view NiPt alloy CE, (c) cross-sectional NiPt CE, (d) top-view NiPd alloy CE, (e) cross-sectional NiPd alloy CE. TEM images of (f) NiPt alloy and (g) NiPd alloy.

the CEs were detected by inductively coupled plasma-atomic emission spectra (ICP-AES). The particle pore sizes were analyzed by an AutoPore IV9500 mercury porosimeter (Micromeritics, USA) in a pressure range of 0.5–30,000 psia.

3. Results and discussion

The microstructure of a CE electrocatalyst has a crucial impact on electrocatalytic activity and therefore solar cell performances. Fig. 1a shows the top-view SEM photograph of ZnO nanorods, suggesting a diameter of ~500 nm and length ranging from 3 to 5 μm. After electrodepositing Ni on ZnO nanorods and galvanic displacement of outward Ni by H_2PtCl_6 as well as suffering final dissolution, the resultant NiPt alloy yields nanoparticle interconnected aggregation with nanoporous structure (Fig. 1b). The average particle size and pore size of around 40 nm and 70 nm, respectively. From the cross-sectional image in Fig. 1c, one can find that the internal holes for NiPt alloy remains the shape of hexagonal ZnO nanorods. The loose structure determined by SEM and TEM (Fig. 1f) techniques is expected to provide gigantic reaction area for I_3^- reduction. Apart from nanoparticle aggregations (~420 nm in diameter and ~2 μm in pore size) on bottom layer and remained hexagonal shape of ZnO nanorods, graphene-like nanosheets are covered on outward surface of NiPd alloys, as shown in Fig. 1d, Fig. 1e, and Fig. 1f. These compact nanosheets may restrict the diffusion of redox electrolyte into nanoporous NiPd alloy electrocatalysts for adsorption and catalytic reaction. The compositions of NiPt and NiPd CE electrocatalysts are determined by ICP-AES to be 1.000: 0.251 and 1.000: 0.406, respectively. The lower Pt or Pd dosages in resultant alloy CEs are expected to significantly reduce the CE cost.

CV characterization is a widespread technique in determining the catalytic processes of electrocatalysts in supporting electrolytes [18,19]. As shown in Fig. 2a, CV curves of NiPt and NiPd alloy CEs are recorded in the I^-/I_3^- redox electrolyte at a scan rate of 50 mV s^{-1}, giving two pairs of redox peaks corresponding to Red_1 ($I_3^- + 2e^- = 3I^-$)/Ox_1 ($3I^- - 2e^- = I_3^-$) and Red_2 ($3I_2 + 2e^- = 2I_3^-$)/Ox_2 ($2I_3^- - 2e^- = 3I_2$) [20]. Due to a fact that the CE is to collected electrons from external circuit and to catalyze I_3^- reduction reaction, therefore the peak current density (J_{Red1}) and potential (ϕ_{Red1}) of Red_1 as well as the peak-to-peak separation (E_{pp}) can be utilized to evaluate the electrocatalytic activity. A higher J_{Red1} value of −9.22 mA cm^{-2} for NiPt alloy CE in comparison to NiPd electrode means that more electrons are collected by NiPt alloy for participating in I_3^- reduction reaction, while the reduced ϕ_{Red1} at −65 mV indicates a lower energy requirement for I_3^- reduction. Moreover, the E_{pp} for NiPt alloy CE is 445 mV in comparison with 1232 mV for NiPd electrode, referring to a lower overpotential requirement for NiPt CE. From the enhanced J_{Red1}, and reduced ϕ_{Red1} and E_{pp}, we can conclude that NiPt alloy CE has superior electrocatalytic activity for reducing I_3^- to I^-. Additionally, diffusion coefficient (D_n) of I^-/I_3^- redox couples at CE/electrolyte interface [21], described as $J_{red} = Kn^{1.5}ACD_n^{0.5}v^{0.5}$ can be employed to compare the diffusion kinetics of I_3^- ions within nanoporous NiM alloy. As summarized in Table 1, the D_n value for NiPt is 4.54×10^{-7} cm^2 s^{-1} in comparable to 3.69×10^{-7} cm^2 s^{-1} for NiPd, suggesting that the nanoporous structure of NiPt alloy is beneficial to electrolyte diffusion. The enhanced diffusion kinetics is believed to accelerate the interconversion between $I_3^- \leftrightarrow I^-$.

By assembling two identical CEs into a symmetric dummy cell, we can measure the Nyquist EIS plots for characterizing the charge-transfer behavior at CE/electrolyte interface. As shown in Fig. 2b, the semicircle refers to the charge-transfer resistance (R_{ct})

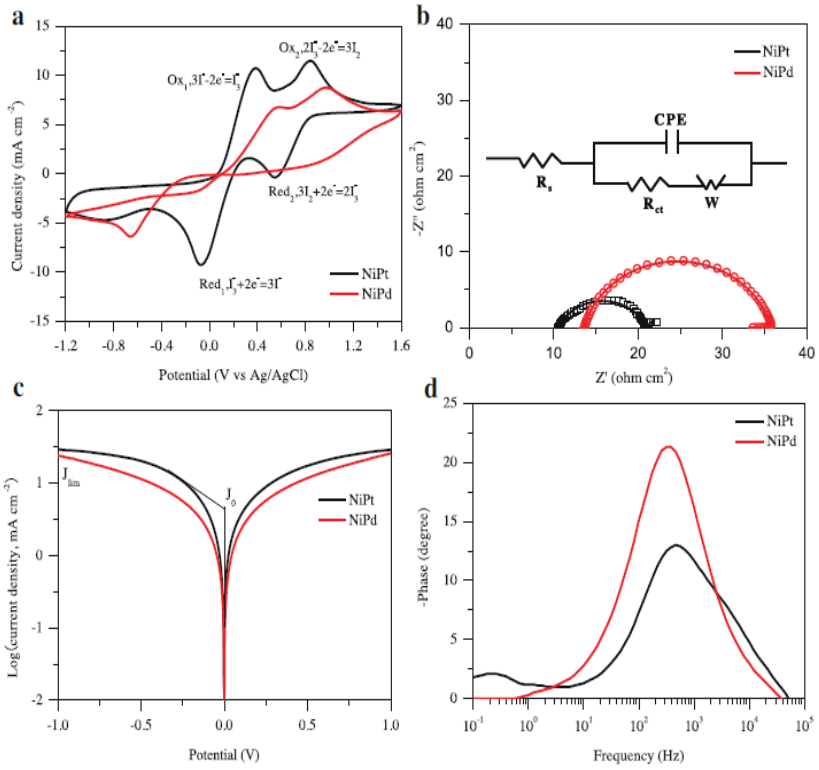

Fig. 2. (a) CV curves of various CEs in I^-/I_3^- redox species recorded at a scan rate of 50 mV s^{-1}, (b) Nyquist EIS plots, (c) Tafel polarization curves, and (d) Bode EIS plots of the symmetric dummy cells with two identical CEs. The inset displays an equivalent circuit extracted by fitting EIS data by Z-view software.

Table 1
Extracted electrochemical parameters from CV, EIS and Tafel characterizations.

CEs	J_{Red1} (mA cm^{-2})	ϕ_{Red1} (mV)	E_{pp} (mV)	logJ_0 (mA cm^{-2})	logJ_{lim} (mA cm^{-2})	D_n (cm^2 s^{-1})	R_{ct} (Ω cm^2)	τ (ms)
NiPt	−9.22	−65	445	0.55	1.47	4.54×10^{-7}	10.34	0.343
NiPd	−6.42	−660	1232	0.24	1.38	3.69×10^{-7}	22.12	0.502

and the corresponding data are extracted by fitting the Nyquist EIS plots with an equivalent circuit. The charges (electrons) will suffer a resistance when involving in the I_3^- reduction reaction at CE/electrolyte interface, and this R_{ct} is dependent on the difference between redox potential of I^-/I_3^- couples (−4.9 eV) [20] and work function of alloy electrocatalyst (Fig. 3). The work functions of NiPt and NiPd alloy CEs (including NiM alloy layer and FTO glass substrate) are measured to be −4.94 and −5.18 eV, yielding energy differences of 0.94 and 1.18 eV, respectively. A reduced R_{ct} and matching work function to redox potential of I^-/I_3^- couples are favorable to rapid participation of electrons in I_3^- reduction reaction. The average lifetime of the electrons (τ) at CE/electrolyte interface can be calculated using $\tau = 1/(2\pi f_{max})$ to cross-check the charge-transfer kinetics, where f_{max} is the frequency at maximum peak for charge-transfer process in Bode EIS plots (Fig. 2d). As summarized in Table 1, the electron lifetimes are 0.343 and 0.502 ms at NiPt/electrolyte and NiPd/electrolyte interfaces, respectively, meaning an enhanced electrocatalytic activity of NiPt alloy CE. This result is in good agreement with CV and Nyquist EIS characterizations.

Tafel polarization curves in Fig. 2c are also provided to reconfirm the catalytic activity and charge-transfer ability. Two crucial parameters including J_0 (exchange current density obtained from the tangent for anodic or cathodic branches, $J_0 = RT/nFRct$) [22] and J_{lim} (limiting diffusion current density from the intersection of the cathodic branch with Y-axis, $J_{lim} = 2nFCD_n/l$) [23] can be determined, as listed in Table 1. The extracted R_{ct} and D_n follow the same order to that from EIS and CV characterizations, respectively. By plotting the peak current densities for Ox_1/Red_1 and Ox_2/Red_2 of stacking CV curves at various scan rates (Fig. 4a), one can find linear relationships between peak current densities and square roots of scan rate, as shown in Fig. 4b. This result suggests that the I_3^- reduction reaction proceeds by a diffusion-controlled mechanism at CE/electrolyte interface [24].

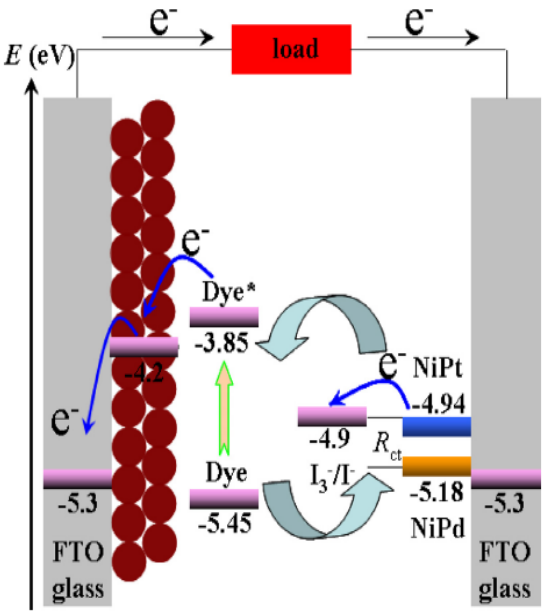

Fig. 3. Diagram for energy levels of the resultant DSSC platform and corresponding charge-transfer processes. The units of the data in diagram are eV.

Apart from electrocatalytic activity, the persistent stability when exposing in I^-/I_3^- redox electrolyte is still an objective for commercial DSSC platforms. We have repeatedly recorded the CV curves at a scan rate of 50 mV s^{-1}, as shown in Fig. 5a and b, and the relationships of J_{Red1} and J_{Ox1} as a function of cycle number are plotted in Fig. 5c and d. The J_{Red1} increases from −6.22 to −6.75 mA cm^{-2} for NiPt alloy CE, yielding an 8.63% enhancement, whereas there is a 22.6% reduction in J_{Red1} for NiPd electrode. The chemical dissolution of alloy species in liquid electrolyte is of highly dependent on the long-term stability [25]. For pristine Pt CE, the Pt species may suffer from dissolution reactions with I_2 [$Pt(s) + 2I_2(aq) = PtI_4(s)$] and I_3^- [$Pt(s) + 2I_3^-(aq) = PtI_4(s) + 2I^-(aq)$], yielding thermodynamical Gibbs free energy ($\Delta_r G_{m,25\,°C}$) of −78.3 and −45.9 kJ mol^{-1}, respectively. The corresponding $\Delta_r G_{m,25\,°C}$ for Pd is −87.5 kJ mol^{-1} in $Pd(s) + I_2(aq) = PdI_2(s)$ and −71.3 kJ mol^{-1} in $Pd(s) + I_3^-(aq) = PdI_2(s) + I^-(aq)$. A negative $\Delta_r G_m$ value means that the reactions between Pt and I_2 or I_3^- ions are spontaneous process, which will result in chemical corrosion of Pt and Pd species in liquid electrolyte. Similarly, the calculated $\Delta_r G_{m,25\,°C}$ values for $Ni(s) + I_2(aq) = NiI_2(s)$ and $Ni(s) + I_3^-(aq) = NiI_2(s) + I^-(aq)$ are −92.6 and −76.4 kJ mol^{-1}, respectively. By alloying Ni with Pt or Pd, the competitive dissolution reactions between Ni with I_2/I_3^- can protect the precious metals from being dissolved by electrolyte [26]. This concept of alloying transition metals having more negative $\Delta_r G_{m,25\,°C}$ with Pt is also applicable to design other stable alloy CEs such as CoPt, FePt, CrPt, etc.

Fig. 6a shows the J–V characteristics on the liquid-junction DSSCs with NiPt and NiPd alloy CEs and the corresponding parameters are summarized in Table 2. The DSSC employing NiPt electrode yields an η of 8.27% (V_{oc} = 0.72 V, J_{sc} = 17.51 mA cm^{-2}, FF = 65.4%) in comparison to η of 6.70% for NiPd based device. As a reference, the photovoltaic performances for the liquid-junction DSSC with pristine Pt electrode have been reported in our previous literatures [27,28]. Under the same conditions, the recorded η is 6.97%, yielding an 18.7% enhancement using NiPt electrode. Although the measured efficiency is still lower than 10.71% for nanoporous Pt [29], 9.16% for nanoporous FeSe [30], and 9.75% for periodically aligned Pt nanocup [31] based devices, the low dosages of previous Pt or Pd (20.06% for NiPt and 28.88% for NiPd from the measured atomic ratios) as well as extraordinary structure demonstrates NiM alloys to be promising CEs candidates for DSSCs. Apart from η, other photovoltaic parameters such as V_{oc} and J_{sc} are also elevated by utilizing NiPt alloy CE. An increased electrocatalytic activity for catalyzing conversion from I_3^- to I^- species means that the excited dye molecules can be rapidly regenerated to their ground state for further excitation and electron injection to conduction band of TiO_2. In this fashion, the density of accumulative electrons on percolating TiO_2 is increased, leading to an elevated J_{sc}. Due to the good matching of conduction band of TiO_2 nanocrystallites, the electrons facilitate transfer the percolating TiO_2 networks instead of involving in the backward recombination reactions with I_3^- species in liquid electrolyte, allowing for a reduced dark current density (Fig. 6b). Theoretically, V_{oc} depends on the difference between Fermi energy level of TiO_2 nanocrystallite and redox potential of I^-/I_3^- electrolyte. A main

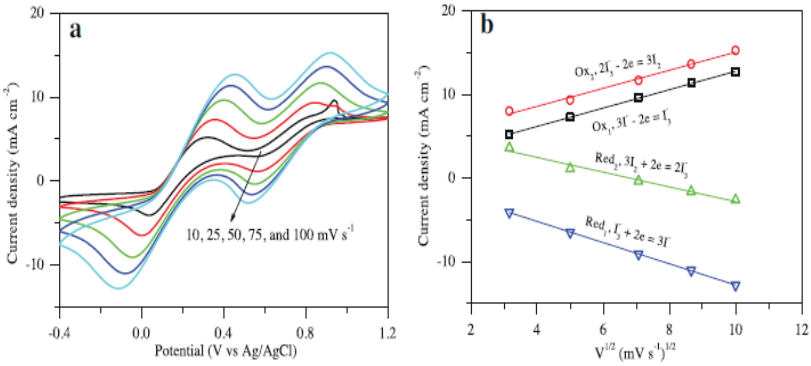

Fig. 4. (a) Stacking CV curves for NiPt alloy CE in I^-/I_3^- redox electrolyte recorded at different scan rates and (b) linear relationships between peak current density and square root of scan rate.

reason behind the reduced V_{oc} in a real device in comparison to this theoretical value is the recombination reactions between the electrons on conduction band of TiO_2 and liquid electrolyte [32]. As has been above-mentioned, the limited backward reaction is beneficial to the enhanced V_{oc} under high voltage drop. By simulating the Nyquist EIS plots using an equivalent circuit, as shown in Fig. 6c, the charge-transfer resistances at dye/TiO_2/electrolyte interface (R_{ct2}) are extracted to be 8.21 and 42.25 Ω cm^2 for NiPt and NiPd based DSSCs, respectively. A lower R_{ct2} value suggests that the I^- species in liquid electrolyte are favorable to diffuse to photoanode/electrolyte interface for dye recovery. *FF* is the parameter depending on the total internal resistance of a DSSC device. Due to the similar photoanodes and electrolytes for two devices, the series resistance (R_s) and R_{ct2} should have crucial impact on the extracted *FF*. Although the R_{ct2} value for NiPt based device is much lower than that for solar cell with NiPd electrode, its R_s value is higher. To our knowledge, there is not an accurate relationship or expression between internal resistance of a solar cell and *FF*, but we can analyze the evolution of *FF* using the cell resistance. The enhanced photovoltaic parameters such as J_{sc}, V_{oc}, and *FF* allow for increased η for NiPt based DSSC in comparison to the device with NiPd CE. Moreover, Bode EIS plots in Fig. 6d are also employed to assess the electron lifetime at photoanode, yielding 9.13 and 0.83 ms for the device with NiPt and NiPd, respectively. The increased electron lifetime demonstrates that the electrons at TiO_2 percolating network have a limited recombination reaction.

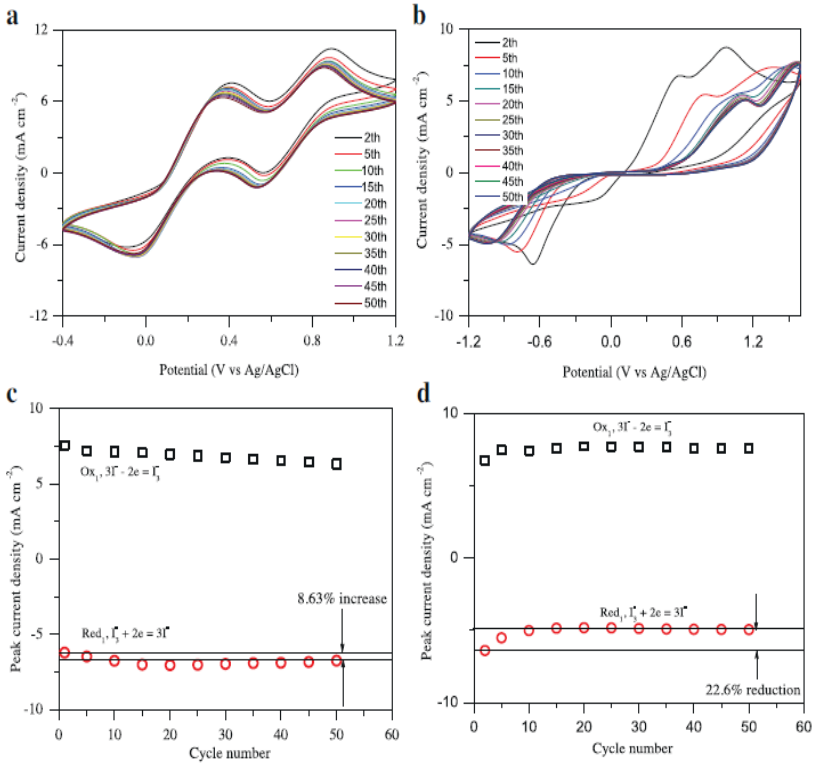

Fig. 5. The 50-stacking CV curves recorded at a scan rate of 50 mV s^{-1} in the supporting electrolyte and the peak current density stability as a function of cycle: (a and c) NiPt alloy CE and (b and d) NiPd alloy CE.

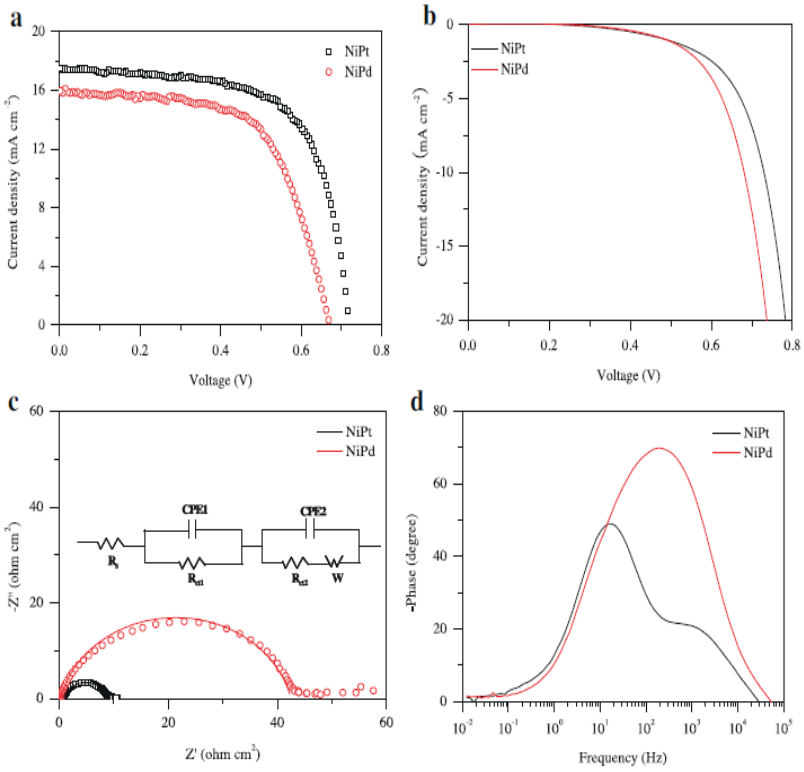

Fig. 6. Characteristics *J–V* curves of the DSSCs recorded (a) under AM 1.5 (100 mW cm^{-2}) irradiation and (b) in the dark. (c) Nyquist EIS and (d) Bode EIS plots of the liquid-junction DSSCs. The inset displays an equivalent circuit matchable to fitting EIS data.

Table 2
Photovoltaic and electrochemical parameters of the DSSCs. V_{oc}: open-circuit voltage; J_{sc}: short-circuit current density, *FF*: fill factor; R_{ct2}: charge-transfer resistance at dye/TiO_2/electrolyte interface; R_s: series resistance.

CEs	V_{oc} (V)	J_{sc} (mA cm^{-2})	*FF* (%)	η (%)	R_{ct2} (Ω cm^2)	R_s (Ω cm^2)
NiPt	0.72	17.51	65.4	8.27	8.21	0.37
NiPd	0.67	15.96	62.6	6.70	42.25	0.23

4. Conclusions

In summary, nanoporous NiPt and NiPt alloy CEs have been experimentally realized by combining electrodeposition of Ni on ZnO nanorods and galvanic displacement of outward Ni by H_2PtCl_6 or $PdCl_2$. The resultant NiPt alloy CE displays superior electrocatalytic activity and charge-transfer ability, arising from good matching of work function to redox potential of liquid electrolyte. Due to the competitive dissolution reactions between Ni and I_2/I_3^- species, the persistent stability of NiPt alloy CE is markedly enhanced. An optimal power conversion efficiency of 8.27% is determined on the DSSC with NiPt alloy electrode in comparison to 6.70% for NiPd based solar cell.

Acknowledgement

The authors would like to acknowledge financial supports from National Natural Science Foundation of China (21503202 and U1037604).

References

[1] B. O'Regan, M. Grätzel, A low-cost, high-efficiency solar cell based on dye-sensitized TiO_2 films, Nature 353 (1991) 737–740.
[2] J.L. Duan, H.H. Zhang, Q.W. Tang, B.L. He, L.M. Yu, Recent advances in critical materials for quantum dot-sensitized solar cells: a review, J. Mater. Chem. A 3 (2015) 17497–17510.
[3] S. Mathew, A. Yella, P. Gao, R. Humphry-Baker, B.F.E. Curchod, N. Ashari-Astani, I. Tavernelli, U. Rothlisberger, M.K. Nazeeruddin, M. Grätzel, Dye-sensitized solar cells with 13% efficiency achieved through the molecular engineering of polyphyrin sensitizers, Nat. Chem. 6 (2014) 242–247.
[4] Q.W. Tang, J.L. Duan, Y.Y. Duan, B.L. He, L.M. Yu, Recent advances in alloy counter electrodes for dye-sensitized solar cells. A critical review, Electrochim. Acta (2015) , doi:http://dx.doi.org/10.1016/electacta.2015.08.072.
[5] Z.B. Yang, M. Liu, C. Zhang, W.W. Tjiu, T. Liu, H.S. Peng, Carbon nanotubes bridged with graphene nanoribbons and their use in high-efficiency dye-sensitized solar cells, Angew. Chem. Int. Ed. 52 (2013) 3996–3999.
[6] H. Chen, T. Liu, N. Wang, L. Zhao, Q. Zhao, J. Ren, H. He, H. Lin, Enhanced dye-sensitized solar cells with catalytic carbon aerogel counter electrodes, Electrochim. Acta 174 (2015) 871–874.
[7] Q.W. Tang, H.Y. Cai, S.S. Yuan, X. Wang, Counter electrodes from double-layered polyaniline nanostructures for dye-sensitized solar cell applications, J. Mater. Chem. A 1 (2013) 317–323.
[8] S. Xu, Y. Luo, G. Liu, G. Qiao, W. Zhong, Z. Xiao, Y. Luo, H. Qu, Bifacial dye-sensitized solar cells using highly transparent PEDOT:PSS films as counter electrodes, Electrochim. Acta 156 (2015) 20–28.
[9] Y.C. Wang, D.Y. Wang, Y.T. Jiang, H.A. Chen, C.C. Chen, K.C. Ho, H.L. Chou, C.W. Chen, FeS_2 nanocrystal ink as a catalytic electrode for dye-sensitized solar cells, Angew. Chem. Int. Ed. 52 (2013) 6694–6698.
[10] F. Gong, H. Wang, X. Xu, G. Zhou, Z.S. Wang, In situ growth of $Co_{0.85}Se$ and $Ni_{0.85}Se$ on conductive substrates as high-performance counter electrodes for dye-sensitized solar cells, J. Am. Soc. Chem. 134 (2012) 10953–10958.
[11] Y.Y. Duan, Q.W. Tang, J. Liu, B.L. He, L.M. Yu, Transparent metal selenide alloy counter electrodes for high-efficiency bifacial dye-sensitized solar cells, Angew. Chem. Int. Ed. 53 (2014) 14569–14574.
[12] X.X. Chen, Q.W. Tang, B.L. He, L. Lin, L.M. Yu, Platinum-free binary Co-Ni alloy counter electrodes for efficient dye-sensitized solar cells, Angew. Chem. Int. Ed. 53 (2014) 10799–10803.
[13] X. Zheng, J. Deng, N. Wang, D. Deng, W.H. Zhang, X. Bao, C. Li, Podlike N-doped carbon nanotubes encapsulating FeNi alloy nanoparticles: high-performance counter electrode materials for dye-sensitized solar cells, Angew. Chem. Int. Ed. 53 (2014) 7023–7027.
[14] J. Huo, J.H. Wu, M. Zheng, Y. Tu, Z. Lan, High performance sponge-like cobalt sulfide/reduced graphene oxide hybrid counter electrode for dye-sensitized solar cells, J. Power Sources 293 (2015) 570–576.
[15] J. Liu, Q.W. Tang, B.L. He, Platinum-free binary Fe-Co nanofiber alloy counter electrodes for dye-sensitized solar cells, J. Power Sources 268 (2014) 56–62.

Electrochimica Acta 184 (2015) 226–232

Contents lists available at ScienceDirect

Electrochimica Acta

journal homepage: www.elsevier.com/locate/electacta

Understanding the catalytic behaviour of NiM (M = Pt, Ru, Pd) counter electrode electrocatalysts in liquid-junction dye-sensitized solar cells

Peizhi Yang[a,1,*], Chunqing Ma[b,1], Qunwei Tang[b,*]

[a] Key Laboratory of Advanced Technique & Preparation for Renewable Energy Materials, Ministry of Education, Yunnan Normal University, Kunming 650500, China
[b] Institute of Materials Science and Engineering, Ocean University of China, Qingdao 266100, China

ARTICLE INFO

Article history:
Received 12 July 2015
Received in revised form 21 September 2015
Accepted 16 October 2015
Available online 20 October 2015

Keywords:
Dye-sensitized solar cell
Counter electrode
Alloy electrocatalyst
Electrocatalytic behavior
Charge transfer

ABSTRACT

Understanding the electrocatalytic behaviours of counter electrode (CE) electrocatalysts favors to tune the sluggish triiodide (I_3^-) reduction kinetics and to compare their catalytic activities. We present here the experimental realization of cost-effective CE electrocatalysts from urchin-like NiM (M = Pt, Ru, Pd) for studying the profounding charge transfer processes without sacrificing photovoltaic performances of DSSCs. Our focus is placed on the systematic studies of catalytic activities along with modeling of I_3^- reduction reaction rate constant, extracting $k = 4\pi Dr_aN_B$ for zero-dimensional electrocatalysts. The DSSCs yield conversion efficiencies of 9.08%, 7.74%, and 6.86% with NiPt, NiRu, and NiPd CEs, respectively.

1. Introduction

Device design for liquid-junction dye-sensitized solar cells (DSSCs) has been explored to operate at varying levels of solar light-to-electricity power conversion efficiency [1,2]. The primary argument in favor of state-of-the-art DSSCs is high consumption of preferred platinum (Pt) electrocatalyst in counter electrodes (CEs) [3]. Therefore, it is highly desirable to engineer DSSC catalysts that utilize significantly lower precious metal loadings and maintain catalytic activity in the desired range. Nevertheless, our ability to control the reduction of fabrication cost of CE catalysts is still limited to utilize Pt hybrids or to completely replace Pt by conductive polymers, carbonaceous materials, or compounds [4,5]. All of these candidates are susceptible to unsatisfactory stability due to structural deviation or electrochemical collapse under cell operations [6]. Therefore, the dilemma of reducing expenses of DSSCs without sacrificing their photovoltaic performances is still unchanged. In this fashion, new synthesis routes to fabricate active and new-structured CE electrocatalysts are desired in the advanced DSSC platforms. Alloying precious noble metals such as Pt, Ru, and Pd with 3d transition metals has been demonstrated as a successful approach toward advanced solution electrocatalysts [7]. Addition of another metal to a catalytically active one to form an alloy can alter the availability of active surface sites and tune both electronic and surface strain effects for optimal catalysis [8]. Fundamental studies of well-defined alloyed CE catalysts are straightforward focused on achieving the same level of triiodide (I_3^-) reduction to Pt by conventional impregnation or coprecipitation synthesis due to the lack of control over size, homogeneity and shape [9–11].

I_3^- reduction reaction is one of the utmost significances in the advanced electrochemical energy conversion of DSSCs. Insights into the relationship between alloy composition, electronic structure and catalytic activity should be determined to tune the sluggish kinetics of I_3^- reduction reaction. It is still subject to considerable uncertainty, however, how do alloy nanocatalysts accelerate the catalytic process. One of the difficulties in determining the catalytic kinetics is that the alloyed nanostructures may not have either the same size or shape. A simple comparison of activity normalized either by mass or surface area is insufficient to identify a true alloying effect. In the current work, we present the experimental realization of bimetallic NiM (M = Pt, Ru, Pd) CE electrocatalysts for efficient DSSCs, and build a model for extracting a commonly used reaction rate constant for evaluating the catalytic activity of zero-dimensional (0D) CE electrocatalysts. Emphasis will be placed on the charge transfer process and mechanism at CE catalyst/liquid electrolyte interface as well as on alloying effects between Ni and M atoms.

* Corresponding author. Tel./Fax: +86 871 5517313.
E-mail addresses: pzhyang@hotmail.com (P. Yang), tangqunwei@ouc.edu.cn (Q. Tang).
[1] The authors have equal contributions.

http://dx.doi.org/10.1016/j.electacta.2015.10.080
0013-4686/

2. Experimental

2.1. Synthesis of NiM CEs

The feasibility of synthesizing NiM electrocatalysts was confirmed by a mild solution approach: 0.237 g of $NiCl_2 \cdot 6H_2O$ was dissolved in 25 mL of distilled water by intensive stirring for 30 min. And then 1 mL of hydrazine monohydrate (85 wt%) was introduced drop by drop to the well-stirred solution at room temperature by simultaneous vigorous agitation for 30 min in succession; then the mixed solution was sealed into a 50 mL Teflon-lined autoclave and cleaned FTO glass substrate (sheet resistance 12 Ω square^{-1}, purchased from Hartford Glass Co., USA) with FTO layer downward was immersed in. After the reaction at 200 °C for 15 min, the FTO substrate supported Ni were rinsed with deionized water and dipped into 1 mM H_2PtCl_6, $RuCl_3$, and $PdCl_2$ aqueous solution for 10, 30, 1 min, respectively.

2.2 Assembly of DSSCs

Under vigorous agitation at room temperature, 100 mL of deionized water was mixed with 10 ml of titanium tetrabutanolate. After 30 min, the mixture was pump-filtrated to obtain dehydrated filter powders. Subsequently, 10 mL of acetic acid and 0.8 mL of nitric acid were added into the above filter powders dropwise in a flask. After an agitation of 15 min at 80 °C, the volume of the mixture was adjusted to 170 mL by adding deionized water. The reactant was further agitated at 80 °C in a sealed atmosphere. Later, the resultant colloid was transferred into a Teflon-lined autoclave and heated at 200 °C for 12 h. A homogeneous mixture consisting of 65 mL of the white colloid and 0.4 g of commercial P25 were made under ultrasonic irradiation for 30 min and then transferred to another Teflon-lined autoclave, which was subsequently heated at 200 °C for 12 h. After removing supernatant liquid, the colloid was mixed with 0.8 g of poly(ethylene glycol) (M_w = 20,000), 1 mL of OP emulsifier (triton X-100), and 0.0405 g of PVP and subsequently concentrated at 80 °C.

The TiO_2 colloid for photoanode fabrication fabrication was prepared by a sol–hydrothermal method. A layer of TiO_2 nanocrystal anode film with a thickness of 10 μm was prepared by a doctor-blade method. Resultant anodes were further sensitized by immersing into a 0.50 mM ethanol solution of N719 dye ([cis–di(thiocyanato)–N,N′–bis(2,2′–bipyridyl–4–carboxylic acid)–4–tetrabutylammonium carboxylate]). The DSSC was fabricated by sandwiching redox electrolyte between a dye-sensitized TiO_2 anode and a CE. A redox electrolyte consisted of 100 mM of tetraethylammonium iodide, 100 mM of tetramethylammonium iodide, 100 mM of tetrabutylammonium iodide, 100 mM of NaI, 100 mM of KI, 100 mM of LiI, 50 mM of I_2, and 500 mM of 4–tert–butyl–pyridine in 50 ml acetonitrile.

2.3. Electrochemical characterizations

The electrochemical performances were recorded on a conventional CHI660E setup comprising an Ag/AgCl reference electrode, a CE of platinum sheet, and a working electrode of FTO glass supported 1D catalysts. The cyclic voltammetry (CV) curves were recorded from −1.0 to +1.6 V and back to −1.0 V. Before the measurement, the supporting electrolyte consisting of 50 mM M LiI, 10 mM I_2, and 500 mM $LiClO_4$ in acetonitrile was degassed using nitrogen for 10 min. Electrochemical impedance spectroscopy (EIS) measurements were also carried out on the CHI660E Electrochemical Workstation in a frequency range of 0.1 Hz ~ 10^5 kHz and an ac amplitude of 10 mV at room temperature. The resultant impedance spectra were analyzed using the Z–view software. The resultant impedance spectra were analyzed using the Z–view software. Tafel polarization curves were recorded on the same Workstation by assembling symmetric cell consisting of CE|redox electrolyte|CE.

2.4. Photovoltaic measurements

The photovoltaic test of the DSSC with an active area of 0.25 cm^2 was carried out by measuring the photocurrent–voltage (J–V) characteristic curves using an Electrochemical Workstation (CHI660E, Shanghai Chenhua Device Company, China) under irradiation of a simulated solar light from a 100 W Xenon arc lamp (XQ–500 W) in ambient atmosphere. The incident light intensity was controlled at 100 mW cm^{-2} (calibrated by a standard silicon solar cell). Each sample was measured at least five times.

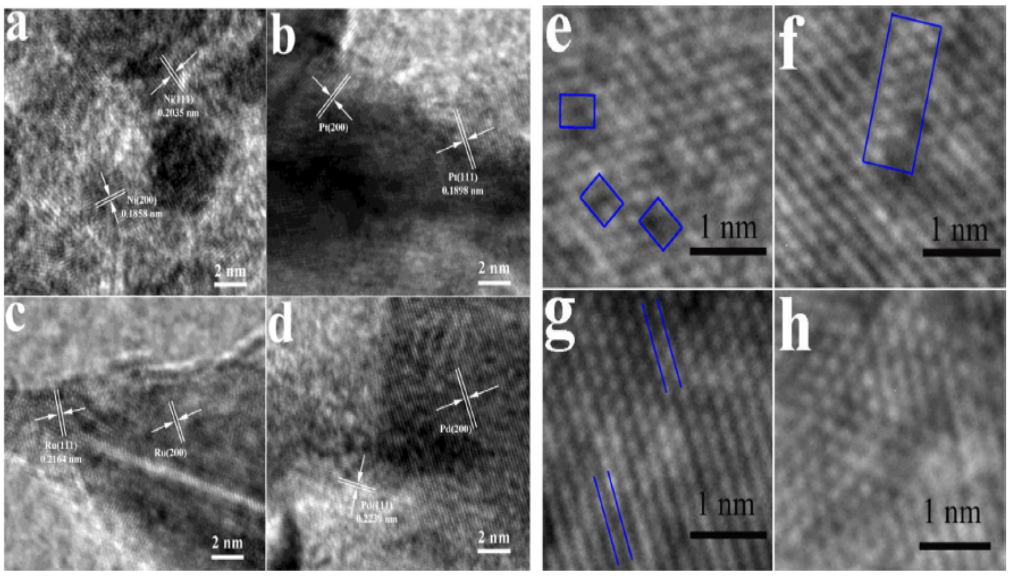

Fig. 1. HRTEM photographs of (a) Ni, (b) NiPt, (c) NiRu, and (d) NiPd electrocatalysts. Lattice strain in (e)&(f) NiPt, (g) NiRu, and (h) NiPd electrocatalysts.

2.5. Other characterizations

The morphologies of the CE catalysts were observed with a scanning electron microscope (SEM, S4800) and a transmission electron microscopy (TEM, JEM2010, JEOL). The work functions of the FTO supported NiM CEs were achieved by a SKP RCH020 Kelvin probe, which features a stainless gold tip as a reference electrode. The contact potential difference extracted from the equipment was defined as the work function of the tip minus the work function of sample [12]. In this fashion, the work function of a CE was obtained by subtracting the standard work function of gold with the recorded contact potential difference. The compositions of the CEs were detected by inductively coupled plasma-atomic emission spectra (ICP-AES).

3. Results and discussion

Fig. S1 and Fig. S2 represent the morphologies of as-prepared Ni and NiM electrocatalysts on fluorine-doped tin oxide substrates, depicting uniform urchin-like shaped structures with average diameter ca. 500 ± 20 nm. No evident alteration in shapes and sizes are detected after a galvanic displacement by $PtCl_6^{2-}$, Ru^{3+}, and Pd^{2+}. It is thermodynamically favorable for noble metal cations to "steal" electrons from the Ni metal because of a lower redox potential for $Ni^{2+} + 2e^- = Ni^0$ ($E^0 = -0.257$ V vs. RHE) than $Pt^{4+} + 4e^- = Pt^0$ ($E^0 = 1.180$ V vs. RHE), $Ru^{3+} + 3e^- = Ru^0$ ($E^0 = 0.455$ V vs. RHE), and $Pd^{2+} + 2e^- = Pd^0$ ($E^0 = 0.951$ V vs. RHE) [13,14]. This galvanic displacement process combines aspects of corrosion of urchin-like Ni and electrodeposition of precious metal cations ($PtCl_6^{2-}$, Ru^{3+}, or Pd^{2+}), enabling the creation of extended surface catalysts through the implementation of extended urchin-structured Ni. The compositions of NiPt, NiRu, and NiPd CE electrocatalysts are determined by ICP-AES to be 1.000: 0.439, 1.000: 2.801, and 1.000: 6.530, respectively. The consistent shapes and sizes of the alloyed NiM electrocatalysts benefit the catalytic activity comparison in DSSCs. This ration design emphasizes the surface-to-volume ratio aspect with respect to increase active sites in per unit volume [15,16], as these catalysts render to be potentially effective placeholders for I_3^- reduction reaction. From the high-resolution TEM images of NiM catalysts in Fig. 1, one can find that the Ni atoms have entered the M lattice due to a lower lattice constent of Ni (3.53 Å for Ni, 3.92 Å for Pt, 4.28 Å for Ru, and 3.89 Å for Pd) [17], creating compressive lattice strain for enhanced catalytic activity [18,19]. As shown in Fig. 1a-d, the lattice distances for Pt (111), Ru (111), and Pd (111) faces are 0.1898, 0.2164, and 0.2239 nm relative to 0.2239, 0.2211, and 0.2285 nm of bulk Pt (PDF#87-0647), Ru (PDF#88-2333), and Pd (PDF#87-0641), respectively. In comparison with pristine Ni, the lattice distance of Ni (111) in three NiM electrocatalysts also has a small lattice strain at the outmost surface. Clear lattice strains can be detected from the atom distribution, as shown in Fig. 1g–h. NiPt electrocatalyst displays atom vacancies in the Pt atom alignments, moreover, dislocations are also produced by the mismatch between host Pt and guest Ni atoms. Although the Ni atoms participate in the alignment of Ru phase, there is apparent changed lattice distance. In the case of NiPd electrocatalyst, a large number of phase boundaries can be determined, leaving more active sites for liquid absorption. The lattice strains in NiM electrocatalysts are

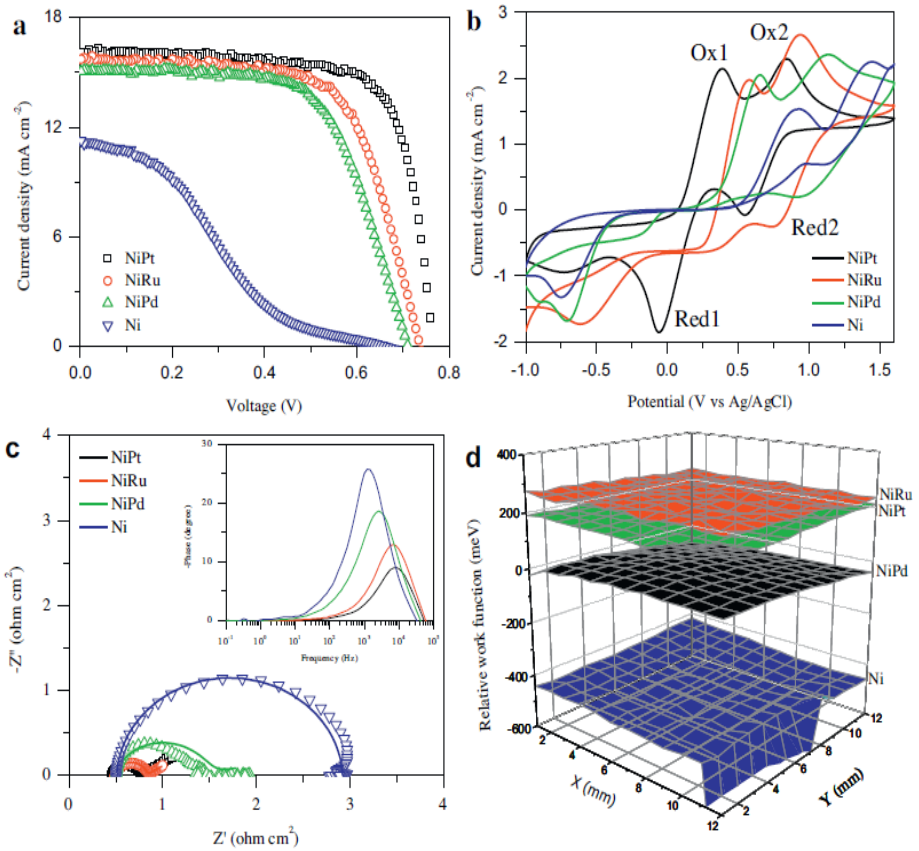

Fig. 2. (a) Characteristic *J-V* curves for the DSSCs with various CEs. (b) CV curves of the CEs for I^-/I_3^- redox electrolyte recorded at a scan rate of 50 mV s^{-1}. (c) Nyquist EIS plots for the symmetric dummy cells from two identical CEs. (d) Relative work functions of various CEs.

expected to tailor the electronic structure and therefore catalytic activity toward I_3^- reduction reaction.

Fig. 2a shows the representative *J-V* curves for the DSSCs with Ni and NiM CEs under air mass 1.5 global sunlight, and the photovoltaic parameters are summarized in Table 1. An η of 1.91% is determined on the DSSC with pristine Ni CE, and this value is enhanced to 9.08%, 7.74%, and 6.86% by replacing partial Ni with Pt, Ru, and Pd, respectively. Moreover, the cell efficiencies for NiPt and NiRu based devices are higher than 7.31% for the DSSC with pristine Pt (Fig. S3 and Table 1). From a small standard deviation (±5%), as shown in Fig. S4, we infer that the DSSCs with promising photovoltaic performances and high reproducibility can be realized using the method reported here.

Two pairs of redox peaks corresponding to Red_1 ($I_3^- + 2e^- = 3I^-$)/Ox_1 ($3I^- - 2e^- = I_3^-$) and Red_2 ($3I_2 + 2e^- = 2I_3^-$)/Ox_2 ($2I_3^- - 2e^- = 3I_2$) are observed in each CV curve recorded at a scan rate of 50 mV s^{-1}, as shown in Fig. 2b. All of the NiM and pristine Ni CEs show similar anodic and cathodic peaks to those obtained with planar Pt electrode [6], allowing for the same catalytic behavior of NiM as CE catalysts. The peak current density (*J*Red1) and potential (*V*Red1) assigned to Red_1 along with peak-to-peak separation (*E*pp) between the potential difference of Red_1 and Ox_1 are three parameters in evaluating the catalytic activity of a CE. The CE giving higher *J*Red1, and lower *V*Red1 and *E*pp is expected to have better catalytic activity toward I_3^- reduction reaction [20]. As summarized in Table S1, the pristine Ni electrode shows a *J*Red1 of −1.328 mA cm^{-2}, *V*Red1 of −0.754 V, and *E*pp of 1.678 V, while *J*Red1 is enhanced to −1.869 mA cm^{-2}, and *V*Red1 and *E*pp are decreased to −0.063 and 0.451 V when alloyed with Pt, respectively. The synthetical catalytic activity is followed by NiRu and NiPd. The electron transfer along Ni-M bonding to M makes an electron-enriched M surface [17], favoring to absorbing I_3^- ions to form I_3^-(M) and subsequently decomposing to I^- according to diffusion-controlled processes (Fig. S5). Nyquist EIS analysis for the symmetric dummy cells by two identical CEs is conducted to gain more insights into charge transfer at CE/electrolyte interface and electrocatalytic property of NiM CEs. As shown in Fig. 2c and Table S2, *R*ct follows an order of NiPt (0.24 Ω cm^2) < NiRu (0.32 Ω cm^2) < NiPd (0.85 Ω cm^2) < Ni (2.26 Ω cm^2). A lower *R*ct value means that the electrons are more facile to participate in the I_3^- reduction reaction ($I_3^- + 2e^- = 3I^-$). In this fashion, the average lifetime of the electrons [$\tau = 1/(2\pi fp)$, *fp* is the peak frequency in Bode EIS plots] at CE/elctrolyte can be utilized to assess the catalytic kinetics. Apparently, the electrons at NiPt CE surface have a lifetime of 19.3 μs in comparison to 23.4, 61.0, and 132.0 μs at interfaces of NiRu/electrolyte, NiPd/electrolyte, and Ni/electrolyte, respectively, allowing for an accelerated reduction process using NiPt CE. This result is in an agreement with that from CV characterization. To understand why and how do the NiM catalysts tune charge-transfer process and electrocatalytic activity, we compare the work functions (WFs) of related CEs with potential of I^-/I_3^- redox reactions (−4.9 eV), as shown in Fig. 2d, the actual WFs for NiPt, NiRu, NiPd, and pristine Ni are calculated to be −4.993, −5.048, −5.111, and −5.32 eV, respectively. The good matching of WF with redox potential of $I_3^- \leftrightarrow I^-$ reaction is beneficial to the electron transfer from catalyst layer to electrolyte for I_3^- reduction, which has been supported by density functional theory calculation in previous report [21]. This potential difference between the WF of a CE and redox potential of I^-/I_3^- can be determined as the energy requirement of an electron jumping at CE/electrolyte interface, i.e. *R*ct of a CE catalyst (Fig. S6). These differences for NiPt, NiRu, NiPd, and Ni are 0.093, 0.148, 0.211, and 0.42 eV, respectively, yielding a consistence with previous analysis for EIS plots.

Table 1
Photovoltaic parameters for the DSSCs with various CEs. V_{oc}: open-circuit voltage; J_{sc}: short-circuit current density; η: power conversion efficiency; *FF*: fill factor.

CE catalysts	V_{oc} (V)	J_{sc} (mA cm^{-2})	η (%)	*FF* (%)
Ni	0.659	11.25	1.91	25.8
NiPt	0.763	16.15	9.08	73.7
NiRu	0.737	15.79	7.74	66.5
NiPd	0.714	15.07	6.86	63.8
Pt	0.703	14.98	7.31	69.4

To further study the investigate the catalytic activities, Tafel polarization curves are scanned on the symmetric dummy cells, as shown in Fig. 3a, the slops for the anodic or cathodic branches are in an order of NiPt > NiRu > NiPd > Ni. A larger slops indicates a higher exchange current density ($J_0 = RT/(nFRct)$, *R* is gas constant, *T* is absolute temperature, *n* is the number of electrons involving in I_3^- reduction, and *F* is Faraday's constant) on the CE. Additionally, limiting diffusion current density ($J_{lim} = 2nFCD/l$, *C* is I_3^- concentration, *l* is the distance between CEs in a symmetric dummy cell, and *D* can be obtained from $J_{red1} = Kn^{1.5}ACD^{0.5}v^{0.5}$) increases in the order of NiPt > NiRu > NiPd > Ni and is proportional to D, while *D* is directly proportional to J_{Red1} in CV curves. Consequently, we conclude from the electrochemical and work function characterizations that NiPt catalyst has a higher electrocatalytic activity than NiRu and NiPd.

Apart from impacting the catalytic behavior, CE catalyst also has a significant effect on photovoltaic performances of a liquid-junction DSSC. When irradiated by incident light, the electrons released by excited dye molecules (dye|$TiO_2 \rightarrow dye^*|TiO_2 \rightarrow dye^+|TiO_2 + e^-|TiO_2$) can transfer to fluorine-doped tin oxide (FTO) glass along percolating TiO_2 networks, while the oxidated dyes will be recovered by I^- ions ($dye^+|TiO_2 + I^- \rightarrow dye|TiO_2 + I_3^-$). The generated I_3^- species diffuse from dye|TiO_2/electrolyte interface to CE/electrolyte and are reduced to I^- again. In this fashion, the higher catalytic activity of a CE catalyst having lower *W* can lead to accelerated processes for dye regeneration, electron excitation, and therefore the electron density on conduction band (CB) of TiO_2. Consequently, the output *J*sc of a DSSC is expected to be enhanced. Moreover, the electrons on CB of TiO_2 favor jumping along percolating channels under such a large potential drop instead of involving in backward reactions with I_3^- due to mismatching of CB of TiO_2 and redox potential of I^-/I_3^- pairs, therefore leading to a decreased dark current (Supporting Information Fig. 3b). *V*oc is determined by the difference between the quasi Fermi energy of the electrons in percolating TiO_2 and redox potential of I^-/I_3^- electrolyte [22]. In a real DSSC device, the recorded *V*oc is generally lower than this theoretical value because of a backward reaction between photogenerated electrons and I_3^- species in electrolyte. As has been abovementioned, the increased electrocatalytic activity is beneficial to restricting the recombination reaction. In this fashion, the real *V*oc value is also elevated by utilizing robust CE. While *FF* is inversely proportional to the internal resistance ($R = RFTO_{/TiO2} + RTiO2 + RTiO2_{/electrolyte} + W + Rct + Rs_{,CE}$) of a DSSC, hence the *FF* should have the same evolution to the catalytic activity of a CE catalyst. All the photovoltaic parameters extracted from liquid-junction DSSCs in Table 1 are consistent with the catalytic activities of CEs.

When applied as windows, roof panels, or portable sources, the DSSCs should have superiorities including fast start up, multiple on/off capability, and stable photocurrent. For evaluating these characteristics, we record the on-off switches by alternatively irradiating and darkening the solar cells, as shown in Fig. 4a. The abrupt increase in photocurrent density and no delay in starting the cell mean the CEs from NiM electrocatalysts are vigorous in catalyzing I_3^- reduction. However, photocurrent densities of the solar cells with NiPt and NiRu are increased by 1.1% and 0.8% and reduced by 13.5% for NiPd after persistent 30 min irradiation (Fig. 4b). In comparison with pristine Pt in Ref [9], the stabilities of the CEs have been markedly enhanced. Pt has been the heart in modern advanced CE electrocatalyst of liquid-junction DSSCs. However, Pt dissolution in state-of-the-art I^-/I_3^- redox electrolyte

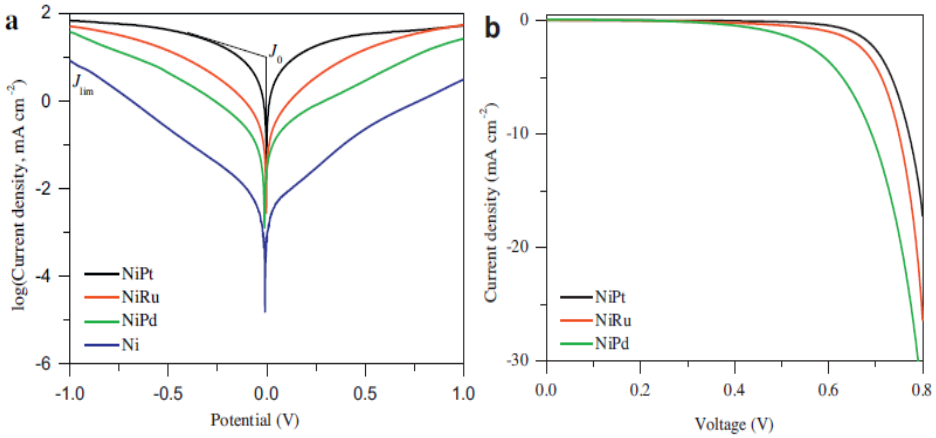

Fig. 3. (a) Tafel polarization curves of the symmetric dummy cells. (b) Dark *J-V* characteristics for the DSSCs.

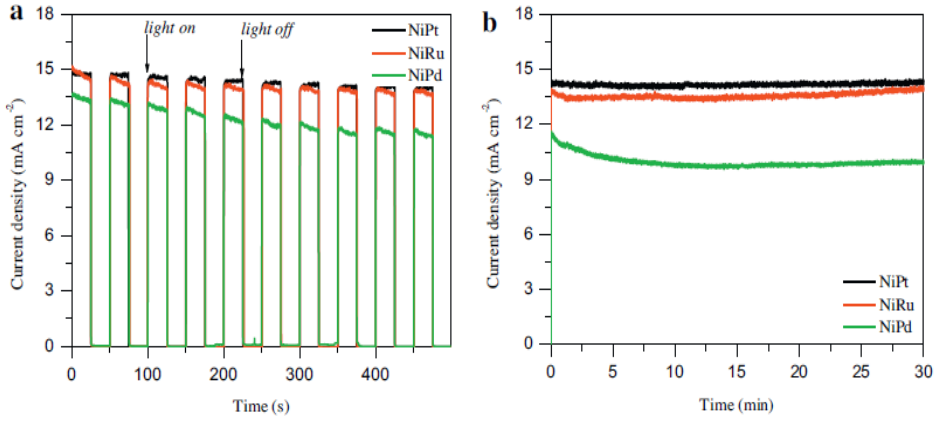

Fig. 4. (a) Start-stop switches and (b) photocurrent stabilities of the DSSCs with NiPt, NiRu, and NiPd CEs.

has been an inevitable issue since the birth of DSSCs. The photocurrent reduction is ascribed to the chemical dissolution of catalysts in I^-/I_3^- redox electrolyte [23], mainly from $Pt(s)+2I_3^-(aq)=PtI_4(s)+2I^-(aq)$ and $Pt(s)+2I_2(aq)=PtI_4(s)$, as shown in Table S3. From Van't hoff isothermal formula, we can calculate the thermodynamical Gibbs free energy (Δ_rG_m) to be −45.9 and −78.3 kJ mol^{-1} for reaction (4) and reaction (3), respectively. The negative values of Δ_rG_m mean that the reactions between metals and I_3^- or I_2 species are spontaneous process, which will lead to the corrosion of metal species. The highly negative of Δ_rG_m for Ni in comparison with that of Pt and Pd indicates that Ni is more easily corroded by I_3^- and I_2, therefore, the more completed reaction of transition metals with I_3^- species protect the high catalytic activity of Pt in coaxially alloyed CEs. The potential mechanism has been

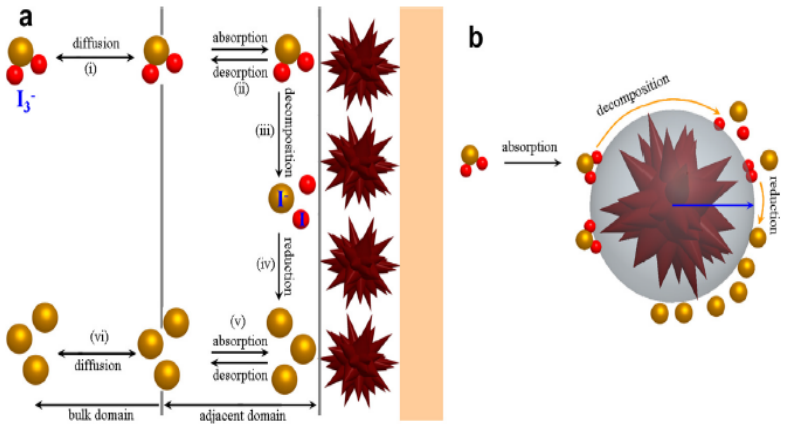

Fig. 5. Schematic diagrams for (a) electrode reaction processes and (b) the diffusion-controlled model.

demonstrated in Fig. S7. From the 100-stacking CV curves of NiPt and NiRu CEs in redox electrolyte, as shown in Fig. S8, one can find that NiPt and NiRu CEs have reasonable stability, arising from the competitive reaction between Ni and I_3^- (and I_2) [23]. However, the NiPd electrode yield marked reduction in J_{Red1} and negative shift for V_{Red1}, suggesting that the catalyst species have been rapidly dissolved in redox electrolyte.

To make the catalytic mechanism of a CE electrocatalyst clear and build an understanding on standard I_3^- reduction rate constant, we launch a model for reaction processes at CE/electrolyte interface, as shown in Fig. 5a. Previously, Hauch and Georg have proposed an insight of charge-transfer reaction at Pt/electrolyte interface by measuring the dependence of *R*ct on I^-/I_3^- concentrations [24], while Dai et al. have revealed the potential reaction mechanism of a I^-/I_3^- redox couple at Pt/electrolyte interface by careful electrochemical characterizations [25]. By integrating the previous works, we demonstrate here that the catalytic reactions of $I_3^- + 2e^- = 3I^-$ during the diffusion-limited processes should include the following six steps: (i) $I_3^-{}_{bulk} \rightarrow I_3^-{}_{diffusion}$, (ii) $I_3^-{}_{diffusion} + NiM \rightarrow I_3^-{}_{NiM}$, (iii) $I_3^-{}_{NiM} \rightarrow 2I^{\bullet}(NiM) + I^-$, (iv) $2I^{\bullet}(NiM) + 2e^- \rightarrow 2I^-(NiM)$, (v) $2I^-(NiM) \rightarrow 2I^-{}_{diffusion} + NiM$, (vi) $2I^-{}_{diffusion} \rightarrow 2I^-{}_{bulk}$. Regardless of the impacts of electrode surface, steps (i) and (ii) happen quickly and the forward rate is proportional to I_3^- concentration and unoccupied active sites on NiM catalysts. Reactions (iii)-(v) are also spontaneous, and the rates of the forward reactions are equal to those of reverse ones. Hauch has indicated that the slowest step (iv) is the rate-determining step for I^-/I_3^- couples. Therefore, one can conclude that the I_3^- reduction reaction at CE/electrolyte interface is faster than the diffusion process of I^- species in the liquid electrolyte, and the electrocatalytic activities of the NiM catalysts along with pristine Ni decrease due to the limitation of diffusion coefficients.

To investigate the reaction kinetics of NiM catalysts toward I_3^- reduction, the rate constant (k) is estimated according to the model in Fig. 5b. Notably, the total reaction rate is controlled by the diffusion rate of generated species at catalyst surface because of fast catalytic processes of reactions (i)-(iv). As the catalytic reaction is limited to the catalyst's surface, therefore the reaction rate is dependent on surface's state. Considering of a high I_3^- concentration in the liquid electrolyte, all the active sites of NiM catalysts have been occupied by I_3^- ions. In this fashion, the slight change in I_3^- concentration during catalytic processes is considered not to have influences on the reaction rate, yielding a zero-order reaction for I_3^- reduction at CE/electrolyte interface. According to the classical diffusion-controlled model, only the I_3^- species close to outside surface of NiM could participate in the reduction reactions and this limit radius for reaction is determined as *r*a. During the reduction processes, the I_3^- concentration around NiM catalyst decreases and forms a concentration gradient. Therefore, a diffusive flux (J) is proportional to the concentration gradient according to Fick's first law:

$$J = -D\frac{dN}{dr} \tag{1}$$

where D is the diffusion coefficient obtained from Tafel polarization curves, N is I_3^- concentration, r is the distance between I_3^- species and NiM catalyst. In this fashion, the reaction rate (I) of a NiM with I_3^- in unit time can be expressed as:

$$I = 4\pi r^2 J = -4\pi r^2 D\frac{dN}{dr} \tag{2}$$

When $r = ra$, $N = 0$, while $r = \infty$, $N = NB$ (NB is the bulk I_3^- concentration). By integrating the equations:

$$\int_{r_a}^{\infty}\frac{1}{r^2}dr = \int_0^{N_B}(-4\pi D)dN \tag{3}$$

$$I = 4\pi D r_a N_B \tag{4}$$

$$r = \frac{dx}{dt} = k \tag{5}$$

The k can be finally determined as:

$$k = 4\pi D r_a N_B \tag{6}$$

This extracted formula for reduction rate constant is also applicable to other 0D CE electrocatalysts. The resultant k values for NiPt, NiRu, NiPd, and pristine Ni are 1.37×10^{-14}, 1.01×10^{-14}, 7.46×10^{-15}, and 1.26×10^{-15} mol s^{-1}, respectively. In definition, the calculated k is the amount of I_3^- (mole) ions reacted with single electrocatalyst species in per time (second). This maximum k for NiPt means there are 8.25×10^9 I_3^- ions can be reduced by a single NiPt electrocatalyst per second. It is noteworthy to mention that equation (6) can be only utilized to evaluate the reduction rate of a single electrocatalyst species. When used to assess the catalytic kinetics of a thin film, the specific surface area of the film should be considered. The study on one-, two-, and three-dimensional electrocatalysts is in progress.

4. Conclusions

In summary, urchin-like NiM (M = Pt, Ru, Pd) have been synthesized for CE electrocatalysts of DSSCs, yielding maximum efficiencies of 9.08%, 7.74%, and 6.86% with NiPt, NiRu, and NiPd in comparison with 1.91% for Ni based cell, respectively. By building a catalytic model for liquid electrolyte at electrolyte/CE interface, a reduction rate constant $k = 4\pi D r_a N_B$ is extracted for comparing the catalytic activity of 0D electrocatalysts. The study presented here is far from being fully optimized, but the preliminary results along with cost-effective and scalable components suggest the alloy NiM CEs holding great promise in developing high-performance DSSCs and the launched reduction rate constant having commonality in comparing the catalytic activity of CE electrocatalysts.

Acknowledgements

The authors would like to acknowledge financial supports from National Natural Science Foundation of China (21503202, U1037604).

Appendix A. Supplementary data

Supplementary data associated with this article can be found, in the online version, at http://dx.doi.org/10.1016/j.electacta.2015.10.080.

References

[1] B. O'Regan, M. Grätzel, Nature 353 (1991) 737–740.
[2] J.H. Wu, Z. Lan, J.M. Lin, M.L. Huang, Y.F. Huang, L.Q. Fan, G.G. Luo, Chem. Rev. 115 (2015) 2136–2173.
[3] S.N. Yun, A. Hagfeldt, T.L. Ma, Adv. Mater. 26 (2014) 6210–6237.
[4] Q.W. Tang, H.Y. Cai, S.S. Yuan, X. Wang, J. Mater. Chem. A 1 (2013) 317–323.
[5] H. Wang, K. Sun, F. Tao, D.J. Stacchiola, Y.H. Liu, Angew. Chem. Int. Ed. 52 (2013) 9210–9214.
[6] F. Gong, H. Wang, X. Xu, G. Zhou, Z.S. Wang, J. Am. Chem. Soc. 134 (2012) 10953–10958.
[7] J. Zhang, K. Sasaki, E. Sutter, R.R. Adzic, Science 315 (2007) 220–222.
[8] F. Maroun, F. Ozanam, O.M. Magnussen, R.J. Behm, Science 293 (2001) 1811–1814.
[9] X.X. Chen, Q.W. Tang, B.L. He, L. Lin, L.M. Yu, Angew. Chem. Int. Ed. 53 (2014) 10799–10803.
[10] Y.Y. Duan, Q.W. Tang, J. Liu, B.L. He, L.M. Yu, Angew. Chem. Int. Ed. 53 (2014) 14569–14574.

[11] X.J. Zheng, J. Deng, N. Wang, D.H. Deng, W.H. Zhang, X.H. Bao, C. Li, Angew. Chem. Int. Ed. 53 (2014) 7023–7027.
[12] Q.W. Tang, J. Liu, H.H. Zhang, B.L. He, L.M. Yu, J. Power Sources 297 (2015) 1–8.
[13] S.M. Alia, Y.S. Yan, B.S. Pivovar, Catal. Sci. Technol. 4 (2014) 3589–3600.
[14] Q.W. Tang, J.L. Duan, Y.Y. Duan, B.L. He, L.M. Yu, Electrochim. Acta 178 (2015) 886–899.
[15] N. Papageorgiou, W.F. Maier, M. Grätzel, J. Electrochem. Sco. 144 (1997) 876–884.
[16] T.C. Wei, C.C. Wan, Y.Y. Wang, Appl. Phys. Lett. 88 (2006) 103122.
[17] S. Zhang, X. Zhang, G. Jiang, H. Zhu, S. Guo, D. Su, G. Lu, S. Sun, J. Am. Chem. Soc. 136 (2014) 7734–7739.
[18] L. Gan, R. Yu, J. Luo, Z. Cheng, J. Zhu, J. Phys. Chem. Lett. 3 (2012) 934–938.
[19] X. Wang, Y. Orikasa, Y. Takesue, H. Inoue, M. Nakamura, T. Minato, N. Hoshi, Y. Uchimoto, J. Am. Chem. Soc. 135 (2013) 5938–5941.
[20] X. Zheng, J. Deng, N. Wang, D. Deng, W.H. Zhang, X.H. Bao, C. Li, Angew. Chem. Int. Ed. 53 (2014) 7023–7027.
[21] J.W. Wan, G.J. Fang, H.J. Yin, X.F. Liu, D. Liu, M.T. Zhao, W.J. Ke, H. Tao, Z.Y. Tang, Adv. Mater. 26 (2014) 8101–8106.
[22] D. Cahen, G. Hodes, M. Grätzel, J.F. Guillemoles, I. Riess, J. Phys. Chem. B 104 (2000) 2053–2059.
[23] Q.W. Tang, H.H. Zhang, Y.Y. Meng, B.L. He, L.M. Yu, Angew. Chem. Int. Ed. 54 (2015) 11448–11452.
[24] A. Hauch, A. Georg, Electrochim. Acta 46 (2001) 3457–3466.
[25] Y. Tang, X. Pan, C. Zhang, S.Y. Dai, F. Kong, L. Hu, Y. Sui, J. Phys. Chem. C 114 (2010) 4160–4167.

Electrochimica Acta 184 (2015) 64–69

Contents lists available at ScienceDirect

Electrochimica Acta

journal homepage: www.elsevier.com/locate/electacta

Cobalt sulfide decorated polyaniline complex counter electrodes for efficient dye-sensitized solar cells

Peizhi Yang[a,*,1], Jialong Duan[b,1], Qunwei Tang[b,*]

[a] Key Laboratory of Advanced Technique & Preparation for Renewable Energy Materials, Ministry of Education, Yunnan Normal University, Kunming 650500, China

[b] Institute of Materials Science and Engineering, Ocean University of China, Qingdao 266100, China

ARTICLE INFO

Article history:
Received 26 July 2015
Received in revised form 21 September 2015
Accepted 9 October 2015
Available online xxx

Keywords:
Dye-sensitized solar cell
Counter electrode
Cobalt sulfide
Polyaniline
Electrocatalyst

ABSTRACT

The practical commercialization of dye-sensitized solar cells (DSSCs) requires persistent exploration of cost-effective counter electrodes (CEs). Aiming at increasing the active sites and accelerating charge transfer of a CE electrocatalyst, cobalt sulfide decorated aniline complexes are synthesized by a reflux technique and subsequently in-situ polymerized for Pt-free polyaniline-cobalt sulfide (PANi-CoS) electrocatalysts in liquid-junction DSSCs. The preliminary results suggest that an enhanced electrocatalytic activity for I_3^- reduction is ascribed to the fast electron-transfer ability of PANi and the high catalytic activity of CoS. The optimized DSSC device based on PANi-7 wt% CoS yields an impressive power conversion efficiency up to 8.55% under an illumination of air mass 1.5 global simulated solar light, which is much higher than 5.65% and 5.79% for the solar cells with pure PANi and pristine Pt CEs, respectively.

1. Introduction

As the third-generation solar cell, dye-sensitized solar cells (DSSCs) have emerged as one of the most promising devices to solve ever-increasing global energy consumption [1,2] due to their inherent properties such as low production cost, environmental friendliness, ease of fabrication, and relatively high power conversion efficiency [3,4]. Enhancement of reduction reaction from triiodide (I_3^-) ions to iodide (I^-) and reduction in electrode cost are two prerequisites to improve the conversion efficiency of a cost-effective DSSC [5]. Preferred Pt electrode has restricted the practical application of DSSCs owing to high expense and scarce resource in the earth [6,7], therefore cost-effective and highly electrocatalytic counter electrode (CE) electrocatalysts have been exploited to substitute for the traditional Pt-based species. Among cost-effective CE electrocatalysts, it has been found that carbonaceous materials [8,9], transition metal oxides [10], nitrides [11], sulfides [12], selenides [13], carbides [14], phosphides [15], and conducting polymers [16,17] can be proposed as candidate alternative CE materials. Polyaniline (PANi) has been of continuous interest because its widespread application in supercapacitor and electrocatalysis field owing to its low cost, easy fabrication and environmental stability as well as good conductivity [18,19]. However, its electrocatalytic activity and long-term stability of pure PANi still can't match up to Pt-based materials, resulting in the unsatisfactory power conversion efficiency when utilized in DSSC platforms.

Utilizing synergistic catalytic effect by combination of several materials provides a promising avenue to fabricate robust CE electrocatalysts [20]. Aiming at improving the electron-migration ability, the combination of carbonaceous materials with conducting polymer for complexes such as PANi-graphene and PANi-carbon nanotube has been extensively studied in our previous studies [21,22]. The electrical conduction and electrocatalysis can be elevated, arising from the easy charge-transfer between carbonaceous materials and PANi. However, one of the drawbacks of carbonaceous materials is the limited active sites for I_3^- reduction and therefore unsatisfactory redox behaviors [23]. To our best of knowledge, cobalt sulfide (CoS) is very effective in catalyzing the I_3^- reduction reaction and is comparable to that of traditional Pt material [24,25]. In order to develop other robust PANi-based composite CEs, we present here the experimental realization of aniline-CoS complexes by a reflux process and subsequent PANi-CoS complexes at F-doped SnO_2 (FTO) conductive glass after suffering an in-situ polymerization. Compared with pristine PANi, the electrocatalytic ability is dramatically enhanced by utilizing PANi-CoS complex. A potential mechanism is attributed to superior properties and the increased active sites of CoS as well as improved charge-transfer kinetics between PANi

* Corresponding authors. Fax: +86 871 5517313.
E-mail addresses: pzhyang@hotmail.com (P. Yang), tangqunwei@ouc.edu.cn (Q. Tang).

[1] The authors have equal contributions.

http://dx.doi.org/10.1016/j.electacta.2015.10.050
0013-4686/

and CoS. The PANi can not only serve as the anchoring matrix to load and hinder agglomeration of CoS, but act as linker to improve the electrical connection between CoS nanoparticles [26]. Due to the highest electrocatalytic activity and more efficient charger migration channel, an impressive power conversion efficiency of DSSC based on PANi-7 wt% CoS complex CE is enhanced to 8.55%, which is much higher than 5.65% for PANi based solar cell and 5.79% for pristine Pt based device.

2. Experimental

2.1. Synthesis of CoS nanoparticles

In a typical synthesis of CoS nanoparticles, 1.0115 g of $CoCl_2{\cdot}6H_2O$ powders was dissolved in 30 mL of deionized water and then 0.646 g of thiourea were added into above solution under vigorous magnetic stirring. Subsequently, the reactants were transferred into a 50 mL of Teflon-lined stainless steel autoclave and heated at 160 °C for 12 h. After cooling naturally, the resultant black powders were centrifuged and rinsed repeatedly by deionized water and anhydrous ethanol, and vacuum dried at 60 °C for 24 h. The resultant CoS powders were used without post-treatment.

2.2. Reflux synthesis of aniline-CoS complexes

CoS powers at dosages of 1, 3, 5, 7, or 9 wt% were added into 10 mL of aniline and the mixtures were sonicated for 15 min. Subsequently, the mixtures were sealed in a three-neck flask and refluxed at 184 °C for 6 h in dark to prepare the aniline-CoS complexes under high-purity N_2 gas flow. When cooling down to room temperature, the complexes were stored under ambient conditions for further use.

2.3. Fabrication of PANi-CoS complex CEs

The PANi-CoS complex CEs were synthesized by an in-situ polymerization process on FTO glasses. Briefly, 1.48 mL of as-synthesized aniline-CoS complexes was dissolved in 50 mL of 1 M HCl aqueous solution and 50 mL of aqueous solution consisting of 1 M HCl and 0.125 M ammonium peroxydisulfate (APS) was dropped into above solution over a 2 h period at 0 °C under mild agitation. Prior to polymerization reaction, a freshly cleaned FTO glass substrate was placed at the bottom of vessel. Then, the polymerization reaction was continued at 4 °C for 10 h. Finally, the FTO supported PANi-CoS complex CE was rinsed thoroughly with 1 M HCl and deionized water, and stored in vacuum.

2.4. Assembly of DSSCs

A TiO_2 film with a thickness of around 10 μm was first deposited on the surface of FTO glass substrate by a traditional doctor-blade method and subsequently calcined at 450 °C for 30 min to obtain the TiO_2 film as photoanode. Afterward, the photoanode with active area of 0.25 cm^2 was sensitized by immersing into an ethanol solution containing 0.50 mM N719 dye for 24 h at room temperature. A typically sandwiched DSSC was fabricated by assembling a sensitized photoanode and a PANi-CoS complex CE with the redox electrolyte.

2.5. Electrochemical characterizations

To evaluate the electrocatalytic activity, all the electrochemical properties of CEs were recorded using a traditional Electrochemical Workstation. The cyclic voltammetry (CV) curves were recorded from −0.6 to +1.2 V and back to −0.6 V in a three electrode system comprising an Ag/AgCl reference electrode, a Pt CE, and the working electrode of PANi-CoS complex in a nitrogen-purged electrolyte solution. Tafel polarization measurements were carried out with the same equipment in a symmetric cell consisting of PANi-CoS complex CE|redox electrolyte|PANi-CoS complex CE with scanning potential window from −1 to 1 V at the scan rate of 10 mV s^{-1}. Electrochemical impedance spectroscopy (EIS) measurements were characterized with symmetric dummy cells, and the frequency range was from 10^5 kHz to 0.01 Hz with an ac modulation signal of 10 mV and zero bias potential at room temperature. The resultant impedance parameters were obtained by fitting with Z-View software.

2.6. Photovoltaic measurements

Photocurrent density-voltage (*J-V*) characteristics of DSSCs were measured under air mass 1.5 global (AM1.5G) illumination at 100 mW cm^{-2} from a 100 W Xenon arc lamp (XQ-500 W) which was calibrated by FZ-A type radiometer in the atmosphere. Each *J-V* curves were repeated measured at least ten times to control the experimental error within ±5%.

2.7. Other characterizations

The morphologies of PANi-CoS complex CEs were investigated by a field-emission scanning electron microscope (SU8020, Hitachi, Japan). The molecular structures of aniline-CoS complexes were determined on a PerkinElmer spectrum 1760 FTIR spectrometer. The optical absorption spectra were measured on a UV–vis spectrophotometer by dissolving the samples in acetone. A Fluorolog 3-P spectrophotometer was used to record the fluorescence emission spectra at room temperature with excitation wavelength of 500 nm.

3. Results and discussion

To reveal the effect of refluxing process on the interaction between CoS and aniline, the fluorescence emission spectra of CoS, pure aniline, aniline/7 wt% CoS mixture and resultant aniline-CoS complexes diluted with acetone solvent was recorded at 500 nm as shown in Fig. 1a. One can find that the maximum emissions of CoS-aniline complexes are at around 560 and 605 nm in acetone, whereas the fluorescence of pure CoS and aniline are significantly quenched. It is noteworthy to mention that the markedly distinction of the fluorescence emission spectra between CoS-aniline complexes and individual components indicates the formation of new light-absorbing species after the refluxing process. Considering the prerequisite of fabricating a robust PANi-CoS complex CEs is the rapid charger-transfer ability, in this fashion, this combination can result in enhanced electrocatalytic active. Furthermore, in order to understand more about the complexing mechanism of aniline monomers and CoS, UV–vis adsorption spectra of pure aniline, aniline/7 wt% CoS mixture and aniline-CoS complexes with various dosages of CoS in acetone are characterized. As shown in Fig. 1b, there is no obvious adsorption peak in the range from 350 to 1100 nm for pure aniline and aniline/7 wt% CoS mixture. In contrast, a new strong and broad adsorption peak between 350 and 600 nm can be observed, which may be attributed to the formation of interaction between CoS and aniline [27,28].

As indicated above, we believe that a new chemical species is produced after refluxing process at 184 °C and therefore the formation of a charge-transfer complex in its ground state because the CoS is a good electron acceptor, whereas the aniline is a common electron donor. At elevated temperature, aniline-CoS complex can be fabricated via the metal (d_π)-nitrogen (p_π)

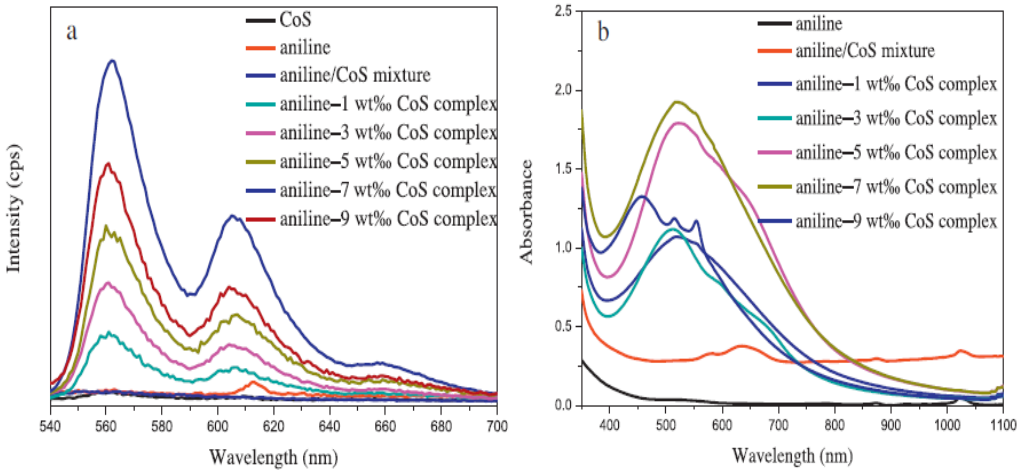

Fig. 1. (a) Emission spectra and (b) UV–vis absorption spectra of pure aniline, CoS, aniline/CoS mixture, and aniline-CoS complexes in acetone at CoS dosages of 1, 3, 5, 7 and 9 wt%.

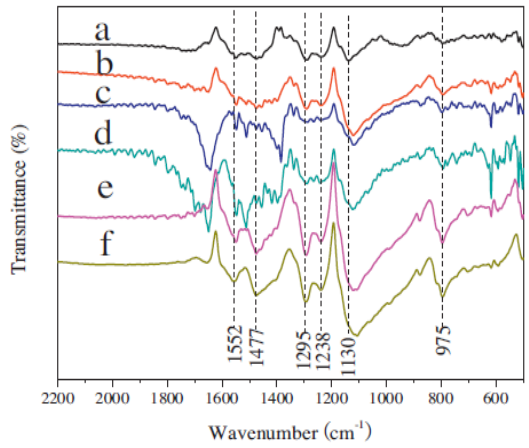

Fig. 2. FTIR spectra of (a) pure PANi and PANi-CoS complexes at CoS dosages of (b) 1, (c) 3, (d) 5, (e) 7, and (f) 9 wt%.

antibonding interaction between Co atom in CoS and N atom in aniline [29]. Fig. 2 shows the FTIR spectra of pure PANi and PANi-CoS complexes at various dosages of CoS to further examine the chemical compositions. The main characteristic adsorption bands located at 1552 and 1478 cm^{-1} are attributed to the C=C stretching of quinoid ring and benzenoid deformation of PANi, respectively. Meanwhile, the C—H bending mode of on benzene ring and C—N bending and stretching mode are also observed at 975, 1238 and 1295 cm^{-1}, respectively [26,30]. In comparison with pure PANi, there is a fact that the C—H bending of the quinoid ring appeared at 1130 cm^{-1} shifts to 1120, 1118, 1116, 1113 and 1106 cm^{-1} in PANi-1 wt% CoS complex, PANi-3 wt% CoS complex, PANi-5 wt% CoS complex, PANi-7 wt% CoS complex, and PANi-9 wt% CoS complex, which can be possibly ascribed to the successful formation of covalent interactions between PANi and CoS. Till now, we can make a conclusion that a charge transfer and a selective interaction of the Co atoms with quinoid rings of PANi backbones can be realized by refluxing process.

As shown in Fig. 3a and b, the top-view SEM images of resultant PANi-7 wt% CoS complex suggest that the CoS nanoparticles are uniformly distributed in the PANi nanofibers on the surface of FTO glass via in-situ polymerization. Meanwhile, as for metal sulfides, the relatively low active surface area and the insufficient interparticles conductive connection due to the large size result in the relatively poor electrocatalytic activity [31]. Notably, we can not detect CoS aggregations, indicating that CoS have been successfully combined with PANi to control the size and distribution of CoS along the PANi network, therefore an increased elecrocatalytic active sites and accelerated the electron transport. The relatively strong interaction between CoS and PANi is expected to improve charge-transfer ability and therefore the electrocatalytic activity.

Fig. 4a shows the representative photocurrent density-voltage (*J-V*) curves of various DSSCs employing pure PANi and PANi-CoS complex CEs under AM1.5G sunlight, and the photovoltaic

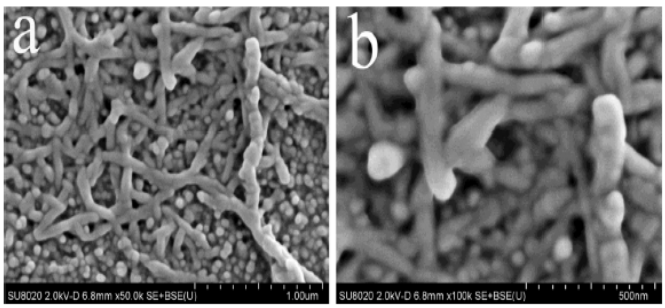

Fig. 3. Top-view SEM photographs of PANi-7 wt% CoS complex CE.

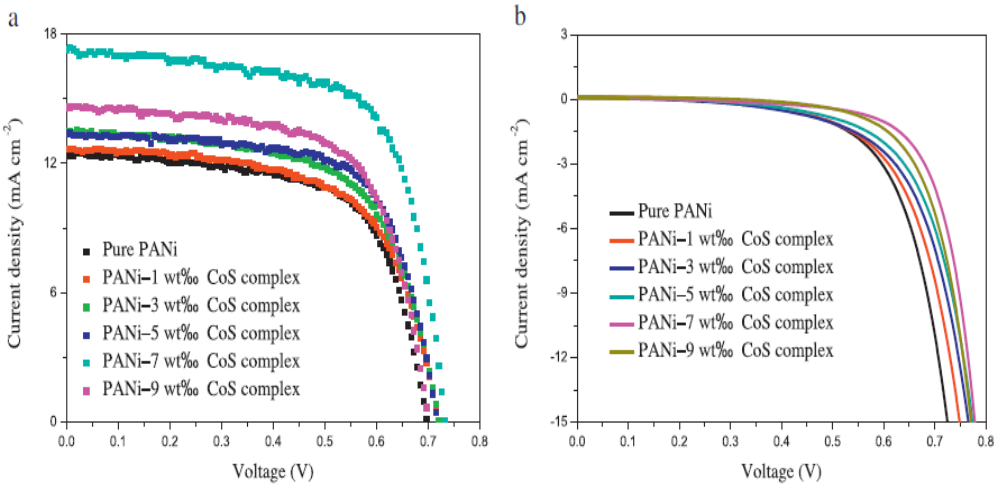

Fig. 4. Photocurrent density-voltage (*J-V*) curves of the DSSCs employing various CEs (a) under an illumination of 100 mW cm^{-2} and (b) in the dark.

Table 1
Photovoltaic parameters of the various DSSCs. J_{sc}: short-circuit current density; V_{oc}: open-circuit voltage, *FF*: fill factor; η: power conversion efficiency.

CEs	V_{oc} (V)	J_{sc} (mA cm^{-2})	η (%)	*FF*
Pure PANi	0.698	12.48	5.65	0.648
PANi-1 wt% CoS complex	0.719	12.67	5.72	0.628
PANi-3 wt% CoS complex	0.721	13.48	6.14	0.632
PANi-5 wt% CoS complex	0.717	13.39	6.47	0.674
PANi-7 wt% CoS complex	0.733	17.29	8.55	0.675
PANi-9 wt% CoS complex	0.700	14.61	6.72	0.657
Pt[a]	0.714	12.47	5.79	0.650

[a] The data were obtained from Ref. [33].

parameters are summarized in Table 1. One can be find that the power conversion efficiency is enhanced to 8.55% (V_{oc} = 0.733, J_{sc} = 17.29 mA cm^{-2}, *FF* = 0.675) from the PANi-7 wt% CoS complex CE by increasing CoS dosage, which is superior to 5.65% for pure PANi. The impressive efficiency may be ascribed to the rapid interconversion between I_3^- and I^- and therefore the accelerated the generation of photoelectrons from dye molecules [32]. Additionally, the efficiency of DSSC with optimized PANi-CoS complex CE has also been markedly enhanced in comparison with 5.79% for pristine Pt based solar cell [33]. Furthermore, the dark *J-V* characteristics are also measured in Fig. 4b, in which the current density follows the order pure PANi > PANi-1 wt% CoS complex > PANi-3 wt% CoS complex > PANi-5 wt% CoS complex > PANi-9 wt% CoS complex > PANi-7 wt% CoS complex at the same voltage. It is well known that the dark current is attributed to backward reaction between electrons in the conduction band of TiO_2 and I_3^- species [33]. The smallest dark current means the retarded recombination of I_3^- species at TiO_2/electrolyte interface and accelerated electron transportation along the conducting network by TiO_2 nanocrystallites. A possible mechanism behind this phenomenon is the good matching of energy levels between percolating TiO_2 (−4.2 eV)-TiO_2 (−4.2 eV) nanocrystallines in comparison with TiO_2 (−4.2 eV)-I^-/I_3^- (−4.9 eV) under an increased voltage drop [34]. Thus, we infer that the enhanced performance of DSSC arises from the elevated electrocatalytic ability.

To demonstrate why the performances of DSSCs employing CoS decorated PANi complex CEs can be improved, cyclic voltammetry

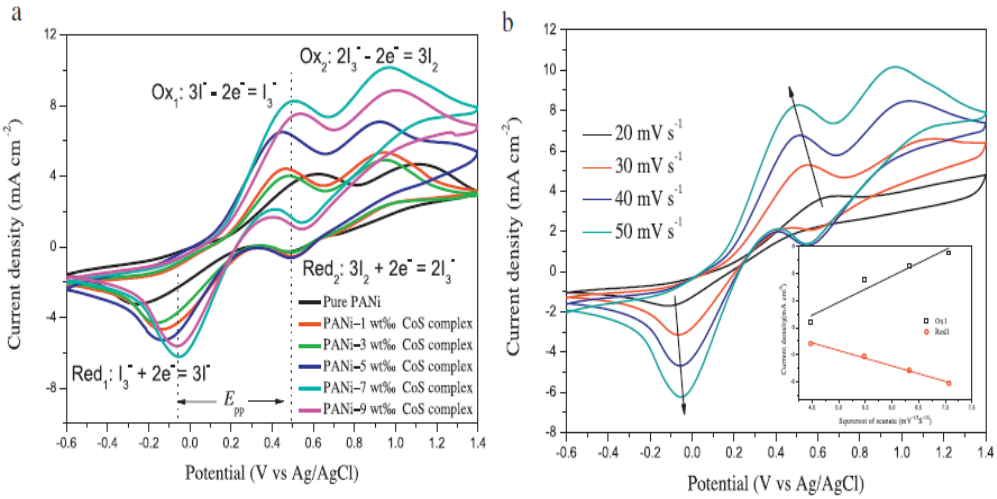

Fig. 5. (a) CV curves of various CEs for I^-/I_3^- redox electrolyte recorded at a scan rate of 50 mV s^{-1}. (b) CV curves of PANi-7 wt% CoS complex CE for I^-/I_3^- redox species at varied scan rates and the inset presents the relationship between peak current density and square root of scan rate.

Table 2
Catalytic parameters of the various PANi-CoS complex CEs toward I^-/I_3^- redox electrolyte.

Parameters	Red_1 (V)	J_{red1} (mA cm^{-2})	Ox_1 (V)	J_{ox1} (mA cm^{-2})	E_{pp} (V)	D_n (cm^2 s^{-1})	R_{ct} (ohm cm^2)
Pure PANi	−0.265	−3.362	0.606	4.056	0.871	3.91×10^{-6}	35.44
PANi-1 wt% CoS complex	−0.164	−4.392	0.482	4.008	0.646	6.66×10^{-6}	29.54
PANi-3 wt% CoS complex	−0.137	−4.733	0.463	4.499	0.600	7.74×10^{-6}	12.02
PANi-5 wt% CoS complex	−0.126	−5.278	0.455	6.559	0.581	9.63×10^{-6}	11.95
PANi-7 wt% CoS complex	−0.052	−6.308	0.497	8.326	0.549	1.37×10^{-5}	6.07
PANi-9 wt% CoS complex	−0.055	−5.668	0.524	7.542	0.579	1.11×10^{-5}	11.61
Pt[a]	−0.129	−2.69	0.556	2.78	0.685	9.85×10^{-7}	7.23

[a] The data were obtained from Ref. [33].

(CV) is carried out to examine the catalytic activity. As shown in Fig. 5a, two pairs of oxidation and reduction peak can be observed, corresponding to the oxidation reaction (Ox_1: $3I^- - 2e^- \rightarrow I_3^-$, Ox_2: $2I_3^- - 2e^- \rightarrow 3I_2$) at positive current peaks and the reduction reaction (Red_1: $I_3^- + 2e^- \rightarrow 3I^-$, Red_2: $3I_2 + 2e^- \rightarrow 2I_3^-$) at negative current peaks. Furthermore, with the aim of exploring the mechanism during reduction of I_3^- to I^-, CV curves of PANi-7 wt % CoS complex CE at various scan rates are shown in Fig. 5b. Linear relationships are observed by plotting the relationship between peak current density and square root of scan rate (inset in Fig. 5b), indicating the reversible $I_3^- + 2e^- \leftrightarrow 3I^-$ redox reactions is controlled by ionic diffusion in the electrolyte [35]. Considering the function of a CE catalyst in DSSC is to reduce the I_3^- to I^-, thus peak current density of the Red_1 (J_{red1}) is used to evaluate the electrocatalytic activity of CE as well as the peak-to-peak separation (E_{pp}) of Ox_1 and Red_1 [36]. It is worthy to mention that the J_{red1} follows an order of pure PANi < PANi-1 wt% CoS complex < PANi-3 wt% CoS complex < PANi-5 wt% CoS complex < PANi-9 wt% CoS complex < PANi-7 wt% CoS complex a nd Epp follows an opposite order as summarized in Table 2. The largest J_{red1} and smallest E_{pp} of PANi-7 wt% CoS complex demonstrate the highest electrocatalytic activity which is consistent with the power conversion efficiency. The rapidly charge-transfer between PANi and CoS and the increased catalytic active sites due to higher amount of CoS attached on the PANi backbone, lead to enhanced electrocatalytic performance. However, much higher CoS dosage may block the charge-transfer because of CoS aggregations. In order to verify the conclusion, the diffusion coefficient (D_n) of the redox species is calculated through the Randles-Sevcik theory [37]: $J_{red1} = Kn^{1.5}ACD_n^{0.5}v^{0.5}$, where K is 2.69×10^5, n is the number of electrons of reduction reaction, A is the electrode area, C is the concentration of I_3^- and v is scan rate of recording CV curves. The largest values of D_n can be obtained from PANi-7 wt% CoS complex CE according to above equation, indicating that the elevated bonding sites between CoS and PANi can provide more active sites to reduce I_3^- and accelerate charge-transfer within PANi-CoS complex CE.

For a real DSSC device, the facile charge-transfer within CE and the enhanced electrocatalytic activity can significantly accelerate the generation of photosensitive dyes. Nyquist EIS plots from the symmetric dummy cells are shown in Fig. 6a. Apparently, two semicircles are observed, which present the R_{ct} at the CE/electrolyte interface at high frequency region and the Nernst diffusion impedance (W) at low frequency region. From Table 2, one can find that the values of R_{ct} extracted by fitting the EIS plots with Z-View software decrease with the various dosages of CoS: pure PANi > PANi-1 wt% CoS complex > PANi-3 wt% CoS complex > PANi-5 wt% CoS complex > PANi-9 wt% CoS complex > PANi-7 wt% CoS complex. The smallest R_{ct} of PANi-7 wt% CoS complex CE suggests a rapid conversion reaction from I_3^- to I^-, therefore resulting in an enhanced FF comparison with other devices. Moreover, V_{oc} is determined by the difference between the quasi Fermi energy of the electrons in percolating TiO_2 and redox potential of I^-/I_3^- electrolyte. In a real DSSC device, the recorded V_{oc} is generally lower than this theoretical value because of a backward reaction between photogenerated electrons and oxided species in electrolyte. As has been abovementioned, the increased electrocatalytic activity is beneficial to restricting the recombination reaction. In this fashion, the real V_{oc} value is also elevated by utilizing robust CE. Tafel polarization curves are also employed to investigated to electrocatalytic activity of pure PANi and PANi-CoS comlplex CEs. Typically, the tafel curve composes of three zones:

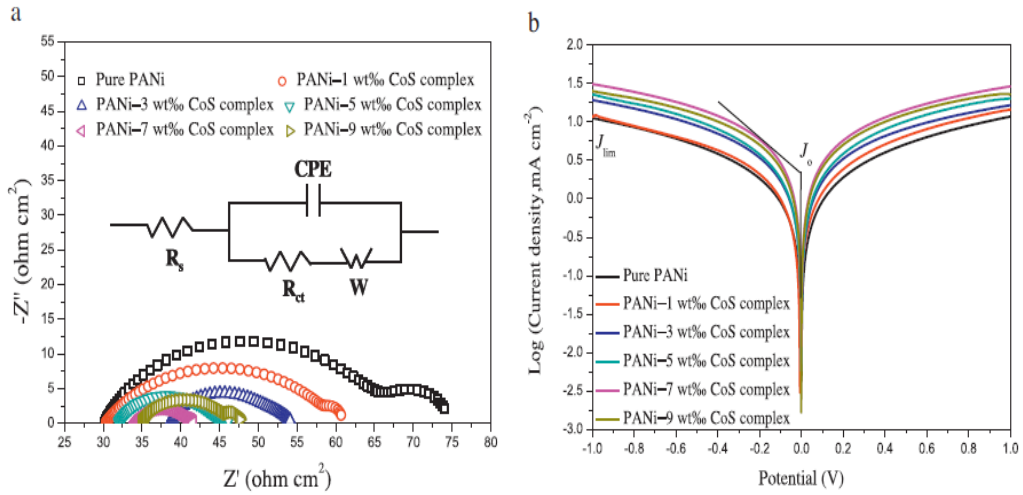

Fig. 6. (a) Nyquist EIS plots and (b) Tafel polarization curves of the symmetric dummy cells fabricated with two identical PANi, and PANi-CoS complex CEs. The inset gives an equivalent circuit to fit EIS parameters by a Z-View software.

the low potential zone ($|U| < 0.12$ V), the high potential zone ($|U| > 0.2$ V) and the Tafel zone ($0.12\,V < |U| < 0.2$ V), corresponding to polarization, limiting diffusion of I^-/I_3^- in the electrolyte and charge transfer at the surface of CE/electrolyte, respectively [38]. As shown in Fig. 6b, the exchange current density (J_o) and limiting diffusion current density (J_{lim}) follow the same order: pure PANi < PANi-1 wt% CoS complex < PANi-3 wt% CoS complex < PANi-5 wt% CoS complex < PANi-9 wt% CoS complex < PANi-7 wt % CoS complex. A higher J_o and J_{lim} indicate the better electrocatalytic activity of CE. Notably, the EIS and Tafel results match well with CV measurement, which can also be obtained by the following relationship [36,24]: $J_0 = RT/nFR_{ct}$, $J_{lim} = 2nFCD_n/l$, where R is the gas constant, T presents the absolute temperature, F is Faraday's constant, l is the distance between the electrodes in a dummy cell. After performing a comprehensive analysis of the CEs, it is evident that the CoS decorated PANi can significantly improve the electrocatalytic activity, which is in agreement with the performance of DSSCs.

4. Conclusion

In summary, we have successfully realized the novel PANi-CoS complex CEs by a reflux approach. The charger transfer between PANi and CoS is accelerated by formation of interaction between Co atom and N atom via the metal (d_π)-nitrogen (p_π) antibonding interaction, resulting in superior electrocatalytic activity toward I_3^- species than pure PANi electrode. Due to the well distribution of CoS along PANi network, the DSSC from PANi-7 wt% CoS complex CE exhibits an impressive power conversion efficiency of 8.55% in comparison with that of 5.65% from pure PANi CE. However, the study presented here is still far from being comprehensive optimized and the conductive ability of PANi-CoS complex is still lower, the advantages along with cost-effective and Pt-free material ensure its wide range of application areas in DSSC as a robust CE candidate.

Acknowledgements

The authors would like to acknowledge financial supports from National Natural Science Foundation of China (U1037604 and 21503202).

References

[1] B. O'Regan, M. Grätzel, Nature 353 (1991) 737–740.
[2] S. Mathew, A. Yella, P. Gao, R. Humphry-Baker, B.F.E. Curchod, N. Ashari-Astani, I. Tavernelli, U. Rothlisberger, M.K. Nazeeruddin, M. Grätzel, Nat. Chem. 6 (2014) 242–247.
[3] G.R. Li, F. Wang, Q.W. Jiang, X.P. Gao, P.W. Shen, Angew. Chem. Int. Ed. 49 (2010) 3653–3656.
[4] X.J. Zheng, J. Deng, N. Wang, D.H. Deng, W.H. Zhang, X.H. Bao, C. Li, Angew. Chem. Int. Ed. 53 (2014) 7023–7027.
[5] M. Zheng, J. Huo, Y.G. Tu, J.H. Wu, L.H. Hu, S.Y. Dai, Electrochim. Acta 173 (2015) 252–259.
[6] W. Zeng, G.J. Fang, T.Y. Han, B.R. Li, N.S. Liu, D.S. Zhao, Z.Q. Liu, D.Y. Wang, X.Z. Zhao, D.C. Zou, J. Power Sources 245 (2014) 456–462.
[7] V.D. Dao, S.H. Kim, H.S. Choi, J.H. Kim, H.O. Park, J.K. Lee, J. Phys. Chem. C 115 (2011) 25529–25534.
[8] H. Ren, H. Shao, L.J. Zhang, D. Guo, Q. Jin, R.B. Yu, L. Wang, Y.L. Li, Y. Wang, H.J. Zhao, D. Wang, Adv. Energy Mater. (2015) , doi:http://dx.doi.org/10.1002/aenm.201500296.
[9] G.Q. Wang, S. Kuang, D.L. Wang, S.P. Zhuo, Electrochim. Acta 113 (2013) 346–353.
[10] M.X. Wu, L. Mu, Y.D. Wang, Y.N. Lin, H.Y. Guo, T.L. Ma, J. Mater. Chem. A 1 (2013) 7519–7524.
[11] M. Chen, L.L. Shao, Z.M. Gao, T.Z. Ren, Z.Y. Yuan, J. Power Sources 286 (2015) 82–90.
[12] J.H. Huo, M. Zheng, Y.G. Tu, J.H. Wu, L.H. Hu, S.Y. Dai, Electrochim. Acta 159 (2015) 166–173.
[13] Y.Y. Duan, Q.W. Tang, J. Liu, B.L. He, L.M. Yu, Angew. Chem. 126 (2014) 14797–14802.
[14] M.X. Wu, X. Lin, Y.D. Wang, L. Wang, W. Guo, D.D. Qi, X.J. Peng, A. Hagfeldt, M. Grätzel, T.L. Ma, J. Am. Chem. Soc. 134 (2012) 3419–3428.
[15] M.S. Wu, J.F. Wu, Chem. Commun. 49 (2013) 10971–10973.
[16] R. Trevisan, M. Döbbelin, P.P. Boix, E.M. Barea, R. Tena-Zaera, I. Mora-Seró, J. Bisquert, Adv. Energy Mater. 1 (2011) 781–784.
[17] J.Y. Lin, W.Y. Wang, S.W. Chou, J. Power Sources 282 (2015) 348–357.
[18] Q.D. Tai, B.L. Chen, F. Guo, S. Xu, H. Hu, B. Sebo, X.Z. Zhao, ACS Nano 5 (2011) 3795–3799.
[19] Y.M. Xiao, G.Y. Han, Y.P. Li, M.Y. Li, Y.Z. Chang, J. Mater. Chem. A 2 (2014) 3452–3460.
[20] C. Bora, C. Sarkar, K.J. Mohan, S. Dolui, Electrochim. Acta 157 (2015) 225–231.
[21] B.L. He, Q.W. Tang, M. Wang, H.Y. Chen, S.S. Yuan, ACS Appl. Mater. Interfaces 6 (2014) 8230–8236.
[22] H.H. Zhang, B.L. He, Q.W. Tang, L.M. Yu, J. Power Sources 275 (2015) 489–497.
[23] L. Wan, S. Wang, X. Wang, B. Dong, Z. Xu, X. Zhang, B. Yang, S. Peng, J. Wang, C. Xu, Solid State Sci. 13 (2011) 468–475.
[24] M.K. Wang, A.M. Anghel, B. Marsan, N.C. Ha, N. Pootrakulchote, S.M. Zakeeruddin, M. Grätzel, J. Am. Chem. Soc. 131 (2009) 15976–15977.
[25] C.W. Kung, H.W. Chen, C.Y. Lin, K.C. Huang, R. Vittal, K.C. Ho, ACS Nano 6 (2012) 7016–7025.
[26] Y.M. Xiao, W.Y. Wang, S.W. Chou, T.W. Lin, J.Y. Lin, J. Power Sources 266 (2014) 448–455.
[27] Y. Sun, S.R. Wilson, D.I. Schuster, J. Am. Chem. Soc. 123 (2001) 5348–5349.
[28] Z.S. Qian, C. Wang, H. Feng, C.C. Chen, J. Zhou, J.R. Chen, Chem. Commun. 47 (2011) 7167–7169.
[29] K.H. Hopmann, A. Ghosh, ACS Catal. 1 (2011) 597–600.
[30] G. Wang, W. Xing, S. Zhou, Electrochim. Acta 66 (2012) 151–157.
[31] X.L. Duan, Z.Y. Gao, J.L. Chang, D.P. Wu, P.F. Ma, J.J. He, F. Xu, S.Y. Gao, K. Jiang, Electrochim. Acta 114 (2013) 173–179.
[32] X.X. Chen, Q.W. Tang, B.L. He, L. Lin, L.M. Yu, Angew. Chem. Int. Ed. 53 (2014) 10799–10803.
[33] P.J. Li, H.Y. Cai, Q.W. Tang, B.L. He, L. Lin, J. Power Sources 271 (2014) 108–113.
[34] Q.W. Tang, J. Liu, H.H. Zhang, B.L. He, L.M. Yu, J. Power Sources 297 (2015) 1–8.
[35] Z.B. Lv, J.F. Yu, H.W. Wu, J. Shang, D. Wang, S.C. Hou, Y.P. Fu, K. Wu, D.C. Zou, Nanoscale 4 (2012) 1248–1253.
[36] F. Gong, H. Wang, X. Xu, G. Zhou, Z.S. Wang, J. Am. Chem. Soc. 134 (2012) 10953–10958.
[37] M.J. Ju, I.Y. Jeon, J.C. Kim, K. Lim, H.J. Choi, S.M. Jung, I.T. Choi, Y.K. Eom, Y.J. Kwon, J. Ko, J.J. Lee, H.K. Kim, J.B. Baek, Adv. Mater. 26 (2014) 3055–3062.
[38] J.W. Wan, G.J. Fang, H.J. Yin, X.F. Liu, D. Liu, M.T. Zhao, W.J. Ke, H. Tao, Z.Y. Tang, Adv. Mater. 26 (2014) 8101–8106.

Applied Surface Science 357 (2015) 666–671

Contents lists available at ScienceDirect

Applied Surface Science

journal homepage: www.elsevier.com/locate/apsusc

A strategy of combining SILAR with solvothermal process for In_2S_3 sensitized quantum dot-sensitized solar cells

Peizhi Yang [a], Qunwei Tang [b,*], Chenming Ji [b], Haobo Wang [b]

[a] Key Laboratory of Advanced Technique & Preparation for Renewable Energy Materials, Ministry of Education, Yunnan Normal University, Kunming 650500, China
[b] Institute of Materials Science and Engineering, Ocean University of China, Qingdao 266100, China

ARTICLE INFO

Article history:
Received 20 July 2015
Received in revised form 23 August 2015
Accepted 4 September 2015
Available online 8 September 2015

Keywords:
Quantum dot-sensitized solar cell
Indium sulfide
Successive ionic layer adsorption and reaction
Solvothermal method
Photoanode

ABSTRACT

Pursuit of an efficient strategy for quantum dot-sensitized photoanode has been a persistent objective for enhancing photovoltaic performances of quantum dot-sensitized solar cell (QDSC). We present here the fabrication of the indium sulfide (In_2S_3) quantum dot-sensitized titanium dioxide (TiO_2) photoanode by combining successive ionic layer adsorption and reaction (SILAR) with solvothermal processes. The resultant QDSC consists of an In_2S_3 sensitized TiO_2 photoanode, a liquid polysulfide electrolyte, and a $Co_{0.85}Se$ counter electrode. The optimized QDSC with photoanode prepared with the help of a SILAR method at 20 deposition cycles and solvothermal method yields a maximum power conversion efficiency of 1.39%.

1. Introduction

Quantum dot-sensitized solar cell (QDSC), a promising photoelectrochemical device directly converting solar energy into electricity, has attracted tremendous attention due to its easy fabrication and cost-effectiveness [1–3]. In comparison with the expensive sensitizers in dye-sensitized solar cells, the quantum dots (QDs) in QDSCs have triggered growing interests because of the tunable band gap and high molar extinction coefficient [4]. Furthermore, the theoretical power conversion efficiency of QDSC can reach as high as 44% according to the multiple exciton generation phenomenon due to the impact ionization effect [5]. In spite of those merits, the highest reported efficiency of QDSCs is limited at 8.55% [6], which is far behind the maximum efficiencies from dye-sensitized solar cells (13%) [7] and perovskite solar cells (20.1%) [8]. The preferred QDs for QDSC applications are highly toxic cadmium and lead chalcogenides (CdS [9], CdSe [2], CdTe [10], and PbS [11]). Although Cd-based and Pb-based QDSCs have higher power conversion efficiencies, their toxic elements may limit the large-scale applications. In this fashion, a prerequisite to develop commercial devices is to replace the Cd-based and Pb-based QDs by nontoxic species.

As a typical III–VI group sulfide, indium sulfide (In_2S_3) with a bulk band gap of 2.0 eV has been extensively investigated in luminescence [12], photocatalysis [13], and Li-ion batteries [14]. Recently, In_2S_3 has been employed in QDSC as light absorber due to its excellent photoactivity, stable chemical and physical properties, high carrier mobility and low toxicity [15]. However, In_2S_3 sensitized solar cell demonstrates a quite poor photovoltaic performance [15–19]. Up to now, the fabrication of In_2S_3 QDs exploit some situ growth methods, such as successive ionic layer adsorption and reaction (SILAR) [19], solvothermal method [20] and electrodeposition technique [21]. In the current work, we present the synthesis of In_2S_3 QDs by combining traditional SILAR with solvothermal processes. SILAR synthesis shows good control over QD stoichiometry and size and can improve surface ligand coverage. However, devices fabricated using SILAR-synthesized materials suffer from QD corrosion, and lead to lower efficiencies than ex situ synthesized QD devices [22]. However, solvothermal synthesis is effective to obtain high-quality inorganic semiconductors [23]. In this fashion, the combination of SILAR and solvothermal processes is expected to optimize the uptake of In_2S_3 QDs and crystal structure. We employ $Co_{0.85}Se$ alloy as the counter electrode (CE), which has a superior catalytic performance for S^{2-}/S_x^{2-} redox electrolyte [24]. In comparison with the QDSCs based on the photoanode prepared using

* Corresponding author.
E-mail addresses: pzhyang@hotmail.com (P. Yang), tangqunwei@ouc.edu.cn (Q. Tang).

http://dx.doi.org/10.1016/j.apsusc.2015.09.049
0169-4332/

SILAR in the current and previous reports [17], the QDSC adopting the photoanode prepared with SILAR at 20 deposition cycles (20C) combined with solvothermal method presents a power conversion efficiency of 1.39%.

2. Experimental

2.1. Fabrication of In_2S_3 sensitized TiO_2 photoanodes

The TiO_2 photoanode on an FTO glass substrate (sheet resistance 12 $\Omega\,sq^{-1}$) was fabricated according to the method in our previous report [25]. The In_2S_3 sensitized TiO_2 anodes were fabricated with a SILAR method. In details, the TiO_2 film was dipped into 0.034 M $InCl_3$ methanol solution for 1 min, rinsed with anhydrous methanol and then dried by N_2 flow, and subsequently dipped into 0.05 M Na_2S ethanol solution for 1 min, rinsed with anhydrous ethanol and then dried by N_2 flow. Each series of the two immersion processes was marked as one deposition cycle. Such deposition cycle was repeated several times to obtain the In_2S_3 sensitized TiO_2 anode, which subsequently suffered solvothermal reaction. The precursor solution for solvothermal reaction includes 1 mM $InCl_3$, 4 mM sulfocarbamide ($SC(NH_2)_2$), and 6 mM citric acid trisodium salt ($C_6H_5Na_3O_7{\cdot}2H_2O$) in ethanol. When transferred the In_2S_3 sensitized TiO_2 anode into a 50 mL Teflon-lined autoclave with the FTO layer downward, the solvothermal reaction was performed at 120 °C. After reaction for 4 h, the final photoanode was thoroughly rinsed with ethanol and dried by N_2 flow.

2.2. Fabrication of $Co_{0.85}Se$ CEs

A mixture aqueous solution consists of 0.0238 g $CoCl_2{\cdot}6H_2O$, 0.01 g Se, 7.5 mL hydrazine hydrate (85%) and 27.5 mL deionized water. After vigorous stirring for 10 min, the resultant solution was transferred into a 50 mL Teflon-lined autoclave holding a cleaned FTO glass substrate with FTO layer downward. After reacting at 120 °C for 12 h, the substrate was taken out and rinsed with deionized water and then vacuum dried at 50 °C.

2.3. Assembly of QDSCs

The typical sandwich configuration of a QDSC was illustrated in Fig. 1a. The liquid polysulfide electrolyte consisting of 1 M Na_2S and 1 M sulphur aqueous solution was injected into the cell through capillary force. The characteristic photocurrent–voltage (J–V) curves of the QDSCs were measured with an Electrochemical Workstation under AM 1.5G irradiation at 100 mW cm^{-2}. The active area of each QDSC was around 0.25 cm^2 defined by applying a black mask on the surface of the device. Due to the good matching of energy levels [26], as shown in Fig. 1b, the electrons can be excited from valence band of In_2S_3 to CB and then transfer to CB of TiO_2.

2.4. Characterizations

The surface morphology of the In_2S_3 sensitized photoanode prepared using SILAR at 20C combined with solvothermal method was characterized using a scanning electron microscope (SEM, S4800). In order to detect the growth of In_2S_3 QDs on TiO_2 anode during the SILAR process, the In_2S_3 sensitized TiO_2 anodes after SILAR and solvothermal processes were subjected to UV–vis absorption at room temperature using bared FTO glass as a benchmark. The UV–vis diffuse reflection spectra were measured on an UV–vis spectrophotometer (Agilent 8453). The electrochemical impedance spectroscopy (EIS) measurements were scanned with a frequency range of 0.1–10^5 Hz at an ac amplitude of 10 mV under dark condition.

3. Results and discussion

The morphology of the photoanode has a powerful influence on the photovoltaic performance of a QDSC. Typical top view SEM images in Fig. 2a and b show the nanoporous structure of In_2S_3 sensitized TiO_2 photoanode synthesized by SILAR at 20C combined with solvothermal method. From Fig. 2a and b, the photoanode has a homogeneous surface without aggregations and the average diameter of the In_2S_3 sensitized TiO_2 nanoparticles is ~25 nm. The photoanode becomes more compact comparing with pristine TiO_2 in our previous report [25], suggesting that the TiO_2 nanoparticles have been covered densely by smaller In_2S_3 QDs and the nanoparticle structure of TiO_2 is retained. As references, the top-view SEM images of the photoanodes synthesized with SILAR at 8C or 24C combined with solvothermal are also provided in Fig. 2c and Fig. 2d, respectively. Top-view SEM photographs in Fig. 2c suggest a low coverage of In_2S_3 quantum dots with an average diameter of ~20 nm on dense TiO_2 film when In_2S_3 quantum dots are deposited for 8 cycles. With further increase in deposition cycle to 28 cycles (Fig. 2d), the TiO_2 surface has been completely covered by porous In_2S_3 quantum dots with a larger size (~50 nm). However, much thicker In_2S_3 layer on TiO_2 provides more interfaces for electron-transfer, therefore, the electron density at CB of TiO_2 nanocrystallite is expected to be decreased.

The In_2S_3 sensitized TiO_2 photoanodes are synthesized based on SILAR combined with solvothermal method. The whole reactions can be demonstrated as:

SILAR process:

$$2InCl_3 + 3Na_2S \rightarrow In_2S_3 \downarrow + 6NaCl \quad (1)$$

Solvothermal process:

$$3A^- + In^{3+} \rightarrow InA_3 \quad (A^- = C_5H_7COO^-) \quad (2)$$

$$SC(NH_2)_2 + C_2H_3OH \rightarrow H_2S + CO_2 + NH_3 \quad (3)$$

$$H_2S \rightarrow HS^- + H^+ \rightarrow S_2^- + 2H^+ \quad (4)$$

$$2In^{3+} + 3S^{2-} \rightarrow In_2S_3 \quad (5)$$

The SILAR process is used to deposit In_2S_3 on percolating TiO_2 film. At the very beginning of the solvothermal process, In^{3+} and A^- form InA_3 complexes. Then the S^{2-} ions released from $SC(NH_2)_2$ react with In^{3+} (released from InA_3 complexes) to form In_2S_3 under solvothermal treatment.

Fig. 3a shows the UV–vis absorption spectra of the In_2S_3 sensitized TiO_2 photoanodes prepared at various deposition cycles using pure TiO_2 photoanode as a benchmark. The typical absorption at around 340 nm is responding to the electron transition in In_2S_3 QDs between valence band and conduction band. Fig. 3b shows the UV–vis diffuse reflectance spectra of the resultant photoanodes, yielding a red shift of the band onset. This may be attributed to the increase of In_2S_3 loading and the increase of size of In_2S_3 QDs. Moreover, the photoanode prepared using SILAR at 20C combined with solvothermal method has the largest band span. In comparison with characteristic band at ca. 640 nm for bulk In_2S_3 [27], a distinct blue shift indicates that the size of In_2S_3 QDs is in the quantum confinement region [28].

The band gap (E_g) of the as-prepared photoanodes can be estimated according to the Kubelka–Munk theory [29]:

$$F(R) = \frac{(1-R)^2}{(2R)} \quad (6)$$

where R is the diffused reflectance. As shown in Fig. 3c, the intercepts of the tangents from the plots of $[F(R)h\nu]^{1/2}$ versus $h\nu$ yield the E_g values of the photoanodes. The E_g are 3.13, 2.44,

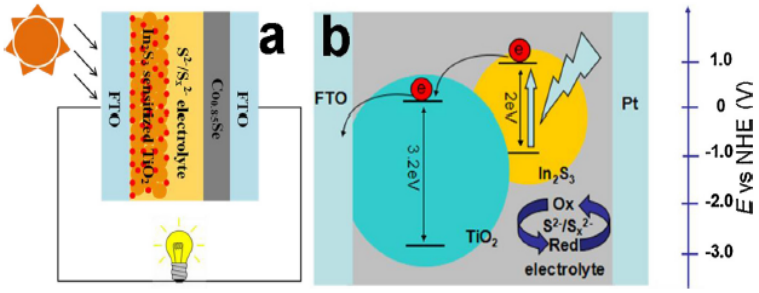

Fig. 1. The schematic diagram for the (a) QDSC with In_2S_3 sensitized TiO_2 photoanodes and (b) charge-transfer process in the QDSSC device.

Table 1
Photovoltaic parameters of various QDSCs. V_{oc}: open-circuit voltage; J_{sc}: short-circuit current density; *FF*: fill factor; η: power conversion efficiency.

Photoanodes	V_{oc} (V)	J_{sc} (mA cm^{-2})	*FF* (%)	η (%)
SILAR at 8C + solvothermal	0.277	1.73	48.0	0.23
SILAR at 12C + solvothermal	0.351	6.46	36.2	0.82
SILAR at 16C + solvothermal	0.355	7.09	43.2	1.09
SILAR at 20C + solvothermal	0.434	7.85	49.9	1.39
SILAR at 24C + solvothermal	0.456	5.93	47.3	1.28
SILAR at 20C	0.425	5.01	47.4	1.01
Solvothermal	0.253	0.42	32.0	0.034

2.35 and 2.64 eV for the photoanodes prepared using solvothermal, SILAR at 16C and 20C combined solvothermal, and SILAR at 20C, respectively. Therefore, the excitation of In_2S_3 QD can be enhanced with the help of a SILAR combined with solvothermal method.

Fig. 4a shows the *J*–*V* curves of QDSCs employing various photoanodes and the photovoltaic parameters are summarized in Table 1. The QDSC with a photoanode prepared using solvothermal method shows a poor efficiency of 0.034%, which is similar to the value in previous report [17]. The optimum efficiency of 1.39% is measured from the QDSC adopting the photoanode prepared using SILAR at 20C combined with solvothermal method, having a significant enhancement of 37.6% comparing with the efficiency of cell employing the anode prepared using SLIAR at 20C. The QDSC based on the photoanode prepared using SILAR combined with solvothermal method displays a higher power conversion efficiency than that reported in the literatures with SILAR method [18]. The improvement can be attributed to the high-quality In_2S_3 QDs by solvothermal process [23,30] for charge transfer between In_2S_3 and TiO_2 nanoparticles, resulting in a smaller interfacial resistance. Moreover, the J_{sc} can also reflect the number of accumulative electrons on conduction band (CB) of TiO_2 injected from CB of In_2S_3. With the increase of In_2S_3 loading, the electrons excited from In_2S_3 can be increased and then transfer to CB of TiO_2. However, the reduction of J_{sc} at 24C with much more In_2S_3 may be attributed to the aggregations and growth of the In_2S_3, which result in the remission of quantum confinement effect on In_2S_3 quantum dots, reduce the number of excitons and then lead to a smaller J_{sc}. V_{oc} is dependent on the difference between the quasi Fermi energy of the electrons in TiO_2 and redox potential (−0.55 eV) of the S^{2-}/S_x^{2-} electrolyte [31]. Due to the same TiO_2 electrodes used for cell assembly, the theoretical V_{oc} values are believed to in the same level. Actually, the real V_{oc} of a QDSC is smaller than the theoretical limit because of a backward reaction between electrons and

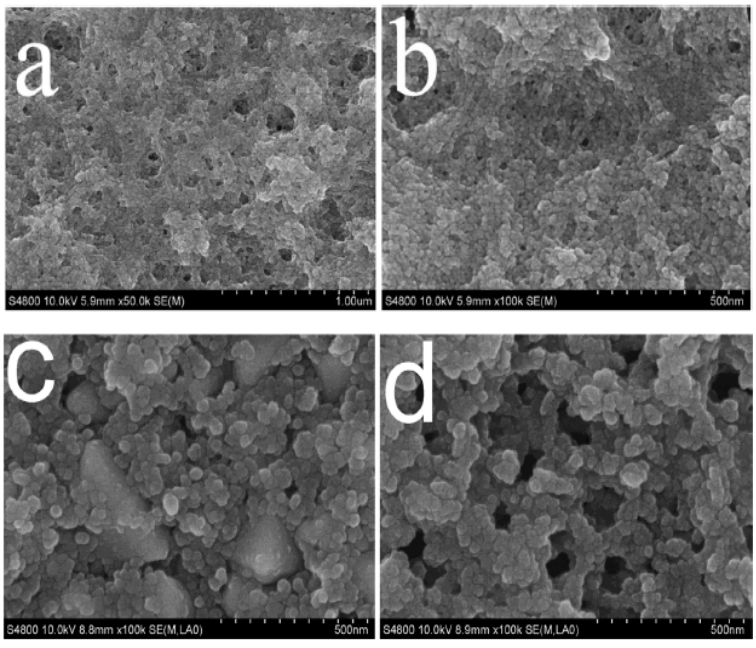

Fig. 2. SEM photograph of In_2S_3 sensitized TiO_2 photoanode prepared using SILAR combined with solvothermal method: (a and b) at 20C, (c) at 8C, and (d) at 24C.

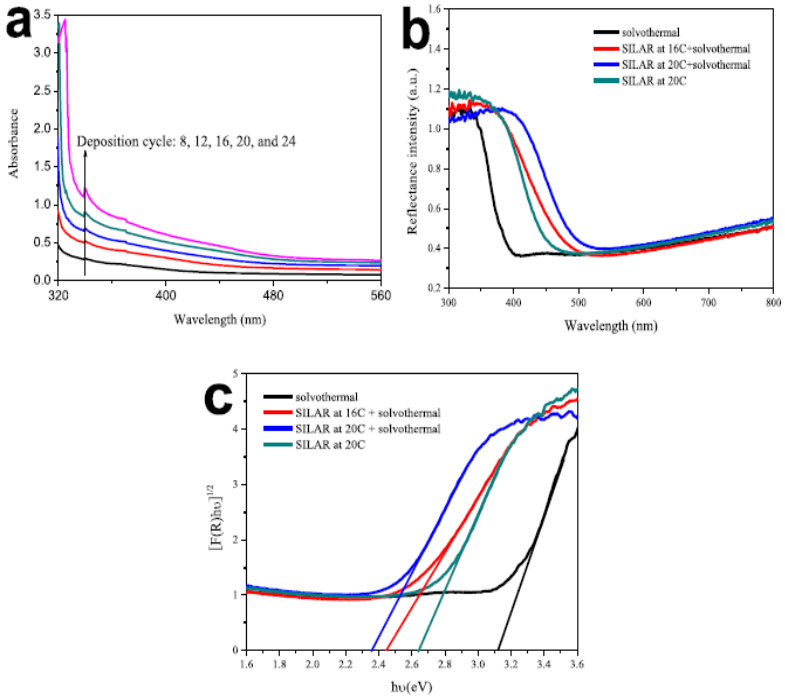

Fig. 3. (a) UV–vis absorption spectra of In_2S_3 sensitized TiO_2 photoanodes at various deposition cycles and subsequent solvothermal process. (b) UV–vis diffuse reflection spectra and (c) plots of $[F(R)h\nu]^{1/2}$ versus the band gap energy of various photoanodes after suffering SILAR and solvothermal processes.

electrolyte, and the backward transport of electrons produces a dark current. Recombination of photogenerated electrons with S_x^{2-} species in polysulfide electrolyte is a primary factor for electron loss. The dark current in QDSC is ascribed to the backward reaction between the S_x^{2-} and electrons on CB of TiO_2. The dark *J–V* curves in Fig. 4b show that the QDSC based on the photoanode prepared using SILAR at 20C combined with solvothermal method has the smallest current density at a given voltage. The smaller dark

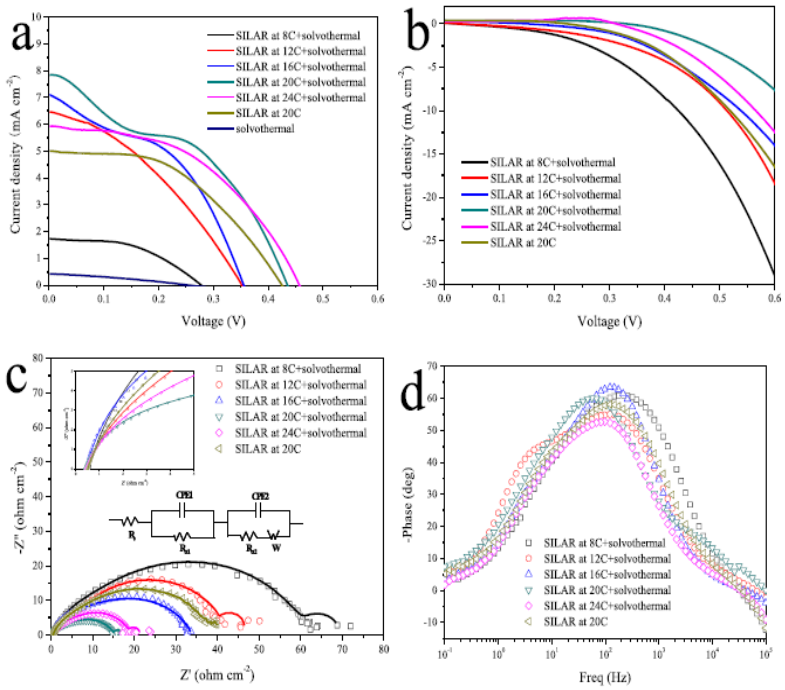

Fig. 4. Characteristic *J–V* curves of QDSCs measured (a) at AM 1.5G irradiation and (b) in the dark; EIS spectra of the QDSCs: (c) Nyquist plots and (d) Bode phase plots.

Table 2
Peak frequency (f_p), electron lifetime (τ), and related parameters of the QDSCs obtained by fitting EIS.

Photoanodes	R_s (Ω cm^2)	R_{ct2} (Ω cm^2)	W (Ω cm^2)	f_p (Hz)	τ (ms)
SILAR at 8C + solvothermal	0.562	50.1	9.40	195.3	0.82
SILAR at 12C + solvothermal	0.449	33.1	4.98	127.6	1.25
SILAR at 16C + solvothermal	0.437	23.9	4.61	118.1	1.35
SILAR at 20C + solvothermal	0.406	11.0	1.08	56.23	2.83
SILAR at 24C + solvothermal	0.449	12.9	2.71	90.10	1.77
SILAR at 20C	0.510	28.2	5.68	123.2	1.29

current density suggests that the recombination at the TiO_2/electrolyte interface is retarded.

As shown in Fig. 4c, the smaller semicircle (high frequency regions) indicates the charge transfer resistance at CE/electrolyte interface (R_{ct1}), the larger semicircle (intermediate frequency regions) indicates the charge transfer resistance at TiO_2/In_2S_3/electrolyte interface (R_{ct2}), the tail (low frequency regions) indicates the Nernst diffusion process corresponding to the diffusion resistance of the S^{2-}/S_x^{2-} redox species (W), respectively. By fitting the Nyquist plots with the equivalent circuit (the inset of Fig. 4c), the sheet resistance (R_s), R_{ct2} and W can be extracted, as summarized in Table 2. Because each device uses the same CE and electrolyte, the differences of the R_s, R_{ct2} and W are responsible for the different photovoltaic properties. It is apparent that the QDSC based on the photoanode prepared using SILAR at 20C combined with solvothermal method has the smallest R_{ct2} of 11.0 Ω cm^2 compared with other devices (Table 2). This result suggests that the photogenerated electrons can rapidly transport to CB of TiO_2 from CB of In_2S_3. Furthermore, the smallest W value indicates that the diffusion kinetics of the S^{2-}/S_x^{2-} redox species within the region between the photoanode and the CE are more facile than other devices, which can quicken the recovery of excited In_2S_3.

The lifetime of the electrons (τ) on various photoanodes are calculated according to Eq. (7) [27]:

$$\tau = \frac{1}{2\pi f_p} \tag{7}$$

where f_p is the peak frequency assigning to the charge-transfer process at anode/electrolyte interface. The electrons on the photoanode prepared using SILAR at 20C combined with solvothermal method have an average lifetime of 2.83 ms, which is the largest one among various photoanodes (Table 2). The longest electron lifetime suggests low electron recombination with holes and electrolyte and an easy electron transport process along the photoanode prepared using SILAR at 20C combined with solvothermal method.

4. Conclusions

In summary, In_2S_3 sensitized TiO_2 photoanodes have been successfully prepared by combing SILAR with solvothermal processes. We have evaluated the dependence of morphology, energy band gap, electrochemical performance, and photovoltaic behavior on SILAR cycles. The preliminary results demonstrate that the QDSC with photoanode prepared using SILAR at 20C combined with solvothermal method yields the maximum power efficiency of 1.39% in comparison with 1.01% on the cell based on photoanode prepared using SILAR at 20C.

Acknowledgements

The authors would like to acknowledge financial supports from National Natural Science Foundation of China (21503202, U1037604) andShandong Province Outstanding Youth Scientist Foundation Plan (BS2013CL015).

References

[1] P.V. Kamat, Quantum dot solar cells. The next big thing in photovoltaics, J. Phys. Chem. B 4 (2013) 908–918.
[2] Y.-L. Lee, Y.-S. Lo, Highly efficient quantum-dot-sensitized solar cell based on co-sensitization of CdS/CdSe, Adv. Funct. Mater. 19 (2009) 604–609.
[3] L. Tao, Y. Xiong, H. Liu, W.Z. Shen, High performance PbS quantum dot sensitized solar cells via electric field assisted in situ chemical deposition on modulated TiO_2 nanotube arrays, Nanoscale 6 (2014) 931–938.
[4] L. Yu, Z. Li, Y. Liu, F. Cheng, S.P. Sun, Mn-doped CdS quantum dots sensitized hierarchical TiO_2 flower-rod for solar cell application, Appl. Surf. Sci. 305 (2014) 359–365.
[5] M.C. Hanna, A.J. Nozik, Solar conversion efficiency of photovoltaic and photoelectrolysis cells with carrier multiplication absorbers, J. Appl. Phys. 100 (2006), 074510.
[6] K. Zhao, Z.X. Pan, I. Mora-Seró, E. Cánovas, H. Wang, Y. Song, X.Q. Gong, J. Wang, M. Bonn, J. Bisquert, X.H. Zhong, Boosting power conversion efficiencies of quantum-dot-sensitized solar cells beyond 8% by recombination control, J. Am. Chem. Soc. 137 (2015) 5602–5609.
[7] T. Umeyama, H. Imahori, Design and control of organic semiconductors and their nanostructures for polymer-fullerene-based photovoltaic devices, J. Mater. Chem. A 2 (2014) 11545–11560.
[8] http://www.nrel.gov/ncpv/images/efficiency_chart.jpg.
[9] P.K. Santra, P.V. Kamay, Mn-doped quantum dot sensitized solar cells: a strategy to boost efficiency over 5%, J. Am. Chem. Soc. 134 (2012) 2508–2511.
[10] Z. Ge, L. Xu, R. Zhang, Z. Xue, H. Wang, J. Xu, Y. Yu, W. Su, Z. Ma, K. Chen, Improved performance of silicon nanowire/cadmium telluride quantum dots/organic hybrid solar cells, Appl. Surf. Sci. 334 (2015) 15–18.
[11] Y. Zhu, R. Wang, W. Zhang, H. Ge, L. Li, CdS and PbS nanoparticles co-sensitized TiO_2 nanotube arrays and their enhanced photoelectrochemical property, Appl. Surf. Sci. 315 (2014) 149–153.
[12] J. Feng, H. Zhu, X.R. Yang, A controllable growth-doping approach to synthesize bright white-light-emitting Cd:In_2S_3 nanocrystals, Nanoscale 5 (2013) 6318–6322.
[13] Y.X. Li, G. Chen, C. Zhou, J.X. Sun, A simple template-free synthesis of nanoporous ZnS-In_2S_3-Ag_2S solid solutions for highly efficient photocatalytic H_2 evolution under visible light, Chem. Commun. 15 (2009) 2020–2022.
[14] Y. Gu, Y. Wang, Microwave hydrothermal growth of In_2S_3 interconnected nanoflowers and nanoparticles on graphene for high-performance Li-ion batteries, RSC Adv. 4 (2014) 8582–8589.
[15] K. Hara, K. Sayama, H. Arakawa, Semiconductor-sensitized solar cells based on nanocrystalline In_2S_3/In_2O_3 thin film electrodes, Sol. Energy Mater. Sol. Cells 62 (2000) 441–447.
[16] S.K. Sarkar, J.Y. Kim, D.N. Goldstein, N.R. Neale, K. Zhu, C.M. Elliott, A.J. Frank, S.M. George, In_2S_3 atomic layer deposition and its application as a sensitizer on TiO_2 nanotube arrays for solar energy conversion, J. Phys. Chem. C 114 (2010) 8032–8039.
[17] Y.H. Zhang, J. Zhu, F. Liu, G.H. Wu, J.F. Wei, L.H. Hu, Y. Huang, C.N. Zhang, J.W. Tang, S.Y. Dai, In_2S_3 sensitized solar cells with a new passivation layer, J. Photochem. Photobiol. A 281 (2014) 53–58.
[18] X.Y. Gan, X.M. Li, X.D. Gao, J.J. Qiu, F.W. Zhuge, TiO_2 nanorod arrays functionalized with In_2S_3 shell layer by a low-cost route for solar energy conversion, Nanotechnology 22 (2011), 305601.
[19] J.L. Duan, Q.W. Tang, B.L. He, L.M. Yu, Efficient In_2S_3 quantum dot-sensitized solar cells: a promising power conversion efficiency of 1.30%, Electrochim. Acta 139 (2014) 381–385.
[20] Y.Q. Wang, Y.C. Rui, Q.H. Zhang, Y.G. Li, H.Z. Wang, A facile in situ synthesis route for $CuInS_2$ quantum-dots/In_2S_3 co-sensitized photoanodes with high photoelectric performance, ACS Appl. Mater. Interfaces 5 (2013) 11858–11864.
[21] Y. Li, S.L. Luo, Z.D. Wei, D.S. Meng, M.Y. Ding, C.B. Liu, Electrodeposition technique-dependent photoelectrochemical and photocatalytic properties of an In_2S_3/TiO_2 nanotube array, Phys. Chem. Chem. Phys. 16 (2014) 4361–4368.
[22] H. Dong, S. Du, X. Zheng, G. Lyu, L. Sun, L. Li, P. Zhang, C. Zhang, C. Yan, Lanthanide nanoparticles: from design toward bioimaging and therapy, Chem. Rev., doi: 10.1021/acs.chemrev.5b00091.
[23] J.H. Bang, P.V. Kamat, Quantum dot sensitized solar cells. A tale of two semiconductor nanocrystals: CdSe and CdTe, ACS Nano 3 (2009) 1467–1476.
[24] C.Q. Ma, Q.W. Tang, Z.Y. Zhao, M.J. Hou, Y.R. Chen, B.L. He, L.M. Yu, Bifacial quantum dot-sensitized solar cells with transparent cobalt selenide counter electrodes, J. Power Sources 278 (2015) 183–189.

[25] Z.B. Wang, Q.W. Tang, B.L. He, X.X. Chen, H.Y. Chen, L.M. Yu, Titanium dioxide/calcium fluoride nanocrystallite for efficient dye-sensitized solar cell. A strategy of enhancing light harvest, J. Power Sources 275 (2015) 175–180.
[26] W. Xiang, H. Zhao, J. Zhong, H. Luo, X. Zhao, Z. Chen, X. Liang, X. Yang, Synthesis and third order optical nonlinearities of In_2S_3 quantum dots glass, J. Alloys Compd. 553 (2013) 135–141.
[27] M.Q. Yang, B. Weng, Y.J. Xu, Synthesis of In_2S_3–CNT nanocomposites for selective reduction under visible light, J. Mater. Chem. A 2 (2014) 1710–1720.
[28] G.D. Stucky, J.E. MacDougail, Quantum confinement and host/guest chemistry: probing a new dimension, Science 247 (1990) 669–678.
[29] H. Tada, M. Fujishima, H. Kobayashi, Photodeposition of metal sulfide quantum dots on titanium(IV) dioxide and the applications to solar energy conversion, Chem. Soc. Rev. 40 (2011) 4232–4243.
[30] B. Feng, J. Cao, J.H. Yang, S. Yang, D.L. Han, Characterization and photocatalytic activity of ZnSe nanoparticles synthesized by a facile solvothermal method, and the effects of different solvents on these properties, Mater Res. Bull. 60 (2014) 794–801.
[31] J.B. Sambur, T. Novet, B.A. Parkinson, Multiple exciton collection in a sensitized photovoltaic system, Science 330 (2010) 63–66.

Materials Letters 161 (2015) 185–188

Contents lists available at ScienceDirect

Materials Letters

journal homepage: www.elsevier.com/locate/matlet

A nanoporous titanium dioxide framework for dye-sensitized solar cell

Peizhi Yang [a], Qunwei Tang [b,*]

[a] Key Laboratory of Advanced Technique & Preparation for Renewable Energy Materials, Ministry of Education, Yunnan Normal University, Kunming 650500, China

[b] Institute of Materials Science and Engineering, Ocean University of China, Qingdao 266100, China

ARTICLE INFO

Article history:
Received 8 July 2015
Received in revised form
7 August 2015
Accepted 22 August 2015
Available online 24 August 2015

Keywords:
Energy storage and conversion
Solar energy materials
Structural

ABSTRACT

Dye-sensitized solar cell (DSSC) is a promising solution to energy depletion, environmental pollution, and ecological destruction. In this communication, we have successfully prepared nanoporous titanium dioxide (TiO_2) framework by etching traditional TiO_2 nanoparticle film for DSSC applications. Due to the enhancement in light-scattering and fast electron transport, a promising power conversion efficiency of 8.29% is recorded from the DSSC employing TiO_2 nanoframework in comparison with 6.24% for the solar cell with pristine TiO_2 anode.

1. Introduction

Dye-sensitized solar cell (DSSC) [1] is a lower cost, simpler preparation process, relatively higher photoelectric conversion efficiency and lighter mass [2] than conventional solar cells, such as silicon-based solar cells. A typical DSSC device is composed of a mesoporous network of TiO_2 nanoparticles for uptaking dye photosensitizer, redox-active electrolyte containing iodide/triiodide (I^-/I_3^-) couples, and Pt counter electrode for converting I_3^- to I^-. An ideal TiO_2 film should simultaneously meet several major requirements such as a large specific surface area for sufficient dye uptakes, a superior scattering effect for enhanced light-harvesting, a prominent electron transport and recombination characteristic for efficient charge-collection, as well as an adequate network and porosity for feasible electrolyte penetration [3]. However, it is still a challenge to integrate such merits into a single photoanode. The conventional porous photoanode is composed of anatase TiO_2 nanoparticles, which have a large specific surface area to load the dye molecules [4]. However, the large interfacial resistance among TiO_2 nanoparticles is expected to trap many photogenerated electrons, reducing the electron lifetime in photoanode. These nanoparticles have abundant defects at surface and grain boundaries, acting as electrons traps for increased charge recombination [5]. In order to solve these issues, one dimensional (1D) TiO_2 nanostructures have been applied in DSSCs [6,7].

We report here a mild one-step hydrothermal method to directly convert pristine TiO_2 nanoparticles into a nanoporous TiO_2 framework. Although the capability of uptaking organic dye molecules on the nanoporous TiO_2 framework reduces in comparison to pristine TiO_2 nanoparticle film, this extraordinary structure can efficiently enhance the light scattering and increase the electron transport and in favor of electrolyte permeation, which contribute to the electron transport in the interface of TiO_2/dye/electrolyte. To the best of our knowledge, this concept of fabricating nanoporous TiO_2 framework for rapid electron transport is also of significance for other solar cells, such as quantum dot-sensitized solar cells, perovskite-sensitized solar cells, and organic–inorganic hybrid solar cells [8].

2. Experimental

2.1. Fabrication of nanoporous TiO_2 photoanodes

The photoanodes from mesoporous TiO_2 crystallites were prepared by coating sol-thermal processed TiO_2 colloid on FTO glass with a doctor-blade method. Subsequently, the as-prepared TiO_2 film on FTO substrates were immersed into 30 mL of 1 M NaOH aqueous solution and placed at an angle against the wall of the Teflon-lined autoclave with the conducting layer facing down performed at 150 °C for 10, 20, 30, 60, 120, and 180 min, respectively. The as-prepared TiO_2/FTO films were thoroughly rinsed with deionized water. The resulted nanoporous TiO_2 frameworks on FTO glass substrates were immersed in a 0.50 mM N719 (cis-di(thiocyanato)-N,N′-bis(2,2′-bipyridyl-4-carboxylic acid)-4-tetrabutylammonium carboxylate) ethanol solution for 24 h to obtain the dye-sensitized TiO_2 photoanodes.

* Corresponding author. Fax: +86 871 5517125.
E-mail addresses: pzhyang@hotmail.com (P. Yang), tangqunwei@ouc.edu.cn (Q. Tang).

http://dx.doi.org/10.1016/j.matlet.2015.08.104
0167-577X/

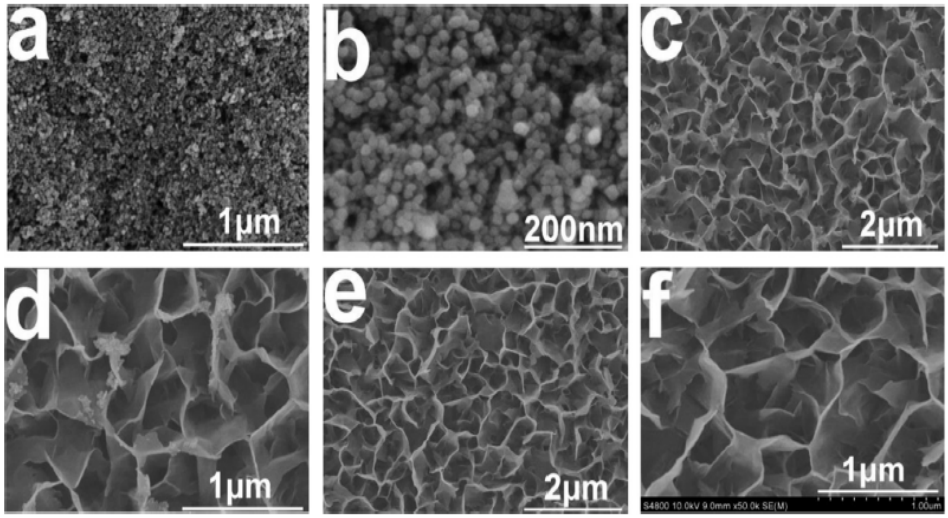

Fig. 1. SEM photographs of (a) and (b) pristine TiO_2 and nanoporous TiO_2 frameworks etched for (c) and (d) 20 min and (e) and (f) 30 min.

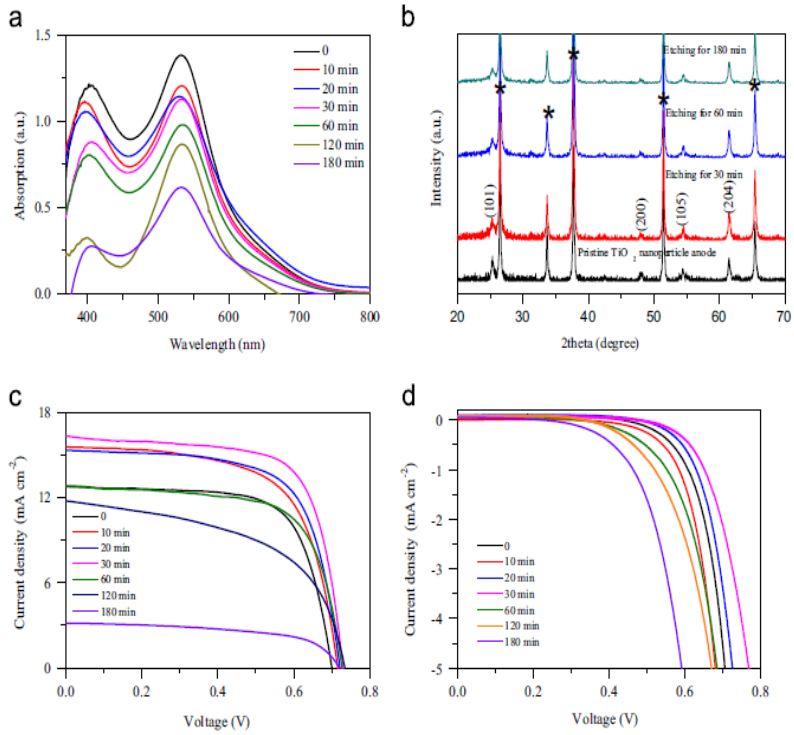

Fig. 2. (a) UV–vis absorption spectra of N719 sensitized TiO_2 anodes. (b) XRD patterns of anodes from pristine TiO_2 nanoparticle film and nanoporous TiO_2 frameworks. The peaks marked by "*" are attributed to FTO glass. *J–V* curves of DSSCs (c) under an AM1.5G illumination and (d) in the dark.

2.2. Assembly of DSSCs and photovoltaic tests

A DSSC was assembled by sandwiching with the liquid electrolyte between a dye-sensitized TiO_2 photoanode and a Pt counter electrode. The photovoltaic tests on the DSSCs were carried out by measuring the characteristic photocurrent–voltage (*J–V*) curves under irradiation from a simulated solar light from a 100 W xenon arc lamp (XQ-500 W) in an ambient atmosphere. The incident light intensity was controlled at 100 mW cm^{-2} (AM 1.5).

3. Results and discussion

Fig. 1a and b shows that the pristine TiO_2 nanoparticle film is apparently synthesized with the average particle size of 20 nm. After being etched for 20 min during the hydrothermal reaction, as shown in Fig. 1c and d, the thin TiO_2 film with nanoparticles has been transferred to nanoporous TiO_2 frameworks decorated with unetched TiO_2 nanoparticles. With further elongation of etching time to 30 min, the TiO_2 nanoparticles have been completely dissolved, leading to homogeneous TiO_2 frameworks, as shown in Fig. 1e and f. These extraordinary TiO_2 frameworks are believed to act as placeholders for dye uptake and percolating channels for electron transportation. The nanoporous TiO_2 frameworks etched for 0, 10, 20, 30, 60, 120, and 180 min are subjected to BET characterization, giving BET values of 89.4, 76.1, 72.6, 68.7, 64.3, 53.8,

Table 1
Comparison of efficiency (η), open-circuit voltage (V_{oc}), short-circuit current density (J_{sc}), fill factor (FF), and electron lifetime ($\tau = 1/2\pi f$, f is the peak frequency in Bode plots).

Etching time (min)	η (%)	V_{oc} (V)	J_{sc} (mA cm^{-2})	FF (%)	R_{ct2} (Ω cm^2)	τ (ms)
0	6.24	0.700	12.76	69.2	13.3	3.43
10	7.13	0.715	15.56	64.1	10.1	2.83
20	7.46	0.720	15.37	67.4	14.9	4.16
30	8.29	0.729	16.32	69.7	3.3	5.04
60	6.32	0.726	12.82	67.9	13.9	1.31
120	4.59	0.734	11.80	53.0	18.3	1.08
180	1.32	0.720	3.21	57.1	26.3	0.74

and 32.1 m^2 g^{-1}, respectively. This result demonstrates that the etching reaction can reduce the specific surface area of TiO_2 film and therefore dye loading, which can also be confirmed by the UV–vis absorption of dye-sensitized TiO_2 photoanodes, as shown in Fig. 2a. The absorption peak intensity has a reduced evolution with etching time from 0 to 180 min, suggesting that the etching of TiO_2 nanoparticle film during hydrothermal process can reduce the specific surface area and therefore dye absorption, which is consistent with BET characterization. Fig. 2b shows the XRD patterns of the pristine TiO_2 and nanoporous TiO_2 framework with an etching time of 30 min. The diffraction peaks at $2\theta = 25.2°$, 38.7°, 48.0°, 54.5°, and 61.6° in the pristine TiO_2 pattern are attributed to diffraction faces of (101), (004), (200), (105), and (204) planes, respectively. All the diffraction peaks corresponding to anatase TiO_2 (PDF#21-1272) can be identified in XRD pattern of nanoporous TiO_2 photoanode. We have carefully compare the XRD patterns of the TiO_2 frameworks synthesized at various etching time, no apparent deviations are observed in the profiles (Fig. 2b).

The DSSC device containing pristine TiO_2 crystallites gives a η of 6.24% (Fig. 2c and Table 1). Interestingly, the optimized DSSC device based on the TiO_2 at an etching time of 30 min performs the η up to 8.29%. Although the dye loading is reduced by etching the pristine TiO_2 nanoparticle film, the light scattering has been markedly enhanced, yielding an enhanced J_{sc} for optimized DSSCs. Moreover, the increase of V_{oc} from 0.700 to 0.729 V is mainly due to the fact that the longer electron lifetimes reduce the electron recombination and improve the electron transport efficiently. It is noteworthy to mention that further elongation of etching time such as higher than 30 min, the FTO layer on glass substrate can be destroyed for electron collection, yielding lower photovoltaic performances in their DSSCs. This conclusion can be supported by the sheet resistance evolution in Table S1. It has been determined that etching time of 30 min is optimum for fabricating nice TiO_2 framework. Dark J–V curves in Fig. 2d demonstrate the dark current density for various DSSCs. Generally, the dark current is formed by the backward recombination of electrons on conduction band of TiO_2 with I_3^- species. Apparently, the dark current density has an order of TiO_2-10 min < pristine TiO_2 < TiO_2-20 min < TiO_2-30 min > TiO_2-60 min > TiO_2-120 min > TiO_2-180 min, which is consistent with electron lifetime in Table 1.

In the EIS Nyquist plots in Fig. 3a, two well-defined semicircles were observed in the high frequency and medium frequency range. One can notice that the R_{ct2} value for the cell device with TiO_2-30 min is the smallest, this demonstrates that the photogenerated electrons can be rapidly transferred to CB of the TiO_2 and the excited dyes are easily recovered by I^- ions. The results can be ascribed to the fact that the etched film is benefit for the electrolyte penetration. However, the destroy of FTO glass substrate can lead to an increased R_{ct2} value. Till now, we can make a conclusion that the enhanced electron lifetimes (Fig. 3b and Table 1) in the DSSCs from TiO_2 anodes with etched 30 min by NaOH can be attributed to the rapid electron transfer.

A sharp increase and no delay in photocurrent density in Fig. 3c

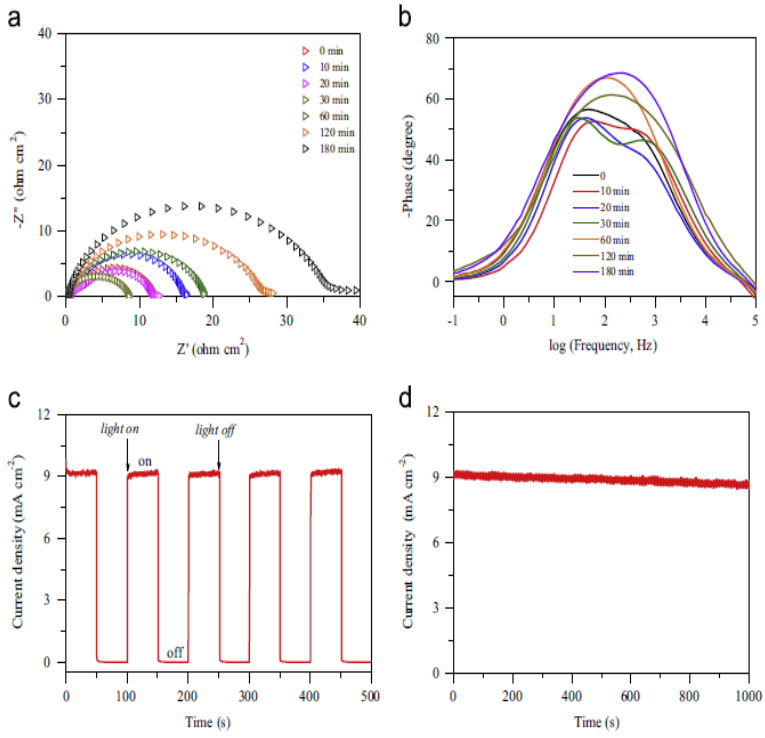

Fig. 3. EIS plots of the DSSCs: (a) Nyquist plots and (b) Bode phase plots. (c) The on-off switches of DSSC with TiO_2-30 min anode achieved by alternately illuminating (100 mW cm^{-2}) and darkening (0 mW cm^{-2}) the DSSC at an interval of 50 s and 0 V. (d) Photocurrent stability of the DSSC device under persistent irradiation at 100 mW cm^{-2}.

suggest a fast start of cell operation at irradiation, demonstrating that the nanoporous TiO_2 framework exhibits a capacity of transporting electrons and reducing backward recombination reaction. Moreover, no obvious reduction in photocurrent density in each "on" state means a good multiple start capability and low electron recombination kinetics. After multiple start-up, the cell still remain properties in its initial level (Fig. 3d), which is an essential prerequisite for the application of DSSCs in engines or vehicles. The photocurrent density as a function of time plots over 1000 s demonstrates photocurrent stability on prolonged exposure to light irradiation (100 mW cm^{-2}).

4. Conclusions

In summary, nanoporous TiO_2 framework has been fabricated by a hydrothermal process for enhancing electron transfer ability, limiting electron recombination, and therefore enhancing power conversion efficiency of DSSCs. The optimized DSSC yields a maximum efficiency of 8.29% in comparison with 6.24% for pristine TiO_2 based device. The high photovoltaic performances are attributed to the nanoporous structure for effective electron transport and electrolyte penetration.

Acknowledgments

The authors would like to acknowledge financial supports from National Natural Science Foundation of China (U1037604).

Appendix A. Supplementary material

Supplementary data associated with this article can be found in the online version at http://dx.doi.org/10.1016/j.matlet.2015.08.104.

References

[1] B. O'Regan, M. Grätzel, Nature 353 (1991) 737–740.
[2] H.H. Zhang, B.L. He, Q.W. Tang, L.M. Yu, J. Power Sources 275 (2015) 489–497.
[3] W.Q. Wu, Y.F. Xu, H.S. Rao, C.Y. Su, D.B. Kuang, J. Am. Chem. Soc. 136 (2014) 6437–6445.
[4] B.B. Hu, Q.W. Tang, B.L. He, L. Lin, H.Y. Chen, J. Power Sources 276 (2014) 445–451.
[5] X.K. Xin, J. Wang, W. Han, M.D. Ye, Z.Q. Lin, Nanoscale 4 (2012) 964–969.
[6] Q.L. Ma, Y.M. Huang, Mater. Lett. 148 (2015) 171–173.
[7] J. Lu, Z. Liu, C. Zhu, M. Zhang., M. Wan, Mater. Lett. 159 (2015) 61–63.
[8] D. Kong, X. Jin, W. Sun, J. Du, J. Tong, C. Chen, X. Yang, Y. Cheng, Q. Li, J. Power Sources 274 (2015) 701–708.

Available online at www.sciencedirect.com

ScienceDirect

Solar Energy 120 (2015) 44–54

SOLAR ENERGY

www.elsevier.com/locate/solener

Diffuse reflections within CPCs and its effect on energy collection

Yamei Yu, Runsheng Tang *

Education Ministry Key Laboratory of Advanced Technology and Preparation for Renewable Energy Materials, Yunnan Normal University, Kunming 650500, PR China

Received 31 October 2014; received in revised form 25 February 2015; accepted 9 July 2015

Communicated by: Associate Editor Brian Norton

Abstract

In practical applications, part of solar rays incidence on reflectors of compound parabolic concentrators (CPC, in short) undergoes diffuse reflections instead of specular reflections due to imperfect reflector profile, rough surface and dust deposition, leading a considerable fraction of solar rays escape from the cavity of CPCs and making their optical performance decrease. In this article, a detailed mathematical procedure to estimate the optical efficiency factor of CPCs with semi-diffuse reflectors and one-sided flat absorber is developed based on the knowledge of two-dimensional radiation transfer, and the effect of diffuse reflections within the CPC on its energy collection is theoretically investigated. Ray-tracing analysis shows that the use of semi-diffuse reflectors in CPCs can not make solar flux on the absorber more uniform except using perfect diffuse reflectors, in turn leads the optical efficiency decrease. Comparisons of the optical efficiency factors between theoretically expected and those obtained by ray-tracing simulation indicate that the mathematical model proposed in this work can accurately estimate the optical performance of such CPC. Theoretical calculations show that the contribution of diffuse reflections within CPCs to the radiation collection of CPCs is limited as a result of the fact that the diffuse radiation transfer shape factor from the reflectors to the absorber is very small, and the annual average optical concentration decreases with the increase of diffuse reflectivity of reflectors for CPCs with a given total reflectivity.

Keywords: CPC with semi-diffuse reflectors; Theoretical analysis; Optical efficiency factor; Effect on energy collection

1. Introduction

With the gradual depletion of fossil fuels in our planet, the application of solar energy becomes more attractive in recent years. It was reported that, by 2011, solar photovoltaic (PV) had been introduced in more than 80 countries and was regarded as the fastest growing power generation technology (Firdaus et al., 2013). However, the use of PV system is limited due to its high cost as compared to the conventional electricity generation, although the cost of electricity generation by PV systems has decreased substantially over the past two decades (Robert, 2005). In a PV system, the PV cell accounts almost 50% of the total cost. Thus, one of effective ways to reduce the cost of electricity generated from a PV system is to reduce the use of solar cells for given power demand by the use of cheep optical concentrators.

In recent years, the compound parabolic concentrator (CPC), an ideal concentrator, sharing advantages of simple structure and no need of sophisticated sun-tacking device (Rabl, 1985), has been widely tested for concentrating solar radiation on solar cells to lower the cost of electricity from a PV system (Mallick et al., 2004; Mallick et al., 2006; Brogren et al., 2003). Theoretically, for a CPC based

* Corresponding author. Tel.: +86 871 65912903; fax: +86 871 65516217.
E-mail address: kingtang01@126.com (R. Tang).

http://dx.doi.org/10.1016/j.solener.2015.07.016
0038-092X/

Nomenclature

C_t	geometric concentration factor of truncated CPCs (dimensionless)
C_{opt}	annual average optical concentration (dimensionless)
$f(\theta_p)$	optical efficiency factor (dimensionless)
$f_b(\theta_p)$	optical efficiency factor contributed by beam radiation (dimensionless)
$f_d(\theta_p)$	optical efficiency factor contributed by diffuse radiation (dimensionless)
F_{x-y}	shape factor from surface x to surface y (dimensionless)
H	daily radiation (J/m^2)
h_t	height of CPCs (m)
I	instantaneous radiation intensity (W/m^2)
J	effective diffuse radiation from reflectors (W/m^2)
S	incident radiation intensity (W/m^2)
t	solar time measuring from the solar noon to afternoon (s)
$\overline{XY}$	length of parabolic reflector from point X to point Y (m)

Greek letters

β	tilt-angle of CPCs' aperture from the horizon (rad.)
δ	declination of the sun (rad.)
λ	site latitude (rad.)
θ_a	acceptance half-angle of CPCs (rad. in expressions, otherwise in deg.)
θ_{in}	real incidence angle of solar rays on the aperture of CPCs (rad.)
θ_b	angle at the incidence angle less than which both reflectors are fully irradiated (rad.)
θ_f	angle at the incidence angle less than which the absorber of CPCs is fully irradiated (rad.)
θ_p	projection incidence angle of solar rays on the cross-section of CPC-trough (rad.)
θ_t	edgy ray angle of truncated CPCs (rad.)
ρ	total reflectivity of reflectors (dimensionless)
ρ_d	diffuse reflectivity of reflectors (dimensionless)
ρ_s	specular reflectivity of reflectors (dimensionless)
τ_{day}	day length (s)
ω	hour angle (rad.)

Subscripts

0	sunset
abs	absorber
ap	aperture
b	beam radiation
d	diffuse radiation

photovoltaic module, the power output should be increased by a factor of its geometric concentration ratio as compared to similar non-concentrating PV panel. However, the actual power output from a CPC based PV module was much less than the theoretical value due to the optical loss resulting from imperfect reflections and the electrical loss partially resulting from non-uniform distribution of solar radiation on solar cells. To make the radiation on solar cells more uniform so as to increase the fill factor of CPC based PV systems, Hatwaambo et al. (2008, 2009) tried to use semi-diffuse reflective materials as CPC reflectors, and experimental results showed that the use of reflectors with rolling mark parallel to the plane of solar cells could slightly increase the fill factor of the photovoltaic system. However, the use of semi-diffuse reflectors would result in the reduction of CPCs' optical efficiency because only a very small fraction of radiation incidence on the reflectors will arrive on the absorber after diffuse reflections.

For a CPC with perfect specular reflectors, all radiation within its acceptance angle will arrive on the absorber directly or from reflectors after reflections, but in practical applications, partial radiation incidence on reflectors will undergo diffuse reflections due to imperfect reflector profile, rough surface and dust deposition, leading a considerable fraction of solar rays escape from the cavity of CPCs and making the optical performance decrease. In this wok, an attempt was made to theoretically investigate the optical efficiency factor contributed by diffuse radiation due to diffuse reflections within the CPC with one-sided flat absorber and semi-diffuse reflectors as well effects of diffuse reflections on its energy collection.

2. Mathematical model to estimate the optical efficiency factor of CPCs

2.1. Reflector equation and key parameters of CPCs

As shown in Fig. 1, the equation of right reflector of a CPC with one-sided flat absorber (the width of absorber

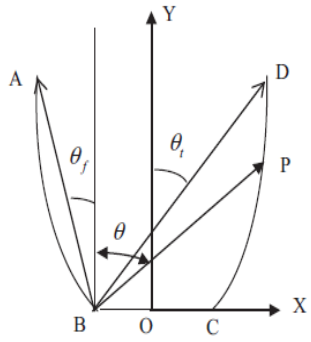

Fig. 1. Geometry of CPC with one-sided flat absorber.

is assumed to be 1 for convenient analysis) in the suggested coordinate system is given by:

$$\begin{cases} x = \frac{(1+\sin\theta_a)\sin\theta}{1-\cos(\theta+\theta_a)} - 0.5 \\ y = \frac{(1+\sin\theta_a)\cos\theta}{1-\cos(\theta+\theta_a)} \end{cases} \quad (\theta_t \leqslant \theta \leqslant 0.5\pi) \tag{1}$$

where θ_a is the acceptance half-angle; θ is the polar angle of any point P on the parabolic reflector; and θ_t is the edge-ray angle of CPCs after truncation. For full CPC, $C_t = 1/\sin\theta_a$, $\theta_t = \theta_a$. Given θ_a and geometric concentration (C_t), the edge-ray angle θ_t can be calculated based on Eq. (1) by:

$$\sin\theta_t = \left(a + \sqrt{b^2 - 4ac}\right)/(2a) \tag{2}$$

where

$$a = [2 + (1 - C_t)\sin\theta_a]^2 + (1 + C_t)^2\cos^2\theta_a \tag{3}$$

$$b = 2(1 + C_t)[2 + (1 - C_t)\sin\theta_a] \tag{4}$$

$$c = (1 + C_t)^2\sin^2\theta_a \tag{5}$$

The parabolic reflector length from its lower end C to any point P can be numerically calculated by:

$$\overline{CP} = \int_{\theta}^{0.5\pi}\sqrt{dx^2 + dy^2} = \sqrt{2}(1 + \sin\theta_a)\int_{\theta}^{0.5\pi}[1 - \cos(\theta + \theta_a)]^{-1.5}d\theta \tag{6}$$

The height of CPCs is given by:

$$h_t = \frac{0.5(C_t + 1)}{\tan\theta_t} \tag{7}$$

The θ_f, as shown in Fig. 1, stands for the angle at the incidence angle less than which the absorber of CPCs is fully irradiated and is given by:

$$\tan\theta_f = \frac{0.5(C_t - 1)}{h_t} = \frac{(C_t - 1)\tan\theta_t}{(C_t + 1)} \tag{8}$$

The θ_b, as shown in Fig. 2, is the angle at the incidence angle less than which both reflectors are fully irradiated. The θ_b is actually the angle formed by the tangent line passing through the upper end point of the reflector and the normal of CPCs' aperture, thus can be calculated based on Eq. (1) by:

$$\tan\theta_b = \left.\frac{dx}{dy}\right|_{\theta=\theta_t} = \frac{\cos\theta_a - \cos\theta_t}{\sin\theta_a + \sin\theta_t} \tag{9}$$

For full CPCs, $\theta_t = \theta_a$ and thus $\theta_b = 0$. As solar rays enter the CPC at $\theta_p > \theta_t$ (θ_p is the projection incidence angle of solar rays on the cross-section of CPC-trough, and is simply referred to as projection incidence angle in this work), the upper part of right (left) reflector is irradiated (see Fig. 7), and the polar angle of point E can be obtained after the lengthy mathematical derivation as follows:

$$\sin\theta_E = \left[BE + \sqrt{B^2E^2 - (D^2 + E^2)(B^2 - D^2)}\right]/(D^2 + E^2) \quad (\theta_t < \theta_p < 0.5\pi) \tag{10}$$

where

$$B = h_t - 0.5(C_t - 1)\mathrm{ctan}\theta_p;$$
$$D = 1 + \sin\theta_a + B\cos\theta_a;$$
$$E = B\sin\theta_a - (1 + \sin\theta_a)\mathrm{ctan}\theta_p.$$

Similarly, as solar rays enter CPCs at $\theta_b < \theta_p < \theta_f$, the lower part of left (right) reflector is irradiated (see Fig. 3), and the polar angle of point F can be calculated as follows:

$$\sin\theta_F = [B'E' + \sqrt{(B'E')^2 - (D'D' + E'E')(B'B' - D'D')}]/(D'D' + E'E') \quad (\theta_b < \theta_p < \theta_f) \tag{11}$$

in which

$$B' = h_t - 0.5(C_t + 1)\mathrm{ctan}\theta_p;$$
$$D' = 1 + \sin\theta_a + B'\cos\theta_a;$$
$$E' = B'\sin\theta_a - (1 + \sin\theta_a)\mathrm{ctan}\theta_p$$

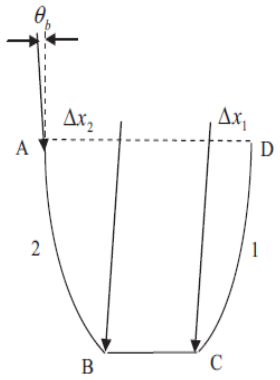

Fig. 2. Irradiation situation within CPCs for the case of $|\theta_p| \leqslant \theta_b$.

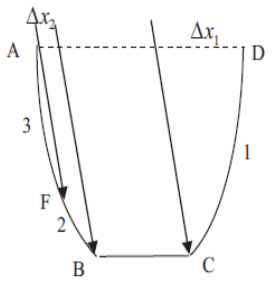

Fig. 3. Irradiation situation within CPCs in the cases of $\theta_b \leqslant |\theta_p| \leqslant \theta_f$ for CPCs with $\theta_f \leqslant \theta_a$ and $\theta_b < |\theta_p| \leqslant \theta_a$ for CPCs with $\theta_f > \theta_a$.

2.2. Optical efficiency factor contributed by beam radiation

When a beam of radiation enters the CPC with semi-diffuse reflectors at $\theta_p \leqslant \theta_a$, partial radiation incidence on reflectors undergoes specular reflections and then arrive on the absorber as beam radiation, the remaining undergoes diffuse reflections within the CPC cavity and only a small fraction will finally fall on the absorber. Thus, for such CPC, the radiation arriving on the absorber includes beam radiation (Q_b), arrived directly or from reflectors after specular reflections, and diffuse radiation (Q_d) from the reflectors after forth-back diffuse reflections within CPCs. Therefore, the optical efficiency factor of the CPC, $f(\theta_p)$, defined as the fraction of radiation incident on the aperture that arrives on the absorber, can be expressed by:

$$f(\theta_p) = \frac{Q_b + Q_d}{S_{ap}} = f_b(\theta_p) + f_d(\theta_p) \tag{12}$$

where S_{ap} is the radiation incidence on the aperture of CPCs; $f_b(\theta_p)$ is the optical efficiency factor contributed by beam radiation due to direct irradiation and specular reflections from reflectors, and $f_d(\theta_p)$ is the optical efficiency factor contributed by diffuse radiation due to diffuse reflections within CPCs. To simplify analysis, multiple specular reflections within the CPCs are not considered, and the one-reflection model is used to calculate $f_b(\theta_p)$ (Tang and Wang, 2013). For full CPCs (F-CPCs), the absorber will be fully irradiated as $|\theta_p| \leqslant \theta_f$ and partially irradiated in the case of $\theta_f < |\theta_p| \leqslant \theta_a$, therefore, the $f_b(\theta_p)$ can be easily obtained as follows (Tang and Wang, 2013):

$$f_b(\theta_p) = \begin{cases} \sin\theta_a + (1-\sin\theta_a)\rho_s & |\theta_p| \leqslant \theta_f \\ \rho_s + 0.5(1-\rho_s)(1+\sin\theta_a)(1-\tan|\theta_p|/\tan\theta_a) & \theta_f < |\theta_p| \leqslant \theta_a \\ 0 & |\theta_p| > \theta_a \end{cases} \tag{13}$$

where ρ_s is the specular reflectivity of CPC's reflectors. For truncated CPCs (T-CPCs) with $\theta_f \leqslant \theta_a$, a fraction of radiation will directly arrive on the absorber as $\theta_a < |\theta_p| < \theta_t$, and the remaining will escape from the CPC cavity after specular reflections; whereas for T-CPCs with $\theta_f > \theta_a$, in the case of $\theta_a < |\theta_p| \leqslant \theta_f$, the absorber will be fully irradiated, and radiation incidence on the lower part of the left (right) reflector (such as EB shown in Fig. 5) will arrive on the absorber after specular reflection, thus, $f_b(\theta_p)$ can be determined based on following two cases (Yu et al., 2014).

Case A: For T-CPCs with $\theta_f \leqslant \theta_a$

$$f_b(\theta_p) = \begin{cases} \rho_s + (1-\rho_s)/C_t & |\theta_p| \leqslant \theta_f \\ \rho_s + 0.5(1-\rho_s)(1+1/C_t)(1-\tan|\theta_p|/\tan\theta_t) & \theta_f < |\theta_p| \leqslant \theta_a \\ 0.5(1+1/C_t)(1-\tan|\theta_p|/\tan\theta_t) & \theta_a < |\theta_p| \leqslant \theta_t \\ 0 & |\theta_p| > \theta_t \end{cases} \tag{14}$$

Case B: For T-CPCs with $\theta_f > \theta_a$

$$f_b(\theta_p) = \begin{cases} \rho_s + (1-\rho_s)/C_t & |\theta_p| \leqslant \theta_a \\ 1/C_t + 0.5\rho_s(1-1/C_t) - h_t\rho_s\tan|\theta_p|/C_t & \theta_a < |\theta_p| \leqslant \theta_f \\ 0.5(1+1/C_t)(1-\tan|\theta_p|/\tan\theta_t) & \theta_f < |\theta_p| \leqslant \theta_t \\ 0 & |\theta_p| > \theta_t \end{cases} \tag{15}$$

2.3. Optical efficiency factor contributed by diffuse radiation

As solar rays incidence on semi-diffuse reflectors, partial radiation will undergoes forth-back diffuse reflections within the cavity of CPC, and a small fraction of diffuse radiation will finally fall on the absorber. To be convenient for the analysis, it is assumed that the radiation from reflectors after diffuse reflections is isotropic, incident solar rays evenly irradiate reflectors, and reflection from the absorber is neglected. With these assumptions together with the knowledge of two-dimensional diffuse radiation transfer, the mathematical procedure to calculate $f_d(\theta_p)$ can be derived. The $f_d(\theta_p)$ not only depends on the projection incidence angle θ_p but also depends on the solar irradiation situation within CPCs, thus depends on the structural parameters of CPCs such as θ_a and C_t. For truncated CPCs (T-CPCs) with $\theta_f \leqslant \theta_a$, the solar irradiation situation within CPCs is dependent on θ_p and classified into five cases: $|\theta_p| \leqslant \theta_b$, $\theta_b < |\theta_p| < \theta_f$, $\theta_f \leqslant |\theta_p| \leqslant \theta_a$, $\theta_a < |\theta_p| \leqslant \theta_t$ and $\theta_t < |\theta_p| < 0.5\pi$; whereas for T-CPCs with $\theta_f > \theta_a$, the solar irradiation situation is classified into another five cases: $|\theta_p| \leqslant \theta_b$, $\theta_b < |\theta_p| \leqslant \theta_a$, $\theta_a < |\theta_p| < \theta_f$, $\theta_f \leqslant |\theta_p| \leqslant \theta_t$ and $\theta_t < |\theta_p| < 0.5\pi$. For full CPCs (F-CPCs), $\theta_b = 0$ and $\theta_t = \theta_a$, thus, it is a special case of T-CPCs with $\theta_f \leqslant \theta_a$. In the consequent analysis, the mathematical expressions to calculate $f_d(\theta_p)$ will be respectively presented based on solar irradiation situations within CPCs.

2.3.1. For the case of $|\theta_p| \leqslant \theta_b$

As shown in Fig. 2, in the case of $|\theta_p| \leqslant \theta_b$, both reflectors 1 and 2 are fully irradiated, and the effective radiation from reflectors 1 and 2 can be expressed by:

$$J_1 = (S_1 + J_2F_{2\text{-}1})\rho_d \tag{16a}$$

$$J_2 = (S_2 + J_1F_{1\text{-}2})\rho_d \tag{16b}$$

where ρ_d is the diffuse reflectivity of reflectors (the total reflectivity $\rho = \rho_s + \rho_d$), J is the effective diffuse radiation from reflectors, S is the solar radiation incidence on reflectors, subscripts 1 and 2 are stands for reflector 1 and 2, respectively, F_{x-y} is the radiation transfer shape factor from surface x to surface y. In Eqs. (16a) and (16b), $F_{1\text{-}2} = F_{2\text{-}1}$ for the symmetric CPCs here, thus, one can obtain J_1 and J_2 as follows:

$$J_1 = (S_1 + S_2\rho_d)\rho_d F_{1\text{-}2}/(1 - F_{1\text{-}2}^2\rho_d^2) \quad (17a)$$

$$J_2 = (S_2 + S_1\rho_d)\rho_d F_{1\text{-}2}/(1 - F_{1\text{-}2}^2\rho_d^2) \quad (17b)$$

Thus one has

$$f_d(\theta_p) = (J_1 F_{1\text{-}BC} + J_2 F_{2\text{-}BC})/S_{ap} \quad (18)$$

In the above equation, shape factor $F_{1\text{-}BC} = F_{2\text{-}BC}$, and $f_d(\theta_p)$ can be found by substituting J_1 and J_2 into Eq. (18) as follows:

$$f_d(\theta_p) = \frac{\rho_d(1 + \rho_d F_{1\text{-}2})F_{1\text{-}BC}(S_1 + S_2)}{(1 - F_{1\text{-}2}^2\rho_d^2)S_{ap}} = \frac{\rho_d(1 + \rho_d F_{1\text{-}2})F_{1\text{-}BC}(1 - 1/C_t)}{(1 - F_{1\text{-}2}^2\rho_d^2)} \quad (19)$$

Based on the reciprocity relation of shape factors and the calculation method of two-dimensional shape factors described by Incropera and Dewitt (1996), one has:

$$F_{1\text{-}2} = \frac{AB}{\overline{CD}}F_{AB-CD} = \frac{2AC - 1 - C_t}{2\overline{CD}} = \frac{1 + C_t}{2\overline{CD}}(1/\sin\theta_t - 1) \quad (20)$$

$$F_{1\text{-}BC} = \frac{BC}{\overline{CD}}F_{BC-CD} = 0.5(h_t/\cos\theta_f - h_t/\cos\theta_t + 1)/\overline{CD} \quad (21)$$

where CD with a bar above ($\overline{CD}$) is the length of reflector CD, and can be calculated based on Eq. (6) by setting $\theta = \theta_t$.

2.3.2. For the cases of $\theta_b < |\theta_p| < \theta_f$ for CPCs with $\theta_f \leqslant \theta_a$ and $\theta_b < |\theta_p| \leqslant \theta_a$ for CPCs with $\theta_f > \theta_a$

As shown in Fig. 3, one reflector is fully irradiated, and the lower part of another reflector is irradiated. Effective radiation from reflectors 1, 2 and 3 can be expressed by:

$$J_1 = (S_1 + J_2 F_{2\text{-}1} + J_3 F_{3\text{-}1})\rho_d \quad (22a)$$

$$J_2 = (S_2 + J_1 F_{1\text{-}2} + J_3 F_{3\text{-}2})\rho_d \quad (22b)$$

$$J_3 = (J_1 F_{1\text{-}3} + J_2 F_{2\text{-}3})\rho_d \quad (22c)$$

By solving the above equation group, one has:

$$J_1 = A_1 S_1 + B_1 S_2 \quad (23a)$$

$$J_2 = BA_1 S_1 + (A + BB_1)S_2 \quad (23b)$$

$$J_3 = DA_1 S_1 + (C + DB_1)S_2 \quad (23c)$$

where

$$A = \rho_d/(1 - F_{2\text{-}3}F_{3\text{-}2}\rho_d^2);$$
$$B = (\rho_d F_{1\text{-}2} + F_{1\text{-}3}F_{3\text{-}2}\rho_d^2)/(1 - F_{2\text{-}3}F_{3\text{-}2}\rho_d^2);$$
$$C = F_{2\text{-}3}\rho_d^2/(1 - F_{2\text{-}3}F_{3\text{-}2}\rho_d^2);$$
$$D = (\rho_d F_{1\text{-}3} + F_{1\text{-}2}F_{2\text{-}3}\rho_d^2)/(1 - F_{2\text{-}3}F_{3\text{-}2}\rho_d^2) \quad (24)$$
$$A1 = \rho_d/[1 - (BF_{2\text{-}1} + DF_{3\text{-}1})\rho_d];$$
$$B1 = \rho_d(AF_{2\text{-}1} + CF_{3\text{-}1})/[1 - (BF_{2\text{-}1} + DF_{3\text{-}1})\rho_d]$$
And $f_d(\theta_p) = (J_1 F_{1\text{-}BC} + J_2 F_{2\text{-}BC} + J_3 F_{3\text{-}BC})/S_{ap}$

Substituting Eqs. (23a)–(23c) into Eq. (24) obtains:

$$f_d(\theta_p) = (A_2 S_1 + B_2 S_2)/S_{ap} = (A_2\Delta x_1 + B_2\Delta x_2)/C_t \quad (25)$$

where

$$\Delta x_1 = 0.5(C_t - 1) + h_t\tan\theta_p \quad (26a)$$

$$\Delta x_2 = 0.5(C_t - 1) - h_t\tan\theta_p \quad (26b)$$

$$A_2 = A_1(F_{1\text{-}BC} + BF_{2\text{-}BC} + DF_{3\text{-}BC}) \quad (27a)$$

$$B_2 = B_1 F_{1\text{-}BC} + (A + BB_1)F_{2\text{-}BC} + (C + DB_1)F_{3\text{-}BC} \quad (27b)$$

where $F_{1\text{-}BC}$ is calculated by Eq. (21). Based on reciprocity relation of shape factors and calculation method of two-dimensional shape factors, one obtains:

$$F_{1\text{-}2} = F_{FB-CD}FB/\overline{CD}; \quad F_{2\text{-}1} = F_{FB-CD}FB/\overline{FB}$$
$$F_{1\text{-}3} = F_{AF-CD}AF/\overline{CD}; \quad F_{3\text{-}1} = F_{AF-CD}AF/\overline{AF}$$
$$F_{2\text{-}3} = F_{AF-FB}AF/\overline{FB}; \quad F_{3\text{-}2} = F_{AF-FB}AF/\overline{AF}$$
$$F_{2\text{-}BC} = F_{BC-FB}BC/\overline{FB}; \quad F_{3\text{-}BC} = F_{BC-AF}BC/\overline{AF}$$

and

$$F_{FB-CD} = 0.5(BD - DF + CF - BC)/BF$$
$$F_{AF-CD} = 0.5(DF - AD + AC - CF)/AF$$
$$F_{AF-FB} = 0.5(BF - AB + AF)/AF$$
$$F_{BC-FB} = 0.5(BF - CF + BC)/BC$$
$$F_{BC-AF} = 0.5(AB - AC + CF - BF)/BC$$

In the above expressions, $BC = 1$, $AD = C_t$, $\overline{XY}$ stands for the reflector length from X to Y. Given C_t, θ_a and θ_p, the coordinate of F can be calculated from Eq. (11), and then AF, BF, CF and DF can be easily calculated, $\overline{AF}$ also can be calculated based on Eq. (6).

2.3.3. For the case of $\theta_f \leqslant |\theta_p| \leqslant \theta_a$ for CPCs with $\theta_f \leqslant \theta_a$

In this case, one of reflector (such as the right reflector as shown in Fig. 4) is fully irradiated and another reflector is fully shaded by itself, thus the effective radiation from both reflectors can be expressed by:

$$J_1 = (S_1 + J_2 F_{2\text{-}1})\rho_d \quad (28a)$$

$$J_2 = J_1 F_{1\text{-}2}\rho_d \quad (28b)$$

where $F_{1\text{-}2} = F_{2\text{-}1}$ and is given by Eq. (20). By solving the above equation group, one obtains J_1 and J_2, then substituting them into Eq. (18) obtains:

$$f_d(\theta_p) = \frac{\rho_d(1 + \rho_d F_{1\text{-}2})F_{1\text{-}BC}\Delta x_1}{(1 - F_{1\text{-}2}^2\rho_d^2)C_t} \quad (29)$$

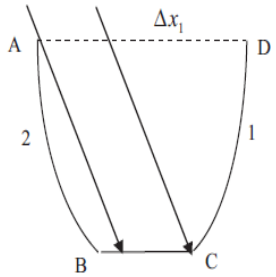

Fig. 4. Irradiation situation within CPCs in the cases of $\theta_f \leqslant |\theta_p| \leqslant \theta_a$ for CPCs with $\theta_f \leqslant \theta_a$.

where $\Delta x_1 = C_t - h_t(\tan\theta_t - \tan\theta_p)$, and $F_{1\text{-}BC}$ is given by Eq. (21).

2.3.4. For the case of $\theta_a < |\theta_p| \leqslant \theta_f$ for CPCs with $\theta_f > \theta_a$

As seen in Fig. 5, in this case, one reflector (such as right reflector) is fully irradiated, but only the lower part of another one is irradiated. When solar rays strike on the right reflector, all rays will arrive on the left reflector after specular reflection, then part of radiation specularly reflected from the left reflector directly escapes from the CPC cavity and the remaining returns back to the right reflector once again then escapes from the CPC cavity after specular reflection. To simplify analysis, it is assumed that solar rays striking on the right reflector will evenly irradiate the left reflector after specular reflection and then escape from the CPC cavity without considering a further specular reflection from one reflector to another reflector, thus one has:

$$J_1 = (S_1 + J_2F_{2\text{-}1} + J_3F_{3\text{-}1})\rho_d \tag{30a}$$

$$J_2 = (S_2 + S_1\rho_s\overline{FB}/\overline{AB} + J_1F_{1\text{-}2} + J_3F_{3\text{-}2})\rho_d \tag{30b}$$

$$J_3 = (S_1\rho_s\overline{FA}/\overline{AB} + J_1F_{1\text{-}3} + J_2F_{2\text{-}3})\rho_d \tag{30c}$$

By solving above equation group, one obtains J_1, J_2 and J_3, then substituting them into Eq. (24) obtains:

$$f_d(\theta_p) = (A_2'\Delta x_1 + B_2\Delta x_2)/C_t \tag{31}$$

where

$$A_2' = A_1'(F_{1\text{-}BC} + BF_{2\text{-}BC} + DF_{3\text{-}BC}) + \rho_s(EF_{2\text{-}BC} + FF_{3\text{-}BC})$$

$$A_1' = \frac{\rho_d(1+E\rho_sF_{2\text{-}1}+F\rho_sF_{3\text{-}1})}{1-(BF_{2\text{-}1}+DF_{3\text{-}1})\rho_d} \quad E = \frac{\rho_d(\overline{FB}+F_{3\text{-}2}\rho_d\overline{FA})}{(1-F_{2\text{-}3}F_{3\text{-}2}\rho_d^2)\overline{AB}}$$

$$F = \frac{\rho_d(\overline{FA}+F_{2\text{-}3}\rho_d\overline{FB})}{(1-F_{2\text{-}3}F_{3\text{-}2}\rho_d^2)\overline{AB}}$$

In above expressions, calculations of shape factors and parameters B, D and B_2 are the same as those in the section of 2.3.2.

2.3.5. For the cases of $\theta_a < |\theta_p| \leqslant \theta_t$ for CPCs with $\theta_f \leqslant \theta_a$ and $\theta_f \leqslant |\theta_p| \leqslant \theta_t$ for CPCs with $\theta_f > \theta_a$

In this case, one reflector is fully irradiated and another one is fully shaded (see Fig. 6). When solar rays strike on the right reflector, all rays will arrive on the left reflector after specular reflection, therefore one has:

$$J_1 = (S_1 + J_2F_{2\text{-}1})\rho_d \tag{32a}$$

$$J_2 = (S_1\rho_s + J_1F_{1\text{-}2})\rho_d \tag{32b}$$

In the above equations, $F_{1\text{-}2} = F_{2\text{-}1}$. By solving above equation group, one obtains J_1 and J_2, then substituting them into Eq. (18) obtains:

$$f_d(\theta_p) = \frac{\rho_d(1+\rho_s)(1+\rho_dF_{1\text{-}2})F_{1\text{-}BC}\Delta x_1}{(1-F_{1\text{-}2}^2\rho_d^2)C_t} \tag{33}$$

Δx_1 here is the same as that in the section of 2.3.3.

2.3.6. For the case of $\theta_t < |\theta_p| < 0.5\pi$

In this case, the upper part of one reflector is irradiated and the other one is fully shaded by itself as shown in Fig. 7, all radiation striking on one reflector will arrive on the opposite reflector after specular reflection, thus, one has:

$$J_1 = (S_{ap} + J_2F_{2\text{-}1} + J_3F_{3\text{-}1})\rho_d \tag{34a}$$

$$J_2 = (S_{ap}\rho_s + J_1F_{1\text{-}2} + J_3F_{3\text{-}2})\rho_d \tag{34b}$$

$$J_3 = (J_1F_{1\text{-}3} + J_2F_{2\text{-}3})\rho_d \tag{34c}$$

By solving the above equation group, one obtains J_1, J_2 and J_3, then substituting them into Eq. (24) obtains:

$$f_d(\theta_p) = A_4F_{1\text{-}BC} + A_5F_{2\text{-}BC} + A_6F_{3\text{-}BC} \tag{35}$$

where

$$A_4 = \rho_d(1 + \rho_sA + \rho_sCF_{3\text{-}1})/[1 - (BF_{2\text{-}1} + DF_{3\text{-}1})\rho_d]$$

$$A_5 = \rho_sA + BA_4$$

$$A_6 = \rho_sC + DA_4$$

The mathematical expressions of A, B, C and D here are the same as those in the Section 2.3.2, $F_{2\text{-}BC}$ in Eq. (35) is the same as $F_{1\text{-}BC}$ in the Section 2.3.1. Given θ_p, θ_a and C_t, the coordinate of point E (see Fig. .7) can be calculated based on Eqs. (1) and (10), then the length of AE, BE, CE, DE and $\overline{DE}$ can be calculated, finally shape factors are calculated as follows:

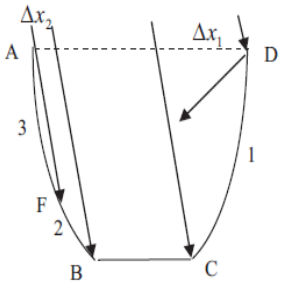

Fig. 5. Irradiation situation within CPCs in the case of $\theta_a < |\theta_p| \leqslant \theta_f$ for CPCs with $\theta_f > \theta_a$.

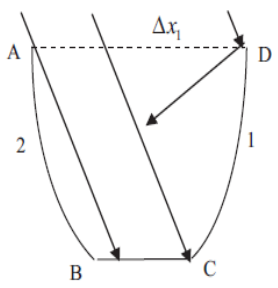

Fig. 6. Irradiation situation within CPCs in the cases of $\theta_a < |\theta_p| \leqslant \theta_t$ for CPCs with $\theta_f \leqslant \theta_a$ and $\theta_f \leqslant |\theta_p| \leqslant \theta_t$ for CPCs with $\theta_f > \theta_a$.

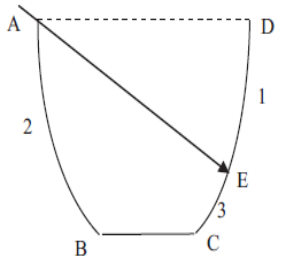

Fig. 7. Irradiation situation within CPCs in the case of $\theta_t < |\theta_p| < 0.5\pi$.

$$F_{1\text{-}2} = ABF_{AB-DE}/\overline{DE} = 0.5(AE - BE + BD - C_t)/\overline{DE};$$
$$F_{2\text{-}1} = ABF_{AB-DE}/\overline{AB} = 0.5(AE - BE + BD - C_t)/\overline{AB};$$
$$F_{1\text{-}3} = CEF_{CE-DE}/\overline{DE} = 0.5(ED - DC + EC)/\overline{DE};$$
$$F_{3\text{-}1} = CEF_{CE-DE}/\overline{CE} = 0.5(ED - DC + EC)/\overline{CE};$$
$$F_{2\text{-}3} = CEF_{CE-AB}/\overline{AB} = 0.5(BE - 1 + AC - AE)/\overline{AB};$$
$$F_{3\text{-}2} = CEF_{CE-AB}/\overline{CE} = 0.5(BE - 1 + AC - AE)/\overline{CE};$$
$$F_{1\text{-}BC} = BCF_{BC-DE}/\overline{DE} = 0.5(DC - BD + BE - EC)/\overline{DE};$$
$$F_{3\text{-}BC} = BCF_{BC-CE}/\overline{CE} = 0.5(EC - BE + 1)/\overline{CE}$$

Given θ_a, C_t, ρ_s and ρ_d, the angular variation of $f_d(\theta_p)$ and $f(\theta_p)$ can be obtained based on mathematical expressions in this work. As seen from Figs. 8–10, given ρ and θ_p, $f_d(\theta_p)$ increases with the increase of diffuse reflectivity (ρ_d) as expected, but the optical efficiency factor, $f(\theta_p)$, decreases. It is also seen that $f_d(\theta_p)$ is very small as compared with $f(\theta_p)$, indicating that the contribution of diffuse radiation due to diffuse reflections within CPCs to the radiation concentration of CPCs is considerably low as a result of fact that the shape factor from the reflectors to the absorber $(F_{1\text{-}BC})$ is very small, such as for F-CPC with $\theta_a = 26°$, $F_{1\text{-}BC} = 0.098$; and for T-CPC with $\theta_a = 20°$, $F_{1\text{-}BC} = 0.086$ for $C_t = 2.8$ and 0.143 for $C_t = 2$. It is also observed that sudden changes of $f_d(\theta_p)$ occur as $\theta_p = \theta_f$ and $\theta_p = \theta_a$ for F-CPC, and as θ_p being θ_f, θ_a and θ_t for T-CPCs, a result of sudden changes of the solar irradiation situation within CPCs when solar rays enter CPCs at the angle near these values.

3. Ray-tracing analysis

To investigate the effect of diffuse reflections on solar flux distribution on the absorber of CPCs, Tracepro software was employed to simulate the flux distribution and analyze the optical efficiency factors. To perform ray-tracing analysis, a physical model of CPCs is constructed by Tracepro first, then a set of parameters, such as specular and diffuse reflectivity of reflectors, solar intensity and incidence angle, are input.

As shown in Fig. 11, for CPCs with perfect diffuse reflectors ($\rho_d = 0.9$ and $\rho_s = 0$), the flux distributions on the absorber are almost uniform, but for CPCs with perfect specular reflectors ($\rho_s = 0.9$ and $\rho_d = 0$), it is non-uniform; whereas for CPCs with semi-diffuse reflectors, the flux distribution patterns are the same as CPCs with perfect specular reflectors ($\rho_s = 0.9$ and $\rho_d = 0$). This implies that the use of semi-diffuse reflectors in a CPC can not make solar flux on the absorber of CPCs more uniform except using perfect diffuse reflectors, but in turn it leads the optical efficiency factor decrease.

Comparison of the optical efficiency factors between theoretically expected and those obtained by ray-tracing simulation is presented in Fig. 12. It is seen that optical efficiency factors obtained by theoretical calculations almost completely agree with those obtained by ray-tracing simulation for the CPC with perfect diffuse reflectors ($\rho_d = 0$ and $\rho_s = 0.9$), and theoretically expected $f(\theta_p)$ are about 0.01 higher than those obtained by ray-tracing simulation for the CPC with semi-diffuse reflectors ($\rho_d = 0.2$ and $\rho_s = 0.7$). This indicates that the mathematical model developed in this work can accurately predict the optical efficiency factors of CPCs with semi-diffuse reflectors.

4. Effects of diffuse reflection on the energy collection of CPCs

Assuming that CPC-troughs are oriented in the east–west direction with the aperture being inclined at β from the horizon, the length of the CPC-trough is infinite as compared to the width of the aperture, and radiation

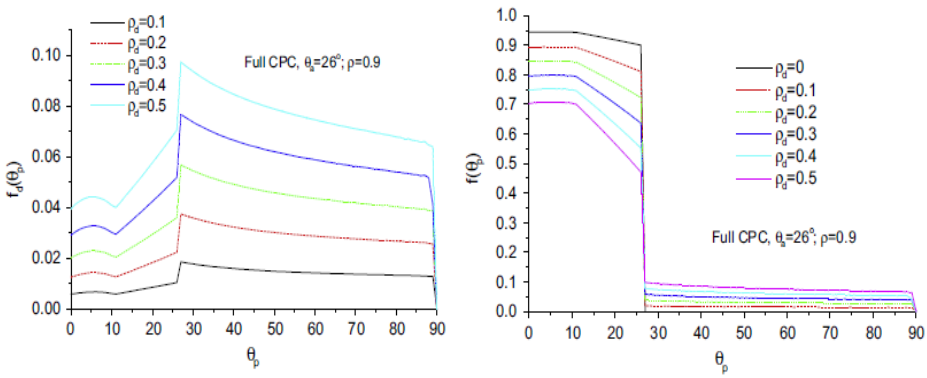

Fig. 8. The angular dependence of $f(\theta_p)$ and $f_d(\theta_p)$ for F-CPC with $\theta_a = 26°$.

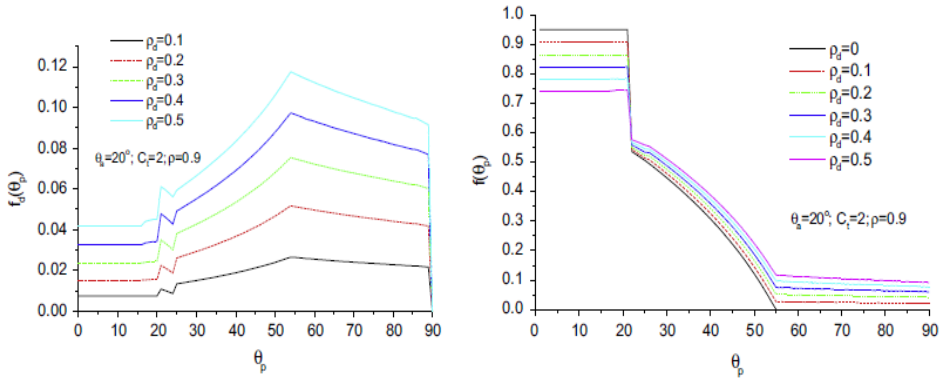

Fig. 9. The angular dependence of $f(\theta_p)$ and $f_d(\theta_p)$ for T-CPC with $\theta_a = 20^\circ$ and $C_t = 2$.

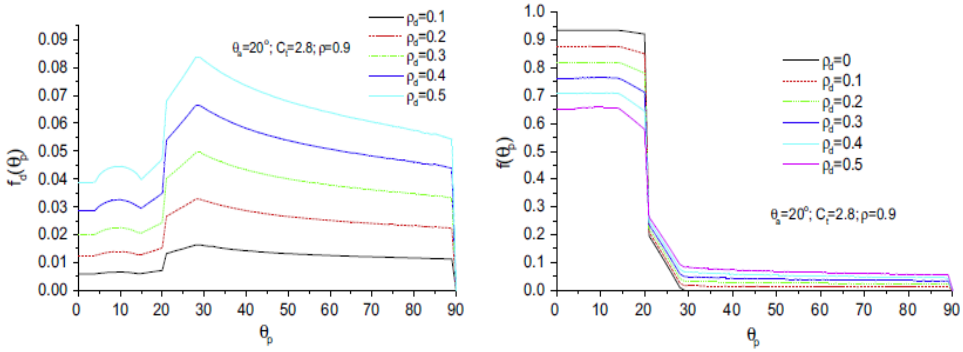

Fig. 10. The angular dependence of $f(\theta_p)$ and $f_d(\theta_p)$ for T-CPC with $\theta_a = 20^\circ$ and $C_t = 2.8$.

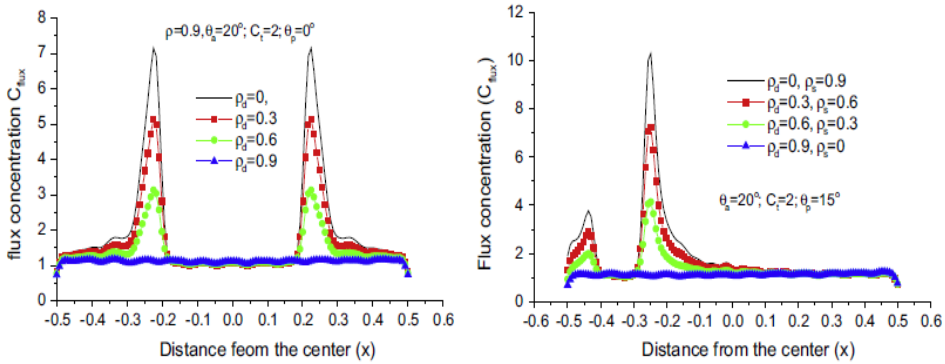

Fig. 11. Flux distribution on the absorber of T-CPC with $\theta_a = 20^\circ$ and $C_t = 2$ for $\theta_p = 0$ and 15°.

reflected from the ground is not considered. To be convenient for calculations, width of the receiver is set to be 1. Thus, solar radiation received by unit area of the CPC's receiver at any moment for isotropic sky diffuse radiation can be expressed by:

$$I_{abs} = C_t I_b f(\theta_{in}) f(\theta_p) \cos\theta_{in} + C_t \int_{-(0.5\pi-\beta)}^{0.5\pi} if\ (\theta_p) \cos\theta_p d\theta_p \tag{36}$$

where i is the directional intensity of sky diffuse radiation on the cross-section of CPC troughs, for CPCs oriented in the east–west direction, $i = 0.5 I_d$ (Tang and Liu, 2011), and I_d is the instantaneous sky diffuse radiation on the horizon. Therefore, Eq. (36) can be simplified as:

$$I_{abs} = C_t I_b f(\theta_{in}) f(\theta_p) \cos\theta_{in} + C_t I_d C_d \tag{37}$$

where

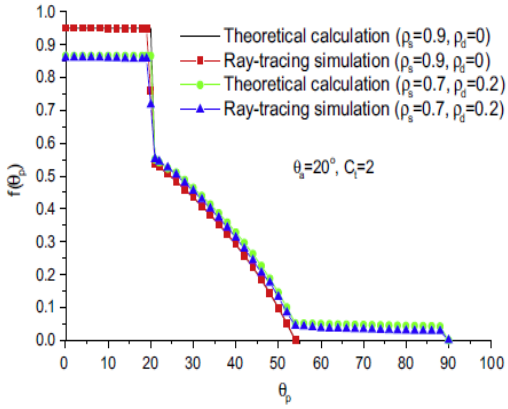

Fig. 12. Comparison of $f(\theta_p)$ between theoretically expected and expected by ray-tracing simulation.

$$C_d = 0.5\left[\int_0^{0.5\pi} f(\theta_p)\cos\theta_p d\theta_p + \int_0^{0.5\pi-\beta} f(\theta_p)\cos\theta_p d\theta_p\right] \tag{38}$$

θ_{in} in Eqs. (36) and (37) is the real incidence angle of solar rays on the aperture of CPCs and is calculated by:

$$\cos\theta_{in} = (\cos\delta\cos\omega\cos\lambda + \sin\delta\sin\lambda)\cos\beta + (\cos\delta\cos\omega\sin\lambda - \sin\delta\cos\lambda)\sin\beta \tag{39}$$

where ω is the solar hour angle measuring from the solar-noon to afternoon, λ is the site latitude, and δ is the declination of the sun. $f(\theta_{in})$ in Eqs. (36) and (37) is a control function, being 1 for the case of $\cos\theta_{in} > 0$ otherwise zero. The projection incidence angle of solar rays on the cross-section of east–west aligned CPC-troughs is expressed by (Tang et al., 2010;Tang and Yu, 2010; Yu et al., 2014):

$$\theta_p = |\beta + \theta_{xoz}| \tag{40}$$

$$\tan\theta_{xoz} = \frac{\sin\delta\cos\lambda - \cos\delta\sin\lambda\cos\omega}{\cos\delta\cos\lambda\cos\omega + \sin\delta\sin\lambda} \tag{41}$$

Daily radiation collected by unit area of CPCs' absorber can be calculated by integrating Eq. (37) over the daytime, i.e.:

$$H_{abs} = C_t\int_{-t_0}^{t_0} f(\theta_{in})f(\theta_p)I_b\cos\theta_{in}dt + C_tH_dC_d \tag{42}$$

And daily radiation on unit area of the CPC's aperture is as follows:

$$H_{ap} = \int_{-t_0}^{t_0} f(\theta_{in})I_b\cos\theta_{in}dt + 0.5H_d(1+\cos\beta) \tag{43}$$

where H_d is the daily sky diffuse radiation on the horizon, $t_0 = \tau_{day}\omega_0/2\pi$ is the sunset time on the horizon, τ_{day} is the day length, and the sunset hour angle on the horizon, ω_0 is the hour angle of sunset on the horizon and determined by the declination of the sun, and δ is determined by the day number counting from the first day of a year (Rabl, 1985).

For a specific east–west aligned CPC inclined at β from the horizon, C_d can be numerically calculated by Eq. (38). At any moment of a day, θ_p and θ_{in} can be calculated, and then optical efficiency factor $f(\theta_p)$ can be determined based on mathematical expressions presented in this work. Therefore, knowing the time variation of I_b and daily sky diffuse radiation (H_d) on the horizon, daily solar gain H_{abs} and H_{ap} can be calculated by numerically integrating Eqs. (42) and (43) over the daytime, then summing H_{abs} and H_{ap} in all days of a year obtain the annual radiation collected by CPCs' receiver and aperture, respectively, and finally the annual average optical concentration of CPCs (C_{opt}), a ratio of annual radiation received by unit area of absorber to that by unit area of the aperture of CPCs, can be obtained.

Given monthly horizontal radiation of a month, the monthly average daily radiation on the horizon, H_h, can be simply calculated by dividing monthly value by days of the month, and then the monthly average daily diffuse radiation, H_d, the instantaneous bean radiation (I_b) can be estimated based on correlations suggested by Collares-Pereira and Rabl (1979).

In the consequent calculations of the daily solar gain, the time step for calculating daily radiation collected by CPCs is taken to 1 min, and the monthly horizontal radiation data used in this work is taken from the book edited by Chen (2001). To investigate effect of diffuse reflection on the energy collection of CPCs in terms of annual average optical concentration, east–west aligned CPCs with the tilt angle of the aperture being yearly fixed and yearly adjusted four times at three tilts are considered. For CPCs with the tilt angle being yearly fixed (1T-CPC), the tilt-angle of CPC's aperture is fixed at the site latitude, and the acceptance half-angle is set to be 26° (Tang et al., 2010). Whereas for CPCs with the tilt-angle being yearly adjusted four times at three tilts (3T-CPC), the tilt-angle of the aperture is set to be site latitude (λ) during periods of 22 days before and after both equinoxes, and adjusted to $\lambda + 24°$ and $\lambda - 24°$ in winters and summers, respectively (Tang and Liu, 2011). In addition, four sites with typical climatic conditions (Beijing: dry land with

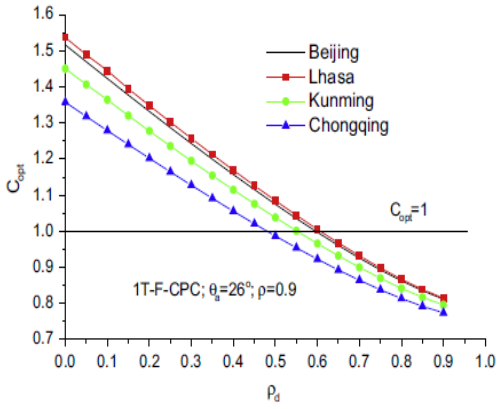

Fig. 13. Effect of ρ_d on C_{opt} for 1T-F-CPC with a given ρ.

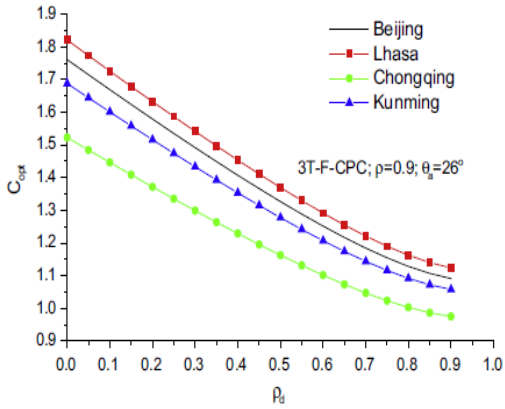

Fig. 14. Effect of ρ_d on C_{opt} for 3T-F-CPC with a given ρ.

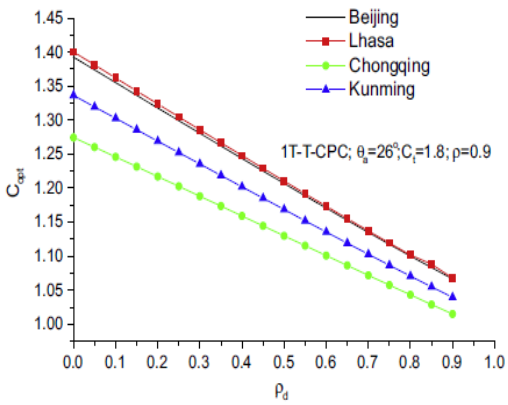

Fig. 15. Effect of ρ_d on C_{opt} for 1T-T-CPC with a given ρ.

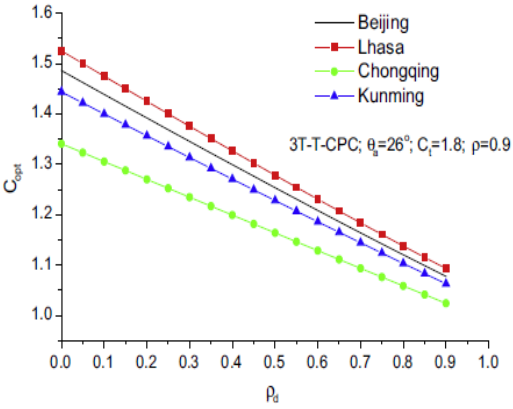

Fig. 16. Effect of ρ_d on C_{opt} for 3T-T-CPC with a given ρ.

abundant solar resource; Lhasa: highland with extremely abundance radiation; Chongqing: a site with poor solar resource; Kunming: characterized by rainy summers and sunny winters) are selected for the analysis.

Effects of diffuse reflectivity (ρ_d) on the annual average optical concentration (C_{opt}) of full CPCs (F-CPC) are presented in Figs. 13 and 14. It is seen that, given the total reflectivity (ρ), the C_{opt} decreases with the increase in ρ_d,

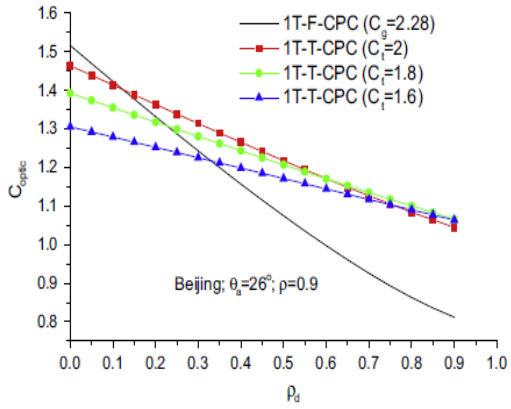

Fig. 17. Effect of ρ_d on C_{opt} for 1T-CPC with a given ρ but different C_t.

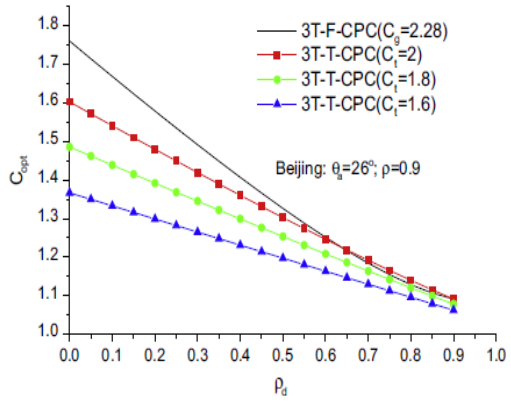

Fig. 18. Effect of ρ_d on C_{opt} for 3T-CPC with a given ρ but different C_t.

this implies that, the use of semi-diffuse reflectors in CPCs will lower its optical performance in terms of C_{opt}. For CPCs with the tilt-angle of the aperture being yearly fixed, the C_{opt} are even less than 1 as $\rho_d > 0.5$, indicating that the use of 1T-F-CPC with a high diffuse reflectivity is meaningless for radiation concentration.

Figs. 15 and 16 present effects of ρ_d on C_{opt} of truncated CPCs (T-CPC). It is also found that C_{opt} decreases with the increase in ρ_d, for T-CPCs with a higher ρ_d, the C_{opt} is close to 1, meaning that the contribution of CPCs with a high diffuse reflectivity to the energy collection of a receiver is limited.

Effect of ρ_d on C_{opt} for 1T and 3T-CPCs with a given ρ but different C_t are shown in Figs. 17 and 18, respectively. It is shown that C_{opt} decrease with the increase in ρ_d, the larger the geometric concentration (C_t), the faster the rate of such decrease, a result of the fact that the larger the geometric concentration, the smaller the shape factor from the reflectors to the absorber.

5. Conclusions

Ray-tracing analysis shows that the use of semi-reflectors in CPCs with the one-sided flat absorber

can not make solar flux on the absorber more uniform except using perfect diffuse reflectors, in turn it leads the optical efficiency factors decrease. Theoretical analysis shows that the optical efficiency factor contributed by diffuse radiation due to diffuse reflections within CPCs not only depends on the projection incidence angle of solar rays on the cross-section of CPC-troughs and diffuse reflectivity of reflectors but also depends on the structural parameters of CPCs such as acceptance half-angle, geometric concentration. For a given CPC with a given total reflectivity of reflectors, the optical efficiency factor decreases with the increase of diffuse reflectivity. Comparisons of the optical efficiency factors between expected from theoretical calculations and those from the ray-tracing analysis indicate that the mathematical model proposed in this work can accurately estimate the optical efficiency factor of such CPC. Theoretical calculations show that the contribution of diffuse reflections to the radiation concentration of CPCs is considerably low as a result of fact that the radiation transfer shape factor from the reflectors to the absorber is very small, and the diffuse reflectivity of reflectors has a considerable effect on the annual energy collection of CPCs, the higher the diffuse reflectivity, the lower the annual average optical concentration.

Acknowledgements

This work is partial fulfillment of funded research program 51466016, financially supported by National Natural Science Foundation of China.

References

Brogren, M., Wennerberg, J., Kapper, R., Karlsson, B., 2003. Design of concentrating elements with CIS thin-film solar cells for façade integration. Sol. Energy Mater. Sol. Cells 75, 567–575.

Chen, Z.Y., 2001. The Climatic Summarization of Yunnan. Weather Publishing House, Beijing.

Collares-Pereira, M., Rabl, A., 1979. The average distribution of solar radiation: correlations between diffuse and hemispherical and between hourly and daily insolation values. Sol. Energy 22, 155–164.

Firdaus, M.S., Siti, H.A.B., Roberto, R.I., Scott, G.B.G.S., Abu, B.M., Ruzairi, A.R., 2013. Performance analysis of a mirror symmetrical dielectric totally internally reflecting concentrator for building integrated photovoltaic systems. Appl. Energy 111, 288–299.

Hatwaambo, S., Hakansson, H., Nilsson, J., Karlsson, B., 2008. Angular characterization of low concentrating PV–CPC using low-cost reflectors. Sol. Energy Mater. Sol. Cells 92, 1347–1351.

Hatwaambo, S., Hakansson, H., Roos, A., Karlsson, B., 2009. Mitigating the non-uniform illumination in low concentrating CPCs using structured reflectors. Sol. Energy Mater. Sol. Cells 93 (11), 2020–2024.

Incropera, F.P., Dewitt, D.P., 1996. Fundamentals of Heat Transfer. Wiley, New York.

Mallick, T.K., Eames, P.C., Hyde, T.J., Norton, B., 2004. The design and experimental characterization of an asymmetric compound parabolic photovoltaic concentrator for building facade integration in the UK. Sol. Energy 77, 319–327.

Mallick, T.K., Eames, P.C., Norton, B., 2006. Non-concentrating and asymmetric compound parabolic concentrating building facade integrated photovoltaic: an experimental comparison. Sol. Energy 80, 834–849.

Rabl, A., 1985. Active Solar Collectors and their Applications. Oxford University Press, Oxford.

Robert, M.C., 2005. Concentrator photovoltaic technologies: review and market prospects. Refocus 6 (4), 35–39.

Tang, R.S., Wu, M.G., Yu, Y.M., Li, M., 2010. Optical performance of fixed east–west aligned CPCs used in China. Renew. Energy 35 (8), 1837–1841.

Tang, R.S., Yu, Y.M., 2010. Feasibility and optical performance of one axis three positions sun-tracking polar-axis aligned CPCs for photovoltaic applications. Sol. Energy 84, 1666–1675.

Tang, R.S., Liu, X.Y., 2011. Optical performance and design optimization of V-trough concentrators for photovoltaic applications. Sol. Energy 85, 2154–2166.

Tang, R.S., Wang, J.F., 2013. A note on multiple reflections of radiation within CPCs and its effect on calculations of energy collection. Renew. Energy 57, 490–496.

Yu, Y.M., Liu, N.Y., Tang, R.S., 2014. Optical performance of CPCs for concentrating solar radiation on flat receivers with a restricted incidence angle. Renew. Energy 62, 679–688.

Journal of Alloys and Compounds 648 (2015) 930–936

Contents lists available at ScienceDirect

Journal of Alloys and Compounds

journal homepage: http://www.elsevier.com/locate/jalcom

Counter electrodes from Mo–Se nanosheet alloys for bifacial dye-sensitized solar cells

Peizhi Yang [a, **, 1], Zhiyuan Zhao [b, 1], Ling Zhu [b], Qunwei Tang [b, *]

[a] Key Laboratory of Advanced Technique & Preparation for Renewable Energy Materials, Ministry of Education, Yunnan Normal University, Kunming 650500, PR China
[b] Institute of Materials Science and Engineering, Ocean University of China, Qingdao 266100, PR China

ARTICLE INFO

Article history:
Received 13 April 2015
Received in revised form
17 June 2015
Accepted 10 July 2015
Available online 15 July 2015

Keywords:
Dye-sensitized solar cell
Transparent counter electrode
Binary alloy
Molybdenum selenide

ABSTRACT

Pursuit of cost-effective counter electrodes (CEs) with no sacrifice of photovoltaic performances is a persistent objective for dye-sensitized solar cells (DSSCs). We launch here the experimental realization of molybdenum selenide (Mo–Se) binary nanosheet CEs by a mild solution method. Due to high optical transparency, the bifacial DSSCs from cost-effective Mo–Se alloy CEs can realize electricity generation from either front or rear side. Particularly, the resultant Mo–Se alloy CEs show superior catalytic activity and charge-transfer ability toward I^-/I_3^- redox electrolyte. The maximum front and rear efficiencies of 8.05% and 5.92% are recorded under simulated air mass 1.5 global irradiation, respectively. The impressive efficiency along with fast start-up, multiple start capability, and simple preparation highlights the potential application of the cost-effective and transparent Mo–Se alloy CE in robust bifacial DSSCs.

1. Introduction

Thin film solar cells are promising devices for cost-effective, environmentally compatible, and large-scale solar energy conversion as alternatives to silicon solar cells [1–3]. Among excitonic cells, dye-sensitized solar cell (DSSC) created in 1991 by Grätzel is a widely studied and longstanding candidate for future energy generation benefiting from cost-effective materials, facile manufacturing methods, high theoretical photovoltaic performances, and low energy expenditure [4–10]. Despite the fact that a maximum efficiency of 13% has been recorded on the optimized DSSC [11], the intrinsic limitation in charge transport is still a gigantic barrier for bringing down the cost of solar-to-electric conversion. A golden rule in solar cell design is to enhance light harvest for photosensitizer excitation and therefore electron production [12]. A strategy of illuminating the DSSC from either side may be promising for cost-effective solar energy utilization [13]. In this fashion, the optical transparency of a counter electrode (CE) in visible-light region is the main issue in designing such a bifacial DSSC [14–17]. Except for high cost, the preferred Pt CE has metallic luster and can reflect incident light on its surface, emerging a low rear efficiency under rear irradiation [13]. Therefore, how to reduce costs by reducing Pt loadings or replacing Pt without loss of photovoltaic performances is the crucial subject of most current CE catalyst research studies. Although colored and transparent species such as polyaniline [18,19], poly(3,4-ethylenedioxythiophene) [20], and graphene [21] are promising candidates for Pt CE, their stabilities and catalytic activities are still modest in developing efficient bifacial DSSCs [22].

Alloys have attracted increasing interest in the quest to develop advanced electrocatalysts. An inspiration is aroused from the alloy catalysts for fuel cells [23–25], where Pt is always alloyed with other transition metals, giving an enhanced catalytic activity for fuels. To the best our knowledge, there are no systematic ageing studies on bifacial DSSCs by combining the merits of cost-effectiveness, optical transparent, and electrocatalytic activity in a CE in other groups. In the current work, we launch an experimental realization of transparent and cost-effective molybdenum selenide (Mo–Se) alloy electrodes on fluorine-doped tin oxide (FTO) glass by a mild solution strategy for bifacial DSSC applications. An original intention of this design is to create Mo–Se alloy CEs having high optical transparency, charge-transfer ability, and electrocatalytic activity. The optimal efficiencies of 8.05% and 5.92% are measured for front and rear irradiations at a simulated air mass 1.5 global (AM1.5G) sunlight, respectively.

* Corresponding author.
** Corresponding author.
E-mail addresses: pzhyang@hotmail.com (P. Yang), tangqunwei@ouc.edu.cn (Q. Tang).
[1] The authors have equal contributions.

http://dx.doi.org/10.1016/j.jallcom.2015.07.082
0925-8388/

2. Experimental

2.1. Synthesis of transparent Mo–Se alloy CEs

The feasibility of synthesizing Mo–Se alloy CEs was confirmed by the experimental procedures: A mixing aqueous solution consisting of Se powders and $MoCl_5$ at stoichiometric ratios was made by agitating 0.0095 g of Se ultrafine powers and 12 mM $MoCl_5$ aqueous solution (2 mL for $Mo_{0.2}Se$, 4 mL for $Mo_{0.4}Se$, 6 mL for $Mo_{0.6}Se$, 8 mL for $Mo_{0.8}Se$, 10 mL for MoSe). The total volume of reagent solution was adjusted to 35 mL by adding deionized water. 2 mL of hydrazine hydrate (85 wt%) was dropped into the above solution, after vigorous agitating for 10 min, the reactant was transferred into a 50 mL of Teflon-lined autoclave and cleaned FTO glass substrate (sheet resistance 12 Ω square^{-1}, purchased from Hartford Glass Co., USA) with FTO layer downward was immersed for Mo–Se alloy uptake. After reaction at 120 °C for 12 h, the FTO substrate was thoroughly rinsed by deionized water and vacuum dried at 50 °C. As references, the pure Se and Mo CEs were also prepared according to the same method at a Se dosage of 0.0095 g of Se or $MoCl_5$ dosage of 10 mL. The pristine Pt CE was purchased from Dalian HepatChroma SolarTech Co., Ltd and used as a standard.

2.2. Assembly of DSSCs

The TiO_2 colloid for mesoscopic TiO_2 thin films with a thickness of ~10 μm was prepared by a sol-hydrothermal method, and the TiO_2 thin films were coated onto FTO glass substrate by a doctor-blade method. After being calcined at 450 °C for 30 min, the resultant nanocrystal films were further sensitized by immersing into a 0.50 mM ethanol solution of N719 dye. The DSSC was fabricated by sandwiching redox electrolyte between a dye-sensitized TiO_2 anode and a CE. A redox electrolyte consisted of 100 mM of tetraethylammonium iodide, 100 mM of tetramethylammonium iodide, 100 mM of tetrabutylammonium iodide, 100 mM of NaI, 100 mM of KI, 100 mM of LiI, 50 mM of I_2, and 500 mM of 4-*tert*-butyl-pyridine in 50 mL acetonitrile. Surlyn film (30 μm) was utilized to seal the device through hot-pressing.

2.3. Electrochemical characterizations

The electrochemical performances were recorded on a conventional CHI660E setup comprising an Ag/AgCl reference electrode, a CE of Pt sheet, and a working electrode of FTO glass supported Mo–Se alloy. The cyclic voltammetry (CV) curves were recorded in a supporting electrolyte consisting of 50 mM LiI, 10 mM I_2, and 500 mM $LiClO_4$ in acetonitrile. EIS measurements were also carried out in a frequency range of 0.1 Hz ~10^5 kHz and an ac amplitude of 10 mV at room temperature. Tafel polarization curves were recorded by assembling symmetric dummy cell consisting of CE|redox electrolyte|CE.

2.4. Photovoltaic measurements

The photovoltaic test of the DSSC with an active area of 0.25 cm^2 was carried out by recording the characteristic photocurrent–voltage (J–V) curves using an Electrochemical Workstation (CHI660E, Shanghai Chenhua Co.) under irradiation of a simulated solar light from a 100 W Xenon arc lamp (XQ-500 W) in ambient atmosphere. The incident light intensity was calibrated by a standard silicon solar cell to control at 100 mW cm^{-2}. Each J–V curve was repeatedly measured for at least five times to control an experimental efficiency error within ±5%. A black mask with an aperture area of around 0.25 cm^2 was applied on the surface of DSSCs to avoid stray light.

2.5. Other characterizations

The compositions of the alloy CEs were detected by inductively coupled plasma-atomic emission spectra (ICP-AES). The optical transmission spectra of resultant CEs were recorded on a UV–vis spectrophotometer at room temperature using a bared FTO glass as a benchmark. X-ray diffraction (XRD) patterns of the resultant alloys were recorded on an X-ray powder diffractometer (X'pert MPD Pro, Philips, Netherlands) with Cu Kα radiation ($\lambda = 1.5418$ Å) in the 2θ range from 10 to 60° operating at 40 kV accelerating voltage and 40 mA current. The morphologies of the resultant $Mo_{0.6}Se$ alloy were observed on a scanning electron microscopy (SEM, S-3500N, Hitachi, Japan) and a transmission electron microscopy (TEM, JEM2010, JEOL). The work functions were achieved by a SKP RCH020 Kelvin probe, which featured a gold tip as a reference electrode. The contact potential difference was defined as the work function of the tip minus the work function of the sample.

3. Results and discussion

The resultant $Mo_{0.6}Se$ alloy was subjected to XRD characterization, as shown in Fig. 1a, the detection of diffraction peaks at $2\theta = 18.6$, 29.7, 32.6, 34.2, 39.2, 39.8, 47.0, 49.2, and 57.9° can be indexed to diffraction faces of (110), (211), (300), (104), (024), (131), (042), (006), and (502) in Mo–Se alloys (PDF# 24-0772). The sharp peak at $2\theta = 28.6$, 31.2, 54.0, and 59.5° are attributed to unreacted Se (PDF# 06-0362). Mo is a typical transition metal having the outermost electronic distribution of $4d^5 5s^1$, the unfilled valences in 4*d* orbital demonstrate the alloying of Mo and Se can accept electrons to form coordinated intermediates for robust electrocatalytic activity. The atomic ratios of Mo/Se in resultant Mo–Se alloys were determined by ICP-AES to be 0.186:1.000, 0.392:1.000, 0.605:1.000, 0.896:1.000, and 1.024:1.000 for $Mo_{0.2}Se$, $Mo_{0.4}Se$, $Mo_{0.6}Se$, $Mo_{0.8}Se$, and MoSe, respectively. The measured atomic ratios for the Mo–Se alloys are nearly consistent to their stoichiometries, therefore the chemical formulas of the Mo–Se alloy electrodes can be represented by their stoichiometric ratios. A prerequisite of realizing irradiation from either side is to create the CEs with high optical transparency in visible-light region. The UV–vis transmission spectra in Fig. 1b show that all the Mo–Se alloys have relatively high optical transmission in visible-light region (>60%) in comparison with only ~35% for pristine Pt. In this fashion, the resultant Mo–Se alloys are promising as transparent and cost-effective CE materials for bifacial DSSC applications [26].

The top-view SEM photographs in Fig. 2a & b reveal a low surface coverage of $Mo_{0.6}Se$ alloys on FTO glass by the mild solution strategy. Monolithic ITO chunks are exposed to air, whereas the deposited $Mo_{0.6}Se$ alloy nanostructures distribute in the narrow gaps among adjacent ITO chunks. To reveal the real morphology, $Mo_{0.6}Se$ powders were collected and subjected to TEM observation, as shown in Fig. 2c. At the first glance, the $Mo_{0.6}Se$ alloy exhibits a nanofibrous topology with a homogeneous distribution. However, a close examination in Fig. 2d reveals a nanosheet structure. The dark tracks refer to the curl of $Mo_{0.6}Se$ nanosheets, which has been labeled in the imaging. Clear lattice fringes can be observed in the high-resolution TEM photograph, as shown in inset of Fig. 2d, the lattice distortions in crystal lattices signal that the alloying of Mo and Se provides numerous defect sites for I_3^- adsorption and reduction. Although the high coverage of FTO glass substrate by Mo–Se at high Mo dosages, as shown in Fig. S3, the poor contact between FTO and Mo–Se could increase the interfacial resistance and electron loss.

The primary feature of a CE is to collect electrons from external circuit and reduce I_3^- to I^- species [27]. In order to better evaluate

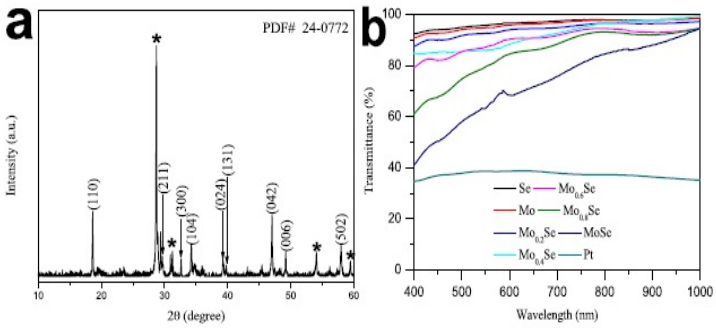

Fig. 1. (a) XRD pattern of $Mo_{0.6}Se$ alloy and (b) UV–vis transmission spectra of the resultant CEs. The optical spectra were achieved using bared FTO glass as a benchmark.

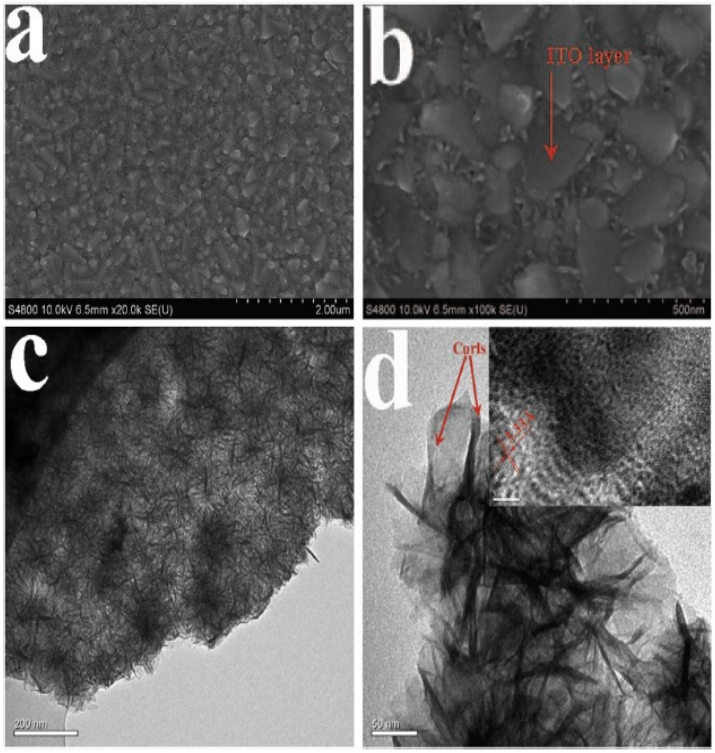

Fig. 2. (a) & (b) Top-view SEM photographs of FTO glass supported $Mo_{0.6}Se$ CE and (c) & (d) TEM photographs of $Mo_{0.6}Se$ nanosheets.

the catalytic activity of a Mo–Se alloy CE toward I^-/I_3^- redox couples, cyclic voltammetry (CV) curves are recorded at a scan rate of 50 mV s^{-1} using alloy CE as a working electrode and redox electrolyte as a supporting medium. Two pairs of redox peaks corresponding to $I_3^- \leftrightarrow I^-$ (Red_1/Ox_1) and $I_3^- \leftrightarrow I_2$ (Red_2/Ox_2) reactions are detected in each CV curve, as shown in Fig. 3a. The peak shapes and positions are very similar to that from Pt electrode, as shown in Fig. S1a, indicating the same catalytic behaviors to Pt species [28]. The peak current density of $I_3^- + 2e = 3I^-$ and peak-to-peak separation (E_{pp}) between Red_1 and Ox_1 are two crucial parameters to compare the catalytic activity of CEs and the data are summarized in Table 1. Among seven CEs, the $Mo_{0.6}Se$ exhibits the highest Red_1 value of −5.78 mA cm^{-2} and a lowest E_{pp} of 0.522 V. After a synergistic evaluation, we find the catalytic performances of all electrodes follow an order of $Mo_{0.6}Se > Mo_{0.4}Se > Mo_{0.8}Se \approx Pt > MoSe > Mo_{0.2}Se > Se > Mo$. Tang et al. have realized Pt–Ni alloy nanoparticle CEs by involving a solvent-based method using octadecylamine as both solvent and reducing regent [29]. The catalytic activity of the alloy electrodes and therefore photovoltaic performances of their DSSCs are optimized by adjusting the Pt/Ni stoichiometry, yielding an optimal alloy CEs from Pt_3Ni with 8.78%-efficiency in its cell device. In order to demonstrate why and how does composition alternation tunes the charge transfer at CE/I_3^- interface and catalytic activity, they calculated the work functions of various CEs and concluded there was a good matching between Pt_3Ni (−4.76 eV) and the potential of I^-/I_3^- (−4.9 eV), which was favorable for the electron transport from CE to electrolyte. From the measured work functions of Mo–Se CEs, as shown in Fig. S2, the work function of $Mo_{0.6}Se$ (−4.931 eV) matches to the redox potential of I^-/I_3^- couples.

From the stacked CV curves of $Mo_{0.6}Se$ electrode at various scan rates along with linear plots between Red_1/Ox_1 peak current densities and square root of scan rate, as shown in Fig. 4, one can see that it is in agreement with modified Cottrell equation ($j = kv^{1/}$

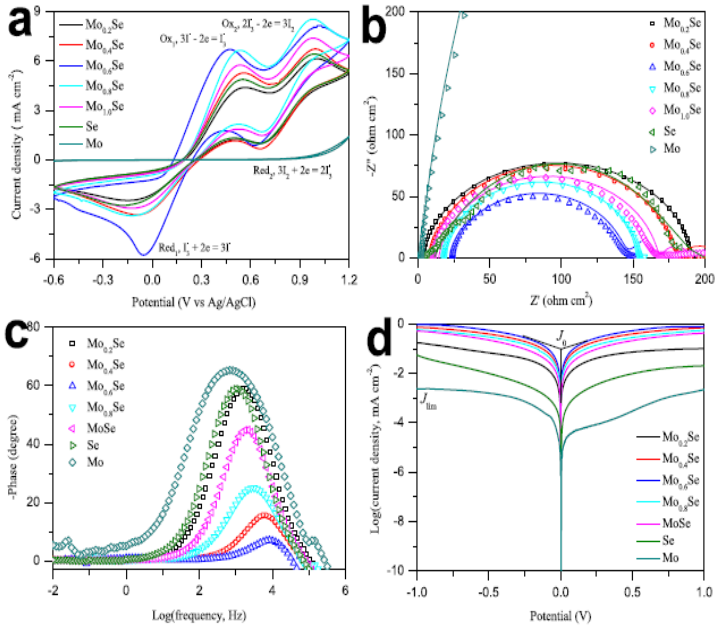

Fig. 3. (a) CV curves of various CEs recorded at a scan rate of 50 mV s^{-1}. (b) Nyquist and (c) Bode EIS plots, and (d) Tafel polarization curves for the symmetric dummy cells fabricated by two identical CEs. The inset shows an equivalent circuit simulated by Z-view software. R_s: series resistance, R_{ct}: charge-transfer resistance, CPE: constant phase element, W: Nernst diffusion resistance.

Table 1
Extracted data from CV and EIS measurements.

CEs	Red$_1$ (mA cm^{-2})	E_{pp} (V)	R_{ct} (Ω cm^2)	τ (μs)
Mo$_{0.2}$Se	−2.42	0.725	172.5	105.2
Mo$_{0.4}$Se	−3.37	0.643	136.1	25.2
Mo$_{0.6}$Se	−5.78	0.522	120.4	17.5
Mo$_{0.8}$Se	−3.36	0.621	152.6	56.5
MoSe	−2.95	0.648	162.7	77.9
Se	−2.73	0.733	187.2	155.6
Mo	–	–	5034.9	241.1
Pt	−3.12	0.603	156.3	56.8

^{2}, where v is the scan rate and k is the collection constant determined by the electrochemical system) [30], which provides evidence for the diffusion-controlled mechanism for the cathodic and anodic reactions and fast electron transfer at the electrolyte/CE interface. The Nyquist EIS plots in Fig. 3b can be utilized to reconfirm the catalytic activities of the alloys and pure Se or pure Mo [31]. The Mo$_{0.6}$Se has an R_{ct} of 120.4 Ω cm^2, which is smaller than the others. This result indicates that the alloying of Mo and Se at an optimized stoichiometry has an acceleration effect on the charge-transfer capability. The rapid diffusion of I_3^- from dye–TiO$_2$/electrolyte interface to CE surface for converting to I^- species and back to dye–TiO$_2$/electrolyte interface is expected to enhance the dye recovery and therefore J_{sc} of a DSSC. A CE is a component of collecting electrons from external circuit and reducing I_3^- to I^- ions, therefore the lifetime of electrons (τ) on a CE is a direct signal for evaluating the catalytic kinetics: a lower τ value refers to an accelerated catalytic process, oppositely, a higher τ value means a decreased catalytic activity. Fig. 3c shows the Bode EIS spectra of the symmetric dummy cells and the τ values ($\tau = 1/(2\pi f)$ [32], f is the peak frequency correspond to charge-transfer process) are listed in Table 1. The τ follows an order of Mo$_{0.6}$Se < Mo$_{0.4}$Se < Mo$_{0.8}$Se < MoSe < Mo$_{0.2}$Se < Se < Mo, suggesting an electrocatalytic activity of Mo$_{0.6}$Se > Mo$_{0.4}$Se > Mo$_{0.8}$Se > MoSe > Mo$_{0.2}$Se > Se > Mo. The conclusion from EIS analysis is in an agreement with CV characterization. The Tafel polarization curves measured on the same symmetric dummy cells, as shown in

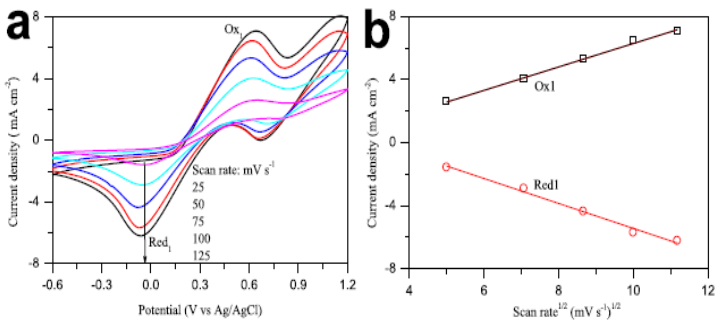

Fig. 4. (a) Stacked CV curves of the Mo$_{0.6}$Se alloy CE recorded at various scan rates and (b) linear relationships between Red$_1$/Ox$_1$ peak current density and square root of scan rate.

Fig. 3d, are recorded to further elucidate the catalytic activity of the alloy electrodes. The slopes for anodic or cathodic branches are in the order of $Mo_{0.6}Se$ > $Mo_{0.4}Se$ > $Mo_{0.8}Se$ > MoSe > $Mo_{0.2}Se$ > Se > Mo. A larger slope in the branch means a higher exchange current density (J_0) on the CE. J_0 is a parameter related to R_{ct} and can be calculated by equation: $J_0 = RT/nFR_{ct}$ [33], where R is the gas constant, T is the absolute temperature, n is the number of electrons involved in I_3^- reduction ($n = 2$), F is Faraday's constant, R_{ct} is charge-transfer resistance obtained from the Nyquist EIS plots. Apparently, the sequence of R_{ct} values from Tafel polarization curves is in an agreement with that from EIS plots. In addition, the limiting diffusion current density (J_{lim}), intersection of cathodic branch with Y-axis, can be used to analyze the diffusion process of I^-/I_3^- redox couples on a CE. J_{lim} is in a linear relationship with diffusion coefficient (D_n): $J_{lim} = 2nD_nCN_A/l$ [34], where l is the spacer thickness, C is the concentration of I_3^- species, N_A is the Avogadro constant. Both J_{lim} and D_n vary in the order of $Mo_{0.6}Se$ > $Mo_{0.4}Se$ > $Mo_{0.8}Se$ > MoSe > $Mo_{0.2}Se$ > Se > Mo, which is consistent with CV analysis. Till now, we can make a conclusion from the catalytic curves and EIS impedance that $Mo_{0.6}Se$ nanosheet has a superior electrocatalytic activity for liquid electrolyte having I^-/I_3^- redox couples.

Fig. 5a compares the characteristic J–V curves of the DSSCs from Mo–Se alloys, Se, Mo, and Pt electrodes and the photovoltaic parameters are summarized in Table 2. The cell with $Mo_{0.6}Se$ yields a front efficiency of 8.05% (J_{sc} = 15.71 mA cm^{-2}, V_{oc} = 0.729, and FF = 70.3%), which is much higher than 6.17% from pristine Pt-based DSSC (J_{sc} = 13.11 mA cm^{-2}, V_{oc} = 0.712, and FF = 66.1%). Notably, J_{sc} increases by an order of $Mo_{0.6}Se$ > $Mo_{0.4}Se$ > $Mo_{0.8}Se$ > MoSe > $Mo_{0.2}Se$ > Se > Mo. It has been demonstrated that the I^- species regenerate excited N719 dyes and subsequently convert to I_3^- ions, after migrating to electrolyte/CE interface the I_3^- are reduced into I^- ions and back to N719–TiO_2/electrolyte interface for dye recovery [35]. In this fashion, the alloy CE with enhanced catalytic activity can accelerate the kinetics for $I_3^- \rightarrow I^-$ conversion and therefore dye recovery. Due to the efficient excitation of

Table 2
Photovoltaic parameters of DSSCs with varied CEs.

CEs	Irradiation	η (%)	V_{oc} (V)	FF (%)	J_{sc} (mA cm^{-2})
$Mo_{0.2}Se$	Front	2.87	0.644	55.4	8.04
	Rear	2.66	0.632	53.4	7.88
$Mo_{0.4}Se$	Front	6.79	0.721	63.3	14.86
	Rear	3.51	0.659	54.7	9.73
$Mo_{0.6}Se$	Front	8.05	0.729	70.3	15.71
	Rear	5.92	0.719	59.3	13.89
$Mo_{0.8}Se$	Front	6.18	0.696	62.7	14.17
	Rear	4.78	0.689	62.2	11.15
MoSe	Front	4.61	0.688	61.5	10.90
	Rear	4.41	0.677	65.3	9.97
Se	Front	3.01	0.621	64.1	7.56
	Rear	2.46	0.611	54.3	7.41
Mo	Front	0.51	0.534	18.1	5.21
	Rear	0.47	0.441	28.7	3.71
Pt	Front	6.17	0.712	66.1	13.11
	Rear	3.56	0.655	57.3	9.49

recovered dyes, the electron density on conduction band (CB) of TiO_2 nanocrystallites and J_{sc} of a solar cell are expected to be markedly elevated. The J–V characteristics obtained by irradiating the solar cells from rear side are shown in Fig. 5b. A rear efficiency as high as 5.92% is recorded on the cell with $Mo_{0.6}Se$ nanosheet alloy electrode, which is also much higher than 3.56% for the DSSC with pristine Pt CE. To our knowledge, the rear efficiency of 5.92% is among the highest reports for the bifacial DSSCs. The remarkable rear efficiency attributes to the promising catalytic activity and high optical transparency. It is noteworthy to mention that both rear J_{sc} and V_{oc} are lower than that under front irradiation. J_{sc} is believed to be dependent on the accumulative electron amount on CB of TiO_2 nanocrystals [36]. In comparison with rear irradiation, the photons penetrating transparent FTO glass can be adsorbed by N719 dyes and the photon distribution is gradient descending (viewed from anode to CE) under front illumination, resulting in a reduced electron distribution on CB of percolating

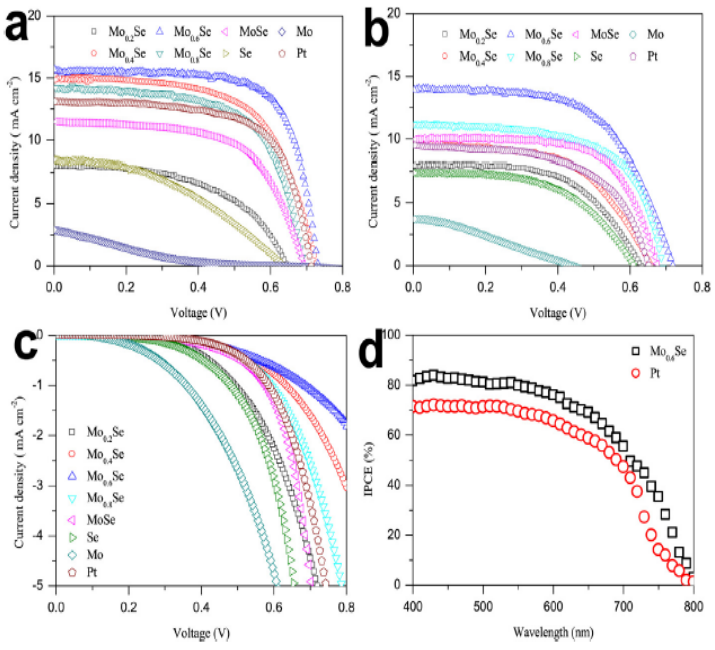

Fig. 5. Characteristic J–V curves for the DSSCs with varied CEs for (a) front and (b) rear irradiations under AM1.5G, and (c) in the dark. (d) IPCE curves for the solar cells with various CEs.

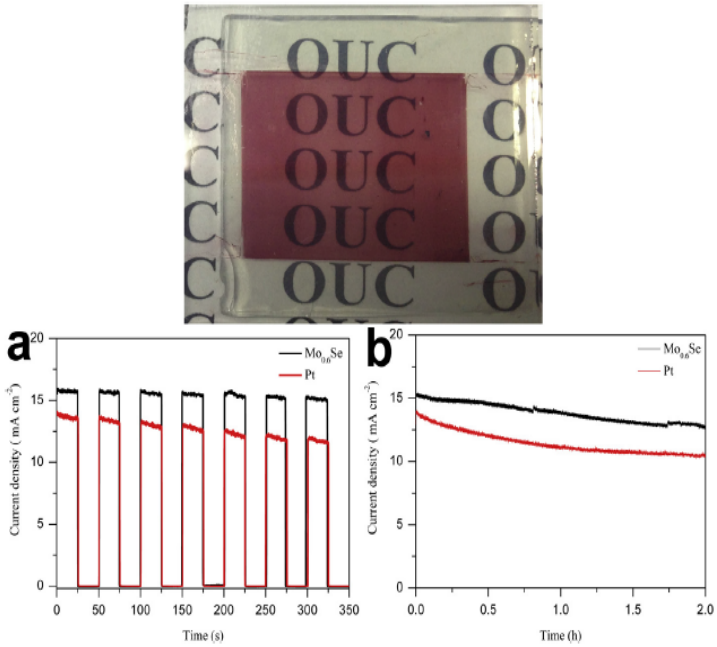

Fig. 6. Top: bifacial DSSC from $Mo_{0.6}Se$ alloy CE. Down: (a) on–off switches and (b) photocurrent stabilities for the DSSCs with $Mo_{0.6}Se$ and pristine Pt CE. The on–off plots were achieved by alternately irradiating (100 mW cm^{-2}) and darkening (0 mW cm^{-2}) the solar cells at a 50 s interval and 0 V. The photocurrent stabilities were obtained by persistently irradiating the cells at a 100 mW cm^{-2} illumination.

TiO_2 networks. When transferred along the percolating channels from mesoscopic TiO_2 thin films, the electrons suffer shorter migration path length and less traps before arriving to FTO layer [37]. Moreover, there is an enhanced light loss from rear irradiation due to light barriers from FTO glass and liquid electrolyte. In addition, the electrons excited under front irradiation have much less trapping events with I_3^- species, giving a restarted backward reaction between electrons and I_3^- ions [15,26]. The restricted recombination reaction can be strongly supported by the lower dark current density, as shown in Fig. 5c. Therefore, the front J_{sc} and V_{oc} values for the cells are higher than that from rear irradiation.

Fig. 5d presents the IPCE plots of the DSSCs from $Mo_{0.6}Se$ alloy and pristine Pt electrodes. The broad IPCE curves, covering the spectrum from 400 to 800 nm, exhibit a maximum IPCE value of ~85% for the cell with $Mo_{0.6}Se$ CE and similar shape to the solar cell with pristine Pt electrode. The result from IPCE characterization reveals that the number of electrons in the external circuit is larger using $Mo_{0.6}Se$ alloy than that from Pt electrode.

Due to the high optical transparency of $Mo_{0.6}Se$ nanosheet electrode in visible-light region, the resultant DSSC device is also transparent, as shown in the top photograph of a large-area bifacially active solar cell realized in this work. When applied as windows, roof panels, or portable sources, the resultant solar panels are expected to have superiorities in fast start-up, multiple start/off capability, and stable photocurrent [34]. Fig. 6a shows the on–off switches in a time slot of 0–350 s. A sharp increase in photocurrent density suggests a fast start-up behavior of the DSSC at front irradiation. After seven start/off cycles, the photocurrent density for the cell with $Mo_{0.6}Se$ alloy CE still remains a reasonable start-up capability, whereas the Pt-based cell has an apparent reduction in photocurrent density. To compare the stability of the $Mo_{0.6}Se$ alloy and pristine Pt CEs under persistent irradiation, the photocurrent densities of the resultant solar cells are measured over 2 h (Fig. 6b). The photocurrent densities decrease by 13.7% and 25.2% for the cells with $Mo_{0.6}Se$ and Pt electrodes, respectively. Although the DSSC is only tested for 2 h, this preliminary result demonstrates that the stability of a cell device can be improved by utilizing $Mo_{0.6}Se$ alloy CE.

4. Conclusions

In summary, we have successfully realized the mild hydrothermal synthesis of Mo–Se nanosheet CEs free of any surfactant or template. Due to the high charge-transfer ability, catalytic activity, and optical transparency, the resultant DSSCs can generate electricity from either side. Maximum front efficiency of 8.05% and rear efficiency of 5.92% are recorded on the cell with $Mo_{0.6}Se$ alloy electrode in comparison to 6.17% and 3.56% for a device based on a pristine Pt CE. Additionally, the bifacial DSSC exhibits fast start-up, high start/off capability, and stable photocurrent. This research is far from being optimized, but these profound superiorities along with cost-effectiveness, mild synthesis, and scalable materials demonstrate the Mo–Se nanosheet CEs to be good candidates for bifacial DSSC applications.

Acknowledgements

The authors would like to acknowledge financial supports from National Natural Science Foundation of China (U1037604), Fundamental Research Funds for the Central Universities (201313001, 201312005), Shandong Province Outstanding Youth Scientist Foundation Plan (BS2013CL015), Shandong Provincial Natural Science Foundation (ZR2011BQ017), and Research Project for the Application Foundation in Qingdao (13-4-198-jch).

Appendix A. Supplementary data

Supplementary data related to this article can be found at http://dx.doi.org/10.1016/j.jallcom.2015.07.082.

References

[1] J.D. Major, R.E. Treharne, L.J. Philips, K. Durose, Nature 511 (2014) 334.
[2] C.H. Lee, D.R. Kim, X.L. Zheng, ACS Nano 8 (2014) 8746.
[3] T.G. Deepak, G.S. Anjusree, S. Thomas, T.A. Arun, S.V. Nair, A.S. Nair, RSC Adv. 4 (2014) 17615.
[4] B. O'Regan, M. Grätzel, Nature 353 (1991) 737.
[5] S. Ito, S.M. Zakeeruddin, P. Comte, P. Liska, D.B. Kuang, M. Grätzel, Nat. Photonics 2 (2008) 693.
[6] Y.C. Wang, D.Y. Wang, Y.T. Jiang, H.A. Chen, C.C. Chen, K.C. Ho, H.L. Chou, C.W. Chen, Angew. Chem. Int. Ed. 52 (2013) 6694.
[7] M.H. Abdullah, M. Rusop, J. Alloy. Compd. 600 (2014) 60.
[8] Y. Dou, F. Wu, C. Mao, L. Fang, S. Guo, M. Zhou, J. Alloy. Compd. 633 (2015) 408.
[9] Y. Xue, J. Liu, H. Chen, R. Wang, D. Li, J. Qu, L. Dai, Angew. Chem. Int. Ed. 51 (2012) 12124.
[10] J.H. Wu, Z. Lan, J.M. Lin, M.L. Huang, S.C. Hao, T. Sato, S. Yin, Adv. Mater 19 (2007) 4006.
[11] S. Mathew, A. Yella, P. Gao, R. Humphry-Basile, B.F.E. Curchod, N. Ashari-Astani, I. Tavernelli, U. Rothlisberger, M.K. Nazeeruddin, M. Grätzel, Nat. Chem. 6 (2014) 242.
[12] J. Kim, J.K. Koh, B. Kim, J.H. Kim, E. Kim, Angew. Chem. Int. Ed. 51 (2012) 6864.
[13] J. Bisquert, Nat. Photonics 2 (2008) 648.
[14] Q. Tai, B. Chen, F. Guo, S. Xu, H. Hu, B. Sebo, X.Z. Zhao, ACS Nano 5 (2011) 3795.
[15] Y.Y. Duan, Q.W. Tang, J. Liu, B.L. He, L.M. Yu, Angew. Chem. Int. Ed. 53 (2014) 14569.
[16] X.P. Wang, Q.W. Tang, B.L. He, R. Li, L.M. Yu, Chem. Commun. 51 (2015) 491.
[17] D.W. Chang, H.J. Choi, A. Filer, J.B. Baek, J. Mater. Chem. A 2 (2014) 12136.
[18] S.S. Jeon, C. Kim, T.H. Lee, Y.W. Lee, K. Do, J. Ko, S.S. Im, J. Phys. Chem. C 116 (2012) 22743.
[19] J.H. Wu, Y. Li, Q.W. Tang, G.T. Yue, J.M. Lin, M.L. Huang, L.J. Meng, Sci. Rep. 4 (2014) 4028.
[20] D. Song, M. Li, Y. Li, X. Zhao, B. Jiang, Y. Jiang, ACS Appl. Mater. Interfaces 6 (2014) 7126.
[21] C. Bu, Y. Liu, Z. Yu, S. You, N. Huang, L. Liang, X.Z. Zhao, ACS Appl. Mater. Interfaces 5 (2013) 7432.
[22] F. Gong, H. Wang, X. Xu, G. Zhou, Z.S. Wang, J. Am. Chem. Soc. 134 (2012) 10953.
[23] C. Baldizzone, S. Mezzavilla, H.W.P. Carvalho, J.C. Meier, A.K. Schuppert, M. Heggen, C. Galeano, J.D. Grunwaldt, F. Schüth, K.J.J. Mayrhofer, Angew. Chem. Int. Ed. 53 (2014) 14250.
[24] D.R. Rolison, P.L. Hagans, K.E. Swider, J.W. Long, Langmuir 15 (1999) 774.
[25] Y. Bing, H. Liu, L. Zhang, D. Ghosh, J. Zhang, Chem. Soc. Rev. 39 (2010) 2184.
[26] Y.Y. Duan, Q.W. Tang, B.L. He, R. Li, L.M. Yu, Nanoscale 6 (2014) 12601.
[27] S.N. Yun, A. Hagfeldt, T.L. Ma, Adv. Mater 26 (2014) 6210.
[28] Y.M. Xiao, G.Y. Han, Y.P. Li, M.Y. Li, Y.Z. Chang, J. Mater. Chem. A 2 (2014) 3452.
[29] J. Wan, G. Fang, H. Yin, X. Liu, D. Liu, M. Zhao, W. Ke, H. Tao, Z. Tang, Adv. Mater. 26 (2014) 8101.
[30] X. Pan, K. Zhu, G. Ren, N. Islam, J. Warzywoda, Z.Y. Fan, J. Mater. Chem. A 2 (2014) 12746.
[31] J.D. Roy-Mayhew, D.J. Bozym, C. Punckt, I.A. Aksay, ACS Nano 4 (2010) 6203.
[32] X. Sang, J. Li, L. Zhang, Z. Wang, W. Chen, Z. Zhu, Z. Su, E. Wang, ACS Appl. Mater. Interfaces 6 (2014) 7876.
[33] A. Hilmi, T.A. Shoker, T.H. Ghaddar, ACS Appl. Mater. Interfaces 6 (2014) 8744.
[34] M.J. Ju, I.Y. Jeon, J.C. Kim, K. Lim, H.J. Choi, S.M. Jung, I.T. Choi, Y.K. Eom, Y.J. Kwon, J. Ko, J.J. Lee, H.K. Kim, J.B. Baek, Adv. Mater. 26 (2014) 3055.
[35] M.X. Wu, T.L. Ma, J. Phys. Chem. C 118 (2014) 16727.
[36] X.X. Chen, Q.W. Tang, B.L. He, L. Lin, L.M. Yu, Angew. Chem. Int. Ed. 53 (2014) 10799.
[37] M. Law, L.E. Greene, J.C. Johnson, R. Saykally, P.D. Yang, Nat. Mater. 4 (2005) 455.

J Mater Sci: Mater Electron (2015) 26:4604–4617
DOI 10.1007/s10854-015-3147-4

Preparation and photovoltaic properties of silicon quantum dots embedded in a dielectric matrix: a review

Xiaobo Chen[1,2] · Peizhi Yang[1]

Received: 1 February 2015 / Accepted: 30 April 2015 / Published online: 7 May 2015

Abstract Over the last few years silicon quantum dots (Si QDs) have come under intensive research because of their interesting physical properties and their potential use in future electronic and optoelectronic applications. Focusing on photovoltaic applications, we review recent progress in silicide-embedded Si QDs films with different fabrication techniques and different characteristics. Some avenues for further material improvements are discussed. The performances of several photovoltaic devices reported in the literature are also reviewed and discussed. We assess the state of the art in the area of Si QDs layer deposition, including fabrication technologies and film properties, and highlight the challenges that need to be overcome. Finally, some existing problems and future work are pointed out.

1 Introduction

Silicon, as a monoatomic crystal, is in general not suitable for optoelectronic applications due to its indirect bandgap and poor light absorption and emission properties. Since the nanostructured silicon has quantum confinement effect, silicon bandgap tuning is possible in different forms of silicon, such as porous silicon [1, 2], silicon nanowires [3–5], silicon nanocrystals (Si NCs) [6–8], and silicon quantum dots (Si QDs) or Si NCs embedded in dielectric [9–12]. It should be explained that a Si NCs with size less than the exciton Bohr radius, which shows quantum size effects are usually called Si QDs [13]. The enhancement of bandgap and indirect-to-direct conversion of QDs of indirect-gap materials are ascribed to quantum confinement effects [14]. Si QDs exhibit strong quantum confinement and therefore their optical, electrical, and photovoltaic properties can be tuned by controlling their size, density, shape, crystalline structure, surrounding matrix, and doping content [15–21].

In terms of photovoltaic market, Si-based solar cells, as they are based on abundant, nontoxic materials and the mature device processing technology, have been identified as the leading photovoltaic technology. Currently, the highest efficiency of ~25.6 % for a crystalline silicon solar cell is obtained [22], which is very close to a recent theoretical limit of 29.43 % [23], so obviously only limited further progress can now be gained. To break through this ideal efficiency limit, the concept of 'all-Si' tandem solar cells [19] has been proposed as a way of improving conversion efficiency. Each cell with different energy bandgap in tandem stack can be optimized for a different part of incident light. Theoretical calculations show that efficiencies of tandem solar cells can be improved up to 42.5 and 47.5 % for two- and three-cell tandem stacks, respectively [24].

Several recent reports have suggested that Si quantum dots (QDs) embedded in different dielectric matrix (such as SiO_2, Si_3N_4, or SiC) are a promising candidate for the upper cell in an 'all-Si' tandem solar cell [18, 25, 26]. The material's effective bandgap can be varied by varying the size of Si QDs, due to three-dimensional quantum confinement. An effective bandgap of about 1.7 eV has been demonstrated for 2 nm diameter Si QDs embedded in silica [27]. The tunneling probability of carriers into Si QDs

✉ Peizhi Yang
pzhyang@hotmail.com

[1] Key Laboratory of Education Ministry for Advance Technique and Preparation of Renewable Energy Materials, Yunnan Normal University, Kunming 650092, China

[2] School of Physics and Mech-tronic Engineering, Sichuan University of Arts and Science, Dazhou 635000, China

embedded in these host matrices is heavily dependent on the barrier height between the Si QDs and the matrix [27]. SiO_2 (bandgap of 9 eV [19]) is a commonly used matrix and Si QDs is generally fabricated in Si-rich silicon oxide films. Another dielectric option is Si_3N_4 (bandgap of 5.3 eV [19]) matrix. SiC has a much lower bandgap energy (2.36 eV in 3C β-SiC [28]) compared to Si_3N_4 and SiO_2, resulting in the highest expected mobility of carriers for a given QDs size and separation [29]. Consequently there is potential for more conductive devices to be produced using a SiC matrix as compared to Si_3N_4 or SiO_2 matrixes [30]. However, both the polarity and length of the bonds decrease towards those of Si–Si for oxide, nitride, or carbide, and SiC is an isoelectronic covalently bonded material as Si is, thus there is a notably smaller tendency for segregation and precipitation of Si than in SiO_2 or Si_3N_4 matrices [24]. Moreover, quantum confinement is relatively weak for Si QDs embedded in Si_3N_4 or SiC matrix compared to in SiO_2 matrix. In summary, these three materials each have their own advantages and are worthwhile to further study. Mangolini [2], Janz et al. [31], Schnable et al. [32] have provided an exhaustive comparison of these three matrices, the readers can find more detailed information in the above reviews.

A lot of research covering materials deposition and device development has already been carried out in relation to Si QDs films. The aim of this paper is to review the past research works mainly on the experimental aspects of Si QDs films for photovoltaic applications. It covers the formation of Si QDs nanostructures, physical properties of the Si QDs, doping, and the performance of photovoltaic devices. This paper is structured as follows. In Sect. 2, we will present a summary of different synthesis approaches. The methods used to improve the properties (such as size control, density improvements, doping, and defect passivation) of Si QDs films will be discussed in Sect. 3. In Sect. 4, we summarize the photovoltaic studies with Si QDs and propose ideas for further exploration. Conclusions are presented in Sect. 5, where the existing problems and outlook for the future work is given.

2 Fabrication techniques of Si QDs

Commonly, in order to obtain Si QDs embedded in a dielectric matrix, firstly silicon-rich thin films [i.e. silicon-rich silicon oxide (SRO) or silicon-rich silicon nitride (SRN) or silicon-rich silicon oxynitride (SRON) or silicon-rich silicon carbide (SRC)] are deposited, and the as-deposited films are generally amorphous. Subjecting the as-deposited films to a post-deposition thermal treatment may result in the phase separation of the excess Si. During post-deposition annealing, the host matrix tends toward a stoichiometric composition, and the extent of phase separation between the excess Si and a dielectric host (i.e. SiO_2 or Si_3N_4 or SiC) and crystallization degree can be modulated through annealing temperature and time [33–35]. As an example, one can see in Fig. 1 that the crystallization degree increased with the increase of annealing temperature, being demonstrated by the increase of intensity of Si NCs peak along with the significant decrease of amorphous Raman contribution. It is important to note here that care must be taken when analyzing the precise position and full width at half maximum of Si NCs peak as it is affected by quantum confinement as well as residual stress [36, 37]. There are two typical approaches to the fabrication of Si QDs embedded in a dielectric matrix: (1) a Si-rich single layer film and (2) a multilayer (or called superlattice) structure film (e.g. SRO/SiO_2 multilayer). In the first approach, the size of Si QDs is controlled through the amount of excess Si in the as-deposited films and the post-annealing parameters [38–40]. In the second approach (for example for SRO/SiO_2 multilayer, SiO_2 layers act as barrier layers), upon high-temperature annealing, diffusion of the excess Si is restricted by the SiO_2 layers, and sizes controlled Si QDs in multilayer structures are formed (see Fig. 2), as discussed further in Sect. 3 below.

Various deposition methods are suitable for such fabrication. There are two primary approaches: chemical vapor deposition (CVD), and magnetron sputtering. In addition, Si QDs can also be prepared by other methods such as evaporation, ion implantation, pulsed laser ablation, and direct ion beam deposition. Table 1 summarizes the representative examples of the Si QDs growth parameters of the above mentioned techniques. It should be noted that the fabrication techniques for silicon quantum dots embedded in nitride or carbide matrices are very similar to those for SiO_2-embedded Si QDs. The quality of material and the degree of phase separation depends not only on the amount

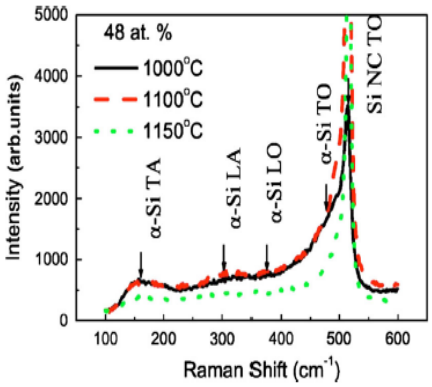

Fig. 1 Raman spectra of 48 at.% Si SRO film deposited on quartz annealed at 1000, 1100, and 1150 °C for 1 h. Reproduced with permission from [33] © 2005 The American Physical Society

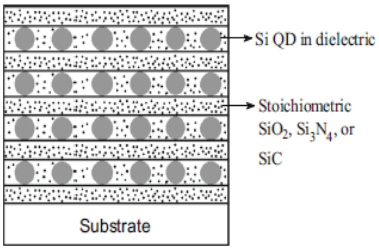

Fig. 2 Multilayer structure of alternating Si-rich dielectric/stoichiometric dielectric after annealing

of excess Si and its post-deposition processing, but also on the fabrication method [41]. The authors of [41] have compared different properties caused by fabrication methods [including sputtering, plasma enhanced chemical vapour deposition (PECVD), and ion implantation], and have presented some speculation on the reasons of difference. But still, a comprehensive understanding is missing. Furthermore, a comparison between CVD method and magnetron cosputtering is given in Refs. [42, 43].

Several kinds of CVD techniques, such as PECVD [44, 45], inductively coupled plasma CVD (ICPCVD) [46], hot-wire CVD (HWCVD) [47], laser-assisted CVD (LACVD) [48], and catalytic CVD (Cat-CVD) [49], have been used to prepare Si QDs. The necessity to use toxic and explosive gases (such as SiH_4, CH_4, and H_2 etc.) and very time consuming in multilayer structure are the common disadvantages of CVD [50]. Process parameters like precursor gas, gas flow rates, chamber pressure, plasma power, and substrate temperature, etc. can significantly affect the film composition and quality, and the size of silicon crystallites [14, 38, 51–53]. Moreover, the film thickness is commonly a direct function of duration time of deposition [46].

From the "Precursor gas" column of Table 1, SiH_4 and NH_3 are often used as the precursor gases for depositing SRN, and SiH_4 and CH_4 are often used for SRC. In the case of SRO, it is noteworthy that N_2O gas is used as the oxygen precursor in many works like [44–46, 54, 55] due to lower activation energy [56] and safety reason [57]. However, N is also incorporated into the film, which blue-shifts the optical bandgap and reduces the absorption efficiency [43]. While, the incorporated N leads to the requirement of a higher annealing temperature as compared to a nitrogen-free film due to the decreased mobility of Si in N containing SRO [57]. By suitably adjusting the flow rates of precursor gases, it is possible to make films with different silicon concentrations [52]. For example, for Si QDs in SiN_x matrix grown by PECVD, with the increase of gas flow ratio of SiH_4 versus NH_3, the crystallization is enhanced, and the amount of dots increases, being demonstrated by the increase of X-ray diffraction intensity of nanocrystalline Si QDs peak (Fig. 3) [58]. Using grazing incidence X-ray diffraction (GIXRD), nanocrystalline Si QDs can be evidenced by the peaks corresponding to the (111), (220), and (311) silicon crystal plane [58]. The sub-stoichiometric Si-based dielectric materials, which can be SiO_x, SiN_x, SiO_xN_y, or SiC_x, undergo phase separation and crystallization during the high-temperature (typically 1100 °C) annealing process, resulting in the formation of Si QDs within the dielectric matrix [44, 52, 59]. However, such high temperatures involve a huge thermal budget, and may not be suitable for device fabrication due either to technical reasons or cost considerations [59]. Recently, progresses for in situ formation of Si QDs in Si-rich silicon nitride matrix [49, 53, 60, 61] and Si-rich silicon carbide matrix [62, 63] by various CVD methods, such as PECVD, Cat-CVD, and ICP-CVD without annealing have been developed. However, the control of the size and the density of Si QDs using these in situ growth methods remains a challenge.

Magnetron sputtering represents another suitable method for obtaining Si-rich films. Argon is excited and ionized, and high energy argon ions are used to sputter material from a target. The production of Si QDs materials are determined by several control control parameters of sputtering: the substrate temperature [64], sputtering power [65], sputtering rate [66], sputtering duration time [67], and reactive gases (N_2, NH_3, or O_2) flow rates in the case of reactive sputtering [68–71] etc. Generally, silicon-rich thin films are deposited on room temperature substrates [36, 65, 66, 72] or on substrates heated at temperatures between 100 and 500 °C [64, 68, 73–75] and the as-deposited films are amorphous. Sputtering is often employed in conjunction with a high-temperature annealing process to form Si QDs in a dielectric matrix [50, 65, 66]. The most efficient annealing temperature for obtaining Si QDs is 1100 °C [16, 65, 73, 74].

Annealing of Si-rich silicide films or multilayers can be made either by rapid thermal processing/annealing (RTP/RTA) or in conventional tube furnace (CTF) [50, 59]. The annealing is typically performed in a gas atmosphere, e.g. N_2 or Ar, and the gas atmosphere can influences the structural characteristics of films [44]. For example, by annealing SRO/SiO_2 multilayer in N_2, Si QDs with small size and low density are observed in comparison with the case of annealing in Ar when bigger QDs with higher density are obtained [44]. The effect of annealing in N_2 on Si NCs formation is often explained in literatures by the suppression of Si diffusion produced by the presence of nitrogen and leading to smaller sizes [76–78]. RTP represents a suitable candidate as a cost- and time-effective technology in current Si-based processing [79]. The major feature of RTP is the rapid heating ramps (up to 100 K/s) and dwell times of seconds to minutes [80]. Hiller et al. [59] pointed that PECVD samples generally contain a

Table 1 Deposition parameter summary of Si QDs embedded in a dielectric matrix

Film structure	Technique	Precursor gas	Substrate temperature	Annealing method/ temperature/time	Experimentation parameter	Ref. No.
Si/SiO_2 multilayer	CVD	SiH_4/Ar, SiH_4/N_2O	50 °C	CTF/1150 °C/1 h	Deposition time	[54]
SRO/SiO_2 multilayer	PECVD	SiH_4, H_2, and N_2O	200 °C	CTF/1100 °C/1 h	Annealing ambient	[44]
SRO single layer	PECVD	SiH_4 and N_2O	400 °C	–/1180 °C/–	Film thickness	[45]
SRO/SiO_2 multilayer	ICPCVD	SiH_4, Ar and N_2O	250 °C	CTF/900 °C/1 h	Deposition time	[46]
SRO single layer	PECVD	SiH_4, Ar and N_2O	–	CTF/1000–1250 °C/30 min	SiH_4 flux and annealing temp.	[55]
SRN single layer	PECVD	SiH_4, NH_3 and He	–	CTF/1100 °C/1 h	NH_3/SiH_4 flow ratio	[82]
SRN/SiO_2 superlattice	PECVD	SiH_4, NH_3 and N_2	375 °C	CTF/500–1200 °C/1 h	Barrier thickness, and annealing temp.	[83]
SRN single layer	LP-PECVD	SiH_4 and NH_3	370 °C	No post annealing	Total pressure	[60]
SRN/Si_3N_4 multilayer	PECVD	SiH_4, NH_3 and N_2	375 °C	CTF/1150 °C/1 h	NH_3/SiH_4 flow ratio, and SRN layer thickness	[84]
SRN/Si_3N_4 multilayer	PECVD	SiH_4, NH_3 and Ar	400 °C	CTF/600–1150 °C/2 h	Annealing temp.	[85]
Si/SRN multilayer	HWCVD	SiH_4 and NH_3	250 °C	CTF/800–950 °C/30 min	Annealing temp.	[47]
SRN single layer	Cat-CVD	SiH_4, NH_3 and H_2	200 °C	No post annealing	NH_3/SiH_4 flow ratio	[49]
$SRON/SiO_2$ superlattice	PECVD	SiH_4, Ar, and N_2O	375 °C	CTF/550–1150 °C/1 h	N_2O/SiH_4 flow ratio, SRON layer thickness, and Annealing temp.	[57]
SRC/SiC multilayer	PECVD	SiH_4, CH_4 and H_2	–	–/1100 °C/either 9 or 30 min	SiH_4/CH_4 flow ratio, pressure, and substrate temp.	[52]
SRC/SiC multilayer	PECVD	SiH_4, CH_4 and H_2	250 °C	CTF/700–1100 °C/30 min	Annealing temp.	[86]
SRC single layer	RF-PECVD	SiH_4, CH_4 and H_2	150 °C	No post annealing	Hydrogen dilution ratio	[62]
Si/SRC multilayer	PECVD	SiH_4 and CH_4	250 °C	CTF/900 °C/1 h	–	[87]
SRC single layer	PECVD	SiH_4, CH_4 and H_2	200 °C	CTF/750–1200 °C/30 min	Annealing temp.	[88]
SRC single layer	PECVD	SiH_4, CH_4 and Ar	250 °C	CTF/500–1100 °C/30 min	SiH_4/CH_4 flow ratio, and annealing temp.	[89]
SRO single layer	Cosputtering	–	Room temp.	CTF/1100 °C/1 h	Sputtering power	[65]
SRO single layer	Cosputtering	–	Room temp.	RTA/1100 and 1200 °C/30 s, Tube furnace/800–1100 °C/3 h	Annealing temp.	[36]
SRO single layer	O_2-reactive sputtering	–	100 °C	CTF/1100 °C/1 h	Sputtering power	[73]
Gradient SRO multilayer	Cosputtering	–	–	CTF/1100 °C/1 h	Film structure	[16]
SRO/SiO_2 multilayer	Cosputtering	–	–	CTF/1100 °C/1 h	Sputtering power,	[90]
Si/SiO_2 superlattice	Cosputtering	–	200–500 °C	CTF/1100 °C/1 h	Substrate temp.	[74]
SRO single layer	Cosputtering	–	Room temp.–673 K.	RTA/1323–1423 K/60 s	Substrate temp., and annealing temp.	[64]
SRO/Si_3N_4 multilayer	Cosputtering	–	–	CTF/1100 °C/–	Doping element	[91]
SRN single layer	Cosputtering	–	Room temp.	CTF/1100 °C/2 h	Sputtering rate	[66]
SRN single layer	Cosputtering	–	Room temp.	CTF/900–1100 °C/30 min-2 h	Annealing temp.	[72]

Table 1 continued

Film structure	Technique	Precursor gas	Substrate temperature	Annealing method/ temperature/time	Experimentation parameter	Ref. No.
SRN/Si_3N_4 multilayer	Cosputtering	–	–	CTF/900–1100 °C/1 h	Annealing temp.	[67]
Gradient SRN multilayer	Cosputtering	–	400 °C	RTA/1050 °C/3 min	Film structure	[75]
SRN single layer	Cosputtering	–	400 °C	LRTP/950–1100 °C/3 min, CRTP/950–1100 °C/3 min	Annealing technique, and annealing temp.	[10]
SRN single layer	N_2-reactive sputtering or cosputtering	–	200 and 500 °C	Tube furnace/1100 °C/2 h	N_2/Ar ratio or power ratio	[68]
SRC single layer	Cosputtering	–	–	CTF/1100 °C/1 h, RTA/ 1100 °C/2 min	Sputtering power, and annealing technique	[50]
SiC or SRC single layer, SiC/ SRC superlattice	Cosputtering	–	200 °C	CTF/800–1000 °C/20 min	Film structure, and annealing technique	[92]
SRC/SiC multilayer	Cosputtering	–	Room temp.	CTF/800–1100 °C/9–25 min	Sputtering power, and annealing temp.	[93]
SRC single layer	Cosputtering	–	–	CTF/900–1200 °C/1 h	Sputtering power, and annealing temp.	[94]
SRC single layer	Cosputtering	–	–	RTA/800 °C/4 min, 900 °C/ 2 min,1000–1200 °C/1 min	Sputtering power, and annealing temp.	[95]
SRC/Si_3N_4 multilayer	Cosputtering	–	–	RTA/1100 °C/2 min	Si_3N_4 barrier layer thickness	[30]
SiO/SiO_2 multilayer	Evaporation	–	100 °C	–/1100 °C/–	SiO layer thichness	[96]
SiO/Si multilayer	Evaporation	–	–	CTF/1100 °C/1 h	Intrinsic and p-type Si layer	[97]
SRO single layer	Ion implantation	–	–	CTF/1100 °C/1 h	–	[7]
SRO single layer	Pulsed laser ablation	–		CTF/1000–1200 °C/ 10–120 min	Annealing temp., and annealing time	[98]
SRC single layer	Direct ion beam deposition	–	700–1220 °C	–	Substrate temp.	[99]

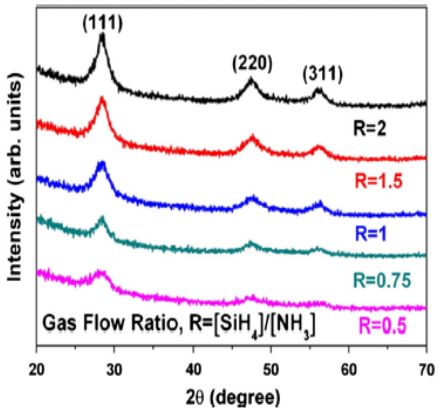

Fig. 3 GIXRD results for silicon rich nitride films deposited at different gas flow ratios and annealed at 1000 °C for 1 h. Reproduced with permission from [58] © 2012 Elsevier

significant amount of hydrogen. If the ramps are too fast, too rapid a heat build-up in the film will results in a blistering of the film because of the hydrogen does not effuse timely. Therefore, the heating ramps should be set reasonable. Wan et al. [50] have shown that RTA treatments can lead to a better degree of crystallization on Si nanocrystal and less amorphous Si residual in SRC thin films with respect to the tube-furnace annealing. However, in Ref. [80] no influence of the type of annealing (RTP or CTF) was observed on the formation and size of Si QDs in SiO_x/SiO_2 multilayers. There may exist a high density of defects at the interface between QDs and matrix, being higher in the RTP annealed multilayers [80]. A H_2-passivation is needed to diminish the defects density [14]. Moreover, high-temperature RTP will also create significant stress in the material due to the fast temperature ramping rate and the thermal shock [36, 81]. Wan et al. and Huang et al. [28, 36] have reported that an additional high-temperature tube-furnace annealing could reduce the residual stress markedly.

3 Material performance improvements

3.1 Si QDs size control and density improvements

The growth of Si QDs can be affected by the barrier layer thickness, Si-rich layer thickness, Si excess, annealing condition, and dopant element [20, 52, 57, 84, 98]. For optoelectronic applications, a high level of size and density control of Si QDs is required to ensure efficient carrier transport [100]. This section reviews several past approaches to size- and density-controlled synthesis of Si QDs.

For example for SRO layers, an early method to obtain Si QDs entails deposition of a thick SRO (SiO_x, $x < 2$) monolayer [45, 55, 64]. High-temperature post-annealing causes a phase separation between the two constituent phases, i.e. Si and SiO_2, and subsequent thermal crystallization to form Si QDs embedded in a SiO_2 matrix [31]. The size of Si QDs can be controlled by the chemical stoichiometry of the SiO_x [101], film thickness [45], and annealing parameters [102]. The QDs size can be reduced by reducing the amount of excess Si. Nevertheless, the dot density is usually reduced simultaneously [70]. The low dot density leads to the disadvantage of poor electrical conductivity of the films. Experimental studies have shown that formation of Si QDs with an average size from 4.3 down to 3 nm from a SiO_x monolayer film requires a stoichiometry x from 1.17 to 1.63 [103]. High-temperature annealing of single-layer thick films (such as SRO, SRN, and SRC) tends to form Si QDs with a broad size distribution and with weak control over spacing of Si QDs. It is indeed possible to fabricate spatially well-ordered, high-density Si QDs in a singly deposited SiO_x layer with appropriate thickness and under favourable annealing conditions [45]. However, this approach is unsuitable to be used as a common approach, because it is difficult to achieve the optimized fabrication parameters.

The growth of Si QDs through the use of multilayer structures is an effective way to control size and spatial locations of Si QDs. High-temperature annealing of amorphous Si/SiO_2 superlattices produces Si QDs, and the dot size is controlled at least in the direction perpendicular to the film surface [104]. The major drawback of this Si/SiO_2 multilayer approach is that most of the crystallites touch each other, tend to form as bricks, and the resultant layers are more like a polycrystalline silicon film [105]. This severely decreases the luminescence efficiency because the grain boundaries often provide an effective route for nonradiative processes [70].

More promising results may be achieved by replacing the a-Si layer with a SRO layer in SRO/SiO_2 multilayers. Zacharias et al. [70] first proposed this new alternative approach to form Si QDs with high density and narrow size distribution. SiO_x/SiO_2 superlattices were deposited by reactive evaporation onto a suitable substrate. The samples were then annealed at 1100 °C for 1 h under N_2 atmosphere. Experimental results have shown that the desired dot size can be controlled by adjusting the thickness of the silicon-rich layer [70]. Figure 4 shows TEM and high-resolution TEM images of Si QDs formed in such a structure. Cho et al. [106] pointed that, under moderate annealing conditions, Si QDs in Si-rich layers as approximately spherical and with a diameter close to the SiO_x sublayer thickness of the as-grown superlattices can be formed. Hao et al. [90] reported the dot size of Si QDs embedded in an oxide matrix as SRO/SiO_2 multilayers decreases with increases in O/Si ratio of the SRO layer.

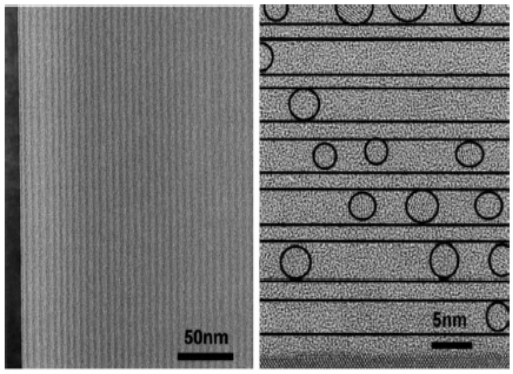

Fig. 4 Cross-sectional TEM images of SiO/SiO_2 multilayer film: **a** multilayer structure of as-prepared SiO/SiO_2 superlattice. The *darker layers* represent the SiO layers. **b** High-resolution TEM of the same film, the *crystalline particles* are *circled* for clarity. Reproduced with permission from [70] © 2002 American Institute of Physics

The density of Si QDs in the SRO layer would be determined by the concentration of excess Si in the layer. It should be noticed that not always the higher O/Si ratio the lower Si QDs density obtained as common expectation. In the work of Kourkoutis et al. [15], it is shown that the Si QDs size, shape and arrangement in SRO/SiO_2 multilayers can be governed by adjusting the SRO stoichiometry. They provided a 3-dimensional view of the Si QDs networks by EFTEM tomography. And the results shown that with decreasing Si concentration the QDs average size decreases, the QDs density increases, the size distribution narrows and the shape becomes more spherical [15]. This multilayer approach was adopted by many researchers [46, 107–109] to create superlattices for Si QDs solar cells.

Besides, another type of structure, multi-alternating layers of Si/SiO superlattice has been widely studied [97, 110, 111]. For instance, in Li et al.'s work [111], the morphology, electroluminescence (EL), and photoluminescence (PL) in annealed Si/SiO multilayers were reported and compared with single-layered one. Si NCs are formed within both Si and SiO layers after high-temperature annealing at 1100 °C for 1 h. The multilayered approach of Si/SiO is found to promote carrier transport and enhance the EL emission of Si NCs [111]. It is supposed that the Si interlayers act as extra carrier paths for carrier transport [111]. Similarly, multilayer such as Si/SiN_x [112], SiN_x/Si_3N_4 [85], SiC_x/SiC [113], Si/SiC [114], SiO_x/Si_3N_4 [115], and SiC/SiO_x [116] also were researched.

Besides, gradient Si-rich oxide multilayer structure [16] was proposed to achieve super-high density Si QDs thin film formation while preserving dot size controllability for better photovoltaic properties. Recently, we have successfully fabricated gradient Si-rich SiN_x multilayer structures [75]. It is proved again that this kind of structure is good at formation of high densities of Si QDs. In our recent work [10], we have proposed a light-filtering rapid thermal processing (LRTP) method, and fabricated high density Si QDs by use of this method. As a result, we have found that the samples treated with LRTP possess higher dot density, PL intensity, and conductivity than the conventional RTP samples. Despite of the obvious advantages of the LRTP method, little is known about the mechanism of growth of Si QDs under LRTP. The solution to this problem probably has to resort to some numerical simulation method such as Monte Carlo simulation.

3.2 Si QDs doping

For Si QDs-based solar cells, highly conductive Si QDs films are necessary [117]. By increasing carrier concentration and decreasing electrical resistivity via doping can be expected to improve the electrical properties of Si QDs films [12, 117, 118]. Moreover, fabrication of p–n junctions by doping with n- and p-type impurities is a key step to form QDs active layers in photovoltaic devices. However, it is proved that the doping of QDs is different from that of the corresponding bulk materials [119–121]. There are several difficulties about the impurity doping in a nanostructured semiconductor [122], including kinetically unfavourable nanocrystal doping caused by self-purification [120], large impurity formation energy [123], and the difficulty in direct quantitative characterization and tracking of the locations of dopants elements with nanometer-resolution [124]. Despite these difficulties, in practice, several researchers have reported successful doping of Si QDs films by several elements including phosphorus [20, 95, 125], boron [73, 126, 127], and antimony [128].

The incorporation of impurity elements in films containing Si QDs has been achieved through several means including sputtering [107], PECVD [21] and ion implantation [129]. In Hao et al.'s experiment [130], the phosphorus doping in the Si QDs superlattices was achieved by cosputtering of Si, SiO_2, and P_2O_5 with a post-deposition anneal. The O/Si ratio and P concentration in the SRO layers were controlled by adjusting the sputtering powers of these three targets. They have found that the resistivity of the sample containing 0.1 at.% P is seven orders of magnitude lower than that of the undoped sample. They have attributed this dramatic decrease in resistivity to effective P-doping in Si QDs. The same authors also reported successful doping of similar layers with boron [117]. Boron doping at a concentration of around 0.5 at.% results in a reduction on the resistivity by six orders of magnitude. They have attributed this decrease in resistivity to the consequence of an increase in mobile carrier concentration. By employing the B-doped Si QDs/SiO_2 multilayer

structure deposited onto an n-type c-Si wafer, a high energy conversion efficiency of 13.4 % has been achieved by Kim's group [124].

To achieve the desired properties in the photovoltaic applications, precise control of the position and concentration of dopant atoms at the nanoscale is crucial [124], and adequate analytical tools are essential in order to trace their properties. However, currently, several commonly used characterization techniques including X-ray photoelectron spectroscopy (XPS) and secondary ion mass spectroscopy (SIMS), can't give exact positioning of dopant atoms. For instance, B has a very low relative sensitivity factor, which makes it difficult to detect by XPS [117]. Figure 5 shows the B1 s peaks of as-deposited and annealed SRO films with boron concentration of ~0.5 at.% in which the peak around 187 eV can be attributed to B–B/B–Si bonding [117]. In the case of SRN films, B was only identified with dopant concentration equal or larger than 1.0 at.% [126]. It should be mentioned that Auger electron spectroscopy is better suitable for the light elements [131] and therefore probably useful for B determination. SIMS was just used to obtain the relative concentration of impurities [124, 132]. In order to overcome the above difficulties, Conibeer et al. [133] suggested that further characterization of the exact positioning of doping elements can be sought from high resolution XPS, scanning transmission electron microscopy, atom probe tomography, and electron paramagnetic resonance. Besides, several characterization techniques based on synchrotron radiation would be useful to attempt in the future, such as soft X-ray absorption spectroscopy, X-ray absorption near-edge structure, which have been employed to probe the surface chemistry of Si nanostructures [134].

In addition, the effects of some doping elements on growth of Si QDs are also worth noting. Hao et al. [135] found that incorporation of B suppressed Si crystallization and has little influence on the quantum dot size [135]. Phosphorus-doping could accelerate the phase separation in SRO layers and also the crystallization of Si NCs [136]. The presence of P atoms improves phase separation in Si-rich SiN_x films and thus Si crystallization rate [20]. Yoon [137] has studied the effects of the addition of Ni on the growth of Si NCs by thermal annealing of Ni-implanted SiO_x films with different content of Ni. It is established that the Ni impurity strongly effect the formation of Si NCs. Moderate Ni concentrations have been found to accelerate the processes of the formation of Si NCs, but the use of high Ni contents leads to the formation of $NiSi_2$ NCs rather than Si NCs. The influence of Sn on the formation of Si NC in an amorphous SiO_x ($x \approx 1.15$) thin film is studied by Voitovych et al. [138]. It is found that the Sn dopant accelerates the processes of crystallization of a-Si clusters and the crystallization temperature could be lowered by 200 °C when adding Sn. Si NCs formed in the Sn-doped samples are smaller in size than those formed in the undoped films, while the volume fraction of the crystalline phase in the Sn-doped films is higher than that in the films free from Sn.

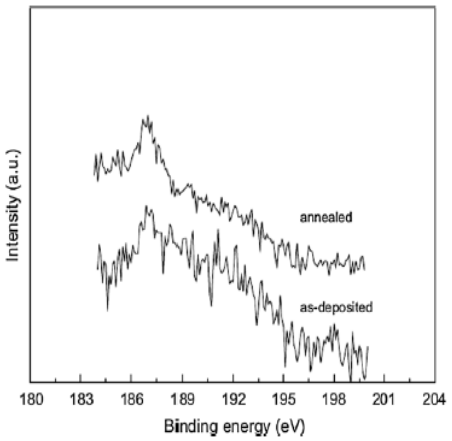

Fig. 5 XPS B1 s spectra of as-deposited and annealed boron-doped SRO film (O/Si = 0.7) with boron concentration of ~0.5 at.%. Reproduced with permission from [117] © 2008 Elsevier

3.3 Defect passivation

Due to the high surface-to-volume ratio presented by the Si QDs size, issues related to the surface of Si QDs and the interface between Si QDs and dielectric matrix come to the fore [82]. Moreover, Si dangling bonds would increase proportionately as the film becomes more Si-rich [139]. As pointed out in Ref. [80], the present challenge is how to minimize the interface defect density which governs both optical [140, 141] and electrical [142] properties. By undertaking passivation step to reduce the high defect density in Si QDs films, it is believed that the performance of Si QDs solar cells can be significantly improved.

There is a strong likelihood that dangling bond, P_b, defects will occur at nanostructure/matrix material interfaces in general [56]. Zacharias et al. [143] summarized different P_b defects in the Si NCs/SiO_2 system. Hydrogen passivation is regarded as an effective method for the passivation of electronically active P_b defects [143]. Many authors have studied the effect on the luminescence of hydrogen incorporation into Si QDs embedded in a dielectric matrix by annealing in a hydrogen-containing gaseous environment such as pure H_2 gas [144, 145] or mixed H_2/N_2 gas [146, 147] or mixed H_2/Ar gas [108, 148]. In addition, passivation treatments can be accomplished using atomic H plasma instead of hydrogen molecules in some experiments [149, 150].

It has been proposed that hydrogen passivation is related to the treatment temperature [108, 151]. The amount of

hydrogen entering into the Si QDs film increases with treatment temperature increase. Meanwhile, dehydrogenation of hydrogen atoms terminating the dangling bonds becomes more prominent during a rise of temperature [151]. The steady-state passivation level is determined by the thermodynamic balance between defect passivation and depassivation [149]. The treatment temperature of 400 °C is considered as optimal in Ref. [151]. For Si-NCs/SiO_2 multilayer thin films, passivation can also be performed by thermal oxidation [152] or exposing the films directly to the atomic oxygen plasma [153].

As for SRC/SiC multilayer, the host matrix consists of amorphous SiC and crystalline SiC phases after annealing, it is possible to contain a high defect density; a hydrogen passivation can be carried out in order to prepare an electronically high-quality film with less recombination-active defects [150]. In Ref. [154], it is shown that the as-annealed Si_xC_{1-x}/SiC superlattices exhibited no PL but once the films were subjected to hydrogen passivation, which decreased the defect density as detected by electron spin resonance, PL emission was observed. Kořínek et al. [150] studied the effect of hydrogen passivation on the PL properties of the B-doped Si-NC/SiC multilayers. They found that hydrogen passivation leads to an additional increase in PL intensities. Ding et al. [155] reported the generation of additional defect states in SiC/SiO_x heterosuperlattice (HSL) during the post deposition annealing. These additional defects are likely to result in a poor device performance of the HSL structure, and thus have to be passivated prior to application of HSL as a solar cell absorber. In their later work [116], the effectiveness of defect passivation methods such as hydrogen plasma in a PECVD reactor, hydrogen dissociation catalysis in a HWCVD reactor, and forming gas annealing (FGA) is examined. They suggest that FGA is the most promising method for the HSL sample passivation. In Di et al.'s work [108], the impact of forming gas (Ar:H_2) anneal on the single junction Si QDs solar cells' electrical and photovoltaic properties has been studied. After annealing in forming gas, the reduction of series resistance is largely (see Fig. 6) and this behavior is attributed to the hydrogen passivation at the interfaces of the Si nanocrystals [108].

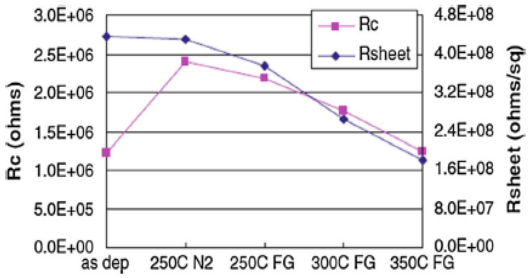

Fig. 6 Contact (R_c) and sheet (R_{sheet}) resistances as a function of annealing conditions. Reproduced with permission from [108] © The Authors 2010

4 Photovoltaic devices

Si QDs have also already been incorporated in solar cells, as will be discussed below. Recently, photovoltaic devices with different structures, such as p-type Si QDs/n-type c-Si heterojunction, n-type Si QDs/p-type c-Si heterojunction, and p–i–n diodes have been successfully fabricated [124, 132, 151]. However, there have been few reports [156] on experimental realization of Si QDs-based 'all-Si' tandem solar cells mainly due to the difficulty in charge transfer between the QDs and the formation of tunnel junctions. In this section we summarize the photovoltaic studies with Si QDs and propose ideas for further exploration.

Table 2 summarizes the photovoltaic parameters of the representative examples of Si QDs photovoltaic devices with QDs as active material. Several characteristics can be drawn from Table 2 as follows: (a) The open circuit voltage obtained from these Si QDs solar cells is much lower than that expected for an absorber layer with a bandgap larger than that of c-Si. (b) The performance of Si QDs solar cells shown in Table 2 is limited by the relatively low short-circuit current density, which can be attributed to the poor carrier transport properties of Si QDs layers. (c) The active cell area was too small to learn the lateral conductivity and charge collection. (d) For photovoltaic properties, the absorption contribution from the Si QDs cannot be established because of the Si substrate absorbs many of the incident light and contributes to the photovoltaic effect. (e) The most efficient Si QDs cells prepared so far was a p-type Si QDs/n-type c-Si heterojunction solar cell with B concentration of 4×10^{20} atoms cm^{-3}, which shows an efficiency of 13.4 % [124]. This corresponds to a short circuit current of 33.7 mA cm^{-2} (AM 1.5), an open circuit voltage of 525 mV, and a fill factor FF of 78.5 %. Although these cell parameters are not comparable to crystalline silicon solar cell efficiencies, they can be viewed as a positive step towards realization of an 'all-Si' tandem cell based on Si QDs materials, as they demonstrate electrical conduction in Si QDs layers.

Usually, these Si QDs solar cells are fabricated on Si wafers. For example, Song et al. [157] reported that p-type Si QDs/n-type c-Si heterojunction devices showed an open circuit voltage of 463 mV, a short circuit current density of 19 mA cm^{-2}, a fill factor of 53 %, and an energy conversion efficiency of 4.66 %. The internal quantum efficiency, external quantum efficiency measurements showed a higher blue response than that of a conventional c-Si single junction solar cell and was due to increasing the

Table 2 Photovoltaic performance of some of the Si QDs solar cells produced in the laboratory by employing different device designs

Device	Si wafer need (Y/N)	A	V_{oc} (mV)	J_{sc}/I_{sc}	FF (%)	ζ (%)	Ref. No.
p-Type Si QDs in SiO_2/n-type c-Si	Y	–	525	33.7 mA cm^{-2}	78.5	13.4	[124]
n-Type Si QDs in SiO_2/p-type c-Si	Y	–	556	29.8 mA cm^{-2}	63.83	10.58	[107]
p-Type Si QDs in SiO_2/n-type Si QDs in SiO_2	N	2–10 mm^2	410	–	–	–	[108]
p-Type Si QDs in SiO_2/intrinsic Si QDs in SiO_2/n-type Si QDs in SiO_2	N	0.12 cm^2	373	–	–	–	[158]
p-Type Si QDs in SiO_2/intrinsic Si QDs in SiO_2/n-type Si QDs in SiO_2	N	2.2 mm^2	492	0.02 mA cm^{-2}	–	–	[25]
n-Type Si QDs in SiO_2/p-type c-Si	Y	–	555.6	29.8 mA cm^{-2}	63.8	10.6	[132]
n-Type Si QDs in Si_3N_4/p-type c-Si	Y	1 mm^2	510	4.96 mA	20.5	–	[18]
n-Type Si QDs in Si_3N_4/p-type c-Si	Y	1 cm^2	500	26.5 mA cm^{-2}	65.2	8.6	[125]
n-Type poly-Si/intrinsic Si QDs in SiC/p-type hydrogenated a-Si	N	–	518	0.34 mA cm^{-2}	51	–	[151]
p-Type Si QDs in SiC/n-type c-Si	Y	–	463	19 mA cm^{-2}	53	4.66	[157]
n-Type a-Si/intrinsic Si QDs in SiC/p-Si	Y	0.8 cm^2	532	24.1 mA cm^{-2}	48.9	6.28	[26]
p-Type a-Si_xC_{1-x}/intrinsic Si QDs in SiC/n-type a-Si_xC_{1-x}	N	–	282	0.339 mA cm^{-2}	–	–	[9]

The parameters: open circuit voltage = V_{oc}; short circuit current/density = J_{sc}/I_{sc}; fill factor = FF; conversion efficiency = ζ; active area = A

bandgap of Si-NC:SiC window layer [157]. However, in this device, the Si substrate masks the effect of the Si QDs layer in this device due to its superior electronic properties. Photovoltaic characterization of Si QDs films without any influence from Si substrate become a challenge. There are a few researches fabricating Si QDs photovoltaic device on an insulating substrate [25, 108, 158]. Such photovoltaic devices have been used for realizations of Si QDs solar cells without electrical wafer influence. Perez-Wurfl et al. [158] have fabricated p–i–n diodes onto quartz substrates with a total active area of 0.12 cm^2. A schematic of such structure is shown in Fig. 7. As shown in the SIMS data,

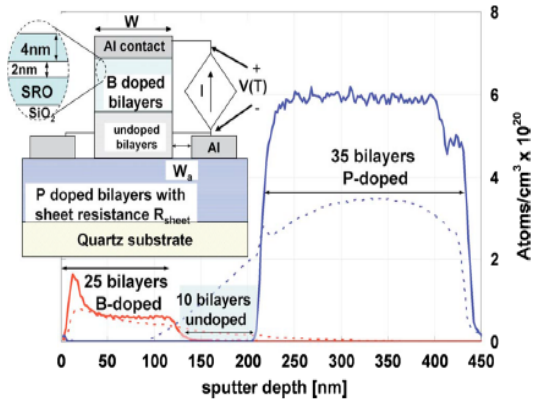

Fig. 7 Schematic of the p–i–n structure photovoltaic device and SIMS profiles of as-deposited (*solid line*) and annealed (*dotted line*) p–i–n structure. Reproduced with permission from [158] © 2009 American Institute of Physics

significant interdiffusion of B and P was occurred in the i-layer after high-temperature annealing and the structure was changed from p–i–n to p–n structure. The resulting p–n structure shows photovoltaic behavior, with an open circuit voltage of 373 mV. The same structure device with a total active area of 2.2 mm^2 was re-fabricated in the same authors' later study [25]. This device yielded 492 mV open-circuit voltage and 0.02 mA cm^{-2} short-circuit current density. The authors believe that the measured short-circuit current density is limited by a large series resistance of 28 kΩ cm^2.

Fabrication a substrate-free photovoltaic device is another way to characterize the photovoltaic performance of Si QDs films without any influence from Si substrate. Löper et al. [9] have developed a membrane-based p–i–n device structure in which the substrate is locally removed by chemical etching and then the rest of substrate be encapsulated after solid-phase crystallization of the Si QDs. This device yielded 282 mV open-circuit voltage and 0.339 mA cm^{-2} short-circuit current density. The apparent weakness of this cell lies in the short-circuit current density; the experimental short-circuit current J_{SC} is only 0.068 idealized maximum photogenerated current J_{gen}, indicating highly recombinative defects in the depletion region [9]. Although the photovoltaic performance is limited by charge carrier recombination, the measured values are directly related to the Si QDs layer, without being affected by the Si substrate [9].

In the fabrication of photovoltaic devices using Si QDs embedded in its silicide matrix, it is still a difficult task to

improve current transport and to reduce carrier recombination [9, 107, 125]. Light trapping techniques will be needed for the development of Si QDs solar cells as the cell absorber layer is very thin. Further device optimization such as optimization of Si QDs growth parameters (film deposition conditions, interface engineering, material passivation, etc.), optimization of the composition of the cell's absorber material, surface plasmons or texturing, and back-surface field are needed to improve the device performance.

5 Conclusions and outlook

We have provided an overview of the selected recent progress with respect to photovoltaic applications of Si QDs films. It has been seen that Si QDs films can be produced by different growth methods. There have been several strategies used to fabricate high density, size-controlled Si QDs with narrow size distribution, including using multilayer structure. With regard to solar cell applications, moderate doping and defects passivation are of high importance to enable better overall material performance. Photovoltaic devices based on Si QDs films have been fabricated by by several groups. This review work shows that Si QDs films has the potential of producing cheap solar cells, which have the possibility to overcome the Shockley–Queisser limit of conventional crystalline Si solar cells.

Although many efforts have been made on improving the conversion efficiency of Si QDs solar cells, it still remains lower than that for conventional crystalline Si solar cells. As far as we know, the best efficiency so far for a Si QDs cell is 13.4 % [124], which is about half of the best efficiency obtained for conventional crystalline Si solar cells (25.6 %) [22]. To further improve the cell performance, the majority of research regarding Si QDs solar cells focuses on three main aspects: (1) developing efficient methods to synthesize size-controllable Si QDs with high dot density, (2) good conductive properties, and (3) judicious and careful device optimization. But problems remain with precise control of doping elements, understanding doping mechanism, improving current transport and increasing V_{oc}. The future research (such as the materials growth, defects passivation, device design, electrode contacts, efficiency of light trapping, etc.) of Si QDs highly relies on the understanding and precise control of doping elements and electronic transport mechanism. Though the current conversion efficiencies reported for the Si QDs solar cells are lower than the conventional crystalline Si solar cells, it is highly expected that further studies at the Si QDs solar cells will lead to a breakthrough that will enable us to realize high-efficiency photovoltaic devices in the near future.

Acknowledgments This work was supported by the National Natural Science Foundation of China (Grant Nos. 51362031, U1037604), A Project Supported by Scientific Research Fund of Sichuan Provincial Education Department (Grant No. 15ZB0317), and Scholarship Award for Excellent Doctoral Student granted by Yunnan Province.

References

1. M. Naddaf, J. Mater. Sci.: Mater. Electron. **23**, 2173 (2012)
2. L. Mangolini, J. Vac. Sci. Technol. B **31**, 020801 (2013)
3. Q. Guo, T. Wang, K. Sheng, B. Yu, J. Mater. Sci.: Mater. Electron. **23**, 334 (2012)
4. J. Ji, H. Zhang, Y. Qiu, Y. Luo, L. Hu, J. Mater. Sci.: Mater. Electron. **24**, 4433 (2013)
5. F. Priolo, T. Gregorkiewicz, M. Galli, T.F. Krauss, Nat. Nanotechnol. **9**, 19 (2014)
6. A.M. Hartel, S. Gutsch, D. Hiller, C. Kübel, N. Zakharov, P. Werner, M. Zacharias, Appl. Phys. Lett. **101**, 193103 (2012)
7. R. Karmouch, G. Savard, D. Barba, D. Koshel, F. Martin, G.G. Ross, J. Mater. Sci.: Mater. Electron. **24**, 1837 (2013)
8. B.T. Goh, C.K. Wah, Z. Aspanut, S.A. Rahman, J. Mater. Sci.: Mater. Electron. **25**, 286 (2014)
9. P. Löper, M. Canino, D. Qazzazie, M. Schnabel, M. Allegrezza, C. Summonte, S.W. Glunz, S. Janz, M. Zacharias, Appl. Phys. Lett. **102**, 033507 (2013)
10. X. Chen, P. Yang, J. Mater. Sci.: Mater. Electron. **25**, 5410 (2014)
11. A. Kole, P. Chaudhuri, AIP Adv. **4**, 107106 (2014)
12. X. Yu, W. Yu, X. Wang, Y. Zheng, J. Zhang, Z. Jiang, G. Fu, Superlattices Microstruct. **78**, 88 (2015)
13. S.K. Ray, S. Maikap, W. Banerjee, S. Das, J. Phys. D Appl. Phys. **46**, 153001 (2013)
14. M.L. Ciurea, A.M. Lepadatu, Dig. J. Nanomater. Bios. **10**, 59 (2015)
15. L.F. Kourkoutis, X. Hao, S. Huang, B. Puthen-Veettil, G. Conibeer, M.A. Green, I. Perez-Wurfl, Nanoscale **5**, 7499 (2013)
16. K.Y. Kuo, P.R. Huang, P.T. Lee, Nanotechnology **24**, 195701 (2013)
17. A.M. Lepadatu, I. Stavarache, M.L. Ciurea, V. Iancu, J. Appl. Phys. **107**, 033721 (2010)
18. D. Di, H. Xu, I. Perez-Wurfl, M.A. Green, G. Conibeer, Prog. Photovolt.: Res. Appl. **21**, 569 (2013)
19. G. Conibeer, M. Green, R. Corkish, Y. Cho, E.C. Cho, C.W. Jiang, T. Fangsuwannarak, E. Pink, Y.D. Huang, T. Puzzer, T. Trupke, B. Richards, A. Shalav, K.L. Lin, Thin Solid Films **511**, 654 (2006)
20. P.J. Wu, Y.C. Wang, I.C. Chen, J. Phys. D Appl. Phys. **46**, 125104 (2013)
21. S. Gutsch, A.M. Hartel, D. Hiller, N. Zakharov, P. Werner, M. Zacharias, Appl. Phys. Lett. **100**, 233115 (2012)
22. M.A. Green, K. Emery, Y. Hishikawa, W. Warta, E.D. Dunlop, Prog. Photovolt.: Res. Appl. **23**, 1 (2015)
23. A. Richter, M. Hermle, S.W. Glunz, IEEE J. Photovolt. **3**, 1184 (2013)
24. G. Conibeer, M. Green, E.C. Cho, D. König, Y.H. Cho, T. Fangsuwannarak, G. Scardera, E. Pink, Y. Huang, T. Puzzer, S. Huang, D. Song, C. Flynn, S. Park, X. Hao, D. Mansfield, Thin Solid Films **516**, 6748 (2008)
25. I. Perez-Wurfl, L. Ma, D. Lin, X. Hao, M.A. Green, G. Conibeer, Sol. Energy Mater. Sol. Cells **100**, 65 (2012)
26. Y. Cao, P. Lu, X. Zhang, J. Xu, L. Xu, K. Chen, Nanoscale Res. Lett. **9**, 1 (2014)
27. T. Saga, NPG Asia Mater. **2**, 96 (2010)

28. Z.Y. Wan, S.J. Huang, M.A. Green, G. Conibeer, Phys. Status Solidi C **8**, 185 (2011)
29. C.W. Jiang, M.A. Green, J. Appl. Phys. **99**, 114902 (2006)
30. Z. Wan, R. Patterson, S. Huang, M. Green, G. Conibeer, EPL-Europhys. Lett. **95**, 67006 (2011)
31. S. Janz, P. Löper, M. Schnabel, Mater. Sci. Eng. B **178**, 542 (2013)
32. M. Schnabel, C. Weiss, P. Löper, P.R. Wilshaw, S. Janz, Phys. Status Solidi A (2015). doi:10.1002/pssa.201431764
33. X.X. Wang, J.G. Zhang, L. Ding, B.W. Cheng, W.K. Ge, J.Z. Yu, Q.M. Wang, Phys. Rev. B **72**, 195313 (2005)
34. R. Ha, S. Kim, H.J. Kim, J.C. Lee, J.S. Bae, Y. Kim, J. Nanosci. Nanotechnol. **12**, 1448 (2012)
35. M. Künle, T. Kaltenbach, P. Löper, A. Hartel, S. Janz, O. Eibl, K.G. Nickel, Thin Solid Films **519**, 151 (2010)
36. J. Huang, Y. Zeng, W. Wang, Y. Yang, J. Huang, R. Tan, S. Dai, N. Dai, W. Song, Phys. Status Solidi A **210**, 528 (2013)
37. S. Hernández, J. López-Vidrier, L. López-Conesa, D. Hiller, S. Gutsch, J. Ibáñez, S. Estradé, F. Peiró, M. Zacharias, B. Garrido, J. Appl. Phys. **115**, 203504 (2014)
38. F. Iacona, G. Franzò, C. Spinella, J. Appl. Phys. **87**, 1295 (2000)
39. D. Nesheva, C. Raptis, A. Perakis, I. Bineva, Z. Aneva, Z. Levi, S. Alexandrova, H. Hofmeister, J. Appl. Phys. **92**, 4678 (2002)
40. M. Molinari, H. Rinnert, M. Vergnat, P. Weisbecker, Mater. Sci. Eng. B **101**, 186 (2003)
41. T. Roschuk, I.F. Crowe, A.P. Knights, M.P. Halsall, Prog. Optics **58**, 251 (2013)
42. T.V. Torchynska, J. Non-Cryst. Solids **352**, 2484 (2006)
43. S. Mirabella, R. Agosta, G. Franzò, I. Crupi, M. Miritello, R.L. Savio, M.A.D. Stefano, S.D. Marco, F. Simone, A. Terrasi, J. Appl. Phys. **106**, 103505 (2009)
44. X. Wang, X. Yu, W. Yu, H. Feng, J. Wang, C. Yin, W. Lu, G. Fu, J. Mater. Sci. **9**, 1353 (2014)
45. K. Surana, H. Lepage, J.M. Lebrun, B. Doisneau, D. Bellet, L. Vandroux, G.L. Carval, M. Baudrit, P. Thony, P. Mur, Nanotechnology **23**, 105401 (2012)
46. N.R. Mavilla, C.S. Solanki, J. Vasi, Phys. E **52**, 59 (2013)
47. A.K. Panchal, C.S. Solanki, J. Cryst. Growth **311**, 2659 (2009)
48. T.C. Tsai, L.Z. Yu, C.T. Lee, Nanotechnology **18**, 275707 (2007)
49. K.M. Lee, T.H. Kim, J.D. Hwang, S. Jang, K. Jeong, M. Han, S. Won, J. Sok, K. Park, W.S. Hong, Scripta Mater. **60**, 703 (2009)
50. Z. Wan, S. Huang, M.A. Green, G. Conibeer, Nanoscale Res. Lett. **6**, 129 (2011)
51. K. Bi, Y. Liu, K. Liu, J. Jiang, W. Peng, Surf. Coat. Technol. **228**, 148 (2013)
52. C. Summonte, M. Allegrezza, M. Bellettato, F. Liscio, M. Canino, A. Desalvo, J. López-Vidrier, S. Hernández, L. López-Conesa, S. Estradé, F. Peiró, B. Garrido, P. Löper, M. Schnabel, S. Janz, R. Guerra, S. Ossicini, Sol. Energy Mater. Sol. Cells **128**, 138 (2014)
53. B. Sain, D. Das, Phys. Chem. Chem. Phys. **15**, 3881 (2013)
54. G. Faraci, G. Mannino, A.R. Pennisi, R. Ruggeri, P. Sberna, V. Privitera, J. Appl. Phys. **113**, 063518 (2013)
55. Y. Li, B. Qian, Z. Sui, C. Jiang, Appl. Phys. Lett. **103**, 161908 (2013)
56. E.G. Barbagiovanni, D.J. Lockwood, P.J. Simpson, L.V. Goncharova, App. Phys. Rev. **1**, 011302 (2014)
57. A.M. Hartel, D. Hiller, S. Gutsch, P. Löper, S. Estradé, F. Peiró, B. Garrido, M. Zacharias, Thin Solid Films **520**, 121 (2011)
58. P.L. Li, C. Gau, C.W. Liu, Thin Solid Films **529**, 185 (2013)
59. D. Hiller, S. Gutsch, A.M. Hartel, P. Löper, T. Gebel, M. Zacharias, J. Appl. Phys. **115**, 134311 (2014)
60. B. Rezgui, A. Sibai, T. Nychyporuk, M. Lemiti, G. Bremond, D. Maestre, O. Palais, Appl. Phys. Lett. **96**, 183105 (2010)
61. B. Sain, D. Das, RSC Adv. **4**, 36929 (2014)
62. J. Ma, J. Ni, J. Zhang, Q. Liu, X. Chen, D. Zhang, X. Zhang, Y. Zhao, Sol. Energy Mater. Sol. Cells **130**, 561 (2014)
63. A. Kole, P. Chaudhuri, Thin Solid Films **522**, 45 (2012)
64. J. Huang, Y. Zeng, R. Tan, W. Wang, Y. Yang, N. Dai, W. Song, Appl. Surf. Sci. **270**, 428 (2013)
65. S. Ilday, G. Nogay, R. Turan, Appl. Surf. Sci. **318**, 256 (2014)
66. P.D. Nguyen, D.M. Kepaptsoglou, Q.M. Ramasse, M.F. Sunding, L.O. Vestland, T.G. Finstad, A. Olsen, J. Appl. Phys. **112**, 073514 (2012)
67. Y.H. So, S. Huang, G. Conibeer, M.A. Green, Thin Solid Films **519**, 5408 (2011)
68. O. Debieu, R.P. Nalini, J. Cardin, X. Portier, J. Perrière, F. Gourbilleau, Nanoscale Res. Lett. **8**, 1 (2013)
69. K. Ma, J.Y. Feng, Z.J. Zhang, Nanotechnology **17**, 4650 (2006)
70. M. Zacharias, J. Heitmann, R. Scholz, U. Kahler, M. Schmidt, J. Bläsing, Appl. Phys. Lett. **80**, 661 (2002)
71. J.M. Terrazas, N. Nedev, E. Manolov, B. Valdez, D. Nesheva, M.A. Curiel, R. Haasch, I. Petrov, J. Mater. Sci.: Mater. Electron. **21**, 481 (2010)
72. P.D. Nguyen, D.M. Kepaptsoglou, Q.M. Ramasse, A. Olsen, Phys. Rev. B **85**, 085315 (2012)
73. M. Xie, D. Li, L. Chen, F. Wang, X. Zhu, D. Yang, Appl. Phys. Lett. **102**, 123108 (2013)
74. Y.-L. Tao, Y.-H. Zuo, J. Zheng, C.-L. Xue, B.-W. Cheng, Q.-M. Wang, J. Xu, Chin. Phys. B **21**, 077402 (2012)
75. X. Chen, W. Yang, L. Duan, L. Zhang, P. Yang, J. Inorg. Mater. **29**, 1270 (2014)
76. A.R. Wilkinson, R.G. Elliman, J. Appl. Phys. **96**, 4018 (2004)
77. V. Mulloni, P. Bellutti, L. Vanzetti, Surf. Sci. **585**, 137 (2005)
78. M. Bolduc, G. Genard, M. Yedji, D. Barbe, F. Martin, G. Terwagne, G.G. Ross, J. Appl. Phys. **105**, 013108 (2009)
79. R.P.S. Thakur, R. Singh, Appl. Phys. Lett. **64**, 327 (1994)
80. D. Hiller, S. Goetze, M. Zacharias, J. Appl. Phys. **109**, 054308 (2011)
81. D.E. Yılmaz, C. Bulutay, T. Çağın, Appl. Phys. Lett. **94**, 191914 (2009)
82. J. Barbé, K. Makasheva, S. Perraud, M. Carrada, B. Despax, J. Phys. D Appl. Phys. **47**, 255302 (2014)
83. A. Zelenina, A. Sarikov, D.M. Zhigunov, C. Weiss, N. Zakharov, P. Werner, L. López-Conesa, S. Estradé, F. Peiró, S.A. Dyakov, M. Zacharias, J. Appl. Phys. **115**, 244304 (2014)
84. D. Hiller, A. Zelenina, S. Gutsch, S.A. Dyakov, L. López-Conesa, J. López-Vidrier, S. Estradé, F. Peiró, B. Garrido, J. Valenta, M. Kořínek, F. Trojánek, P. Malý, M. Schnabel, C. Weiss, S. Janz, M. Zacharias, J. Appl. Phys. **115**, 204301 (2014)
85. G. Scardera, T. Puzzer, I. Perez-Wurfl, G. Conibeer, J. Cryst. Growth **310**, 3680 (2008)
86. M. Künle, S. Janz, K.G. Nickel, A. Heidt, M. Luysberg, O. Eibl, Sol. Energy Mater. Sol. Cells **115**, 11 (2013)
87. J. Ma, J. Ni, J. Zhang, Q. Liu, G. Hou, X. Chen, X. Zhang, Y. Zhao, Sol. Energy Mater. Sol. Cells **123**, 228 (2014)
88. G. Wen, X. Zeng, W. Liao, C. Cao, Thin Solid Films **552**, 18 (2014)
89. A.M. Hartel, M. Künle, P. Löper, S. Janz, A.W. Bett, Sol. Energy Mater. Sol. Cells **94**, 1942 (2010)
90. X.J. Hao, A.P. Podhorodecki, Y.S. Shen, G. Zatryb, J. Misiewicz, M.A. Green, Nanotechnology **20**, 485703 (2009)
91. D. Di, H. Xu, I. Perez-Wurfl, M.A. Green, G. Conibeer, Nanoscale Res. Lett. **6**, 1 (2011)
92. J. Moon, S.J. Baik, O. Byungsung, J.C. Lee, Nanoscale Res. Lett. **7**, 1 (2012)
93. D. Song, E.C. Cho, G. Conibeer, Y. Huang, C. Flynn, M.A. Green, J. Appl. Phys. **103**, 083544 (2008)
94. A.G. Imer, I. Yildiz, R. Turan, Phys. E **42**, 2358 (2010)
95. Y. Zeng, N. Dai, Q. Cheng, J. Huang, X. Liang, W. Song, Mater. Sci. Semicond. Process. **16**, 598 (2013)

96. A.E. Naciri, P. Miska, A.S. Keita, Y. Battie, H. Rinnert, M. Vergnat, J. Nanopart. Res. **15**, 1 (2013)
97. D.C. Wang, J.R. Chen, J. Zhu, C.T. Lu, M. Lu, J. Nanopart. Res. **15**, 1 (2013)
98. J. Gan, Q. Li, Z. Hu, W. Yu, K. Gao, J. Sun, N. Xu, J. Wu, Appl. Surf. Sci. **257**, 6145 (2011)
99. I.V. Mirgorodskiy, L.A. Golovan, V.Y. Timoshenko, A.V. Semenov, V.M. Puzikov, Semiconductors **48**, 711 (2014)
100. J.W. Luo, P. Stradins, A. Zunger, Energy Environ. Sci. **4**, 2546 (2011)
101. S. Hernández, A. Martínez, P. Pellegrino, Y. Lebour, B. Garrido, E. Jordana, J.M. Fedeli, J. Appl. Phys. **104**, 044304 (2008)
102. A. Coyopol, T. Díaz-Becerril, G. García-Salgado, H. Juárez-Santisteban, R. López, E. Rosendo-Andrés, J. Lumin. **145**, 88 (2014)
103. U. Kahler, H. Hofmeister, Opt. Mater. **17**, 83 (2001)
104. T. Zheng, Z. Li, Superlattices Microstruct. **37**, 227 (2005)
105. G.F. Grom, D.J. Lockwood, J.P. McCaffrey, H.J. Labbe, P.M. Fauchet, B. White, J. Diener, D. Kovalev, F. Koch, L. Tsybeskov, Nature **407**, 358 (2000)
106. E.C. Cho, M.A. Green, G. Conibeer, D.Y. Song, Y.H. Cho, G. Scardera, S.J. Huang, S. Park, X.J. Hao, Y.D. Huang, L.V. Dao, Adv. Opt. Electron. **2007**, 69578 (2007)
107. S. Park, E. Cho, D. Song, G. Conibeer, M.A. Green, Sol. Energy Mater. Sol. Cells **93**, 684 (2009)
108. D. Di, I. Perez-Wurfl, A. Gentle, D.H. Kim, X. Hao, L. Shi, G. Conibeer, M.A. Green, Nanoscale Res. Lett. **5**, 1762 (2010)
109. G. Zatryb, A. Podhorodecki, X.J. Hao, J. Misiewicz, Y.S. Shen, M.A. Green, Nanotechnology **22**, 335703 (2011)
110. D. Li, Y.B. Chen, M. Lu, Mater. Lett. **89**, 9 (2012)
111. D. Li, Y.B. Chen, Y. Ren, J. Zhu, Y.Y. Zhao, M. Lu, Nanoscale Res. Lett. **7**, 1 (2012)
112. A.K. Panchal, D.K. Rai, M. Mathew, C.S. Solanki, J. Nanopart. Res. **13**, 2469 (2011)
113. J. López-Vidrier, S. Hernández, J. Samà, M. Canino, M. Allegrezza, M. Bellettato, R. Shukla, M. Schnabel, P. Löper, L. López-Conesa, S. Estradé, F. Peiró, S. Janz, B. Garrido, Mater. Sci. Eng. B **178**, 639 (2013)
114. Y. Rui, S. Li, Y. Cao, J. Xu, W. Li, K. Chen, Appl. Surf. Sci. **269**, 37 (2013)
115. D. Di, I. Perez-Wurfl, G. Conibeer, M.A. Green, Sol. Energy Mater. Sol. Cells **94**, 2238 (2010)
116. K. Ding, U. Aeberhard, O. Astakhov, U. Breuer, M. Beigmohamadi, S. Suckow, B. Berghoff, W. Beyer, F. Finger, R. Carius, U. Rau, J. Non-Cryst. Solids **358**, 2145 (2012)
117. X.J. Hao, E.C. Cho, C. Flynn, Y.S. Shen, S.C. Park, G. Conibeer, M.A. Green, Sol. Energy Mater. Sol. Cells **93**, 273 (2009)
118. C. Summonte, M. Canino, M. Allegrezza, M. Bellettato, A. Desalvo, R. Shukla, I.P. Jain, I. Crupi, S. Milita, L. Ortolani, L. López-Conesa, S. Estradé, F. Peiró, B. Garrido, Mater. Sci. Eng. B **178**, 551 (2013)
119. D.J. Norris, N. Yao, F.T. Charnock, T.A. Kennedy, Nano. Lett. **1**, 3 (2000)
120. S.C. Erwin, L. Zu, M.I. Haftel, A.L. Efros, T.A. Kennedy, D.J. Norris, Nature **436**, 91 (2005)
121. G.M. Dalpian, J.R. Chelikowsky, Phys. Rev. Lett. **96**, 226802 (2006)
122. S. Ossicini, F. Iori, E. Degoli, E. Luppi, R. Magri, R. Poli, G. Cantele, F. Trani, D. Ninno, IEEE J. Sel. Top. Quant. **12**, 1585 (2006)
123. G. Cantele, E. Degoli, E. Luppi, R. Magri, D. Ninno, G. Iadonisi, S. Ossicini, Phys. Rev. B **72**, 113303 (2005)
124. S.H. Hong, Y.S. Kim, W. Lee, Y.H. Kim, J.Y. Song, J.S. Jang, J.H. Park, S.-H. Choi, K.J. Kim, Nanotechnology **22**, 425203 (2011)
125. P.-J. Wu, Y.-C. Wang, I.-C. Chen, Nanoscale Res. Lett. **8**, 457 (2013)
126. S. Huang, Y.H. So, G. Conibeer, M. Green, Jpn. J. Appl. Phys. **51**, 10NE10 (2012)
127. J. Ma, J. Ni, J. Zhang, Z. Huang, G. Hou, X. Chen, X. Zhang, X. Geng, Y. Zhao, Sol. Energy Mater. Sol. Cells **114**, 9 (2013)
128. Y.H. So, S. Huang, G. Conibeer, M.A. Green, EPL-Europhys. Lett. **96**, 17011 (2011)
129. T. Nakamura, S. Adachi, M. Fujii, K. Miura, S. Yamamoto, Phys. Rev. B **85**, 045441 (2012)
130. X.J. Hao, E.C. Cho, G. Scardera, Y.S. Shen, E. Bellet-Amalric, D. Bellet, G. Conibeer, M.A. Green, Sol. Energy Mater. Sol. Cells **93**, 1524 (2009)
131. P.J. Smith, Materials and Chemical Analysis of Electronic Devices, in *Microelectronics Manufacturing Diagnostics Handbook*, ed. by A.H. Landzberg (Springer, NewYork, 1993), pp. 396–424
132. E.C. Cho, S. Park, X. Hao, D. Song, G. Conibeer, S.C. Park, M.A. Green, Nanotechnology **19**, 245201 (2008)
133. G. Conibeer, M.A. Green, D. König, I. Perez-Wurfl, S. Huang, X. Hao, D. Di, L. Shi, S. Shrestha, B. Puthen-Veetil, Y. So, B. Zhang, Z. Wan, Prog. Photovolt.: Res. Appl. **19**, 813 (2011)
134. J. Zhong, H. Zhang, X. Sun, S.T. Lee, Adv. Mater. **26**, 7786 (2014)
135. X.J. Hao, E.C. Cho, C. Flynn, Y.S. Shen, G. Conibeer, M.A. Green, Nanotechnology **19**, 424019 (2008)
136. X.J. Hao, E.C. Cho, G. Scardera, E. Bellet-Amalric, D. Bellet, Y.S. Shen, S. Huang, Y.D. Huang, G. Conibeer, M.A. Green, Thin Solid Films **517**, 5646 (2009)
137. J.H. Yoon, Mater. Lett. **136**, 237 (2014)
138. V.V. Voitovych, R.M. Rudenko, A.G. Kolosiuk, M.M. Krasko, V.O. Juhimchuk, M.V. Voitovych, S.S. Ponomarov, A.M. Kraitchinskii, V.Y. Povarchuk, V.A. Makara, Semiconductors **48**, 73 (2014)
139. H. Miyashita, Y. Watabe, J. Appl. Phys. **70**, 2452 (1991)
140. C. Delerue, G. Allan, M. Lannoo, Phys. Rev. B **48**, 11024 (1993)
141. M. Jivanescu, D. Hiller, M. Zacharias, A. Stesmans, Europhys. Lett. **96**, 27003 (2011)
142. S. Gutsch, J. Laube, A.M. Hartel, D. Hiller, N. Zakharov, P. Werner, M. Zacharias, J. Appl. Phys. **113**, 133703 (2013)
143. M. Zacharias, D. Hiller, A. Hartel, S. Gutsch, Phys. Status Solidi A **209**, 2449 (2012)
144. J. Xu, W. Mu, Z. Xia, H. Sun, D. Wei, W. Li, Z. Ma, K. Chen, J. Non-Cryst. Solids **358**, 2141 (2012)
145. S. Cheylan, R.G. Elliman, Appl. Phys. Lett. **78**, 1225 (2001)
146. M. Lopez, B. Garrido, C. Garcıa, P. Pellegrino, A. Perez-Rodriguez, J.R. Morante, C. Bonafos, M. Carrada, A. Claverie, Appl. Phys. Lett. **80**, 1637 (2002)
147. S. Godefroo, M. Hayne, M. Jivanescu, A. Stesmans, M. Zacharias, O.I. Lebedev, G. van Tendeloo, V.V. Moshchalkov, Nat. Nanotechnol. **3**, 174 (2008)
148. D. Comedi, O.H.Y. Zalloum, P. Mascher, Appl. Phys. Lett. **87**, 213110 (2005)
149. Y.J. Jung, J.H. Yoon, R.G. Elliman, A.R. Wilkinson, J. Appl. Phys. **104**, 083518 (2008)
150. M. Kořínek, M. Schnabel, M. Canino, M. Kozák, F. Trojánek, J. Salava, P. Löper, S. Janz, C. Summonte, P. Malý, J. Appl. Phys. **114**, 073101 (2013)
151. S. Yamada, Y. Kurokawa, S. Miyajima, M. Konagai, Nanoscale Res. Lett. **9**, 1 (2014)
152. M.L. Brongersma, A. Polman, K.S. Min, E. Boer, T. Tambo, H.A. Atwater, Appl. Phys. Lett. **72**, 2577 (1998)
153. J.H. Yoon, Curr. Appl. Phys. **11**, 827 (2011)
154. Y. Kurokawa, S. Tomita, S. Miyajima, A. Yamada, M. Konagai, in *Proceedings of the 22nd EU PVSEC*, Milan, 233 (2007)

155. K. Ding, U. Aeberhard, O. Astakhov, F. Köhler, W. Beyer, F. Finger, R. Carius, U. Rau, Energ. Procedia **10**, 249 (2011)
156. S. Janz, M. Schnabel, P. Löper, C. Summonte, M. Canino, J. López-Vidrier, S. Hernández, B. Garrido, S. W. Glunz, in *Proceedings of the 28th EU PVSEC*, Paris, 142 (2013)
157. D. Song, E.C. Cho, G. Conibeer, C. Flynn, Y. Huang, M.A. Green, Sol. Energy Mater. Sol. Cells **92**, 474 (2008)
158. I. Perez-Wurfl, X. Hao, A. Gentle, D.H. Kim, G. Conibeer, M.A. Green, Appl. Phys. Lett. **95**, 153506 (2009)

Applied Energy 155 (2015) 284–293

Contents lists available at ScienceDirect

Applied Energy

journal homepage: www.elsevier.com/locate/apenergy

Performance comparison of CPCs with and without exit angle restriction for concentrating radiation on solar cells

Yamei Yu, Nianyong Liu, Guihua Li, Runsheng Tang *

Education Ministry Key Laboratory of Advanced Technology and Preparation for Renewable Energy Materials, Yunnan Normal University, Kunming 650500, PR China

HIGHLIGHTS

- CPCs with and without exit angle restriction based PV modules were fabricated and tested.
- Performance of both CPVs was investigated and compared.
- Results showed that CPV-65 performed slightly but insignificantly better as compared to CPV-90.

ARTICLE INFO

Article history:
Received 15 March 2015
Received in revised form 9 May 2015
Accepted 8 June 2015

Keywords:
CPC with exit angle restriction
CPC based PV module
Performance comparison
Experimental investigation
Theoretical analysis

ABSTRACT

To perform this comparison, the compound parabolic concentrator with a restricted exit angle of 65° (CPC-65) and the one without exit angle restriction (CPC-90) were fabricated and tested for concentrating radiation on multi-crystalline solar cells. Both CPC-65 and CPC-90 are identical in the acceptance half-angle (20°) and geometrical concentration factor (2×). Theoretical calculations showed that CPC-90 based PV system (CPV-90) annually concentrated about 3–5% more radiation on solar cells as compared to CPC-65 based PV system (CPV-65). For CPV-65, all radiation would arrive on the solar cells at the incidence angle less than 65°, but for CPV-90, about 8–10% of annual collectible radiation would arrive on solar cells at the incidence angle larger than 65°. Measurements at outdoor conditions showed that the CPV-65 performed slightly better than CPV-90 in terms of short-circuit current and power output as the projection incidence angle of solar rays on the cross-section of CPC-troughs (θ_p) less than the acceptance half-angle, otherwise the CPV-90 did better. Compared to CPV-90, the power output at maximum power points from CPV-65 were slightly higher, and increases of 2.1%, 5.4% and 8.17% were measured for θ_p = 0°, 10° and 16°, respectively. Analysis indicated that effect of solar flux distribution over solar cells on power output of both CPVs was almost identical and insignificant, and the CPV-65 performed slightly but insignificantly better than the CPV-90 in terms of annual power output except in areas with poor solar resources where the annual power output from both systems was almost identical.

1. Introduction

With the gradual depletion of fossil fuels in our planet, the application of solar energy becomes more attractive currently over the world. Solar energy can be directly utilized through a variety of devices such as solar collectors or photovoltaic cells. It was reported that, by 2011, solar photovoltaic (PV) had been introduced in more than 80 countries and was considered to be the fastest growing power generation technology. The total installation of PV over the world reached 70 GW in 2011, an increase of 79% as compared to 2010 [1]. However, the use of PV system is limited due to its high cost as compared to the conventional electricity generation, although the cost of electricity generation by PV systems has decreased substantially over the past two decades [2]. Enterprisers of PV over the world have been relying on subsides from governments for surviving, this severely resists a further development of PV technology, and the unique solution is to further lower the cost of electricity generated from PV systems. In a PV system, the PV cell material contributes about 50% of the total cost. Thus, one of potential ways to lower the cost of electricity generated from a PV system is to reduce the use of solar cells for given power demand by the use of cheep optical concentrators.

In recent years, the compound parabolic concentrator (CPC), sharing advantages of simple structure and no need of sophisticated sun-tacking device [3], has been widely tested for

* Corresponding author. Tel.: +86 871 65516229; fax: +86 871 65516217.
E-mail address: kingtang01@126.com (R. Tang).

http://dx.doi.org/10.1016/j.apenergy.2015.06.012
0306-2619/

concentrating solar radiation on solar cells to lower the cost of electricity generation from a photovoltaic system [4,5]. Experimental studies performed by Mallick and Eames [6,7] showed that, compared with similar non-concentrating PV panel, the use of an asymmetric CPC with a geometric concentration factor of 2.01 increased the maximum power point of photovoltaic modules by 62%, the temperature of solar cells was only 12 °C higher. Brogren et al. tested a CPC (3×) based Cu(In, Ga)Se_2 PV module, and 1.9 times of maximum power output as that of identical modules without using CPCs was experimentally observed [8]. Theoretically, for a CPC based photovoltaic module (referred to as CPV to distinguish with CPC), the power output should be increased by a factor of the geometric concentration ratio of the CPC as compared to similar non-concentrating PV panel. However, the actual power output from a CPV system was much less than the theoretical value due to the optical loss partially resulting from the poor solar absorption of solar cells for radiation incident at a large angle and the electrical loss partially resulting from uneven distribution of solar radiation on solar cells. To make the radiation on solar cells more even so as to increase the fill factor of CPVs, Hatwaambo tried to use semi-diffuse reflective materials as CPC reflectors, and experimental results showed that the use of reflectors with rolling mark parallel to the plane of solar cells slightly increased the fill factor of the photovoltaic system [9,10]. However, the use of semi-diffuse reflectors in CPVs cannot make solar flux on solar cells more uniform except using perfect diffuse reflectors, in turn leads the collectible radiation decrease greatly [11]. Li et al. designed and tested a lens-walled CPC for photovoltaic/thermal applications with the aims to increase the optical concentration and improve the solar flux distribution on solar cells, and the average optical efficiencies of above 60% were measured on two typical days under the actual outdoor condition considering direct and diffuse solar radiation [12,13]. Compared to CPCs, V-trough concentrators are extremely easy to be constructed, the distribution of solar intensity on the base of V-trough is more uniform, however the increase of power output from V-trough based PV modules is limited as a result of the fact that the V-trough is not an ideal concentrator for solar radiation [14–16].

For a CPV system, the incidence angle on solar cells for radiation reflecting from the lower part of reflectors is considerably large, and this part of solar radiation cannot be efficiently converted into electrical power due to the poor solar absorptance [17,18]. To improve the solar absorption of receivers, Rabl and Winston suggested a CPC with a restricted exit angle (CPC-θ_e, $\theta_e < 90°$) [19], and the use of CPC-θ_e in a PV system can make the incidence angle of solar rays less than desired value thus increase the solar absorption of solar cells. The previous studies of the authors showed that the use of CPC-θ_e could slightly but insignificantly improve the uniform of irradiation on solar cells [20], and CPC-θ_e is more efficient to concentrate solar radiation on receivers with a restricted incidence angle (namely, the receiver cannot absorb the radiation incident at the angle larger than θ_e) as compared to the CPC without exit angle restriction (CPC-90) [21], but the performance of them for concentrating radiation on solar cells was not investigated. Given the acceptance half-angle, the use of CPC-θ_e in a PV system (CPV-θ_e, in short) would reduce its geometrical concentration factor as compared to the CPC-90 based PV system (CPV-90, in short) [3], thus less radiation would be collected, but in the other hand, partial radiation on solar cells of CPV-90 cannot be efficiently converted into electrical output due to the poor solar absorption resulting from large incidence angle. To date, comparative studies on the performance of CPV-θ_e and CPV-90 were not found in the literatures. In this work, an attempt was made to experimentally and theoretically investigate the performance of CPC-θ_e and CPC-90 for concentrating radiation on solar cells with the aim to ascertain whether the use of CPC-θ_e can really improve the photovoltaic performance of CPC based PV systems.

2. Design and fabrication of CPC based PV systems

2.1. CPC design

Ideal concentrators are designed based on the principles of edge-rays and identical total ray path length of non-imaging optics [3,19,22]. As shown in Fig. 1, for CPC-90 with one-sided flat absorber, the reflector is parabola, and the maximum exit angle of solar rays from the concentrator is 90° for solar rays incident at the acceptance half-angle (θ_a); whereas for CPC-θ_e with one-sided flat absorber, the upper portion of reflectors is parabola and the lower portion is flat reflector, and the exit angle of solar rays from the concentrator is less than the desired value θ_e.

CPCs are usually oriented in the east–west direction with the aperture being inclined from the horizon for efficient radiation concentration, and the acceptance half-angle (θ_a) is a key design parameter. To make CPCs efficiently operate in any day of a year, θ_a should be selected based on the scheduled number of tilt-angle adjustment in a year and the requirement of least daily

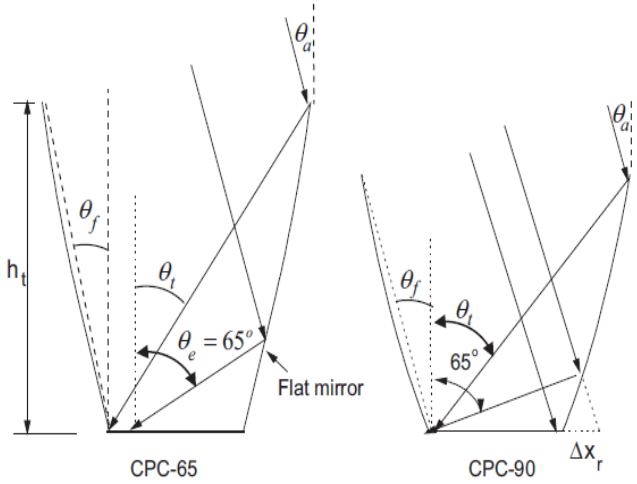

Fig. 1. Geometry of CPC-90 and CPC-65.

Table 1
Design parameters of CPC-90 and CPC-65.

	θ_a	θ_e	a (mm)	θ_t	θ_f	C_t	h_t (mm)
CPC-90	20	90	63	53.9	24.56	2	68.84
CPC-65	20	65	63	46.9	19.61	2	88.44

operation hours. In this work, the θ_a of both CPC-90 and CPC-θ_e is set to be 20°, and thus suitable to be employed for two cases that the tilt-angle of the aperture is yearly adjusted two times at two tilts and four times at three tilts [22]. θ_e in the CPC-θ_e is set to be 65° considering that the solar cells have poor solar absorption as the incidence angle lager than 65° [18]. For fair comparisons, both CPCs are truncated with identical geometrical concentration factor (C_t = 2) but different edge-ray angle (θ_t) and height (h_t). Design parameters of both CPCs are listed in Table 1. It is seen that the height (h_t) of CPC-65 is about 1.28 times as that of CPC-90, thus more reflective materials are used.

2.2. Reflector substrate

The computer generated data points were transferred to CAD files to generate CPC reflector profile first, then steel molds of reflector substrate were subsequently processed with the aid of a CNC machine, finally "triangle-shaped" aluminum ducts of 6 mm in thickness were produced by using the technique of heating squeezing (see Fig. 2). The self-adhesive reflector film of 0.12 mm in thickness with the solar reflectivity of 0.862, measured by a spectrophotometer (Cary 5000, Varian, Inc.), was attached to the aluminum reflector substrate, and aluminum reflector substrates were fixed on the solar cell panel with thermally conductive adhesive to form CPC-troughs (Fig. 3).

2.3. CPV modules

To perform comparisons of photovoltaic performance, two identical solar panels were fabricated with the one equipped with CPC-65 concentrators (referred to as CPV-65 to distinguish with CPC-65) and another one equipped with CPC-90 concentrators (CPV-90). The PV panels consisted of three strings of solar cells connected in parallel, each string consisted of 4 half-size multi-crystalline silicon solar cells (measuring 125 × 62.5 mm), and a space of 63 mm between two adjacent strings was left to accommodate the CPC reflector substrate (see Fig. 4). Four CPC reflector substrates were used in a PV panel to form three trough-like concentrators (Fig. 5). 2-mm thick aluminum sheet was used as the back plate of solar panels, 2 layers of TPT (Tedlar/PET/Tedlar) were sandwiched in between solar cells and back plate as the electrical insulator with the EVA (ethylene–vinyl acetate) at solar cells, TPT and the back plate. 1-mm thick polyethylene naphthalate sheet covered on solar cells, and solar cells were encapsulated within the panel by the vacuum press technique. To make two PV panels identical in the performance as possibly, all solar cells used in two PV panels were carefully picked up with almost identical PV performance. Performance parameters of two PV panels measured in the laboratory are presented in Table 2. It is seen that two solar panels are almost identical in the performance.

3. Optical performance of CPV-65 and CPV-90

3.1. Optical efficiency of CPVs

The optical efficiency factor of CPVs is defined as the fraction of radiation incident on the aperture that arrives on solar cells at any incidence angle. Assuming that the reflection of solar rays on reflectors of CPVs is perfect specular, thus the optical efficiency factor is a function of projection incidence angle (θ_p). For CPVs investigated in this work, the upper portion of CPC reflectors was truncated, and all radiation arrives on solar cells either directly or indirectly from reflectors after just one reflection based on the theoretical analysis presented by Tang and Wang [23]. Thus, one-reflection model can be used to accurately calculate optical efficiency factors of both CPV-90 and CPV-65. The optical efficiency factor of CPV-90 can be expressed by [21]:

$$f(\theta_p)=\begin{cases}\rho+(1-\rho)/C_t & |\theta_p|\le 20^\circ\\ 1/C_t+0.5\rho(1-1/C_t)-0.5\rho(1+1/C_t)\tan|\theta_p|/\tan 53.9 & 20^\circ<|\theta_p|\le 24.56\\ 0.5(1+1/C_t)(1-\tan|\theta_p|/\tan 53.9 & 24.56<|\theta_p|\le 53.9\\ 0 & |\theta_p|>53.9\end{cases} \quad (1)$$

and for CPV-65

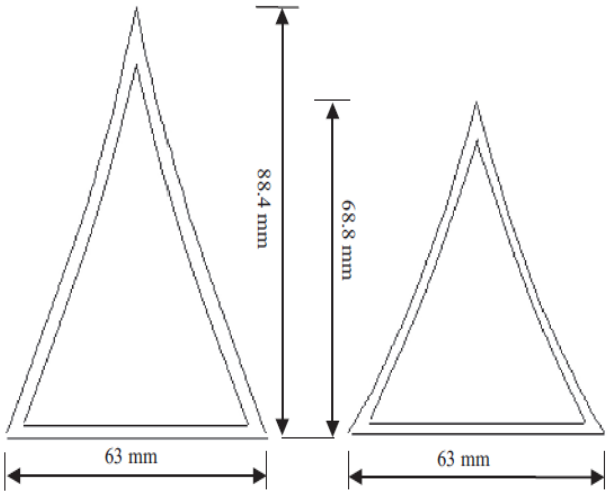

Fig. 2. Triangle-shaped reflector substrate (Left: CPC-65; Right: CPC-90).

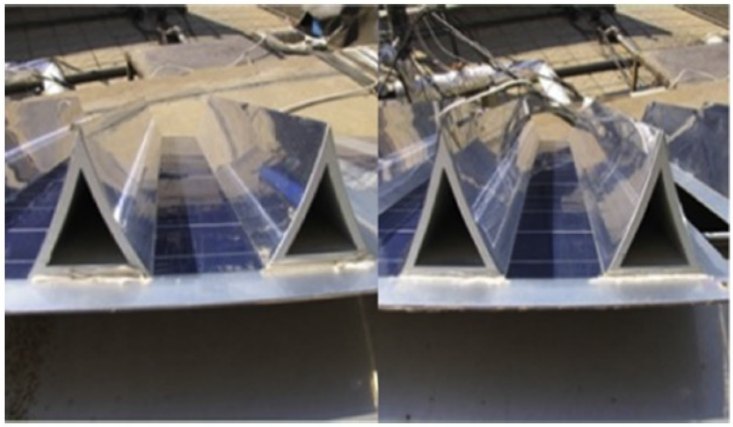

Fig. 3. Photo of CPC-troughs. Left: CPC-90; Right: CPC-65.

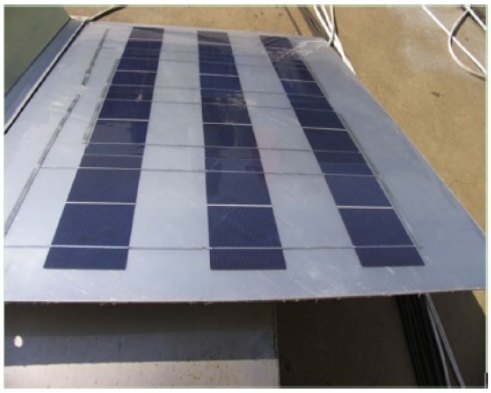

Fig. 4. Photo of PV panels without using CPCs.

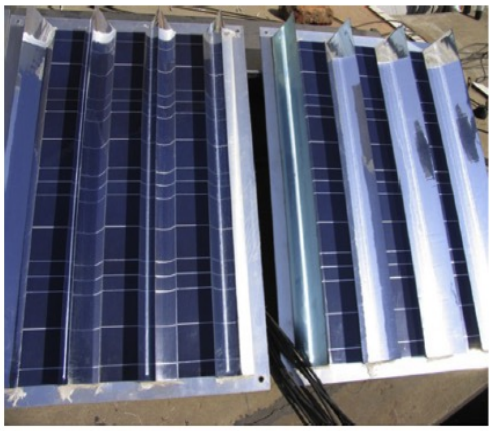

Fig. 5. Photo of CPV modules. Left: CPV-65; Right: CPV-90.

$$f(\theta_p)=\begin{cases}\rho+(1-\rho)/C_t & |\theta_p|\le 19.62\\ \rho+0.5(1-\rho)(1+1/C_t)(1-\tan|\theta_p|/\tan 46.9) & 19.62<|\theta_p|\le 20\\ 0.5(1+1/C_t)(1-\tan|\theta_p|/\tan 46.9) & 20<|\theta_p|\le 46.9\\ 0 & |\theta_p|>46.9\end{cases} \quad (2)$$

where $\rho = 0.862$ is the solar reflectivity of reflectors. As seen from Fig. 6, the optical efficiency of both CPV-90 and CPC-65 are identical for solar rays within the acceptance angle ($\theta_a = 20°$), otherwise the optical efficiency of CPV-90 is larger than that of CPV-65.

3.2. Incidence angle of solar rays on solar cells

For CPV-65, all radiation arrives on solar cells at the incidence angle less than 65°, but for the CPV-90, as shown in Fig. 1, the fraction, $F(\theta_{in} > 65) = \Delta x/C_t$, of radiation arrives on solar cells at the angle larger than 65°. $F(\theta_{in} > 65)$ as a function of θ_p can be determined based on the method presented in the previous work of the authors [21].

As seen from Fig. 7, it is found that, for the CPV-90, $F(\theta_{in} > 65)$ increases with the increase of θ_p, and are 0.062 and 0.2793 for $\theta_p = 0°$ and 20°, respectively. This means that a fraction of solar radiation arrives on solar cells of CPV-90 at the angle larger than 65°, and this part of radiation cannot be efficiently converted into photovoltaic output by solar cells due to poor solar absorption.

3.3. Annual collectible radiation on solar cells

Assuming that CPC-troughs in CPVs are oriented in the east–west direction with the aperture being inclined at β from the horizon, the length of the CPC-trough is infinite as compared to its width, and solar radiation reflecting from the ground is not considered. Thus, the daily solar gain on unit area of solar cells can be calculated as follows:

$$H_{day} = C_t \int_{-t_0}^{t_0} g(\theta_{ap}) f(\theta_p) I_b \cos\theta_{ap} dt + 0.5 H_d (C_d + C_{d\beta}) \quad (3)$$

where H_d is the daily sky diffuse radiation on the horizon, t_0 is the sunset time on the horizon, and C_d and $C_{d\beta}$ are determined by:

$$C_d = C_t \int_0^{\theta_t} f(\theta_p)\cos\theta_p d\theta_p \quad (4)$$

$$C_{d\beta} = C_t \int_0^{\theta_\beta} f(\theta_p)\cos\theta_p d\theta_p \quad (5)$$

$$\theta_\beta = \mathrm{Min}(\theta_t, 0.5\pi - \beta)$$

Similarly, the daily radiation on solar cells of the CPV-90 at the angle larger than 65° after reflection from reflectors can be calculated by:

Table 2
Performance parameters of two PV panels measured in laboratory.

No	V_{oc} (V)	I_{sc} (A)	V_p (V)	I_p (A)	P_p (W)
1	7.05	3	5.2	2.8	14.56
2	7.05	3.01	5.22	2.79	14.5638

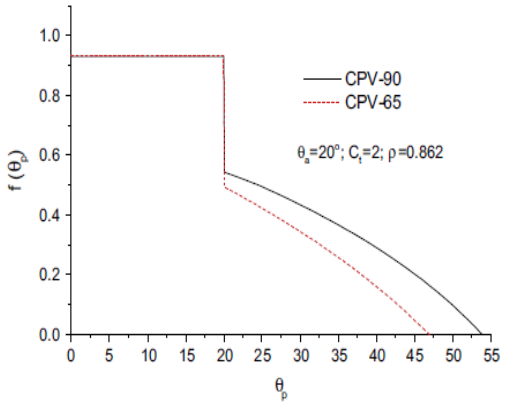

Fig. 6. Angular dependence of optical efficiency of CPV-90 and CPV-65.

$$H_{day,65^\circ} = C_t\rho\int_{-t_0}^{t_0} g(\theta_{ap})F(\theta_{in} > 65)I_b\cos\theta_{ap}dt + 0.5H_d\rho(C_{x,1}+C_{x,2}) = \rho\int_{-t_0}^{t_0} g(\theta_{ap})\Delta x I_b\cos\theta_{ap}dt + 0.5H_d\rho(C_{x,1}+C_{x,2}) \quad (6)$$

$$C_{x,1} = \int_0^{\theta_a}\Delta x\cos\theta_p d\theta_p \quad (7)$$

$$C_{x,2} = \int_0^{\theta_x}\Delta x\cos\theta_p d\theta_p \quad (8)$$

And $$\theta_x = \mathrm{Min}(\theta_a, 0.5\pi-\beta) \quad (9)$$

The θ_{ap} in above expressions is the incidence angle of solar rays on the aperture of CPVs, and $g(\theta_{ap})$ is a control function, being 1 for the case of $\cos\theta_{ap} > 0$ otherwise zero.

At any moment of a day, θ_p and θ_{ap} can be determined based on the solar geometry [3,21], then $f(\theta_p)$ and $F(\theta_{in} > 65)$ can be calculated. Therefore, H_{day} and $H_{day,65}$ can be numerically calculated based on Eqs. (3) and (6), then summing H_{day} and $H_{day,65}$ in all days of a year obtains annual radiation collected by unit area of solar cells (S_a) and the annual radiation on solar cells of CPV-90 at the incidence angle larger than 65° ($S_{a,65}$).

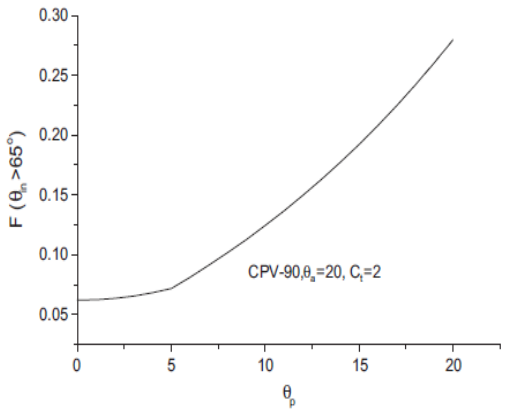

Fig. 7. Angular variation of $F(\theta_{in} > 65)$ for the CPV-90.

In the subsequent calculations, monthly horizontal radiation averaged over many years were used, and the monthly average daily diffuse radiation, H_d, the instantaneous sky diffuse radiation (I_d), horizontal radiation (I_h), and beam radiation (I_b) were estimated based on correlations suggested by Collares-Pereira and Rabl [24–27]. The monthly horizontal radiation data used in this work was taken from the book edited by Chen [28]. Two cases, the tilt-angle of CPVs' aperture being yearly adjusted two times at two tilts (2T-CPV) and four times at three tilts (3T-CPV), were considered for the analysis. For the 3T-CPVs, the tilt-angle of CPVs' aperture was set to be site latitude (λ) during periods of 23 days before and after both equinoxes, and adjusted to $\lambda+23$ and $\lambda-23$ in winters and summers, respectively [16,27]; whereas for the 2T-CPVs, the tilt-angle was set to be $\lambda+19$ and $\lambda-19$ in winters ($\delta<0$) and summers ($\delta<0$), respectively. 31 sites in China were selected as the representative for the analysis. These sites cover a variety of climatic conditions and a wide range of site latitude [27], thus the results are of representative for the use of CPV-65 and CPV-90 in China even over the world.

As shown in Tables 3 and 4, solar cells of the CPV-90 annually received about 3–5% more radiation as compared to the CPV-65 (see the column of $S_{a,CPV\text{-}90}/S_{a,CPV\text{-}65}$ in Tables). For CPV-65, all radiation would arrive on the solar cells at the incidence angle less than 65°, but for CPV-90, the radiation arriving on solar cells at incidence angle larger than 65° ($S_{a,65}$) took about 8.3% and 9.5% of annual collectible radiation (S_a) for the cases of the tilt-angle of the aperture being yearly adjusted four times and two times, respectively (see the column of $S_{a,65}/S_a$ in Tables). It was also found that solar cells of 3T-CPVs annually collected about 1.2–2.5% more radiation as compared to 2T-CPVs.

4. Photovoltaic performance of CPV-90 and CPV-65

4.1. Angular dependence of the photovoltaic efficiency of PV panels

First, the *I–V* characteristics of PV panels without using CPCs were measured to determine their angular dependence of maximum power points. In this measurement, a PV panel was fixed on a two-axis sun-tracking platform, and the orientation of which can be arbitrarily adjusted manually. The incidence angle of solar rays on the PV panel was measured by a sundial, one pyranometer (CM11, Kipp & Zonen) and one pyrheliomter (TBS-2-2, Jingzhou Sunlight Co. of China) with measuring error less than 1% were employed to measure the total radiation on the PV panel (I_t) and beam radiation (I_b), respectively. Two digital multiple meters with 1 mA current resolution and 1 mV voltage resolution were employed to monitor current and voltage of the PV panel, respectively. A slide rheostat was used as the variable resistance during *I–V* measurements. Measurements of *I–V* were performed around the solar noon on January 26 of 2014, and each *I–V* measurement lasted about 3 min. After one measurement, the PV panel was moved into a shelter for cooling and the orientation of the platform was manually changed for next measurement. During measurements, radiation data were recorded at intervals of 10 s by a computerized data logger (TRM-2, Jingzhou Sunlight Co. of China) and the value averaged over the period of *I–V* measurements was used to calculate the photovoltaic conversion efficiency of the PV panel. It can be seen from Fig. 8 that, the *I–V* characteristics of the PV panel strongly depended on the incidence angle of solar rays, the voltage of open-circuit was almost independent on the incidence

Table 3
Performance comparison between 3T-CPV-90 and 3T-CPV-65.

Sites	S_a (MJ/m^2)		$S_{a,65}$ (MJ/m^2)		$S_{a,CPV\text{-}90}/S_{a,CPV\text{-}65}$	$S_{a,65}/S_a$ (CPV-90)	P_a (MJ/m^2)		$P_{a,CPV\text{-}65}/P_{a,CPV\text{-}90}$
	CPV-90	CPV-65	CPV-90	CPV-65			CPV-90	CPV-65	
Beijing	10125	9824	833	0	1.031	0.082	1428	1452	1.0168
Harbin	9785	9505	809	0	1.029	0.083	1380	1405	1.0182
Changchun	10051	9765	830	0	1.029	0.083	1417	1443	1.0183
Shenyang	9587	9295	792	0	1.031	0.083	1352	1374	1.0163
Urumqi	11051	10755	913	0	1.028	0.083	1558	1590	1.0201
Xining	11466	11146	942	0	1.029	0.082	1617	1647	1.0187
Lanzhou	10401	10084	855	0	1.031	0.082	1467	1490	1.016
Xi'an	7860	7558	647	0	1.04	0.082	1109	1117	1.0076
Yinchuan	11590	11275	952	0	1.028	0.082	1635	1666	1.0194
Hohhot	11686	11392	961	0	1.026	0.082	1648	1684	1.0216
Taiyuan	10329	10019	849	0	1.031	0.082	1457	1481	1.0165
Shijiazhuang	10022	9715	825	0	1.032	0.082	1413	1436	1.0158
Tianjin	10605	10298	872	0	1.03	0.082	1496	1522	1.0176
Jinan	10077	9764	829	0	1.032	0.082	1421	1443	1.0154
Zhengzhou	8993	8682	739	0	1.036	0.082	1268	1283	1.0116
Hefei	8450	8135	697	0	1.039	0.082	1192	1202	1.009
Shanghai	7648	7342	630	0	1.042	0.082	1078	1085	1.0061
Nanjing	8168	7857	673	0	1.04	0.082	1152	1161	1.0081
Hangzhou	7476	7170	616	0	1.043	0.082	1054	1060	1.0052
Nanchang	7292	6987	599	0	1.044	0.082	1029	1033	1.0039
Wuhan	7781	7471	640	0	1.042	0.082	1097	1104	1.0061
Changsha	6781	6480	557	0	1.046	0.082	956	958	1.0014
Chengdu	5461	5197	449	0	1.051	0.082	769	770	1.0003
Chongqing	5450	5187	450	0	1.051	0.083	768	769	1.0002
Guiyang	6108	5813	503	0	1.051	0.082	861	859	0.9973
Kunming	9842	9499	807	0	1.036	0.082	1388	1404	1.0114
Lhasa	15869	15495	1302	0	1.024	0.082	2238	2290	1.0231
Fuzhou	7274	6959	598	0	1.045	0.082	1026	1029	1.0025
Guangzhou	7611	7284	622	0	1.045	0.082	1074	1077	1.0026
Nanning	7223	6901	592	0	1.047	0.082	1019	1020	1.0012
Taipei	6533	6237	536	0	1.047	0.082	921	922	1.0003

Table 4
Performance comparison between 2T-CPV-90 and 2T-CPV-65.

Sites	S_a (MJ/m^2)		$S_{a,65}$ (MJ/m^2)		$S_{a,CPV\text{-}90}/S_{a,CPV\text{-}65}$	$S_{a,65}/S_a$ (CPV-90)	P_a (MJ/m^2)		$P_{a,CPV\text{-}65}/P_{a,CPV\text{-}90}$
	CPV-90	CPV-65	CPV-90	CPV-65			CPV-90	CPV-65	
Beijing	9946	9639	946	0	1.031	0.095	1392	1425	1.0232
Harbin	9601	9318	917	0	1.03	0.095	1344	1377	1.0249
Changchun	9866	9575	943	0	1.03	0.095	1381	1415	1.0249
Shenyang	9416	9120	902	0	1.032	0.095	1318	1348	1.023
Urumqi	10861	10652	1041	0	1.019	0.095	1520	1574	1.0358
Xining	11264	10933	1057	0	1.03	0.093	1578	1616	1.024
Lanzhou	10224	9898	957	0	1.032	0.093	1432	1463	1.0212
Xi'an	7744	7436	715	0	1.041	0.092	1086	1099	1.0121
Yinchuan	11386	11061	1073	0	1.029	0.094	1595	1635	1.0252
Hohhot	11477	11162	1094	0	1.028	0.095	1606	1650	1.0269
Taiyuan	10151	9833	956	0	1.032	0.094	1422	1453	1.0222
Shijiazhuang	9851	9538	931	0	1.032	0.094	1379	1410	1.0218
Tianjin	10424	10110	984	0	1.031	0.094	1460	1494	1.0236
Jinan	9908	9587	935	0	1.033	0.094	1388	1417	1.0212
Zhengzhou	8852	8534	823	0	1.037	0.093	1241	1261	1.0166
Hefei	8329	8007	770	0	1.04	0.092	1168	1183	1.0134
Shanghai	7544	7232	698	0	1.043	0.092	1058	1069	1.0106
Nanjing	8052	7735	746	0	1.041	0.092	1129	1143	1.0127
Hangzhou	7378	7066	681	0	1.044	0.092	1035	1044	1.0095
Nanchang	7204	6891	673	0	1.045	0.093	1009	1019	1.0091
Wuhan	7679	7362	713	0	1.043	0.092	1076	1088	1.0109
Changsha	6699	6399	622	0	1.046	0.092	939	946	1.0071
Chengdu	5394	5126	491	0	1.052	0.091	757	758	1.001
Chongqing	5385	5116	496	0	1.052	0.092	755	756	1.0014
Guiyang	6033	5736	561	0	1.051	0.093	845	848	1.0028
Kunming	9669	9308	902	0	1.038	0.093	1355	1376	1.0152
Lhasa	15578	15178	1474	0	1.026	0.094	2181	2243	1.0284
Fuzhou	7185	6863	664	0	1.046	0.092	1007	1014	1.007
Guangzhou	7511	7171	695	0	1.047	0.092	1053	1060	1.0065
Nanning	7143	6811	662	0	1.048	0.092	1001	1007	1.0053
Taipei	6457	6152	600	0	1.049	0.092	905	909	1.0048

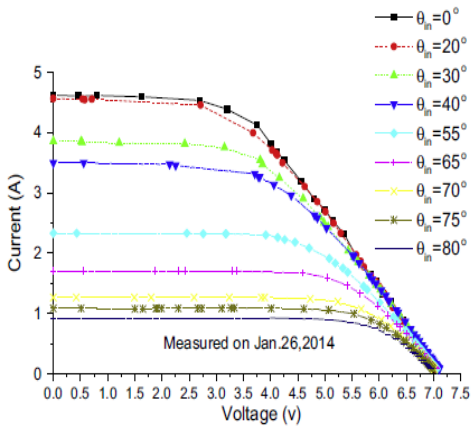

Fig. 8. *I–V* characteristics of PV panels without using CPCs.

angle, but the current of short-circuit decreased with the increase of the incidence angle.

The photovoltaic conversion efficiency of the PV panel at the maximum power point calculated based on the total radiation (including beam and sky diffuse radiation), η_t, is presented in Fig. 9. It was seen that η_t was almost kept unchanged as the incidence angle (θ_{in}) less than 40°, and then linearly decreased as $\theta_{in} > 40°$. Usually, in the case of θ_{in} being close to 90°, the η_t should be very lower due to poor solar absorptance of solar cells, but a 9.6% of η_t was measured at $\theta_{in} = 80°$, a result of the fact that the total radiation on solar cells included beam and sky diffuse radiation, and in the case of θ_{in} close to 90°, most of radiation fallen on solar cells was sky diffuse radiation and solar absorptance of solar cells for isotropic sky diffuse radiation was approximately equal to that of solar cells for beam radiation incident at $\theta_{in} = 60°$ [17,29]. To find the angular dependence of photovoltaic efficiency of solar cells for beam radiation (η_b), it was assumed that the photovoltaic efficiency of solar cells for the isotropic sky diffuse radiation (η_d) was approximately equal to η_t of solar cells for radiation incident at $\theta_{in} = 60°$ (i.e. $\eta_d = 12\%$), therefore, η_b could be estimated based on measured power output at the maximum power point (P_m), beam radiation (I_b), total radiation (I_t) and assumed η_d as follow:

$$\eta_b = \frac{P_m - A_s(I_t - I_b\cos\theta_{in})\eta_d}{A_s I_b \cos\theta_{in}} \tag{10}$$

where $A_s = 0.09375\ m^2$ is the total area of 12 solar cells. As shown in Fig. 9, η_b sharply decreased with the increase of incidence angle as

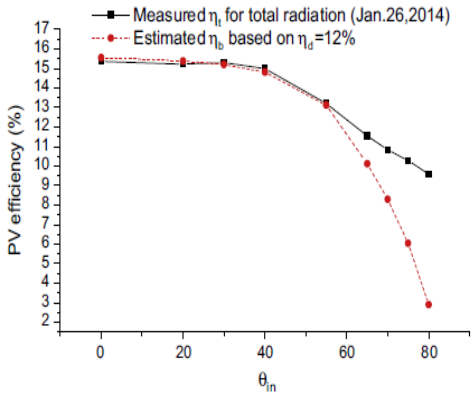

Fig. 9. Angular dependence of measured η_t and estimated η_b.

the $\theta_{in} > 60°$, and were 10.1% and 2.8% for $\theta_{in} = 65°$ and 80°, respectively. This implied that the photovoltaic conversion efficiency of solar cells was very lower as the incidence angle of solar rays larger than 65°. By fitting estimated η_b to the polynomial, one obtained following correlations:

$$\eta_b = 15.5494 + 0.02325\theta_{in} - 0.00301\theta_{in}^2 + 9.4685\times10^{-5}\theta_{in}^3 - 1.134\times10^{-6}\theta_{in}^4 \quad (0° < \theta_{in} < 65°) \tag{11}$$

$$\eta_b = 41.52 - 0.4784\theta_{in} \quad (65° < \theta_{in} < 90°) \tag{12}$$

Therefore, the average efficiency of solar cells for the isotropic radiation over the angle from 0° to 65° can be calculated based on Eq. (11) by numerical calculations as follow:

$$\overline{\eta}_{0-65} = \frac{\int_0^{65}\eta_b\cos\theta_{in}d\theta_{in}}{\int_0^{65}\cos\theta_{in}d\theta_{in}} = 14.78\% \tag{13}$$

Similarly, the average efficiency of solar cells for the isotropic solar radiation over the angle from 65° to 90° was found to be $\overline{\eta}_{65-90} = 6.56\%$.

4.2. Comparison of photovoltaic performance between CPV-65 and CPV-90

To make comparisons fair, an electrical circuit as shown in Fig. 10 was used to measure the electrical output from both CPVs with the aid of a two-way switch. Both CPV systems were placed on the same platform, and the tilt-angle of which from the horizon can be accurately adjusted based on requirement of experiments. Experimental measurements were conducted on the roof of a six-storey building in the campus of Yunnan Normal University (site latitude $\lambda = 25.02°$) from March 10 to 26 in 2014.

4.2.1. I–V characteristics

In this experiment, CPC-troughs of both systems were oriented in the east–west direction with the aperture being tilted at the angle of $\lambda - \delta - \theta_p$, thus the projection incidence angle of solar rays on the cross-section of CPC-troughs was just equal to θ_p near the solar noon, and the θ_p can be arbitrarily selected based on experimental requirement. Experimental measurements were conducted about 5 min around the solar-noon.

As shown in Figs. 11–13, it was observed that the open-circuit voltage (V_{oc}) of both systems were almost identical, but the short-circuit current (I_{sc}) of CPV-65 was always larger than that of CPV-90. Compared to CPV-90, the power output from CPV-65 (P_m) at the maximum power points were slightly higher, and increases of 2.1%, 5.4% and 8.17% were measured for $\theta_p = 0°$, 10° and 16°, respectively. It was also found that the fill factor of CPV-65 was slightly higher than that of CPV-90. This implied that

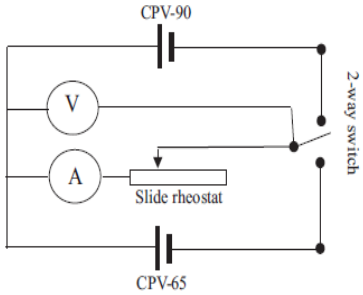

Fig. 10. Circuit used to measure electrical outputs from CPV-90 and CPV-65.

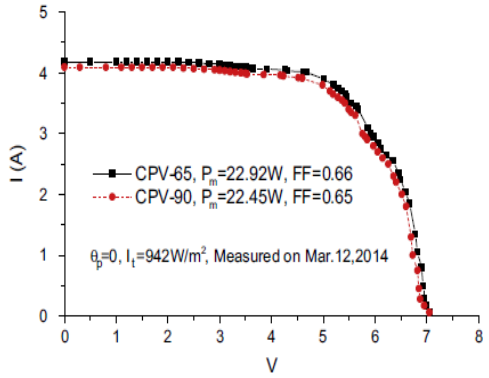

Fig. 11. *I–V* characteristics of CPV-65 and CPV-90 in the case of $\theta_p = 0°$.

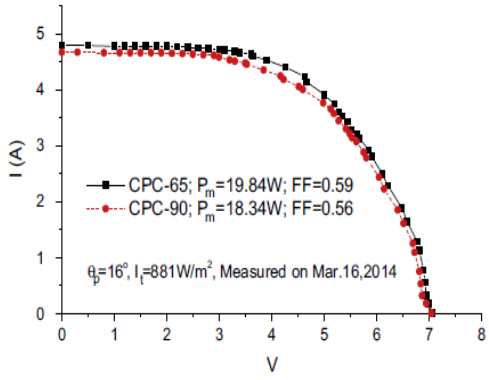

Fig. 13. The same as in Fig. 11 but $\theta_p = 16°$.

CPV-65 was more electrically efficient than CPV-90 as solar rays within the acceptance angle of CPVs.

4.2.2. Short-circuit current and open-circuit voltage

This comparative experiment was purposefully scheduled on days near the spring equinox (δ is near zero), CPC-troughs of both systems were south-north oriented and the aperture of CPC-troughs was inclined at $\lambda - \delta$ so as to eliminate the end effect of CPC-troughs during the period of measurements, and θ_p can be easily calculated based on solar time or clock time. As shown in Fig. 14, the short-circuit current (I_{sc}) from CPV-65 was slightly higher than that from CPV-90 as $\theta_p < \theta_a$, otherwise the situation was reversed. This could be explained by the fact that, in the case of $\theta_p < \theta_a$, the optical efficiency of both systems were identical, a fraction of radiation reflecting from reflectors of CPV-90 arrived on solar cells at the angle larger than 65°, but the incidence angle of all solar rays on solar cells of CPV-65 was less than 65°, whereas in the case of $\theta_p > \theta_a$, the optical efficiency of CPV-90 was larger than that of CPV-65. Angular variations of open-circuit voltage of both systems are presented in Fig. 15, and it was found that open-circuit voltage of both systems was almost identical.

4.2.3. Power output of CPVs with fixed electrical load

In this experiment, both systems were placed on a south-facing platform tilted at $\lambda - \delta$, CPC-troughs of both systems were south–north oriented, and the slide rheostat (see Fig. 11) was fixed at a point corresponding to a resistance of 1.5 ohm with which the power output of both systems was close to their maximum power points. Experimental measurements started at the solar-noon and ended at 15:40 (solar time) on March 25 of 2014 (a clear day). As seen from Fig. 16, it was found that, in the case of $\theta_p < \theta_a$, the power

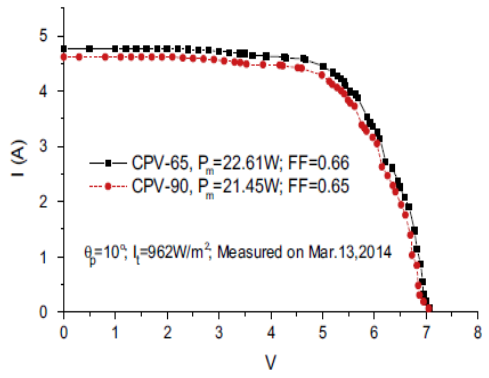

Fig. 12. The same as in Fig. 11 but $\theta_p = 10°$.

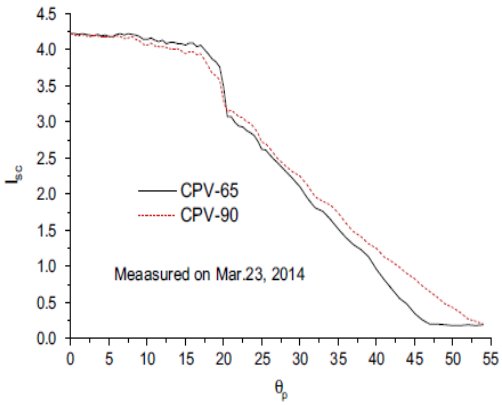

Fig. 14. Comparison of short-circuit current from CPV-65 and CPV-90.

output from CPV-65 (P_{65}) was always higher than that from CPV-90 (P_{90}), the ratio of P_{65}/P_{90} was kept in a narrow range of 1.02–1.06 for $\theta_p < 16°$ and then sharply increased from 1.04 to 1.18 as θ_p close to θ_a (20°); whereas in the case of $\theta_p > \theta_a$, the power output from CPV-65 was slightly less than that from CPV-90.

5. Long-term performance comparison between CPV-90 and CPV-65

5.1. Effect of solar flux distribution on the power out of CPVs

Experimental results in the above showed that the CPV-65 performed slightly better than CPV-90 as solar rays within the acceptance angle of CPVs under identical operation conditions, and this is a result of the joint effect of more uniform irradiation and smaller incidence angle of solar rays on solar cells of CPV-65. To identify which one is the dominant factor affecting photovoltaic performance of both CPVs, an attempt was made to theoretically estimate the power output from both CPVs based on the radiation measured at the solar-noon on days of *I–V* measurements for comparison with measured power output by assuming that the power output of both CPVs is dependent on θ_{in} but independent on solar flux distribution. Thus the power output from CPVs at any moment can be estimated by:

$$P = A_s(I_s - I_{s,65})\overline{\eta}_{0-65} + A_s I_{s,65}\overline{\eta}_{65-90} \quad (14)$$

where $\overline{\eta}_{0-65} = 14.78\%$ and $\overline{\eta}_{65-90} = 6.56\%$. The collectible radiation on solar cells in the case of $|\theta_p| < \theta_a$ is expressed by:

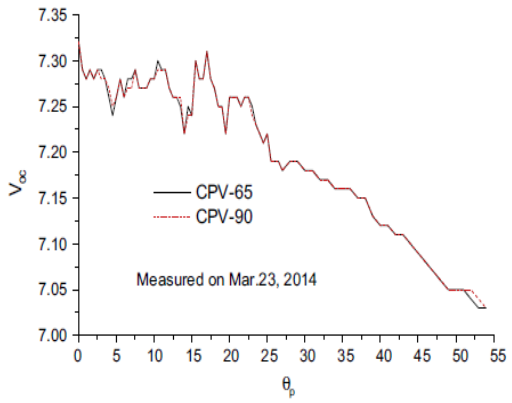

Fig. 15. Comparison of open-circuit voltage between CPV-65 and CPV-90.

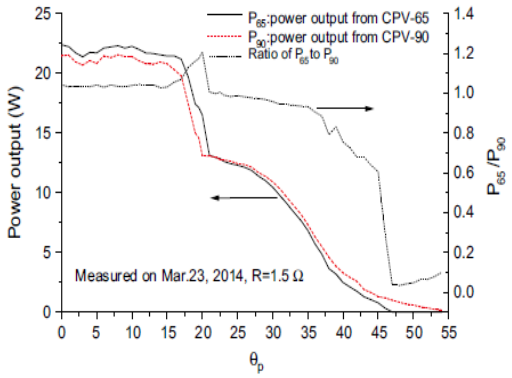

Fig. 16. Power output from both systems at fixed electrical load.

$$I_s = C_t I_b f(\theta_p)\cos\theta_{ap} + 0.5 I_d (C_d + C_{d\beta}) \quad (15)$$

For CPV-65, the radiation on solar cells of CPV-90 at the angle larger than 65° is zero, and for CPV-90, it is given by:

$$I_{s,65} = C_t \rho F(\theta_{in} > 65) I_b \cos\theta_{ap} + 0.5 I_d \rho (C_{x1} + C_{x2}) \quad (16)$$

On the days of *I–V* measurements of both CPVs, $\beta = \lambda - \delta - \theta_p$, thus for CPV-90, $C_d = C_{d\beta} = 0.9874$, $C_{x1} = C_{x2} = 0.1488$; whereas for CPV-65, $C_d = C_{d\beta} = 0.8591$. $f(\theta_p) = 0.931$ for both CPVs in the case of $\theta_p = 0, 10°$ and 16°. Knowing the beam radiation I_b and sky diffuse radiation on the horizon I_d, the power output can be estimated. Table 5 presents the expected power output from CPVs at the solar-noon on the days of *I–V* measurements. It is seen that the expected power outputs from both CPVs were slightly lower than those measured at the maximum point of *I–V* measurements (see Figs. 11–13), and this is because, for both CPVs here, half of radiation on the aperture will directly irradiate solar cells for solar rays at $\theta_p < \theta_f$, and the actual photovoltaic efficiency of solar cells for this part radiation is higher than $\overline{\eta}_{0-65}$ due to small incidence angle. However, it is seen that the expected increases in power output from CPV-65 as compared to CPV-90 were highly in agreement with those actually measured. This implied that the assumption "the power output of both CPVs is dependent on θ_{in} but independent on solar flux distribution" was reasonable. However, the solar flux distribution on solar cells of both CPVs are different, this indicated that the effect of solar flux distribution on the photovoltaic performance of both CPVs was identical and insignificant.

5.2. Long-term photovoltaic performance of CPV-65 and CPV-90

The annual power output from CPVs is complex and affected by many factors such as electrical load and climatic conditions. Analysis in the above showed that under identical operation conditions, effects of all parameters with an exception of θ_{in} on the power output of both systems can be regarded to be identical. Thus, the annual power output from unit solar cells' area of both systems could be simply estimated by:

$$P_a = (S_a - S_{a,65})\overline{\eta}_{0-65} + S_{a,65}\overline{\eta}_{65-90} \quad (17)$$

For the long-term performance, $\overline{\eta}_{0-65}$ and $\overline{\eta}_{65-90}$ depend on the annually angular distribution of radiation over solar cells of CPVs. From the long-term point of view, the radiation from the sun can be regarded to be isotropic over the acceptance angle of CPVs, thus the radiation on the solar cells of CPVs also can be regarded as to be angularly isotropic based on the optical characteristics of CPC [30], therefore $\overline{\eta}_{0-65}$ and $\overline{\eta}_{65-90}$ here can be determined based on Eq. (13), namely: $\overline{\eta}_{0-65} = 14.78\%$ and $\overline{\eta}_{65-90} = 6.56\%$. As shown in Tables 3 and 4, the annual power output of CPV-65 was slightly higher than that from CPV-90 except in the areas with poor solar resources, such as Chengdu, Chongqing, Guiyang and Taipei, where the annual power output from both systems was almost identical. It is also found that 2T-CPV-65 was more favorable as compared to 2T-CPV-90, a result of fact that, in the case of the tilt-angle of the aperture being yearly adjusted two times at two tilts, more radiation arrived on solar cells of CPV-90 at the angle larger than 65° as seen from Tables 3 and 4. This implied that the CPV-65 performed slightly but insignificantly better than the CPC-90 in terms of annual power output especially in the areas with abundant solar resources.

6. Conclusions

Theoretical calculations showed that the optical efficiency of CPV-65 and CPV-90 was identical for solar rays within the acceptance angle of CPVs, and optical efficiency of CPV-65 was slightly lower than that of CPV-90 for solar rays out the acceptance angle. As compared to CPV-65, solar cells of CPV-90 annually received 3–5% more radiation. For CPV-65, all radiation would arrive on the solar cells at the incidence angle less than 65°, but for CPV-90, about 8–10% of annual collectible radiation would arrive on solar cells at the incidence angle larger than 65°, and this part of radiation could not be efficiently converted into electrical power output by solar cells due to the poor solar absorption.

Measurements under outdoor conditions indicated that the photovoltaic efficiency of PV panels without using CPCs for total radiation was almost kept unchanged as the incidence angle (θ_{in}) less than 40°, and then linearly decreased as $\theta_{in} > 40°$. Calculation based on measured photovoltaic efficiency of solar cells for total radiation and assumed photovoltaic efficiency for sky diffuse radiation indicated that photovoltaic efficiency of PV panels for beam

Table 5
Expected power out of CPV-90 and CPV-65 at solar noon on days of *I–V* measurements.

θ_p	I_b	I_d	$F(\theta_{in} \geq 65)$	I_s		$I_{s,65}$	P		$P_{cpc\text{-}65}/P_{cpc\text{-}90}$
				CPV-90	CPV-65		CPV-90	CPV-65	
0	734	233	0.062	149.7	146.89	10.16	21.29	21.71	1.0198
10	717	246	0.1244	143.07	143.07	17.16	20.17	21.15	1.0483
16	699	252	0.2077	137.59	137.59	25.59	18.68	20.34	1.0886

radiation sharply decreased with the increase of incidence angle as the $\theta_{in} > 60°$, and was only 2.8% in the case of $\theta_{in} = 80°$.

It was observed that the open-circuit voltage of both systems were almost identical, but the short-circuit current of CPV-65 was always larger than that of CPV-90 as $\theta_p < \theta_a$, otherwise the situation was reversed. As compared to the CPV-90, the power output at the maximum power points from CPV-65 were slightly higher, and increases of 2.1%, 5.4% and 8.17% were measured for $\theta_p = 0°$, 10° and 16°, respectively. Analysis showed that effect of solar flux distribution over solar cells on the power output of both CPVs was almost identical and insignificant, but the incidence angle of solar rays on solar cells had a significant influence.

Experimental results showed that, for both systems with the identical electrical load, CPV-65 performed better than CPV-90 in terms of power output as solar rays within the acceptance angle especially as θ_p close to θ_a, otherwise CPV-90 did better. Analysis indicated that the CPV-65 performed slightly but insignificantly better than the CPV-90 in terms of annual power output except in the areas with poor solar resources where the annual power output of both systems was almost identical, a result of the fact that a part of radiation arrived on solar cells of CPV-90 at the angle larger than 65°, and this part of radiation would not be efficiently converted into electrical power by solar cells.

Given the acceptance half-angle and geometric concentration factor, the height of CPV-65 was larger than that of CPV-90, thus more reflective materials are used, therefore, a further experimental investigation on the long-term performance of both CPVs is required to ascertain whether CPV-65 is more attractive in economy and performance.

Acknowledgement

This work is partial fulfillment of funded research programs 51066007 and 51466016, financially supported by Natural Science Foundation of China.

References

[1] Firdaus MS, Siti HAB, Roberto RI, Scott GBGS, Abu BM, Ruzairi AR. Performance analysis of a mirror symmetrical dielectric totally internally reflecting concentrator for building integrated photovoltaic systems. Appl Energy 2013;111:288–99.
[2] Robert MC. Concentrator photovoltaic technologies: review and market prospects. Refocus 2005;6(4):35–9.
[3] Rabl A. Active solar collectors and their applications. Oxford: Oxford University Press; 1985.
[4] Bahaidarah HM, Tanweer B, Gandhidasan P, Ibrahim N, Rehman S. Experimental and numerical study on non-concentrating and symmetric unglazed compound parabolic photovoltaic concentration systems. Appl Energy 2014;136:527–36.
[5] Sellami N, Mallick TK. Optical efficiency study of PV crossed compound parabolic concentrator. Appl Energy 2013;102:868–76.
[6] Mallick TK, Eames PC, Hyde TJ, Norton B. The design and experimental characterization of an asymmetric compound parabolic photovoltaic concentrator for building façade integration in the UK. Sol Energy 2004;77:319–27.
[7] Mallick TK, Eames PC, Norton B. Non-concentrating and asymmetric compound parabolic concentrating building façade integrated photovoltaic: an experimental comparison. Sol Energy 2006;80:834–49.
[8] Brogren M, Wennerberg J, Kapper R, Karlsson B. Design of concentrating elements with CIS thin-film solar cells for façade integration. Sol Energy Mater Sol Cells 2003;75:567–75.
[9] Hatwaambo S, Hakansson H, Nilsson J, Karlsson B. Angular characterization of low concentrating PV–CPC using low-cost reflectors. Sol Energy Mater Sol Cells 2008;92:1347–51.
[10] Hatwaambo S, Hakansson H, Roos A, Karlsson B. Mitigating the non-uniform illumination in low concentrating CPCs using structured reflectors. Sol Energy Mater Sol Cells 2009;93(11):2020–4.
[11] Yamei Yu. Studies on performance of CPCs with a restricted exit angle. Thesis of Doctor. Yunnan Normal University; 2015.
[12] Guiqiang Li, Gang Pei, Yuehong Su, Yunyun Wang, Jie Ji. Design and investigation of a novel lens-walled compound parabolic concentrator with air gap. Appl Energy 2014;125:21–7.
[13] Li Guiqiang, Pei Gang, Ji Jie, Su Yuehong. Outdoor overall performance of a novel air-gap-lens-walled compound parabolic concentrator (ALCPC) incorporated with photovoltaic/thermal system. Appl Energy 2015;144:214–23.
[14] Sangani CS, Soanki CS. Experimental evaluation of V-trough (2 suns) PV concentrator system using commercial PV modules. Sol Energy Mater Sol Cells 2007;91(5):453–9.
[15] Solanki CS, Sangani CS, Gunasheka D, Antony G. Enhanced heat dissipation of V-trough PV modules for better performance. Sol Energy Mater Sol Cells 2008;92:1634–8.
[16] Tang Runsheng, Liu Xinyue. Optical performance and design optimization of V-trough concentrators for photovoltaic applications. Sol Energy 2011;85:2154–66.
[17] Duffie JA, Beckman WA. Solar engineering of thermal processes. 2nd ed. New York: John Wiley & Sons, Inc.; 1991.
[18] Hein M, Dimroth F, Siefer G, Bett AW. Characterisation of a 300× photovoltaic concentrator system with one-axis tracking. Sol Energy Mater Sol Cells 2003;75:277–83.
[19] Rabl A, Winston R. Ideal concentration for finite sources and restricted exit angle. Appl Opt 1976;15:2880–3.
[20] Yu Yamei, Tang Runsheng, Xia Chaofeng. Irradiation distribution on solar cells inside CPCs with a restricted exit angle. Adv Mater Res 2012;588–589:603–7.
[21] Yu Yamei, Liu Nianyong, Tang Runsheng. Optical performance of CPCs for concentrating solar radiation on flat receivers with a restricted incidence angle. Renew Energy 2014;62:679–88.
[22] Rabl A. Comparison of solar concentrators. Sol Energy 1976;18:93–111.
[23] Tang Runsheng, Wang Jinfu. A note on multiple reflections of radiation within CPCs and its effect on calculations of energy collection. Renew Energy 2013;57:490–6.
[24] Collares-Pereira M, Rabl A. The average distribution of solar radiation: Correlations between diffuse and hemispherical and between hourly and daily insolation values. Sol Energy 1979;22:155–64.
[25] Li Zhimin, Liu Xinyue, Tang Runsheng. Optical performance of vertical single-axis tracked solar panels. Renew Energy 2011;36:64–8.
[26] Tang Runsheng, Wu Maogang, Yu Yamei, Ming Li. Optical performance of fixed east-west aligned CPCs used in China. Renewable Energy 2010;35:1837–41.
[27] Ma Yi, Li Guihua, Tang Runsheng. Optical performance of vertical axis three azimuth angles tracked solar panels. Appl Energy 2011;88/5:1784–91.
[28] Chen ZY. The climatic summarization of Yunnan. Beijing: Weather Publishing House; 2001.
[29] Wu Hongbo, Tang Runsheng, Li Zhimin, Zhong Hao. A mathematical procedure to estimate absorptance of shallow water ponds. Energy Convers Manage 2009;50:1828–33.
[30] Rabl A, Goodman NB, Winston R. Practical design considerations for CPC collectors. Sol Energy 1919;22:373–81.

Glossary

a: width of CPC troughs (m)
A_s: total area of solar cells (m^2)
C_t: geometric concentration factor of truncated CPCs (dimensionless)
$f(\theta_p)$: optical efficiency factor (dimensionless)
$F(\theta_{in} > 65)$: fraction of radiation incidence on the aperture of CPCs that arrives on solar cells at the angle larger than 65° (dimensionless)
H: daily radiation on solar cells (MJ/m^2)
h_t: height of CPCs (m)
I: instantaneous radiation intensity (W/m^2); current (A)
P_a: annual power output of CPVs (MJ/m^2)
S_a: annual radiation on solar cells (MJ/m^2)
V: voltage (V)
t: solar time measuring from solar noon to afternoon (s)
Greek letters
β: tilt-angle of the aperture of CPVs from horizon (°)
δ: declination of the sun (°)
λ: site latitude (°)
θ_a: acceptance half-angle of CPVs (°)
θ_{ap}: incidence angle of solar rays on the aperture of CPVs or solar panels (radian)
θ_{in}: incidence angle of solar rays on solar cells (°)
θ_e: restricted exit angle of CPCs (°)
θ_f: angle for solar radiation incident at the angle larger than which the absorber of CPC will be fully irradiated (°)
θ_p: projection incidence angle of solar rays on the cross-section of CPC-trough (°)
θ_t: edgy-ray angle of truncated CPCs (°)
ρ: reflectivity of reflectors (dimensionless)
ω: hour angle (radian)
Subscripts
0: sunset
b: beam radiation
d: sky diffuse radiation
day: daily solar gain
h: hemisphere radiation
m: maximum value
s: solar cell

PLOS ONE

RESEARCH ARTICLE

Pectin Enhances Bio-Control Efficacy by Inducing Colonization and Secretion of Secondary Metabolites by *Bacillus amyloliquefaciens* SQY 162 in the Rhizosphere of Tobacco

Kai Wu[1,2☯], Zhiying Fang[1☯], Rong Guo[1], Bin Pan[1], Wen Shi[1], Saifei Yuan[1], Huilin Guan[2]*, Ming Gong[3], Biao Shen[1]*, Qirong Shen[1]

1 National Engineering Research Center for Organic-based Fertilizers, College of Resources and Environmental Sciences, Nanjing Agricultural University, Nanjing, 210095, China, 2 Engineering Research Center of Sustainable Development and Utilization of Biomass Energy, Key Laboratory of Ministry of Education, College of Energy and Environmental Sciences, Yunnan Normal University, Kunming, 650500, China, 3 School of Life Sciences, Yunnan Normal University, Kunming, 650500, China

☯ These authors contributed equally to this work.
* ghl0871@aliyun.com (HG); shenbiao@njau.edu.cn (BS)

OPEN ACCESS

Citation: Wu K, Fang Z, Guo R, Pan B, Shi W, Yuan S, et al. (2015) Pectin Enhances Bio-Control Efficacy by Inducing Colonization and Secretion of Secondary Metabolites by *Bacillus amyloliquefaciens* SQY 162 in the Rhizosphere of Tobacco. PLoS ONE 10(5): e0127418. doi:10.1371/journal.pone.0127418

Academic Editor: Rita Grosch, Leibniz-Institute of Vegetable and Ornamental Crops, GERMANY

Received: November 3, 2014

Accepted: April 15, 2015

Published: May 21, 2015

Data Availability Statement: All relevant data are within the paper and its Supporting Information files.

Funding: This research was financially supported by Programs of Study and Application of Key Technologies for Soil Bioremediation in Guizhou Province (110201002019), the projects of the 111 project (B12009), the Priority Academic Program Development of Jiangsu Higher Education Institutions (PAPD), the Chinese Ministry of Agriculture (201103004), the National Natural Science Foundation of China (41361075), the Applied and Basic Research Foundation of Yunnan province

Abstract

Bacillus amyloliquefaciens is a plant-beneficial Gram-positive bacterium involved in suppressing soil-borne pathogens through the secretion of secondary metabolites and high rhizosphere competence. Biofilm formation is regarded as a prerequisite for high rhizosphere competence. In this work, we show that plant extracts affect the chemotaxis and biofilm formation of *B. amyloliquefaciens* SQY 162 (SQY 162). All carbohydrates tested induced the chemotaxis and biofilm formation of the SQY 162 strain; however, the bacterial growth rate was not influenced by the addition of carbohydrates. A strong chemotactic response and biofilm formation of SQY 162 were both induced by pectin through stimulation of surfactin synthesis and transcriptional expression of biofilm formation related matrix genes. These results suggested that pectin might serve as an environmental factor in the stimulation of the biofilm formation of SQY 162. Furthermore, in pot experiments the surfactin production and the population of SQY 162 in the rhizosphere significantly increased with the addition of sucrose or pectin, whereas the abundance of the bacterial pathogen *Ralstonia* decreased. With increased production of secondary metabolites in the rhizosphere of tobacco by SQY 162 and improved colonization density of SQY 162 in the pectin treatment, the disease incidences of bacterial wilt were efficiently suppressed. The present study revealed that certain plant extracts might serve as energy sources or environmental cues for SQY 162 to enhance the population density on tobacco root and bio-control efficacy of tobacco bacterial wilt.

(2013FA015), and the Science Research Program of Provincial Education Department of Yunnan province (ZD2013008). The funders had no role in study design, data collection and analysis, decision to publish, or preparation of the manuscript.

Competing Interests: The authors have declared that no competing interests exist.

Introduction

The use of plant growth promoting rhizobacteria (PGPR) to bio-control soil-borne diseases and promote plant growth is a promising way to improve agriculture sustainability [1–2]. One PGPR example, the Gram-positive bacteria *Bacillus*, is widely used as biofertilizer to control *fusarium* and bacterial wilt [3–5]. *Bacillus amyloliquefaciens* produces lipopeptides (LPs) to protect the plant from pathogens [6]. Furthermore, *B. amyloliquefaciens* also induces the systemic resistance in plants against pathogens [7–9].

Successful root colonization of bio-control agents in the rhizosphere was essential for bio-control efficacy [4,9–10]. Chowdhury et al. [10] demonstrated that successful control of lettuce bottom rot was achieved through high rhizosphere competence of *B. amyloliquefaciens* FZB42 in the field. Additionally, the bio-control of *Fusarium oxysporum* on cucumber was facilitated by the biofilm formation of *B. amyloliquefaciens* on cucumber roots [11]. Biofilms are complex architectures in which numerous cells are embedded within a matrix consisting of exopolysaccharides (EPS), DNA and proteins [12–13]. The extracellular matrix was affected by the expression of the *epsA-O* operon and *tasA*, which are responsible for the synthesis of EPS and amyloid-like fibers, respectively [12,14]. *tasA* is indirectly controlled by the global transcriptional regulator Spo0A, which is controlled by various histidine kinases (KinA-KinE) under different environmental conditions [15–16]. Therefore, when appropriate environmental cues are present, the kinases are active and induce biofilm formation and root colonization.

Plants change the rhizobacterial living habitat through the secretion of root exudates, which act as nutrient sources or signal compounds in the rhizosphere [17–18]. Chen et al. [19] illustrated that tomato root exudates induced the biofilm formation of *B. subtilis* 3610 via a KinD-dependent pathway. Tan et al. [20] demonstrated that the concentration of organic acids from root exudates from different tomato cultivars affected the biofilm formation and rhizosphere colonization of *B. amyloliquefaciens* T-5. Furthermore, structural carbohydrates from *Arabidopsis* acted as a more important factor than the root exudates in triggering the biofilm formation and root colonization of *B. subtilis* [15].

Surfactin secreted from *B. amyloliquefaciens* may be important in biofilm formation, root colonization, plant defense stimulation and the effective suppression of plant disease [7,21–23]. Recently, our study found that *B. amyloliquefaciens* SQY 162 (SQY 162) could suppress tobacco bacterial wilt caused by *Ralstonia solanacearum* through changing the bacterial community composition in rhizosphere [24]. However, interaction between the bio-control activity of the strain SQY 162 and the plant polysaccharides is unknown. Therefore, we hypothesized that plant polysaccharides could improve the colonization of SQY 162 and bio-control activity against tobacco bacterial wilt due to enhancing surfactin production and reducing the population density of the pathogen. The effects of plant root extracts and different carbohydrates on the chemotaxis and biofilm formations of strain SQY 162 were identified *in vitro* with capillary and microtitre plate assay, respectively. The expression analyses of several genes involved in the production of the matrix and surfactin of strain SQY 162 were performed in defined medium with carbohydrates *in vitro* and pot experiments were used to analyze the disease incidences. The *Bacillus*-tobacco plant model system could be useful for understanding the bacteria-plant interactions in future plant protection studies.

Materials and Methods

Ethics statement

The *B. amyloliquefaciens* strain SQY 162 was isolated from the soil from the farmland (26° 74′ N, 107° 49′ E) in Guizhou, China, with property rights. We collaborate with the Institute of

Guizhou Tobacco Science Research on the study about biological control of tobacco bacterial wilt. Therefore, we have obtained permission from the chairman of the institute. The chairman of the institute, Yonggang Feng, should be contacted for future permission. The locations are not protected, and the field studies did not involve endangered or protected species.

Strain

B. amyloliquefaciens SQY 162 (SQY162, CGMCC accession No.7500, China General Microbiology Culture Collection Center) was isolated from the rhizosphere soil in a diseased field in Fuquan, China and showed strong antagonistic ability against the tobacco bacterial wilt pathogen *Ralstonia solanacearum in vitro* (S1 Fig) [24]. SQY 162 was spotted on the nutrient medium (for 1 L liquid nutrient medium containing 3 g beef extracts, 10 g tryptone, 10 g NaCl) with sterile toothpicks. The beef extracts and tryptone were purchased from Oxoid Ltd., Basingstoke, UK. After 24 h incubation, the plates were sprayed with cell suspension of *R. solanacearum* (nearly 10^7 cfu/ml) and then incubated for an additional 24h to observe the inhibition activity.

R. solanacearum with its strong pathogenicity was isolated from diseased tobacco plants in Sansui as described by Wu et al. [24]. The strain was grown in Casamino acid-Peptone-Glucose (CPG) medium (Oxoid Ltd., Basingstoke, UK) [25]. If necessary, antibiotics were used in following concentration: ampicillin, 100 mg/L; kanamycin, 25 mg/L; tetracycline, 15 mg/L; and gentamicin, 12.5 mg/L. Antibiotics were purchased from Sigma-Aldrich (St Louis, Mo, USA).

Plant root exudates and root extracts preparation

Tobacco seeds were surface-sterilized and sown in floating polystyrene trays. Tobacco plants cultured for 30 days were used for root exudate collection. The root exudates collection procedure was conducted as described previously by Hao et al. [26] with a few modifications. Briefly, plants were gently washed three times with sterilized double-distilled water and then transplanted in plastic cups containing 300 ml sterilized double-distilled water. Each treatment was conducted in triplicate (each cup consisted of three tobacco plants). After incubation in the plant growth chamber at 28°C for 24 h (16 h light/8 h dark), root exudates were collected, lyophilized and sterilized by passing through a 0.2-μm filter, and stored at -80°C for further analysis.

For plant root extracts, the plant roots were frozen with liquid nitrogen and ground with mortar and pestle, re-suspended in 100 ml sterile water, lyophilized and filtered with a 0.2-μm filter, and stored at -80°C for further analysis [15].

Chemotaxis experiments

The capillary assay was performed according to the previously published methods with several modifications [27]. The SQY 162 strain was grown in 3 ml Luria-Bertani (LB) broth (Oxoid Ltd., Basingstoke, UK) overnight. Then, 1 ml liquid culture was transferred to 100 ml fresh LB broth with 170 r/min shaking at 30°C until the OD_{600} reached 0.3 to 0.7. Cells were then collected by centrifugation, washed twice in sterile phosphate buffer (10 mM potassium phosphate, pH 7.0, 0.1 mM EDTA, and 1 mM $MgSO_4$) [28], and diluted to an OD_{600} of 0.1 for future testing. A 200-μl pipette tip was used as a chamber to incubate 100 μl SQY 162 suspended in phosphate buffer and harvested as described above. A 4 cm-25-gauge needle (Becton-Dickinson) was used as the capillary for chemotaxis and was attached to a 1 ml tuberculin syringe containing 100 μl of the 15 × root exudates or plant root extracts or different types of compounds. After 2 h incubation at 30°C in the incubation chamber, the needle syringe was removed and the contents were serially diluted in sterile phosphate buffer and plated on LB

medium. The bacterial number in the capillaries was calculated as the average from the colony forming units (CFU) ml^{-1} counted in triplicate plates. Each treatment was presented with three separate capillary assays.

Biofilm formation assay

Biofilm formation was quantified with a modified version of the polyvinylchloride (PVC) microtitre plate assay as described previously by Hamon and Lazazzera [29]. The cells of strain SQY 162, growing in LB medium to the mid-exponential growth stage, were collected and diluted to an OD_{600} of 0.01 in LB medium. SQY 162 suspensions (100 μl) containing the 15 × tobacco root exudates, root extracts or different types of compounds were then added to each well of a 96-well PVC microtiter plate. The inoculated plates were incubated under stationary conditions at 30°C for 18 h. Medium and non-adherent cells were removed, and adherent cells were washed twice with phosphate buffer, as described above, and air-dried. Adherent cells were then stained with 1% crystal violet (CV) in phosphate buffer at room temperature for 20 min. Excess CV was then removed, and the wells were rinsed with water. The bound CV was solubilized in 200 μl of 80% ethanol and 20% acetone. Biofilm formation was then measured at A_{570} for each well.

Effects of carbohydrates on the growth of SQY 162 and *R. solanacearum*

The cells of SQY 162 were incubated overnight in 3 ml LB medium as described above. One milliliter SQY 162 liquid culture was inoculated into 100 ml LB medium containing carbohydrates at a final concentration of 0.5% (w:v). For *R. solanacearum*, the pathogen strain was incubated for 48 h in 3 ml nutrient medium as described above. One milliliter *R. solanacearum* liquid culture was inoculated into 100 ml nutrient medium containing carbohydrates at a final concentration of 0.5% (w:v). The cultures were then incubated for 60 h at 30°C with 170 rpm shaking. Cultures were measured at OD_{600} for each treatment.

Effects of carbohydrates on the lipopeptide production of SQY 162

The cells were incubated overnight in 3 ml LB medium. One milliliter SQY 162 liquid culture was inoculated into 100 ml LB medium containing compounds at a final concentration of 0.5% (w:v). The cultures were then incubated for 60 h at 30°C with 170 rpm shaking. To isolate lipopeptide products, the liquid medium was centrifuged at 10,000 rpm at 4°C, and 6 mol/L HCl was added into the supernatant to a final pH of 2.0 to precipitate the crude lipopeptides. The precipitates were than stored at 4°C overnight. The crude LPs were harvested by 10,000 rpm centrifugation for 10 min at 4°C and then extracted with methanol. The solutions were evaporated with a rotary evaporator, and the resulting residues were re-suspended in distilled water and lyophilized at -80°C. The lyophilized compounds were separated into two parts, one for HPLC analysis and the other for calculation of crude LPs production. The total amounts of crude LPs were calculated as the average value of three replicates.

HPLC analysis

The crude LPs were dissolved in methanol and passed through a 0.22 μm filter. HPLC analysis using an XDB-C18 column (4.6 mm × 250 mm, Agilent Technologies, Santa Clara, CA, USA) was performed at 30°C with the mobile phase consisting of 10 mM trifluoroacetic acid (TFA): acetonitrile (30:70,for surfactin; 60:40, for iturin A, v:v) buffer solution. Each sample solution (10 μl) was eluted for 10 min at a flow rate of 0.8 ml min^{-1} and detected at 280 nm. Standards

for surfactin and iturin A were purchased from Sigma-Aldrich (St Louis, MO,USA) and chromatographed alone.

Pot experiment

The effects of SQY162 plus carbohydrates on the control of tobacco bacterial wilt were evaluated in a green house. Cells of SQY162 were cultured in LB media overnight. The cells were harvested by centrifugation and washed twice with sterile phosphate buffer (10 mM potassium phosphate, pH 7.0, 0.1 mM EDTA, and 1 mM $MgSO_4$) [28] and adjusted to a cell density of 1.5×10^9/ml. The sandy loam soil (pH 5.31, Organic Carbon 12.37 g/Kg, total N 1.74 g/Kg, and available K, P contents 214.26, 53.81 mg/Kg, respectively) collected from a diseased field in Sansui County in Guizhou province was steam-sterilized twice at 121°C for 40 min. For the preparation of cell suspension of *R. solanacearum*, the overnight liquid culture of *R. solanacearum* in CPG broth as described above was centrifuged and obtained cells were suspended in sterile phosphate buffer (3.0×10^8/ml). The steam-sterilized soil was inoculated with *R. solanacearum* at a final concentration of 10^6 cfu/g of soil. The numbers of *R. solanacearum* were determined using semi-selective medium from South Africa (Oxoid Ltd., Basingstoke, UK) composed of peptone 10 g, glycerol 5 ml, casamino acid 1 g, agar 20 g; crystal violet 5 mg; polymyxin B sulfate 100 mg; bacitracin 25 mg; chloromycetin 5 mg; penicillin 0.5 mg; and cycloheximide 100 mg [30]. Antibiotics were purchased from Sigma-Aldrich (St Louis, Mo, USA). Surface-sterilized tobacco seeds (cultivar K326, provided by the Institute of Guizhou Tobacco Science Research) were sown in floating polystyrene trays. After growing for 7 weeks, seedlings were washed three times with sterile water and then transferred to plastic cups (700-g soil). The treatments were designed as follows: (1) Control, soil treated with nothing; (2) PC, yeast extract at a final concentration of 1% was inoculated into each cup; (3) Su, sucrose at a final concentration of 1% was inoculated into each cup; and (4) Pectin, pectin at a final concentration of 1% was inoculated into each cup. Each sample was inoculated with SQY 162 at a final concentration of 10^7 cfu/g of soil before tobacco transplanting and was performed with three replicates. Each replicate consisted of 5 cups (one tobacco seedling was transplanted in each cup). All the plants were placed in a green house (16 h light/8 h dark, 28–32°C). The disease incidence was calculated as the percentage of diseased plants to the total number of transplanted plants in each replicate. Thirty days after transplanting (in the fast growing stage of tobacco), ten-gram rhizosphere soil from the pot was extracted with 40 ml sterile water and was centrifuged. The supernatant was collected for further crude LPs determination. Crude LPs containing surfactin and iturin in the supernatant were extracted and analyzed according to the procedures described above.

The populations of SQY 162 were counted with plate counting methods at 30 days after transplanting. The population of SQY 162 was counted on selective medium supplemented with polymyxin B (35 μg/ml), lincomycin (5 μg/ml) and cycloheximide (50 μg/ml) [24]. The number of *R. solanacearum* was determined using semi-selective medium from South Africa as described above.

Transcription analysis of genes involved in biofilm formation

Biofilm of strain SQY 162 formed under stationary conditions at 30°C for 18 h was harvested, and RNA from SQY 162 was extracted according to the procedure described by Xu et al. [31]. Briefly, after biofilm formation at 30°C for 18 h, the cells from the sucrose and pectin treatments described above were centrifuged at 11000 rpm for 2 min (4°C). Total RNA was extracted using a Bacterial RNA Kit (Omega Bio-Tek, Inc., Norcross, GA, USA) according to the manufacturer's protocol. RNA samples were then reverse transcribed into cDNA in a 20 μl

reverse transcription system (TransGen Biotech, Beijing, China) according to the manufacturer's protocol.

Transcription levels of *epsD*, *yqxM*, *sft*, and *kinC* of SQY 162 cells from the different carbohydrate treatments were measured relative to SQY 162 (control) using quantitative reverse transcription-PCR (qRT-PCR) with a SYBR Premix Ex Taq (Perfect Real Time) Kit (TaKaRa). *epsD* (from the epsA-O operon) and *yqxM* (from the yqxM-sipW-tasA operon) are two genes critical in the production of exopolysaccharide (EPS) and TasA, respectively, which are essential for biofilm formation [31]. The *recA* gene was used as a control. qRT-PCR was performed with an ABI 7500 system under the following conditions: cDNA was denatured for 10 s at 95°C, followed by 40 cycles of 5 s at 95°C and 34 s at 60°C. The data of qRT-PCR were analyzed according to the method of $2^{-\triangle\triangle CT}$ described by Livark and Schmittgen [32].

Statistical analysis

Differences among treatments were assessed with ANOVA, and the means were analyzed with Microsoft Excel 2007 and then subjected to Duncan's multiple range tests at $P < 0.05$ using SPSS 13.0 statistical software (SPSS Inc., Chicago, USA).

Results

Chemotaxis response of SQY 162

The chemotaxis assay indicated that the effects of attracting SQY 162 differed with root exudates and root extracts. The population density of SQY 162 attracted in the syringe in the KL treatments was higher than that in the K treatments (Fig 1). The attracted population of SQY 162 in the KL treatments was 6.20 log cfu/ml, whereas the attracted number of SQY 162 in the K treatments was 6.03 log cfu/ml. The population densities of SQY 162 in treatments amended with individual carbohydrates were all significantly higher than the control (Fig 2), indicating that all the carbohydrates could efficiently attract the strain. SQY 162 was strongly attracted by sucrose, with as many as 6.62 log cfu/ml observed in the syringe.

Biofilm assay

The effects of tobacco root exudates and root extracts on the biofilm formation of SQY 162 are determined. The results indicated that both root exudates and root extracts could induce the biofilm formation of SQY 162 (Fig 3). The effects of carbohydrates on the biofilm formation of SQY 162 were tested using the crystal violet staining method. All the individual carbohydrates induced the biofilm formation of SQY 162, whereas their influence abilities differed (Fig 4). The highest biofilm intensity of SQY 162 was observed in the presence of sucrose, followed by fructose and pectin.

Effects of carbohydrates on the LPs production

The effects of carbohydrates on the crude LPs production of SQY 162 were summarized in Table 1. Seven carbohydrates, except xylan and glycerol, could induce the production of LPs. In the presence of sucrose, the amount of crude LPs increased to 592.7 mg/L compared to the control. The lowest LPs level, 261.0 mg/L, was observed in the glycerol treatment. Using HPLC analysis, two carbohydrates, pectin and sucrose, induced the production of surfactin (Table 2). However, the five other carbohydrates exhibited little effect on the production of surfactin.

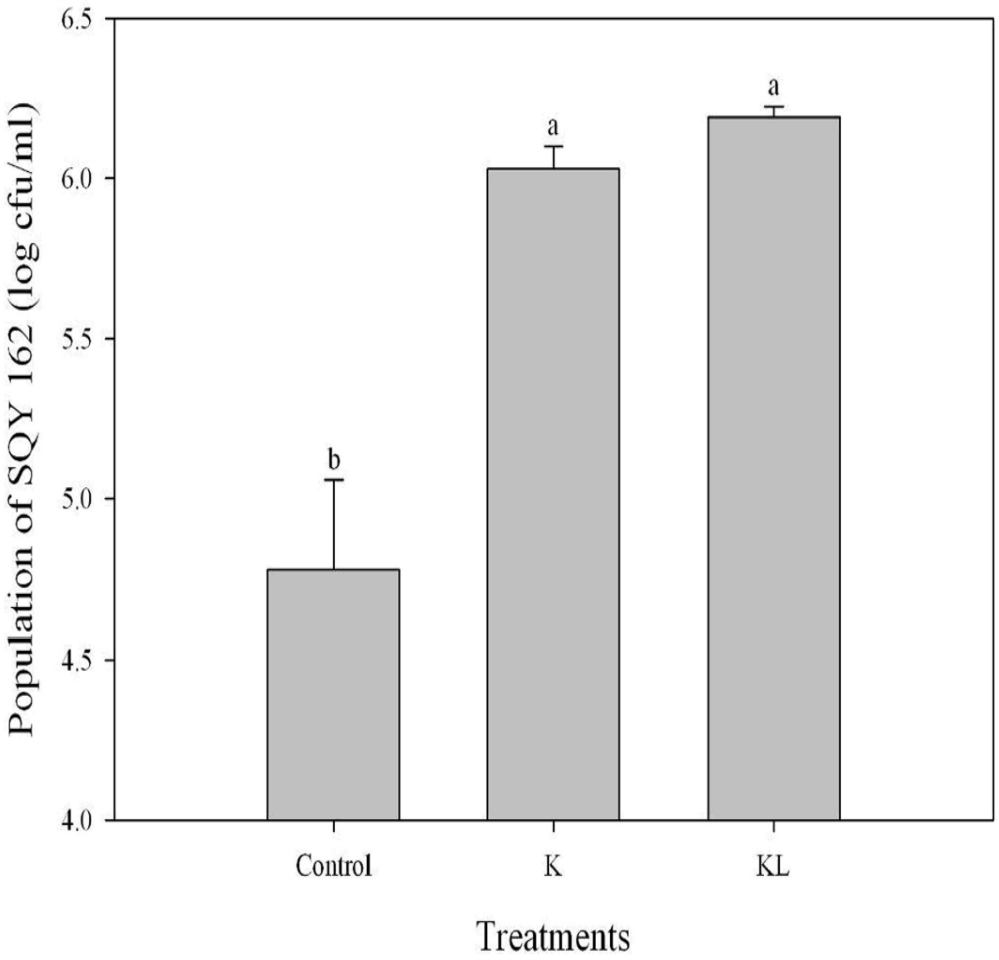

Fig 1. Chemotactic response of SQY 162 towards tobacco root exudates and root extracts from K326 evaluated by capillary assay. Control (chemotaxis buffer), K (inoculated with 15 × root exudates from K326), KL (inoculated with 15 × root extracts from K326).

doi:10.1371/journal.pone.0127418.g001

Effects of carbohydrates on the growth of SQY 162 and *R. solanacearum*

As shown in Fig 5, there were no significant effects of carbohydrates on the growth of SQY 162, indicating carbohydrates might act as induced factors to promote lipopeptide production. For *R. solanacearum*, the growth rates of *R. solanacearum* in presence of different carbohydrates were different, indicating *R. solanacearum* could not equally utilize these carbohydrates (Fig 6).

Effects of sucrose and pectin on the expression of genes involved in biofilm formation

For the sucrose and pectin treatments, the transcription levels were determined for four genes, *epsD*, *yqxM*, *sft*, and *kinC*, relative to the control. The results suggested that application of sucrose and pectin both significantly increase the transcription levels of *eps*D, *yqx*M and *kin*C in *B. amyloliquefaciens* SQY 162. As shown in Fig 7, application of sucrose increased the transcription levels of *eps*D and *yqx*M by 6.89- and 3.43-fold, respectively. However, the *sft* transcription levels showed no significant difference with the addition of sucrose. Furthermore, in

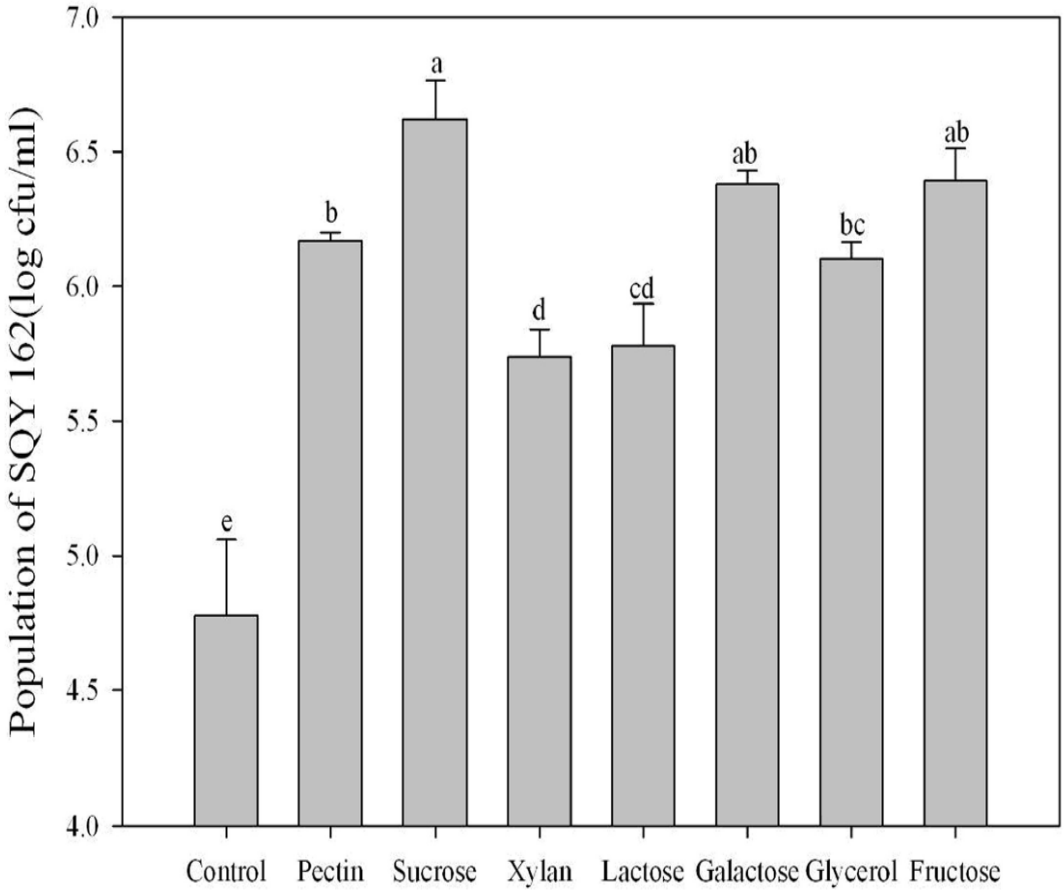

Fig 2. The chemotactic response of SQY 162 to treatment with different carbohydrates. The means and standard errors are shown. The different letters above each bar refer to the Duncan's test, $p < 0.05$. Phosphate buffer was amended with sucrose (Sucrose), fructose (Fructose), pectin (Pectin), xylan (Xylan), galactose (Galactose), lactose (Lactose), or glycerol (Glycerol) at a final concentration of 0.5% (w:v).

doi:10.1371/journal.pone.0127418.g002

contrast to the control, application of pectin significantly increased the transcription levels of *kin*C, *eps*D and *sft* by 26.77-, 8.32- and 5.84-fold, respectively. The results also indicated that addition of pectin had little effect on the *yqx*M transcription levels.

Pot experiment

The results suggested that treatments amended with carbohydrates efficiently suppressed tobacco bacterial wilt compared to the control treatment (Fig 8). Application of sucrose significantly reduced the disease incidence by 25.55% compared to the control treatment (Fig 8A). However, the suppression efficacy in the Su treatment was equivalent to or slightly higher than that in the PC treatment. The results also showed that the disease incidences of the pectin treatment decreased by 27.34 and 42.83% compared to the PC and control treatments, respectively.

Fig 8B shows that the population of the antagonistic strain SQY 162 decreased with plant growth; however, the decrease ratio differed among treatments. Thirty days after transplanting, the number of SQY 162 in the control treatment remained at 5.57 log cfu/g dry weight (log cfu/g dw) soil. With the application of carbon sources, the populations of SQY 162 in the PC, Su

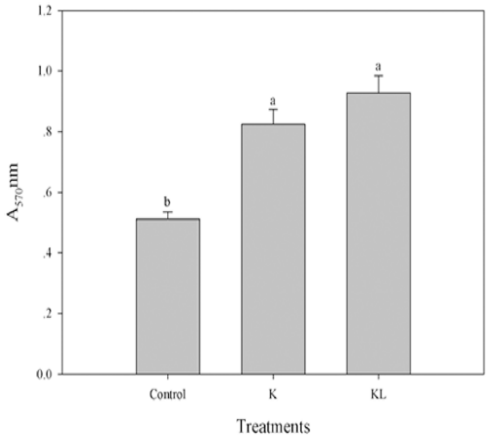

Fig 3. Effects of tobacco root exudates and root extracts from K326 on the biofilm formation of SQY 162. The assays were performed in triplicate and quantified by measuring A_{570} of crystal violet-stained wells rinsed with 80% ethanol and 20% acetone. Control (amended with nothing), K (amended with 15 × root exudates from K326), KL (inoculated with 15 × root extracts from K326).

doi:10.1371/journal.pone.0127418.g003

and pectin treatments were all higher than that in the control treatment. The highest population of SQY 162 was observed in the pectin treatment (6.40 log cfu/g dw soil), which was nearly ten times higher than the population in the control. Furthermore, the result also revealed a negative correlation between the population of SQY 162 and *R. solanacearum* ($r = -0.812$, $p < 0.001$). The population of *R. solanacearum* in the Control treatment was the highest, up to 6.79 log cfu/g dw soil (Fig 8C). The result showed few differences in the population of *R. solanacearum* between the PC and Su treatments. However, with the application of pectin, the population of *R. solanacearum* was significantly reduced compared to that of the control treatment.

Using HPLC analysis, the amount of surfactin in the control treatment was 36.17 μg/kg rhizosphere soil (Fig 8D). In contrast, the application of all carbon sources tested significantly increased the production of surfactin in the rhizosphere soil. Application of sucrose and pectin both increased the production of surfactin by 9.86 and 32.96%, respectively, compared to the PC treatment. However, iturin A was not detected in the rhizosphere soil of any treatments.

Discussion

Bacillus spp. is a well-known biological control agent that suppresses bacterial and fungal diseases through competition, the secretion of antibiotics, and the induction of plant systemic resistance. Because the colonization of plant roots by *B. amyloliquefaciens* displayed striking similarity to the process of biofilm formation *in vitro* [15], the responses of chemotaxis and biofilm involvement in root colonization are prerequisites for successful biological control [33]. In the present study, tobacco root extracts significantly induced the chemotaxis activity and biofilm formation of SQY 162 compared to the root exudates. These findings corroborated the results of Beauregard et al. [15]. Because the carbohydrates acted not only as energy sources but also as environmental cues to induce the EPS production [34–35], it was not surprising to find that all the carbohydrates tested increased the chemotaxis activity and biofilm formation of the strain SQY 162.

Several studies showed that LPs produced by *Bacillus* increased the formation of biofilm or fruiting bodies [36] and are heavily involved in the antagonistic activities against pathogens *in*

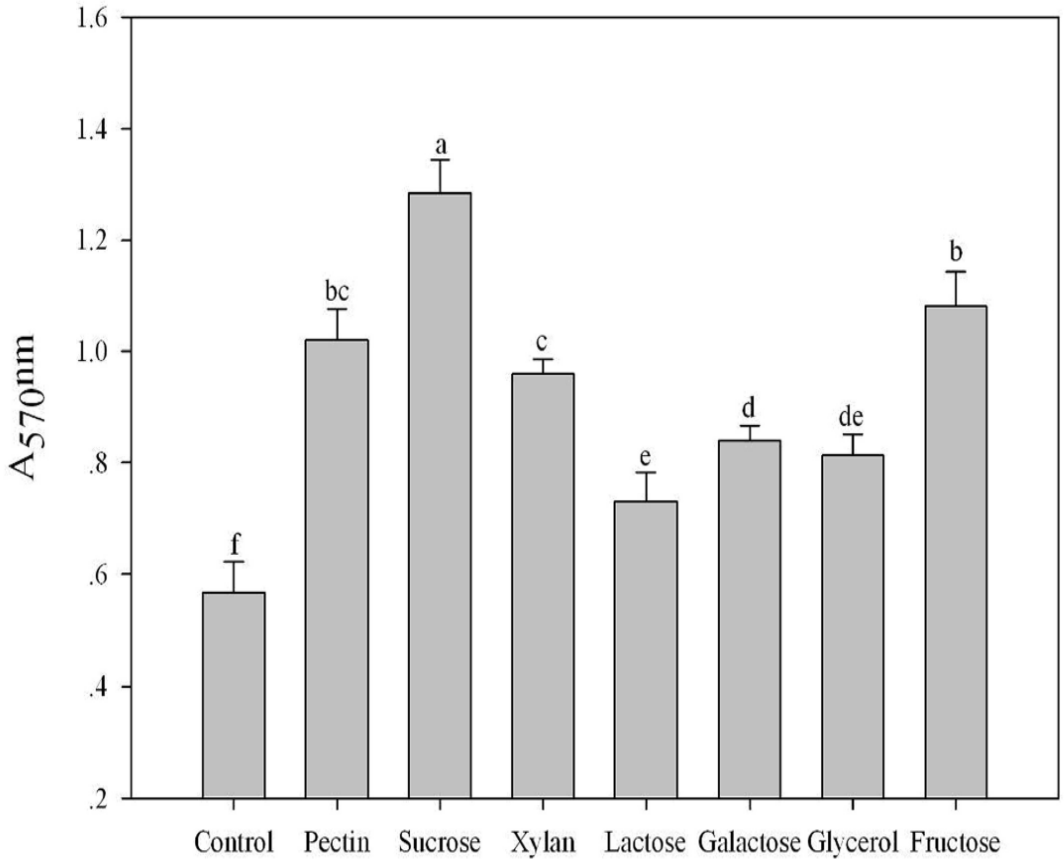

Fig 4. Effects of different carbohydrates on the biofilm formation of SQY 162. The assays were performed in triplicate and quantified by measuring A_{570} nm of crystal violet-stained wells rinsed with 80% ethanol and 20% acetone. The different letters above each bar refer to the Duncan's test, $p < 0.05$. Control (amended with nothing). LB medium was amended with sucrose (Sucrose), fructose (Fructose), pectin (Pectin), xylan (Xylan), galactose (Galactose), lactose (Lactose), or glycerol (Glycerol) at a final concentration of 0.5% (w:v).

doi:10.1371/journal.pone.0127418.g004

Table 1. Effects of different carbohydrate treatments on the lipopeptide production of antagonistic strain SQY 162. Control (amended with nothing).

Treatments	Lipopeptide (mg/L)
Control	295.6±24.4de
Sucrose	592.7±27.2a
Fructose	323.5±43.7cd
Pectin	490.3±16.6b
Xylan	277.0±18.5de
Galactose	359.3±13.5c
Lactose	303.5±28.1de
Glycerol	261.0±17.7e

LB medium amended with sucrose (Sucrose), fructose (Fructose), pectin (Pectin), xylan (Xylan), galactose (Galactose), lactose (Lactose), and glycerol (Glycerol) at a final concentration of 0.5% (w:v).

doi:10.1371/journal.pone.0127418.t001

Table 2. Effects of different carbohydrate treatments on the surfactin and Iturin A production of antagonistic strain SQY 162. Control (amended with nothing).

Treatments	Lipopeptides (mg/L)	
	Surfactin	Iturin A
Control	26.29±2.23c	2.69±0.13c
Sucrose	42.40±4.83b	14.38±0.45a
Fructose	27.99±2.16c	2.95±0.10c
Pectin	62.60±7.96a	3.86±0.13b
Xylan	24.23±2.34c	1.85±0.16e
Galactose	24.06±2.18c	1.78±0.11e
Lactose	26.44±1.93c	2.21±0.07d
Glycerol	23.29±1.37c	2.10±0.06de

LB medium amended with sucrose (Sucrose), fructose (Fructose), pectin (Pectin), xylan (Xylan), galactose (Galactose), lactose (Lactose), and glycerol (Glycerol) at a final concentration of 0.5% (w:v).

doi:10.1371/journal.pone.0127418.t002

vitro [6,37]. In response to different substrates, the production of surfactin and other LPs may be diverse at different levels [38–39]. In the present study, surfactin and iturin were detected in the *B. amyloliquefaciens* SQY 162 culture. Pectin and sucrose treatments significantly increased the surfactin and iturin production, resulting in the increase of biofilm biomass. Moreover, analysis of the transcription levels revealed that the increasing production of LPs by the addition of pectin and sucrose were related to the transcriptional stimulation of *sft*, which is involved in surfactin production.

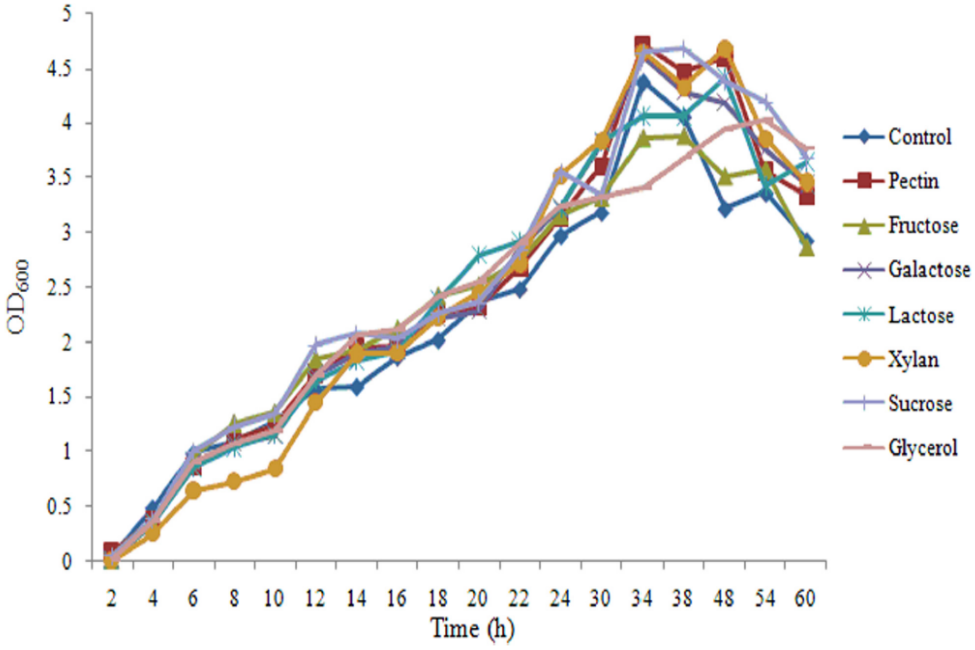

Fig 5. Effects of different carbohydrate treatments on the growth of SQY 162. Control (amended with nothing). LB medium was amended with pectin (Pectin), fructose (Fructose), galactose (Galactose), lactose (Lactose), xylan (Xylan), sucrose (Sucrose), or glycerol (Glycerol) at a final concentration of 0.5% (w:v).

doi:10.1371/journal.pone.0127418.g005

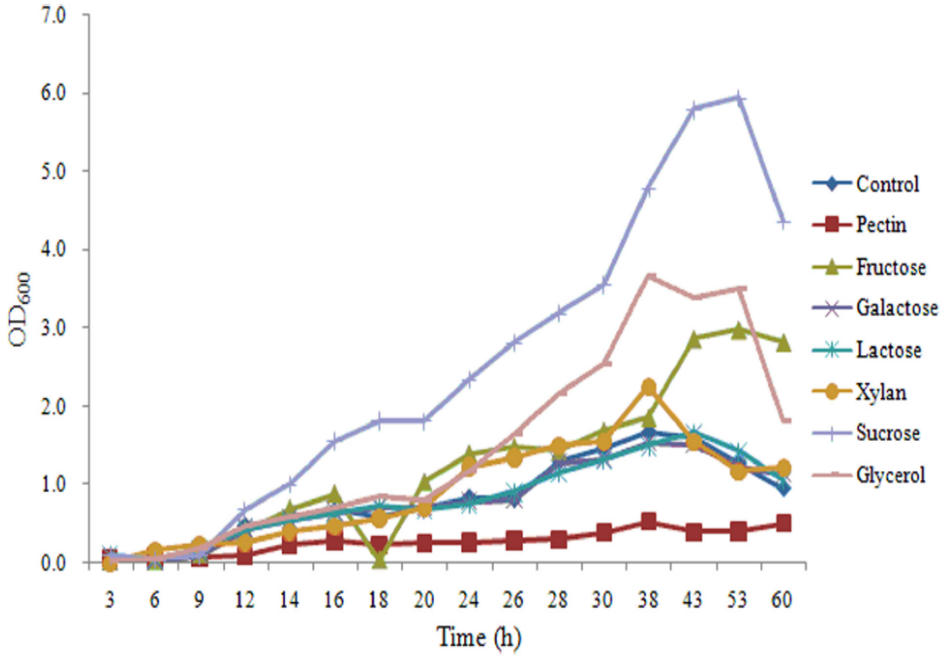

Fig 6. Effects of different carbohydrate treatments on the growth of *R. solanacearum*. Control (amended with nothing). Nutrient medium was amended with pectin (Pectin), fructose (Fructose), galactose (Galactose), lactose (Lactose), xylan (Xylan), sucrose (Sucrose), or glycerol (Glycerol) at a final concentration of 0.5% (w:v).

doi:10.1371/journal.pone.0127418.g006

A previous study demonstrated that a *B. subtilis* mutant unable to produce surfactin would fail to colonize the root [37]. In addition, surfactin induces potassium leakage, which stimulates the activity of a membrane protein kinase (KinC) and thereby increases expression of the genes involved in matrix synthesis [40]. Due to the stimulation of *Kin*C, addition of pectin could significantly increase the transcription levels of *eps*D and *yqx*M, triggering biofilm formation.

Recent studies have indicated that organic acids significantly increase LPs production in the rhizosphere, resulting in a population increase of *B. amyloliquefaciens* S499 on the root [23]. Here, the results of the pot experiment showed that the amount of surfactin in the pectin treatments was significantly higher than that in the control and PC treatments, which was possibly because transcription of *sft* was stimulated by the addition of pectin, as described above. Several studies revealed that inconsistency in bio-control of plant disease by bacterial inoculants in the field could be the result of poor root colonization and insufficient production of antimicrobial metabolites [9,41]. In the present study, we suggested that the bio-control activity of SQY 162 against tobacco bacterial wilt could be enhanced in the presence of pectin. There are several possible mechanisms of the bio-control of the pathogen in the presence of pectin, like enhanced production of surfactin. Since recent studies suggested that surfactin produced by *B. amyloliquefaciens* FZB 42 might be most important in colonizing plant roots [22] and the antibiotic effects of the surfactin on *R. solanacearum* [42], enhanced production of surfactin in the presence of pectin could reduce the population of the pathogen at the rhizosphere. In contrast, iturin A was not detected in the rhizosphere, mainly due to the detection limits for LPs from the soil extracts [43]. It was also found that the fengycin and iturin with antifungal activities produced by *B. amyloliquefaciens* S499 were both poorly expressed *in planta*. Therefore, whether surfactin could be expressed in plant needs further study. Enhanced production of

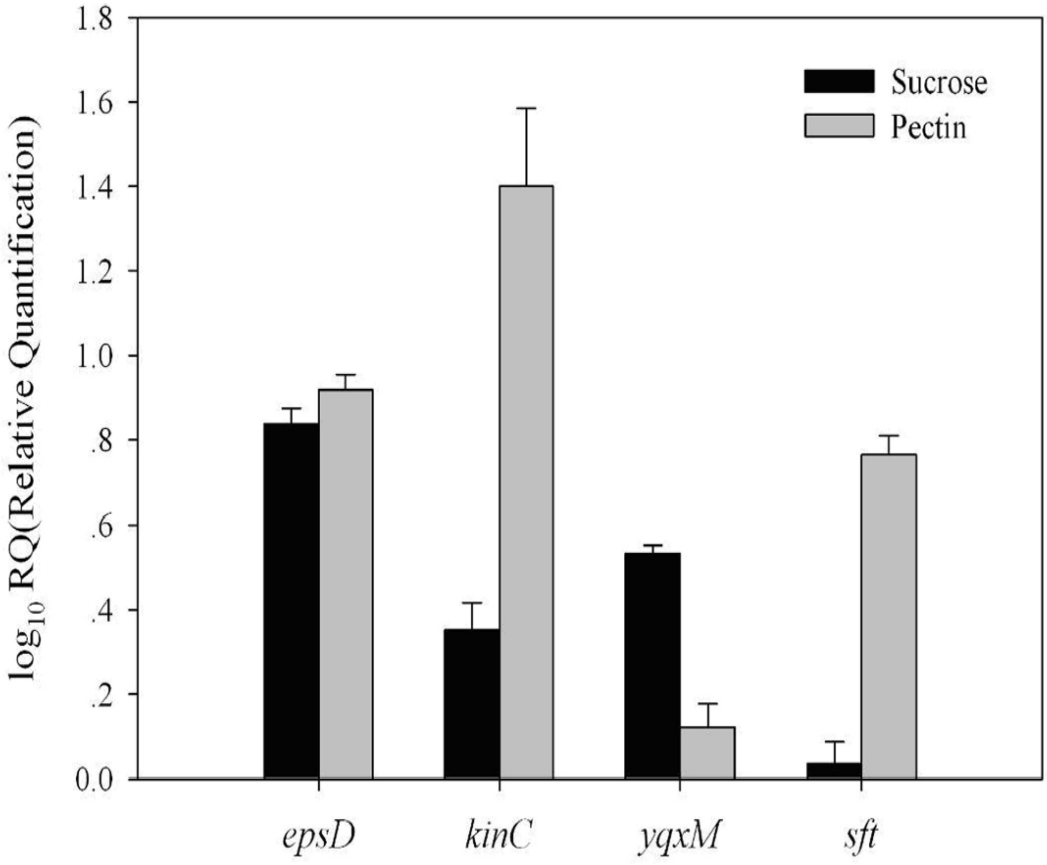

Fig 7. Effects of sucrose or pectin treatments on the transcription levels of biofilm related genes (*eps*D, *kin*C, *yqx*M, and *sft*). LB medium was amended with sucrose (Sucrose) or pectin (Pectin) at a final concentration of 0.5% (w:v).

doi:10.1371/journal.pone.0127418.g007

surfactin by pectin amendment could enable the bacterium to successful colonize the highly competitive rhizosphere niche. It was suggested that an inoculant strain with high rhizosphere competence ability is a key factor for successful disease control [44]. The addition of pectin and sucrose both significantly increased the population of SQY 162 in the rhizosphere, which decreased the pathogen population to some degree. Furthermore, surfactin produced by *B. subtilis* may trigger induced systemic resistance to protect the plant from pathogen infection [45]. It was also suggested oligogalacturonides released by bacterial pectinases could also induce plant defense [46]. Interestingly, *R. solanacearum* was found to grow slower in nutrient medium in the presence of pectin than other carbohydrates amendment in present study, reducing the disease incidence in some aspects. However, *R. solanacearum* was found to utilize pectin as carbon source with pectinase [47]. Therefore, another interest was to study whether the plant extracts could affect the biofilm and colonization of *R. solanacearum* on the root.

In conclusion, our results suggest that plant root extracts from tobacco supply nutrient sources for bacterial growth in the rhizosphere, and induce chemotaxis and biofilm formation. Addition of pectin decreased the abundance of *R. solanacearum* and disease incidence of tobacco bacterial wilt by inducing antibiotic secretion and SQY 162 colonization in the rhizosphere.

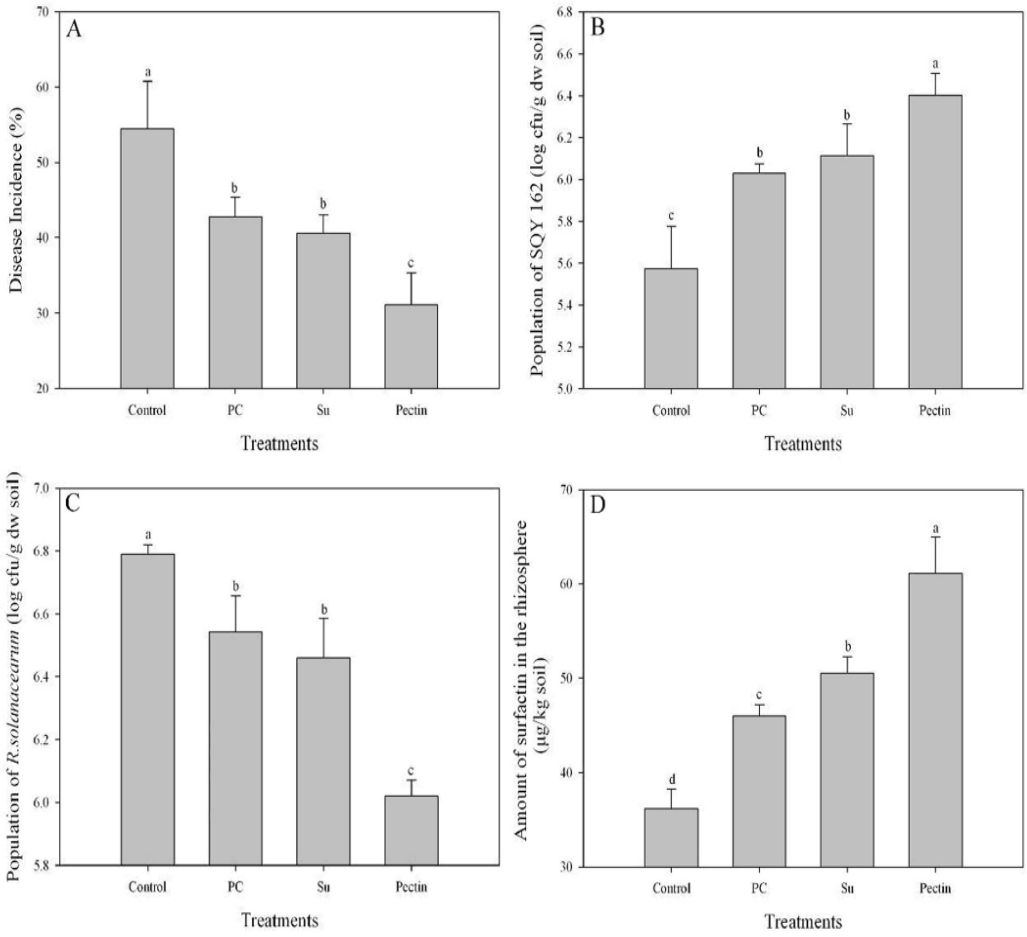

Fig 8. The suppression of tobacco bacterial wilt and quantification of surfactin in pot experiments. Disease incidence, abundance of SQY 162 and *R. solanacearum*, and the amount of surfactin were determined in plants 30 days after transplanting. The different letters above each bar refer to the Duncan's test, $p < 0.05$. Control (soil treated with nothing), PC (yeast extract at a final concentration of 1% was inoculated into each cup), Su (sucrose at a final concentration of 1% was inoculated into each cup), and Pectin (pectin at a final concentration of 1% was inoculated into each cup). Each treatment was inoculated with SQY 162 at a final concentration of 10^7 cfu/g of soil and performed in triplicate.

doi:10.1371/journal.pone.0127418.g008

Although many factors in the rhizosphere affect antibiotic secretion and *Bacillus* colonization, these results increase our understanding of optimizing bio-control strategies using this strain.

Supporting Information

S1 Fig. Antibiotic activity of SQY 162 against the pathogen *in vitro*.
(TIF)

Author Contributions

Conceived and designed the experiments: QS BS KW. Performed the experiments: KW ZF RG BP WS SY. Analyzed the data: KW ZF. Contributed reagents/materials/analysis tools: SY RG BP WS. Wrote the paper: KW BS QS HG MG.

References

1. Compant S, Duffy B, Nowak J, Clément C, Barka EA. Use of plant growth-promoting bacteria for biocontrol of plant diseases: principles, mechanisms of action, and future prospects. Appl Environ Microb. 2005; 71: 4951–4959. PMID: 16151072
2. Handelsman J, Stabb EV. Biocontrol of soilborne plant pathogens. Plant Cell. 1996; 8: 1855–1869. PMID: 12239367
3. Zhao Q, Dong C, Yang X, Mei X, Ran W, Shen Q, et al. Biocontrol of *Fusarium* wilt disease for *Cucumis melo* melon using bio-organic fertilizer. Appl Soil Ecol. 2011; 47: 67–75.
4. Yuan S, Wang L, Wu K, Shi J, Wang M, Yang X, et al. Evaluation of *Bacillus*-fortified organic fertilizer for controlling tobacco bacterial wilt in greenhouse and field experiments. Appl Soil Ecol. 2014; 75: 86–94.
5. Ding C, Shen Q, Zhang R, Chen W. Evaluation of rhizosphere bacteria and derived bio-organic fertilizers as potential biocontrol agents against bacterial wilt (*Ralstonia solanacearum*) of potato. Plant Soil. 2013; 366: 453–466.
6. Chen XH, Koumoutsi A, Scholz R, Eisenreich A, Schneider K, Heinemeyer I, et al. Comparative analysis of the complete genome sequence of the plant growth–promoting bacterium *Bacillus amyloliquefaciens* FZB42. Nat Biotechnol. 2007; 25: 1007–1014. PMID: 17704766
7. Pertot I, Puopolo G, Hosni T, Pedrotti L, Jourdan E, Ongena M. Limited impact of abiotic stress on surfactin production in planta and on disease resistance induced by *Bacillus amyloliquefaciens* S499 in tomato and bean. FEMS Microbiol Ecol. 2013; 86: 505–519. doi: 10.1111/1574-6941.12177 PMID: 23829709
8. Tan S, Dong Y, Liao H, Huang J, Song S, Xu Y, et al. Antagonistic bacterium *Bacillus amyloliquefaciens* induces resistance and controls the bacterial wilt of tomato. Pest Manag Sci. 2013; 69: 1245–1252. doi: 10.1002/ps.3491 PMID: 23519834
9. Weller DM, Raaijmakers JM, Gardener BBMS, Thomashow LS. Microbial Populations Responsible for Specific Soil Suppressiveness to Plant Pathogens[1]. Annu Rev Phytopathol. 2002; 40: 309–348. PMID: 12147763
10. Chowdhury SP, Dietel K, Rändler M, Schmid M, Junge H, Borriss R, et al. Effects of *Bacillus amyloliquefaciens* FZB42 on lettuce growth and health under pathogen pressure and its impact on the rhizosphere bacterial community. Plos One. 2013; 8: e68818. doi: 10.1371/journal.pone.0068818 PMID: 23935892
11. Weng J, Wang Y, Li J, Shen Q, Zhang R. Enhanced root colonization and biocontrol activity of *Bacillus amyloliquefaciens* SQR9 by *abrB* gene disruption. Appl Microbiol Biot. 2013; 97: 8823–8830. doi: 10.1007/s00253-012-4572-4 PMID: 23196984
12. Branda SS, Vik Å, Friedman L, Kolter R. Biofilms: the matrix revisited. Trends Microbiol. 2005; 13: 20–26. PMID: 15639628
13. O'Toole G, Kaplan HB, Kolter R. Biofilm formation as microbial development. Annu Rev Microbiol. 2000; 54: 49–79. PMID: 11018124
14. Romero D, Aguilar C, Losick R, Kolter R. Amyloid fibers provide structural integrity to *Bacillus subtilis* biofilms. Proc Natl Acad Sci USA. 2010; 107: 2230–2234. doi: 10.1073/pnas.0910560107 PMID: 20080671
15. Beauregard PB, Chai Y, Vlamakis H, Losick R, Kolter R. *Bacillus subtilis* biofilm induction by plant polysaccharides. Proc Natl Acad Sci USA. 2013; 110: E1621–E1630. doi: 10.1073/pnas.1218984110 PMID: 23569226
16. Jiang M, Shao W, Perego M, Hoch JA. Multiple histidine kinases regulate entry into stationary phase and sporulation in *Bacillus subtilis*. Mol Microbiol. 2000; 38: 535–542. PMID: 11069677
17. Badri DV, Quintana N, El Kassis EG, Kim HK, Choi YH, Sugiyama A, et al. An ABC transporter mutation alters root exudation of phytochemicals that provoke an overhaul of natural soil microbiota. Plant Physiol. 2009; 151: 2006–2017. doi: 10.1104/pp.109.147462 PMID: 19854857
18. Bais HP, Weir TL, Perry LG, Gilroy S, Vivanco JM. The role of root exudates in rhizosphere interactions with plants and other organisms. Annu Rev Plant Biol. 2006; 57: 233–266. PMID: 16669762
19. Chen Y, Cao S, Chai Y, Clardy J, Kolter R, Guo J, et al. A *Bacillus subtilis* sensor kinase involved in triggering biofilm formation on the roots of tomato plants. Mol Microbiol. 2012; 85: 418–430. doi: 10.1111/j.1365-2958.2012.08109.x PMID: 22716461
20. Tan S, Yang C, Mei X, Shen S, Raza W, Shen Q, et al. The effect of organic acids from tomato root exudates on rhizosphere colonization of *Bacillus amyloliquefaciens* T-5. Appl Soil Ecol. 2013; 64: 15–22.

21. Cawoy H, Mariutto M, Henry G, Fisher C, Vasilyeva N, Thonart P, et al. Plant defense stimulation by natural isolates of *Bacillus* depends on efficient surfactin production. Mol Plant Microbe In. 2014; 27: 87–100.
22. Fan B, Chen XH, Budiharjo A, Bleiss W, Vater J, Borriss R. Efficient colonization of plant roots by the plant growth promoting bacterium *Bacillus amyloliquefaciens* FZB42, engineered to express green fluorescent protein. J Biotechnol. 2011; 151: 303–311. doi: 10.1016/j.jbiotec.2010.12.022 PMID: 21237217
23. Nihorimbere V, Cawoy H, Seyer A, Brunelle A, Thonart P, Ongena M. Impact of rhizosphere factors on cyclic lipopeptide signature from the plant beneficial strain *Bacillus amyloliquefaciens* S499. FEMS Microbiol Ecol. 2012; 79: 176–191. doi: 10.1111/j.1574-6941.2011.01208.x PMID: 22029651
24. Wu K, Yuan S, Wang L, Shi J, Zhao J, Shen B, et al. Effects of bio-organic fertilizer plus soil amendment on the control of tobacco bacterial wilt and composition of soil bacterial communities. Biol Fert Soils. 2014; 50: 961–971.
25. Hendrick CA, Sequeira L. Lipopolysaccharide-defective mutants of the wilt pathogen *Pseudomonas solanacearum*. Appl Environ Microb. 1984; 48: 94–101.
26. Hao WY, Ren LX, Ran W, Shen QR. Allelopathic effects of root exudates from watermelon and rice plants on *Fusarium oxysporum* f. sp. *niveum*. Plant Soil. 2010; 336: 485–497.
27. Rudrappa T, Czymmek KJ, Paré PW, Bais HP. Root-secreted malic acid recruits beneficial soil bacteria. Plant Physiol. 2008; 148: 1547–1556. doi: 10.1104/pp.108.127613 PMID: 18820082
28. Yao J, Allen C. Chemotaxis is required for virulence and competitive fitness of the bacterial wilt pathogen *Ralstonia solanacearum*. J Bacteriol. 2006; 188: 3697–3708. PMID: 16672623
29. Hamon MA, Lazazzera BA. The sporulation transcription factor Spo0A is required for biofilm development in *Bacillus subtilis*. Mol Microbiol. 2001; 42: 1199–1209. PMID: 11886552
30. Elphinstone J, Hennessy J, Wilson J, Stead D. Sensitivity of different methods for the detection of *Ralstonia solanacearum* in potato tuber extracts. EPPO B. 1996; 26: 663–678.
31. Xu Z, Shao J, Li B, Yan X, Shen Q, Zhang R. Contribution of bacillomycin D in *Bacillus amyloliquefaciens* SQR9 to antifungal activity and biofilm formation. Appl Environ Microb. 2013; 79: 808–815. doi: 10.1128/AEM.02645-12 PMID: 23160135
32. Livark K, Schmittgen T. Analysis of relative gene expression data using real-time quantitative PCR and the 2 (-Delta Delta C (T)) method. Methods. 2001; 25: 402–408. PMID: 11846609
33. Xu Z, Zhang R, Wang D, Qiu M, Feng H, Zhang N, et al. Enhanced control of cucumber wilt disease by *Bacillus amyloliquefaciens* SQR9 by altering the regulation of its DegU phosphorylation. Appl Environ Microb. 2014; 80: 2941–2950. doi: 10.1128/AEM.03943-13 PMID: 24584252
34. Chai Y, Beauregard PB, Vlamakis H, Losick R, Kolter R. Galactose metabolism plays a crucial role in biofilm formation by *Bacillus subtilis*. MBio. 2012; 3: e00184–00112. doi: 10.1128/mBio.00184-12 PMID: 22893383
35. Bartholdson SJ, Brown AR, Mewburn BR, Clarke DJ, Fry SC, Campopiano DJ, et al. Plant host and sugar alcohol induced exopolysaccharide biosynthesis in the *Burkholderia cepacia* complex. Microbiol. 2008; 154: 2513–2521. doi: 10.1099/mic.0.2008/019216-0 PMID: 18667584
36. Branda SS, González-Pastor JE, Ben-Yehuda S, Losick R, Kolter R. Fruiting body formation by *Bacillus subtilis*. P Natl Acad Sci USA. 2001; 98: 11621–11626. PMID: 11572999
37. Bais HP, Fall R, Vivanco JM. Biocontrol of *Bacillus subtilis* against infection of *Arabidopsis* roots by *Pseudomonas syringae* is facilitated by biofilm formation and surfactin production. Plant Physiol. 2004; 134: 307–319. PMID: 14684838
38. Zhu Z, Zhang J, Wu Y, Ran W, Shen Q. Comparative study on the properties of lipopeptide products and expression of biosynthetic genes from *Bacillus amyloliquefaciens* XZ-173 in liquid fermentation and solid-state fermentation. World J Microb Biot. 2013; 29: 2105–2114.
39. Zhu Z, Zhang F, Wei Z, Ran W, Shen Q. The usage of rice straw as a major substrate for the production of surfactin by *Bacillus amyloliquefaciens* XZ-173 in solid-state fermentation. J Environ Manage. 2013; 127: 96–102. doi: 10.1016/j.jenvman.2013.04.017 PMID: 23685270
40. López D, Fischbach MA, Chu F, Losick R, Kolter R. Structurally diverse natural products that cause potassium leakage trigger multicellularity in *Bacillus subtilis*. Proc Natl Acad Sci USA. 2009; 106: 280–285. doi: 10.1073/pnas.0810940106 PMID: 19114652
41. Raaijmakers JM, Paulitz TC, Steinberg C, Alabouvette C, Moënne-Loccoz Y. The rhizosphere: a playground and battlefield for soilborne pathogens and beneficial microorganisms. Plant Soil. 2009; 321: 341–361.
42. Chen Y, Yan F, Chai Y, Liu H, Kolter R, Losick R, et al. Biocontrol of tomato wilt disease by *Bacillus subtilis* isolates from natural environments depends on conserved genes mediating biofilm formation. Environ Microbiol. 2013; 15: 848–864. doi: 10.1111/j.1462-2920.2012.02860.x PMID: 22934631

43. Kinsella K, Schulthess CP, Morris TF, Stuart JD. Rapid quantification of *Bacillus subtilis* antibiotics in the rhizosphere. Soil Biol Biochem. 2009; 41: 374–379.

44. Kamilova F, Validov S, Azarova T, Mulders I, Lugtenberg B. Enrichment for enhanced competitive plant root tip colonizers selects for a new class of biocontrol bacteria. Environ Microbiol. 2005; 7: 1809–1817. PMID: 16232295

45. Ongena M, Jourdan E, Adam A, Paquot M, Brans A, Joris B, et al. Surfactin and fengycin lipopeptides of *Bacillus subtilis* as elicitors of induced systemic resistance in plants. Environ Microbiol. 2007; 9: 1084–1090. PMID: 17359279

46. Nakaho K, Allen C. A Pectinase-deficient *Ralstonia solanacearum* Strain Induces Reduced and Delayed Structural Defences in Tomato Xylem. J Phytopathol. 2009; 157: 228–234.

47. Tans-Kersten J, Guan Y, Allen C. *Ralstonia solanacearum* pectin methylesterase is required for growth on methylated pectin but not for bacterial wilt virulence. Appl Environ Microb. 1998; 64: 4918–4923. PMID: 9835583

Electrochimica Acta 173 (2015) 331–337

Contents lists available at ScienceDirect

Electrochimica Acta

journal homepage: www.elsevier.com/locate/electacta

Multi-interfacial polyaniline-graphene/platinum counter electrodes for dye-sensitized solar cells

Peizhi Yang [a], Jialong Duan [b,*], Danyang Liu [b], Qunwei Tang [b,*], Benlin He [b]

[a] Key Laboratory of Advanced Technique & Preparation for Renewable Energy Materials, Ministry of Education, Yunnan Normal University, Kunming 650500, PR China

[b] Institute of Materials Science and Engineering, Ocean University of China, Qingdao 266100, PR China

ARTICLE INFO

Article history:
Received 13 March 2015
Received in revised form 13 April 2015
Accepted 12 May 2015
Available online 15 May 2015

Keywords:
Dye-sensitized solar cells
Counter electrode
Multilayer
Self-assembly
Polyaniline-graphene complex

ABSTRACT

Pursuit of multi-interfacial counter electrodes (CEs) for enhanced triiodide (I_3^-) reduction reaction has been a persistent objective for dye-sensitized solar cells (DSSCs). Here we report the synthesis of multilayer CEs consisting of positively charged polyaniline-graphene (PANi-G) complex and negatively charged platinum (Pt) nanoparticles. The $(PANi\text{-}G/Pt)_n$ (n represents the bilayer number) multilayer displays multi-interfaces for I_3^- reduction and charge transfer. Moreover, the complexation between PANi and G can markedly accelerate the electron migration from G to PANi. The DSSC with $(PANi\text{-}10wt‰G/Pt)_9$ electrode yields an impressive power conversion efficiency of 7.45% under simulated air mass 1.5 global sunlight. The promising efficiency along with cost-effectiveness and scalable materials demonstrates the multi-interfacial CEs to be good candidates for robust DSSCs.

1. Introduction

Nowadays, dye-sensitized solar cells (DSSCs) have become one of the most promising photovoltaic devices due to their superiorities in cost-effectiveness, easy fabrication, environmental friendliness, and relatively high conversion efficiency [1–3]. Since the first prototype described by O'Regan and Grätzel in 1991 [1], a power conversion efficiency as high as 13% has been achieved on DSSCs [4]. Generally, a classical DSSC device comprises of three key components: dye-sensitized photoanode, a redox electrolyte, and a counter electrode (CE). The CE is a prerequisite to collect electrons from external circuit and to reduce triiodides (I_3^-) into iodide (I^-) species [5]. The maximum open-circuit voltage (V_{oc}) is determined by the difference between quasi Fermi energy of electrons in an anode and redox potential energy of electrolyte. Although commonly used Pt electrode exhibits excellent catalytic performance, the high expense of Pt species has restricted the commercialization of DSSCs. Therefore, it seems to be great significance to search for Pt-free or at least low-Pt electrodes.

Significant achievements have been made in previous studies on CE materials, such as Pt alloys [6–8], Pt-free alloys [9,10], carbonaceous materials [11,12], and conducting polymers [13,14]. Among various CE candidates, carbonaceous materials and conducting polymers have applicable prospects as alternative CEs. Conducting polymers, in particular polyaniline, attract more and more research interests due to their excellent electrocatalytic abilities and extremely low cost, meanwhile they have good conductivity and environmental stability [15]. Aiming at improving the electron-migration ability, conducting polymer-carbonaceous complex materials (single wall carbon nanotube [16], multiwalled carbon nanotube [17], and graphene [18]) have been synthesized by a reflux method and employed as CE materials. In our previous work, we develop an avenue of assembling CEs with enormous interfacial area and rapid charge-transfer by a layer-by-layer self-assembly technique from polyaniline-carbon nanotube complex and graphene oxide [16]. However, graphene oxide has relatively low catalytic and conductive property, which reducing the power conversion efficiency of the DSSCs.

In search for other efficient and multi-interfacial CEs with enhanced catalytic activity and charge-transfer capability, here we have successfully synthesized polyaniline-graphene (PANi-G) complex by a reflux technique and homogeneous Pt hydrosol via reducing the chloroplatinic acid with sodium citrate. The multi-interfacial $(PANi\text{-}G/Pt)_n$ electrodes are fabricated by a layer-by-layer self-assembly strategy utilizing the electrostatic interactions. Results reveal that the both PANi-G and Pt nanoparticles have acceleration effects on the electrocatalytic activity and therefore

* Corresponding author. Tel./fax: +86 532 66782533.
E-mail addresses: djl140122009005@163.com (J. Duan), tangqunwei@ouc.edu.cn (Q. Tang).

http://dx.doi.org/10.1016/j.electacta.2015.05.073
0013-4686/

photovoltaic performances of solar cells. An impressive efficiency of 7.45% is recorded on the solar cells with $(PANi\text{-}10wt‰G/Pt)_9$ electrode.

2. Experimental

2.1. Reflux synthesis of aniline-G complexes

The aniline-G complexes were synthesized by a reflux process similar to our previous work [16]. In details, three aniline-G mixtures at G dosages of 4, 8, and 10wt‰ were sealed in a three-neck flask filled with high-purity N_2 gas. In dark, the mixtures were refluxed for 6 h at 184 °C to obtain the target aniline-G complexes, which were subsequently stored in a dark and cold atmosphere.

2.2. Synthesis of PANi-G complexes

50 ml of aqueous solution consisting of HCl (1 M) and $(NH_4)_2S_2O_8$ (APS, 0.5 wt%) was dipped into 50 ml of a mixture consisting of HCl (1 M) and aniline-G (0.325 M) at 0 °C within 2 h. After reaction at 4 °C for 10 h, the resultant product was successively rinsed with1 M HCl aqueous solution and deionized water to remove unreacted aniline monomers and oligomers. Finally, the PANi-G complexes were vacuumly desiccated at 50 °C for 24 h and then dissolved in deionized water to prepare a solution with concentration of around 1 mg ml^{-1}.

2.3. Reflux synthesis of Pt-hydrosol

A mixture consisting of 1 mL of chloroplatinic acid aqueous (0.4 mM) and 15 ml polyvinylpyrrolidone aqueous (10 mg ml^{-1}) was added into a sealed three-neck flask. Then, the mixture was heated to 100 °C with oil bath under magnetic stirring to make reactant dissolved thoroughly, subsequently adding 3 ml sodium citrate aqueous (10 mM) into the above reagent and keeping this temperature for 30 min.

2.4. Assembly of multi-interfacial $(PANi\text{-}G/Pt)_n$ CEs

$(PANi\text{-}G/Pt)_n$ multilayer CEs were fabricated on FTO glass substrates (sheet resistance 12 Ω sqr^{-1}, purchased from Hartford Glass Co., USA). Prior to assembly, the substrates were carefully cleaned with deionized water and anhydrous ethanol. FTO substrates were subsequently immersed in a piranha solution [7/3 (v/v) of H_2SO_4/H_2O_2 at room temperature] for 1 h. To assemble CE, the pretreated FTO glass was immersed in PANi-G aqueous solution for 5 min, rinsed with deionized water for 1 min and dried by N_2 gas stream, then immersed in Pt-hydrosol for 5 min, then rinsed again by deionized water for 1 min and dried by N_2 gas stream. By repeating the previous procedures, we can obtain FTO supported $(PANi\text{-}G/Pt)_n$ multilayer CE (n represents the deposition cycle or bilayer number). The growth process was determined by recording the UV-vis absorption spectra of the multilayer CEs with a Mapada 3200 UV-visible spectrometer. The bared FTO glass substrate was used as a benchmark for each UV-vis spectrum. The errors of the absorption peak were controlled within ± 5%.

2.5. Assembly of DSSCs

FTO-coated glass substrates were cleaned by ultrasonication with acetone, ethanol and deionized water. A layer of TiO_2 nanocrystal anode film with a thickness of 10 μm and active area of 0.16 cm^2 was prepared by coating the TiO_2 colloid using a screen printing technique, and sintered in air at 450 °C for 30 min. Afterward, the photoanodes were sensitized with 0.5 mM N719 [cis-di(thiocyanato)-N,N′-bis(2,2-bipyridyl-4-carboxylic acid-4-tetrabutylammonium carboxylate, purchased from Dyesol LTD, Australia] in ethanol solution for 24 h at room temperature. Then the DSSC was fabricated by sandwiching a sensitized photoanode and a multilayer CE injected with redox electrolyte. A redox electrolyte consisted of 100 mM of tetraethylammonium iodide, 100 mM of tetramethylammonium iodide, 100 mM of tetrabutylammoniumiodide, 100 mM of NaI, 100 mM of KI, 100 mM of LiI, 50 mM of I_2, and 500 mM of 4-tert-butylpyridine in 50 ml acetonitrile.

2.6. Electrochemical characterizations

The electrochemical properties of FTO supported $(PANi\text{-}G/Pt)_n$ multilayer CEs were characterized by a traditional three-electrode method on a conventional CHI660E Electrochemical Workstation (CHI660E, Shanghai Chenhua Device Company, China) comprising an Ag/AgCl reference electrode,a CE of platinum sheet, and a working electrode of FTO glass supported $(PANi\text{-}G/Pt)_n$ multilayer. The cyclic voltammetry (CV) curves were recorded at room temperature from -0.8 to +1.8 V and back to -0.8 V in a supporting electrolyte consisting of 50 mM LiI, 10 mM I_2, and 500 mM $LiClO_4$ in acetonitrile degassed using nitrogen before the measurement. The active area of the CE could be determined by measuring the area below the liquid electrolyte. Electrochemical impedance spectroscopy (EIS) measurements on the symmetric dummy cells consisting two identical CEs were also carried out on the CHI660E Electrochemical Workstation in a frequency range of 0.01 Hz-

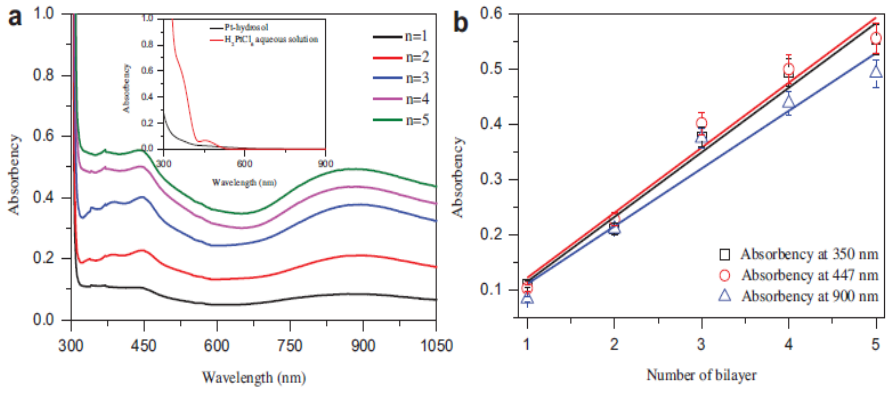

Fig. 1. (a) UV-vis absorption spectra of $(PANi\text{-}10wt‰G/Pt)_n$ (n = 1, 3, 5, 7, and 9) multilayers. (b) Linear plots of the absorbance intensity of PANi as a function of bilayer number. The inset in (a) represents the UV-vis absorption spectra of H_2PtCl_6 and Pt–hydrosol.

10^6 Hz and an open circuit potential at room temperature. The resultant impedance spectra were analyzed using the Z-view software. Tafel polarization curves was recorded on the same Workstation by assembling symmetric dummy cell consisting of FTO/$(PANi\text{-}G/Pt)_n$ multilayer|redox electrolyte|FTO/$(PANi\text{-}G/Pt)_n$ multilayer and scanning potential window of -1 to +1 V at a scan rate of 10 mV s^{-1}. All the curves from CV, EIS, and Tafel were repeatedly measured at least five time to control the errors within 5%.

2.7. Photovoltaic measurements

The photocurrent-voltage (*J-V*) curves of the assembled DSSCs were measured on an Electrochemical Workstation (CHI600E) under irradiation of a simulated solar light from a 100 W xenon-mercury arc lamp (CHF-XM-500W, Beijing Trusttech Co., Ltd) in ambient atmosphere. The incident light intensity was calibrated using a FZ-A type radiometer from Beijing Normal University Photoelectric Instrument Factory to control it at 100 mW cm^{-2} (AM 1.5). Each DSSC device was measured at least five times to eliminate experimental error and a compromise *J-V* curve was employed.

2.8. Other characterizations

The optical absorption spectra were recorded on a UV-vis spectrophotometer (Mapada 3200) at room temperature. The top-view morphologies of the multilayer CEs were observed on a scanning electron microscope (SEM, S4800). For electrochemical impedance spectroscopy (EIS) measurements, the DSSCs were scanned from 0.01 Hz to 1 MHz at an open circuit potential and analyzed using the Z-view modeling software to fit the data according to equivalent circuit derived from transmission line model.

3. Results and discussion

Fig. 1a shows the UV-vis absorption spectra of the multi-interfacial $(PANi\text{–}10wt‰G/Pt)_n$ electrodes prepared by a layer-by-layer self-assembly technique. The absorption spectra indicates that the Pt hydrosol has been successfully prepared due to the disappeared absorption peak of chloroplatinic acid (Inset in Fig. 1a) [19]. $(PANi\text{-}10wt‰G/Pt)_n$ multilayer exihibits three bands at 350, 447 and 900 nm, which are assigned to the bands of Pt species [19], π→localized polaron band of PANi [20,21]. The band at 350 nm is relatively weak in comparison to the absorbance of PANi, therefore, the absorbance of intensities of PANi can be employed to detect the growth of $(PANi\text{-}10wt‰G/Pt)_n$ multilayer electrodes. The absorbance at 447 and 900 nm increases linearly with the deposition cycles (Fig. 1b), which suggests that the same amount of PANi-G and Pt are deposited during each cycle [16]. Our previous studies have confirmed that the covalent-bonding between PANi and G can be formed between carbon atom in conjugation structure and the nitrogen atom in PANi. Due to the rapid electron transfer from G to PANi and high catalytic activity of Pt, nanoporous $(PANi\text{-}G/Pt)_n$ multilayer electrodes can be realized and are expected to provide multi-interfaces for I_3^- reduction.

From the top-view SEM images of $(PANi\text{-}10wt‰G/Pt)_n$ multilayers, as shown in Fig. 2, one can find that the resultant multilayers have nanoporous instead of layered structure, which is beneficial to the diffusion and rapid exchange of I^-/I_3^- redox couples within the CE material. Moreover, the Pt nanoparticles with the diameter of ~50 nm can be observed in Fig. 2c, and the size of Pt particles become larger at an increased bilayer from $n = 3$ to 9, resulting in the improvement of electrocatalytic activity toward I_3^- reduction.

In order to explore the influence of the number of deposition cycle to the electrocatalytic performance transferring I_3^- to I^-, $(PANi\text{-}10wt‰G/Pt)_n$ multilayer CEs with various deposition cycles ($n = 1, 3, 5, 7, 9$) are used to record the CV curves. For all the five CEs, two pairs of oxidation and reduction peaks (Ox_1/Red_1 and Ox_2/Red_2 in Fig. 3a) are well distinguished, which are very similar

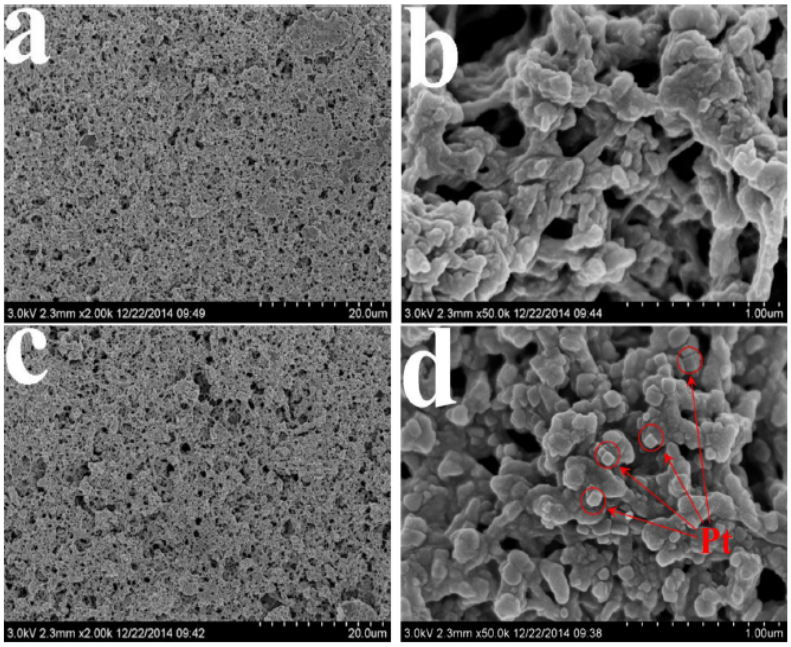

Fig. 2. Top-view SEM photographs of CEs from (a)&(b) $(PANi\text{-}10wt‰G/Pt)_3$ and (c)&(d) $(PANi\text{-}10wt‰G/Pt)_9$.

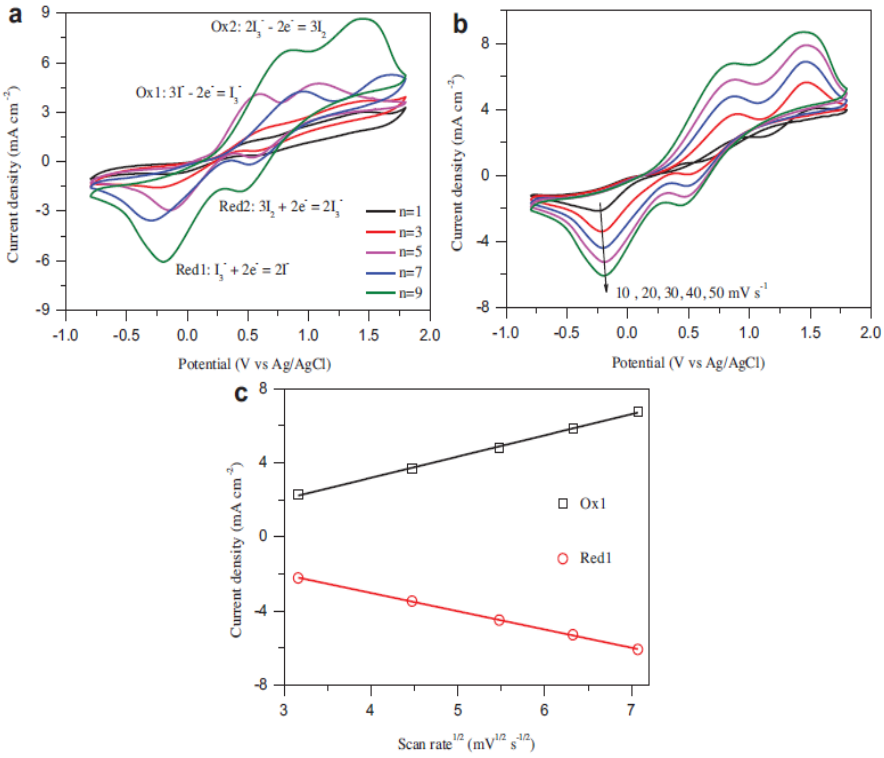

Fig. 3. (a) CV curves of $(PANi\text{-}10wt‰G/Pt)_n$ ($n = 1, 3, 5, 7$, and 9) multilayer CEs toward I^-/I_3^- redox species recorded at a scan rate of 0.05 V s^{-1}, (b) CV curves of $(PANi\text{-}10wt‰G/Pt)_9$ CE for I^-/I_3^- redox species at varied scan rates, and (c) the linearly relationship between peak current density and square root of scan rates.

to those of Pt CE [22]. Considering the task of CE is to collect electrons from external circuit to the multilayer and reduce I_3^- to I^- [5], the characteristics of Red_1 are significant to evaluate the catalytic activity of the multi-interfacial CEs. Generally, a larger peak current intensity (J_{Red1} or J_{Ox1}) and a small E_{pp} refer to a higher electrocatalytic activity. It is noteworthy to mention that there is an increasing trend in electrocatalytic activity toward I_3^- reduction with increased deposition cycle from $n = 1$ to 9. Due to the experimental restriction, in the current work we can not find the most optimal deposition cycle.

From the stacking CV curves of $(PANi\text{-}10\ wt‰G/Pt)_9$ CE at scan rates of 10, 20, 30, 40, and 50 mV s^{-1}, one can find an outward extension of all the peaks (Fig. 3b). By plotting peak current density corresponding to $I_3^- \rightarrow I^-$ and $I^- \rightarrow I_3^-$ versus square root of scan rate, as shown in Fig. 3c, a linear relationship is observed. This result indicates that the redox reaction is a diffusion-controlled mechanism on the surface of multilayer CEs. This result also suggests that the adsorption of redox species is hardly affected by the redox reaction on the $(PANi\text{-}10wt‰\ G/Pt)_9$ CE surface and no specific interaction occurred between I^-/I_3^- and the CE.

The origin of different catalytic activities of the CEs toward I_3^- reduction is further elucidated by EIS measurements using the symmetric dummy cells fabricated with two identical CEs. Nyquist plots in Fig. 4a and the charge-transfer resistance at CE/electrolyte

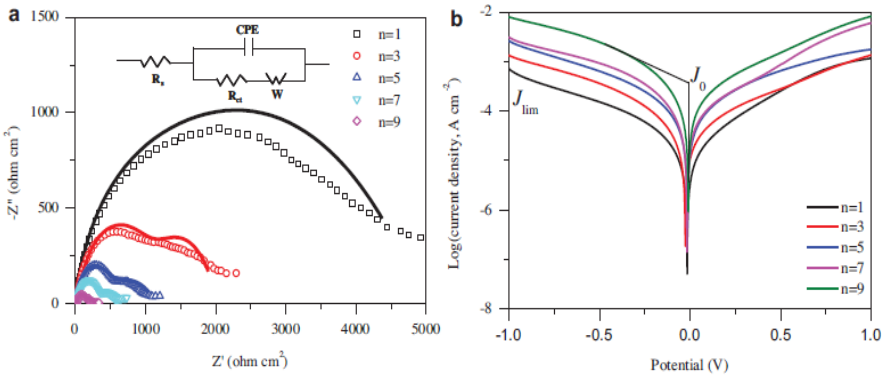

Fig. 4. (a) Nyquist plots and (b) Tafel polarization curves for symmetric dummy cells fabricated with $(PANi\text{-}10wt‰G/Pt)_n$ ($n = 1, 3, 5, 7$, and 9) multilayer CEs. The insert in (a) shows the equivalent circuit.

Table 1
Parameters of charge-transfer resistance (R_{ct}) and electron lifetime (τ_1) obtained by fitting EIS of the symmetric dummy cells using a Z-view software.

Deposition cycles	R_{ct} (Ω cm^2)	f_p (Hz)	τ_1 (μs)
1	4938	276.1	576.7
3	985.9	439.5	362.3
5	290	1386.8	114.8
7	205.5	1618.1	98.4
9	136.3	1945.4	81.9

interface (R_{ct}) values obtained from the equivalent circuit (Insert in Fig. 4a) are summarized in Table 1. In order to better compare the extracted resistances and evaluate the catalytic activity, the same model is utilized in fitting the plots at various bilayers. Although there are deviations for the EIS plots at low bilayers, the fitted curves and measured plots match well for the CEs with high bilayers. This may be attributed to the surface of conductive glass substrate has not been thoroughly covered by multilayers at low bilayer number, therefore leading to an incomplete charge diffusion process at CE/electrolyte interface. The results indicate that there is a significant decrease on R_{ct1} values from 4938 to 136.3 Ω cm^2. The improvement of charge-transfer ability results from the formation of multilayers between PANi-G complex and Pt as well as the multi-interfaces. The rapid reduction of I_3^- to I^- is attributed to the facile electron transfer between PANi and G as well as high catalytic activity of Pt nanoparticles. Since R_{ct1} varies inversely with the electrocatalytic activity, such enormous decrease demonstrates that the (PANi-10wt‰G/Pt)$_9$ has the higher electrocatalytic activity [23,24]. The conclusions for the electrocatalytic activity derived from EIS and CV data are in a good agreement.

Tafel polarization curves in Fig. 4b are recorded to reconfirm the electrocatalytic activity of multilayer CEs on the symmetrical dummy cells used in the EIS experiment. Theoretically, the larger slope in the anode or cathodic branches indicates the higher exchange current density (J_o) on the CEs and better electrocatalytic activity. Apparently, the J_o of multilayer CEs are in the order: (PANi-10wt‰G/Pt)$_9$ > (PANi-10wt‰G/Pt)$_7$ > (PANi-10wt‰G/Pt)$_5$ > (PANi-10wt‰G/Pt)$_3$ > (PANi-10wt‰G/Pt)$_1$, which is consist with EIS experiment because the J_o can be calculated from $J_0 = RT/nFR_{ct1}$ [25], where the R is the gas constant, T is the absolute temperature, n is the number of electrons contributing to the charge transfer at the interface, F is Faraday's constant, and R_{ct1} is charge-transfer resistance obtained from the EIS plots. Additionally, the limiting diffusion current density (J_{lim}) can be as a parameter that depends on the diffusion coefficient of I^-/I_3^- redox couples in the electrolyte. According to the J_{lim}, the diffusion coefficient (D_n) can be calculated through $D_n = lJ_{lim}/2nFC$ [26], where l is the spacer thickness, C is the concentration of I_3^- ions. One can see that the J_{lim} also follows an order of (PANi-10wt‰G/Pt)$_9$ > (PANi-10wt‰G/Pt)$_7$ > (PANi-10wt‰G/Pt)$_5$ > (PANi-10wt‰G/Pt)$_3$ > (PANi-10wt‰G/Pt)$_1$. The enhanced J_0 and D_n for multilayer CE at higher bilayer derive from the increased interface area and rapid charge-transfer between Pt and PANi-G complexes.

Fig. 5a compares the characteristic J-V curves of the DSSCs with (PANi-10wt‰G/Pt)$_n$ multilayer CEs and the parameters from the J-V curves are summarized in Table 2. The DSSC employing multi-interfacial (PANi-10wt‰G/Pt)$_9$ electrode yields the highest power conversion efficiency of η = 7.45 % (J_{sc} = 15.22 mA cm^{-2}, V_{oc} = 0.725 V, and FF = 0.675). This might be attributed to the elevated interface area and the rapid charge-transfer within the CE and the enhanced electrocatalytic activity utilizing the Pt as the negatively charged

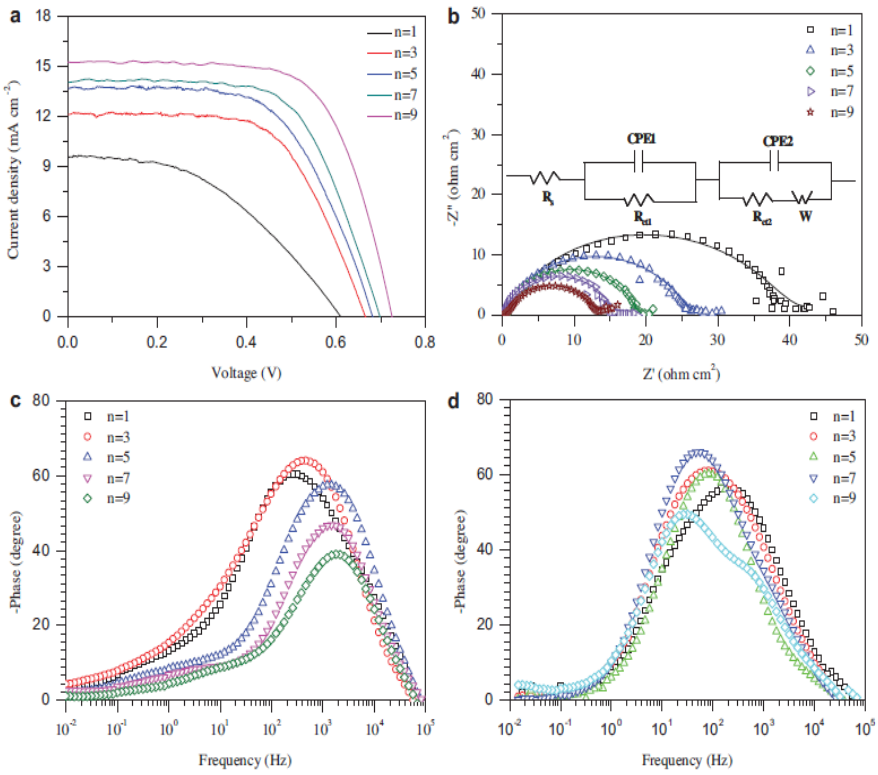

Fig. 5. (a) J-V characteristics of the DSSCs under AM1.5 irradiation and (b) Nyquist plots for DSSCs from various (PANi-10wt‰G/Pt)$_n$ (n = 1, 3, 5, 7, and 9) CEs. Bode phase plots of (c) symmetric dummy cells and (d) DSSCs with various CEs. The insert shows an equivalent circuit.

Table 2
Photovoltaic parameters of the DSSCs. J_{sc}: short-circuit current density; V_{oc}: open-circuit voltage, *FF*: fill factor; η: power conversion efficiency.

Deposition cycle	V_{oc} (V)	J_{sc} (mA cm^{-2})	η (%)	*FF*	R_{ct2} (Ω cm^2)	f_p(Hz)	τ_2 (ms)
1	0.610	9.58	2.58	0.441	23.83	214.8	0.74
3	0.665	12.09	4.99	0.621	21.36	85.9	1.85
5	0.681	13.67	5.63	0.605	16.52	81.7	1.95
7	0.697	14.23	6.29	0.634	10.96	50.6	3.15
9	0.725	15.22	7.45	0.675	10.57	26.2	6.08

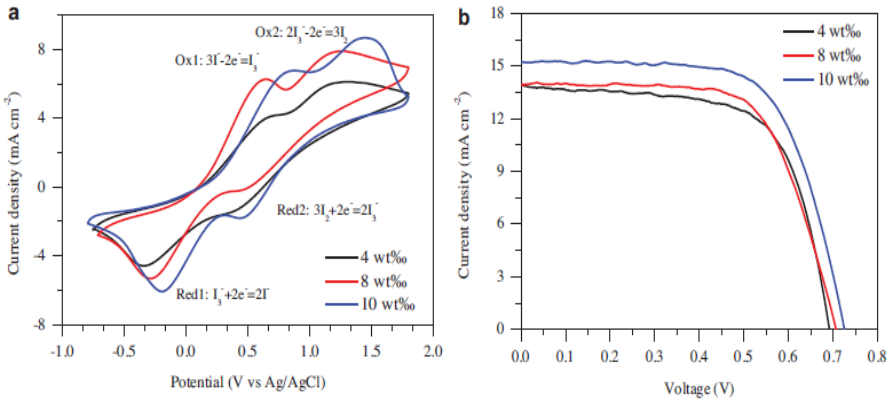

Fig. 6. (a) CV curves of $(PANi\text{-}G/Pt)_9$ multilayer CEs toward I^-/I_3^- redox species recorded at a scan rate of 0.05 V s^{-1}, and (b) *J-V* characteristics of DSSCs under AM1.5. The G dosage is 4, 8, 10 wt‰.

material to fabricate the multilayer CE. This conclusion can be supported by the EIS and Tafel characterizations. The lifetimes of electrons participating in the I_3^- reduction reaction (τ_1) can be represented as $\tau_1 = 1/2\pi f_p$ [27], where f_p is the peak frequency in the Bode spectra, and the parameters are summarized in Table 1. A lower τ_1 value implies the electrons on a CE can rapidly participate in the I_3^- reduction and therefore has a higher electrocatalytic activity. Meanwhile, a larger τ_2 value and smaller charge-transfer resistance at the TiO_2/dye/electrolyte interface (R_{ct2}), as shown in Fig. 5c,d and Table 2 means that the enhanced electrocatalytic activity has an accelerating effect for dye excitation, electron generation, and therefore electron flow from the excited dye to the conduction band of the TiO_2 [28]. After performing a comprehensive analysis of the DSSCs, it can be concluded that the photovoltaic performance is in agreement with the EIS and Tafel polarization results.

With an aim to further study the effect of bonding sites between PANi and G as mentioned above, CV curves of the resultant different $(PANi\text{-}G/Pt)_9$ multilayers CEs at G dosages of 4, 8, and 10 wt‰ are also scanned in liquid electrolyte to determine their electrocatalytic performances. As shown in Fig. 6a, $(PANi\text{-}G/Pt)_9$ multilayers CEs at a higher graphene dosage has an enhanced catalytic activity toward I_3^- reduction. It is expected that more bonding sites between PANi and G have been formed when 10wt‰ G is utilized to synthesis the PANi-G complexes [16]. The results indicate that the increased bonding sites can accelerate the charge transfer, which is consistent with the previous studies [29,30]. The DSSC using $(PANi\text{-}10wt‰G/Pt)_9$ multilayer CE exhibits an efficiency of 7.45% in comparison with 6.48% for $(PANi\text{-}4wt‰G/Pt)_9$, and 6.65% for $(PANi\text{-}8wt‰G/)_9$ (Fig. 6b). Although the higher G dosages gives more bonding sites for rapid charge transfer and higher power conversion efficiency, black precipitates can be observed in the as-synthesized aniline-G solution at further high G dosage because the dissolution of G in aniline monomer has reached its saturation.

4. Conclusion

In summary, we have fabricated the multi-interfacial $(PANi\text{-}G/Pt)_n$ CEs by layer-by-layer self-assembly strategy for DSSCs. The integration of Pt with PANi-G complex can provide enormous interfaces for I_3^- reduction. Moreover, the covalent-bonding sites between PANi and G also have acceleration effect on charge transfer and catalytic activity. An efficiency of 7.45% has been recorded on the solar cell with $(PANi\text{-}10wt‰G/Pt)_9$ multilayer electrode by optimizing G dosage and bilayer number. This research presented here provides a strategy to assemble CEs with cost-effectiveness, easy technique and environment friendly. The profound advantages in easy synthesis, versatile electrical and photovoltaic performances promise the multilayer films to be excellent CE materials in DSSCs.

Acknowledgements

The authors would like to acknowledge financial supports from National Natural Science Foundation of China (U1037604), Fundamental Research Funds for the Central Universities (201313001, 201312005), Shandong Province Outstanding Youth Scientist Foundation Plan (BS2013CL015), Shandong Provincial Natural Science Foundation (ZR2011BQ017), and Research Project for the Application Foundation in Qingdao (13-4-198-jch).

References

[1] B. O'Regan, M. Grätzel, Nature 353 (1991) 737–740.
[2] U. Bach, D. Lupo, P. Comte, J.E. Moser, F. Weissortel, J. Salbeck, M. Grätzel, Nature 395 (1998) 583–585.
[3] D. Kim, A. Ghicov, S.P. Albu, P. Schmuki, J. Am. Chem. Soc. 130 (2008) 16454–16455.

[4] S. Mathew, A. Yella, P. Gao, R. Humphry, B. Curchod, N. Ashari-Astani, I. Tavernelli, U. Rothlisberger, M. Nazeeruddin, M. Grätzel, Nature Chemistry 6 (2014) 242–247.
[5] J.L. Duan, Q.W. Tang, B.L. He, L.M. Yu, Electrochim. Acta 137 (2014) 175–182.
[6] A. Kojima, K. Teshima, Y. Shirai, T. Miyasaka, J. Am. Chem. Soc. 131 (2009) 6050–6051.
[7] T.W. Hamann, R.A. Jensen, A.B.F. Martinson, H.V. Ryswyk, J.T. Hupp, Energy Environ. Sci. 1 (2008) 66–78.
[8] H.Y. Cai, Q.W. Tang, B.L. He, P.J. Li, J. Power Sources 258 (2014) 117–121.
[9] B.L. He, X. Meng, Q.W. Tang, P.J. Li, S.S. Yuan, P.Z. Yang, J. Power Sources 260 (2014) 180–185.
[10] J.W. Wan, G.J. Fang, H.J. Yin, X.F. Liu, D. Liu, M.T. Zhao, W.J. Ke, H. Tao, Z.Y. Tang, Adv. Mater. 26 (2014) 8101–8106.
[11] Y.Y. Duan, Q.W. Tang, J. Liu, B.L. He, L.M. Yu, Angew. Chem. Int. Ed. 53 (2014) 14569–14574.
[12] J. Liu, Q.W. Tang, B.L. He, J. Power Sources 268 (2014) 56–62.
[13] K. Suzuki, M. Yamaguchi, M. Kumagai, S. Yanagida, Chem. Lett. 32 (2003) 28–29.
[14] G.Q. Wang, W. Xing, S.P. Zhuo, J. Power Sources 194 (2009) 568–573.
[15] Q.D. Tai, B.L. Chen, F. Guo, S. Xu, H. Hu, B. Sebo, X.Z. Zhao, ACS Nano 5 (2011) 3795–3799.
[16] J.J. He, N.W. Duffy, J.M. Pringle, Y.B. Cheng, Electrochim. Acta 137 (2014) 34–40.
[17] D. Li, J.X. Huang, R.B. Kaner, Acc. Chem. Res. 42 (2008) 135–145.
[18] M. Wang, Q.W. Tang, H.Y. Chen, B.L. He, Electrochim. Acta 125 (2014) 510–515.
[19] H.H. Zhang, B.L. He, Q.W. Tang, L.M. Yu, J. Power Sources 275 (2015) 489–497.
[20] M. Wang, Q.W. Tang, P.P. Xu, B.L. He, L. Lin, H.Y. Chen, Electrochim. Acta 137 (2014) 175–182.
[21] T. Teranishi, M. Hosoe, T. Tanaka, M. Miyake, J. Phys. Chem. B 103 (1999) 3818–3827.
[22] T. Cassagneau, J.H. Fendler, J. Phys. Chem. B 103 (1999) 1789–1793.
[23] Q.W. Tang, J.H. Wu, X.M. Sun, Q.H. Li, J.M. Lin, L.Q. Fan, Polymer 50 (2009) 752–755.
[24] Y.D. Wang, C.Y. Zhao, M.X. Wu, W. Liu, T.L. Ma, Electrochim. Acta 105 (2013) 671–676.
[25] G.Q. Wang, W. Xing, S.P. Zhuo, Electrochim. Acta 92 (2013) 269–275.
[26] B. Lee, D.B. Buchholz, R.P.H. Chang, Energy Environ. Sci. 5 (2012) 6941–6952.
[27] M.X. Wu, X. Lin, Y.D. Wang, L. Wang, W. Guo, D.D. Qi, X.J. Peng, A. Hagfeldt, M. Grätzel, T.L. Ma, J. Am. Chem. Soc. 134 (2012) 3419–3428.
[28] M.K. Wang, A.M. Anghel, B. Marsan, N.C. Ha, N. Pootrakulchote, S.M. Zakeeruddin, M. Grätzel, J. Am. Chem. Soc. 131 (2009) 15976–15977.
[29] J. Yoon, M. Jin, M. Lee, Adv. Mater. 23 (2011) 3974–3978.
[30] X.X. Chen, Q.W. Tang, B.L. He, L. Lin, L.M. Yu, Angew. Chem. Int. Ed. 53 (2014) 10799–10803.

Electrochimica Acta 158 (2015) 397–402

Contents lists available at ScienceDirect

Electrochimica Acta

journal homepage: www.elsevier.com/locate/electacta

Cost–effective alloy counter electrodes as a new avenue for high–efficiency dye–sensitized solar cells

Benlin He [a,b], Qunwei Tang [a,b,*], Liangmin Yu [a,*], Peizhi Yang [c]

[a] Key Laboratory of Marine Chemistry Theory and Technology, Ministry of Education, Ocean University of China, Qingdao 266100, PR China
[b] Institute of Materials Science and Engineering, Ocean University of China, Qingdao 266100, PR China
[c] Key Laboratory of Advanced Technique & Preparation for Renewable Energy Materials, Ministry of Education, Yunnan Normal University, Kunming 650092, PR China

ARTICLE INFO

Article history:
Received 22 October 2014
Received in revised form 19 January 2015
Accepted 30 January 2015
Available online 31 January 2015

Keywords:
Dye–sensitized solar cell
Counter electrode
Binary alloy
Electrochemical deposition

ABSTRACT

Pursuit of cost–effective and efficient counter electrodes (CEs) has been a persistent objective for dye–sensitized solar cells (DSSCs). Aiming at reducing fabrication cost without sacrificing power conversion efficiency of DSSCs, here we report the successful design of binary Pt–Ni alloy CEs by a simple cyclic voltammetry technique. Due to the rapid charge transfer ability and electrocatalytic activity, the power conversion efficiency of the DSSC employing binary $PtNi_{0.75}$ alloy CE has been elevated to 8.59% in comparison with 6.98% from Pt–based solar cell. The impressive results along with simple synthesis highlight the potential application of low–Pt alloys in robust DSSCs.

1. Introduction

Fossil fuels such as coal, oil, and natural gas have occupied energy market for hundreds of years. However, the combustion of these non–renewable fuels can release sulfides, carbides and dusts which will damage ecology and pollute environment. By addressing these issues, it is a prerequisite to develop renewable, green, and environment–friendly energy resources to resolve energy and environment crisis [1]. Among various energy candidates, dye–sensitized solar cells (DSSCs) [2–5], electrochemical devices converting solar energy into electrical power honored by a high efficiency and no environmental impact, are promising solutions to global energy and environmental problems because of clean, high efficiency, good durability, and relatively simple fabrication. Since the first prototype reported by Grätzel in 1991 [6], DSSCs have attracted growing interests and great achievements have been made. However, it is still premature for their commercialization. Until now, the most limiting factor in the development of commercial DSSCs has been their cost [7,8]. The historically high prices for Pt feedstock, a traditional counter electrode (CE) material, have meant that a cell could not be fabricated at a cost low enough to compete with conventional silicon solar cells. The task of a CE is to collect electrons from external circuit and to reduce triiodide (I_3^-) into iodide (I^-), therefore, an efficient CE electrocatalyst should display good charge–transfer ability and excellent electrocatalytic activity. Other candidates such as carbonaceous materials [9,10], conducting polymers [11,12], or their composites [13–15] present either modest electrocatalysis, unsatisfactory electron–conduction, or large interfacial resistance. More importantly, such CEs have a fast attenuation in electrocatalytic activity and long–term stability [16]. Therefore, it is a prerequisite to develop cost–effective but stable CEs before DSSCs are becoming a commercial reality.

Alloy materials have established themselves as the alternative electrocatalysts for fuel cell applications in the past two decades [17,18]. Aiming to increase the catalytic activity of the electrode kinetics and to lower the cost of electrocatalysts, it has been shown that alloying of Pt metal with transition metals could be an efficient route to meet the cell requirements. However, the employment of Pt–free or low–Pt alloys in DSSCs is still at preliminary stage. Previous studies in our group have revealed that binary M–Pt (where M = Co, Ru) alloys have exceptional electrocatalysis toward I^-/I_3^- redox couples [19,20]. However, Co species in Co–Pt alloys are easily oxided and Ru sources are relative price high. In searching for other robust M–Pt alloys, here we report the synthesis and characterization of a new class binary Ni–Pt alloy CEs. The resultant Pt–Ni alloys show supercatalytic behavior toward I^-/I_3^- redox couples, allowing the rapid interconversion

* Corresponding authors. Tel.: +86 532 66781690; fax: +86 532 66782533.
E-mail addresses: tangqunwei@ouc.edu.cn (Q. Tang), yuyan@ouc.edu.cn (L. Yu).

http://dx.doi.org/10.1016/j.electacta.2015.01.194
0013-4686/

between $I_3^- \rightarrow I^-$. The Pt–Ni alloy CEs are expected to significantly enhance the electron conduction, charge-transfer ability, and therefore power conversion efficiency of the DSSCs.

2. Experimental

2.1. Preparation of binary Pt–Ni alloy CEs

The feasibility of this strategy was confirmed by a cyclic voltammetry (CV) method: A cleaned FTO glass substrate was used as a working electrode, and the CV curves were recorded from –0.4 to +0.3 V and back to –0.4 V for 10 cycles. Before the measurement, the supporting electrolyte consisting of 2 mM H_2PtC1_6, 1 mM of $Ni(NO_3)_2$, and 5 mM of HCl aqueous solution was degassed using nitrogen for 10 min.

2.2. Assembly of DSSCs

A layer of TiO_2 nanocrystal anode film with a thickness of 10 μm was prepared by a sol-hydrothermal method [21] and a layer of TiO_2 nanocrystal anode film with a thickness of 10 μm and an active area of 0.25 cm^2 was prepared by coating TiO_2 colloid onto conducting glass using a doctor blade technique, followed by sintering in air at 450 °C for 30 min. Resultant anodes were further sensitized by immersing into a 0.50 mM ethanol solution of N719 dye ([cis–di(thiocyanato) –N,N' –bis(2,2' –bipyridyl–4–carboxylic acid)–4–tetrabutylammonium carboxylate]). The DSSC was fabricated by sandwiching redox electrolyte between dye–sensitized TiO_2 anode and FTO supported Pt–Ni alloy CEs. A redox electrolyte consisted of 100 mM of tetraethylammonium iodide, 100 mM of tetramethylammonium iodide, 100 mM of tetrabutylammonium iodide, 100 mM of NaI, 100 mM of KI, 100 mM of LiI, 50 mM of I_2, and 500 mM of 4–tert–butyl–pyridine in 50 ml acetonitrile.

2.3. Electrochemical characterizations

The electrochemical performances were recorded on a conventional CHI660E setup comprising an Ag/AgCl reference electrode, a CE of platinum sheet, and a working electrode of FTO glass supported Pt–Ni alloy. The CV curves were recorded from –1.0 to +1.4 V and back to –1.0 V. Before the measurement, the supporting electrolyte consisting of 50 mM M LiI, 10 mM I_2, and 500 mM $LiClO_4$ in acetonitrile was degassed using nitrogen for 10 min. Electrochemical impedance spectroscopy (EIS) measurements were also carried out on the CHI660E Electrochemical Workstation in a frequency range of 0.01 Hz ~ 10^6 kHz and an ac amplitude of 5 mV at room temperature. The resultant impedance spectra were analyzed using the Z–view software. Tafel polarization curves were recorded on the same Workstation by assembling symmetric cell consisting of Pt–Ni alloy CE|redox electrolyte|Ni–Pt alloy CE.

2.4. Photovoltaic measurements

The photocurrent–voltage (*J–V*) curves of the assembled DSSCs were recorded on an Electrochemical Workstation (CHI600E) under irradiation of a simulated solar light from a 100 W xenon–mercury arc lamp (CHF–XM–500 W, Beijing Trusttech Co., Ltd) in an ambient atmosphere. The incident light intensity was calibrated using a FZ–A type radiometer from Beijing Normal University Photoelectric Instrument Factory to control it at 100 mW cm^{-2} (AM1.5 calibrated by a standard silicon solar cell). Each DSSC device was measured at least five times to eliminate experimental error and a compromise *J–V* curve was employed.

2.5. Other characterizations

The morphologies of the Pt–Ni alloy CE were observed with a scanning electron microscope (SEM, S4800). The XRD data were

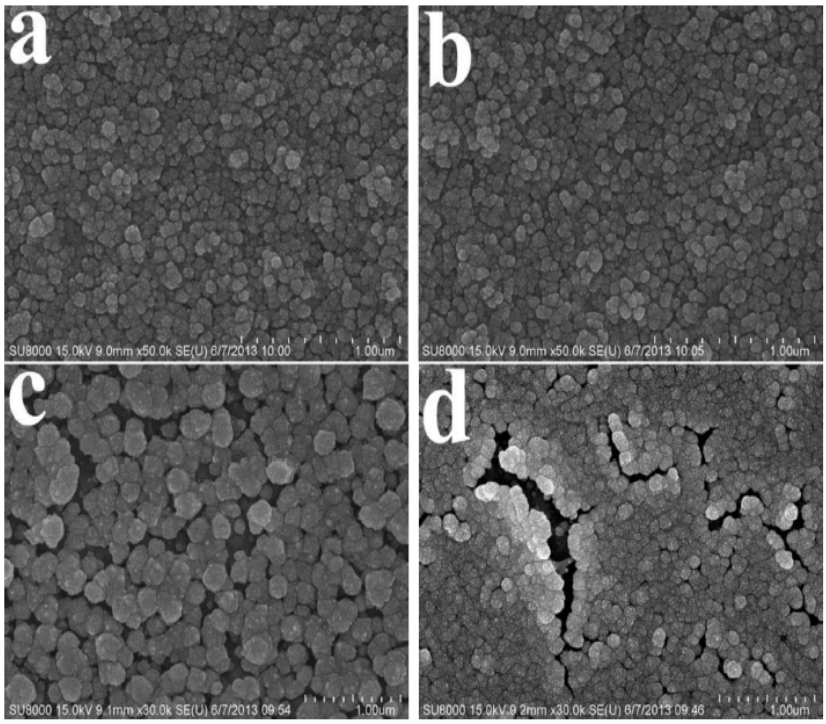

Fig. 1. Top–view SEM photographs of (a) $PtNi_{0.25}$, (b) $PtNi_{0.50}$, (c) $PtNi_{0.75}$, and (d) PtNi alloy CEs.

collected in a scan mode with a scanning speed of 10 ° min^{-1} in the 2θ range between 20 and 80°. XPS experiment was carried out on a RBD upgraded PHI–5000C ESCA system (Perkin Elmer) with Mg Kα radiation ($h\nu$ = 1253.6 eV).

3. Results and discussion

SEM photographs in Fig. 1 suggest a high surface coverage and loading of alloys on FTO glass. Deep examination gives homogeneously spherical aggregations. However, the compact structures in $PtNi_{0.25}$ and $PtNi_{0.50}$ alloy CEs can hinder the diffusion of I^-/I_3^- redox couples at CE/electrolyte interface. By optimizing stoichiometry of Pt and Ni sources, a loose structure with an average aggregation size of ~200 nm is obtained for $PtNi_{0.75}$ alloy CE, providing channels for I^-/I_3^- species across the alloy layer [22]. At a high Ni dosage, such as PtNi alloy, the cracks and large interfacial resistance may limit electron migration from FTO back to alloy layer.

Energy–dispersive X–ray spectra (EDS), as shown in Fig. 2a, demonstrate that Pt and Ni elements as well as partial elements from FTO glass are detected, indicating a successful deposition of Pt and Ni on FTO substrate. The measured atomic ratios by EDS for $PtNi_{0.25}$, $PtNi_{0.50}$, $PtNi_{0.75}$, and PtNi alloys are 1.000:0.266, 1.000:0.518; 1.000:0.752, and 1.000:1.083, respectively. The measured atomic ratios are relatively close to their stoichiometries, therefore the chemical formulae of the alloy CEs can be expressed according to the stoichiometric ratios [23]. XPS characterization is carried out to determine the chemical structure and composition of $PtNi_{0.75}$ alloy. As shown in Fig. 2b and Fig. 2c, the peaks for Pt4f and Ni2p are centered at 71.28 eV ($Pt4f_{7/2}$), 71.45 eV ($Pt4f_{5/2}$), and 852.5 eV ($Ni2p_{3/2}$), confirming the metallic nature of as–synthesized $PtNi_{0.75}$ alloy [24]. It has been mentioned that the alloying of transition metals can favor the electronic perturbation of other metals [25] and therefore accelerate the electrocatalytic activity of the alloys for their electrocatalyst applications. The binary alloy CEs synthesized by a CV method are subjected to XRD measurements. As shown in Fig. 2d, XRD results indicate that the alloy CEs consist of alloy materials at 2θ = 39.96° and FTO glass substrate marked with (*). Moreover, unalloyed Pt is also detected because of the appearance of diffraction peak at 2θ = 46.24°.

A golden rule in determining an efficient CE is to evaluate its electrocatalytic activity toward electrolyte [26]. As displayed in Fig. 3a, the CV peak shapes and positions of alloy CEs are similar to that of pristine Pt electrode, suggesting that the alloys have a similar electrocatalytic function to Pt CE. However, the peak current densities of CV curves have been elevated by alloying Pt with Ni in comparison with pristine Pt electrode. Considering the task of a CE is to collect electrons from external circuit and to reduce I_3^- to I^-, therefore, Red1 peak can be employed to assess the catalytic activity of alloy CEs. The ratio of $J_{ox1}/|J_{red1}|$ is a parameter to elevate the reversibility of the redox reaction toward I^-/I_3^- species [27]. The obtained values for pristine Pt, $PtNi_{0.25}$, $PtNi_{0.50}$, $PtNi_{0.75}$, and PtNi are 1.155, 0.985, 0.990, 1.007, and 0.966,

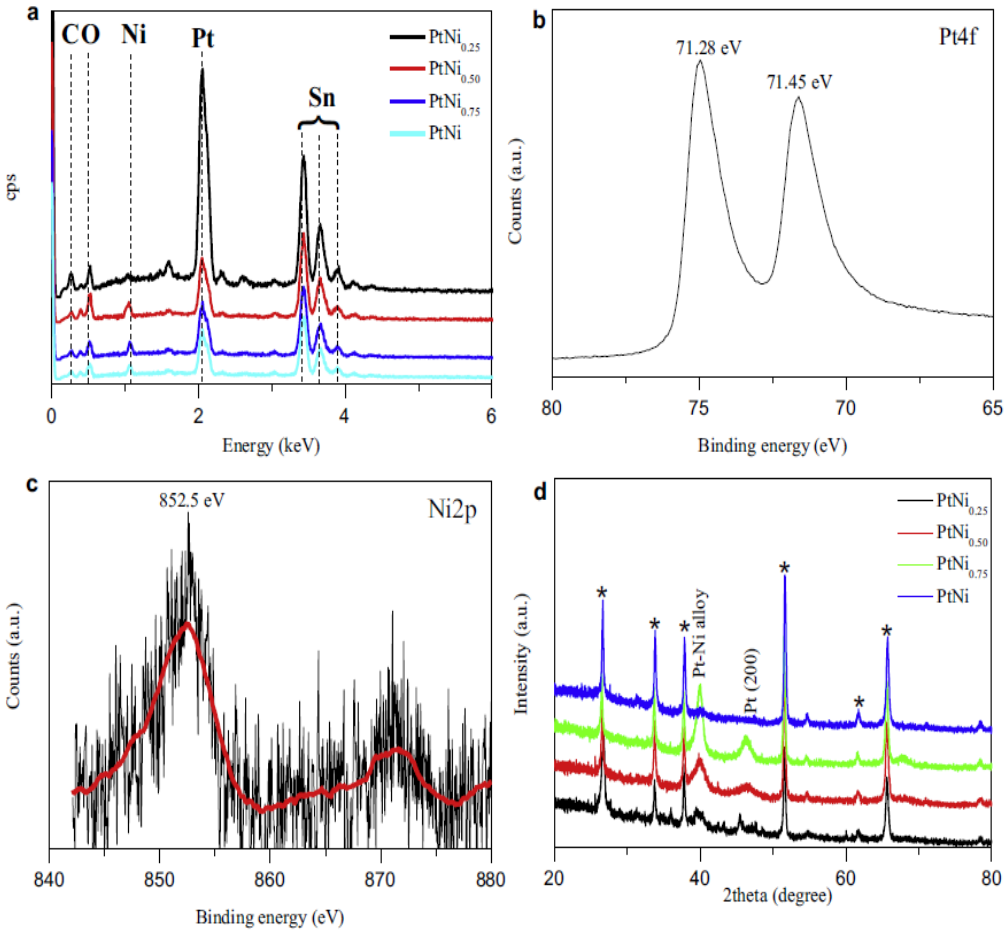

Fig. 2. (a) EDS of Pt–Ni alloy CEs, XPS spectra of (b) Pt4f and (c) Ni2p in $PtNi_{0.75}$ alloy, and (c) XRD patterns of FTO glass supported alloy CEs.

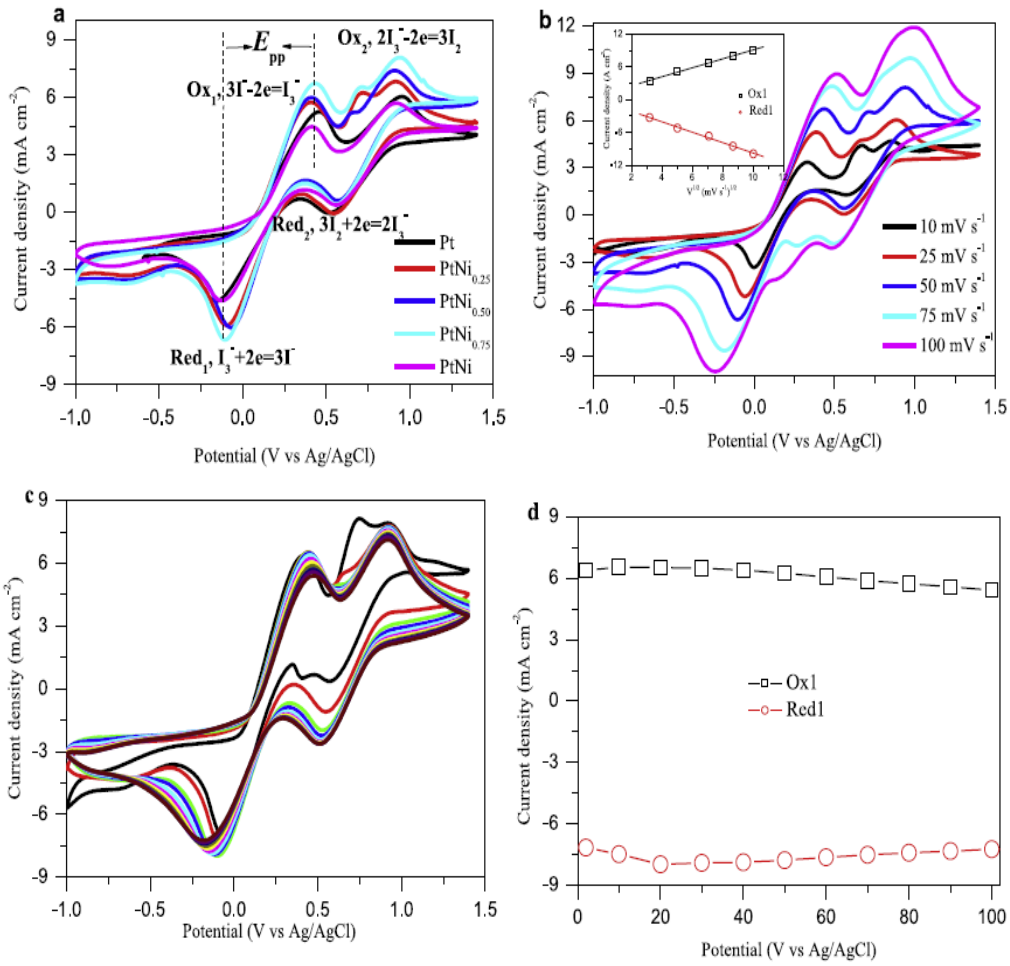

Fig. 3. (a) CV curves of various CEs for I^-/I_3^- redox species recorded at a scan rate of 50 mV s^{-1}. (b) CV curves of $PtNi_{0.75}$ alloy CE for I^-/I_3^- redox species at different scan rates. The insert gives the plots of peak current density versus scan rate. (c) A total of 100 consecutive CVs for the I^-/I_3^- system using the $PtNi_{0.75}$ alloy CE at a scan rate of 50 mV s^{-1}. (d) Relationship between the cycle time and the redox peak current for the $PtNi_{0.75}$ alloy CE.

respectively. The high peak current density, low peak–to–peak separation (E_{pp}, 0.528 V for $PtNi_{0.75}$ and 0.632 V for Pt) [28], and good reversibility demonstrate the alloying of Pt with Ni can markedly enhance the reversibility of $I_3^- \leftrightarrow I^-$ reaction, and $PtNi_{0.75}$ alloy has superiority of catalyzing liquid electrolyte containing I^-/I_3^- redox couples. From the stacking CV curves of $PtNi_{0.75}$ alloy CE at different scan rates, one can find an outward extension of redox peaks (Fig. 3b). By plotting peak current density corresponding to $I_3^- \leftrightarrow I^-$ versus square root of scan rate, linear relationships are observed, indicating a diffusion controlled mechanism of redox reaction on alloy CE [29]. A total of 100 consecutive CV curves for the I^-/I_3^- system using the $PtNi_{0.75}$ alloy CE at a scan rate of 50 mV s^{-1} are shown in Fig. 3c, no obvious attenuation of peak current densities in Ox1/Red1 means the alloy CE is relatively stable for reducing I_3^- ions (Fig. 3d).

Nyquist EIS plots of the symmetric dummy cells by two identical CEs are employed to demonstrate the intrinsic interfacial charge–transfer kinetics at CE/electrolyte interface. As presented in Fig. 4a, the R_{ct} value of the $PtNi_{0.75}$ alloy CE is 3.03 Ω cm^2, smaller than 5.75 Ω cm^2 for pristine Pt electrode (Table 1). The R_{ct} of CEs follows an order of $PtNi_{0.75} < PtNi_{0.50} < PtNi_{0.25} < Pt < PtNi$. The sequence is consistent with the results of CV curves. Enhanced electrocatalytic kinetics and charge–transfer ability could accelerate dye regeneration and therefore elevate the J_{sc} of cells. Due to the participation of electrons in I_3^- reduction reaction, therefore the electron lifetime (τ) at CE/electrolyte interface can be calculated from $\tau = 1/(2\pi f_p)$ and utilized to assess the reduction reaction kinetics [30], where f_{max} is the maximum frequency of the mid–frequency peak in the Bode phase plots (Fig. 4b). The τ at CE/electrolyte interface has an order of $PtNi_{0.75}$ (42 μs) < $PtNi_{0.50}$ (50 μs) < $PtNi_{0.25}$ (61 μs) < Pt (74 μs) < PtNi (90 μs). A low τ value refers to a rapid reduction reaction occurred at CE/electrolyte interface. Moreover, the exchange current density (J_0, the slope for anodic or cathodic branches) and limiting diffusion current density (J_{lim}, the intersection of cathodic branch with *Y*-axis), in the Tafel polarization curves can also be uitilized to reconfirm the catalytic activity of CEs. As shown in Fig. 4c, both J_0 and J_{lim} have an order of $PtNi_{0.75} > PtNi_{0.50} > PtNi_{0.25} > Pt > PtNi$. From equations $J_0 = RT/nFR_{ct}$ [31] $J_{lim} = 2nFCD_n/l$ [32], and $J_{red1} = Kn^{1.5}ACD_n^{0.5}v^{0.5}$ [33] (*R* is the gas constant, *F* is Faraday's constant, *n* is number of electrons participating in I_3^- reduction reaction, *l* is the distance between electrodes in a symmetric dummy cell, *C* is concentration of I_3^- ions), one can conclude that the results from Tafel polarization curves, EIS plots, and CV curves are in good agreement. Fig. 4d compares characteristic *J*–*V* curves of the DSSCs with pristine Pt and alloy CEs. The solar cell from $PtNi_{0.75}$ electrode yields a maximum η of 8.59% (V_{oc} = 0.716 V, J_{sc} = 17.50 mA cm^{-2}, *FF* = 68.6%), which are much higher than the photovoltaic parameters with pristine Pt CE and those in literatures [34,35], The solar cell from $PtNi_{0.75}$ electrode. This may be attributed to a fact that the rapid

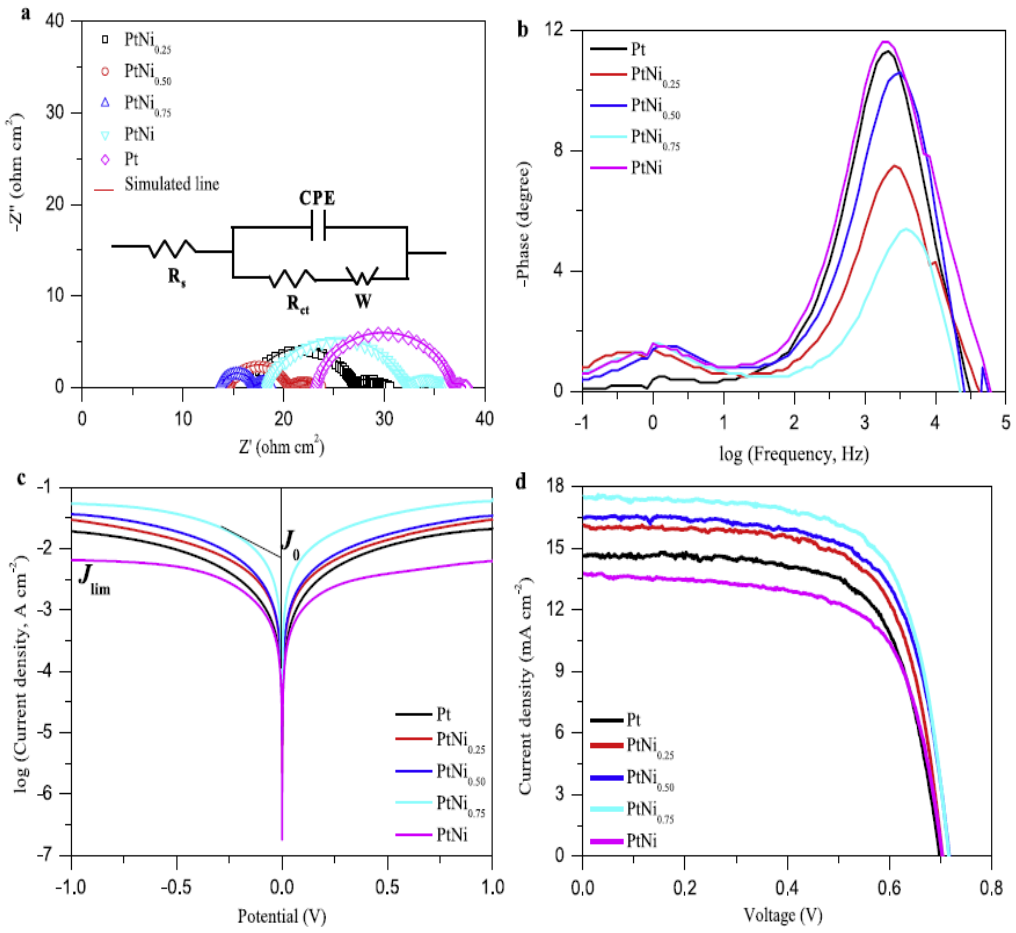

Fig. 4. (a) Nyquist and (b) Bode EIS plots and (c) Tafel polarization curves for symmetric dummy cells fabricated two identical CEs. (d) Characteristic *J–V* curves for the DSSCs with various CEs. The insert gives an equivalent circuit for the symmetric dummy cells.

interconvertion between I_3^- and I^- can accelerate electron generation from N719 dye and therefore elevate the electron flow from excited dye to conduction band of TiO_2, therefore the electron density on TiO_2 conduction band is markedly enhanced. The recorded η from $PtNi_{0.75}$ alloy is impressive for the DSSCs with low–Pt CEs.

Critical requirements of the engines and vehicles drived by solar panels are high power conversion efficiency, cost–effectiveness, fast start–up, multiple start capability, and operational stability. The efficiency and expenses greatly depend on the design of CEs, in which Pt–free or low–Pt materials are always required. However, a robust catalyst in CE is desirable for fast start–up, multiple start, and stability [36]. As shown in Fig. 5a, the photocurrent of the cell device employing $PtNi_{0.75}$ alloy electrode has an abrupt increase at full irradiation. No delay in time is detected in starting the cell, this observation supports a fact that the alloy CEs are robust in catalyzing I^-/I_3^- redox couples. After five start–stop cycles, there is no failure in photocurrent density, however, the current density from Pt based solar cell has an apparent decrease in the first two cycles. These results suggest that $PtNi_{0.75}$ alloy is a preferred CE material for efficient DSSCs. Additionally, the relationship between photocurrent density and time demonstrates cell stability on prolonged exposure to light irradiation ($100\,mW\,cm^{-2}$). As displayed in Fig. 5b, the photocurrent densities for DSSCs with $PtNi_{0.75}$ and Pt decrease by 6.75% and 14.69% over 5 h, respectively. In comparison with the solar cell with Pt electrode [37], the DSSC employing $PtNi_{0.75}$ alloy electrode displays enhanced stability. In order to explore potential mechanism for enhanced catalytic activity and stability, the Gibbs energy of the possible dissolving reaction of $PtNi_{0.75}$ alloy is calculated [38]. The values of Gibbs free

Table 1
Comparison of photovoltaic and electrochemical parameters as well as electron lifetime and transparency for the DSSCs. η: power conversion efficiency; V_{oc}: open–circuit voltage; J_{sc}: short–circuit current density; *FF*: fill factor; R_{ct}: charge–transfer resistance; *W*: Nernst diffusion resistance corresponding to I^-/I_3^- couples; τ: electron lifetime at CE/electrolyte interface.

CEs	η (%)	V_{oc} (V)	J_{sc} ($mAcm^{-2}$)	*FF* (%)	R_{ct} ($\Omega\,cm^2$)	*W* ($\Omega\,cm^2$)	τ (μs)
Pristine Pt	6.98	0.698	14.63	68.4	13.00	5.75	74
$PtNi_{0.25}$	7.70	0.703	16.07	68.2	9.18	3.88	61
$PtNi_{0.50}$	8.05	0.717	16.45	68.3	5.42	2.92	50
$PtNi_{0.75}$	8.59	0.716	17.50	68.6	3.03	1.85	42
PtNi	6.46	0.703	13.75	66.8	13.26	8.47	90

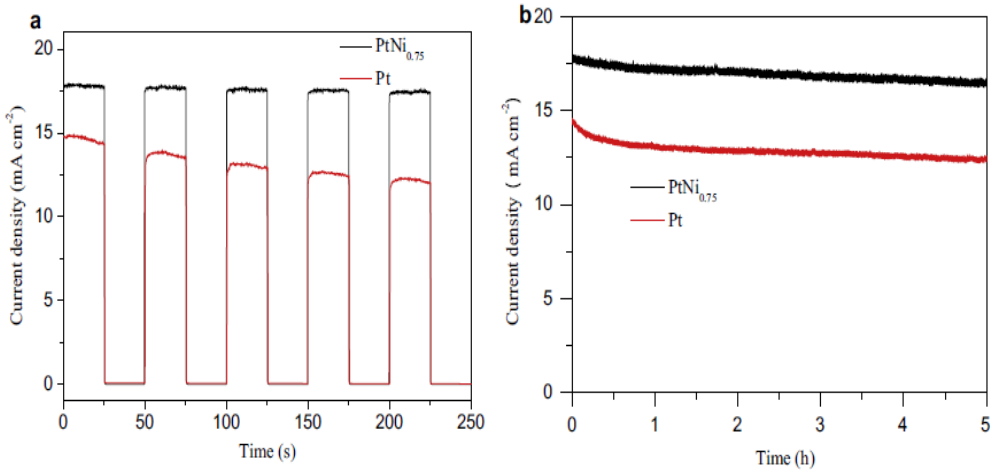

Fig. 5. (a) Start–stop switches and (b) photocurrent stabilities of the DSSCs employing $PtNi_{0.75}$ alloy and Pt electrodes. The on–off plots were achieved by alternatively irradiating (100 mW cm^{-2}) and darkening (0 mW cm^{-2}) the DSSC devices at an interval of 25 s and 0 V, whereas the photocurrent stabilities were carried out under sustained irradiation of 100 mW cm^{-2}.

energy ($\Delta_r G_m$) were calculated for the possible reactions between Ni or Pt and triiodide species [Reaction 1: Pt (s) + $2I_3^-$ (aq) = PtI_4 (s) + $2I^-$ (aq); Reaction 2: Ni (s) + I_3^- (aq) = NiI_2 (s) + I^- (aq)]. The $\Delta_r G_m$ values for reaction 1 and reaction 2 are −45.9 and −76.4 kJ mol^{-1}, respectively. In this fashion, the reaction between Ni species and triiodides is easier. The alloying of Ni with Pt can form a competed reaction between Ni and Pt, therefore protecting the high catalytic activity of Pt species by sacrificing Ni species. The presented results demonstrate the superiority of $PtNi_{0.75}$ alloy CE than pristine Pt electrode for DSSC application.

4. Conclusions

In summary, binary Pt–Ni alloys have been fabricated by an electrochemical codeposition strategy free of any surfactant or template and employed as CE materials in DSSCs. It is demonstrated that $PtNi_{0.75}$ alloy CE has an optimal charge–transfer ability and electrocatalytic activity toward I_3^- reduction. The DSSC employing $PtNi_{0.75}$ alloy CE exhibits impressive power conversion efficiency of 8.59% in comparison with 6.98% from pristine Pt CE based device. The research presented here is far from being optimized but these profound advantages along with cost–effectiveness, mild synthesis and scalable materials promise the binary Pt–Ni alloy CEs to be strong candidates in robust DSSCs.

Acknowledgements

The authors would like to acknowledge financial supports from Fundamental Research Funds for the Central Universities (201313001, 201312005), Shandong Province Outstanding Youth Scientist Foundation Plan (BS2013CL015), Shandong Provincial Natural Science Foundation (ZR2011BQ017), Research Project for the Application Foundation in Qingdao (13-4-198-jch), National Natural Science Foundation of China (51102219, 51342008, U1037604), National Key and National Key Technology Support Program (2012BAB15B02).

References

[1] J.M. Tour, C. Kittrell, V.L. Colvin, Nat. Mater. 9 (2010) 871–874.
[2] N. Memarian, I. Concina, A. Braga, S.M. Rozati, A. Vomiero, G. Sberveglieri, Angew. Chem. Int. Ed. 50 (2011) 12321–12325.
[3] A. Yella, H.W. Lee, H.N. Tsao, C. Yi, A.K. Chandiran, M.K. Nazeeruddin, E.W.G. Diau, C.Y. Yeh, S.M. Zakeeruddin, M. Grätzel, Science 334 (2011) 629–634.
[4] J.H. Wu, Y.M. Xiao, Q.W. Tang, G.T. Yue, J.M. Lin, M.L. Huang, Y.F. Huang, L.Q. Fan, Z. Lan, S. Yin, T. Sato, Adv. Mater. 24 (2012) 1884–1888.
[5] X.X. Chen, Q.W. Tang, B.L. He, L. Lin, L.M. Yu, Angew. Chem. Int. Ed. 53 (2014) 10799–10803.
[6] B. O'Regan, M. Grätzel, Nature 353 (1991) 737–740.
[7] M.X. Wu, T.L. Ma, J. Phys. Chem. C 118 (2014) 16727–16742.
[8] J. Liu, Q.W. Tang, B.L. He, J. Power Sources 268 (2014) 56–62.
[9] J.D. Roy-Mayhew, D.J. Bozym, C. Punckt, I.A. Aksay, Nano 4 (2010) 6203–6211.
[10] B. Tang, G.X. Hu, H.Y. Gao, Z.X. Shi, J. Power Sources 234 (2013) 60–68.
[11] Q.W. Tang, H.Y. Cai, S.S. Yuan, X. Wang, J. Mater. Chem. A 1 (2013) 317–323.
[12] J.H. Wu, Y. Li, Q.W. Tang, G.T. Yue, J.M. Lin, M.L. Huang, L.J. Meng, Sci. Rep. 4 (2014) 4028.
[13] B.L. He, Q.W. Tang, T.L. Liang, Q.H. Li, J. Mater. Chem. A 2 (2014) 3119–3126.
[14] B.L. He, Q.W. Tang, M. Wang, H.Y. Chen, S.S. Yuan, ACS Appl. Mater. Interfaces 6 (2014) 8230–8236.
[15] J. Ma, L. Zhou, C. Li, J. Yang, T. Meng, H. Zhou, M. Yang, F. Yu, J. Chen, J. Power Sources 247 (2014) 999–1004.
[16] F. Gong, H. Wang, X. Xu, G. Zhou, Z.S. Wang, J. Am. Chem. Soc. 134 (2012) 10953–10958.
[17] X. Chen, Y. Jiang, J. Sun, C. Jin, Z. Zhang, J. Power Sources 267 (2014) 212–218.
[18] Y. Bing, H. Liu, L. Zhang, D. Ghosh, J. Zhang, Chem. Soc. Rev. 39 (2010) 2184–2202.
[19] B.L. He, X. Meng, Q.W. Tang, ACS Appl. Mater. Interfaces 6 (2014) 4812–4818.
[20] H.Y. Cai, Q.W. Tang, B.L. He, P.J. Li, J. Power Sources 258 (2014) 117–121.
[21] B.B. Hu, Q.W. Tang, B.L. He, L. Lin, H.Y. Chen, J. Power Sources 267 (2014) 445–451.
[22] S. Cho, S.H. Hwang, C. Kim, J. Jang, J. Mater. Chem. 22 (2012) 12164–12171.
[23] Y.Y. Duan, Q.W. Tang, B.L. He, R. Li, L.M. Yu, Nanoscale 6 (2014) 12601–12608.
[24] K. Park, J. Choi, B. Kwon, S. Lee, Y. Sung, H. Ha, S. Hong, H. Kim, A. Wieckowski, J. Phys. Chem. B 106 (2002) 1869–1877.
[25] C. Xu, J. Hou, X. Pang, X. Li, M. Zhu, B. Tang, Int. J. Hydrogen Energy 37 (2012) 10489–10498.
[26] S. Thomas, T.G. Deepak, G.S. Anjusree, T.A. Arun, S.V. Nair, A.S. Nair, J. Mater. Chem. A 2 (2014) 4474–4490.
[27] H. Tributsch, Coordin. Chem. Rev. 248 (2004) 1511–1530.
[28] B.L. He, Q.W. Tang, J.H. Luo, Q.H. Li, X.X. Chen, H.Y. Cai, J. Power Sources 256 (2014) 170–177.
[29] Z.B. Lv, J.F. Yu, H.W. Wu, J. Shang, D. Wang, S.C. Hou, Y.P. Fu, K. Wu, D.C. Zou, Nanoscale 4 (2012) 1248–1253.
[30] J. Yoon, M. Jin, M. Lee, Adv. Mater. 23 (2011) 3974–3978.
[31] M. Wu, X. Lin, Y. Wang, L. Wang, W. Guo, D. Qi, X. Peng, A. Hagfeldt, M. Grätzel, T.L. Ma, J. Am. Chem. Soc. 134 (2014) 3419–3428.
[32] M.K. Wang, A.M. Anghel, B. Marsan, N.C. Ha, N. Pootrakulchote, S.M. Zakeeruddin, M. Grätzel, J. Am. Chem. Soc. 131 (2009) 15976–15977.
[33] T. Daeneke, A.J. Mozer, T.H. Kwon, N.W. Duffy, A.B. Holmes, U. Bach, L. Spiccia, Energy Environ. Sci. 5 (2012) 7090–7099.
[34] Y. Gong, C. Li, X. Huang, Y. Luo, D. Li, Q. Meng, B.B. Iversen, ACS Appl. Mater. Interfaces 5 (2013) 795–800.
[35] V.-D. Dao, S.-H. Kim, H.-S. Choi, J.-H. Kim, H.-O. Park, J.-K. Lee, J. Phys. Chem. C 115 (2011) 25529–25534.
[36] D. Papadias, S.H.D. Lee, Ind. Eng. Chem. Res. 45 (2006) 5841–5858.
[37] G. Syrrokostas, A. Siokou, G. Leftheriotis, P. Yianoulis, Sol. Energy Mater. Sol. Cells 103 (2012) 119–127.
[38] E. Olsen, G. Hagen, S.E. Lindquist, Sol. Energy Mater. Sol. Cells 63 (2000) 267–273.

RSC Advances

PAPER

View Article Online
View Journal | View Issue

Cite this: RSC Adv., 2015, 5, 46260

Toward elevated light harvesting: efficient dye-sensitized solar cells with titanium dioxide/silica photoanodes†

Peizhi Yang,*[a] Qunwei Tang*[b] and Benlin He[b]

Received 13th April 2015
Accepted 30th April 2015

DOI: 10.1039/c5ra06584d

www.rsc.org/advances

Pursuit of light harvesting is a persistent objective for dye-sensitized solar cells (DSSCs). Here we report the synthesis of titanium dioxide/silica (TiO_2/SiO_2) nanocrystallite photoanodes, aiming at elevating the light harvesting for dye excitation. Due to light interference effect of the reflected light beams from TiO_2/SiO_2 and SiO_2/electrolyte interfaces, the dye excitation and therefore the photocurrent density are markedly enhanced. The photovoltaic performances of the resultant DSSCs are optimized by utilizing three TiO_2/SiO_2 photoanodes from different synthetic strategies. A maximum power conversion efficiency of 8.56% is measured under simulated air mass 1.5 global sunlight in comparison with 7.06% from pristine TiO_2 based DSSC. The high power conversion efficiency in combination with simple preparation demonstrates the potential for utilization of TiO_2/SiO_2 nanocrystallite anodes in efficient DSSCs.

1. Introduction

The depletion of fossil fuels and global warming pose a challenge against sustainable development of the world. One of the efficient solutions is to explore renewable energy resources. Solar energy accounts for 99% of energy on earth, therefore the direct conversion of solar energy into electricity has attracted widespread attention due to low environmental impact.[1–3] A dye-sensitized solar cell (DSSC), a photoelectrochemical device comprising of a dye-sensitized anode, a redox electrolyte having I^-/I_3^- couples, and a counter electrode, has attracted growing interests because of its merits on cost-effectiveness, relatively high power conversion efficiency, easy fabrication, and environmental friendliness.[4–8] Since the first DSSC prototype created by Grätzel in 1991,[9] a maximum efficiency of ~13% has been recorded under simulated air mass 1.5 (AM1.5) global sunlight.[10] One of the main problems in restricting the enhancement in power conversion efficiency is the incompleted dye excitation, therefore resulting in a modest electron density on the conduction band (CB) of the TiO_2 anode.[11] There has been much effort to enhance the dye excitation, such as building a reflecting layer[12,13] and designing bifacial DSSC that can be simultaneously illuminated from both front and rear sides.[14] Recently, a bifacial DSSC device has been successfully designed in our group by splitting incident light into two beams.[14] The device is simultaneously irradiated from the TiO_2 photoanode and a transparent polyaniline counter electrode. The incident light from the transparent polyaniline counter electrode can compensate for the light penetrated from the photoanode, leading to a significantly enhanced dye excitation and a promising power conversion efficiency of 8.35%.

In searching for other alternative strategies, here we present three hydrothermal methods for the design of TiO_2/SiO_2 anodes in an attempt to increase the electron density on CB of TiO_2 nanocrystallites. The light intensity for dye excitation is expected to be markedly enhanced due to the interference light reflected from TiO_2/SiO_2 and SiO_2/air (electrolyte) interfaces. The concept toward light harvesting is also significant for other solar cells, such as quantum dot-sensitized solar cells, perovskite solar cells.

2. Experimental

2.1. Materials

Unless noted otherwise, all chemicals were purchased from Sigma-Aldrich and used as received. The average diameter of commercial SiO_2 nanoparticles is around 20 nm.

2.2. Preparation of TiO_2/SiO_2 nanocrystallites

The TiO_2/SiO_2 nanocrystallites can be prepared according to the following procedures: (1) under vigorous agitation at room temperature, 100 mL of deionized water was mixed with 10 mL of titanium tetrabutanolate. After 30 min, the mixture was pump-filtrated to obtain dehydrated filter powders. (2)

[a]Key Laboratory of Advanced Technique & Preparation for Renewable Energy Materials, Ministry of Education, Yunnan Normal University, Kunming 650500, P. R. China. E-mail: pzhyang@hotmail.com; Fax: +86 532 66782533; Tel: +86 532 66782533

[b]Institute of Materials Science and Engineering, Ocean University of China, Qingdao 266100, P. R. China. E-mail: tangqunwei@ouc.edu.cn

† Electronic supplementary information (ESI) available. See DOI: 10.1039/c5ra06584d

Subsequently, 10 mL of acetic acid and 0.8 mL of nitric acid were added into the above filter powders dropwise in a flask. After agitation of 15 min at 80 °C, the volume of the mixture was adjusted to 170 mL by adding deionized water. The reactant was further agitated at 80 °C in a sealed atmosphere. (3) Later, the resultant colloid was transferred into a Teflon-lined autoclave and heated at 200 °C for 12 h. (4) A homogeneous mixture consisting of 65 mL of the white colloid and 0.4 g of commercial P25 were prepared under ultrasonic irradiation for 30 min and (5) then transferred to another Teflon-lined autoclave, which was subsequently heated at 200 °C for 12 h. (6) After removing the supernatant liquid, the colloid was mixed with 0.8 g of poly(ethylene glycol) ($M_w = 20\,000$) and 1 mL of OP emulsifier and subsequently concentrated at 80 °C. To obtain the TiO_2/SiO_2 colloid, 0.0275 g of SiO_2 nanoparticles were added to the above reagent after steps (2), (4), and (6). The as-synthesized samples were denoted as TiO_2/SiO_2-(i), TiO_2/SiO_2-(ii), and TiO_2/SiO_2-(iii), respectively.

2.3. Fabrication of photoanodes

Fluorine doped tin oxide (FTO) glass substrates (sheet resistance: 12 Ω square^{-1}) with a size of 2 × 2 cm^2 were thoroughly rinsed with deionized water and anhydrous ethanol, and dried by N_2 gas flow. The photoanodes from TiO_2/SiO_2 were fabricated using a screen printing technique. The size of the resultant photoanodes was controlled at 0.5 × 0.5 cm^2 with an average thickness of TiO_2/SiO_2 layer of 10 μm. The air-dried colloids were calcined in a muffle furnace at 450 °C for 30 min. The increase of heating temperature was controlled at a speed of 2 °C min^{-1} till 130 °C, and then at a speed of 6 °C min^{-1} until 450 °C. The resultant TiO_2/SiO_2 films were immersed in 0.50 mM N719 ethanol solution for 24 h to obtain dye-sensitized TiO_2/SiO_2 photoanodes.

2.4. Assembly of DSSCs

Each DSSC was assembled by sandwiching a dye-sensitized TiO_2/SiO_2 photoanode, a liquid electrolyte having I^-/I_3^- redox couples, and a Pt counter electrode. The redox electrolyte consisted of 100 mM of tetraethylammonium iodide, 100 mM of tetramethylammonium iodide, 100 mM of tetrabutylammonium iodide, 100 mM of NaI, 100 mM of KI, 100 mM of LiI, 50 mM of I_2, and 500 mM of 4-*tert*-butyl-pyridine in 50 mL acetonitrile. The photocurrent–voltage (J–V) curves of the assembled DSSCs were recorded on an Electrochemical Workstation (CHI600E) under irradiation of a simulated solar light (Xe Lamp Oriel Sol^{3}A™ Class AAA Solar Simulators 94023A, USA) at a light intensity of 100 mW cm^{-2} (calibrated by a standard silicon solar cell) in ambient atmosphere. A black mask with an aperture area of around 0.25 cm^2 was applied on the surface of DSSCs to avoid stray light. Each DSSC device was measured at least five times to eliminate experimental error (±5%) and a suitable J–V curve was constructed.

2.5. Other characterizations

The morphologies of the resultant TiO_2/SiO_2 and pure TiO_2 anodes were observed with a scanning electron microscope (SEM, S-3500N, Hitachi, Japan) and a transmission electron microscopy (TEM, JEM2010, JEOL). The optical absorption spectra were recorded on a UV-vis spectrophotometer (Agilent 8453) at room temperature. Fourier transformed Raman spectroscopic measurements in the ultraviolet light were performed on a Renishaw inVia Reflex Raman Spectrometer. High-resolution gratings were used to give a spectral resolution of 2 cm^{-1}. The spectra were recorded at room temperature from 3200 to 100 cm^{-1} using 16 scans with an exposure time of 1 s per scan. X-ray diffraction (XRD) profiles of the resultant nanocrystallites were recorded on an X-ray powder diffractometer (X'pert MPD Pro, Philips, Netherlands) with Cu Kα radiation ($\lambda = 1.542$ Å) in the 2θ range from 10 to 70° operating at 40 kV accelerating voltage and 40 mA current. Fourier transform infrared spectrometry (FTIR) spectra were recorded on a Vertex 70 FTIR spectrometer (Bruker). For electrochemical impedance spectroscopy (EIS) measurements, the DSSCs were scanned from 0.1 Hz to 1 MHz at an ac amplitude of 10 mV.

3. Results and discussion

The morphology of a TiO_2 nanocrystallite photoanode is crucial for use in a DSSC device.[15] Here, we mainly describe the morphological difference of resultant TiO_2/SiO_2 and pure TiO_2 prepared by the sol–hydrothermal method. As is shown in Fig. 1, no apparent deviations in morphologies are observed from SEM images, indicating that the synthetic strategy does not influence the morphology of resultant TiO_2/SiO_2 anodes. The BET surface areas of the samples are 46.2, 62.0, 96.7, and 73.5 m^2 g^{-1} for pure TiO_2, TiO_2/SiO_2-(i), TiO_2/SiO_2-(ii), and TiO_2/SiO_2-(iii), respectively. The task of a photoanode is to adsorb dyes and to transfer photogenerated electrons from the excited dye to the FTO layer along the percolating networks of TiO_2. Therefore, a mesoporous structure having a high specific surface area demonstrates that it is feasible to upload more photosensitive dyes for electron generation. As a reference, the

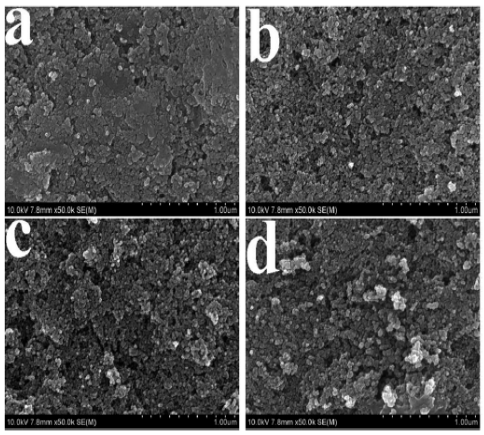

Fig. 1 SEM photographs of the TiO_2/SiO_2 and pure TiO_2 nanocrystallites: (a) TiO_2/SiO_2-(i), (b) TiO_2/SiO_2-(ii), (c) TiO_2/SiO_2-(iii), and (d) pure TiO_2.

surface morphology of pristine TiO_2 anode is also provided, giving no apparent difference from TiO_2/SiO_2-(ii). Moreover, we can not distinguish SiO_2 from TiO_2 nanoparticles in SEM photographs, or amorphous SiO_2 nanoparticles maybe suffer from dissolution and reorganization during the rigorous hydrothermal conditions.

Fig. 2 displays the high-resolution TEM images of TiO_2/SiO_2 and pure TiO_2 nanocrystallites. It can be seen that the crystal lattice of the pure TiO_2 is homogeneous with no amorphous regions, indicating that the organics and carbonaceous materials have been removed during the calcination process. However, a great deal of lattice distortions and plenty of defects are detected in the three TiO_2/SiO_2 nanocrystallites. Due to the presence of SiO_2 amorphous phase, we deduce that the amorphous regions refer to the SiO_2 phase and the crystal phase means anatase TiO_2. These results reveal that TiO_2 has been successfully incorporated or partially incorporated with amorphous SiO_2 by entering the lattice fringes of TiO_2 by Si^{4+} ions.[16] It has been known that the ionic radius of Si^{4+} (0.039 nm) is much smaller than that of Ti^{4+} (0.068 nm), suggesting that Si^{4+} ions can enter into the TiO_2 crystal lattice to substitute for Ti^{4+}, which is consistent with the morphology analysis.

In order to describe the photo-absorption behavior of the TiO_2/SiO_2 nanocrystallites, the UV-vis diffuse reflection spectra have been recorded and are shown in Fig. 3. As a comparison, the absorption spectrum of pristine TiO_2 is also conducted at the same conditions. No obvious shape alteration is observed after integration with SiO_2. Pristine TiO_2 exhibits an absorption band at *ca.* 396 nm. However, the absorption shifts towards the ultraviolet-light region. Reflectance spectra have been converted to the absorbance spectra using Kubelka–Munk equations (eqn (1) and (2)).[17]

$$F(R_\infty(\lambda)) = \frac{(1-R_\infty)^2}{2R_\infty} \quad (1)$$

$$R_\infty = \frac{R}{R_{BaSO_4}} \quad (2)$$

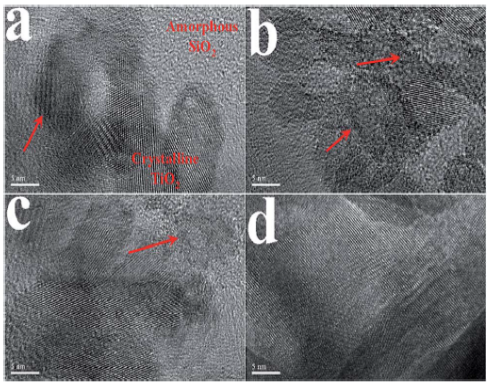

Fig. 2 TEM photographs of the TiO_2/SiO_2 and pure TiO_2 nanocrystallites: (a) TiO_2/SiO_2-(i), (b) TiO_2/SiO_2-(ii), (c) TiO_2/SiO_2-(iii), and (d) pure TiO_2. The distortions and defects have been marked in the figures.

where R is the reflectance recorded for a sample and R_{BaSO_4} is the reflectance recorder for a reference. To calculate the band-gap energy, the Kubelka–Munk function is converted to the form $(F(R_\infty)E)^{1/2}$ and the wavelength is changed to energy units (eV). The direct band gap energy can be obtained by an extrapolation method (see Fig. 3b–e). The direct E_g values of pure TiO_2, TiO_2/SiO_2-(i), TiO_2/SiO_2-(ii), and TiO_2/SiO_2-(iii) are 2.96, 3.00, 3.02, and 3.16 eV, respectively. Notably, TiO_2 is a typical photocatalyst and has been utilized for dye removal from pollutions.[18–20] When irradiated by incident light, the electrons on the valence band of TiO_2 can absorb energy and jump to its conduction band, leaving holes in the TiO_2 surface. Both photogenerated electrons and holes by TiO_2 can participate in the degradation reactions of organic dyes. In this way, the N719 molecule, one of the organic dyes, is expected to be photodegradated by TiO_2, while the wavelength of the light for dye degradation depends on the E_g of the TiO_2 ($E_g \approx 1240/\lambda$). Apparently, the as-synthesized TiO_2/SiO_2-(ii) has the highest E_g, which indicates the excitation of photogenerated electrons and holes requires an increased photon energy. Therefore, fewer electron–hole pairs can be produced in the TiO_2/SiO_2-(ii) for participating in the photodegradation of organic N719 dye molecules, leading to an enhanced dye stability by utilizing strategy (ii) for photoanode fabrication.

The XRD technique has been widely employed for the identification of the crystal phase as well as crystallite size of TiO_2. The detection of diffraction peaks reveals that pristine TiO_2 is featured by anatase phase (Fig. 4). No diffraction peaks of the rutile phase are detected in the XRD patterns. The crystallite size can be determined from the broadening of the corresponding XRD peaks by the Scherrer formula:[21]

$$L = \frac{K\lambda}{\beta \cos\theta} \quad (3)$$

where L is the crystallite size, λ is the wavelength of the X-ray radiation (CuKα = 0.15418 nm), K is usually taken as 0.89, and β is the line width at half-maximum height (FWHM). In addition, the crystal lattice distortion ($\Delta d/d$) can also be evaluated from the equation:[22]

$$\frac{\Delta d}{d} = \frac{\beta}{4tg\theta} \quad (4)$$

At the first glance, all the diffraction peaks belonging to the diffraction faces of anatase TiO_2 can be detected in the TiO_2/SiO_2 nanocrystallites. However, the relative intensity of the diffraction peak belonging to the (101) face of anatase TiO_2 phase dramatically decreases after being doped with Si^{4+}, indicating an inhibition effect of phase transformation from amorphous to anatase TiO_2. Moreover, the crystallite size of the TiO_2/SiO_2 has an order of decreasing and the TiO_2/SiO_2-(ii) has the smallest crystallite size (Table 1), suggesting that the doping of Si^{4+} in TiO_2 can hinder the growth of crystallite size due to the segregation of dopant cations at the grain boundary.[23] The crystal lattice distortion ($\Delta d/d$) is also elevated by doping Si^{4+} ions in comparison with that of pure TiO_2, indicating that the substitution of Ti by Si can generate more defects for dye

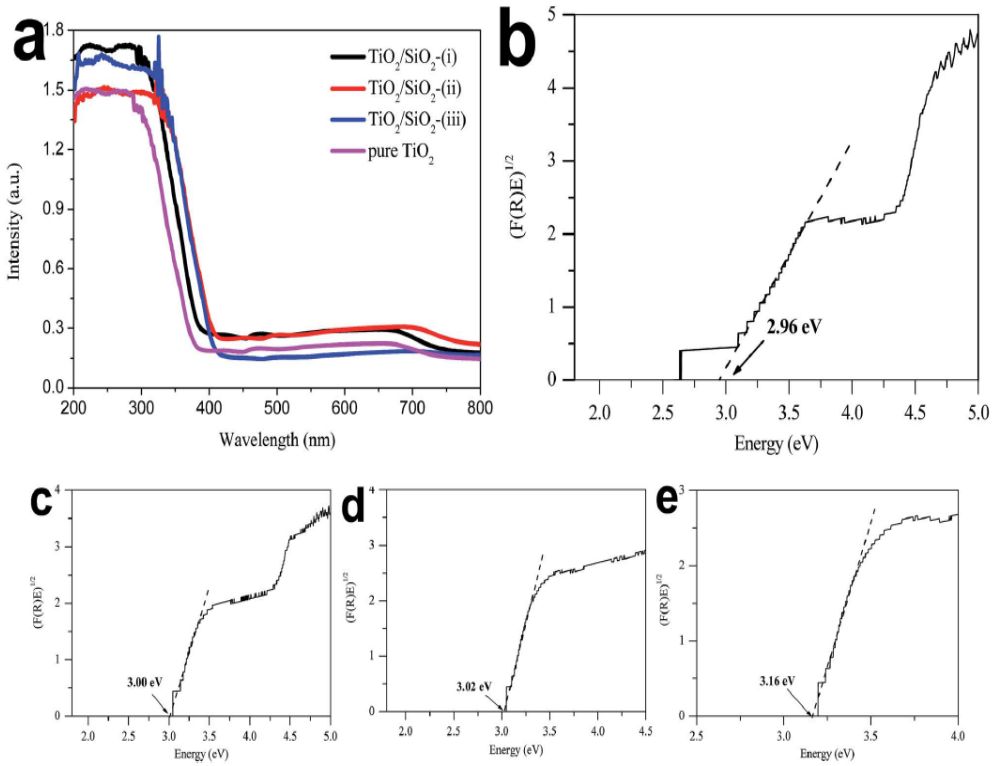

Fig. 3 (a) UV-vis diffuse reflection spectra of the TiO_2/SiO_2 and pure TiO_2 nanocrystallites. Plots of $(F(R_\infty)E)^{1/2}$ as a function of energy for (b) pristine TiO_2, (c) TiO_2/SiO_2-(i), (d) TiO_2/SiO_2-(ii), and (e) TiO_2/SiO_2-(iii).

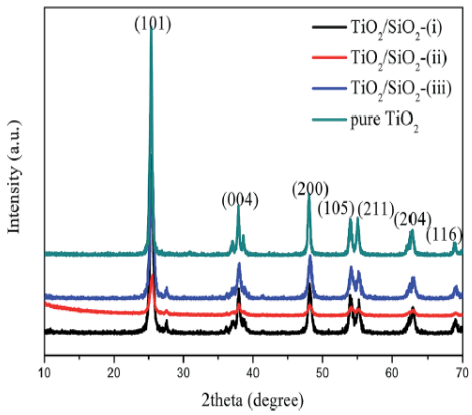

Fig. 4 XRD patterns of the TiO_2/SiO_2 and pure TiO_2 nanocrystallites.

adsorption. This result is in an agreement with TEM observations.

The crystallographic structures of the TiO_2/SiO_2 and pure TiO_2 nanocrystallites were investigated by Raman spectroscopy and shown in Fig. 5a. The whole set of spectra shows three main Raman peaks at 394, 515, and 639 cm^{-1} that can be ascribed to the B_{1g} (1), A_{1g}/B_{1g} (2), and E_g (3) modes of anatase phase of pure TiO_2, respectively. However, the mode positions have shifted in

Table 1 Structure parameters obtained from XRD patterns of pure TiO_2 and TiO_2/SiO_2 nanocrystallites

Nanocrystallites	β (°)	2θ (°)	Crystallite size (nm)	$\Delta d/d$
Pure TiO_2	0.32	25.45	25.19	0.00752
TiO_2/SiO_2-(i)	0.48	25.45	16.66	0.0113
TiO_2/SiO_2-(ii)	0.58	25.45	13.79	0.0136
TiO_2/SiO_2-(iii)	0.56	25.45	14.28	0.0132

comparison with pure TiO_2. It is attributed to the decrease in crystallite size (Table 1) and lack of adjacent atoms for the surface atoms. Therefore, the surface atoms are in a relaxation state and the red shift results from a surface relaxation effect.[24] Although the positions have deviations, the doping of Si^{4+} does not influence and change the structure of TiO_2.[25] The conclusion is consistent with that of XRD analysis. No Raman peaks corresponding to SiO_2 can be detected in the doped TiO_2, indicating that Si^{4+} may present in the substitutional positions in the crystal lattice of TiO_2. The detection of 1059 cm^{-1} in the FTIR spectra (Fig. 5b) is a signal of Si–O–Ti bond,[26,27] indicating that there is a covalent bond between SiO_2 and TiO_2 instead of a simple mixture. The coverage of TiO_2 by SiO_2 layer along with the doping of TiO_2 by SiO_2 and detection of Si–O–Ti bond may be used to support the hypothesis that the amorphous SiO_2

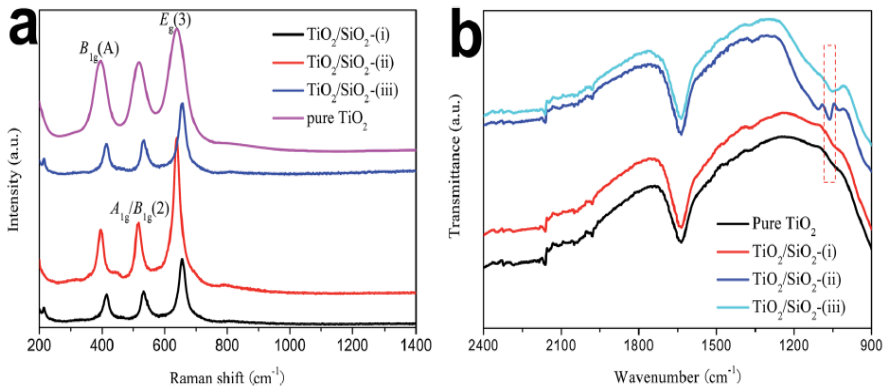

Fig. 5 (a) Raman and (b) FTIR spectra of TiO_2/SiO_2 and pure TiO_2 nanocrystallites.

nanoparticles have been dissolved and reorganized in the hydrothermal process.

Incident light intensity of 100 mW cm^{-2} (AM1.5G) has been widely employed as a standard in evaluating DSSC performances. In our previous study,[11] we found that ~85 and ~40 mW cm^{-2} of incident light remains after penetrating FTO glass and 10 μm-thickness FTO–TiO_2 photoanode (Fig. 6), respectively. This indicates that the dye molecules adsorbed at the interface of TiO_2/FTO are irradiated by incident light with an intensity of ~85 mW cm^{-2}, whereas it is ~40 mW cm^{-2} for the dyes at the interface of TiO_2/electrolyte. The incident light shows a gradient descent within the dye-sensitized TiO_2 film because of reflection and absorption of TiO_2 nanocrystallites. It is well known that the DSSC performances are highly dependent on incident light intensity.[28–30] Therefore, the transmission enhancement is of great significance in improving the photovoltaic performances. Interestingly, the transmission is dramatically enhanced by synthesizing TiO_2/SiO_2 by route (ii), it is ~80 mW cm^{-2} in light intensity across the 10 μm-thickness FTO-TiO_2/SiO_2 anode. To explore the potential mechanism, we think it is subject to the compensation effect of reflected light from TiO_2/SiO_2 and SiO_2/electrolyte interfaces. The transmission enhancement is attributed to a good matching of $\sqrt{n_{TiO_2}}$ with n_{SiO_2} (ESI†).[11] Until now, we conclused that the dye excitation efficiency is expected to be significantly enhanced, which is contributive to the elevation of electron density on CB of TiO_2 and therefore the photocurrent density of the DSSC.

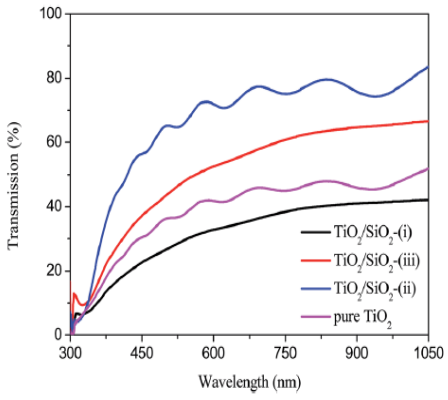

Fig. 6 Transmission spectra of TiO_2/SiO_2 and pure TiO_2 nanocrystallites.

Fig. 7a displays *J–V* curves of the DSSCs from TiO_2/SiO_2 and pure TiO_2 photoanodes and the photovoltaic parameters are summarized in Table 2. The DSSC device containing pure TiO_2 crystallites gives a J_{sc} of 14.06 mA cm^{-2} and η of 7.06%. Both of these parameters are enhanced by employing TiO_2/SiO_2 anodes. The optimal photovoltaic performances result from TiO_2/SiO_2-(ii) based DSSC: J_{sc} of 18.06 mA cm^{-2} and η of 8.56%. J_{sc} is a reflection of accumulative electron density injected from the excited state of dye to CB of TiO_2, whereas the low excitation efficiency and photodegradation of dye molecules on TiO_2 nanocrystallites have been tremendous obstacles for current loss. Owing to the compensation effect of TiO_2/SiO_2 nanocrystallines and enhancement of E_g of SiO_2 doped TiO_2, the excitation efficiency and photostability of dye molecules can be significantly improved, giving an enhanced J_{sc} in their DSSC devices. From a small standard deviation (±5%), as shown in ESI Fig. S1,† we infer that the DSSCs with promising photovoltaic performances and high reproducibility can be realized using the method reported here (Table 3).

From the dark *J–V* curves in Fig. 7b, one can see that the DSSC from TiO_2/SiO_2-(ii) anode shows the smallest dark current density at the same voltage. The dark current density in DSSC device is attributed to the triiodides combination with electrons on CB of TiO_2 at the TiO_2/electrolyte interface.[31] The smaller dark current density indicates that the reduction of triiodides on the TiO_2/electrolyte interface is slower. This is another factor for the elevated J_{sc} for TiO_2/SiO_2-(ii) anode based DSSC.

Fig. 8a shows the impedance spectra for the DSSCs, giving two semicircles which are assigned to electrochemical reaction at CE (a smaller one in high frequency region) and charge transfer at the TiO_2|dye|electrolyte (a larger one in low frequency region). An equivalent circuit (see the inset of Fig. 8a) is used to fit the Nyquist plots to estimate the electron transport

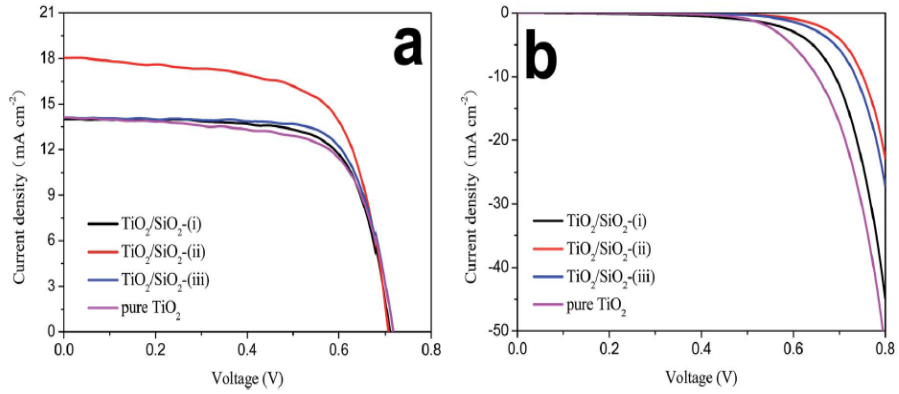

Fig. 7 J–V characteristics of DSSCs from various nanocrystallite anodes: (a) illuminated under AM1.5 and (b) in the dark.

Table 2 Photovoltaic parameters of the DSSCs using various nanocrystallite anodes. J_{sc}: short-circuit current density; V_{oc}: open-circuit voltage, FF: fill factor; PCE: power conversion efficiency

DSSCs	V_{oc} (V)	J_{sc} (mA cm^{-2})	FF	PCE (%)
TiO$_2$/SiO$_2$-(i)	0.710	14.13	0.73	7.30
TiO$_2$/SiO$_2$-(ii)	0.708	18.06	0.65	8.56
TiO$_2$/SiO$_2$-(iii)	0.770	14.10	0.69	7.52
Pure TiO$_2$	0.718	14.06	0.70	7.06

Table 3 Parameters of lifetime of electrons and the equivalent circuit obtained by fitting EIS of the DSSCs using a Z-view software. τ: lifetime

Parameters	TiO$_2$/SiO$_2$-(i)	TiO$_2$/SiO$_2$-(ii)	TiO$_2$/SiO$_2$-(iii)	Pure TiO$_2$
R_s (Ω cm^2)	0.89	0.73	0.97	0.95
R_{ct2} (Ω cm^2)	5.33	3.46	9.09	9.32
W (Ω cm^2)	18.72	6.84	18.18	19.06
τ (μs)	124.2	399.7	214.9	105.1

parameters, such as sheet resistance (R_s), charge-transfer resistance at CE/electrolyte (R_{ct1}), charge-transfer resistance at the TiO$_2$/dye/electrolyte interface (R_{ct2}), and Nernst diffusion impedance corresponding to the diffusion resistance of I^-/I_3^- redox species (W). CPE1 and CPE2 are constant phase elements. It is found that the R_{ct2} of TiO$_2$/SiO$_2$-(ii) anode based DSSC is the smallest in comparison with other devices. The results demonstrate that the photogenerated electrons can be rapidly transferred to CB of TiO$_2$ and the excited dyes are easily recovered by iodide ions. Moreover, the smallest W value suggests that the I^-/I_3^- redox couples have a high diffusion kinetics within TiO$_2$/SiO$_2$-(ii) anode.

$$\tau = 1/2\pi f_p \quad (5)$$

Finally, the lifetimes of electrons on various anodes are determined according to eqn (4),[32] where f_p is second peak frequency (Fig. 8b), giving a lifetime of 124.2 μs for TiO$_2$/SiO$_2$-(i), 399.7 μs for TiO$_2$/SiO$_2$-(ii), 214.9 μs for TiO$_2$/SiO$_2$-(iii), and 105.1 μs for pure TiO$_2$. The enhanced electron lifetime in TiO$_2$/SiO$_2$

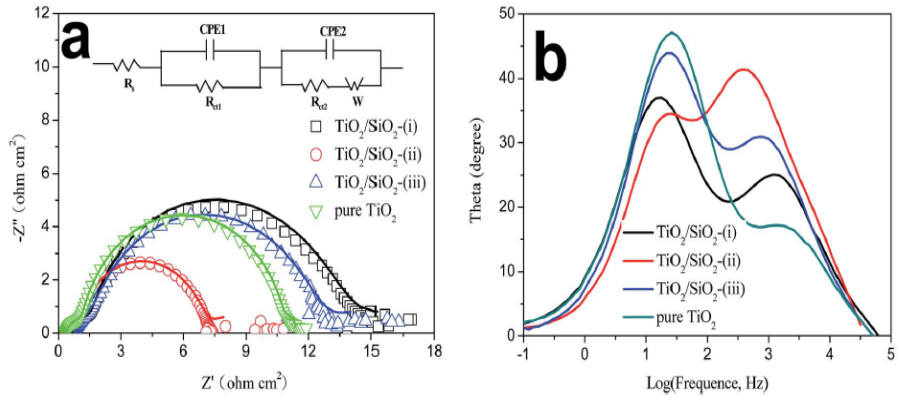

Fig. 8 EIS spectra of the DSSCs from varied nanocrystallite anodes. The inset gives the equivalent circuit used to fit the impedance data. (a) Nyquist plot, (b) Bode phase plot.

based DSSCs can be attributed to the elevated formation of connected channels by TiO_2 and enhanced electron density.

4. Conclusions

In summary, we have demonstrated that the combination of TiO_2 with SiO_2 is an effective strategy for enhancing dye illumination and excitation, and increasing dye photostability. Due to the light interference reflected from TiO_2/SiO_2 and SiO_2/air (electrolyte) interfaces, more active sites for dye adsorption and high electron lifetime, the DSSC from TiO_2/SiO_2-(ii) nanocrystallite provides an impressive power conversion efficiency of 8.56% in comparison with that of 7.06% from a pure TiO_2 anode based device. The research presented here is far from being optimized but these profound advantages along with low-cost synthesis and scalable materials show the new nanocrystallites to be strong candidates for robust DSSCs.

Acknowledgements

The authors would like to acknowledge financial support from the National Natural Science Foundation of China (U1037604), the Shandong Province Outstanding Youth Scientist Foundation Plan (BS2013CL015), the Shandong Provincial Natural Science Foundation (ZR2011BQ017), and the Research Project for the Application Foundation in Qingdao (13-4-198-jch).

References

1 P. Krogstrup, H. I. Jorgensen, M. Heiss, O. Demichel, J. V. Holm and M. Aagesen, *et al.*, *Nat. Photonics*, 2013, **7**, 306–310.
2 J. Oh, H. C. Yuan and H. M. Branz, *Nat. Nanotechnol.*, 2012, **7**, 743–748.
3 Y. Chiba, A. Islam, Y. Watanabe, R. Komiya, N. Koide and L. Han, *Jpn. J. Appl. Phys.*, 2006, **45**, L638–L640.
4 X. X. Chen, Q. W. Tang, B. L. He, L. Lin and L. M. Yu, *Angew. Chem., Int. Ed.*, 2014, **53**, 10799–10803.
5 Y. Y. Duan, Q. W. Tang, J. Liu, B. L. He and L. M. Yu, *Angew. Chem., Int. Ed.*, 2014, **53**, 14569–14574.
6 T. G. Deepak, G. S. Anjusree, S. Thomas, T. A. Arun, S. V. Nair and A. S. Nair, *RSC Adv.*, 2014, **4**, 17615–17638.
7 Q. W. Tang, H. Y. Cai, S. S. Yuan and X. Wang, *J. Mater. Chem. A*, 2013, **1**, 317–323.
8 K. Ladomenou, T. N. Kitsopoulos, G. D. Sharma and A. G. Coutsolels, *RSC Adv.*, 2014, **4**, 21379–21404.
9 B. O'Regan and M. Grätzel, *Nature*, 1991, **353**, 737–740.
10 A. Yella, H. W. Lee, H. N. Tsao, C. Yi, A. K. Chandiran and M. K. Nazeeruddin, *et al.*, *Science*, 2011, **334**, 629–634.
11 S. S. Yuan, Q. W. Tang, B. L. He, L. Men and H. Y. Chen, *Electrochim. Acta*, 2014, **125**, 646–651.
12 H. S. Jung and J. K. Lee, *J. Phys. Chem. Lett.*, 2013, **4**, 1682–1693.
13 X. L. He, G. J. Yang, C. J. Li, C. X. Li and S. Q. Fan, *J. Power Sources*, 2014, **251**, 122–129.
14 J. H. Wu, Y. Li, Q. W. Tang, G. T. Yue, J. M. Lin and M. L. Huang, *et al.*, *Sci. Rep.*, 2014, **4**, 4028.
15 Z. Weng, H. Guo, X. Liu, S. Wu, K. W. K. Yeung and P. K. Chu, *RSC Adv.*, 2013, **3**, 24758–24775.
16 L. Lin, Y. C. Yang, L. Men, X. Wang, D. N. He and Y. C. Chai, *et al.*, *Nanoscale*, 2013, **5**, 588–593.
17 K. M. Reddy, S. V. Manorama and A. R. Reddy, *Mater. Chem. Phys.*, 2002, **78**, 239–245.
18 L. Lin, Y. Yang, L. Men, X. Wang, D. He, Y. Chai, B. Zhao, S. Ghoshroy and Q. W. Tang, *Nanoscale*, 2013, **5**, 588–593.
19 L. Lin, Y. Chai, Y. Yang, X. Wang, D. He, Q. W. Tang and S. Ghoshroy, *Int. J. Hydrogen Energy*, 2013, **38**, 2634–2640.
20 H. Y. Cai, X. X. Chen, Q. H. Li, B. L. He and Q. W. Tang, *Appl. Surf. Sci.*, 2013, **284**, 837–842.
21 Q. H. Zhang, L. Gao and J. K. Guo, *Appl. Catal., B*, 2000, **26**, 207–215.
22 L. Q. Jing, X. J. Sun, B. F. Xin, B. Q. Wang, W. M. Cai and H. G. Fu, *J. Solid State Chem.*, 2004, **177**, 3375–3382.
23 Y. H. Zhang, H. X. Zhang, Y. X. Xu and Y. G. Wang, *J. Mater. Chem.*, 2003, **13**, 2261–2265.
24 C. H. Yang, Z. Q. Ma, F. Li, B. He, J. H. Yuan and Z. H. Zhang, *Acta Phys.-Chim. Sin.*, 2010, **26**, 1349–1354.
25 I. Cacciotti, A. Bianco, G. Pezzotti and G. Gusmano, *Chem. Eng. J.*, 2011, **166**, 751–764.
26 S. Cheng, X. Liu, S. Yun, H. Luo and Y. Gao, *Ceram. Int.*, 2014, **40**, 13781–13786.
27 Y. Li, X. Ge, X. Pang, X. Yu, X. Zhen, L. Geng and Y. Wang, *Mater. Lett.*, 2015, **152**, 170–172.
28 T. Trupke, P. Würfel and I. Uhlendorf, *J. Phys. Chem. B*, 2000, **104**, 11484–11488.
29 I. Gonzalez-Valls, Y. Yu, B. Ballesteros, J. Oro and M. Lira-Cantu, *J. Power Sources*, 2011, **196**, 6609–6621.
30 X. Z. Guo, Y. H. Luo, C. H. Li, D. Qin, D. M. Li and Q. B. Meng, *Curr. Appl. Phys.*, 2012, **12**, e54–e58.
31 Z. Y. Tang, J. H. Wu, M. Zheng, J. H. Huo and Z. Lan, *Nano Energy*, 2013, **2**, 622–627.
32 T. Hoshikawa, T. Ikebe, R. Kikuchi and K. Eguchi, *Electrochim. Acta*, 2006, **51**, 5286–5294.

Journal of Materials Chemistry A

PAPER

View Article Online
View Journal | View Issue

Cite this: J. Mater. Chem. A, 2015, 3, 5368

Solid-state dye-sensitized solar cells from poly(ethylene oxide)/polyaniline electrolytes with catalytic and hole-transporting characteristics

Yanyan Duan,[ab] Qunwei Tang,*[ab] Yuran Chen,[b] Zhiyuan Zhao,[b] Yang Lv,[b] Mengjin Hou,[b] Peizhi Yang,[d] Benlin He*[b] and Liangmin Yu*[ac]

Received 24th November 2014
Accepted 20th January 2015

DOI: 10.1039/c4ta06393g

www.rsc.org/MaterialsA

The pursuit of cost-effective and efficient solid-state electrolytes is a persistent objective for dye-sensitized solar cells (DSSCs). Herein, we present the experimental design of iodide/triiodide (I^-/I_3^-)-incorporated poly(ethylene oxide)/polyaniline (PEO/PANi) solid-state electrolytes, aiming at expanding the catalytic event of I_3^- reduction from the electrolyte/counter electrode interface to both the interface and electrolyte system and shortening the charge diffusion path length. Except for I^- species, the conjugated PANi is also responsible for dye regeneration and hole transfer to the counter electrode. A DSSC with (I^-/I_3^-)-incorporated PEO/1.0 wt% PANi electrolyte yields a maximum efficiency of 6.1% in comparison with 0.8% obtained from a PANi-free electrolyte-based solar cell and 0.1% for a PANi-based solar cell.

1. Introduction

Solar energy, accounting for 99% of the total energy on Earth, has been considered as one of the promising green energy resources for developing a low-carbon economy. The direct conversion of solar energy into electricity is an efficient solution to current energy problems. Among diversified photovoltaic devices,[1–4] dye-sensitized solar cells (DSSCs) have received widespread attention as inexpensive and remarkably efficient energy conversion devices.[5–8] The configuration of a typical DSSC consists of an electrolyte containing redox couples that is dissolved in an organic solvent, which is sandwiched between an organic dye-sensitized TiO_2 anode and a counter electrode (CE).[9] Researchers are currently focusing on understanding and improving charge generation, transport, recombination, and collection along with optimizing materials for liquid electrolyte DSSC operation.[10–12] Until now, a maximum efficiency of 13% has been measured under air mass 1.5 (AM1.5) global sunlight.[13] Due to flaws in solvent leakage and evaporation, the mass production and long-term stability of such DSSC devices have been limited. One solution to this impasse is to employ microstructured polymer gel electrolytes with three-dimensional (3D) frameworks and all-solid-state electrolytes.[14–17] Although liquid electrolyte can be imbibed and remains in the 3D structures of polymer gel electrolytes by osmotic pressure or capillary force,[18] the dilemma of organic solvent evaporation still remains. Therefore, the challenge of achieving commercial success will be in designing efficient all-solid-state electrolytes with facile synthesis processes and cost-effectiveness.

The focus of the current solid-state systems is always on enhancement of charge-transfer ability. An emerging avenue by our group is to explore conducting polymers or carbonaceous materials with integrated electrolytes having catalytic activities for triiodide (I_3^-) reduction. In our previous works,[19,20] conducting species such as polyaniline (PANi), polypyrrole, and graphene were successfully imbibed into 3D frameworks of polymer gel electrolytes, aiming at extending the reduction reaction of I_3^- from the electrolyte/CE interface to the whole structure due to the catalytic nature of such conducting polymers. Moreover, organic hole transporting materials (HTMs) such as 2,2′,7,7′-tetrakis(*N*,*N*-di-4-methoxyphenylamino)-9,9′-spirobifluorene (*spiro*-OMeTAD) have also been employed to replace electrolytes,[21,22] which leads to >5% efficiency for solid DSSCs. The oxidized dye can be regenerated by the hole injection into the HTM, which is subsequently collected by the CE to fulfill an electronic circuit. These results demonstrate the great potential of developing solid-state DSSCs based on organic HTMs. Although spiro-OMeTAD is the most favorable organic HTM for such solid solar cells, it is limited by low hole mobility and high fabrication cost.[23,24] Consequently, conjugated polymers such as polyaniline have been investigated as an alternative HTM due to their thermal stability, high conductivity, and good solubility as well as tunable optoelectronic features.[25,26]

[a]Key Laboratory of Marine Chemistry Theory and Technology, Ministry of Education, Ocean University of China, Qingdao 266100, P.R. China. E-mail: tangqunwei@ouc.edu.cn; yuyan@ouc.edu.cn; Fax: +86 532 66782533; Tel: +86 532 66782533

[b]Institute of Materials Science and Engineering, Ocean University of China, Qingdao 266100, P.R. China. E-mail: blhe@ouc.edu.cn

[c]Qingdao Collaborative Innovation Center of Marine Science and Technology, Ocean University of China, Qingdao 266100, P.R. China

[d]Key Laboratory of Advanced Technique and Preparation for Renewable Energy Materials, Ministry of Education, Yunnan Normal University, Kunming 650092, P.R. China

To explore versatile full-solid-state electrolytes having catalytic and hole-transporting features, here, we launch an experimental strategy of synthesizing simple composite electrolytes from (I^-/I_3^-)-incorporated poly(ethylene oxide)/polyaniline (PEO/PANi) for solid-state DSSC application. The resultant PEO/PANi displays intrinsic electrocatalytic activity toward the reduction of I_3^- ions, rapid charge-transfer ability, easy synthesis, and cost-effectiveness, which demonstrates the merits of extraordinary solid-state electrolytes in efficient DSSCs. In addition, the integration of conjugated structure from PANi can shorten the charge diffusion path length. More importantly, the conjugated PANi structures participate in the dye regeneration by hole injection into the PANi. To our knowledge, there are no systematic ageing studies on efficient DSSCs from solid-state electrolytes with catalytic and hole-transporting functions. DSSCs employing PEO/1.0 wt% PANi show an efficiency as high as 6.1%, which is much higher than 0.8% from the cells with (I^-/I_3^-)-incorporated PEO electrolyte and 0.1% for pristine PANi hole material.

2. Experimental

2.1 Synthesis of solid-state electrolytes

A homogenous mixture was obtained by dissolving 0.592 mL of aniline in 20 mL of 1 M HCl aqueous solution. For polymerization, 20 mL of 0.125 M ammonium peroxydisulfate aqueous solution was dipped in the above mixture within 30 min, and the polymerization reaction was carried out at 0 °C. After 3 h, the resultant reactant was rinsed with 1 M HCl aqueous solution, filtered, and finally vacuum dried at 60 °C for 24 h. The feasibility of synthesizing (I^-/I_3^-)-incorporated PEO/PANi electrolytes was confirmed by the following experimental procedures: a mixing solution consisting of I^-/I_3^- redox couples, PEO, and PANi was made by agitating 0.1 g of LiI, 0.019 g of I_2, 0.264 g of PEO ($M_w = 2\,000\,000$), and stoichiometric PANi (the dosages of PANi were adjusted to be 0.2, 0.4, 0.6, 0.8, 1.0, and 2.0 wt% of PEO weight). After vigorous agitating for 24 h, the reactant with a viscosity of approximately 100 mPa s^{-1} was cast onto a dye-sensitized TiO_2 anode for consolidation at vacuum. As a reference, the (I^-/I_3^-)-incorporated PEO electrolyte was also prepared according to the above approach at the same stoichiometric ratio.

2.2 Assembly of DSSCs

A layer of TiO_2 nanocrystal anode film with a thickness of approximately 10 μm was prepared by a sol-hydrothermal method.[27] The resultant anodes were further sensitized by immersion in a 0.50 mM ethanol solution of N719 dye. The DSSC was fabricated by sandwiching redox electrolyte between a dye-sensitized TiO_2 anode and a Pt CE (purchased from Dalian HepatChroma SolarTech Co., Ltd). The redox electrolyte consisted of 100 mM of tetraethylammonium iodide, 100 mM of tetramethylammonium iodide, 100 mM of tetrabutylammonium iodide, 100 mM of NaI, 100 mM of KI, 100 mM of LiI, 50 mM of I_2, and 500 mM of 4-*tert*-butyl-pyridine in 50 mL acetonitrile. Surlyn film (30 μm) was utilized to seal the device through hot-pressing.

2.3 Electrochemical characterizations

The electrochemical performances were recorded on a conventional CHI660E electrochemical workstation setup comprising an Ag/AgCl reference electrode, a CE composed of a Pt sheet, and a working electrode of fluorine-doped tin oxide (FTO) glass-supported electrolyte. The CV curves were recorded in a supporting electrolyte consisting of 50 mM M LiI, 10 mM I_2, and 500 mM $LiClO_4$ in acetonitrile. Bode phase measurements were carried out in a frequency range of 0.1 Hz to 10^5 kHz and an ac amplitude of 10 mV at room temperature. Both Bode plots and Tafel polarization curves were recorded by assembling symmetric dummy cells consisting of Pt CE|solid-state electrolyte|Pt CE.

2.4 Photovoltaic measurements

The photovoltaic test of the DSSC with an active area of 0.25 cm^2 was carried out by measuring the photocurrent–voltage (*J–V*) characteristic curves using a CHI660E electrochemical workstation under irradiation from simulated solar light produced by a 100 W xenon arc lamp (XQ-500 W) in an ambient atmosphere. The incident light intensity was controlled at 100 mW cm^{-2} (calibrated by a standard silicon solar cell). A black mask with an aperture area of approximately 0.25 cm^2 was applied on the surface of the DSSCs to avoid stray light.

2.5 Other characterizations

The ionic conductivity of the electrolyte was measured using a conductivity meter (DSSJ-308A, LeiCi Instruments) by consolidating electrolyte into the space between two electrodes. The instrument was calibrated with 0.01 M KCl aqueous solution prior to experiments. Fourier transform infrared (FTIR) spectrometry spectra were recorded on a Vertex 70 FTIR spectrometer (Bruker).

3. Results and discussion

Fig. 1a illustrates the synthesis process of (I^-/I_3^-)-incorporated PEO/PANi solid electrolyte as well as H-bonding between PEO and PANi.[28] Li^+ ions are embedded into the free volume regions of PEO surrounded by I^- and I_3^- counter ions. The conformational transformation of PEO segments at relaxation motion precipitates the migration of Li^+ and therefore I^-/I_3^- couples. Due to the redox nature of PANi, PANi nanostructures have been widely utilized as CE material for Pt candidates.[29–31]

Spectroscopy techniques were employed to examine the formation of functional bands and reaction mechanisms. The FTIR spectrum of the PEO/1.0 wt% PANi electrolyte is shown in Fig. 2. The observation of the bands at 800–900 cm^{-1} indicates the occurrence of PANi polymerization *via* a head-to-tail mechanism.[32] The oxygenic species are expected to interact with the conjugated structure of PANi, especially through the Q-ring (semiquinone radical cation), as has been reported in the case of nanocrystalline TiO_2 and Au.[33] Once the PANi is integrated

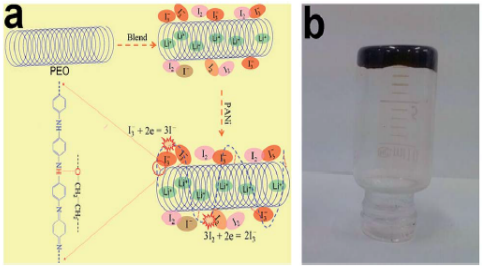

Fig. 1 (a) Schematic illustration of the synthesis of (I^-/I_3^-)-incorporated PEO/PANi solid-state electrolytes. The PANi chains are bonded onto PEO backbones by H-bonding for catalyzing I_3^- reduction. (b) Digital photograph showing the inverted PEO/1.0 wt% PANi solid electrolyte.

with PEO, the bands belonging to C–N stretching the secondary aromatic amine, and C–N–C stretching vibration in the polaron structure move from 1292 and 1231 cm^{-1} to 1280 and 1242 cm^{-1}, respectively. Additionally, the bands for C–O–C stretching and C–O stretching at 1098 and 836 cm^{-1} have also shifted to 1102 and 845 cm^{-1}, respectively. These signal the interaction between PANi (C–N) and PEO (C–O–C) through H-bonds.

Close contact of the PEO/PANi electrolyte with the Pt electrode results in a conduction of reflux electrons (the electrons traveling from the external circuit to the Pt CE) from the Pt layer to the whole solid-state electrolyte. The conducting channels formed by PANi chains function as pathways for electron transfer and can be optimized by adjusting the PANi dosage. Activated by electrons, PANi will catalyze the reduction reaction of I_3^- (Red_1: $I_3^- + 2e = 3I^-$) and I_2 (Red_2: $3I_2 + 2e = 2I_3^-$), in which Red_1 governs the entire reaction kinetics. Fig. 1b demonstrates the solid nature of PEO/PANI and shows how inversion of the vessel containing the PEO/1.0 wt% PANi electrolyte results in the electrolyte staying on the bottom with no observable flow, thus exhibiting its suitability as a solid support for solid-state PEO/PANi. Cyclic voltammetry (CV) is a commonly used technique for determining catalytic activity. The CV curve of the solid-state electrolyte was measured using a

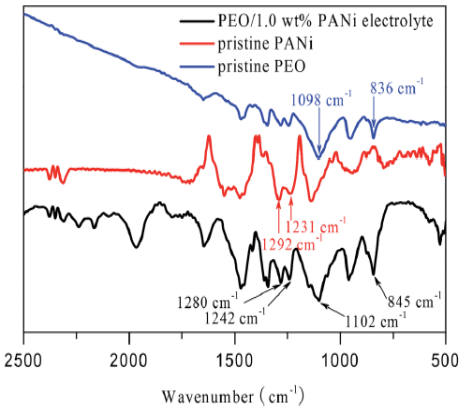

Fig. 2 FTIR spectra of PEO/1.0 wt% PANi electrolyte, pristine PANi, and PEO.

conversional three-electrode system comprising a working electrode of Cu foil-supported solid electrolyte, a Pt wire CE, and liquid electrolyte containing I^-/I_3^- redox couples. As shown in Fig. 3a, two pairs of redox peaks are observed in (I^-/I_3^-)-incorporated PEO/1.0 wt% PANi solid-state electrolyte, and the peak shape and positions are similar to pure PANi CE,[29–31] indicating that the solid-state PEO/PANi electrolyte has the same catalytic activity toward I_3^- reduction. As a reference, no redox peaks were detected from the (I^-/I_3^-)-incorporated PEO electrolyte, suggesting no catalysis of (I^-/I_3^-)-incorporated PEO.

With the aim of demonstrating the catalytic activity of solid electrolyte, the (I^-/I_3^-)-incorporated PEO/PANi film was sandwiched between two Pt electrodes. As shown in Fig. 3b, the τ of electrons at the electrolyte/Pt electrode can be calculated by the equation[34] $\tau = 1/2\pi f_p$, where f_p is the second peak frequency. Once the electrons migrate from the external circuit to the Pt layer, they either participate in the I_3^- reduction at the electrolyte/CE or transfer to the PEO/PANi system, and therefore, the average τ of electrons can be utilized to compare the synthetical kinetics of Pt and PANi toward I_3^- reduction. Apparently, the PEO/1.0 wt% PANi electrolyte exhibits a lifetime of 2.53 ms, as summarized in Table 1, which is shorter than that for other solid electrolytes.[35,36] Considering that the Pt electrode has the same catalytic performance, the enhancement of synthetical kinetics reflects the highest catalytic activity in PEO/1.0 wt% PANi electrolyte. Fig. 3c shows Tafel polarization curves recorded on the same symmetrical dummy cell as that used for Bode phase measurement. The slope for the anodic or cathodic branch represents exchange current density ($J_0 = RT/nFR_{ct}$).[37] It is apparent that the PEO/1.0 wt% PANi electrolyte has a maximum J_0 and therefore charge-transfer ability. Additionally, the intersection of the cathodic branch with the y-axis is a limiting diffusion current density ($J_{lim} = 2nFCD_n/l$),[38] a parameter dependent on the diffusion coefficient of I^-/I_3^- redox couples. The extracted J_{lim} and diffusion coefficient of redox species (D_n) from PEO/1.0 wt% PANi are much higher than those of pure PEO electrolyte, indicating that the resultant ionic conductivity is significantly elevated.

Another creative feature of the PEO/PANi electrolyte is to shorten charge (I^-/I_3^- redox couples) diffusion path length. In the DSSC with pure PEO electrolyte, the I^- ions must migrate from the electrolyte/Pt CE interface to the electrolyte/anode interface for dye recovery, whereas the I_3^- species have to transfer across the whole electrolyte system to the electrolyte/Pt CE for reduction. However, the energy from the PEO/PANi solid electrolyte can assist with accelerating $I_3^- \leftrightarrow I^-$ conversion. Assisted by the schematic diagram in Fig. 1, we can reveal the potential mechanism. It has been previously described that the interconnected channels from PANi chains distribute through the whole electrolyte, and the I_3^- ions originating from the electrolyte/anode interface only transfer to conjugated chain segments of PANi for reduction reaction instead of the electrolyte/Pt CE interface. The as-reduced I^- species also quickly return to the electrolyte/anode interface. Therefore, we can make the conclusion that the integration of PANi can shorten the I^-/I_3^- diffusion path length. Although we cannot determine the accurate path and length in the current study, it is still

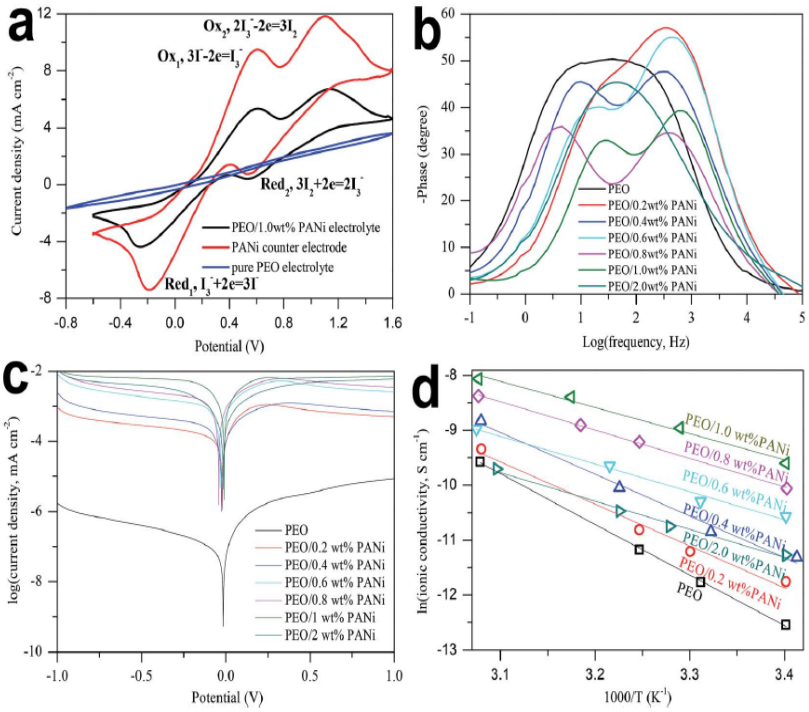

Fig. 3 (a) CV curves of (I^-/I_3^-)-incorporated PEO/1.0 wt% PANi solid-state electrolyte, PANi CE, and (I^-/I_3^-)-incorporated PEO electrolyte, (b) Bode phase plots and (c) Tafel polarization curves of symmetric dummy cells from solid electrolytes. (d) Temperature dependence of ionic conductivity for various solid-state electrolytes.

Table 1 Parameters for electrochemical data and electron lifetime

Electrolytes	R_{ct1} (Ω cm^2)	R_{ct2} (Ω cm^2)	τ (ms)	W (Ω cm^2)
PEO	36.1	621.9	—	255.2
PEO/0.2 wt% PANi	21.6	57.9	4.59	123.0
PEO/0.4 wt% PANi	9.13	21.2	4.55	108.7
PEO/0.6 wt% PANi	9.08	16.4	3.93	31.9
PEO/0.8 wt% PANi	8.82	9.59	3.90	20.4
PEO/1.0 wt% PANi	4.19	5.72	2.53	7.74
PEO/2.0 wt% PANi	8.74	58.6	3.34	86.1

pioneering to demonstrate preliminary new insights on how to elevate I_3^- reduction, shorten charge diffusion path length, and therefore markedly enhance the photovoltaic performances of solid-state DSSCs.

The ionic conductivity of the solid electrolyte is crucial to the photovoltaic performances of DSSCs. Fig. 3d shows the temperature dependence of ionic conductivities for the solid-state electrolytes, and the data are summarized in Table 2. (I^-/I_3^-)-incorporated PEO/1.0 wt% PANi exhibits the highest conductivity of 67.73 μS cm^{-1} at approximately 20 °C in comparison to 3.59 μS cm^{-1} for (I^-/I_3^-)-incorporated PEO. Compared with 5.76 mS cm^{-1} for ester-functionalized solid-state electrolyte,[17] the measured conductivity is still unimpressive, and therefore, the enhanced photovoltaic performances are responsible for the peculiar catalytic activity. The ionic conductivities of the electrolytes measured under dry air from approximately 20 to 50 °C follow an Arrhenius relationship: $\sigma = \sigma_0 \exp(-E_a/RT)$, where σ is ionic conductivity, E_a represents activation energy, T refers to absolute temperature, and R is a molar gas constant. It was found that all plots of ln σ against $1000/T$ give straight lines, which is a typical ion-conducting behavior. The E_a,[39] which is the minimum energy required for ionic conduction through (I^-/I_3^-)-incorporated PEO/PANi solid-state electrolytes at 0, 0.2, 0.4, 0.6, 0.8, 1.0, and 2.0 wt% PANi, was obtained from the slopes in the linear fit, showing 76.66, 63.46, 63.07, 43.08, 41.98, 39.66, and 42.71 kJ mol^{-1}, respectively. The E_a of the electrolyte at 1.0 wt% PANi is the lowest, indicating that ion (I^- and I_3^-) movement becomes easier in the (I^-/I_3^-)-incorporated PEO/PANi system.

Table 2 Photovoltaic parameters of DSSCs with varied solid-state electrolytes and the conductivity data. V_{oc}: open-circuit voltage; J_{sc}: short-circuit current density, FF: fill factor; η: power conversion efficiency; σ: ionic conductivity at approximately 20 °C

Electrolytes	η (%)	V_{oc} (V)	FF (%)	J_{sc} (mA cm^{-2})	σ (μS cm^{-1})
PEO	0.8	0.633	61.4	2.06	3.59
PEO/0.2 wt% PANi	1.9	0.628	75.3	4.02	7.87
PEO/0.4 wt% PANi	2.5	0.616	71.2	5.70	12.26
PEO/0.6 wt% PANi	3.8	0.642	76.1	7.78	25.82
PEO/0.8 wt% PANi	4.2	0.633	66.9	9.92	42.84
PEO/1.0 wt% PANi	6.1	0.636	70.6	13.59	67.73
PEO/2.0 wt% PANi	3.1	0.623	65.1	7.64	12.76
PANi	0.1	0.516	34.6	0.56	4.37

View Article Online
Journal of Materials Chemistry A Paper

Fig. 4a displays *J–V* curves of the DSSCs using (I^-/I_3^-)-incorporated PEO/PANi, (I^-/I_3^-)-incorporated PEO solid electrolytes, and pristine PANi hole-transporting material. The DSSC with PEO/1.0 wt% PANi electrolyte yields an optimal η of 6.1% (J_{sc} = 13.59 mA cm^{-2}, V_{oc} = 0.636 V, FF = 70.6%). The recorded efficiency is very high for the solid-state DSSCs with either pristine solid-state electrolytes or HTMs.[40–43] It is noteworthy to mention that the efficiencies for the solar cells with (I^-/I_3^-)-incorporated PEO and pristine PANi hole layers are 0.8% and 0.1%, respectively. The marked enhancement in efficiency is attributed to the synergistic effects of catalytic activity and shortened charge diffusion path length of the PEO/PANi electrolyte and hole injection into PANi. Notably, the J_{sc}, having the same order to η, signals that the rapid interconversion between I_3^- and I^- can accelerate the generation of photoelectrons from dye molecules and therefore elevate the accumulative electron density on the conduction band of TiO_2. The recorded efficiency from (I^-/I_3^-)-incorporated PEO/1.0 wt% PANi is impressive in comparison with other full-solid-state DSSCs.[27,35,44,45] In comparison with liquid-system DSSCs, the efficiency is still modest. The dye regeneration by organic HTM is generally on the picosecond time scale and at least one order of magnitude faster than that in a typical liquid electrolyte device.[46] This indicates that the charge separation and dye regeneration are not the major bottlenecks for the low device performance of the resultant DSSCs. Other limitations such as low hole mobility of organic HTMs and incomplete filling of HTM into mesoporous TiO_2 film have been considered because the derivative problems could lead to excessive interfacial recombination loss and dye regeneration hysteresis.

EIS experiments were carried out for the DSSCs to confirm the charge-transfer abilities of the resultant solid electrolytes. Nyquist plots in Fig. 4b illustrate that the R_{ct1} follows an order of PEO/1.0 wt% PANi (4.19 Ω cm^2) < PEO/2.0 wt% PANi (8.74 Ω cm^2) < PEO/0.8 wt% PANi (8.82 Ω cm^2) < PEO/0.6 wt% PANi (9.08 Ω cm^2) < PEO/0.4 wt% PANi (9.13 Ω cm^2) < PEO/0.2 wt% PANi (21.6 Ω cm^2) < PEO (36.1 Ω cm^2), which is consistent with the sequence of τ and therefore catalytic activity. However, W represents the Nernst diffusion resistance of I^-/I_3^- redox couples. A lower W denotes that I^-/I_3^- species have higher diffusion kinetics. The results of W match the ionic conductivity well.

Fast startup, multiple start/stop cycles, and good photocurrent stability are prerequisite merits for efficient solar panels that will be mounted on windows or roofs or used as portable sources. Fig. 5a exhibits the start-stop switches of a cell device employing (I^-/I_3^-)-incorporated PEO/1.0 wt% PANi electrolyte. As a reference, the switching of the cell device with (I^-/I_3^-)-incorporated PEO was also measured under the same conditions. An abrupt increase in photocurrent density at "light on" indicates the fast startup of the DSSC, whereas no delay in reaching the highest current density suggests that the incorporation of PANi with PEO accelerates hole injection and the interconversion between I_3^- and I^- as well as shortening the charge transfer path length. Interestingly, there is a depressed process in each "on" stage, indicating a diffusion-limited transport mechanism in the solid electrolytes. The schematic sketch in Fig. 5 illuminates the transfer avenues of electrons within a real solid-state DSSC employing (I^-/I_3^-)-incorporated PEO/PANi electrolyte. Generally, there are two possibilities for the photogenerated electrons released from excited dye molecules: (i) The majority of electrons flow to the conduction band of TiO_2 and further migrate to the FTO layer along conducting channels; (ii) only a minority of electrons transfer to the TiO_2/electrolyte interface and recombine with I_3^- ions.[47] Due to the fact that PANi has the ability to conduct electrons, the electrons at the TiO_2/electrolyte interface are expected to transfer to the electrolyte layer along the PANi chains and recombine with any encountered I_3^-, resulting in a decreased electron density in TiO_2 and therefore photocurrent density of a cell device. However, the conducted electrons from electrolyte/Pt interfaces participate in the reduction reaction of $I_3^- + 2e \rightarrow 3I^-$, accelerating the interconversion kinetics of I_3^- species. Although there is also a decreased process for the cell with (I^-/I_3^-)-incorporated PEO electrolyte, the reduction degree is apparently confined in the absence of PANi, whereas the lower photocurrent density reflects a relatively poor I^-/I_3^- interconversion and therefore dye recovery kinetics.

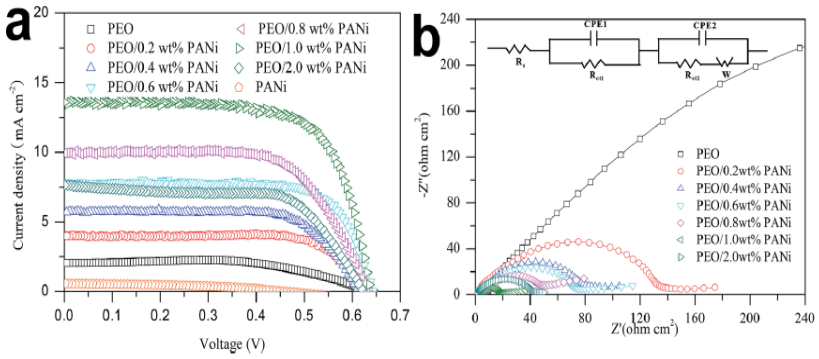

Fig. 4 (a) Characteristic *J–V* curves and (b) Nyquist EIS plots of the DSSCs with solid electrolytes. The inset gives an equivalent circuit. R_s: sheet resistance; R_{ct1}: charge-transfer resistance at the CE/electrolyte; R_{ct2}: charge-transfer resistance at the TiO_2/electrolyte interface; W: Nernst diffusion resistance corresponding to the diffusion resistance of I^-/I_3^- redox couples; CPE1/CPE2: constant phase elements.

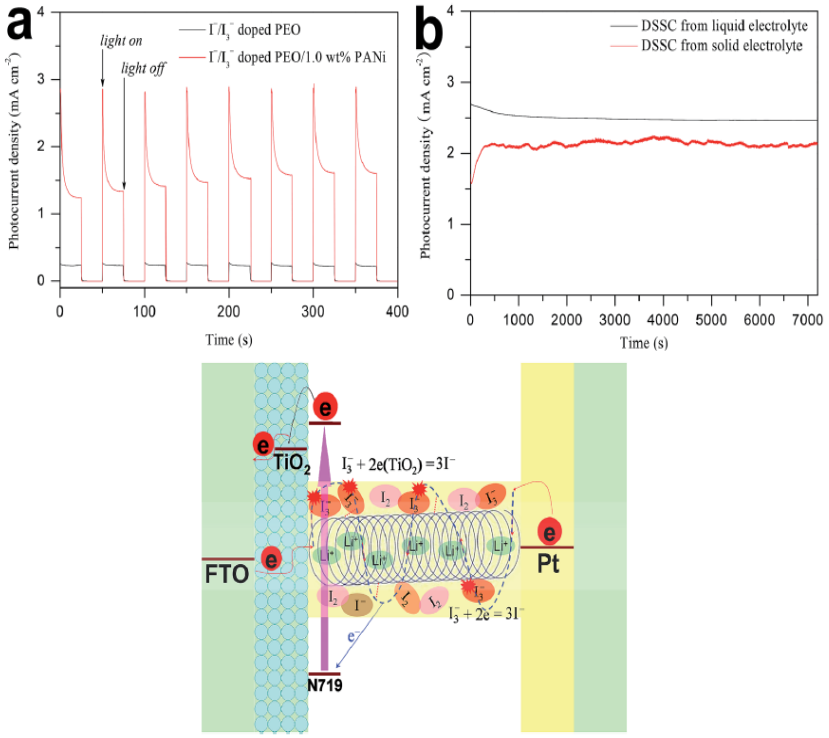

Fig. 5 (a) The start-stop switches for the DSSCs with (I^-/I_3^-)-incorporated PEO/1.0 wt% PANi and PEO solid electrolytes. (b) Photocurrent stabilities recorded on the DSSCs obtained from traditional liquid electrolyte and (I^-/I_3^-)-incorporated PEO/1.0 wt% PANi solid electrolyte. The schematic sketch illustrates the electron migration routes along PANi chains from the Pt electrode and TiO_2 anode in a real solid-state DSSC.

These conclusions are in agreement with electrochemical and photovoltaic characterizations. Moreover, the conjugated PANi can also participate in the dye regeneration by hole injection into the PANi, which is favorable to the photovoltaic performance. After eight startup cycles, no obvious decrease in photocurrent density was observed, suggesting that the solid-state DSSC has multiple startup capability. In order to compare the stability of DSSCs with traditional liquid electrolyte containing I^-/I_3^- redox couples and (I^-/I_3^-)-incorporated PEO/PANi electrolyte, their photocurrent stabilities were obtained using a chronoamperometry mode. As shown in Fig. 5b, the photocurrent densities increased by 35.1% and decreased by 8.5% for solid and liquid electrolytes under durative irradiation over 2 h,[48] respectively. Although additional research will be necessary before two-hour tests for a stable DSSC can be conducted, this preliminary result demonstrates that the stability of the cell device can be significantly enhanced by utilizing (I^-/I_3^-)-incorporated PEO/PANi solid electrolyte.[49]

4. Conclusions

In summary, full-solid-state electrolytes from (I^-/I_3^-)-incorporated PEO/PANi featuring strong catalytic activity and shortened charge diffusion path length have been fabricated by a facile blending process free of any additives and employed in assembling efficient DSSCs. It was demonstrated that (I^-/I_3^-)-incorporated PEO/1.0 wt% PANi electrolyte has an optimal charge-transfer ability and electrocatalytic activity toward I_3^- reduction. Due to the expanded reaction area where electrons can travel from the electrolyte/Pt interface to the solid-state electrolyte system and the shortened charge transfer path length, the kinetics for $I_3^- \leftrightarrow I^-$ interconversion and dye recovery and therefore electron density on the conduction band of TiO_2 have been markedly enhanced. The DSSC employing (I^-/I_3^-)-incorporated PEO/1.0 wt% PANi electrolyte exhibits an impressive power conversion efficiency of 6.1% in comparison with 0.8% from (I^-/I_3^-)-incorporated PEO and 0.1% from pristine PANi-hole-transporting-based devices. The research presented here is far from being optimized, but these profound advantages along with cost-effectiveness, mild synthesis, and scalable materials indicate that (I^-/I_3^-)-incorporated PEO/1.0 wt% PANi electrolytes are strong candidates for incorporation in full-solid-state DSSCs. Further studies are now in progress to extend this approach to other solid-state electrolytes for better photovoltaic performances.

Acknowledgements

The authors gratefully acknowledge Fundamental Research Funds for the Central Universities (201313001, 201312005), Shandong Province Outstanding Youth Scientist Foundation Plan (BS2013CL015), Shandong Provincial Natural Science Foundation (ZR2011BQ017), Research Project for the Application Foundation in Qingdao (13-1-4-198-jch), National Natural

Science Foundation of China (51102219, 51342008, U1037604), National High Technology Research and Development Program of China (2010AA09Z203, 2010AA065104), and National Key Technology Support Program (2012BAB15B02).

References

1 S. S. Li and C. W. Chen, *J. Mater. Chem. A*, 2013, **1**, 10574–10591.
2 Q. Zhang, E. Uchaker, S. L. Candelaria and G. Z. Cao, *Chem. Soc. Rev.*, 2013, **42**, 3127–3171.
3 Q. H. Li, Y. Yuan, Z. Chen, X. Jin, T. H. Wei, Y. Li, Y. C. Qin and W. F. Sun, *ACS Appl. Mater. Interfaces*, 2014, **6**, 12798–12807.
4 O. Adebanjo, B. Vaagensmith and Q. Q. Qiao, *J. Mater. Chem. A*, 2014, **2**, 10331–10349.
5 B. O'Regan and M. Grätzel, *Nature*, 1991, **353**, 737–740.
6 U. Bach and T. Daeneke, *Angew. Chem., Int. Ed.*, 2012, **51**, 10451–10452.
7 D. Kim, A. Ghicov, S. P. Albu and P. Schmuki, *J. Am. Chem. Soc.*, 2008, **130**, 16454–16455.
8 X. X. Chen, Q. W. Tang, B. L. He, L. Lin and L. M. Yu, *Angew. Chem., Int. Ed.*, 2014, **53**, 10799–10803.
9 E. J. W. Crossland, N. Noel, V. Sivaram, T. Leijtens, J. A. Alexander-Webber and H. J. Snaith, *Nature*, 2013, **495**, 215–219.
10 H. Choi, W. T. Chen and P. V. Kamat, *ACS Nano*, 2012, **6**, 4418–4427.
11 Q. W. Tang, H. Y. Cai, S. S. Yuan and X. Wang, *J. Mater. Chem. A*, 2013, **1**, 317–323.
12 M. Cheng, X. C. Yang, F. G. Zhang, J. H. Zhao and L. C. Sun, *Angew. Chem., Int. Ed.*, 2012, **51**, 9896–9899.
13 S. Mathew, A. Yella, P. Gao, R. Humphry-Baker, B. F. E. Curchod, N. Ashari-Astani, I. Tavernelli, U. Rothlisberger, M. K. Nazzeruddin and M. Grätzel, *Nat. Chem.*, 2014, **6**, 242–247.
14 J. H. Wu, Z. Lan, J. M. Lin, M. L. Huang, S. C. Hao, T. Sato and S. Yin, *Adv. Mater.*, 2007, **19**, 4006–4011.
15 Q. Dai, D. R. MacFarlane, P. C. Howlett and M. Forsyth, *Angew. Chem., Int. Ed.*, 2005, **44**, 313–316.
16 H. H. Snaith and L. Schmidt-Mende, *Adv. Mater.*, 2007, **19**, 3187–3200.
17 H. Wang, X. Zhang, F. Gong, G. Zhou and Z. S. Wang, *Adv. Mater.*, 2012, **24**, 121–124.
18 S. S. Yuan, Q. W. Tang, B. B. Hu, C. Q. Ma, J. L. Duan and B. L. He, *J. Mater. Chem. A*, 2014, **2**, 2814–2821.
19 S. S. Yuan, Q. W. Tang, B. L. He and P. Z. Yang, *J. Power Sources*, 2014, **254**, 98–105.
20 S. S. Yuan, Q. W. Tang, B. L. He and Y. Zhao, *J. Power Sources*, 2014, **260**, 225–232.
21 N. Cai, S. J. Moon, L. Cevey-Ha, T. Moehl, R. Humphry-Baker, P. Wang, S. M. Zakeeruddin and M. Grätzel, *Nano Lett.*, 2011, **11**, 1452–1456.
22 W. Zhang, Y. M. Cheng, X. Yin and B. Liu, *Macromol. Chem. Phys.*, 2011, **212**, 15–23.
23 H. J. Snaith and L. Schmidt-Mende, *Adv. Mater.*, 2007, **19**, 3187–3200.
24 I. K. Ding, J. Melas-Kyriazi, N. L. Cevey-Ha, K. G. Chittibabu, S. M. Zakeeruddin, M. Grätzel and M. D. McGehee, *Org. Electron.*, 2010, **11**, 1217–1222.
25 S. Günes, H. Neugebauer and N. S. Sariciftci, *Chem. Rev.*, 2007, **107**, 1324–1338.
26 Y. C. Hsu, L. C. Tseng and R. H. Lee, *J. Polym. Sci., Part B: Polym. Phys.*, 2014, **52**, 321–332.
27 S. S. Yuan, Q. W. Tang, B. L. He, L. Men and H. Y. Chen, *Electrochim. Acta*, 2014, **125**, 646–651.
28 J. H. Wu, Y. Li, Q. W. Tang, G. T. Yue, J. M. Lin, M. L. Huang and L. J. Meng, *Sci. Rep.*, 2014, **4**, 4028.
29 Q. Tai, B. Chen, F. Guo, S. Xu, H. Hu, B. Sebo and X. Z. Zhao, *ACS Nano*, 2011, **5**, 3795–3799.
30 Q. H. Li, J. H. Wu, Q. W. Tang, Z. Lan, P. J. Li, J. M. Lin and L. Q. Fan, *Electrochem. Commun.*, 2008, **10**, 1299–1302.
31 J. Yoon, M. Jin and M. Lee, *Adv. Mater.*, 2011, **23**, 3974–3978.
32 Q. W. Tang, J. H. Wu, X. M. Sun, Q. H. Li and J. M. Lin, *Langmuir*, 2009, **25**, 5253–5257.
33 Q. W. Tang, L. Lin, X. Zhao, K. Huang and J. H. Wu, *Langmuir*, 2012, **28**, 3972–3978.
34 X. Jiang, K. M. Karlsson, E. Gabrielsson, E. M. J. Johansson, M. Quintana, M. Karlsson, L. C. Sun, G. Boschloo and A. Hagfeldt, *Adv. Funct. Mater.*, 2011, **21**, 2944–2952.
35 Y. S. Kwon, J. Lim, I. Song, I. Y. Song, W. S. Shin, S. J. Moon and T. Park, *J. Mater. Chem.*, 2012, **22**, 8641–8648.
36 M. Wu, X. Lin, Y. Wang, L. Wang, W. Guo, D. Qi, X. Peng, A. Hagfeldt and M. Grätzel, *J. Am. Chem. Soc.*, 2012, **134**, 3419–3428.
37 M. K. Wang, A. M. Anghel, B. Marsan, N. C. Ha, N. Pootrakulchote, S. M. Zakeeruddin and M. Grätzel, *J. Am. Chem. Soc.*, 2009, **131**, 15976–15977.
38 Q. W. Tang, S. S. Yuan and H. Y. Cai, *J. Mater. Chem. A*, 2013, **1**, 630–636.
39 J. H. Yum, B. E. Hardin, S. J. Moon, E. Baranoff, F. Nüesch, M. D. McGehee, M. Grätzel and M. K. Nazeeruddin, *Angew. Chem., Int. Ed.*, 2009, **48**, 9277–9280.
40 D. Xu, C. Z. Shi, L. Wang, L. H. Qiu and F. Yan, *J. Mater. Chem. A*, 2014, **2**, 9803–9811.
41 P. J. Li, Y. Y. Duan, Q. W. Tang, B. L. He and R. Li, *J. Power Sources*, 2015, **273**, 180–184.
42 E. Lancelle-Beltran, P. Prene, C. Boscher, P. Belleville, P. Buvat and C. Sanchez, *Adv. Mater.*, 2006, **18**, 2579–2582.
43 G. K. Mor, S. Kim, M. Paulose, O. K. Varghese, K. Shankar, J. Basham and C. A. Grimes, *Nano Lett.*, 2009, **9**, 4250–4257.
44 S. R. Jang, K. Zhu, M. J. Ko, K. Kim, C. Kim, N. G. Park and A. J. Frank, *ACS Nano*, 2011, **5**, 8267–8274.
45 V. Armel, J. M. Prinkgle, P. Wagner, M. Forsyth, D. Officer and D. R. MacFarlane, *Chem. Commun.*, 2011, **47**, 9327–9329.
46 U. Bach, D. Lupo, P. Comte, J. E. Moser, F. Weissortel, J. Salbeck, H. Spreitzer and M. Grätzel, *Nature*, 1998, **395**, 583–585.
47 Z. Y. Tang, J. H. Wu, M. Zheng, J. H. Huo and Z. Lan, *Nano Energy*, 2013, **2**, 622–627.
48 B. L. He, X. Meng and Q. W. Tang, *ACS Appl. Mater. Interfaces*, 2014, **6**, 4812–4818.
49 L. Xi, X. C. Yang, J. J. Gao, H. N. Tian, J. Z. Zhao, A. Hagfeldt and L. C. Sun, *J. Am. Chem. Soc.*, 2011, **133**, 8458–8460.

ARTICLE IN PRESS JGR108_proof ■ 5 June 2015 ■ 1/8

J Ginseng Res xxx (2015) 1–8

Contents lists available at ScienceDirect

Journal of Ginseng Research

journal homepage: http://www.ginsengres.org

Research article

Diversity, distribution, and antagonistic activities of rhizobacteria of *Panax notoginseng*

Ze-Yan Fan [1,2,4], Cui-Ping Miao [2,4], Xin-Guo Qiao [2], You-Kun Zheng [2], Hua-Hong Chen [3], You-Wei Chen [2], Li-Hua Xu [2], Li-Xing Zhao [2,*], Hui-Lin Guan [1,**]

[1] School of Energy and Environment Science, Yunnan Normal University, Kunming, PR China
[2] Key Laboratory of Microbial Diversity in Southwest China of Ministry of Education and Laboratory for Conservation and Utilization of Bio-Resources, Yunnan Institute of Microbiology, Yunnan University, Kunming, PR China
[3] Department of Chemistry and Life Science, Chuxiong Normal University, Chuxiong, PR China

ARTICLE INFO

Article history:
Received 9 February 2015
Received in Revised form
2 May 2015
Accepted 9 May 2015
Available online xxx

Keywords:
antagonistic activities
diversity
Panax notoginseng
rhizobacteria

ABSTRACT

Background: Rhizobacteria play an important role in plant defense and could be promising sources of biocontrol agents. This study aimed to screen antagonistic bacteria and develop a biocontrol system for root rot complex of *Panax notoginseng*.
Methods: Pure-culture methods were used to isolate bacteria from the rhizosphere soil of notoginseng plants. The identification of isolates was based on the analysis of 16S ribosomal RNA (rRNA) sequences.
Results: A total of 279 bacteria were obtained from rhizosphere soils of healthy and root-rot notoginseng plants, and uncultivated soil. Among all the isolates, 88 showed antagonistic activity to at least one of three phytopathogenic fungi, *Fusarium oxysporum*, *Fusarium solani*, and *Phoma herbarum* mainly causing root rot disease of *P. notoginseng*. Based on the 16S rRNA sequencing, the antagonistic bacteria were characterized into four clusters, *Firmicutes*, *Proteobacteria*, *Actinobacteria*, and *Bacteroidetesi*. The genus *Bacillus* was the most frequently isolated, and *Bacillus siamensis* (Hs02), *Bacillus atrophaeus* (Hs09) showed strong antagonistic activity to the three pathogens. The distribution pattern differed in soil types, genera *Achromobacter*, *Acidovorax*, *Brevibacterium*, *Brevundimonas*, *Flavimonas*, and *Streptomyces* were only found in rhizosphere of healthy plants, while *Delftia*, *Leclercia*, *Brevibacillus*, *Microbacterium*, *Pantoea*, *Rhizobium*, and *Stenotrophomonas* only exist in soil of diseased plant, and *Acinetobacter* only exist in uncultivated soil.
Conclusion: The results suggest that diverse bacteria exist in the *P. notoginseng* rhizosphere soil, with differences in community in the same field, and antagonistic isolates may be good potential biological control agent for the notoginseng root-rot diseases caused by *F. oxysporum*, *Fusarium solani*, and *Panax herbarum*.

1. Introduction

Panax notoginseng F. H. Chen, known as Sanqi or Tianqi in Chinese, is a well-known traditional Chinese medicine [1], widely used for promotion of blood circulation, removal of blood stasis, induction of blood clotting, relief of swelling, alleviation of pain, and cure of coronary heart disease and cardiovascular disease [2]. Roots of *P. notoginseng* have been used as a variety of raw materials in Chinese medicinal products in China [3]. It has been mainly cultivated for 400 years in the Southwest regions of China, especially in Wenshan, Yunnan Province [4].

* Corresponding author. Li-Xing Zhao, Key Laboratory of Microbial Diversity in Southwest China of Ministry of Education and Laboratory for Conservation and Utilization of Bio-Resources, Yunnan Institute of Microbiology, Yunnan University, Kunming 650091, PR China.
** Corresponding author. Hui-Lin Guan, School of Energy and Environment Science, Yunnan Normal University, Kunming 650092, PR China.
E-mail addresses: zlx70@163.com (L-X. Zhao), ghl0871@163.com (H.-L. Guan).

[4] These two authors contributed equally to this work.

1226-8453/$ – see front matter Copyright © 2015, The Korean Society of Ginseng, Published by Elsevier. All rights reserved.
http://dx.doi.org/10.1016/j.jgr.2015.05.003

Please cite this article in press as: Fan Z-Y, et al., Diversity, distribution, and antagonistic activities of rhizobacteria of *Panax notoginseng*, Journal of Ginseng Research (2015), http://dx.doi.org/10.1016/j.jgr.2015.05.003

ARTICLE IN PRESS JGR108_proof ■ 5 June 2015 ■ 2/8

P. notoginseng should be grown in the field for at least 3 y to obtain high-quality raw roots [5]. However, the long period planting conditions make *P. notoginseng* vulnerable to attacks by many soil-borne pathogens including fungi, bacteria, and nematodes [5–14]. Soil-borne pathogens of *P. notoginseng* have been reported by fungi including *Fusarium oxysporum*, *Fusarium solani*, *Phoma herbarum*, *Alternaria tenuis*, *Alternaria panax*, *Cylindrocarpon destructans*, *Cylindrocarpon didynum*, *Phytophthora cactorum*, *Rhizoctonia solani*, and by bacterial pathogens including *Pseudomonas* sp., *Ralstonia* sp., and by parasitic nematodes, such as *Ditylenchus* sp., *Rhabditis elegans*, and *Meloidogyne* spp. [15,16]. In this case, the control of soil-borne diseases mainly relies on chemical pesticides, fungicides, and crop rotation. Chemical pesticides and fungicides are less effective on the soil-borne diseases, and lead to reduction of *P. notoginseng* quality. Meanwhile, pesticides may be toxic to crops, humans, animals [17,18]. However, a 15–20 y replanting interval leads to the lack of appropriate fields, resulting in searching for a new field or/and transferring to a less appropriate field to grow *P. notoginseng*.

It is obvious that pesticides and less appropriate cultivation soil are not suitable to control the qualities of *P. notoginseng* required by the good agriculture practice (GAP). Friendly approaches are urgently needed to effectively manage or solve the questions. Biological control, a bioeffector method with other living organisms to control pests (insects, mites, weeds, and plant diseases) [19], has been considered as effective approaches. Soil bacteria, especially rhizospheric ones with antagonistic properties, demonstrate biological control effectiveness to some plant diseases, and are the most potential for development of biological control agents (BCAs) [20–29]. However, little is known about the bacterial diversity, distribution, and ecological effects in the cultivation soil of *P. notoginseng*. In this study, we developed the investigation of rhizobacteria of 3-y-old *P. notoginseng* from Wenshan, Yunnan Province, by culture-dependent methods. The bacterial isolates were also challenged by three pathogens, *F. oxysporum*, *F. solani*, and *P. herbarum*, which are associated with the root rot disease of *P. notoginseng*.

2. Materials and methods

2.1. Soil sample collection and isolation of soil bacteria

Soil samples were collected from a 3-y-old *P. notoginseng* plantation in Wenshan, Yunnan Province, in July 2014. Ten healthy and 10 root-rot notoginseng plants were uprooted. Soil was collected around 3 cm from the main roots, and rhizosphere soil was gently stripped from the roots. Root-adjacent soil and rhizospheric soil were mixed together, recorded as healthy plant soil and diseased plant soil, respectively. Uncultivated soil sample was obtained without planting notoginseng at the same field. All the soil samples were placed into sterile plastic bags, transferred to the laboratory in 24 h, and kept at 4°C before treatment.

Bacterial isolation were developed using serial dilution spread plate method. Ten grams of soil was mixed with 90 mL of sterile phosphate buffered saline (PBS, pH 7.4) and stirred for 30 min at 200 rpm. The soil suspension was left to stand for 10 min at room temperature to allow settling of large particles, tenfold serial diluted in PBS (from 10^{-2} to 10^{-5}). Then, 80 μL of the first to fourth and fifth diluents were transferred to petri dishes with LB agar medium (10.0 g peptone, 5.0 g yeast extract, 10.0 g NaCl, and 13.0 g agar, 1.0 L distilled water, pH 7.2) and nutrition agar (NA) medium (3.0 g beef extract, 5.0 g peptone, 5.0 g NaCl, 13.0 g agar, 1.0 L distilled water, pH 7.0). The plates were incubation at 28°C, and bacterial colonies were selected and purified according to their morphological characteristics.

2.2. Screening of antagonistic bacteria against fungal pathogens

Three fungal pathogens *F. oxysporum*, *F. solani*, and *P. herbarum* were isolated from the rotten root of *P. notoginseng*, and their pathogenicity was verified [15,16]. The target fungi were cultured on potato dextrose agar (PDA) medium (200.0 g fresh potato, 20.0 g starch, 13.0 g agar, 1.0 L distilled water, pH not adjusted). The antagonism of all bacterial isolates was checked with respect to the ability to suppress fungal growth. Antifungal bioassay was performed with the dual culture and agar well diffusion plate on PDA.

In dual culture tests, a 5-mm mycelial disk of pathogenic fungus, collected from the edge of actively growing colonies, was placed into the center of plates containing fresh PDA. Bacterial isolates were grown around the target fungus with a distance of 3.0 cm (Fig. 1A, 1B). The dual culture plates were incubation at 28°C, and checked every 12 h after inoculation. All treatments were tested in duplicate.

In agar well plate tests, a 200-μL fresh culture of pathogenic fungus with concentration of 10^8 spores/mL was mixed with 250 mL PDA and evenly distributed into 10 petri dishes (90 mm). On each plate, four wells of 5 mm in diameter were made (Fig. 1C). Bacterial isolates were cultured in nutrient broth medium at 28°C, 135 rpm for 72 h. The bacterial suspension was adjusted to the final cell concentration of 10^7 cfu/mL with nutrient broth medium. Next, 200 μL of suspension was added to each well, and the same volume of nutrient broth was used as control. All treatments were tested in duplicate.

2.3. Phylogenetic analysis

The genomic DNA of bacteria was extracted using a bacterial genomic DNA extraction kit (BioTeke Corporation, China, Cat#:

Fig. 1. Bioassay of soil bacteria toward (A) *Fusarium solani*, (B) *Phoma herbarum*, and (C) *Fusarium oxysporum*.

Please cite this article in press as: Fan Z-Y, et al., Diversity, distribution, and antagonistic activities of rhizobacteria of *Panax notoginseng*, Journal of Ginseng Research (2015), http://dx.doi.org/10.1016/j.jgr.2015.05.003

ARTICLE IN PRESS JGR108_proof ■ 5 June 2015 ■ 3/8

DP2001) and 16S ribosomal RNA (rRNA) genes were amplified by PCR using the primer pair of PA (5′-AGAGTTTGATCCTGGCTCAG-3′) and PB (5′-AAGGAGGTGATCCAGCCGCA-3′) [30]. The PCR reaction was performed in 50 μL reaction mixture containing 1 μL of DNA, 1 μL forward primer (10μM), 4 μL reverse primer (10μM), 5 μL reaction buffer (10×), 4 μL dNTP (each 2.5μM), 0.5 μL of *Taq* DNA polymerase (500 U), and 37.5 μL sterile double-distilled water. The PCR cycling protocol consisted of an initial denaturation at 94 °C for 4 min, followed by 32 cycles of 94 °C for 1 min, 56 °C for 1 min and 72 °C for 1 min, and a final elongation step of 72 °C for 10 min. As a negative control, the DNA was replaced by sterile double-distilled water. The PCR amplified products were separated by agarose gel electrophoresis, and sequenced on an ABI Prism 3730 sequencer at Sangon Biotech (Shanghai, China). The sequences of the isolates were searched in EzBioCloud (http://www.ezbiocloud.net/). The approximate phylogenetic affiliations and 16S rRNA gene sequence similarities were determined according to Altschul et al [31]. Sequences chimera checking were performed by the program CHIMERA CHECK of the Ribosomal Database Project (RDP) [32], and sequences with a potential chimeric structure were excluded. The alignments of 16S rRNA genes sequences were performed using Clustal X [33]. The 16S rRNA sequences were used to construct a phylogenetic tree with the Kimura 2-parameter model and MEGA (version 5.05) by bootstrap analysis of 1,000 replications [34,35]. The partial 16S rRNA gene sequences obtained for rhizosphere antagonistic bacteria have been deposited in GenBank with accession numbers: KP214596–KP214641.

3. Results

3.1. Number of bacteria in different soil samples

A total of 279 bacterial isolates were obtained from healthy soil, diseased soil, and uncultivated soil. The distribution is 132 isolates (47.3%) in diseased soil, 77 isolates (27.6%) in healthy soil, and 70 isolates (25.1%) in uncultivated soil (Table 1). Bacteria in diseased soil are much richer than that in healthy and uncultivated soil.

3.2. Antagonistic soil bacteria associated with P. notoginseng

All the soil bacterial isolates were evaluated for their antagonistic activity to three fungal pathogens, *F. oxysporum*, *F. solani*, and *P. herbarum*. Eighty-eight isolates (31.5% of the total) displayed antagonistic activities against at least one of fungal pathogens (Table 1). The large number of bacterial antagonists was isolated from healthy plant soil which offered 37 strains (48.1% of 77 isolates from healthy plant soil), followed by uncultivated soil (27, 38.6% of 70 isolates from uncultivated land), diseased soil (24, 18.2% of 132 isolates from diseased soil).

Among the 88 antagonists, 33 displayed antagonistic activity only against one of three fungal pathogens (Table 2), which included four strains obtained from healthy plant soil toward *F. oxysporum* and 19 toward *F. solani*, and 10 toward *P. herbarum*.

Table 1
Number of Rhizospheric Bacteria in Different Soil Samples of *Panax notoginseng*

No. of bacteria	Soil sample			Sum
	Healthy plant soil	Root rot plant soil	Uncultivated soil	
Total	77	132	70	279
Antagonistic bacteria	37	24	27	88
Percent of antagonistic bacteria (%)	48.1	18.2	38.6	31.5

Table 2
The Number of Rhizobacteria Obtained from Different Soil of *Panax notoginseng* with Antagonisitic Activities Toward Three Host Plant Pathogens of Root Rot Disease

Pathogens	No. of rhizosphere antagonistic bacteria			Sum
	Healthy plant soil	Root rot plant soil	Uncultivated soil	
Fo	4	0	0	4
Fs	8	7	4	19
Ph	4	5	1	10
Fo & Fs	1	1	4	6
Fo & Ph	1	1	0	2
Fs & Ph	9	5	10	24
Fo, Fs, & Ph	10	5	8	23
Total	37	24	27	88

[a]Fo = Fusarium oxysporum, Fs = Fusarium solani, Ph = Phoma herbarum. Q1

There were 32 bacterial isolates showing antagonistic activities against two of three pathogens (Table 2). Among them, six isolates had antagonistic activity to *F. oxysporum* and *F. solani*, two isolates against *F. oxysporum* and *P. herbarum*, and 24 isolates against *F. solani* and *P. herbarum*.

Furthermore, there were 23 isolates exhibiting different antagonistic activities against all the three fungal pathogens (Table 2).

3.3. Phylogeny of bacterial antagonists from P. notoginseng

The molecular analysis revealed that the 88 strains belonged to four bacterial groups, *Actinobacteria*, *Bacteroidetes*, *Firmicutes*, and *Proteobacteria* (Table 3, Fig. 2). Over half of the soil antagonistic bacteria (46 isolates, 52.3% of total) were accommodated in the *Firmicutes* group. In this group, *Bacillus* spp. represented the majority, with 42 isolates (91.3%). Phylogenetic analysis based on the 16S rRNA gene sequences indicated that most active *Bacillus* isolates were closely related to the species *Bacillus thuringiensis* (12 isolates, 28.6%), *Bacillus aryabhattai* (9 isolates, 21.4%) and *Bacillus siamensis* (5 isolates, 11.9%) with the sequence similarities of 99.9–100.0%, 98.9–100.0%, and 99.1–100.0%, respectively. Other 16 *Bacillus* isolates were assigned to nine species according to their sequence similarities: *Bacillus subtilis* subsp. *subtilis* (2 isolates), *Bacillus simplex* (1), *Bacullus anthracis* (1), *B. atrophaeus* (2), *Bacillus cereus* (4), *Bacillus licheniformis* (1), *Bacillus safensis* (1), *Bacillus toyonensis* (3), and *Bacillus acidiceler* (1). The four remaining *Firmicutes* were respectively assigned to *Paenibacillus chitinolyticus (1)*, *Paenibacillus jamilae* (2), and *Brevibacillus brevis (1)* with similarity > 99.4%. Twenty-six isolates belonging to *Proteobacteria* were assigned to 10 genera: *Achromobacter*, *Acinetobacter*, *Acidovorax*, *Brevundimonas*, *Delftia*, *Ensifer*, *Leclercia*, *Pseudomonas*, *Rhizobium*, and *Stenotrophomonas*. *Pseudomonas* included nine species: *Pseudomonas baetica* (1 isolates), *Pseudomonas helmanticensis* (1), *Pseudomonas hunanensis* (2), *Pseudomonas koreensis* (2), *Pseudomonas libanensis* (1), *Pseudomonas moorei* (1), *Flavimonas oryzihabitans* (1), *Pseudomonas chlororaphis* subsp. *aurantiaca* (1), and *Pseudomonas chlororaphis* subsp. *piscium* (2) with sequence similarities of 98.3–100.0%.

In *Actinobacteria*, 11 isolates were assigned to nine species of five genera (*Arthrobacter*, *Microbacterium*, *Brevibacterium*, *Pantoea*, and *Streptomyces*) based on their similarities of 98.8–100.0%. Five isolates in *Bacteroidetes* were phylogenetically related to *Chryseobacterium vrystaatense* (1), *Chryseobacterium joostei* (2), *Chryseobacterium contaminans* (1), and *Chryseobacterium stationis* (1) with a similarity > 98.0%.

3.4. Distribution of antagonists in different soil types

The distribution of active isolates obtained from healthy plant soil, diseased plant soil, and uncultivated soil of *P. notoginseng* is

Please cite this article in press as: Fan Z-Y, et al., Diversity, distribution, and antagonistic activities of rhizobacteria of *Panax notoginseng*, Journal of Ginseng Research (2015), http://dx.doi.org/10.1016/j.jgr.2015.05.003

Table 3
Antagonistic Activities of Rhizospheric Bacteria Towards *Fusarium oxysporum* (Fo), *Fusarium solani* (Fs), and *Panax herbarum* (Ph) in Different Soil Types from *Panax notoginseng* and Their Closest Phylogenetic Affiliation (Based on Partial 16S Ribosomal RNA Gene Sequences)

Isolate(Accession No.)	Closest NCBI library strain & accession No.	Antagonistic activities			Similarity(%)	Origin of strains
		Fo	Fs	Ph		
Hs02(KP214617)	*Bacillus siamensis* KCTC 13613(AJVF01000043)	+++	+++	+++	100.0	Hs
Hs03(KP214604)	*Streptomyces cinnamonensis* NBRC 15873(AB184707)	+	++	++	100.0	Hs
Hs04(KP214608)	*Brevibacterium epidermidis* NCDO 2286(X76565)	–	–	+	100.0	Hs
Hs05(KP214613)	*Bacillus subtilis* subsp. *subtilis* NCIB 3610(ABQL01000001)	–	+	–	99.7	Hs
Hs07(KP214619)	*Bacillus toyonensis* BCT-7112(CP006863)	–	+	–	100.0	Hs
Hs08(KP214632)	*Bacillus safensis* FO-36b(ASJD01000027)	–	+	++	99.9	Hs
Hs09(KP214630)	*Bacillus atrophaeus* JCM 9070(AB021181)	+++	+++	+++	99.9	Hs
Hs10(KP214629)	*Pseudomonas hunanensis* LV(JX545210)	–	+	–	98.6	Hs
Hs11(KP214626)	*Pseudomonas baetica* a390(FM201274)	–	+	–	99.6	Hs
Hs13(KP214612)	*Pseudomonas chlororaphis* subsp. *piscium* JF3835(FJ168539)	+	+	++	98.1	Hs
Hs14(KP214624)	*Paenibacillus jamilae* CECT 5266(AJ271157)	+	+	++	100.0	Hs
Hs16(KP214618)	*Bacillus thuringiensis* ATCC 10792(ACNF01000156)	–	+	–	99.9	Hs
Hs18(KP214628)	*Pseudomonas libanensis* CIP 105460(AF057645)	–	+	++	99.9	Hs
Hs20(KP214602)	*Acidovorax radicis* N35(AFBG01000030)	–	+	–	97.3	Hs
Hs22(KP214611)	*Bacillus cereus* ATCC 14579(AE016877)	–	+	–	100.0	Hs
Hs23(KP214640)	*Arthrobacter pascens* DSM 20545(X80740)	–	–	+	99.6	Hs
Hs24(KP214631)	*Flavimonas oryzihabitans* IAM 1568(D84004)	–	–	++	98.3	Hs
Hs25(KP214622)	*Chryseobacterium vrystaatense* LMG 22846(AJ871397)	–	+	+	97.2	Hs
Hs26(KP214627)	*Pseudomonas moorei* RW10(AM293566)	+	+	–	99.5	Hs
Hs31(KP214606)	*Ensifer adhaerens* LMG 20216(AM181733)	+	–	+	100.0	Hs
Hs33(KP214603)	*Achromobacter spanius* LMG 5911 (AY170848)	+	–	–	99.9	Hs
Hs35(KP214609)	*Brevundimonas olei* MJ15(GQ250440)	+	–	–	99.7	Hs
Rw01(KP214601)	*Leclercia adecarboxylata* GTC 1267(AB273740)	+	+	+	99.9	Rw
Rw04(KP214633)	*Bacillus licheniformis* ATCC 14580(AE017333)	+++	+++	+++	98.9	Rw
Rw07(KP214610)	*Chryseobacterium joostei* LMG 18212(AJ271010)	+	+	+	98.6	Rw
Rw12(KP214634)	*Bacillus sonorensis* NBRC 101234(AYTN01000016)	–	–	++	98.8	Rw
Rw14(KP214600)	*Delftia lacustris* DSM 21246(EU888308)	++	+	–	99.3	Rw
Ry07(KP214638)	*Arthrobacter ureafaciens* DSM 20126(X80744)	–	+	++	99.5	Ry
Ry09(KP214614)	*Arthrobacter nicotinovorans* DSM 420(X80743)	–	+	++	100.0	Ry
Ry11(KP214615)	*Pseudomonas koreensis* Ps 9-14(AF468452)	++	–	++	99.6	Ry
Rn02(KP214616)	*Pseudomonas helmanticensis* OHA11(HG940537)	–	+	++	99.7	Rn
Rn06(KP214623)	*Paenibacillus chitinolyticus* IFO 15660(AB021183)	–	++	–	99.9	Rn
Rn08(KP214607)	*Brevibacillus brevis* NBRC 100599 (AP008955)	+++	+++	+++	99.4	Rn
Rn11(KP214620)	*Bacillus aryabhattai* B8W22(EF114313)	+	+	+	100.0	Rn
Rn12(KP214605)	*Stenotrophomonas chelatiphaga* LPM-5 (EU573216)	–	+	–	98.2	Rn
Rn13(KP214639)	*Arthrobacter arilaitensis* Re117(FQ311875)	–	+	–	100.0	Rn
Rn16(KP214597)	*Rhizobium radiobacter* ATCC 19358(AJ389904)	–	+++	+++	100.0	Rn
Rn17(KP214598)	*Pantoea septica* LMG 5345(EU216734)	–	+	–	98.8	Rn
Rn18(KP214599)	*Microbacterium maritypicum* DSM 12512(AJ853910)	–	–	++	99.4	Rn
Ul06(KP214596)	*Acinetobacter calcoaceticus* DSM 30006(AIEC01000170)	+	+	+	99.9	Ul
Ul07(KP214625)	*Pseudomonas chlororaphis* subsp. *aurantiaca* NCIB 10068(DQ682655)	–	+	+	99.7	Ul
Ul09(KP214637)	*Bacillus anthracis* ATCC 14578(AB190217)	+	+	+	100.0	Ul
Ul10(KP214636)	*Bacillus acidiceler* CBD 119(DQ374637)	+	+	–	99.9	Ul
Ul11(KP214635)	*Bacillus simplex* NBRC 15720(AB363738)	–	+	–	100.0	Ul
Ul16(KP214621)	*Acinetobacter oleivorans* DR1(CP002080)	+	+	–	100.0	Ul
Ul21(KP214641)	*Chryseobacterium contaminans* C26(KF652079)	–	+	–	99.3	Ul

+++, highly active; ++ medially active; +, showing active; –, not active; Hs, rhizosphere soil of healthy plants; NCBI, National Center of Biotechnology Information; Rw, Ry Rn, rhizosphere soil of root-rotten plants; Ul, uncultivated soil.

presented in Fig. 2. At the phylum level, isolates in *Firmicutes*, *Proteobacteria*, *Actinobacteria*, and *Bacteroidetes* were widely distributed in all types of the soils. *Firmicutes* was dominant and accounted for 45.9%, 29.2%, and 66.7% in healthy plant soil, diseased plant soil, and uncultivated soil, respectively. The isolates in *Bacteroidetes* are much less than that in the other three phyla. Analysis at the genera level showed that *Bacillus* and *Pseudomonas* were present in all soil types and represented the majority of antagonists, especially *Bacillus* spp. which accounted for 45.9% of antagonists in healthy plant soil, 29.2% in diseased plant soil, and 66.7% in uncultivated soil. *Arthrobacter* was distributed in soils with *P. notoginseng*, and not found in the uncultivated soil (Fig. 3).

For all isolated genera, *Acidovorax*, *Brevibacterium*, and *Flavimonas* were exclusively found in healthy plant soil, whereas *Delftia*, *Leclercia*, *Brevibacillus*, *Microbacterium*, *Pantoea*, *Rhizobium*, and *Stenotrophomonas* were only present in diseased plant soil. *Acinetobacter* was only found in uncultivated soil (Fig. 3).

4. Discussion

Soil-plant-microorganisms shape a complex soil ecosystem, and soil microorganisms are regarded as an important and essential component of soil quality due to their crucial activities in many ecosystem processes [36–38]. Soil bacteria exist in almost every soil type. Some soil bacteria are developed as biocontrol agents (BCAs), an environment-friendly approach to control pests (insects, mites, weeds, and plant diseases) [19]. *Panax* plants, *P. ginseng*, *P. notoginseng*, and *Panax quniquefolius*, are perennial plants and mainly cultivated in artificial shads for several years. Cultivation can be affected by diseases caused by soil-borne and foliar pathogens [16,39–42]. In recent years, using antagonistic microorganisms to control ginseng diseases is increasing [40–43], but few researches on *P. notoginseng* [44]. In our study, we screened 88 antagonistic strains out of 279 soil bacterial isolates of *P. notoginseng* with three pathogens as targets, and analyzed their

Please cite this article in press as: Fan Z-Y, et al., Diversity, distribution, and antagonistic activities of rhizobacteria of *Panax notoginseng*, Journal of Ginseng Research (2015), http://dx.doi.org/10.1016/j.jgr.2015.05.003

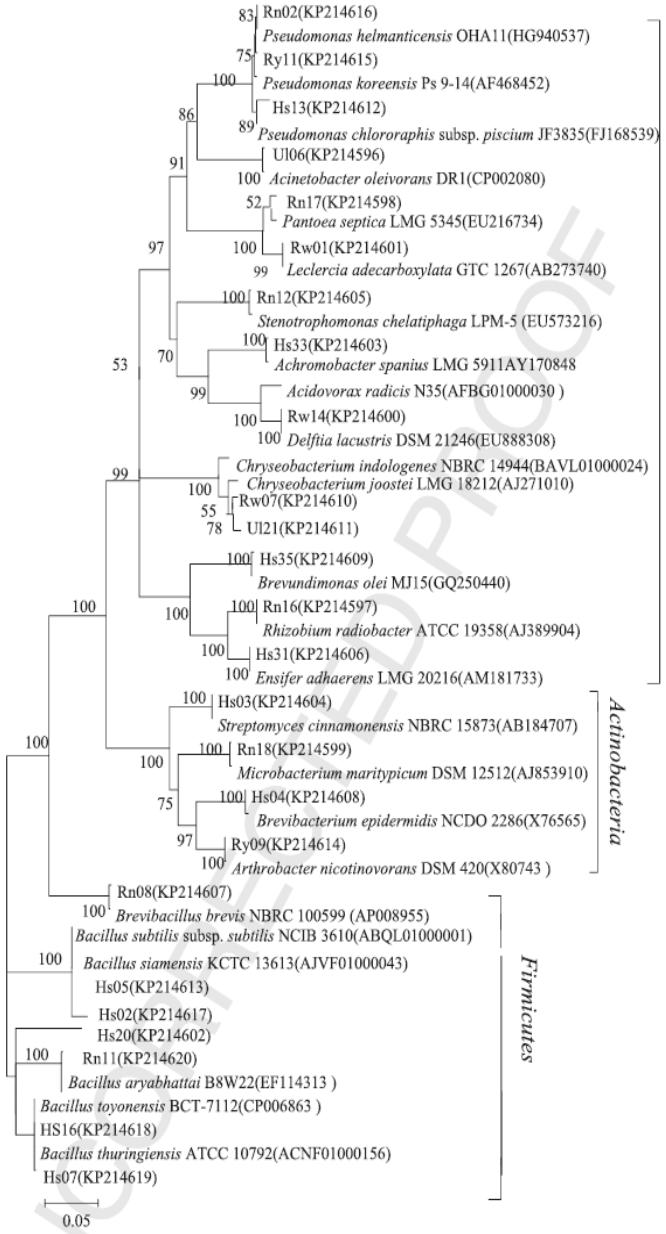

Fig. 2. Neighbor-joining tree of partial rhizospheric antagonistic bacteria obtained from five different soil types (healthy plant soil, root rot plant soil, uncultivated soil) of *Panax notoginseng* and their closest relatives based on the 16S ribosomal RNA gene sequences. The significance of each branch is indicated by a bootstrap value calculated for 1,000 subsets. The scale bar represents 0.05 substitutions per base position. Accession numbers are given in parenthesis. Only values above 50% were shown. The rhizospheric antagonistic bacteria of *P. notoginseng* were encoded as Hs01-37, Ry01-15, Rw01-14, Rn01-19, and Ul01-27.

phylogenetic diversity and distribution in healthy plant soil, diseased plant soil, and uncultivated soil.

Phylogenetic analysis indicated that soil antagonistic bacteria of *P. notoginseng* were assigned into four bacterial groups: *Actinobacteria*, *Bacteroidetes*, *Firmicutes*, and *Proteobacteria*. In four bacterial groups, *Firmicutes*, especially *Bacillus* species, represented the majority of the active isolates. This result is similar to that of endophytic bacteria [15]. Meanwhile, the member of *Proteobacteria* showed high diversity in taxonomy, and were assigned into 10 genera, 19 species. *Actinobacteria* and *Proteobacteria* were also discovered from two types of soil associated to *P. notoginseng*. Most of the *Bacillus* species exist in the rhizosphere soil of *P. notoginseng*. This is the same as other results described in medical plants [43]. Additionally, species in *Arthrobacter*, *Brevibacterium*, *Microbacterium*, *Streptomyces*, *Pantoea*, *Brevibacillus*, *Paenibacillus*, *Delftia*, *Leclercia*, *Achromobacter*, *Brevundimonas*, *Ensifer*, *Stenotrophomonas*, and *Pseudomonas* detected as antagonistic endophytic bacteria from *P. notoginseng* have not been reported from cultivation soil of

Please cite this article in press as: Fan Z-Y, et al., Diversity, distribution, and antagonistic activities of rhizobacteria of *Panax notoginseng*, Journal of Ginseng Research (2015), http://dx.doi.org/10.1016/j.jgr.2015.05.003

ARTICLE IN PRESS JGR108_proof ■ 5 June 2015 ■ 6/8

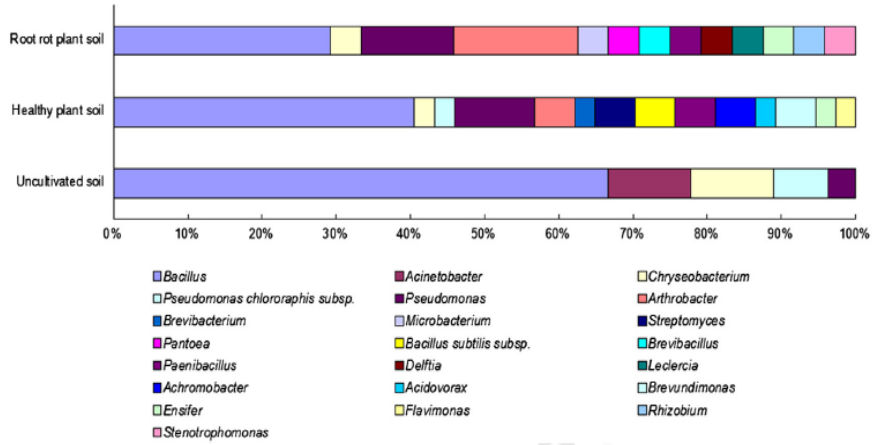

Fig. 3. Comparative taxonomic distribution of rhizospheric antagonistic bacteria from different soil types of *P. notoginseng*. The different color show to different taxa.

Table 4
Species Affiliations of Rhizobacteria from *Panax notoginseng* with Antagonistic Activities Toward *Fusarium oxysporum* (Fo), *Fusarium solani* (Fs), and *Panax Herbarum* (Ph) Q12

Phylogenetic species	Antagonistic activities						
	Fo[a]	Fs[b]	Ph[c]	Fo & Fs	Fo & Ph	Fs & Ph	Fo, Fs, & Ph
Bacillus siamensis						1	4
Bacillus atrophaeus							1
Bacillus cereus		2				2	
Bacillus safensis						1	
Bacillus thuringiensis		2	1			8	1
Bacillus toyonensis		2					1
Bacillus licheniformis							1
Bacillus sonorensis			1				
Bacillus simplex		1					
Bacillus acidiceler				1			
Bacillus anthracis							1
Bacillus aryabhattai			1	2		4	2
Bacillus subtilis subsp. *subtilis*		1				1	
Brevibacterium epidermidis			1				
Brevundimonas olei	2						
Brevibacillus brevis							1
Paenibacillus chitinolyticus		1					
Paenibacillus jamilae							2
Ensifer adhaerens		1			1		
Chryseobacterium vrystaatense						1	
Chryseobacterium indologenes		1					
Coryseobacterium contaminans							2
Corynebacterium stationis		1					
Flavimonas oryzihabitans			1				
Pseudomonas hunanensis		1					1
Pseudomonas libanensis						1	
Pseudomonas moorei				1			
Pseudomonas baetica		1					
Pseudomonas koreensis			1		1		
Pseudomonas helmanticensis						1	
Pseudomonas chlororaphis subsp. *piscium*							2
Pseudomonas chlororaphis subsp. *aurantiaca*						1	
Streptomyces cinnamonensis							2
Stenotrophomonas chelatiphaga		1					
Arthrobacter nitroguajacolicus			1				
Arthrobacter nicotinovorans			1			1	
Arthrobacter ureafaciens						1	
Arthrobacter arilaitensis		1					
Arthrobacter pascens			1				
Achromobacter spanius	2						
Acidovorax radicis		1					
Leclercia adecarboxylata							1
Delftia lacustris				1			
Microbacterium maritypicum			1				
Pantoea septica		1					
Rhizobium radiobacter						1	
Acinetobacter calcoaceticus		1					1
Acinetobacter oleivorans				1			
Total	4	19	10	6	2	24	23

Please cite this article in press as: Fan Z-Y, et al., Diversity, distribution, and antagonistic activities of rhizobacteria of *Panax notoginseng*, Journal of Ginseng Research (2015), http://dx.doi.org/10.1016/j.jgr.2015.05.003

ARTICLE IN PRESS JGR108_proof ■ 5 June 2015 ■ 7/8

P. notoginseng [15]. Antagonistic bacteria existed in all types of tested soil in the same field of *P. notoginseng*, but the number and species of antagonists are different (Table 1). There are 23 species in 11 genera in healthy plant soil, 14 species in four genera in uncultivated soil, and 20 species in 13 genera in diseased soil, respectively. The biodiversity of antagonistic bacteria in diseased soil is much lower than that in healthy plant soil and uncultivated soil (Table 1). It is unclear what affect the patterns of distribution and diversity of soil bacteria as the soil properties and agromanagement approaches are not different in the same plantation, especially for healthy plant soil and diseased soil. Further studies might focus on the interaction between fungal pathogens and soil bacteria.

More than half of soil antagonistic bacteria of *P. notogingseng* (55 strains, 62.5% of antagonistic bacteria) showed antagonistic activities against two or three pathogens (Table 4). Most of these antagonists were assigned into the genus *Bacillus*. *Bacillus* spp. have been frequently reported as the major rhizobacteria for diverse host plants and used to suppress pathogens. In this study, *Bacillus siamensis*, *Bacillus thuringiensis*, and *Bacillus aryabhattai* were the most dominant and widespread species within different rhizosphere soil types of *P. notoginseng*, inferring that the three species can offer a promising way to screen biocontrol *Bacillus* strains for *P. notoginseng*. Moreover, other *Bacillus* spp. isolates, such as *Bacillus atrophaeus*, *Bacillus toyonensis*, *Bacillus licheniformis*, and *Bacillus subtilis* subsp. *subtilis*, with broad-spectrum antagonisms also are promising candidates to resist root rot disease of *P. notoginseng*. Further studies should be taken to evaluate their antagonistic ability in pot and field condition.

In conclusion, this investigation provides the first evidence of bacterial differences in healthy plant soil and diseased plant soil of *P. notoginseng*, although antagonistic bacteria are harbored in all types of tested soil. This will provide some clues for us to understand the interaction among soil bacteria, pathogenic fungi, and plant.

Acknowledgments

This work was partly supported by the grants from the National Natural Science Foundation of China (Nos. 31100009 and 41361075), Yunnan Natural Science Foundation (No. 2013FA015), and Foundation of Yunnan Educational Committee (No. ZD2013008).

References

[1] Park HJ, Kim DH, Park SJ, Kim JM, Ryu JH. Ginseng in traditional herbal prescriptions. J Ginseng Res 2012;36:225–41.
[2] Kim JH. Cardiovascular diseases and *Panax ginseng*: a review on molecular mechanisms and medical applications. J Ginseng Res 2012;36:16–26.
[3] Dong TT, Cui XM, Song ZH, Zhao KJ, Ji ZN, Lo CK, Tsim KW. Chemical assessment of roots of *P. notoginseng* in China: regional and seasonal variations in its active constituents. J Agric Food Chem 2003;51:4617–23.
[4] Wei JX, Du YC. Modern science research and application of *P. notoginseng*. Kunming: Yunnan Science and Technology Press; 1996.
[5] Guo HB, Cui XM, An N, Cai GP. Sanchi ginseng (*P. notoginseng* (Burkill) F. H. Chen) in China: distribution, cultivation and variations. Genet Resour Crop Evol 2006;57:453–60.
[6] Chen YJ, Wang YY, Feng GQ, Li ZY. Relationship between root rot of *P. notoginseng* and ecological conditions. Yunnan Agric Sci Technol 2001;6:33–5.
[7] Wang CL, Cui XM, Li ZY, He CF, Yu SF, Luo WF. Studies on relationship between root rot on *P. notoginseng* (Burk). F. H. Chen and its environmental conditions. Chin J Chin Materia Medica 1998;23:714–6.
[8] Kim JH, Jeon YH, Park H, Lee BD, Cho DH, Park BY, Khan Z, Kim YH. The root lesion nematode, *Pratylenchus subpenetrans*, on ginseng (*Panax ginseng*) in Korea. Nematology 2006;8:637–9.
[9] Lee SK. *Fusarium* species associated with ginseng (*Panax ginseng*) and their role in the root-rot of ginseng plants. Res Plant Dis 2004;10:248–59.
[10] Lee JH, Yu YH, Kim YH, Ohh SH, Park WM. Morphological characteristics and pathogenicity of *Alternaria* isolates causing leaf and stem blights and black root rot of Korea ginseng. Korea J Plant Pathol 1990;6:13–20.
[11] Jeon YH, Park H, Lee BD, Yu YH, Chang SP, Kim SG, Hwang I, Kim YH. First description of crown gall disease on ginseng. Plant Pathol J 2008;24:207–10.
[12] Ohh SH, Lee SK, Lee JH, Han SC. New root rot disease of *Panax ginseng* due to *Ditylenchus* destructor Thorne. Korea J Plant Prot 1983;22:181–5.
[13] Ohh SH, Yu YH, Cho DH, Lee JH, Kim YH. Effect of chemical treatments on population changes of *Ditylenchus* destructor and responses of *Panax ginseng*. Korea J Plant Prot 1986;25:169–73.
[14] Yu YH, Ohh SH. Research on ginseng diseases in Korea. Korea J Ginseng Sci 1993;17:61–8.
[15] Ma L, Cao YH, Cheng MH, Huang Y, Mo MH, Wang Y, Yang JZ, Yang FX. Phylogenetic diversity of bacterial endophytes of *P. notoginseng* with antagonistic characteristics towards pathogens of root-rot disease complex. Antonie van Leeuwenhoek 2013;103:299–312.
[16] Miao ZQ, Li SD, Liu XZ, Chen YJ, Li YH, Wang Y, Xia ZY, Zhang KQ. The causal microorganisms of *P. notoginseng* root rot disease. Scientia Agricultura Sinica 2006;39:1371–8.
[17] Handelsman J, Stabb EV. Biocontrol of soil borne plant pathogens. Plant Cell 1996;8:1855–69.
[18] Ma CZ, Li SD, Gu ZR, Chen YJ, Zhou W, Wang Y, Liu YZ, Xia ZY, Li YH. Measures of integrated control of root rot complex of continuous cropping *P. notoginseng* and their control efficacy. Acta Agriculture Shanghai 2006;22:63–8.
[19] Flint ML, Dreistadt SH, Clark JK. Natural Enemies Handbook: the illustrated guide to biological pest control. Oakland: University of California Press; 1998.
[20] Hameeda B, Rupela OP, Reddy G. Antagonistic activity of bacteria inhabiting composts against soil-borne plant pathogenic fungi. Indian J Microbiol 2006;46:389–96.
[21] Berg G, Opelt J, Zachow C, Lottmann J, Götz M, Costa R, Smalla K. The rhizosphere effect on bacteria antagonistic towards the pathogenic fungus *Verticillium differs* depending on plant species and site. FEMS Microbiol Ecol 2006;56:250–61.
[22] Patkowska E, Konopiński M. Antagonistic activity of selected bacteria occurring in the soil after root chicory cultivation. Plant Soil Environ 2014;60:320–4.
[23] Landa BB, Hervás A, Bettiol W, Jiménez-Díaz RM. Antagonistic activity of bacteria from the chickpea rhizosphere against *Fusarium oxysporum* f. sp. *Ciceris*. Phytoparasitica 1997;25:305–18.
[24] Raaijmakers JM, Paulitz TC, Steinberg C, Alabouvette C, Yvan ML. The rhizosphere: a playground and battlefield for soilborne pathogens and beneficial microorganisms. Plant Soil 2009;321:341–61.
[25] Whipps JM. Ecological considerations involved in commercial development of biological control agents for soil-borne diseases. In: JD van Elsas, Trevors JT, Wellington EMH, editors. Modern Soil Microbiology. New York: Marcel Dekker Inc; 1997. p. 525–46.
[26] Huang Y, Ma L, Fang DH, Xi JQ, Zhu ML, Mo MH, Zhang KQ, Jie YP. Isolation and characterisation of rhizosphere bacteria active against *Meloidogyne incognita*, *Phytophthora nicotianae* and the root knot-black shank complex in tobacco. Pest Manag Sci 2014. http://dx.doi.org/10.1002/ps.3820. Q
[27] Adam M, Heuer H, Hallmann J. Bacterial antagonists of fungal pathogens also control root-knot nematodes by induced systemic resistance of tomato plants. PLoS One 2014;9:e90402.
[28] Haas D, Défago G. Biological control of soil-borne pathogens by fluorescent pseudomonads. Nat Rev Microbiol 2005;3:307–19.
[29] Essghaier B, Fardeau ML, Cayol JL, Hajlaoui MR, Boudabous A, Jijakli H, Sadfi-Zouaoui N. Biological control of grey mould in strawberry fruits by halophilic bacteria. J Appl Microbiol 2009;106:833–46.
[30] Qin S, Li J, Chen HH, Zhao GZ, Zhu WY, Jiang CL, Xu LH, Li WJ. Isolation, diversity, and antimicrobial activity of rare actinobacteria from medicinal plants of tropical rain forests in Xishuangbanna, China. Appl Environ Microbiol 2009;75:6176–86.
[31] Altschul SF, Madden TL, Schaffer AA, Zhang J, Zhang Z, Miller W, Lipman DJ. Gapped BLAST and PSI-BLAST: a new generation of protein database search programs. Nucleic Acids Res 1997;25:3389–402.
[32] Maidak BL, Olsen GJ, Larsen N, Overbeek R, Mc-Caughey MJ, Woese CR. The RDP (ribosomal database project). Nucleic Acids Res 1997;25:109–10.
[33] Thompson JD, Gibson TJ, Plewniak F, Jeanmougin F, Higgens DG. The Clustal X windows interface, flexible strategies for multiple sequences alignment aided by quality analysis tools. Nucleic Acids Res 1997;24:4876–82.
[34] Kimura M. A simple method for estimating evolutionary rate of base substitutions through comparative studies of nucleotide sequences. J Mol Evol 1980;16:111–20.
[35] Tamura K, Peterson D, Peterson N, Stecher G, Nei M, Kumar S. MEGA 5: molecular evolutionary genetics analysis using maximum likelihood, evolutionary distance, and maximum parsimony methods. Mol Biol Evol 2011;28:2731–9.
[36] Garbeva P, van Veen JA, van Elsas JD. Microbial diversity in soil: selection of microbial populations by plant and soil type and implications for disease suppressiveness. Annu Rev Phytopathol 2004;42:243–70.
[37] Atkinson A, Watson CA. The beneficial rhizosphere: a dynamic entity. Appl Soil Ecol 2000;48:99–104.
[38] Kent AD, Triplett EW. Microbial communities and their interactions in soil and rhizosphere ecosystems. Annu Rev Microbiol 2002;56:211–36.
[39] Song JY, Seo MW, Kim SI, Nam MH, Lim HS, Kim HG. Genetic diversity and pathogenicity of *Cylindrocarpon destructans* isolates obtained from Korean *Panax ginseng*. Mycobiology 2014;42:174–80.

Please cite this article in press as: Fan Z-Y, et al., Diversity, distribution, and antagonistic activities of rhizobacteria of *Panax notoginseng*, Journal of Ginseng Research (2015), http://dx.doi.org/10.1016/j.jgr.2015.05.003

[40] Lee SG. *Fusarium* species associated with ginseng (*Panax ginseng*) and their role in the root-rot of ginseng plants. Res Plant Dis 2004;10:248–59.
[41] Rahman M, Punja ZK. Biological control of damping-off on American ginseng (*Panax quinquefolius*) by *Clonostachys rosea* f. *catenulate* (= *Gliocladium catenulatum*). Can J Plant Pathol 2007;29:203–7.
[42] Ryu H, Park H, Suh DS, Jung GH, Park J, Lee BD. Biological control of *Colletotrichum panacicola* on *Panax ginseng* by *Bacillus subtilis* HK-CSM-1. J Ginseng Res 2014;38:215–9.
[43] Song M, Yun HY, Kim YH. Antagonistic *Bacillus* species as a biological control of ginseng root rot caused by *Fusarium* cf. *incarnatum*. J Ginseng Res 2014;38:136–45.
[44] Guo R, Liu X, Li S, Miao Z. In vitro inhibition of fungal root-rot pathogens of *Panax notoginseng* by rhizobacteria. Plant Pathol J 2009;25:70–6.

Please cite this article in press as: Fan Z-Y, et al., Diversity, distribution, and antagonistic activities of rhizobacteria of *Panax notoginseng*, Journal of Ginseng Research (2015), http://dx.doi.org/10.1016/j.jgr.2015.05.003

Antonie van Leeuwenhoek (2015) 108:627–632
DOI 10.1007/s10482-015-0518-z

ORIGINAL PAPER

Skermanella rubra sp. nov., a bacterium isolated from the desert of Xinjiang, China

Zheng-Yun Zhang · Xu-Hong Gao · Yun-Jiao Zhang · Man Jia · Xiao-Ju Lu · Yong-Chun Ma · Fei Tian · Qiong Xie · Shu-Kun Tang

Received: 16 February 2015 / Accepted: 23 June 2015 / Published online: 30 June 2015

Abstract A Gram-negative, pink-coloured, rod-shaped, motile bacterium, designated YIM 93097^T, was isolated from the desert soil collected from Xinjiang province of China. Strain YIM 93097^T was found to grow at 20–45 °C (optimum 28–37 °C), pH 5.0–7.0 (optimum pH 7.0) and 0–8 % (w/v) NaCl (optimum 1 %, w/v). Based on 16S rRNA gene sequence similarity studies, it belongs to the genus *Skermanella*. The 16S rRNA gene sequence similarity was identified to be 98.7 % to *Skermanella xinjiangensis* CCTCC AB 207153^T while the DNA–DNA hybridization value was found to be only 48.1 %. The predominant isoprenoid quinone was determined to be Q-10. The major fatty acids were identified to be $C_{16:0}$, $C_{18:1}\omega7c$ and summed feature 4 (consisting of $C_{17:1}$ anteiso B/iso I). The major polar lipids were identified as phosphatidylcholine, phosphatidylglycerol, phosphatidylethanolamine, diphosphatidylglycerol, two unidentified phospholipids and one unidentified aminolipid. The DNA G+C content was found to be 67.2 mol %. The analysis of the genotypic and phenotypic data indicated that strain YIM 93097^T belongs to a novel species of the genus *Skermanella*, for which the name *Skermanella rubra* sp. nov. is proposed. The type strain is YIM 93097^T (=DSM 21389^T=CCTCC AB 2015161^T).

Keywords *Skermanella rubra* · Polyphasic taxonomy · 16S rRNA gene

Zheng-Yun Zhang and Xu-Hong Gao contributed equally to this work.

Electronic supplementary material The online version of this article (doi:10.1007/s10482-015-0518-z) contains supplementary material, which is available to authorized users.

Z.-Y. Zhang · X.-H. Gao · X.-J. Lu
Energy and Environment Science College, Yunnan Normal University, Education Ministry Key Laboratory of Renewable Energy Advanced Materials and Manufacturing Technology, Kunming 650092, People's Republic of China

Z.-Y. Zhang · M. Jia · X.-J. Lu · Y.-C. Ma · F. Tian · S.-K. Tang (✉)
Key Laboratory of Microbial Diversity in Southwest China, Ministry of Education, and Laboratory for Conservation and Utilization of Bio-resources, Yunnan Institute of Microbiology, Yunnan University, Kunming 650091, People's Republic of China
e-mail: tangshukun@ynu.edu.cn

Y.-J. Zhang
Department of Microbiology and Immunology, Faculty of Basic Medical Sciences, Kunming Haiyuan Medical College, Kunming 650031, People's Republic of China

Q. Xie
State Key Laboratory of Space Medicine Fundamentals and Application, China Astronaut Research and Training Center, Beijing 100094, People's Republic of China

Introduction

Conglomeromonas largomobilis subsp. *parooensis* was first proposed by Skerman et al. (1983). Later, this species was transferred to the new genus *Skermanella* as the type species, *Skermanella parooensis*, based on polyphasic taxonomic data (Sly and Stackebrandt 1999). The genus *Azospirillum* of the *Alphaproteobacteria* is phylogenetically closely related to the genus *Skermanella*. At present, this genus comprises four species with validly published names: *S. parooensis* (Sly and Stackebrandt 1999), *Skermanella aerolata* (Weon et al. 2007), *Skermanella xinjiangensis* (An et al. 2009) and *Skermanella stibiiresistens* (Luo et al. 2012). These species were isolated from fresh water, air, desert and coal-mining soil, respectively. Species of this genus are characterized as being Gram-negative, motile, possessing a high DNA G+C content (mol %), strictly aerobic and unable to fix nitrogen. The aim of the present study is to clarify the taxonomic position of strain YIM 93097^T within the genus *Skermanella*.

Materials and methods

Isolation and maintenance of organism

Strain YIM 93097^T was isolated from a desert soil sample collected from Xinjiang province, China. Strain YIM 93097^T was isolated by the standard dilution plating technique at 37 °C on Glucose-Tryptone-Yeast (GTY) medium (Tang et al. 2010) and incubated at 37 °C for 2 weeks. Colonies were picked off and repeatedly re-streaked onto GTY medium to confirm its purity. Strain YIM 93097^T was maintained on GTY slants at 4 °C, and as glycerol suspension (20 %, v/v) at −80 °C for long-term preservation. The reference type strain *S. xinjiangensis* CCTCC AB 207153^T was obtained from the China Center for Type Culture Collection (CCTCC), and used in physiological, biochemical and chemotaxonomic analysis. For chemotaxonomic and molecular studies strain YIM 93097^T and the reference type strain were growth on GTY medium at 37 °C for 3 days.

Phylogenetic and genetic analysis

PCR amplification of the 16S rRNA gene was carried out according to established procedures (Li et al. 2007). The 16S rRNA gene sequences of related taxa were obtained from the EzTaxon-e server Database (http://eztaxon-e.ezbiocloud.net/) (Kim et al. 2012). Multiple alignments were carried out using CLUSTAL_X (Thompson et al. 1997). Phylogenetic analyses were performed using three tree-making algorithms, the neighbour-joining (NJ; Saitou and Nei 1987), maximum-likelihood (ML; Felsenstein 1981) and maximum-parsimony (MP; Fitch 1971) methods. The NJ, MP and ML phylogenetic trees were reconstructed using MEGA version 5.0 (Tamura et al. 2011). The topology of the phylogenetic trees was assessed using bootstrap analysis based on 1000 replications (Felsenstein 1985).

The G+C content of the DNA was determined as described elsewhere (Mesbah et al. 1989). DNA–DNA hybridization between strain YIM 93097^T and *S. xinjiangensis* CCTCC AB 207153^T was carried out according to previously described method (Huß et al. 1983).

Morphological, physiological and biochemical characteristics

Cell morphology was examined by using transmission electron microscopy after growth on modified GTY medium at 37 °C for 3 days. Cells were prepared for transmission electron microscopy as described by Golyshina et al. (2000). Gram staining was performed using the standard Gram reaction test and confirmed by using the KOH lysis (Cerny 1978). Cell motility was detected by the presence of turbidity throughout the semisolid medium (Leifson 1960) and the hanging-drop method (Skerman 1967). The presence of endospores was examined using malachite green staining (Smibert and Krieg 1994) under a light microscope. Catalase activity was tested by production of bubbles after the addition of a drop of 3 % H_2O_2. Oxidase activity was tested by oxidation of tetramethyl-*p*-phenylenediamine. Anaerobic growth was determined on modified GTY medium, using the GasPak Anaerobic System (BBL) according to the manufacturer's instructions at 37 °C for 15 days. Salt tolerance was examined in GTY medium supplemented with 0-20 % (w/v, from 0 to 20 at intervals of 1 % NaCl increment). The effects of temperature on growth were assessed at 4, 10, 15, 20, 28, 37, 45, 50 and 55 °C. Growth at different pH concentrations (from 4.0 to 10.0 at intervals of 1 pH unit) was tested as described

by Xu et al. (2005). Carbon and nitrogen source utilization was tested using Biolog GEN III Micro-Plates according to the manufacturer's instructions. Several other physiological and biochemical features were assessed using API 20E, API 50CH and API ZYM test systems and tests were conducted according to the manufacturers' instructions (bioMérieux).

Chemotaxonomy analysis

Bacterial cells were collected after their growth on TSA, pH 7.0 at 37 °C for 3 days, under aerobic conditions. Isoprenoid quinones were isolated according to the method of Minnikin et al. (1984) and separated by HPLC (Collins 1985). Cellular fatty acids were extracted, methylated and analyzed using the Microbial Identification System (MIDI) according to the manufacturer's instructions (Sasser 1990). The fatty acid methyl esters were analyzed by using the Microbial Identification software package of TSBA6 (Sherlock Version 6.1). Polar lipids were extracted and examined by using two-dimensional Thin Layer Chromatography (TLC) and identified as described elsewhere (Minnikin et al. 1984).

Results and discussion

Molecular characterization

Phylogenetic analysis revealed that strain YIM 93097^T is a member of the genus *Skermanella* and closely related to *S. xinjiangensis* CCTCC AB 207153^T, with 16S rRNA gene sequence similarity of 98.7 %. The sequence similarities between strain YIM 93097^T and other validly named species of the genus *Skermanella* were all lower than 97 % (*S. aerolata* 5416T-32^T, 93.8 %; *S. stibiiresistens* SB22^T, 92.7 %; *S. parooensis* ACM 2042^T, 92.3 %). In the phylogenetic tree based on the neighbour-joining algorithm, strain YIM 93097^T clustered with the type strain of *S. xinjiangensis* CCTCC AB 207153^T at a high bootstrap resampling value of 100 % (Fig. 1). The topology was

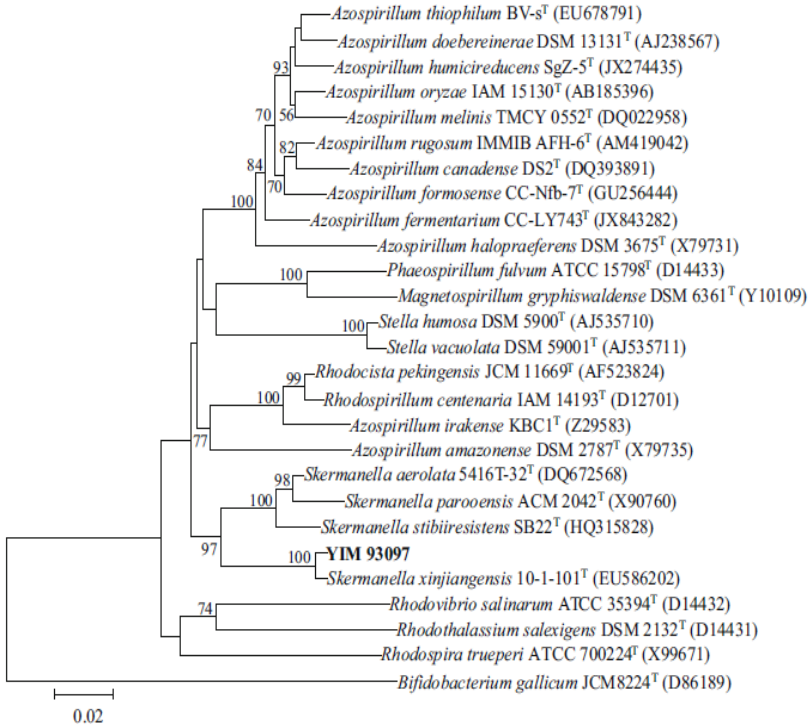

Fig. 1 The phylogenetic afficiation of strain YIM 93097^T on the neighbor-joining phylogenetic tree based on 16S rRNA gene. Numbers on branch nodes are bootstrap values (1000 resamplings, only values above 50 % are shown). *Bar*, 0.02 substitutions per nucleotide position

similar to those of the phylogenetic trees constructed using maximum-parsimony and maximum-likelihood methods.

The DNA G+C content was found to be 67.2 mol %, which is within the range of the DNA G+C content of the genus *Skermanella* (65.0–69.6 mol %). The DNA–DNA hybridization value between strain YIM 93097^T and *S. xinjiangensis* CCTCC AB 207153^T was found to be 48.1 %. This value is below the 70 % cut-off recommended for genomic species discrimination (Wayne et al. 1987), clearly suggesting strain YIM 93097^T represents a novel species in the genus *Skermanella*.

Phenotypic and biochemical characteristics

Strain YIM 93097^T was found to be a strictly aerobic, Gram-negative, rod-shaped bacterium. The cells were found to be motile (Fig. S1), and endospores were not observed. While strain YIM 93097^T was observed to form circular, convex and pink colonies with wrinkles on GTY medium at 37 °C after 3 days, the reference type strain *S. xinjiangensis* CCTCC AB 207153^T formed circular, convex and light-pink colonies without wrinkles. The physiological and biochemical characteristics of strain YIM 93097^T are given in the species description and other phenotypic characteristics of strain YIM 93097^T and other species of the genus *Skermanella* are presented in Table 1.

Chemotaxonomic characterisation

The major isoprenoid quinone of YIM 93097^T and the reference strain *S. xinjiangensis* CCTCC AB 207153^T was determined to be Q-10. The major fatty acids of YIM 93097^T comprise $C_{16:0}$, $C_{18:1}\omega7c$ and summed feature 4 (consisting of $C_{17:1}$ anteiso B/iso I). The differences between fatty acids composition of strain YIM 93097^T and other species of the genus *Skermanella* are as follows (Table 2). Strain YIM 93097^T contains

Table 1 Phenotypic characteritics of strain YIM 93097^T and type strains of the genus *Skermanella*

Characteristic	1	2	3	4	5
Source	Soil	Soil	Air	Soil	Fresh water
Temperature range (°C)	20–45	17–37	5–35	4–37	10–37
Growth pH range	5–7	6–9	4–9	5–9	6–9
Salinity range (%, w/v)	0–8	0–4	0–5	0–4	0–2
Urease	−	+	−	−	+
Gelatin hydrolysis	−	−	+	−	+
Glucose fermentation	−	−	+	−	+
Tween 80 hydrolysis	−	−	+	−	+
Assimilation of					
Acetate	−	+	−	−	+
L-Arabinose	−	W	+	−	+
Propionate	−	+	+	−	+
Mannitol	−	+	+	−	+
Salicin	+	−	−	+	−
L-Fucose	+	−	+	−	+
D-Sorbitol	−	−	+	−	+
Rhamnose	−	+	−	+	+
N-Acetylglucosamine	W	−	W	−	−
Inositol	−	−	+	+	−
Enzyme activities					
Esterase lipase (C8)	+	+	−	−	+
α-Glucosidase	−	−	−	W	+
β-Glucosidase	+	+	−	W	+
DNA G + C content (mol %)	67.2	68.8	65.0	69.6	67.2

Strains: 1, YIM 93097^T; 2, *S. xinjiangensis* CCTCC AB 207153^T; 3, *S. aerolata* 5416T-32^T; 4, *S. stibiiresistens* SB22^T; 5, *S. parooensis* ACM 2042^T. Data are taken from Luo et al. (2012) and from this study

+ positive, − negative, *w* weak

Table 2 Cellular fatty acids composition of strain YIM 93097^T and *Skermanella xinjiangensis* CCTCC AB 207153^T

Fatty acid	YIM 93097^T	CCTCC AB 207153^T
$C_{16:0}$	6.7	8.0
$C_{16:0}$ 3-OH	1.1	1.2
$C_{16:1}\omega11c$	1.2	0.8
$C_{17:1}\omega6c$	1.0	1.0
$C_{18:0}$	0.6	1.0
$C_{18:1}\omega5c$	3.6	2.0
$C_{18:1}\omega7c$	66.5	74.5
$C_{18:1}$ 2-OH	tr	1.7
Summed features*		
2	2.5	2.0
3	1.3	1.3
4	8.7	–

* Fatty acids that could not be separated by gas chromatography using the Microbial Identification System software were considered as summed features. Summed feature 2 contains $C_{14:0}$ 3-OH and/or iso-$C_{16:1}$ I; Summed feature 3 consists $C_{16:1}\omega6c$ and/or $C_{16:1}\omega7c$ and summed feature 4 contains $C_{17:1}$ anteiso B/iso I. Data are percentages of total fatty acids; fatty acids that represent <0.5 % in the two strains are omitted. Fatty acids were determined in this study; the two strains were incubated to the exponential phase under the same conditions. The analysis was performed with two replications for each strain

– not detected, *tr* trace amount (<0.5 %)

higher amounts of the major fatty acids summed feature 4 ($C_{17:1}$ anteiso B/iso I), and significantly lower amounts of $C_{16:0}$ and summed feature 3 ($C_{16:1}\omega6c$ and/or $C_{16:1}\omega7c$). The polar lipids of strain YIM 93097^T were identified as phosphatidylcholine, phosphatidylglycerol, phosphatidylethanolamine, diphosphatidylglycerol, two unidentified phospholipids and one unidentified aminolipid (Fig. S2). This polar lipid profile is typical for the genus *Skermanella*.

Taxonomic conclusion

Phylogenetic and chemotaxonomic analyses (major fatty acids, polar lipids and isoprenoid quinone) support the assignment of strain YIM 93097^T to the genus *Skermanella*. However, several characteristic physiological and biochemical features (listed in Table 1) and genetic distinctness support taxonomic standing of strain YIM 93097^T at the species level. On the basis of genotypic, phenotypic and phylogenetic evidence, strain YIM 93097^T should be classified as a novel species of the genus *Skermanella*, for which the name *Skermanella rubra* sp. nov. is proposed.

Description of *Skermanella rubra* sp. nov

Skermanella rubra (rub'ra. L. fem. adj. rubra red).

Cells are Gram-negative, aerobic, rod-shaped and motile by means of a single polar or subpolar flagellum. Endospores are not observed. Colonies are circular, convex and pink with wrinkles on GTY medium after 3 day-growth at 37 °C. Growth occurs on GTY medium at 20–45 °C (optimum 28–37 °C), 0–8.0 % (w/v) NaCl (optimum 0–2.0 %, w/v) and pH 5.0–7.0 (optimum pH 7.0). Positive for catalase and oxidase. The following compounds are utilized as sole carbon or nitrogen sources: acetoacetic acid, aztreonam, dextrin, D-fructose-6-PO_4, L-fucose, fusidic acid, L-galactonic acid lactone, D-galacturonic acid, glucuronamide, D-glucuronic acid, guanidine HCl, lincomycin, minocycline, nalidixic acid, niaproof 4, potassium tellurite, rifamycin SV, sodium butyrate, tetrazolium blue, tetrazolium violet, troleandomycin and vancomycin (Biolog GEN III MicroPlates). Positive for β-galactosidase activity (API 20E). Negative for arginine dihydrolase, gelatin hydrolysis, glucose fermentation, indole production and urea hydrolysis (API 20E). Assimilates acetonate. Does not assimilate lysine, sodium citrate and sodium thiosulfate (API 20E). Acid is produced from *N*-acetylglucosamine (weakly), aesculin, amygdalin, D-arabinose (weakly), L-arabinose, arbutin, cellobiose (weakly), D-fucose (weakly), L-fucose (weakly), 5-ketogluconate (weakly), D-lyxose, maltose, potassium gluconate, D-ribose (weakly), salicin, D-tagatose, D-xylose, L-xylose and methyl β-D-xylopyranoside (API 50CH). Enzyme activities are positive for alkaline phosphatase, esterase lipase (C4), esterase lipase (C8), β-glucosidase, leucine arylamidase and naphthol-AS-BI-phosphohydrolase. Negative for acid phosphatase, α-chymotrypsin, cystine arylamidase, β-fucosidase, α-galactosidase, β-galactosidase, β-glucuronidase, α-glucosidase, N-acetylb-glucosaminidase, lipase (C14), trypsin and valine arylamidase,α-mannosidase (API ZYM system). The predominant isoprenoid

quinone is Q-10. The major fatty acids are $C_{16:0}$, $C_{18:1}\omega7c$ and summed feature 4 (consisting of $C_{17:1}$ anteiso B/iso I). The polar lipids are phosphatidylcholine, phosphatidylglycerol, phosphatidylethanolamine, diphosphatidylglycerol, two unidentified phospholipids and one unidentified aminolipids The DNA G+C content of the type strain is 67.2 mol %.

Acknowledgments This research was supported by grants from the National Natural Science Foundation of China (No. 31270055) and China Space Medico-Engineering Advanced Research Project (No. 2012SY541106).

References

An H, Zhang L, Tang Y, Luo X, Sun T, Li Y, Wang Y, Dai J, Fang C (2009) *Skermanella xinjiangensis* sp. nov., isolated from the desert of Xinjiang, China. Int J Syst Evol Microbiol 59:1531–1534

Cerny G (1978) Studies on the aminopeptidase test for the distinction of gram-negative from gram-positive bacteria. Appl Micorbiol Biot 5:113–122

Collins MD (1985) Analysis of isoprenoid quinones. Methods Microbiol 18:329–366

Felsenstein J (1981) Evolutionary trees from DNA sequences: a maximum likelihood approach. J Mol Evol 17:368–376

Felsenstein J (1985) Confidence limits on phylogenies: approach using the bootstrap. Evolution 39:783–791

Fitch WM (1971) Toward defining the course of evolution: minimum change for a specific tree topology. Syst Zool 20:406–416

Golyshina OV, Pivovarova TA, Karavaiko GI, Kondratéva TF, Moore ER, Abraham WR, Lünsdorf H, Timmis KN, Yakimov MM, Golyshin PN (2000) *Ferroplasma acidiphilum* gen. nov., sp. nov., an acidophilic, autotrophic, ferrous-iron-oxidizing, cell-walllacking, mesophilic member of the *Ferroplasmaceae* fam. nov., comprising a distinct lineage of the *Archaea*. Int J Syst Evol Microbiol 50:997–1006

Huß VAR, Festl H, Schleifer KH (1983) Studies on the spectrophotometric determination of DNA hybridization from renaturation rates. Syst Appl Microbiol 4:184–192

Kim OS, Cho YJ, Lee K, Yoon SH, Kim M, Na H, Park SC, Jeon YS, Lee JH et al (2012) Introducing EzTaxon-e: a prokaryotic 16S rRNA gene sequence database with phylotypes that represent uncultured species. Int J Syst Evol Microbiol 62:716–721

Leifson E (1960) Atlas of bacterial flagellation. Academic Press, London

Li WJ, Xu P, Schumann P, Zhang YQ, Pukall R, Xu LH, Stackebrandt E, Jiang CL (2007) *Georgenia ruanii* sp. nov., a novel actinobacterium isolated from forest soil in Yunnan (China) and emended description of the genus *Georgenia*. Int J Syst Evol Microbiol 57:1424–1428

Luo G, Shi Z, Wang H, Wang G (2012) *Skermanella stibiiresistens* sp. nov., a highly antimony-resistant bacterium isolated from coal-mining soil, and emended description of the genus *Skermanella*. Int J Syst Evol Microbiol 62:1271–1276

Mesbah M, Premachandran U, Whitman WB (1989) Precise measurement of the G+C content of deoxyribonucleic acid by high-performance liquid chromatography. Int J Syst Bacteriol 39:159–167

Minnikin DE, O'Donnell AG, Goodfellow M, Alderson G, Athalye M, Schaal A, Parlett JH (1984) An integrated procedure for the extraction of bacterial isoprenoid quinones and polar lipids. J Microbiol Methods 2:233–241

Saitou N, Nei M (1987) The neighbor-joining method: a new method for reconstructing phylogenetic trees. Mol Biol Evol 4:406–425

Sasser M (1990) Identification of bacteria by gas chromatography of cellular fatty acids. USFCC Newslett 20:1–6

Skerman VBD (1967) A guide to the identification of the genera of bacteria, 2nd edn. Williams & Wilkins, Baltimore

Skerman VBD, Sly LI, Williamson ML (1983) *Conglomeromonas largomobilis* gen. nov., sp. nov., a sodium-sensitive, mixedflagellated organism from fresh waters. Int J Syst Bacteriol 33:300–308

Sly LI, Stackebrandt E (1999) Description of *Skermanella parooensis* gen. nov., sp. nov. to accommodate *Conglomeromonas largomobilis* subsp. *parooensis* following the transfer of *Conglomeromonas largomobilis* subsp. *largomobilis* to the genus *Azospirillum*. Int J Syst Bacteriol 49:541–544

Smibert RM, Krieg NR (1994) Phenotypic characterization. In: Gerhardt P, Murray RGE, Wood WA, Krieg NR (eds) Methods for general and molecular bacteriology. American Society for Microbiology, Washington, pp 607–654

Tamura K, Peterson D, Peterson N, Stecher G, Nei M, Kumar S (2011) MEGA5: molecular evolutionary genetics analysis using maximum likelihood, evolutionary distance, and maximum parsimony methods. Mol Biol Evol 28:2731–2739

Tang SK, Zhi XY, Wang Y, Wu JY, Lee JC, Kim LJ, Lou K, Xu LH, Li WJ (2010) *Haloactinobacterium album* gen. nov., sp. nov., a halophilic actinobacterium, and proposal of *Ruaniaceae* fam. nov. Int J Syst Evol Microbiol 60:2113–2119

Thompson JD, Gibson TJ, Plewniak F, Jeanmougin F, Higgins DG (1997) The CLUSTAL_X windows interface: flexible strategies for multiple sequence alignment aided by quality analysis tools. Nucleic Acids Res 25:4876–4882

Wayne LG, Brenner DJ, Colwell RR, Grimont PAD, Kandler O, Krichevsky MI, Moore LH, Moore WEC, Murray RGE et al (1987) Report of the ad hoc committee on reconciliation of approaches to bacterial systematics. Int J Syst Bacteriol 37:463–464

Weon HY, Kim BY, Hong SB, Joa JH, Nam SS, Lee KH, Kwon SW (2007) *Skermanella aerolata* sp. nov., isolated from air, and emended description of the genus *Skermanella*. Int J Syst Evol Microbiol 57:1539–1542

Xu P, Li WJ, Tang SK, Zhang YQ, Chen GZ, Chen HH, Xu LH, Jiang CL (2005) *Naxibacter alkalitolerans* gen. nov., sp. nov., a novel member of the family 'Oxalobacteraceae' isolated from China. Int J Syst Evol Microbiol 55:1149–1153

Phys. Status Solidi B **252**, No. 12, 2751–2757 (2015) / **DOI** 10.1002/pssb.201552159

Structural and thermodynamic properties of Cu-doped Sn-based single-crystalline clathrates

Jingsong Wang[1], Feng Cheng[1], Hongxia Liu[1], Decong Li[2], Lanxian Shen[1], Kaiyuan Shen[1], and Shukang Deng[*,1]

[1] Education Ministry Key Laboratory of Renewable Energy Advanced Materials and Manufacturing Technology, Yunnan Normal University, Kunming 650500, P.R. China
[2] Photoelectric Engineering College, Yunnan Open University, Kunming 650500, P.R. China

Received 24 March 2015, revised 13 July 2015, accepted 13 July 2015
Published online 10 August 2015

Keywords $Ba_8Ga_{16}Sn_{30}$, clathrates, Cu-doping, electronic properties, thermoelectric materials

[*] Corresponding author: e-mail skdeng@126.com, Phone: +86-0871-65940972, Fax: +86-0871-65940974

This work is a joint experimental and theoretical study on the structural properties and thermodynamic stability of Cu-doped $Ba_8Ga_{16}Sn_{30}$ single-crystalline clathrates. Different synthesis temperatures were adopted to prepare type-I and type-VIII $Ba_8Ga_{16-x}Cu_xSn_{30}$ ($x = 0$, 1, 2) by the Sn-flux method. Experimental results revealed that the reaction transformation temperature from type-VIII to type-I clathrates is approximately 773 K, and Cu doping can increase the critical preparation temperature of type-I phase. The Cu-doped samples possess high conductivity resulting from the significant enhancement of carrier mobility. Theoretical calculation revealed that the density of states (DOS) near the Fermi level increased for Cu doping, which may lead to reduction in structural stability.

1 Introduction Over the past decades, thermoelectric materials have attracted the attention of workers because of their capability to transform waste heat directly into high-quality electrical energy [1, 2]. The performance of a thermoelectric material depends on the figure of merit $ZT = \alpha^2\sigma T/\kappa$, where α is the Seebeck coefficient, σ is the electrical conductivity, κ is the thermal conductivity, T is the absolute temperature, and a high ZT is the value that thermoelectric material must possess [2]. In recent decades, the performance of the thermoelectric materials has significantly improved through intensive research [3–6]; however, the ZT value is still maintained at around unity and is still difficult to be applied. Therefore, researching high-performance thermoelectric materials is a vital task in developing clean energy.

A promising thermoelectric material is the semiconducting clathrate compound with phonon-glass property that satisfies the "phonon glass-electron crystal" (PGEC) [7]. Among the many types of clathrates [8–10] is the Sn-based clathrate, which possesses promising applications in the thermoelectric generation because of its low thermal conductivity and high Seebeck coefficient [11–13].

$Ba_8Ga_{16}Sn_{30}$ (BGS) [14, 15] and $Eu_8Ga_{16}Ge_{30}$ (EGG) [16, 17] are two known members in the family of clathrates that exist in two modifications of type-I and type-VIII phases. Both types have the same chemical formula $A_8X_{16}Y_{30}$ (A = Ba, Eu; X = Ga; Y = Sn, Ge). Type-I clathrate with space group $Pm\bar{3}n$ has a simple cubic structure (PDF No. 223). The unit cell of type-I clathrate consists of two dodecahedra and six tetrakaidecahedra comprising X/Y atoms [18, 19]. The alkali metal or alkali-earth metal (guest atom) can be accommodated in both polyhedrons. The anharmonic vibration of the guest atom in the cages can scatter heat-carrying lattice phonons effectively, thereby reducing lattice thermal conductivity [20, 21]. By contrast, the sp^3 hybridization of the framework atoms X/Y can significantly enhance electronic transmission.

Figure 1a shows the structure of type-I clathrates. The guest atoms occupy the 2*a* and 6*d* sites, while the framework atoms occupy the framework sites of 6*c*, 16*i*, and 24*k* [22].

The structure of type-VIII clathrate is shown in Fig. 1b. Type-VIII clathrate with space group $I\bar{4}3m$ also has a cubic structure (PDF No. 217). The guest atoms are encapsulated in the polyhedrons composed of 23 framework atoms, while

physica status solidi b

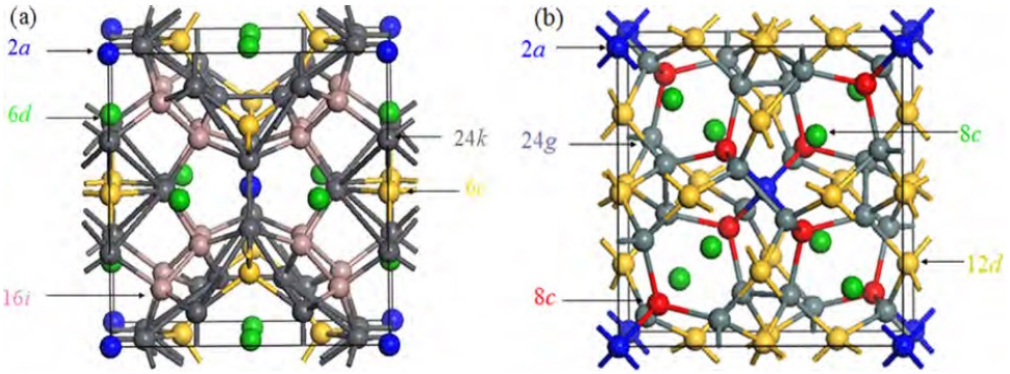

Figure 1 The structure of type-I (a) and type-VIII (b) clathrates.

the adjacent two polyhedrons are connected by a polyhedron composed of eight framework atoms [23]. The guest atoms occupy only the 8*c* site, while the framework atoms occupy the framework sites of 2*a*, 8*c*, 12*d*, and 24*g* [22].

Avila et al. [24] reported that the thermal conductivity of type-I $Ba_8Ga_{16}Sn_{30}$ is only half that of type-I $Ba_8Ga_{16}Ge_{30}$ at 700 K, but type-I $Ba_8Ga_{16}Sn_{30}$ possesses lower carrier concentration. The researchers conjectured that thermoelectric performance can be optimized by doping or changing the stoichiometric ratio. Meng et al. [25] synthesized n-type single-crystal VIII-$Ba_8Ga_{16-x}Ge_xSn_{30}$ and found that its conductivity improved by 62% through Ge doping. The obtained maximum *ZT* value reached 1.25 for the sample with $x = 0.5$ at around $T = 500$ K. Deng et al. [26] found that n-type VIII-$Ba_8Ga_{16-x}Cu_xSn_{30}$ clathrates doped with Cu possess high electrical conductivity with maximum *ZT* of 1.35 for $x = 0.03$. The *ZT* value of the n-type BGS is enhanced by partial substitution of Ge or Cu for Ga in the framework. In particular, Cu doping can effectively improve the thermoelectric performance of the material. Conversely, Takabatake and coworkers [27] reported that type-I $Ba_8Ga_{16}Sn_{30}$ is only stable in a certain temperature range and will transform into type-VIII $Ba_8Ga_{16}Sn_{30}$ above 739 K. In the preparation of Sn-based clathrate through the Sn-flux method, higher reaction temperatures will produce type-I clathrate, while lower reaction temperatures will reduce type-VIII clathrate [12]. No study to date has reported the reaction transformation temperature from type-VIII to type-I clathrate in the preparation process. Therefore, the present work explores the critical temperature of synthesized type-I $Ba_8Ga_{16}Sn_{30}$ by controlling the synthesis temperature. Based on the results, the influence of Cu doping on the critical temperature and the thermoelectric property of Cu doped I-$Ba_8Ga_{16}Sn_{30}$ are analyzed. In addition, the formation E_f and the binding E_0 energies of Cu-doped I-$Ba_8Ga_{16}Sn_{30}$ and VIII-$Ba_8Ga_{16}Sn_{30}$ are calculated and the electronic properties of Cu-doped VIII-$Ba_8Ga_{16}Sn_{30}$ are explored.

2 Experimental The Cu-doped $Ba_8Ga_{16}Sn_{30}$ single crystals were prepared by the Sn-flux method. High-purity elements Ba (ingot, 99.9%), Ga (ingot, 99.999%), Sn (ingot, 99.999%), and Cu (ingot, 99.999%) were mixed according to the $Ba_8Ga_{16-x}Cu_xSn_{30}$ ($x = 0$, 1, 2) formula. The mixtures were sealed in the evacuated quartz tube, placed in a furnace, and then heated for 3 h to 763 and 773 K for $x = 0$; 813, 823, and 833 K for $x = 1$; and 813, 833, and 853 K for $x = 2$. The mixtures were cooled to 663 K for 50 h after being soaked for 10 h at the above-mentioned temperatures. The quartz tube was removed from the furnace at 663 K. The crystals were separated from the molten Sn solvent by centrifugation.

Phase composition was characterized by powder X-ray diffraction (XRD, Bruker D8 CuK_α). Electron probe microanalysis (EPMA, JXA-8230) was used for chemical composition analysis. A comparative method was adopted using constantan (Ni: 40%) as a reference sample with a known $\alpha(T)$ to measure the Seebeck coefficient α. The electrical conductivity $\sigma(T)$ of the samples was measured by the DC current method, with the DC current kept at 20 mA. The carrier density *n* was measured at room temperature by the DC method in a magnetic field of 0.75 T.

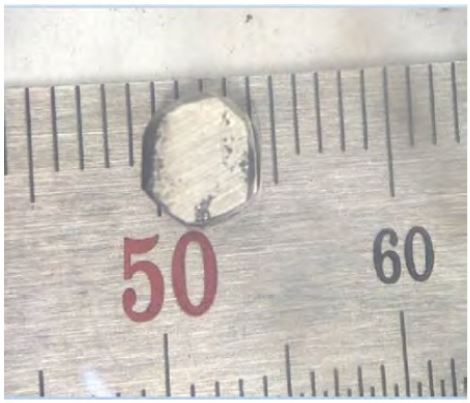

Figure 2 Single-crystal sample of type-I $Ba_8Ga_{16-x}Cu_xSn_{30}$ with $x = 1$, grown with soaking temperature of 833 k.

Original Paper

Table 1 Crystal compositions, carrier mobility μ_H, carrier density n, effective mass m^*/m_0, electrical conductivity σ at room temperature for all samples.

sample	starting composition				carrier mobility μ_H ($cm^2/V\,s$)	carrier density n ($10^{19}\,cm^{-3}$)	effective mass m^*/m_0	electrical conductivity σ ($10^3\,S\,m^{-1}$)
	Ba	Ga	Sn	Cu				
I-Cu_1	7.98	15.8	30.2	0.023	5.6	4.1	0.51	3.6
I-BGS	8.0	15.9	30.1	0.000	4.5	3.2	0.39	2.35
VIII-Cu_1	7.98	15.8	30.2	0.018	45.2	3.1	0.23	22.8
VIII-BGS	7.96	15.9	30.1	0	27.8	4.2	0.38	18.9

3 Results and discussion Single-crystalline samples were obtained for $x = 0$, 1, and 2 under different synthesis temperatures. The obtained samples were denoted by Cu_x-T, where x is the starting content of Cu and T is the soaking temperature.

The crystal sizes of type-I single crystals with $x = 1$ (Cu_1) are about 4 mm. Figure 2 shows the grown crystal of Cu_1-833K with a shiny metallic luster. By contrast, the crystal size of Cu_2-853K is less than 2 mm. The obtained reactant is partially composed of plate-like crystals with $BaNiSn_3$-type structure, which can be easily removed from the clathrate sample.

The crystal composition, room-temperature values of carrier mobility μ_H, carrier density n, and electrical conductivity σ of some samples with type-I and type-VIII structures are listed in Table 1. Tin clathrate-VIII are consistent with other experimental results [26]. Notably, the actual Cu content is much lower than the starting composition for all Cu-doped samples. The Ga composition is slightly smaller than the ideal value of 16; nevertheless, the composition of the framework elements is close to 46 because the total content of Sn and Cu is a little larger than the ideal value of 30.

Figure 3 displays the powder XRD patterns of the clathrate samples. The pattern of Cu_0-763K is well indexed by type-VIII clathrates, while that of Cu_0-773K is typical type-I phase. The reaction transformation temperature from type-VIII BGS to type-I BGS clathrate is around 773 K. To explore the effect of Cu doping on the reaction transformation temperature, I- and VIII-$Ba_8Ga_{16-x}Cu_xSn_{30}$ ($x = 1$ and 2) are synthesized in different temperatures. As shown in Fig. 3, the pattern of Cu_1-813K is well indexed by the VIII-phase diffraction peak; the pattern of Cu_1-823K is composed of type-I and type-VIII clathrates; and Cu_1-833K is type-I clathrate. The critical preparation temperature of type-I Cu_2 is elevated to 853 K with the increase in initial Cu content. Therefore, Cu doping can increase the reaction transformation temperature from type-VIII to type-I phase for Sn-based BGS prepared by the Sn-flux method. Furthermore, higher initial Cu content has a higher reaction transformation temperature. The reason for this phenomenon is discussed in the computational part.

The results of the present work corroborate the report of Deng et al. [26] on the thermoelectric performance of Cu-doped VIII-BGS. Hence, the present work focused only on the analysis of Cu-doped I-BGS. The temperature dependence of the Seebeck coefficient α for type-I Cu_0 and

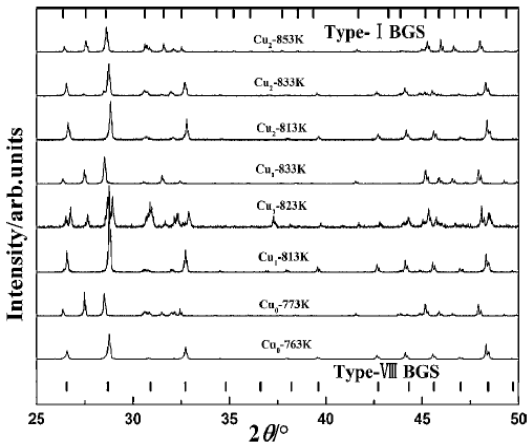

Figure 3 Powder X-ray diffraction patterns of all samples prepared at different temperature.

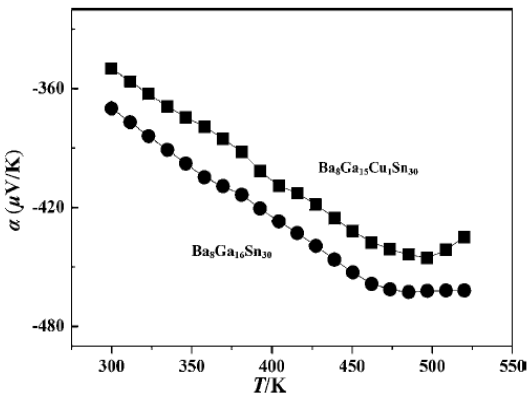

Figure 4 Temperature dependence of Seebeck coefficient for type-I $Ba_8Ga_{16-x}Cu_xSn_{30}$ with $x = 0$ and 1.

physica status solidi b

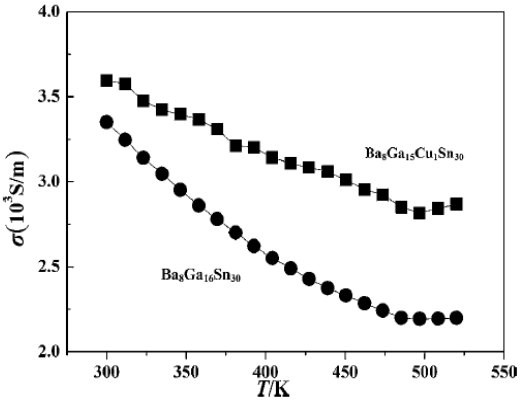

Figure 5 Temperature dependence of electrical conductivity for type-I $Ba_8Ga_{16-x}Cu_xSn_{30}$ with $x = 0$ and 1.

Cu_1 samples is presented in Fig. 4. Both α are negative, indicating n-type conduction. The n-type character is maintained because the Sn composition is larger than the ideal value of 30. Cu doping reduces the α and increases the temperature of intrinsic excitation, indicating that Cu doping changes the band structure of the compound. Nolas et al. [28] found that the α and the electrical conductivity σ of $Sr_8Ga_{16}Ge_{30}$ are significantly influenced by fine tuning the ratio of Ga to Ge, and α decreases with the decrease in the value of Ga/Ge. The present work confirms these findings.

Figure 5 shows the σ of type-I Cu_0 and Cu_1 samples as a function of temperature from 300 K to 520 K. The σ of type-I Cu_1 decreases as the temperature T increases from 300 to 500 K, and then increases because of intrinsic conduction. The electrical conductivity is enhanced by Cu doping. To understand this phenomenon, the Hall coefficient is measured and the carrier mobility and carrier density at room temperature are estimated. As shown in Table 1, With Cu-doped, for both I- and VIII-Cu_0, the carrier mobility and carrier density are increased and subtly changed, respectively.

4 Computational approach and formation energies To evaluate the effect of Cu doping on the structure and thermoelectric property of I-$Ba_8Ga_{16}Sn_{30}$ and VIII-$Ba_8Ga_{16}Sn_{30}$, the first-principles calculation is performed based on the $Ba_8Ga_{15}Cu_1Sn_{30}$ (BGCS) chemical formula. The density-functional theory is adopted in the first-principles calculations. The interaction between the ion solid and the valence electrons is described by the ultrasoft pseudopotentials [29], and the electron configuration is described by Ba: [Xe]$6s^2$, Ga: [Ar]$3d^{10}4s^24p^1$, Sn: [Kr] $4d^{10}5s^25p^2$, and Cu: [Ar]$3d^{10}4s^1$. The exchange and correlation energy of the electrons are calculated by the generalized gradient approximation (GGA) [30, 31]. Through the convergence test, the cutoff energy for plane-wave expansion of the wave functions is set at 300 eV, and k-mesh of $4 \times 4 \times 4$ is adopted for all samples of space [30]. The cell shape, volume, and atomic coordinates are optimized to minimize the energy of configuration. The equilibrium structural parameters, electronic band, and densities of states (DOS) are calculated based on the minimum-energy configurations.

Table 2 Energy difference between Cu occupying different sites and the lowest energy structure for type-I and type-VIII clathrates.

type	Cu site occupancy	ΔE (eV)
I-BGCS	6*c*	0
	24*k*	0.57
	16*i*	1.21
VIII-BGCS	8*c*	0
	12*d*	0.32

To find the most stable BGCS structure, energy is minimized by changing the Cu site in the $Ba_8Ga_{16}Sn_{30}$ framework. As shown in Table 2, Cu did not randomly occupy the framework for both types $Ba_8Ga_{16}Sn_{30}$, but occupied the 6*c* and 8*c* sites in I- and VIII-$Ba_8Ga_{16}Sn_{30}$, respectively.

The calculated lattice constants of type-VIII and type-I BGCS are 11.81 and 11.92 Å, respectively, which are slightly longer than those of the experimental valves. Overestimating the bond strength results in larger lattice parameters in using the GGA approximation [32]. The values deviate from the present experimental data, but agree with the theoretical results in other reports [33, 34]. Cu doping decreases the lattice constant because Cu has a smaller atomic radius than Ga.

The formation E_f and binding E_0 energies are listed in Table 3. The total energy difference between the compound and its corresponding isolate bulk constituent elements is

Table 3 The calculated binding energy E_0, lattice constant, bandgap E_g, and formation energy E_f, for the series. Some reported theoretical results [33,34] are also listed.

	lattice constant (Å)	E_g (eV)	E_0 (eV/atom)	E_f (eV/atom)
VIII-BGS	11.86, 11.88[34]	0.20, 0.19[34]	–2.96, –2.98[34]	–1.17
VIII-BGCS	11.81	0.14	–2.71	–1.03
I-BGS	12.09, 12.22[34]	0.30, 0.24[34]	–2.69, –2.67[33]	–0.95, –0.91[33]
I-BGCS	11.92	0.16, 0.17[33]	–2.51, –2.48[33]	–0.88, –0.86[33]

Original Paper

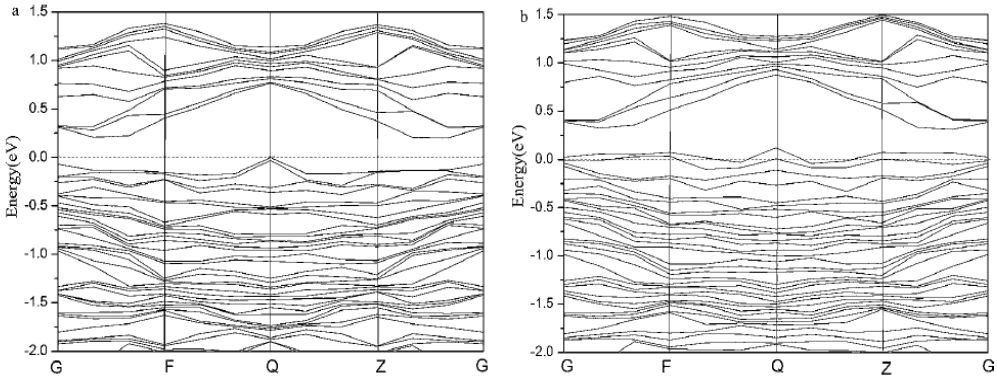

Figure 6 The electronic band structure of (a) VIII-$Ba_8Ga_{16}Sn_{30}$ and (b) VIII-$Ba_8CuGa_{15}Sn_{30}$ calculated by first principles.

called the formation energy [22], which can be calculated by

$$E_f(Ba_8Ga_{15}CuSn_{30}) = E_{Ba_8Ga_{15}CuSn_{30}} - 8E_{Ba} - 15E_{Ga} - E_{Cu} - 30E_{Sn},$$

where E_{Ba} is the energy of one Ba atom in Ba metal; E_{Cu}, E_{Ga}, and E_{Sn} are defined similarly [22]. E_f and E_0 are negative and increased by Cu substitution, which indicated that the synthesis of BGCS by the experimental method satisfies the thermodynamics condition, however, the stability of BGCS is poor compared with BGS, therefore, the framework site is more easily occupied by Ga atom than Cu. Moreover, the actual composition of Cu in the sample is also determined by the migration at the reaction temperature, and we conjecture that the migration of Cu is lower than that of Ga, thus, Ga is preferentially combined with framework atoms, consequently the actual Cu content is far less than the starting content and the critical temperatures of synthesis of the Cu-doped type-I clathrate are higher than that of type-I BGS.

5 Electronic properties Li et al. [33] reported the electronic property of Cu-doped I-BGS; their results are in good agreement with the present results. Hence, the present paper focuses only on the analysis of VIII-BGCS. The electronic band structures of VIII-BGCS and VIII-BGS are shown in Fig. 6, where G (0, 0, 0), F (0, 1/2, 0), Q (0, 1/2, 1/2), and Z (0, 0, 1/2) are high-symmetry points in the Brillouin zone. The VIII-BGS and VIII-BGCS are indirect semiconductors. The binding energy E_0, lattice constant, bandgap E_g, formation energy E_f are summarized in Table 3. VIII-BGS is an intrinsic semiconductor with a bandgap $E_g = 0.20$ eV. The electronic property of VIII-BGS is in good agreement with other theoretical results [34]. The effect of Cu doping on the minimum of the conduction band is negligible, indicating that the electronic effective mass remains nearly unchanged by Cu doping. The top of the valence bands is changed dramatically, especially near the valence-band maximum. Two states between the Fermi level and the bottom of the conduction band are in VIII-BGCS, indicating two excess holes per unit cell, and the Cu atom acts as acceptors with two holes. However, the

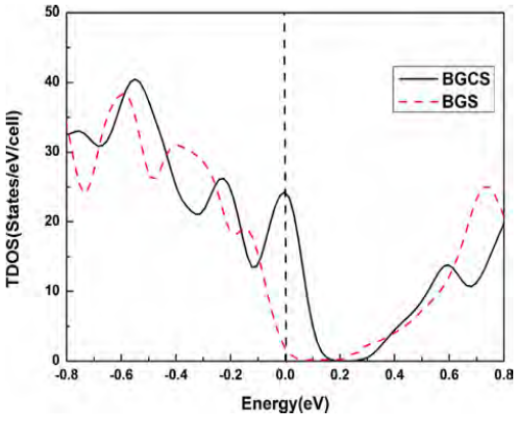

Figure 7 The total electronic densities of states for the VIII-$Ba_8Ga_{16}Sn_{30}$ and VIII-$Ba_8CuGa_{15}Sn_{30}$ calculated by first principles.

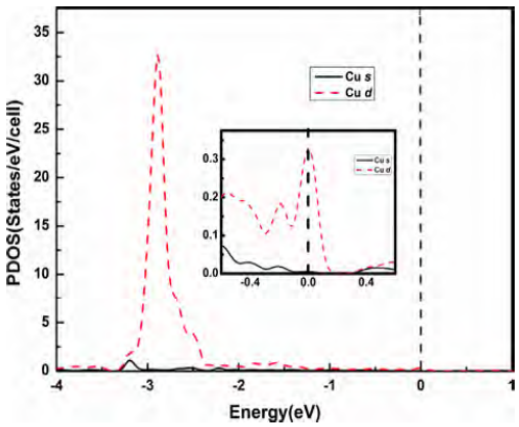

Figure 8 The partial electronic densities of states of Cu orbitals in VIII-$Ba_8CuGa_{15}Sn_{30}$ calculated by first principles.

physica status solidi b

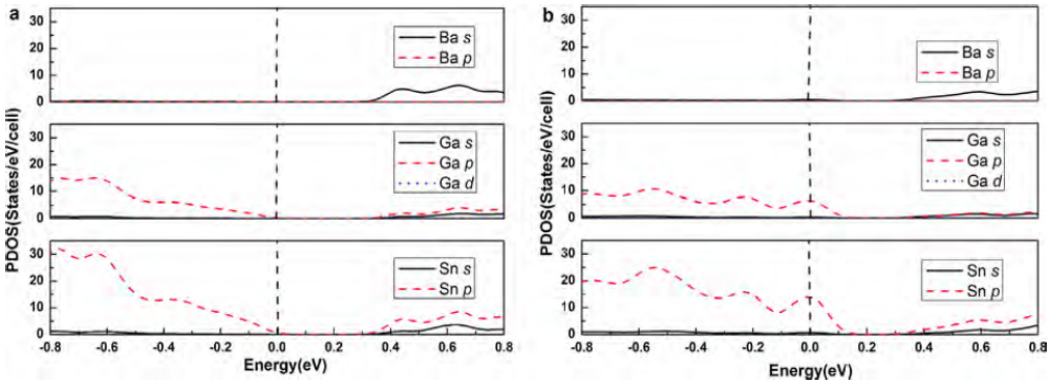

Figure 9 The partial electronic densities of states of (a) free-doped and (b) Cu-doped clathrates by first principles.

present samples show n-type character because the value of (Cu + Ga)/Sn is lower than the ideal value of 16/30. In addition, Cu doping also narrows the energy gap; thus, the carrier concentration should increase with Cu doping. However, the actual Cu content in the VIII-BGCS samples is relatively low, thus the carrier concentration is almost invariable.

The total electronic density of states (DOS) of VIII-BGS and VIII-BGCS are shown in Fig. 7. Cu doping increases the electronic DOS near Fermi level, which may reduce structure stability [35]. Furthermore, the bottom of the conduction bands shifts to a higher energy level by the coupling between Cu 3*d* states and the conduction bands of clathrate, thereby enhancing the intrinsic excitation temperature, which is in good accordance with our experimental result.

Figure 8 shows the partial DOS of Cu. Obviously, the effect of Cu 4*s* states on the total DOS is negligible. The Cu 3*d* states are mainly located between −3.0 and −2.0 eV, suggesting the localized character of Cu 3*d* electrons. The calculated partial electronic DOS in Cu-free clathrate and Cu-doped clathrate are shown in Fig. 9. Each partial DOS is the total contribution from the same atomic element in the unit cell. Figure 9 shows that the contribution of the Ba *p* electrons to the total DOS near the Fermi level of both compounds is negligible. The hybridization between the Ba *s* orbital and the framework atoms form the conduction band of clathrate. The top of the valence bands of clathrate mostly consist Sn *p* and Ga *p* states that hybridize with the *s* states. Blake [36] indicated that the valence bands of the clathrate are almost exclusively localized on the framework, but the lowest conduction bands are formed by the bonding orbitals between the metal atoms and antibonding molecular orbitals of the framework. Figure 8 shows that the Cu 3*d* states possess a sharp peak around the Fermi energy level, indicating that the DOS at the band edges is primarily contributed by the Cu 3*d* states.

6 Conclusions In this work, single-crystal samples of I- and VIII-$Ba_8Ga_{16-x}Cu_xSn_{30}$ ($x = 0, 1, 2$) were prepared by controlling the synthesis temperature. The results showed that the reaction transformation temperature from type-VIII to type-I clathrate is about 773 K, which was increased by Cu doping. By contrast, the Seebeck coefficient was reduced by Cu doping for I- and VIII-BGS. The carrier mobility was significantly enhanced by Cu doping and consequently resulted in the higher electrical conductivity for the Cu-doped I- and VIII-BGS samples. The theoretical calculation results reveal that the contribution of Cu 4*s* states to the total DOS is negligible, and the Cu 3*d* states are located mainly between −3.0 and −2.0 eV, which suggests the localized character of Cu 3*d* electrons. Moreover, Cu doping increases the electronic DOS near the Fermi level, which may lead to the reduction of the structure stability.

Acknowledgement This work was supported by the National Nature Science Foundation of China (Grant No.51262032).

References

[1] G. S. Nolas, in: The Physics and Chemistry of Inorganic Clathrates, edited by G. S. Nolas (Springer, Netherlands, 2014).
[2] F. Ioffe, Semiconductor Thermoelements and Thermoelectric Cooling (Infosearch Limited, London, 1957).
[3] M. H. Phan, V. Franco, A. Chaturvedi, S. Stefanoski, H. Kirby, G. S. Nolas, and H. Srikanth, J. Appl. Phys. **107**, 09A910 (2010).
[4] A. Popescu, A. Datta, G. S. Nolas, and L. M. Woods, J. Appl. Phys. **109**, 103709 (2011).
[5] J. Martin, G. S. Nolas, H. Wang, and J. Yang, J. Appl. Phys. **102**, 103719 (2007).
[6] J. Martin, S. Erickson, G. S. Nolas, P. Alboni, T. M. Tritt, and J. Yang, J. Appl. Phys. **99**, 044903 (2006).
[7] G. A. Slack, in: CRC Handbook of Thermoelectrics (CRC, Boca Raton, 1995).
[8] S. K. Deng, Y. Saiga, K. Suekuni, and T. Takabatake, J. Appl. Phys. **108**, 073705 (2010).
[9] B. L. Du, Y. Saiga, K. Kajisa, and T. Takabatake, J. Appl. Phys. **111**, 013707 (2012).
[10] S. K. Deng, D. C. Li, L. X. Shen, R. T. Hao, and T. Takabatake, Chin. Phys. B **21**, 017401 (2012).

Original Paper

[11] Y. Saiga, K. Suekuni, B. Du, and T. Takabatake, Solid State Commun. **152**, 1902 (2012).
[12] K. Suekuni, M. A. Avila, K. Umeo, H. Fukuoka, S. Yamanaka, T. Nakagawa, and T. Takabatake, Phys. Rev. B **77**, 235119 (2008).
[13] D. Huo, T. Sakata, T. Sasakawa, M. A. Avila, M. Tsubota, F. Iga, H. Fukuoka, S. Yamanaka, S. Aoyagi, and T. Takabatake, Phys. Rev. B **71**, 075113 (2005).
[14] M. A. Avila, K. Suekuni, K. Umeo, H. Fukuoka, S. Yamanaka, and T. Takabatake, Phys. Rev. B **74**, 125109 (2006).
[15] K. Suekuni, M. A. Avila, K. Umeo, H. Fukuoka, S. Yamanaka, T. Nakagawa, and T. Takabatake, Phys. Rev. B **77**, 235119 (2008).
[16] M. H. Phan, G. T. Woods, A. Chaturvedi, S. Stefanoski, G. S. Nolas, and H. Srikant, Appl. Phys. Lett. **93**, 252505 (2008).
[17] V. Pacheco, A. Bentien, W. Carrillo-Cabrera, W. Paschen, F. Steglish, and Y. Grin, Phys. Rev. B **71**, 165205 (2005).
[18] B. C. Chakoumakos, B. C. Sales, and D. G. Mandrus, J. Alloys Compd. **322**, 127 (2001).
[19] M. Christensen, S. Johnsen, and B. B. Iversen, Dalton Trans. **39**, 978 (2010).
[20] B. C. Sales, B. C. Chakoumakos, R. Jin, J. R. Thompson, and D. Mandrus, Phys. Rev. B **63**, 245113 (2001).
[21] K. Suekuni, M. A. Avila, K. Umeo, H. Fukuoka, S. Yamanaka, T. Nakagawa, and T. Takabatake, Phys. Rev. B **77**, 235119 (2008).
[22] N. P. Blake, D. Bryan, S. Latturner, L. Møllnitz, G. D. Stucky, and H. Metiu, J. Chem. Phys. **114**, 10063 (2001).
[23] S. Paschen, W. Carrillo-Cabrera, A. Bentien, V. H. Tran, M. Baenitz, Y. Grin, and F. Steglich, Phys. Rev. B **64**, 214404 (2001).
[24] M. A. Avila, K. Suekuni, and K. Umeo, Appl. Phys. Lett. **92**, 041901 (2008).
[25] D. Y. Meng, L. X. Shen, X. X. Shen, G. J. Dong, and S. K. Deng, Acta Phys. Sin. **62**, 247401 (2013).
[26] S. K. Deng, Y Saiga, K. Kajisa, and T. Takabatake, J. Appl. Phys. **109**, 103704 (2011).
[27] B. L. Du, Y. Saiga, K. Kajisa, and T. Takabatake, Philos. Mag. **92**, 2541 (2012).
[28] G. S. Nolas, J. L. Cohn, and G. A. Slack, Appl. Phys. Lett. **73**, 178 (1998).
[29] M. C. Payne, M. P. Teter, D. C. Allan, T. A. Arias, and J. D. Joannopoulos, Rev. Mod. Phys. **64**, 1045 (1992).
[30] H. J. Monkhorst and J. D. Pack, Phys. Rev. B **13**, 5188 (1976).
[31] J. P. Perdew, K. Burke, and M. Ernzerhof, Phys. Rev. Lett. **77**, 3865 (1996).
[32] J. M. Zuo, P. Blaha, and K. Schwarz, J. Phys.: Condens. Matter **9**, 1741 (1997).
[33] D. C. Li, L. Fang, S. K. Deng, K. Y. Kang, W. H. Wei, and H. B. Ruan, Indian J. Phys. **86**, 447 (2012).
[34] D. C. Li, L. Fang, S. K. Deng, K. Y. Kang, and W. H. Wei, Physica B **407**, 1238 (2012).
[35] P. Ravindran and R. A. Sokamani, Bull. Mater. Sci. **20**, 4 (1997).
[36] N. P. Blake, S. Latturner, J. D. Bryan, G. D. Stucky, and H. Metiu, J. Chem. Phys. **115**, 8060 (2001).

Phys. Status Solidi B **252**, No. 4, 795–799 (2015) / **DOI** 10.1002/pssb.201451366

physica status solidi b
www.pss-b.com
basic solid state physics

Preparation, thermal stability, and electrical transport properties of In/Sn codoped β-Zn_4Sb_3 single crystal

Xuxia Shai[1], Shukang Deng[*,1], Lanxian Shen[1], Daiyi Meng[1], Decong Li[2], Yanjun Zhang[1], and Xianyan Jiang[1]

[1] Education Ministry Key Laboratory of Renewable Energy Advanced Materials and Manufacturing Technology, Yunnan Normal University, Kunming 650500, P. R. China
[2] Photoelectric Engineering College, Yunnan Open University, Kunming 650500, P. R. China

Received 16 July 2014, revised 27 November 2014, accepted 27 November 2014
Published online 20 January 2015

Keywords carrier mobility, carrier transport, electrical properties, single crystals, thermoelectric materials, Zn_4Sb_3

* Corresponding author: e-mail skdeng@126.com, Phone: +86-0871-65940972, Fax: +86-0871-65940974

In and Sn codoped β-Zn_4Sb_3 single crystals were prepared by a Sn-flux method according to the formula $Zn_{4.4}Sb_3Sn_3In_x$(x = 0–0.5). The thermal weight loss is suppressed completely until the melting point of the single crystals. All crystals exhibit p-type conduction. The carrier mobility of the single crystals is increased, compared to a β-Zn_4Sb_3 polycrystalline sample. All samples possess relatively high electrical conductivity, reaching 6.3×10^4 S/m for the sample with x = 0.18. The Seebeck coefficient is enhanced on increasing of the total content of In and Sn. The sample with x = 0.5 exhibits excellent electrical properties, and shows a maximal power factor of 1.53×10^{-3} W/m/K^2 at 603 K.

1 Introduction The performance of thermoelectric (TE) material is assessed with the figure of merit ZT defined as $ZT = \alpha^2\sigma T/\kappa$, where α, σ, κ, and T are the Seebeck coefficient, electrical conductivity, thermal conductivity, and absolute temperature, respectively, and the electrical part $\alpha^2\sigma$ is called the power factor and κ is divided into two parts of lattice contribution κ_L and carrier component κ_C. At a specific temperature, material possessing a higher ZT shows a better performance [1–4]. β-Zn_4Sb_3 has attracted much attention because of its outstanding TE performance in midrange temperatures (473–673 K) [5, 6] due to the complex crystal structure and atomic disorder. β-Zn_4Sb_3 possesses a hexagonal unit cell with space group of $R\bar{3}c$. There are at least three disorderly distributed interstitial Zn atoms in each unit cell. This structure means that the compound has a very low thermal conductivity of 0.65 W/(m K) at room temperature [7, 8]. A record high ZT of 1.3 at 670 K for β-Zn_4Sb_3 was reported by Caillat et al. [5].

Although β-Zn_4Sb_3 has a relativity higher ZT at moderate temperatures compared to other TE materials, further improvement in its properties is necessary for the practical application on the large scale, in this respect, many approaches have been explored to enhance its ZT. Among them, metal doping has been widely studied to optimize its TE performance. Elements such as Ge, Cd, Hg, In, Si, Ag, Cu, and Nb have been used to substitute Zn [9–17], and Sb has been replaced by Ti, Te, or Bi [18–21], but the TE performance has not been improved significantly. Moreover, the poor thermal stability and weak mechanical property resulting from cracks in polycrystalline β-Zn_4Sb_3 [22–25] are the main reasons restricting its practical application.

In the present work, we focus on the effects of In/Sn codoping on the thermal stability and electrical properties of β-Zn_4Sb_3 single crystals prepared by the Sn-flux method. The results show that the thermodynamic stabilities and electrical transport properties of the β-Zn_4Sb_3 single crystals are simultaneously optimized.

2 Experimental The In/Sn codoped β-Zn_4Sb_3 single crystals were prepared by the Sn-flux method. High-purity elemental Zn (grain, 99.999%), Sb (grain, 99.999%), Sn (ingot, 99.999%), and In (ingot, 99.99%) were weighed according to the formula of $Zn_{4.4}Sb_3Sn_3In_x$(x = 0–0.5). The weighed elements were put into a quartz tube and sealed under vacuum. The sealed tube was placed into a furnace and heated to 853 K in 2 h, held at this temperature for 10 h, and then cooled to 753 K in 15 min, followed by cooling

physica status solidi b

to 593 K in 40 h. The remaining molten Sn was separated from the β-Zn_4Sb_3 single crystals by the technique of centrifugation.

The phase identification of the samples was carried out by a powder X-ray diffraction (XRD, Bruker D8 X-ray diffraction) using CuKα radiation ($\lambda = 1.5406$ Å). Electron probe microanalysis (EPMA, JXA-8230) was used for chemical composition analyses. The melting point and thermal stability were measured by thermogravimetric-differential thermal analysis (TG-DTA, STA449F3 Jupiter). The Hall coefficient R_H was measured by a DC method in a magnetic field of 0.75 T. The electrical conductivity σ and Seebeck coefficient α were measured from 300 to 660 K in a vacuum. The Seebeck coefficient α was measured by a comparative method using constantane (Ni:40%) as a reference sample of which the α in the measured temperature range is known. The electrical conductivity σ of the samples was measured by a DC current method with $I = 20$ mA.

3 Results and discussions

3.1 Structure and chemical compositions According to the formula of $Zn_{4.4}Sb_3Sn_3In_x$($x = 0$–0.5), single crystals with crystal size about 6 mm were obtained by the Sn-flux method. As an example, Fig. 1 shows a typical photo of the grown crystal with $x = 0.3$.

Figure 2 shows the powder XRD patterns of the crystals with different In and Sn contents. All the diffraction peaks can be indexed to the β-Zn_4Sb_3 with hexagonal symmetry (space group $R\bar{3}c$). The peak at $2\theta \sim 32°$ for the sample with $x = 0$ becomes less obvious in the patterns of $x = 0.3$ and 0.5, which can be attributed to the different grain size of the powder prepared for the XRD measurement. In addition, the peak at $2\theta \sim 52°$ in the sample with $x = 0.3$ splits into three peaks, due to the impurities in the Zn–Sn–In eutectic compound that has not been separated completely from the surface of the single crystals. Compared to the sample with $x = 0$, the Bragg positions shift to higher angles, indicating smaller lattice parameters for the In/Sn codoped samples.

The actual compositions, lattice parameters, and some electrical properties at room temperature of all the samples are summarized in Table 1. As can be seen from the actual compositions, both Sn and In atoms are preferred to replace Zn. The In contents in the crystals are increased on increasing the starting content of In, while the Sn contents in the crystals are decreased on raising x, and the total contents of In and Sn in the crystals are increased synchronously. It is seen from Table 1 that the lattice parameter of the sample with $x = 0$ is larger than that of the In-doped samples, but for the In-doped samples, the lattice parameters are nearly invariable. Also, it can be seen in Table 1 that the carrier densities of the present samples are consistent with each other and consistent with that of the β-Zn_4Sb_3 polycrystalline materials prepared by the MS-SPS [11]. It can be inferred that the substitution of In and Sn for Zn is the isoelectronic substitution. So the chemical state of Sn in the compounds should be Sn^{4+}, a Sn^{4+} ion should replace 2 Zn^{2+} ions, and a In^{3+} ions should replace 1.5 Zn^{2+} ions. Compared to the sample with $x = 0$, the content of Sn in the In-doped compounds are decreased, and the lattice parameters of the corresponding samples should be decreased for the radius of Sn^{4+} (0.71 Å) is smaller than that of Zn^{2+}(0.74 Å). At the same time, the lattice parameters of the In-doped samples should be increased as the radius of In^{3+} (0.80 Å) is larger than that of Zn^{2+}. Hence, the smaller lattice parameters of In-doped samples can be attributed to the fact that the contribution of Sn^{4+} to the decrease of the lattice parameter is greater than that of In^{3+} to the increase of the lattice parameter.

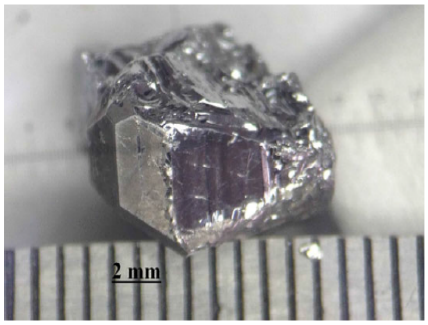

Figure 1 The picture of the single crystal sample with $x = 0.3$ prepared by the Sn-flux method according to the formula of $Zn_{4.4}Sb_3Sn_3In_x$ ($x = 0$–0.5).

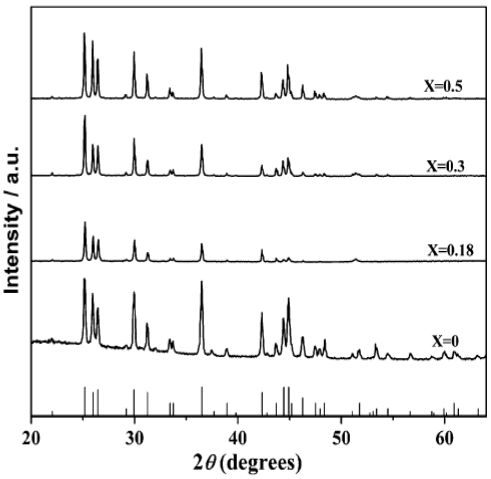

Figure 2 Powder XRD patterns for single-crystal samples prepared by the Sn-flux method according to the formula of $Zn_{4.4}Sb_3Sn_3In_x$ ($x = 0$–0.5): $x = 0$, $x = 0.18$, $x = 0.3$, and $x = 0.5$. (CuKα radiation, $\lambda = 1.5406$ Å).

3.2 Thermal analysis of samples The thermal stability of all Sn-flux samples has been studied in this paper. All of the samples have no weight loss under the melting temperature of β-Zn_4Sb_3. As an example, Fig. 3

Original Paper

Table 1 The actual compositions, the room-temperature lattice constants (*a*/*b*/*c*), Hall coefficients (R_H), carrier concentrations (*n*), and carrier mobilities (μ_H) of the prepared β-Zn_4Sb_3 crystals prepared by the Sn-flux method according to the formula of $Zn_{4.4}Sb_3Sn_3In_x$ ($x = 0$–0.5).

sample	actual content				lattice constant (*a*/*b*/*c*)		*n* (10^{19} cm^{-3})	R_H (10^{-8} m^3/C)	μ_H (cm^2/V/s)
	Zn	Sb	In	Sn	$a = b$ (Å)	c (Å)			
$x = 0$	3.82	3.00	0	0.084	12.2478	12.4394	5.47	11.4	67.97
$x = 0.18$	3.74	3.00	0.025	0.066	12.2412	12.4222	6. 64	9.41	58.98
$x = 0.3$	3.65	3.00	0.066	0.042	12.2395	12.4206	6.11	10.2	57.04
$x = 0.5$	3.62	3.00	0.098	0.038	12.2394	12.4151	5.79	10.7	56.41

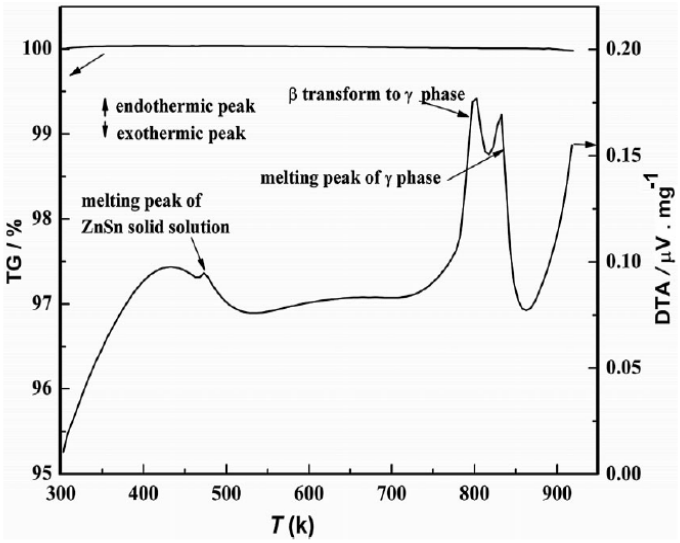

Figure 3 Thermal analysis of sample with $x = 0.3$ prepared by the Sn-flux method according to the formula of $Zn_{4.4}Sb_3Sn_3In_x$ ($x = 0$–0.5) performed in an open alumina crucibles with a heating rate of 10 K/min and high-purity nitrogen was used as purge gas and protective gas.

shows the TG-DTA curve of the sample with $x = 0.3$ performed in an open alumina crucible. From the TG curve, the weight loss has not been observed in the temperature range from 300 K to the melting point of 919 K, indicating the evaporation of Zn is suppressed completely in the present single crystals. The thermal stability of the present β-Zn_4Sb_3 single crystal is superior to that of the Cd-substituted β-Zn_4Sb_3 polycrystal, which has only 85% of the original phase left at 625 K [10]. The recent study shows that the reason for phase decomposition of β-Zn_4Sb_3 is the evaporation of Zn [24] and it is known that the diffusion mechanism of materials is mainly based on the mechanism of vacancy diffusion. In this study, the lattice perfection and fewer vacancy defects of the single crystals are the reason for the suppression of Zn evaporation in the heating process of TG-DTA, and this leads to the stability of single crystals up to 800 K compared with polycrystalline samples.

The endothermic peak (see Fig. 3) at 474 K is the melting peak of the Zn–Sn–In eutectic compound, which is not completely separated from the surface of single crystals. The endothermic peak at 833 K is the melting peak of the sample and the melting point is about 829 K, which is lower than the 837 K of Zn_4Sb_3 [26]. The reason for the lower melting point is due to the Sn and In codoping, which have a lower melting point than Zn_4Sb_3. The phase transformation of β to γ phase takes place at 791 K in this work, which is higher than that of 767 K as shown in the phase diagram [26].

The location of the endothermic peak for the melting Zn–Sn–In eutectic compound, melting point of the sample, and the phase transformation temperature of β to γ phase of all samples are listed in Table 2. It is obvious that the melting temperature of both the solid solution and Zn_4Sb_3 are

Table 2 The location of the endothermic peak for the melting of the Zn–Sn–In eutectic compound, melting of the sample, and the phase transformation of β to γ phase of the present β-Zn_4Sb_3 crystals prepared by the Sn-flux method according to the formula of $Zn_{4.4}Sb_3Sn_3In_x$ ($x = 0$–0.5).

sample	melting temperature of eutectic compound (K)	temperature of phase transformation (K)	melting point of Zn_4Sb_3 (K)
$x = 0$	482	774	835
$x = 0.18$	478	785	832
$x = 0.3$	474	791	829
$x = 0.5$	467	793	827

physica status solidi b

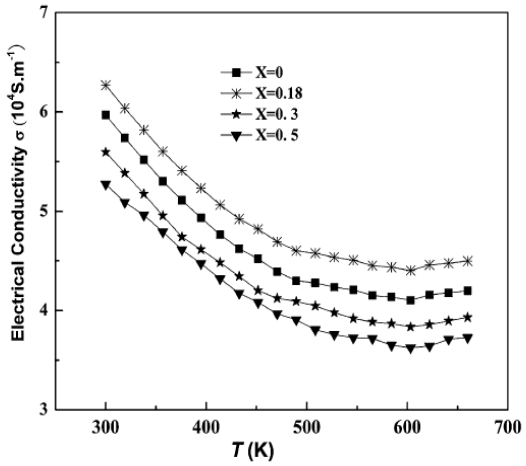

Figure 4 The temperature dependence of the electrical conductivity for all samples prepared by the Sn-flux method according to the formula of $Zn_{4.4}Sb_3Sn_3In_x$ ($x=0$–0.5) ($x=0$, $x=0.18$, $x=0.3$, $x=0.5$) in the temperature range from 300 to 660 K.

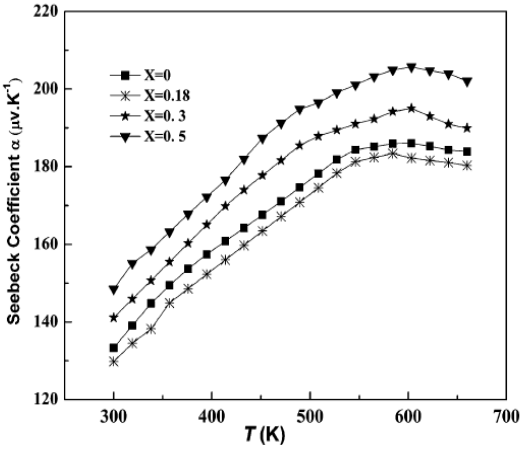

Figure 5 The temperature dependence of the Seebeck coefficient for all samples prepared by the Sn-flux method according to the formula of $Zn_{4.4}Sb_3Sn_3In_x$ ($x=0$–0.5) ($x=0$, $x=0.18$, $x=0.3$, $x=0.5$) in the temperature range from 300 to 660 K.

decreased on increasing x, and this is due to the Sn and In codopants that have lower melting points than Zn_4Sb_3. However, with increasing In and Sn total content, the temperature of the phase transformation of β phase to γ phase shows a gradual increase, indicating that the stability of β-Zn_4Sb_3 single crystals are improved.

3.3 Electrical transport properties The temperature dependence of electrical conductivity σ for all samples is presented in Fig. 4. All the samples possess higher electrical conductivity at the room temperature, which reaches to 6.26×10^4 S/m for the sample with $x=0.18$. In order to explore the other electrical properties, the Hall coefficient R_H was measured at room temperature, and then using the measured σ and R_H at 300 K, the carrier mobility μ_H was calculated by $\mu_H = |R_H| \times \sigma$. As shown in Table 1, the carrier densities are consistent with that of the Cd-doped β-Zn_4Sb_3 polycrystalline materials prepared by the MS-SPS [11]. However, as for the lower grain-boundary scattering of single crystals, the μ_H of the present materials are increased compared to polycrystalline materials.

The Seebeck coefficients as a function of temperature for the prepared samples are shown in Fig. 5. All Seebeck coefficients are positive, illustrating the prepared samples show p-type conductivity, which is consistent with the positive Hall coefficients (see Table 1). The Seebeck coefficient α gradually increases to a maximum value at around 603 K with increasing temperature and then decreases gradually due to the intrinsic activation. The value of the intrinsic conduction temperature of the sample with $x=0.18$ is lower than that of other samples. It is known that the intrinsic conduction temperature is dependent on the bandgap of materials, according to the formula $E_g = 2eS_{max}T_{max}$, where S_{max} is the maximum Seebeck coefficient and T_{max} is the temperature at S_{max}. As shown in Fig. 5, the sample with $x=0.18$ should possess the narrowest bandgap. Additionally, the Seebeck coefficient of the sample with $x=0.5$ is as high as 205 μV/K at 603 K, which is comparable to that of 212 μV/K for the In-doped β-Zn_4Sb_3 polycrystal at 600 K [14]. As can been seen in Fig. 5, the Seebeck coefficient of the sample with $x=0.18$ with less content of In and Sn is lower than that of other samples, presumably due to the fact that scattering intensity of impurity scattering is weaker than that of other samples.

The temperature dependence of the power factor $\alpha^2\sigma$ for all compounds is shown in Fig. 6. The power factor of the

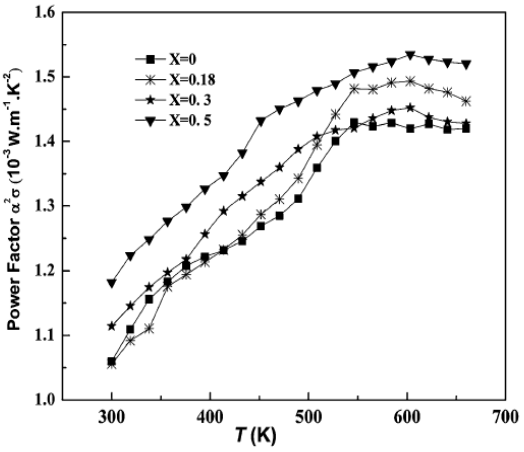

Figure 6 The temperature dependence of the power factor for all samples prepared by the Sn-flux method according to the formula of $Zn_{4.4}Sb_3Sn_3In_x$ ($x=0$–0.5) ($x=0$, $x=0.18$, $x=0.3$, $x=0.5$) in the temperature range from 300 to 660 K.

Original Paper

sample with $x = 0$ is lower than those of the other samples, while the sample with $x = 0.5$ gave the highest power factor with the maximum value of 1.53×10^{-3} W/m/K^2 at 603 K due to the higher electrical conductivity and higher Seebeck coefficient.

4 Conclusions In this paper, In/Sn codoped β-Zn_4Sb_3 single crystals with space group $R\bar{3}c$ were prepared by the Sn-flux method according to the formula of $Zn_{4.4}Sb_3Sn_3In_x$ ($x = 0$–0.5). The prepared samples exhibit excellent high temperature thermal stability, and it is enhanced by the increasing codoped content of In and Sn. All the prepared samples show p-type conduction. Compared to the β-Zn_4Sb_3 polycrystal sample, the carrier mobility is increased significantly. Also, the prepared single crystals possess higher electrical conductivity. The Seebeck coefficient of the crystal samples is increased by the increasing total content of In and Sn. The sample with $x = 0.5$ exhibits excellent electrical properties, which shows maximal power factor of 1.53×10^{-3} W/m/K^2 at 603 K.

Acknowledgments We would like to thank Dr. M. J. Yang for EPMA performed at Wuhan University of Technology. This work was supported by National Nature Science Foundation of China (Grant No.51262032).

References

[1] D. M. Rowe (ed.), Thermoelectrics Handbook: Macro to Nano (CRC Press, Taylor & Francis Group, Boca Raton, 2006).
[2] L. E. Bell, Science **321**, 1457 (2008).
[3] T. M. Tritt, Science **283**, 804 (1999).
[4] F. J. DiSalvo, Science **285**, 703 (1999).
[5] T. Caillat, J.-P. Fleurial, and A. Borshchevsky, J. Phys. Chem. Solids **58**, 1119 (1997).
[6] T. Caillat, A. Borshchevsky, and J.-P. Fleurial, Mater. Res. Soc. Symp. Proc. **478**, 103 (1997).
[7] G. J. Snyder, M. Christensen, E. Nishibori, T. Caillat, and B. B. Iversen, Nature Mater. **3**, 458 (2004).
[8] F. Cargnoni, E. Nishibori, P. Rabiller, L. Bertini, G. J. Snyder, M. Christensen, C. Gatti, and B. B. Iversen, Chem. Eur. J. **10**, 3861 (2004).
[9] S. Y. Wang, X. J. Tan, G. J. Tan, X. Y. She, W. Liu, H. Li, H. J. Liu, and X. F. Tang, J. Mater. Chem. **22**, 13977 (2012).
[10] B. L. Pedersen, H. Yin, H. Birkedal, M. Nygren, and B. B. Iversen, Chem. Mater. **22**, 2375 (2010).
[11] S. Y. Wang, H. Li, D. K. Qi, W. J. Xie, and X. F. Tang, Acta Mater. **59**, 4805 (2011).
[12] B. L. Pedersen, H. Birkedal, E. Nishibori, A. Bentien, M. Sakata, M. Nygren, P. T. Frederiksen, and B. B. Iversen, Chem. Mater. **219**, 6304 (2007).
[13] A. P. Litvinchuk, J. Nylen, B. Lorenz, A. M. Guloy, and U. Haussermann, J. Appl. Phys. **103**, 123524 (2008).
[14] M. Tsutsui, L. T. Zhang, K. Ito, and M. Yamaguchi, Intermetallics **12**, 809–813 (2004).
[15] L. Pan, X. Y. Qin, H. X. Xin, C. J. Song, Q. Q. Wang, J. H. Sun, and R. R. Sun, Solid State Sci. **12**, 1511 (2010).
[16] M. Liu, X. Y. Qin, C. S. Liu, L. Pan, and H. X. Xin, Phys. Rev. B **81**, 245215 (2010).
[17] D. Li, H. H. Hng, J. Ma, and X. Y. Qin, J. Mater. Res. **24**, 430 (2009).
[18] W. Li, L. M. Zhou, Y. L. Li, J. Jiang, and G. J. Xu, J. Alloys Compd. **486**, 335 (2009).
[19] D. Li and X. Y. Qin, Intermetallics **19**, 1651–1655 (2011).
[20] L. M. Zhou, W. Li, J. Jiang, T. Zhang, Y. Li, G. J. Xu, and P. Cui, J. Alloys Compd. **503**, 464 (2010).
[21] X. Y. Qin, M. Liu, L. Pan, H. X. Xin, J. H. Sun, and Q. Q. Wang, J. Appl. Phys. **109**, 033714 (2011).
[22] W. J. Xie, X. F. Tang, Y. G. Yan, Q. J. Zhang, and T. M. Tritt, J. Appl. Phys. **105**, 113713 (2009).
[23] H. Li, X. F. Tang, Q. J. Zhang, and C. Uher, Appl. Phys. Lett. **94**, 102114 (2009).
[24] H. Yin, M. Christensen, N. Lock, and B. B. Iversen, Appl. Phys. Lett. **101**, 043901 (2012).
[25] E. Chalfin, H. X. Lu, and R. Dieckmann, Solid State Ion. **178**, 447 (2007).
[26] O. Chinatsu, U. Takashi, and H. Kazuhiro, Mater. Trans. **51**, 152 (2010).

第35卷,第7期 光 谱 学 与 光 谱 分 析 Vol. 35, No. 7, pp -
2015年7月 Spectroscopy and Spectral Analysis July, 2015

磁控共溅射法沉积的硅量子点 SiN_x 薄膜的光谱特性

陈小波[1,2], 杨 雯[1], 段良飞[1], 张力元[1], 杨培志[1*], 宋肇宁[3]

1. 云南师范大学可再生能源材料先进技术与制备教育部重点实验室, 太阳能研究所, 云南 昆明 650092
2. 四川文理学院物理与机电工程学院, 四川 达州 635000
3. Department of Physics and Astronomy, University of Toledo, Toledo OH 43606, USA

摘 要 采用双极脉冲和射频磁控共溅射沉积法在不同温度的Si(100)衬底和石英衬底上制备了富硅 SiN_x 薄膜。在氮气氛中, 于1 050 ℃下采用快速光热退火热处理, 获得了包含硅量子点的 SiN_x 薄膜。采用Fourier变换红外光谱、Raman光谱、掠入射X射线衍射和光致发光光谱对退火后的薄膜样品进行了表征。结果显示: Fourier变换红外光谱中出现了富硅Si—N键, 表明薄膜为富硅 SiN_x 薄膜; 当衬底温度不低于200 ℃时, 薄膜样品的拉曼光谱中出现了硅纳米晶的Si—Si振动横光学模, 掠入射X射线衍射中出现了明显的Si(111)和Si(311)的衍射峰, 证实了硅量子点的形成; 发现存在一最佳衬底温度(300 ℃), 该条件下获得的硅量子点的数量和晶化率最高; 衬底温度为300和400 ℃的样品的光致发光光谱中均有3个可见荧光峰, 结合拉曼光谱结果, 用纳米晶硅的量子限域效应和辐射复合缺陷态对荧光峰进行了合理解释; 由光致发光光谱计算出的衬底温度为300和400 ℃的样品的硅量子点平均尺寸分别为3.5和3.4 nm。这些结果有助于优化含硅量子点的 SiN_x 薄膜的制备参数, 在硅基光电子器件的应用方面有重要意义。

关键词 Si量子点, SiN_x 薄膜, 磁控溅射, 光致发光

中图分类号: O484.5 **文献标识码**: A **DOI**: 10.3964/j.issn.1000-0593(2015)07-00-04

引 言

硅的间接带隙特性限制了其在光电子器件中的应用。然而镶嵌有硅量子点的绝缘基质薄膜材料, 可通过调节量子点尺寸而调控其带隙[1], 因此在光电子器件中有良好的应用前景。其中, 研究得较多的是氧化硅基质和氮化硅基质的硅量子点薄膜。相比于氧化硅基质, 氮化硅具有相对较低的势垒, 更有利于载流子的隧穿输运。因此, 含硅量子点的 SiN_x 薄膜被认为是制备硅基光电子器件[1-3]的优秀候选材料。制备硅量子点薄膜的主要方法有: 化学气相沉积[4]、离子注入[5]和磁控溅射[6]等。研究发现, 采用不同制备方法得到的硅量子点薄膜的微结构和室温光致发光性能存在很大的差异[4]。因此有必要对各工艺制备的富硅 SiN_x 薄膜的结构和光致发光性能进行深入的研究。磁控溅射沉积法作为一种成本低、稳定性好、适合于大面积薄膜的制备方法, 已获得广泛应用。在磁控溅射沉积过程中, 衬底温度对薄膜结构和性能有很大的影响。然而, 迄今为止, 还未见针对脉冲和射频磁控共溅射沉积富硅 SiN_x 薄膜过程中的衬底温度对薄膜的结构和发光性能影响的报道。

本文采用双极脉冲和射频磁控共溅射沉积法在不同的衬底温度下制备了富硅 SiN_x 单层薄膜, 并通过快速光热退火处理凝析出硅量子点。采用Raman光谱, 掠入射X射线衍射(grazing incident X-ray diffraction, GIXRD), Fourier变换红外(Fourier transform infrared, FTIR)光谱和光致发光(photoluminescence, PL)光谱对薄膜的微结构和发光特性进行了研究。

1 实验部分

在JCP-450型磁控溅射系统中采用磁控共溅射技术, 采用Si(100)和石英片作为衬底生长 SiN_x 薄膜。其中石英衬底上的薄膜样品用于Raman光谱的测试, 单晶硅衬底上的薄膜用于FTIR光谱、GIXRD谱和PL光谱的测试。镀膜前, 先将溅射腔室的真空度抽至 5×10^{-4} Pa以下, 通入高纯Ar至工作气压 2.9×10^{-1} Pa, Si靶和 Si_3N_4 靶分别接双极脉冲

收稿日期: 2012-00-00, **修订日期**: 2012-00-00

基金项目: 国家自然科学基金项目(51362031, U1037604), 四川省教育厅资助科研项目(15ZB0317)资助

作者简介: 陈小波, 1982年生, 云南师范大学太阳能研究所博士研究生 e-mail: chenxbok@126.com

* 通讯联系人 e-mail: pzhyang@hotmail.com

电源和射频电源。在溅射过程中，脉冲电源和射频电源的功率分别固定在 100 和 50 W，溅射时间为 90 min。采用 RTP-500 型快速光热退火设备将沉积的薄膜样品在氮气氛中、1 050 ℃进行 3 min 退火处理。为研究不同的衬底温度对薄膜的结构和发光特性的影响，本实验制备了编号为 S_{RT}，S_{100}，S_{200}，S_{300} 和 S_{400} 的样品，分别对应于衬底温度：室温(RT)，100 ℃，200 ℃，300 ℃和 400 ℃。

采用岛津 FTIR-8400S 型傅里叶变换红外光谱仪测量不同样品中的键合作用。采用 DXR 显微拉曼光谱仪测量样品的 Raman 谱，其激发源波长为 532 nm。采用型号为 X'Pert PRO (Cu Kα radiation)的 X 射线衍射仪进行掠入射 X 射线衍射测试，入射角为 1°，2θ 范围为 20°～80°。室温 PL 光谱的测试采用型号为 inVia-Reflex 的激光显微共聚焦拉曼光谱仪，功率为 10 mW、波长为 325 nm 的 He-Cd 激光器作为激发光源。

2 结果与讨论

图 1 给出了不同衬底温度下薄膜样品的 FTIR 谱，不同的峰位对应着薄膜中各种红外活性振动模式吸收，从中可获悉样品的化学键结构和薄膜成分信息。中心在 820～836 cm^{-1}范围的吸收峰带对应于 Si—N 键的非对称伸缩振动模式[7]。根据文献[6]，Si_3—N 键的频率范围在 790～890 cm^{-1}之间，这一范围主要与富硅 Si—N 键相联系，表明制备出了富硅 SiN_x 薄膜。中心在 985～1 045 cm^{-1}范围的峰或肩峰归结于 Si—O—Si 伸缩振动[7]，可能来自溅射过程和退火过程设备中的残余氧的影响。

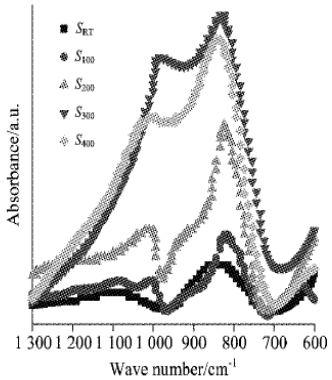

Fig. 1 FTIR spectra of the films for different substrate temperature

拉曼散射是一种可以探测纳米结构材料的晶化程度的无损探测技术。图 2 给出了不同衬底温度下制备的样品的拉曼光谱。样品 S_{RT} 和 S_{100} 的 Raman 谱为典型的 SiO_2(石英衬底)的拉曼光谱[8]，表明在 S_{RT} 和 S_{100} 样品中没有硅量子点形成；样品 S_{200}，S_{300} 和 S_{400} 的拉曼谱中，存在中心位于 150 cm^{-1}和～515 cm^{-1}的峰，归因于非晶硅的一级横声学声子散射和纳米晶硅的 Si—Si 振动横光学模[6]，表明在样品中已有晶硅量子点的形成。当衬底温度从 200 ℃增加到 300 ℃时，位于～515 cm^{-1}的峰强度明显增加，然而衬底温度为 400 ℃时，该峰强反而减小，表明衬底温度为 300 ℃时所制备的薄膜经退火后，其晶硅量子点的数量最大。为了进一步研究样品的结晶情况，对样品 S_{200}，S_{300} 和 S_{400} 的 Raman 谱进行了最佳高斯分峰拟合。薄膜样品晶化率可由式(1)得出[4]

$$X_c = I_c/(I_c + I_a) \quad (1)$$

其中，I_c 和 I_a 分别为晶硅高斯峰和非晶硅高斯峰的积分面积。样品 S_{200}，S_{300} 和 S_{400} 的晶化率分别为 22.1%，25.1%和 24.9%，可见衬底温度以 300 ℃为最佳。对以上结果解释如下：随着衬底温度的升高，沉积在衬底上的硅原子的迁移速率变大，更易形成硅悬挂键反应活性位置(退火时就成为晶核)，从而导致薄膜样品更容易晶化。然而，衬底温度越高，沉积的薄膜越致密，在退火处理时 Si 原子的迁移率就越低，形成硅量子点的难度增加。因此，存在一最佳的衬底温度 300 ℃。

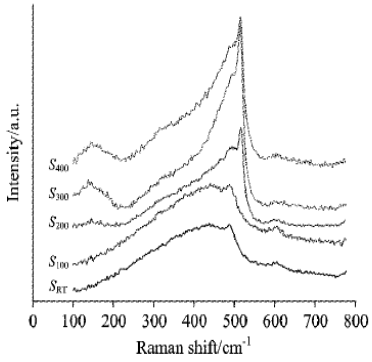

Fig. 2 Raman spectra of the films for different substrate temperature

图 3 显示了不同的衬底温度下制备的薄膜样品在退火后的 GIXRD 谱图，证实了与衬底温度相关的纳米晶硅的形成。样品 S_{300} 和 S_{400} 的 GIXRD 谱中均有中心位置位于 28.3°和 56.1°的衍射峰，分别对应 Si(111)和 Si(311)的布拉格峰，与 S_{400} 样品相比，S_{300} 样品的衍射峰的强度更大、锋形更尖锐，表明 S_{300} 样品中形成的纳米晶硅量子点的数量更多[7]；样品 S_{200} 仅在 28.3°处有一弱的宽衍射峰；样品 S_{RT} 和 S_{100} 则没有明显的衍射峰。以上结果表明，在衬底温度为 300 ℃下制备的薄膜更易于形成晶硅量子点，与 Raman 谱的结果一致。

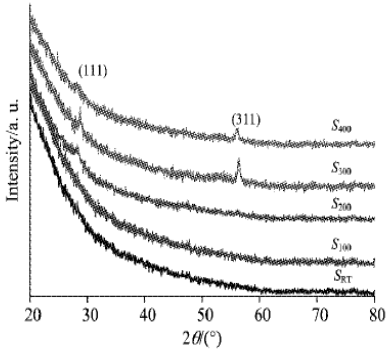

Fig. 3 GIXRD results of the films for different substrate temperature

PL 光谱技术是表征含硅量子点的 SiNx 薄膜的一种常规技术，通过样品的 PL 光谱可分析薄膜内的缺陷和硅量子点生长情况。如图 4 为样品的 PL 光谱，结合拉曼光谱和 GIXRD 的分析，我们重点研究了样品 S_{300} 和 S_{400} 的光致发光特性。通常，经过退火处理后得到的含纳米晶硅量子点的 SiN_x 薄膜的发光主要源于量子点的量子限域效应，同时可能伴随有缺陷态跃迁[9]。两种样品的 PL 谱均有 3 个可见荧光峰。较弱的两个峰 P2 (2.4 eV)和 P3 (2.7 eV)，除强度外，其峰位无变化，因此将其归因于薄膜内的缺陷态[10]：P2 峰(2.4 eV)源于≡Si^0 缺陷到氮化硅的价带的跃迁[11]；P3 峰(2.7 eV)则源于电子从≡Si^- →＝N^- 的跃迁[4]。由于样品 S_{300} 中的硅量子点的数量和尺寸的增加，导致≡Si^- 和≡Si^0 减少，因此样品 S_{300} 的 P2 发光峰和 P3 发光峰的强度均比样品 S_{400} 的小。样品 S_{300} 和 S_{400} 的主要峰位 P1 分别位于 2.1 eV 和 2.2 eV，与通常观察到的 SiN_x 薄膜中量子点的发光峰位一致[4]。因此，我们将 P1 峰归因于硅量子的发光，两样品 P1 峰位的差异源于量子点平均尺寸的不同。发光峰位 E 和晶硅量子点平均尺寸 d 的关系可用式(2)表示[12]

$$E = 1.16 + 11.8/d^2 \quad (2)$$

由式(2)可算出样品 S_{300} 和样品 S_{400} 中的晶硅量子点平均尺寸分别为 3.5 和 3.4 nm。由于样品 S_{300} 中的硅量子点的数量要高于样品 S_{400}，因此样品 S_{300} 中源于量子点的量子限域效应的发光峰 P1 强度较样品 S_{400} 的要稍大。

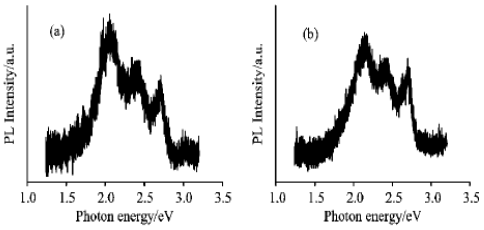

Fig. 4　PL spectra of (a) sample S_{300} and (b) sample S_{400}

3　结　论

衬底温度对脉冲和射频磁控共溅射法制备含硅量子点的富硅 SiN_x 薄膜的微结构和发光性能有显著影响。FTIR 光谱显示各衬底温度下制备的薄膜均出现了富硅 Si—N 键，表明不同的衬底温度下均能制备出富硅 SiN_x 薄膜。Raman 光谱、GIXRD 谱分析表明，在衬底温度不低于 200 ℃时所制备的薄膜经 1050 ℃高温退火后有晶硅量子点的形成。PL 光谱结果显示衬底温度为 300 和 400 ℃的样品均有 3 个可见荧光峰，分别源于硅量子点的量子限域效应和缺陷态跃迁。在衬底温度为 300 ℃时薄膜具有最好的结晶质量和光致发光峰。这些结果有助于优化含硅量子点的富硅 SiN_x 薄膜的制备参数。

References

[1] Nguyen P D, Kepaptsoglou D M, Ramasse Q M, et al. Physical Review B, 2012, 85(8): 085315.
[2] Huang R, Song J, Wang X, et al. Optics letters, 2012, 37(4): 692.
[3] Rodriguez-Gómez A, García-Valenzuela A, Haro-Poniatowski E, et al. Journal of Applied Physics, 2013, 113(23): 233102.
[4] LIAO Wu-gang, ZENG Xiang-bin, WEN Guo-zhi, et al(廖武刚，曾祥斌，文国知，等). Acta Phys. Sin.(物理学报), 2013, 62(12): 126801.
[5] Cen Z H, Chen T P, Liu Z, et al. Optics Express, 2010, 18(19): 20439.
[6] Ha R, Kim S, Kim H J, et al. Journal of Nanoscience and Nanotechnology, 2012, 12(2): 1448.
[7] Li P L, Gau C, Liu C W. Thin Solid Films, 2013, 529: 185.
[8] Mavilla N R, Solanki C S, Vasi J. Physica E: Low-Dimensional Systems and Nanostructures, 2013, 52: 59.
[9] Delachat F, Carrada M, Ferblantier G, et al. Nanotechnology, 2009, 20: 415608.
[10] Jiang L, Zeng X, Zhang X. Journal of Non-Crystalline Solids, 2011, 357(10): 2187.
[11] Wang M, Li D, Yuan Z, et al. Applied Physics Letter, 2007, 90(13): 131903.
[12] Liao W, Zeng X, Wen X, et al. Journal of Electronic Materials, 2013, 42(12): 3445.

Spectral Characteristics of Si Quantum Dots Embedded in SiN_x Thin Films Prepared by Magnetron Co-Sputtering

CHEN Xiao-bo[1,2], YANG Wen[1], DUAN Liang-fei[1], ZHANG Li-yuan[1], YANG Pei-zhi[1*], SONG Zhao-nin[3]

1. Key Laboratory of Education Ministry for Advance Technique and Preparation of Renewable Energy Materials, Institute of Solar Energy, Yunnan Normal University, Kunming 650092, China
2. School of Physics and Mech-Tronic Engineering, Sichuan University of Arts and Science, Dazhou 635000, China
3. Department of Physics and Astronomy, University of Toledo, Toledo OH 43606, USA

Abstract　The silicon-rich SiN_x films were fabricated on Si(100) substrate and quartz substrate at different substrate tempera-

tures varying from room temperature to 400 ℃ by bipolar pulse ane RF magnetron co-sputtering deposition technique. After deposition, the films were annealed in a nitrogen atmosphere by rapid photo-thermal annealing at 1 050 ℃ for 3 minutes. This thermal step allows the formation of the silicon quantum dots. Fourier transform infrared spectroscopy, Raman spectroscopy, grazing incidence X-ray diffraction and photoluminescence spectroscopy were used to analyze the bonding configurations, microstructures and luminescence properties of the films. The experimental results showed that: silicon-rich Si-N bonds were found in Fourier transform infrared spectra, suggesting that the silicon-rich SiN_x films were successfully prepared; when the substrate temperature was not lower than 200 ℃, the Raman spectra of the films showed the transverse optical mode of Si-Si vibration, while the significant diffraction peaks of Si(111) and Si(311) were shown in grazing incidence X-ray diffraction spectra, confirming the formation of silicon quantum dots; our work indicated that there was an optimal substrate temperature (300 ℃), which could significantly increase the amount and the crystalline volume fraction of silicon quantum dots; three visible photoluminescence bands can be obtained for both 300 ℃ sample and 400 ℃ sample, and in combination with Raman results, the emission peaks were reasonably explained by using the quantum confinement effect and radiative recombination defect state of Si nanocrystals; the average size of the silicon quantum dots is 3.5 and 3.4 nm for the 300 ℃ sample and 400 ℃ sample, respectively. These results are useful for optimizing the fabrication parameters of silicon quantum dots embedded in SiN_x thin films and have valuable implications for silicon based photoelectric device applications.

Keywords Silicon quantum dots; Silicon nitride; Magnetron sputtering; Photoluminescence

(Received 2012; accepted 2012)

* Corresponding author

Journal of Power Sources 284 (2015) 369–376

Contents lists available at ScienceDirect

Journal of Power Sources

journal homepage: www.elsevier.com/locate/jpowsour

Multifunctional graphene incorporated polyacrylamide conducting gel electrolytes for efficient quasi-solid-state quantum dot-sensitized solar cells

Jialong Duan [a, b], Qunwei Tang [a, b, *], Ru Li [a], Benlin He [b, **], Liangmin Yu [a, c, ***], Peizhi Yang [d]

[a] Key Laboratory of Marine Chemistry Theory and Technology, Ministry of Education, Ocean University of China, Qingdao 266100, PR China
[b] Institute of Materials Science and Engineering, Ocean University of China, Qingdao 266100, PR China
[c] Qingdao Collaborative Innovation Center of Marine Science and Technology, Ocean University of China, Qingdao 266100, PR China
[d] Key Laboratory of Advanced Technique & Preparation for Renewable Energy Materials, Ministry of Education, Yunnan Normal University, Kunming 650092, PR China

HIGHLIGHTS

- Graphene is incorporated into microporous PAAm matrix.
- The catalytic reaction of redox couples is conducted into conducting gel electrolyte.
- Liquid electrolyte is driven by osmotic pressure and capillary diffusion.
- A power conversion efficiency of 2.34% is recorded in the quasi-solid-state QDSC.

GRAPHICAL ABSTRACT

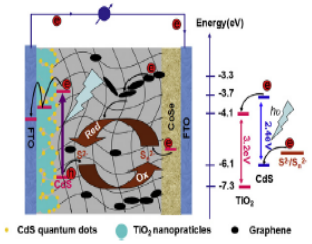

ARTICLE INFO

Article history:
Received 7 January 2015
Received in revised form
6 March 2015
Accepted 9 March 2015
Available online 10 March 2015

Keywords:
Quasi-solid-state quantum dot-sensitized solar cell
Conducting gel electrolyte
Polyacrylamide
Graphene
Hydrogel

ABSTRACT

Pursuit of a high efficiency and stability has been a persistent objective for quantum dot-sensitized solar cells (QDSCs). Here we launch a strategy of synthesizing graphene implanted polyacrylamide (PAAm-G) conducting gel electrolytes for quasi-solid-state QDSCs. With an aim of elevating the dosage of S^{2-}/S_x^{2-} redox couples and therefore charge-transfer ability, both osmotic press across the PAAm-G and capillary force within the three-dimensional micropores are utilized as driving forces. A promising power conversion efficiency of 2.34% is recorded for the QDSCs by optimizing graphene dosage in the conducting gel electrolyte. The enhanced conversion efficiency of solar cell is attributed to the expanded catalytic area from counter electrolyte/electrolyte interface to both interface and the conducting gel electrolyte.

1. Introduction

Quantum dot-sensitized solar cell (QDSC) has drawn considerable attentions as an impressive candidate for the third generation solar cells [1–3]. A typical QDSC comprises a quantum dot-sensitized photoanode, liquid electrolyte containing S^{-}/S_x^{2-} redox

* Corresponding author.
** Corresponding author.
*** Corresponding author.
E-mail addresses: tangqunwei@ouc.edu.cn (Q. Tang), blhe@ouc.edu.cn (B. He), yuyan@ouc.edu.cn (L. Yu).

http://dx.doi.org/10.1016/j.jpowsour.2015.03.060
0378-7753/

couples, and metal sulfide counter electrode. In comparison with dye-sensitized solar cells (DSSCs) [4], the QDSCs demonstrate some bewitching characteristics, such as tunable bad gap [5], high absorption coefficient [6], multiple exciton generation [7], and hot electron transfer of quantum dots (QDs) [8]. A class of narrow bandgap semiconductor QDs such as CdS [9], CdSe [10], CdTe [11], PbS [12], and In_2S_3 [13] have been successfully explored to substitute the organic dyes. In the previous studies, considerable attentions have been focused on improving the power conversion efficiencies of QDSCs by launching new strategies or techniques for synthesizing versatile QDs [14]. Recently, a power conversion efficiency as high as 7.04% has been achieved for the QDSC comprising of a liquid polysulfide (S^{-}/S_x^{2-}) electrolyte and ternary $CuInS_2$ QDs [15]. A remaining issue for the liquid QDSCs is the leakage of liquid electrolyte from the sandwiched solar cell [16]. By addressing this issue, significant achievements have been made by employing solid-state electrolytes [17,18]. Due to the low charge transfer kinetics and the serious photogenerated electron recombination loss and inner energy loss occurring at the electrolyte/electrode interfaces [19,20], the photovoltaic performances are still unsatisfactory. Therefore, it is a prerequisite to explore cost-effective and stable electrolytes for storing redox species.

Polymer gel electrolytes, combination of the stability of solid-state electrolytes and high charge–transfer ability of liquid electrolyte, exhibit promising performances in both quasi-solid-state DSSCs and QDSCs [21,22]. To realize these gel electrolytes, the osmotic pressure across the gel matrix is a mainly driving force for uploading the liquid electrolyte into three-dimensional (3D) gel matrix. In mechanism, the imbibition of liquid electrolyte by the gel matrix is controlled by Flory theory and the imbibed liquid electrolyte has migration kinetics similar to that in liquid system [23]. Once the gel electrolyte is sandwiched between a photoanode and a counter electrode, the reduction reaction occurs at electrolyte/counter electrode interface. Aiming at accelerating the reduction reaction of redox species in the DSSCs, conducting polymers (polyaniline, polypyrrole) [24] and carbonaceous materials (graphene, graphene oxide) [25] have been incorporated into the gel systems to fabricate conducting gel electrolytes in DSSCs, in which the electrocatalytic reaction has been expanded from electrolyte/counter electrode interface to both interface and the gel electrolyte. Moreover, the interconnected conducting channels also shorten the charge diffusion path length and yield a significantly enhanced efficiency in quasi-solid-state DSSCs. Therefore, a promising strategy of fabricating efficient QDSCs with high stability is to design conducting gel electrolytes for quasi-solid-state devices. We present here the synthesis of graphene implanted polyacrylamide (PAAm-G) conducting polymer gel electrolytes by incorporating graphene into the 3D polyacrylamide matrix under the driving force of both osmotic pressure across the gel matrix and capillary diffusion from micropores. The synergistic effect of both osmotic pressure and capillary force is believed to further elevate the dosage of liquid electrolyte in per unit volume of gel electrolyte. Moreover, CoSe alloy is utilized as a counter electrode material to substitute metal sulfides owing to its reasonable electronic conduction and electrocatalytic ability [26]. In comparison with the QDSC from pristine PAAm gel electrolyte, the photovoltaic performances of the solar cells have been markedly enhanced by employing PAAm-G conducting gel electrolytes.

2. Experimental

2.1. Synthesis of microporous PAAm-G composites

The PAM–G matrices were synthesized by an aqueous polymerization route. In details, 10 g of acrylamide monomer and stoichiometric graphene (The percentages of graphene were confined at 3, 5, 7, and 9 wt‰ of the acrylamide monomer) was thoroughly dissolved in 15 mL of deionized water. After vigorous agitation, the reactant was degassed for 10 min and heated in a water bath of 80 °C, 0.0015 g of N,N'-(methylene)bisacrylamide and 0.06 g of ammonium persulfate were successively added into the above mixture. With the proceeding of polymerization, the viscosity increased gradually. When the viscosity of the PAAm-G prepolymers reached around 180 mPa s^{-1}, the reagent was poured into a Petri dish and cooled to room temperature with the formation of an elastic black gel. After being rinsed with excess deionized water, the samples were vacuum dried at 80 °C for more than 12 h. The pristine PAAm matrix was also synthesized with the same method. The microporous PAAm-G matrices were prepared by immersing the dense PAAm-G composites into deionized water for 2 days to reach swelling equilibrium, subsequently the swollen PAAm-G hydrogels were freeze-dried under vacuum at −60 °C for 48 h. The closed 3D framework of PAAm-G matrix will open during the swelling process, whereas the freeze-dry technique can realize the elimination of water with no morphological variation.

2.2. Preparation of conducting PAAm-G gel electrolytes

To realize PAAm-G gel electrolytes, the dense or microporous PAAm and PAAm-G matrices were immersed in a liquid electrolyte consisting of 1 M S and 1 M Na_2S aqueous solution for 5 days to reach their swelling equilibriums. The imbibed liquid electrolyte having S^{2-}/S_n^{2-} redox couples will be reserved in the 3D frameworks of PAAm or PAAm-G gel matrices.

2.3. Fabrication of CdS sensitized TiO_2 anodes

FTO glass substrates (12 Ω cm^{-2}) with a size of 2 × 2 cm^2 were thoroughly rinsed by deionized water and anhydrous ethanol, and dried by N_2 gas flow. The TiO_2 colloid was prepared according to a sol-hydrothermal method [27]. The TiO_2 anode films with an average thickness of 10 μm and an active area of 0.5 × 0.5 cm^2 were fabricated by a screen printing technique. The air-dried colloids were calcined in a muffle furnace at 450 °C for 30 min. The elevation of heating temperature was controlled at a speed of 2 °C min^{-1} till 130 °C, and then at a speed of 6 °C min^{-1} until 450 °C.

To fabricate CdS sensitized TiO_2 anodes, the TiO_2 film was immersed into 0.1 M $Cd(NO_3)_2$ ethanol solution for 1.5 min, rinsed with anhydrous ethanol and dried by N_2 gas stream, then soaked in 0.1 M Na_2S methanol solution for 1.5 min, rinsed with anhydrous methanol and dried by N_2 gas. By repeating the previous procedures for 12 times, we could obtain CdS sensitized TiO_2 anodes.

2.4. Synthesis of CoSe alloy counter electrodes

The CoSe alloy counter electrode was synthesized following previous reports [18]. In details, 0.01 g of Se powers and 0.0238 g of $CoCl_2{\cdot}6H_2O$ were mixed in 27.5 mL of deionized water by vigorous agitation to obtain a homogeneous mixture. Subsequently, 7.5 mL of hydrazine hydrate (85 wt%) was dropped into the above solution. After vigorous agitating for 10 min, the reactant was transferred into a 50 ml of Teflon-lined autoclave and cleaned FTO glass substrate with FTO layer downward was immersed in. After the reaction at 120 °C for 12 h, the FTO substrate was rinsed by deionized water and vacuum dried at 50 °C.

2.5. Assembly and characterizations of quasi-solid-state QDSCs

The quasi-solid-state QDSC was fabricated by sandwiching a slice of gel electrolyte with thickness of around 500 μm between a

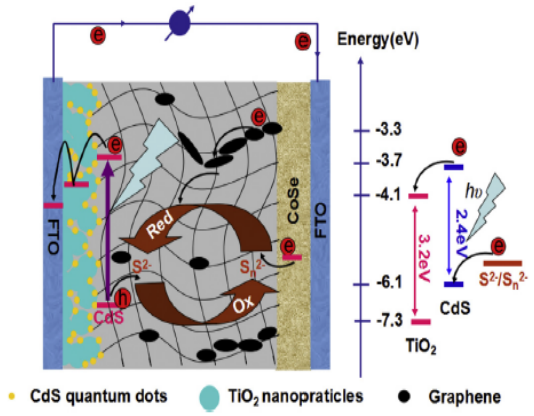

Fig. 1. The schematic diagram of a quasi-solid-state QDSC device from a CdS-sensitized TiO_2 photoanode and a PAAm-G conducting gel electrolyte.

CdS sensitized TiO_2 anode and a CoSe alloy counter electrode, as shown in Fig. 1.

The photocurrent–voltage (J–V) curves of the QDSCs with an active area of 0.25 cm^2 were recorded on an Electrochemical Workstation (CHI600E) under irradiation of a simulated solar light from a 100 W xenon–mercury arc lamp (CHF-XM-500W, Beijing Trusttech Co., Ltd) in ambient atmosphere. The incident light intensity was calibrated using an FZ-A type radiometer from Beijing Normal University Photoelectric Instrument Factory to control it at 100 mW cm^{-2}. Each QDSC device was measured at least five times to eliminate experimental errors and a compromise J–V curve was employed. A black mask with an aperture area of around 0.25 cm^2 was applied on the surface of the cell to avoid stray light.

2.6. Other characterizations

The morphology of the microporous PAAm-7‰G matrix was observed with a scanning electron microscope (SEM). The morphologies of the conducting gel electrolyte with PAAm-7‰G were observed confocal laser scanning microscopy. The ionic conductivities of gel electrolytes were measured by using a pocket conductivity meter (DSSJ-308A, Leici Instrument) by filling the gel electrolytes into the interspace between two electrodes. Prior to experiments, the instrument was calibrated with 0.01 M KCl aqueous solution. For electrochemical impedance spectroscopy (EIS) measurements, the QDSCs were scanned from 0.01 Hz to 10^6 Hz at an ac amplitude of 10 mV.

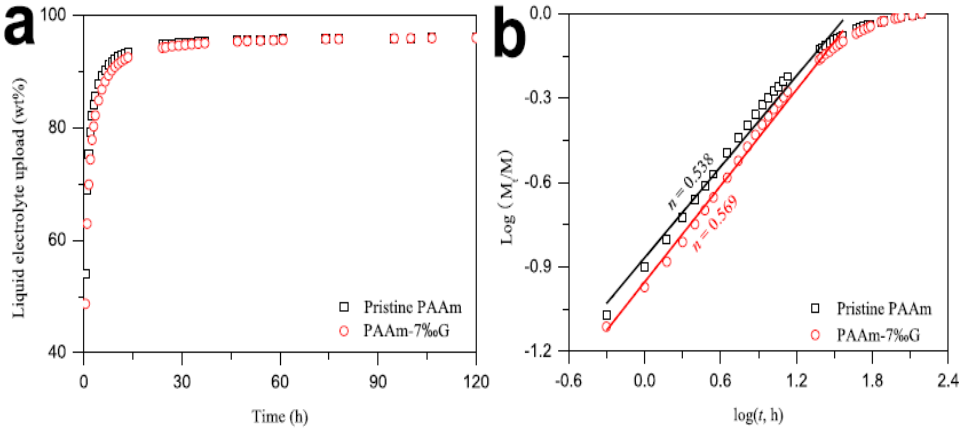

Fig. 2. The time dependences of liquid electrolyte loading for pure PAAm and PAAm-7wt‰G gel electrolytes.

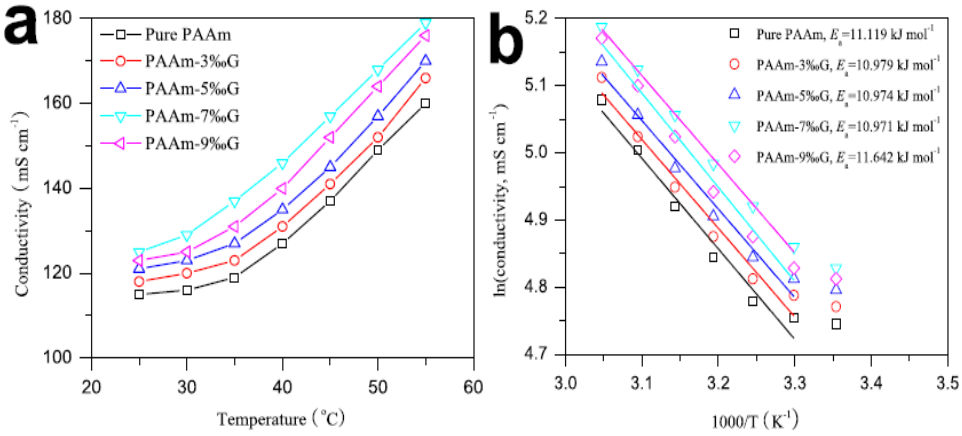

Fig. 3. (a) The temperature dependence of ionic conductivity and (b) Arrhenius plots of various gel electrolytes.

3. Results and discussion

Fig. 2a shows the imbibition kinetics of PAAm and PAAm-7‰G in the liquid electrolyte with no graphene. The swelling of a gel matrix in liquid electrolyte can be involved into three processes: (i) liquid electrolyte enters gel matrix, (ii) relaxation of the macromolecular chains, and (iii) stretch of the whole chains in liquid electrolyte. The liquid electrolyte loading can be obtained according to the equation [25].

$$Liquid\ electrolyte\ loading = \frac{M_{gel} - M_{matrix}}{M_{gel}} \times 100\% \quad (1)$$

where M_{gel} (g) and M_{matrix} (g) are masses of polymer gel electrolyte and anhydrous polymer matrix, respectively. The sharp increase in liquid electrolyte loading within one day means a superabsorbing ability of PAAm or PAAm-7‰G toward liquid electrolyte, yielding a final liquid electrolyte loading of 96.04 or 95.98 wt%, respectively. No apparent deviation in liquid electrolyte uptake suggests that the incorporation of graphene does not alter the imbibition capability and molecular structure of PAAm. The 3D PAAm provides a framework for reserving and migrating liquid electrolyte having S^{2-}/S_n^{2-} redox couples like that in a liquid system, where the implanted graphene can form interconnected channels for conducting reflux electrons (the electrons from external circuit to counter electrode) from CoSe counter electrode to the conducting gel electrolyte. Generally, the swelling of PAAm or PAAm-7‰G in liquid electrolyte obeys Flory theory under the driving of osmotic pressure across the gel matrix [28]. In order to further study the imbibition mechanism, the relationship between the accumulative amount of liquid electrolyte loading and the imbibition time has been fitted by the Fickian theory [29]:

$$\frac{M_t}{M_\infty} = kt^n \quad (2)$$

where M_t and M_∞ are the masses of the imbibed liquid electrolyte at time t and at equilibrium, k is a characteristic rate constant relating to the properties of gel matrix, and n is a transport number characterizing the transport mechanism. $n \leq 0.5$ suggests a Fickian or Case I transport behavior in which the chain relaxation is much faster than the diffusion; $n = 1$ gives a non-Fickian or Case II mode of transport where liquid electrolyte uptake is controlled by diffusion process. $0.5 < n < 1$ refers to an anomalous or a Case III mode in which structural relaxation is comparable to diffusion. According to the plots of $\log(M_t/M_\infty) - \log(t)$ and extracted n values in Fig. 2b, it is clearly that an anomalous mechanism in which structural relaxation is comparable to diffusion in either PAAm or PAAm-7wt‰G matrix.

Fig. 3a shows the conductivity–temperature (σ–t) plots of various gel electrolytes. In comparison with ~115 mS cm^{-2} for pristine PAAm gel electrolyte, the room-temperature ionic conductivities of the conducting gel electrolytes have been markedly enhanced and the maximum conductivity is 125 mS cm^{-2} for PAAm-7wt‰G. The elevated conductivity is expected to enhance the charge–transfer ability of gel electrolyte and therefore

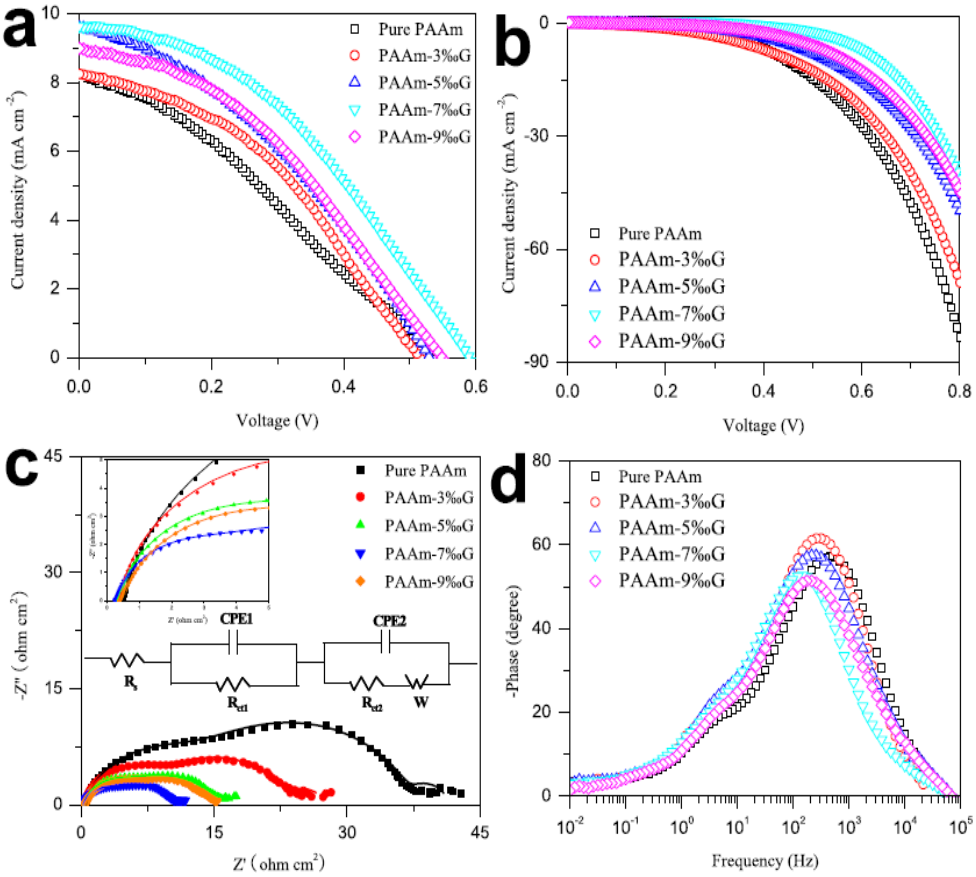

Fig. 4. *J–V* characteristics of quasi-solid-state QDSCs from conducting gel electrolytes under (a) illuminated of AM1.5 and (b) in the dark. (c) Nyquist plots and (d) Bode phase plots for the QDSCs. The inset gives an equivalent circuit by fitting the impedance data.

Table 1
Photovoltaic parameters of the quasi-solid-state QDSCs with dense gel electrolytes. J_{sc}: short-circuit current density; V_{oc}: open-circuit voltage, *FF*: fill factor; η: power conversion efficiency.

Gel electrolytes	V_{oc} (V)	J_{sc} (mA cm^{-2})	η (%)	*FF* (%)
Pure PAAm	0.533	8.21	1.36	31.1
PAAm-3wt‰G	0.515	8.24	1.67	39.4
PAAm-5wt‰G	0.529	9.59	1.84	36.3
PAAm-7wt‰G	0.590	9.63	2.24	39.4
PAAm-9wt‰G	0.548	8.98	1.88	38.2

Table 2
Peak frequency (f_p), electron lifetime (τ), and related parameters of the QDSCs using various gel electrolytes.

Gel electrolytes	R_s (Ω cm^2)	R_{ct1} (Ω cm^2)	R_{ct2} (Ω cm^2)	f_p (Hz)	τ (ms)
Pure PAM	0.513	12.57	23.66	463.90	0.343
PAAm-3wt‰G	0.389	8.718	13.36	285.17	0.558
PAAm-5wt‰G	0.294	3.381	11.94	240.86	0.661
PAAm-7wt‰G	0.265	2.075	8.23	145.43	1.095
PAAm-9wt‰G	0.369	3.094	11.35	190.94	0.834

photovoltaic performances of QDSC device. Arrhenius theory is utilized to study the charge–transfer mechanism by plotting lnσ against 1000/T, as shown in Fig. 3b.

$$\sigma = \sigma_0 \exp\left(-\frac{E_a}{RT}\right) \quad (3)$$

where σ is ionic conductivity, E_a represents activation energy, the minimum energy required for charge conduction through 3D gel matrix. The extracted E_a values are 11.119, 10.979, 10.974, 10.971, and 11.642 kJ mol^{-1} for pure PAAm, PAM-3wt‰G, PAM-5wt‰G, PAM-7wt‰G, and PAM-9wt‰G, respectively. The lowest E_a value at PAM-7wt‰G gel electrolyte indicates that charge movement becomes easier at a graphene dosage of 7wt‰. Till now, we can make a conclusion that the increased conductivity as well as E_a for charge transfer can result in enhanced reaction kinetics in the QDSCs.

The *J*–*V* curves of QDSCs from various gel electrolytes are shown in Fig. 4a and the photovoltaic parameters are summarized in Table 1. An efficiency of 1.36% (V_{oc} = 0.533 V, J_{sc} = 8.21 mA cm^{-2}, *FF* = 31.1%) is recorded for the pristine PAAm gel electrolyte based QDSC, which is in the same level to the liquid QDSC with CdS QDs [30]. After being incorporated with graphene, the efficiency has been elevated to 2.24% (V_{oc} = 0.590 V, J_{sc} = 9.63 mA cm^{-2}, *FF* = 39.4%) for the quasi-solid-state solar cell with PAAm-7wt‰G gel electrolyte. The significant enhancement in photovoltaic performances is attributed to the expansion of catalytic reaction from electrolyte/CoSe electrode interface to both interface and 3D gel electrolyte. It has been widely demonstrated that the combination of conducting species such as carbonaceous materials and conductive polymers with insulating polymers such as PAAm can form interconnected conducting channels for electron transfer [24,25]. When applied as gel electrolyte, the channels by graphene are therefore believed to conduct reflux electrons from CoSe layer to the PAAm framework. In this fashion, the catalytic area for S_n^{2-} reduction is dramatically expanded [31,32], leading to rapid conversion kinetics of $S_n^{2-} \rightarrow S^{2-}$ recation. The S^{2-} ions can further react with photogenerated holes, leaving increased accumulative electrons in photoanode. Contrarily, the S_n^{2-} species at anode/electrolyte must migrate to electrolyte/CoSe electrode interface for conversion and then back to anode/electrolyte interface in pristine PAAm based solar cell. Viewed from this point, the incorporation of graphene into PAAm may shorten the diffusion path length of S^{2-}/S_n^{2-} redox couples. This conclusion can be solidly supported by the elevation of J_{sc} from 8.21 mA cm^{-2} in pristine PAAm electrolyte based solar cell to 9.63 mA cm^{-2} for the cell with PAAm-7wt‰G gel electrolyte. Moreover, the two-view SEM image of PAAm-7wt‰G matrix in Fig. S1b also suggests that the interconnected graphene can conduct reflux electrons to 3D framework of conducting gel electrolyte for expanding catalytic area and shortening charge diffusion path length. However, excessive graphene such as at 9 wt‰, the graphene may weaken the hydrophilicity of PAAm, resulting in a decreased liquid electrolyte loading, charge–transfer ability (as shown in Fig. 3) and therefore photovoltaic performances in its QDSC.

Fig. 4b shows dark *J*–*V* characteristics of the quasi-solid-state QDSCs, in which the cell with PAAm-7wt‰G gel electrolyte displays the smallest dark current density at the same voltage. The dark current originates from a back reaction of electrons on conduction band of TiO_2 nanocrystallites with S_n^{2-} ions. The increased voltage drop from an elevated electron density will accelerate the electron migration to FTO layer along the TiO_2 percolating channels for the PAAm-G gel electrolyte, which limits the recombination reaction between electrons and S_n^{2-} species. The V_{oc} of QDSC is determined by the difference between the quasi Fermi energy of electrons in TiO_2 anode and valence band of CdS QDs. However, the real V_{oc} is generally smaller than this theoretical limit, and the main reason is a backward reaction between electrons and electrolyte.

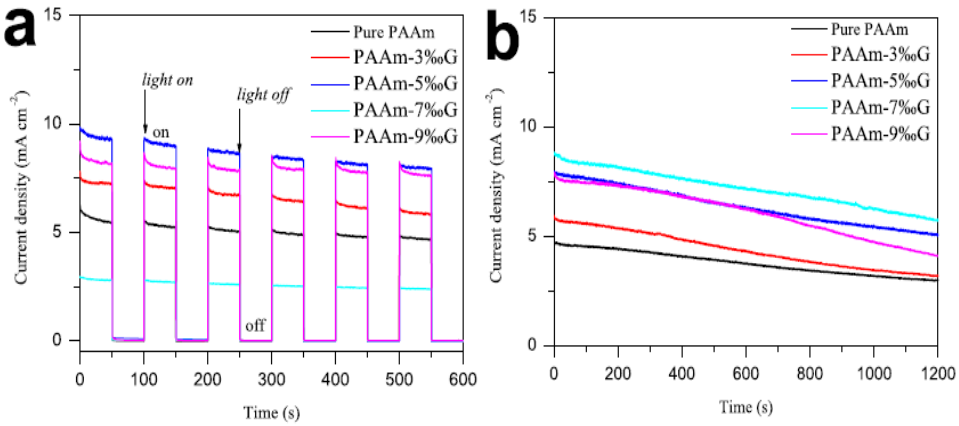

Fig. 5. (a) Start–stop switches and (b) photocurrent stability of the quasi-solid-state QDSCs. The start–stop switches were achieved by alternately irradiating (100 mW cm^{-2}) and darkening (0 mW cm^{-2}) the solar cells at a 50 s interval and 0 V. The photocurrent stabilities were obtained by persistently irradiating the cells at a 100 mW cm^{-2} illumination.

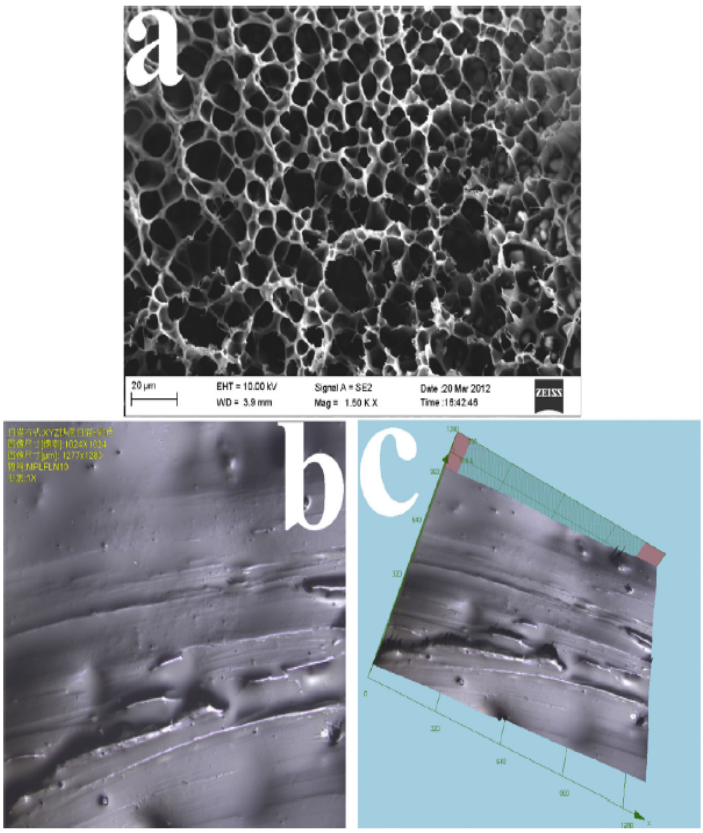

Fig. 6. (a) SEM image of microporous PAAm-7wt‰G matrix and confocal microscope photographs of the conducting gel electrolyte from microporous PAAm-7wt‰G in (b) 2D and (c) 3D modes.

From the dark J–V characteristics in Fig. 4b, we can make a conclusion that the backward reaction between electrons and S_n^{2-} species has been restricted, leading to the largest V_{oc} value.

Electrochemical impedance spectra (EIS) in Fig. 4c were recorded to evaluate the electrochemical performances of QDSCs and the electrochemical parameters such as series resistance (R_s), charge–transfer resistance at the electrolyte/CoSe counter electrode interface (R_{ct1}), and charge–transfer resistance at CdS–TiO_2/electrolyte interface (R_{ct2}) are summarized in Table 2. Apparently, two semicircles assigning to the electrochemical reactions at electrolyte/CoSe counter electrode interface (the smaller one in high frequency region) and charge–transfer process at CdS–TiO_2/electrolyte interface (the larger one in low frequency region). Meanwhile, the average electrons lifetime (τ) is calculated according to the following equation [33]:

$$\tau = \frac{1}{2\pi f_p} \tag{4}$$

where the f_p is the peak frequency attributing to electrochemical reaction at CdS–TiO_2/electrolyte interface, as shown in the Bode spectra (Fig. 4d). The largest τ of 1.095 ms is detected for the QDSC employing PAAm-7wt‰G gel electrolyte. The enhanced τ value is attributed to the decreased R_{ct2} for S^{2-}/S_n^{2-} redox couples and the rapid reaction of holes with S_n^{2-} ions. This result leads to fast electron-transfer process along TiO_2 percolating channels and easy flow of the electrons from CB of CdS to TiO_2 [27]. After performing a comprehensive analysis of the QDSCs, it can be concluded that the solar cell from PAAm-7wt‰G gel electrolyte displays optimal photovoltaic performances.

When applied as photovoltaic curtain walls or portable sources, the solar panels are expected to have superiorities on fast start-up, multiple start/stop capability, and the long-term stability [34]. Fig. 5a shows the start-stop switches of QDSCs with various gel electrolytes in a time slot of 1–600 s. A sharp increase in photocurrent density suggests a quick start-up ability of the cell during operation under irradiation. The high photoelectrochemical kinetics on the quasi-solid-state QDSCs originates from the high charge-transfer ability of PAAm-G gel electrolytes and reasonable catalytic activity of CoSe alloy counter electrode. The interconnected conducting channels from graphene are crucial in expanding catalytic area of $S_n^{2-} \rightarrow S^{2-}$ and shortening charge diffusion path length. Meanwhile, the slightly decreased current density in "on" state indicates that the charges obey a diffusion mechanism within the conducting gel electrolytes. As shown in Fig. 5b, the photocurrent densities of the solar cells over 1200 s demonstrate that the quasi-solid-state QDSCs have reasonable stability on prolonged exposure to light irradiation (100 mW cm^{-2}). The photocurrent densities decrease by 33.3%, 40.5%, 34.7%, 28.6%, and 44.0% for the cells with pure PAAm, PAAm-3wt‰G, PAAm-5wt‰G, PAAm-7wt‰G, and PAAm-9wt‰G gel electrolytes, respectively. This is mainly attributed to the volatilization of water medium from the 3D frameworks.

With an aim of further improving the photovoltaic performances of quasi-solid-state QDSCs, the dense matrices were swollen in deionized water and subsequently freeze-dried at −60 °C. As shown in Fig. 6a, the freeze-dried PAAm-7wt‰G matrix displays homogeneous microporous structure, which is

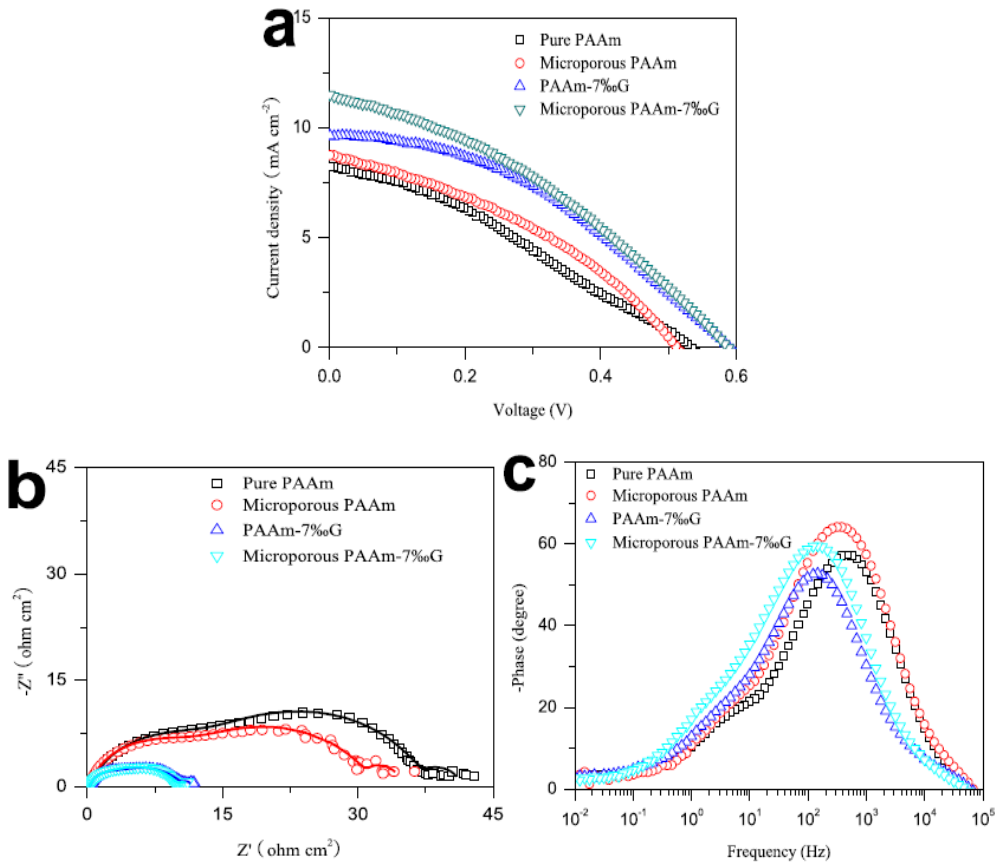

Fig. 7. *J–V* characteristics of quasi-solid-state QDSCs and their EIS spectra: (b) Nyquist plots, (c) Bode phase plot.

superior to enhancing liquid electrolyte uptake. When suffered in liquid attack, both osmotic press across the PAAm-G and capillary force within the 3D micropores are utilized as driving forces. In the fashion, the liquid electrolyte percentage in per unit gel electrolyte is markedly enhanced, leading to enhanced photovoltaic performances in QDSC device. From Fig. 6b and c, the micropores have been filled by liquid electrolyte, therefore the migration mode of S^{2-}/S_n^{2-} redox couples in the 3D framework of PAAm-7wt‰G is similar to that in a liquid system (Fig. S3). The characteristic *J–V* curves of the resultant cells are shown in Fig. 7a and the detailed parameters are summarized in Table 3, yielding an efficiency of 1.64% for the cell with microporous PAAm gel electrolyte in comparison with 1.36% from dense PAAm gel electrolyte based solar cell. These results reveal that the elevation in liquid electrolyte loading has an acceleration effect on photovoltaic performances. Similarly, the power conversion efficiency for the solar cell with conducting gel electrolyte has also been enhanced from 2.24% to 2.34% by utilizing microporous PAAm-7wt‰G gel electrolyte. The enhancement in efficiency is attributed to the elevation in charge–transfer ability and catalytic activity, which can be confirmed by the EIS spectra in Fig. 7b, c, and Table 4.

4. Conclusions

In summary, we have demonstrated that the integration of grapheme with PAAm is an effective strategy of expanding catalytic regions of $S_n^{2-} \rightarrow S^{2-}$ reaction, shortening charge migration path length, and accelerating charge–transfer kinetics. The physicochemical behaviors can be further enhanced by imbibing the liquid electrolyte by osmotic press across the PAAm-G and capillary force within the 3D micropores. An impressive efficiency of 2.34% is recorded for the quasi–solid–state QDSC with microporous PAAm-7wt‰G gel electrolyte in comparison with 1.64% for microporous PAAm based cell. The research presented here is far from being optimized but these profound advantages and cost–effective

Table 3
Photovoltaic parameters of the quasi-solid-state QDSCs from microporous gel electrolytes.

Gel electrolytes	V_{oc} (V)	J_{sc} (mA cm^{-2})	η (%)	FF (%)
Pure PAAm	0.533	8.21	1.36	31.1
Microporous PAAm	0.554	8.78	1.64	33.7
PAAm-7wt‰G	0.590	9.63	2.24	39.4
Microporous PAAm-7wt‰G	0.590	11.47	2.34	34.6

Table 4
Electrochemical parameters of the quasi-solid-state QDSCs from microporous gel electrolytes.

Gel electrolytes	R_s (Ω cm^2)	R_{ct1} (Ω cm^2)	R_{ct2} (Ω cm^2)	f_p (Hz)	τ (ms)
Pure PAAm	0.513	12.57	23.66	463.90	0.343
Microporous PAAm	0.301	10.67	20.11	352.76	0.451
PAAm-7wt‰G	0.265	2.075	8.23	145.43	1.095
Microporous PAAm-7wt‰G	0.250	1.792	7.97	136.49	1.167

synthesis demonstrate the technique to be promising in quasi-solid-state QDSCs.

Acknowledgements

The authors would like to acknowledge financial supports from Fundamental Research Funds for the Central Universities (201313001, 201312005), Shandong Province Outstanding Youth Scientist Foundation Plan (BS2013CL015), Shandong Provincial Natural Science Foundation (ZR2011BQ017), Research Project for the Application Foundation in Qingdao (13-4-198-jch), National Key Technology Support Program (2012BAB15B02), National Natural Science Foundation of China (U1037604), and National High-Tech Research and Development Programme of China (2010AA09Z203, 2010AA065104).

Appendix A. Supplementary data

Supplementary data related to this article can be found at http://dx.doi.org/10.1016/j.jpowsour.2015.03.060.

References

[1] X.Z. Lan, S. Masala, E.H. Sargent, Nature 13 (2014) 233–240.
[2] G.E. Jabbour, D. Doderer, Nat. Photonics 4 (2010) 604–605.
[3] L. Tao, Y. Xiong, H. Liu, W.Z. Shen, Nanoscale 6 (2014) 931–938.
[4] B. O'Regan, M. Grätzel, Nature 353 (1991) 737–740.
[5] D.D. Sarma, A. Nag, P.K. Santra, A. Kumar, S. Sapra, P. Mahadevan, J. Phys. Chem. Lett. 1 (2010) 2149–2153.
[6] W.W. Yu, L.H. Qu, W.Z. Guo, X.G. Peng, Chem. Mater. 15 (2003) 2854–2860.
[7] M.C. Beard, J. Phys. Chem. Lett. 2 (2011) 1282–1288.
[8] W.A. Tisdale, K.J. Williams, B.A. Timp, D.J. Norris, E.S. Aydil, X.Y. Zhu, Science 328 (2010) 1543–1547.
[9] C.Q. Ma, Q.W. Tang, D.Y. Liu, Z.Y. Zhao, B.L. He, H.Y. Chen, L.M. Yu, J. Power Sources 276 (2015) 215–221.
[10] X.H. Song, M.Q. Wang, H. Zhang, J.P. Deng, Z. Yang, C.X. Ran, X. Yao, Electrochim. Acta 108 (2013) 449–457.
[11] J. Luo, H. Wei, F. Li, Q. Huang, D. Li, Y. Luo, Q.B. Meng, Chem. Commun. 50 (2014) 3464–3466.
[12] X.N. Li, W.H. Lu, Y.N. Wang, Y.Y. Fang, L.L. Wang, Q.L. Ai, X.W. Zhou, Y. Lin, Electrochim. Acta 144 (2014) 71–75.
[13] J.L. Duan, Q.W. Tang, B.L. He, L.M. Yu, Electrochim. Acta 137 (2014) 175–182.
[14] G.P. Xu, S.L. Ji, C.H. Miao, G.D. Liu, C.H. Ye, J. Mater. Chem. 22 (2012) 4890–4896.
[15] Z.X. Pan, I. Mora-Sero, Q. Shen, H. Zhang, K. Zhao, J. Wang, X.H. Zhong, J. Bisquert, J. Am. Chem. Soc. 136 (2014) 9203–9210.
[16] K.F. Chen, C.H. Liu, C.K. Hsieh, C.L. Lin, H.K. Huang, C.H. Tsai, et al., J. Power Sources 247 (2014) 939–946.
[17] B.H. Lee, H.C. Leventis, S.J. Moon, P. Chen, S. Ito, S.A. Haque, T. Torres, F. Nüesch, T. Geiger, S.M. Zakeeruddin, M. Grätzel, M.K. Nazeeruddin, Adv. Funct. Mater. 19 (2009) 2735–2742.
[18] J.L. Duan, Q.W. Tang, Y.N. Sun, B.L. He, H.Y. Chen, RSC Adv. 4 (2014) 60478–60483.
[19] M.A. Hossain, J.R. Jennings, Z.Y. Koh, Q. Wang, ACS Nano 5 (2011) 3172–3181.
[20] P.V. Kamat, K. Tvrdy, D.R. Baker, J.G. Radich, Chem. Rev. 110 (2010) 6664–6688.
[21] S.S. Yuan, Q.W. Tang, B.B. Hu, C.Q. Ma, J.L. Duan, B.L. He, J. Mater. Chem. A 2 (2014) 2814–2821.
[22] Z.X. Yu, Q.X. Zhang, D. Qin, Y.H. Luo, D.M. Li, Q. Shen, T. Toyoda, Q.B. Meng, Electrochem. Commun. 12 (2010) 1776–1779.
[23] S.S. Yuan, Q.W. Tang, B.L. He, H.Y. Chen, Q.H. Li, C.Q. Ma, et al., J. Power Sources 249 (2014) 277–284.
[24] S.S. Yuan, Q.W. Tang, B.L. He, P.Z. Yang, J. Power Sources 254 (2014) 98–105.
[25] S.S. Yuan, Q.W. Tang, B.L. He, Y. Zhao, J. Power Sources 260 (2014) 225–232.
[26] J.G. Radich, R. Dwyer, P.V. Kamat, J. Phys, Chem. Lett. 2 (2011) 2453–2460.
[27] Y.Y. Duan, Q.W. Tang, Z.H. Chen, B.L. He, H.Y. Chen, J. Mater. Chem. A 2 (2014) 12459–12465.
[28] J.H. Wu, Y.L. Wei, J.M. Lin, S.B. Lin, Polymer 44 (2003) 6513–6520.
[29] N.W. Franson, N.A. Peppas, J. Appl, Polym. Sci. 28 (1983) 1299–1310.
[30] H.N. Chen, L.Q. Zhu, H.C. Liu, W.P. Li, J. Power Sources 245 (2014) 406–410.
[31] X.L. Zhang, X.M. Huang, Y.Y. Yang, S. Wang, Y. Gong, Y.H. Luo, D.M. Li, Q.B. Meng, ACS Appl. Mater. Interfaces 5 (2013) 5954–5960.
[32] D.M. Li, L.Y. Cheng, Y.D. Zhang, Q.X. Zhang, X.M. Huang, Y.H. Luo, Q.B. Meng, Sol. Energ. Mat. Sol. C 120 (2014) 454–461.
[33] M.X. Wu, X. Lin, Y.D. Wang, L. Wang, W. Guo, D.D. Qi, X.J. Peng, A. Hagfeldt, M. Grätzel, T.L. Ma, J. Am. Chem. Soc. 134 (2012) 3419–3428.
[34] C. Laberty-Robert, K. Vallé, F. Pereira, C. Sanchez, Chem. Soc. Rev. 40 (2011) 961–1005.

Journal of Power Sources 284 (2015) 178–185

Contents lists available at ScienceDirect

Journal of Power Sources

journal homepage: www.elsevier.com/locate/jpowsour

A dye-sensitized solar cell having polyaniline species in each component with 3.1%-efficiency

Yanyan Duan [a, b, 1], Yuran Chen [a, b, 1], Qunwei Tang [a, b, *], Zhiyuan Zhao [b], Mengjin Hou [b], Ru Li [a, c], Benlin He [b, *], Liangmin Yu [a, c, **], Peizhi Yang [d], Zhiming Zhang [a, c]

[a] Key Laboratory of Marine Chemistry Theory and Technology, Ministry of Education, Ocean University of China, Qingdao 266100, PR China
[b] Institute of Materials Science and Engineering, Ocean University of China, Qingdao 266100, PR China
[c] Qingdao Collaborative Innovation Center of Marine Science and Technology, Ocean University of China, Qingdao 266100, PR China
[d] Key Laboratory of Advanced Technique & Preparation for Renewable Energy Materials, Ministry of Education, Yunnan Normal University, Kunming 650092, PR China

HIGHLIGHTS

- The DSSC having PANi species in each component yield an efficiency of 3.1%.
- The solar cell consists of a PANi/TiO_2 anode, a PANi CE, and a PANi electrolyte.
- The PANi electrolyte can shorten charge diffusion path length.
- The new concept is also applicable to all-carbon solar cells, etc.

GRAPHICAL ABSTRACT

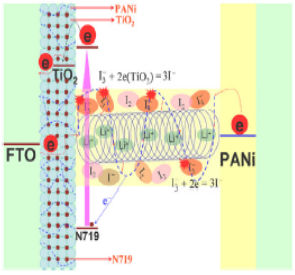

ARTICLE INFO

Article history:
Received 22 December 2014
Received in revised form
4 February 2015
Accepted 5 March 2015
Available online 5 March 2015

Keywords:
Dye-sensitized solar cell
Polyaniline
Counter electrode
Solid-state electrolyte

ABSTRACT

Pursuit of technological implementation with no sacrifice of photovoltaic performances has been a persistent objective for dye-sensitized solar cells (DSSCs). We launch here the experimental realization of a class of DSSCs consisting of polyaniline (PANi) incorporated TiO_2 anodes, PANi counter electrodes (CEs), and iodide doped PANi solid-state electrolytes. The PANi filled in photoanode can inject electrons for dye recovery, whereas the PANi CE fulfills the function of reducing triiodide into iodide ions. In particular, the solid PANi electrolyte has an ability of catalyzing triiodide species, shortening charge diffusion path length, and recovering dye molecules at anode/electrolyte interface. The photovoltaic performances are optimized by adjusting assembly process and lithium iodide dosage, yielding a maximum efficiency as high as 3.1% in the resultant DSSC device accompanied with fast start-up, multiple start/stop cycling, and good stability under persistent irradiation.

1. Introduction

Photovoltaic conversion is a promising solution to the energy requirement for nowaday's low-carbon economy [1–4]. Among excitonic cells, dye-sensitized solar cell (DSSC) [5–9], an electrochemical device converting solar energy into electricity with no emission, has attracted considerable interests because of its

* Corresponding authors. Institute of Materials Science and Engineering, Ocean University of China, Qingdao 266100, PR China.
** Corresponding author. Key Laboratory of Marine Chemistry Theory and Technology, Ministry of Education, Ocean University of China, Qingdao 266100, PR China.
E-mail addresses: tangqunwei@ouc.edu.cn (Q. Tang), blhe@ouc.edu.cn (B. He), yuyan@ouc.edu.cn (L. Yu).
[1] The authors have the same contributions to the work.

http://dx.doi.org/10.1016/j.jpowsour.2015.03.032
0378-7753/

superiorities on simple fabrication, promising power conversion efficiency, and scalable materials. Since the first prototype created by Grätzel in 1991 [10], an efficiency of 13% has been measured for the cell with Pt counter electrode (CE), dye-sensitized TiO_2 photoanode along with liquid electrolyte containing $I^-/I_3^-I_3^-$ redox couples [11]. However, the bleak commercialization prospect of DSSCs mainly arises from the intrinsic limitations in poor stability resulting from leakage of liquid electrolyte [12–14]. A promising approach of overcoming such an impasse is to design solid-state electrolytes of either enhancing charge transfer ability (I^-, I_3^-) or injecting holes into hole transporting materials (HTMs) [15,16]. Another economic burden for DSSCs is high fabrication cost of Pt Ces [17]. Therefore, many efforts have been made to explore candidates for Pt species, such as conducting polymers [18,19], carbonaceous materials [20,21], metal sulfonates [22], and binary alloys [23,24]. In particular, the DSSC employing either solid-state electrolyte or HTM can not realize the rapid recovery of organic dyes located far from the TiO_2/electrolyte (or HTM) interface, generating an unsatisfactory conversion efficiency [25].

The structure of a solar cell is crucial in determining the functional properties of a photoelectrochemical system. Early works in this area were mainly focused on either replacing TiO_2 by other wide-band-gap oxide semiconductors [26] or using cost-effective CEs [27] or solid-state electrolytes [28,29] for enhanced charge transport and hole injection. To our knowledge, there are no systematic aging studies on efficient DSSCs by combining these three components, particularly using the same species. Here we launch an experimental realization of a class of DSSCs consisting of polyaniline (PANi) incorporated TiO_2 anodes with shortened electron migration length, cost-effective H^+ doped PANi CEs, and I_2 doped PANi solid-state electrolytes having shortened charge diffusion path length along with electrocatalytic and hole-transporting functions. The original intention of this design is to elevate the cell stability, to reduce fabrication cost, and to simplify the preparation techniques. An optimal efficiency as high as 3.1% under air mass 1.5 (AM1.5) global sunlight as well as simple synthesis and scalable components demonstrate the concept to be applicable in enabling the technological implementation of solid DSSCs.

2. Experimental

2.1. Synthesis of I_2 doped PANi

In the dark, 2 g of I_2 was dissolved in 50 mL of ethanol aqueous solution ($V_{water}/V_{ethanol}$ = 1/1) to obtain a homogeneous mixture. 3 mL of aniline was dipped in the above mixture within 30 min. The polymerization reaction was carried out at 4 °C. After 48 h, the resultant reactant was air-blowing dried at 50 °C.

2.2. Synthesis of H^+ doped PANi

1.48 mL of aniline was dissolved in 50 mL of 1 M HCl aqueous solution to obtain a homogeneous mixture. A freshly cleaned FTO glass was put at the bottom of the reaction vessel with FTO layer upward. 50 mL of 0.125 M ammonium peroxydisulfate aqueous solution was dipped in the above mixture within 1 h. The polymerization reaction was carried out at 4 °C for 24 h. The H^+ doped PANi CE and resultant reactant were both rinsed by 1 M HCl aqueous solution, filtrated, and finally air-blowing dried at 60 °C for 24 h.

2.3. Preparation of photoanodes

A layer of TiO_2 nanocrystal anode film with a thickness of ~10 μm was prepared by a sol-hydrothermal method. The resultant anodes were further immersed in an N-methyl-2-pyrrolidone solution dissolved H^+ doped PANi solution (0.5 mg mL^{-1}) for 10 min, after being rinsed by anhydrous ethanol and dried by N_2 gas flow, the TiO_2/PANi photoanodes were sensitized by immersing into a 0.25 mM ethanol solution of N719 dye for 24 h.

2.4. DSSC assembly

The DSSC was fabricated by sandwiching solid-state electrolyte between a dye-sensitized TiO_2/PANi anode and a PANi CE. Four strategies were utilized to assemble the solar cell devices: (i) Before the cell assembly, a viscous electrolyte was prepared by dissolving 0.061 g of I_2 doped PANi, 0.11 g of LiI, and 0.25 g of PEO in 50 mL of acetonitrile. After vigorous agitation for 24 h, the reactant was vacuum-dried at 55 °C for 14 h to control the volume at around 5 mL. The viscous electrolyte was dipped on a dye-sensitized anode, after being covered by a PANi CE, the solar cell was air-blowing dried at 60 °C for 15 min and sealed by a Surlyn film (30 μm) through hot-pressing. (ii) The viscous electrolyte was dipped on dye-sensitized anode and then covered by a PANi CE and subsequently sealed by a Surlyn film through hot-pressing. Afterward, the device was air-blowing dried at 60 °C for 30 min (iii) The viscous electrolyte was thoroughly vacuum-dried at 55 °C for 48 h. A slice of the solid electrolyte was sandwiched between a dye-sensitized anode and a PANi CE and then sealed by a Surlyn film through hot-pressing. (iv) The device in approach (ii) was vacuum-dried at 60 °C for 30 min.

2.5. Photovoltaic measurements

The photovoltaic test of the DSSC with an active area of 0.25 cm^2 was carried out by measuring the photocurrent–voltage (J–V) characteristic curves using a CHI660E Electrochemical Workstation under irradiation of a simulated solar light from a 100 W Xenon arc lamp (XQ-500 W) in ambient atmosphere. The incident light intensity was controlled at 100 mW cm^{-2} (calibrated by a standard silicon solar cell). A black mask with an aperture area of around 0.25 cm^2 was applied on the surface of DSSCs to avoid stray light. Each J–V curve was repeatedly measured at least five time to control the experimental error within ±5%.

2.6. Electrochemical characterizations

The electrochemical performances were recorded on a conventional CHI660E setup comprising an Ag/AgCl reference electrode, a CE of Pt sheet, and a working electrode of FTO glass supported electrolyte. The CV curves were recorded in a supporting electrolyte consisting of 50 mM M LiI, 10 mM I_2, and 500 mM $LiClO_4$ in acetonitrile. Bode phase measurements were carried out in a frequency range of 0.1 Hz ~ 10^5 kHz and an ac amplitude of 10 mV at room temperature. Both Bode plots and Tafel polarization curves were recorded by assembling symmetric dummy cell consisting of PANi CE|solid-state electrolyte|PANi CE.

2.7. Other characterizations

The absorption spectra of resultant anode, electrolyte, and CE were recorded on a UV–vis spectrophotometer at room temperature. The morphologies of the resultant TiO_2/PANi anode and PANi CE were observed with a scanning electron microscope (SEM, S-3500N, Hitachi, Japan). The X–ray diffraction (XRD) data were collected in the 2θ range between 10 and 50° at a scanning speed of 10° min^{-1}. Fourier transform infrared spectrometry (FTIR) spectra were recorded on a PerkinElmer spectrum 1760 FTIR spectrometer. The UV–vis spectra were measured on a UV-3200

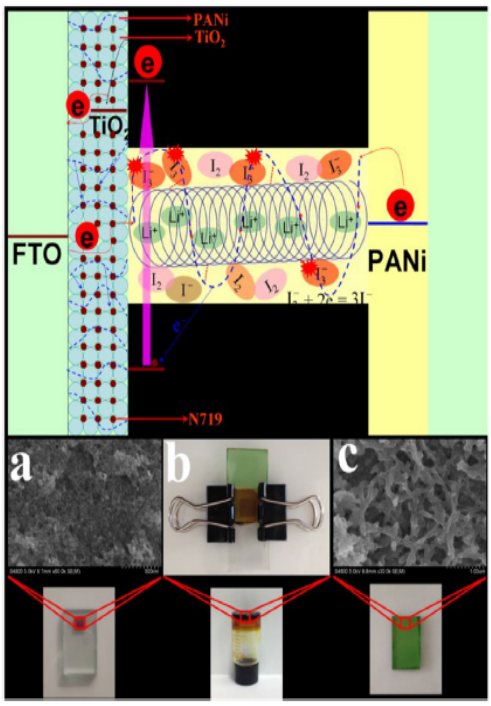

Fig. 1. (Top) Schematic illustration of a DSSC and charge-transfer mechanism. (Down) topologies of (a) TiO_2/PANi photoanode and top-view SEM photograph, (b) I_2 doped PANi solid-state electrolyte and solar cell, (c) H^+ doped PANi CE and top-view SEM image.

spectrophotometer. Fourier transformed Raman spectroscopic measurements in the ultraviolet light were performed on a Renishaw inVia Reflex Raman Spectrometer. High–resolution gratings were used to give a spectral resolution of 2 cm^{-1}.

3. Results and discussion

The topologies of the TiO_2/PANi photoanode, I_2 doped PANi solid-state electrolyte, and H^+ doped PANi CE are subjected to morphological examinations. As shown in Fig. 1a, the TiO_2 has been colored after immersion in H^+ doped PANi aqueous solution, meaning that positively charged PANi has been bonded onto negatively charged TiO_2 nanoparticles. Once the photogenerated electrons flow from excited dyes to conduction band (CB) of TiO_2 nanocrystallites, they can transfer to FTO layer along the TiO_2 nanocrystallite channels. Due to a solid-state feature of the electrolyte, the oxidated dye molecules at anode/electrolyte interface can be recovered by both I^- species and electron injection from the PANi in electrolyte, whereas the PANi filled in photoanode will regenerate the dyes far away the interface by electron injection. In order to further demonstrate the solid nature of the electrolyte having I_2 doped PANi and PEO, the container is inverted, as shown in Fig. 1b, the electrolyte stays on the bottom of a vessel and no flow is observed, which is a powerful support for solid-state electrolyte. Notably, moderate PEO is prerequisite to prevent the formation of a short circuit between a TiO_2/PANi photoanode and a PANi CE.

Fig. 2a displays the FTIR spectra of I_2 doped PANi and the resultant solid electrolyte. The observation of absorption bands at 800–900 cm^{-1} indicates the occurrence of PANi polymerization via a head-to-tail mechanism [30]. The oxygenic species are expected to interact with conjugated structure of PANi, especially through

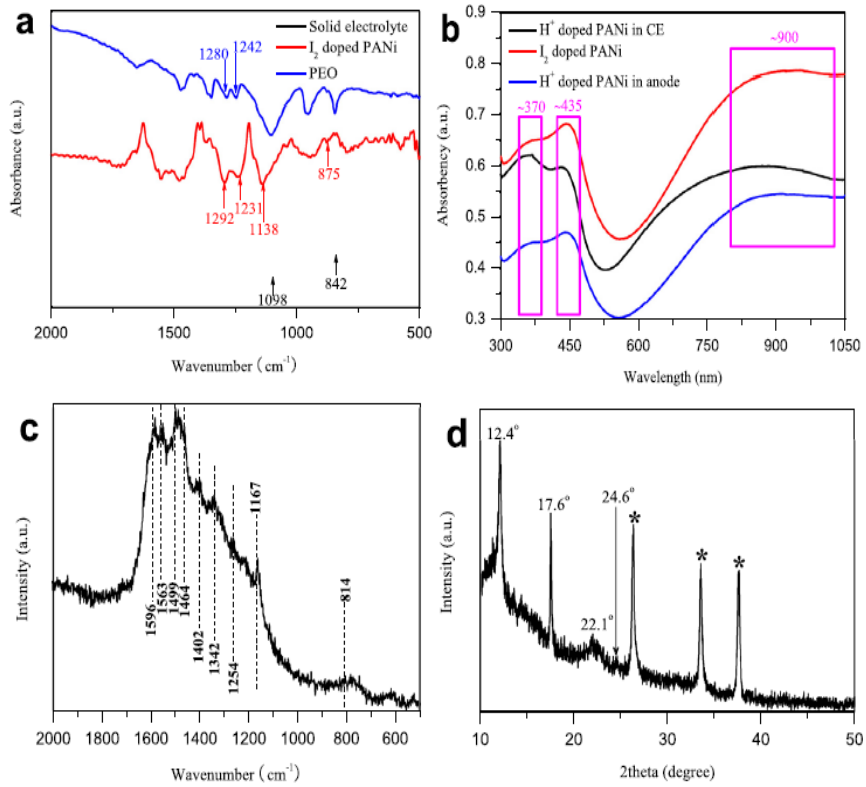

Fig. 2. (a) FTIR spectra of PEO incorporated PANi electrolyte, I_2 doped PANi, and pristine PEO. (b) UV–vis spectra of H^+ doped PANi for CE and anode, and I_2 doped PANi for solid electrolyte. FTO glass and FTO glass supported TiO_2 were utilized as benchmarks for recording UV–vis spectra of a CE and an anode, respectively. (c) Raman spectrum and (d) XRD pattern of the H^+ doped PANi CE. The peaks labeled with (*) are attributed to FTO glass.

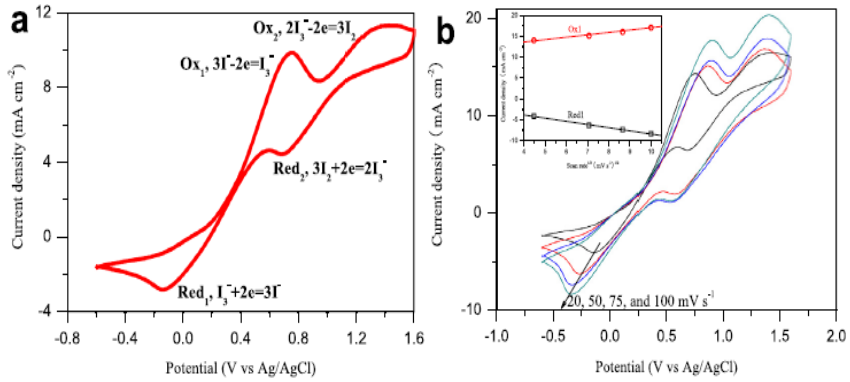

Fig. 3. (a) CV curve of the PANi CE in a liquid electrolyte consisting of 50 mM M LiI, 10 mM I_2, and 500 mM $LiClO_4$ in acetonitrile. The CV curve was recorded at a scan rate of 20 mV cm^{-1} and at room temperature. (b) Stacking CV curves of the PANi CE recorded at various scan rates. The inset gives the linear relationships between peak current densities and square root of scan rate.

the quinoid ring (semiquinone radical cation), as has been reported in the case of nanoscrystalline TiO_2 and Au [31]. Once the PANi is integrated with PEO, the bands attributing to C–N stretching in the secondary aromatic amine and C–N–C stretching vibration in the polaron structure move from 1292 to 1231 cm^{-1} to 1280 and 1242 cm^{-1}, respectively. Additionally, the bands for C–O–C stretching and C–O stretching at 1098 and 842 cm^{-1} in pristine PEO have also shifted to 1138 and 875 cm^{-1} in the solid electrolyte, respectively. These signal the possible interaction between PANi (C–N) and PEO (C–O–C) through H-bonds. Fig. 1c shows SEM image of the H^+ doped PANi CE, exhibiting well-defined fibrous morphology with a diameter of around 100 nm. The nanofiber network characteristic of a PANi electrode can significantly facilitate the redox reaction of I^-/I_3^- redox couples. The absorption curves for PANi in a photoanode, a CE, and a solid electrolyte are shown in Fig. 2b, giving a similar shape and three absorption bands at ~370, ~435, and ~900 nm. The bands at ~370 and ~435 nm can be attributed to $\pi \rightarrow \pi^*$ transitions and the polaron band $\rightarrow \pi^*$ transition in the centers of benzenoid rings, respectively [32]. The band at infrared region originates from the charged cationic species, known as $\pi \rightarrow$ localized polaron transition [33]. This broad band may be caused by the interband charge transfer from

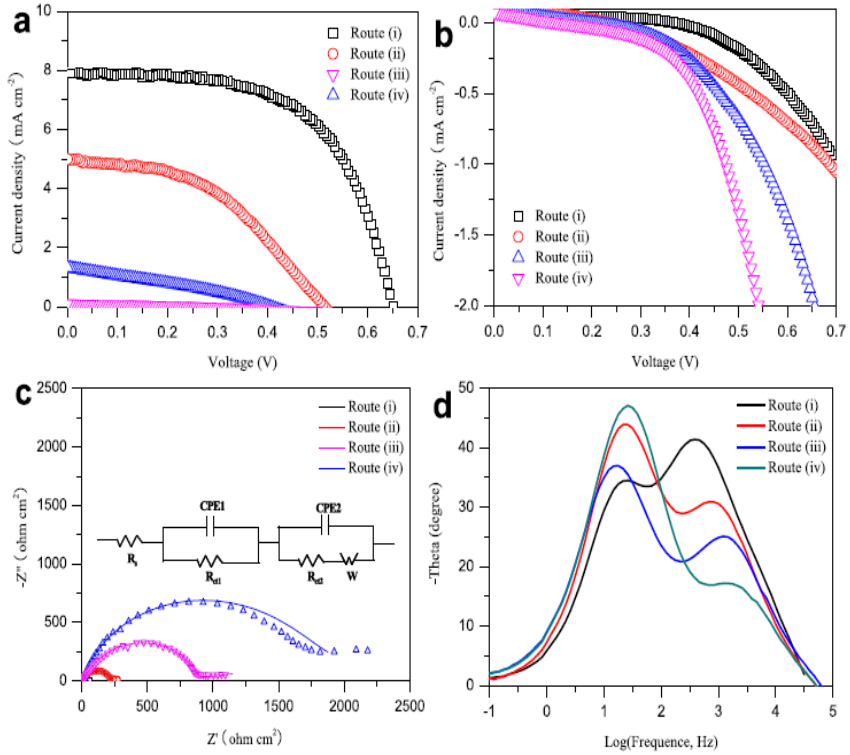

Fig. 4. Characteristic *J–V* curves of the DSSCs recorded (a) at AM1.5G irradiation and (b) in the dark. (c) Nyquist and (d) Bode EIS spectra for the DSSCs with different assembly strategies. The mass ratio of LiI to I_2 doped PANi was 1.8. R_s: series resistance; R_{ct1}: charge-transfer resistance at CE/electrolyte interface; R_{ct2}: charge-transfer resistance at anode/dye/electrolyte interface; *W*: Nernst diffusion resistance corresponding to the I^-/I_3^- redox couples; CPE1 and CPE2: constant phase elements.

Table 1
Photovoltaic parameters of DSSCs from various strategies: V_{oc}: open-circuit voltage; J_{sc}: short-circuit current density, *FF*: fill factor; η: power conversion efficiency; τ: electron lifetime.

Strategies	η (%)	V_{oc} (V)	J_{sc} (mA cm^{-2})	*FF* (%)	τ (μs)
Route (i)	3.1	0.649	7.92	60.3	404
Route (ii)	1.2	0.512	4.99	47.0	207
Route (iii)	0.2	0.422	1.38	34.3	125
Route (iv)	0.01	0.412	0.13	18.7	118

Table 2
Electrochemical parameters of the DSSCs from various strategies. R_{ct1}, R_{ct2}, and *W* are extracted from the EIS spectra of the solar cells.

Strategies	R_{ct} (Ω cm^2)	τ (ms)	R_{ct1} (Ω cm^2)	R_{ct2} (Ω cm^2)	*W* (Ω cm^2)
Route (i)	169.3	10.1	1.2	29.8	87.5
Route (ii)	931.1	30.4	3.0	204.8	255.2
Route (iii)	755.7	34.2	14.9	864.9	2017
Route (iv)	5972	206.3	29.3	1384	8178

benzenoid to quinoid rings of the conjugated PANi. As shown in Fig. 2c, the appearance of Raman bands indicates that the as-synthesized PANi doped by H^+ and I_2 are in their emeraldine state [34]. The detection of three characteristic bands at 1596 cm^{-1} (C=C stretching vibration in the quinoid rings), 1563 cm^{-1} (C–C stretching of intermediates between quinoid and semiquinoid rings), and 1499 cm^{-1} (C=N stretching of quinoid rings) suggests the conjugated structure of PANi. Moreover, the diffraction peaks at $2\theta = 12.4$, 17.6, 22.1, and 24.6° demonstrates that the resultant PANi has highly ordered molecular structure (Fig. 2d) [35,36]. This ordering structure is expected to provide superhighways for charge transfer.

In this fashion, cyclic voltammetry (CV) technique can be utilized to determine the catalytic activity, as shown in Fig. 3a, giving two pairs of redox peaks (Red_1/Ox1, Red_2/Ox_2) corresponding to interconversion reactions between I^- and I_3^- species in the CV curves. The similar peak positions and shapes to those of pristine Pt electrode indicate that the resultant PANi CE has catalytic behavior toward I^-/I_3^- redox couples [37]. From the stacked CV curves of the PANi electrode, as shown in Fig. 3b, we can make a conclusion that the cathodic and anodic reactions obey a diffusion-limited mechanism and there is no specific interaction between I^-/I_3^- redox couples and electrodes due to linear relationships for both Ox1 and Red1 reactions between the square root of scan rate and peak current density [38,39].

Fig. 4a compares *J–V* characteristics of the DSSCs and the detailed photovoltaic parameters are summarized in Table 1. The cell assembled by route (i) yields an optimal efficiency of 3.1% J_{sc} of 7.92 mA cm^{-2}, V_{oc} of 0.649 V, and *FF* of 60.3%, which are much higher than the values from other strategies. The results demonstrate that it is realizable to design DSSC with a PANi CE, a PANi electrolyte, and a PANi incorporated TiO_2 anode by optimizing the assembly technologies. J_{sc} is dependent on the accumulative electron density on the CB of TiO_2 injected from excited dyes [40]. In route (i), the viscous electrolyte in acetonitrile has a close contact with TiO_2/PANi anode but can not diffuse into its mesoporous structure, therefore the dye recovery is derived from electron injection of PANi in the anode as well as I^- reduction and electron injection of PANi in the electrolyte. This conclusion can be supported by the characteristic *J–V* curve of the solar cell with I^-/I_3^-

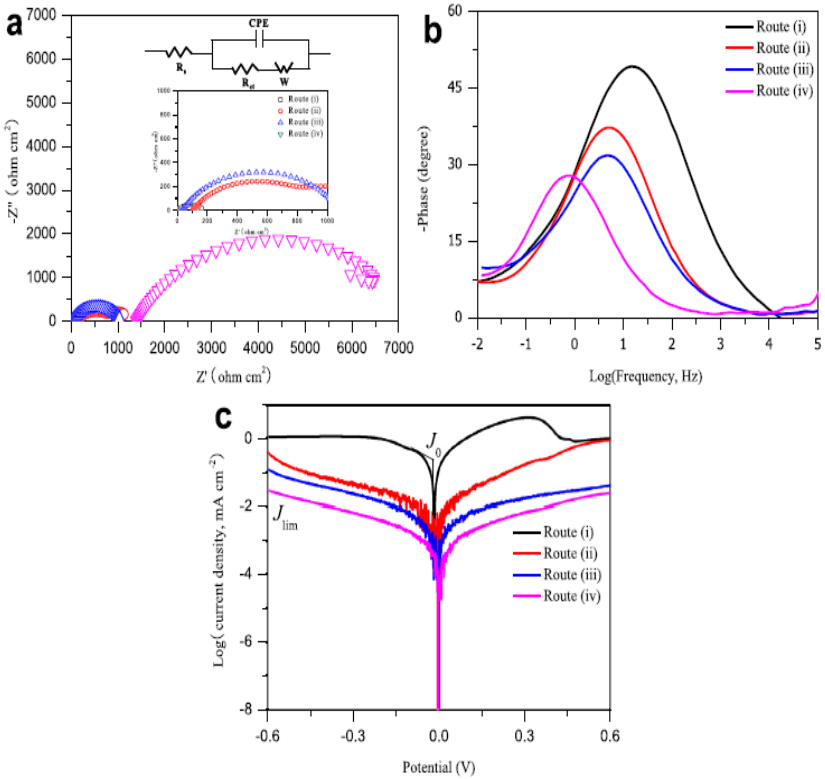

Fig. 5. (a) Nyquist and (b) Bode EIS plots and (c) Tafel polarization curves of the symmetric dummy cells from two identical CEs. The mass ratio of LiI to I_2 doped PANi was 1:8. The inset shows an equivalent circuit: R_s–series resistance, R_{ct}–charge-transfer resistance at PANi CE/electrolyte interface, *W*–Nernstian diffusion resistance, *CPE*–constant phase element.

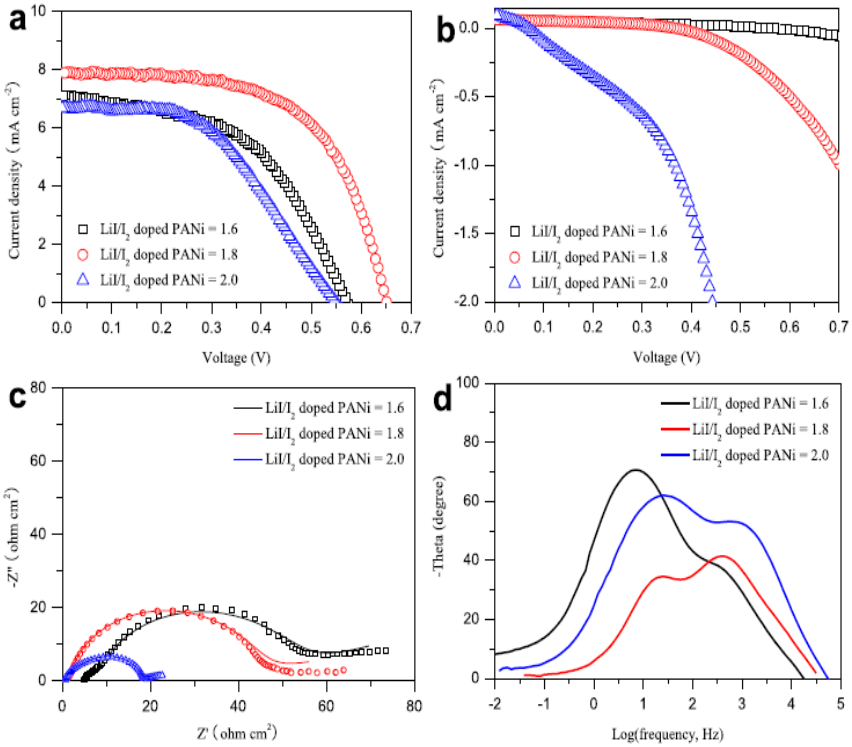

Fig. 6. (a) Characteristic *J–V* curves of the DSSCs for the electrolytes at various LiI/PANi ratios recorded (a) at AM1.5G irradiation and (b) in the dark. (c) Nyquist and (d) Bode EIS spectra of the DSSCs assembled by route (i).

incorporated PEO electrolyte, as shown in Fig. S1. A J_{sc} value of 2.08 mA cm^{-2} and an efficiency of 0.82% are recorded in the solid solar cell. For the cell with PEO electrolyte, the dye recovery is realized by I^- reduction. The reduced kinetics in dye recovery is therefore expected to have a low J_{sc}. For the cell assembled by TiO_2 anode, I^-/I_3^- incorporated PEO electrolyte, and PANi CE, the absence of PANi in directly transferring electrons from CB of TiO_2 to PANi chains and subsequently FTO layer, there are more electron loss during the migration process. This can be confirmed by the reduced J_{sc} of 1.13 mA cm^{-2}. When incorporated by PANi in the solid electrolyte, the participation of PANi in expanding catalytic area, shortening I^-/I_3^- diffusion path length, and recovering dyes, there is a little elevation in J_{sc}. In consideration of the same dosage and distribution of PANi structure in anode, the deviation mainly results from solid electrolyte. In route (ii), the cell has been sealed before air-blowing dry, therefore the evaporated acetonitrile can not exclude from the cell. A remaining problem for the impasse is resolution and flow of solid electrolyte. The inhomogeneous distribution of the solid electrolyte triggers incompletable dye regeneration. However, the physical contact of the solid electrolyte slice with photoanode generates a large interfacial resistance for charge diffusion.

As shown in Fig. 4c and Table 2, the R_{ct2} for the cell from route (iii) is 864.9 Ω cm^2, which is much higher than 29.8 Ω cm^2 in route (i). The result demonstrates that the charge-transfer resistance at anode/dye/electrolyte interface is markedly decreased by employing route (i). That is not surprising to have unsatisfactory photovoltaic performances in its solar cell. In comparison with route (ii), the device is dried under vacuum conditions, producing enormous macropores in the solid-state electrolyte. This macroporous structure prolongates the charge diffusion path length and blocks either successive transportation of I^-/I_3^- redox couples or electron injection. Once the excited dye molecules can not successively recover to their ground state, the accumulative electron density on CB of TiO_2 and therefore J_{sc} will be brought down. Moreover, the maximum V_{oc} is determined by the difference between the quasi Fermi energy of electrons in TiO_2 and the redox potential energy of the electrolyte [41], whereas the real V_{oc} of a solar cell is smaller than this theoretical limit due to a backward reaction between photogenerated electrons in TiO_2 and I_3^- ions or PANi. In a real DSSC, the backward reaction of photogenerated electron with I_3^- species is restricted by either inhomogeneous I_3^- distribution, poor contact or macroporous structure in the solar cells from routes (ii)–(iv). Therefore, the electrons mainly suffer to recombination with PANi chains. As shown in Fig. 4b, the dark current increases for the cell from route (i) to (iv), meaning an elevated dark reaction and hence a decreased V_{oc}. The electron loss can be further confirmed by the Bode EIS spectra (Fig. 4d) and average lifetime of the electrons in photoanode, as listed in Table 1. The τ ($\tau = 1/2\pi f$) value is 404 μs in the DSSC from route (i), whereas it reduces to 118 μs for the cell from route (iv).

In addition, *FF* is a photovoltaic parameter inversely proportional to internal resistance of a cell. R_{ct} can be demonstrated by the EIS plots and Tafel polarization curves of the symmetric dummy cells in Fig. 5. From the extracted data in Table 2, one can see that

Table 3
Photovoltaic parameters of DSSCs from various strategies and the simulated data from EIS spectra.

LiI/I$_2$ doped PANi	η (%)	V_{oc} (V)	J_{sc} (mA cm^{-2})	*FF* (%)	R_{ct2} (Ω cm^2)	τ (μs)
1.6	2.1	0.574	7.09	51.6	34.4	578
1.8	3.1	0.649	7.92	60.3	29.8	404
2.0	1.8	0.548	6.67	49.2	11.7	241

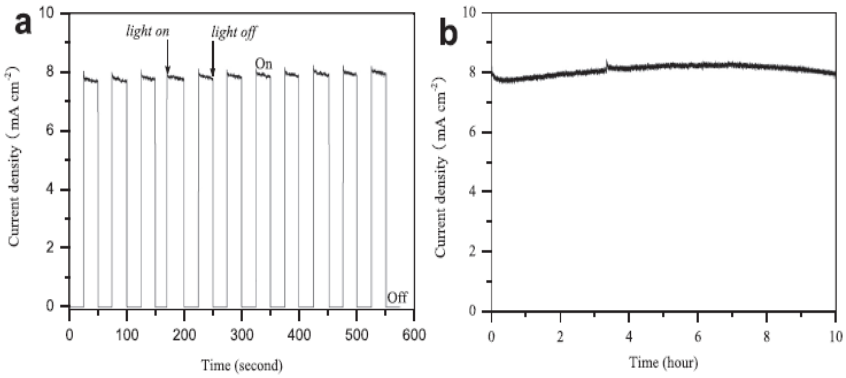

Fig. 7. (a) The start-stop switch by alternatively irradiating (100 mW cm^{-2}) and darking (0 mW cm^{-2}) the cell device at an internal of 25 s and 0 V. (b) Photocurrent stability with durative irradiation under 100 mW cm^{-2} for the solar cell. The mass ratio of LiI to I_2 doped PANi was 1.8.

R_{ct1}, R_{ct2}, and R_{ct} are all increscent for the cell from route (i) to route (iv), therefore leading to an order of *FF* value: Route (i) >Route (ii) >Route (iii) >Route (iv).

The cations in the electrolyte have significant influences on the photovoltaic performances of a DSSC [42], as shown in Fig. 6a. The addition of LiI ions at a modest dosage such as mass ratio of LiI to I_2 doped PANi of 1.8, the active Li^+ cations can both adsorb on TiO_2 surface and implant into TiO_2 nanocrystallite. In this fashion, the Li^+ cations on TiO_2 surface can form Li^+–e^- dipoles with photogenerated electrons at CB of TiO_2 nanocrystallites [43]. Due to a fact of shortened transportation length and decreased resistance attributing to the diffusion of the Li^+–e^- dipoles on TiO_2 surface, the addition of LiI can markedly enhance the electron-transfer capability of the TiO_2 anode and therefore J_{sc}. However, the recombination kinetics between Li^+–e^- dipoles and I_3^- or PANi is also elevated, leading to an enhanced dark current and decreased *FF* [44]. The DSSCs are characterized by Nyquist EIS, as shown in Fig. 6c, and the data are summarized in Table 3. The R_{ct2} at anode/electrolyte interface decreases from 34.4 to 11.7 by varying LiI/I_2 doped PANi ratio from 1.6 to 2.0. However, the dark current in Fig. 6b and electron lifetime from Bode EIS spectra (Fig. 6d) reveal an enhanced electron recombination at higher LiI dosage. After a comprehensive evaluation, the DSSC at LiI/I_2 doped PANi ratio of 1.8 displays the maximum efficiency.

When applied as windows, roof panels, or portable sources, the solar panels should be expected to have superiorities of fast start-stop behavior, multiple start/stop capability, and persistent stability. The start-stop switches are recorded by alternatively illuminating (100 mW cm^{-2}) and darkening (0 mW cm^{-2}) the solid DSSC from route (i), aiming at evaluating the start-up performances. As shown in Fig. 7a, an abrupt increase in photocurrent density with no time delay under irradiation means a fast start-up characteristic. The photocurrent density after eleven start/stop cycles is still unchanged in comparison to its initial state, which is a prerequisite for a durable solar panel. Additionally, the *J*–*t* curve of the solar cell is measured under prolonged irradiation over 10 h to study the stability, as shown in Fig. 7b, there is no sign of degradation in photocurrent. Although the DSSC is only tested for 10 h, this preliminary result demonstrates that stable solar cell can be realized in the current work.

4. Conclusions

In summary, stable and solid-state DSSC has been successfully fabricated by utilizing a TiO_2/PANi photoanode, a PEO/PANi electrolyte, and a PANi CE. It is demonstrated that the PANi in anode participate in dye recovery, the function of PANi in solid-state electrolyte is to reduce I_3^- species, to shorten charge diffusion path length, and to recover dye molecules, whereas PANi CE mainly realize the interconversion between I_3^- and I^-. The DSSC from route (i) yields an efficiency of 3.1% by optimizing assembly strategy and LiI dosage. The research presented here is far from being optimized, but these profound superiorities along with low cost, mild synthesis, and scalable materials promise the DSSC to be a promising technological implementation. Further studies are now in progress to extend this approach to all-carbon quantum dot solar cells.

Acknowledgements

The authors gratefully acknowledge Fundamental Research Funds for the Central Universities (201313001, 201312005), Shandong Province Outstanding Youth Scientist Foundation Plan (BS2013CL015), Shandong Provincial Natural Science Foundation (ZR2011BQ017), Research Project for the Application Foundation in Qingdao (13-1-4-198-jch), National Natural Science Foundation of China (51102219, 51342008), National High Technology Research and Development Program of China (2010AA09Z203, 2010AA065104), National Natural Science Foundation of China (U1037604), and National Key Technology Support Program (2012BAB15B02).

Appendix A. Supplementary data

Supplementary data related to this article can be found at http://dx.doi.org/10.1016/j.jpowsour.2015.03.032.

References

[1] J. Burschka, N. Pellet, S.J. Moon, R. Humphry-Baker, P. Gao, M.K. Nazeeruddin, M. Grätzel, Nature 499 (2013) 316.
[2] M.C. Beard, J.M. Luther, A.J. Nozik, Nat. Nanotechnol. 9 (2014) 951.
[3] S. Kazim, M.K. Nazeeruddin, M. Grätzel, S. Ahmad, Angew. Chem. Int. Ed. 53 (2014) 2812.
[4] S. Pan, Z. Yang, P. Chen, J. Deng, H. Li, H.S. Peng, Angew. Chem. Int. Ed. 53 (2014) 6110.
[5] B.E. Hardin, H.J. Snaith, M.D. McGehee, Nat. Photonics 6 (2012) 162.
[6] J.H. Wu, Z. Lan, J.M. Lin, M.L. Huang, S.C. Hao, T. Sato, S. Yin, Adv. Mater. 19 (2007) 4006.
[7] X. Wu, G.Q. Lu, L.Z. Wang, Adv. Energy Mater. 3 (2013) 704.
[8] N. Memarian, I. Concina, A. Braga, S.M. Rozati, A. Vomiero, G. Sberveglieri, Angew. Chem. Int. Ed. 50 (2011) 12321.
[9] S.S. Li, Y.H. Luo, W. Lv, W.J. Yu, S. Wu, P. Hou, Q. Yang, Q.B. Meng, C. Liu, H.M. Cheng, Adv. Energy Mater. 1 (2011) 486.
[10] B. O'Regan, M. Grätzel, Nature 353 (1991) 737.
[11] S. Mathew, A. Yella, P. Gao, R. Humphry-Baker, B.F.E. Curchod, N. Ashari-Astani, I. Tavernelli, U. Rothlisberger, M.K. Nazeeruddin, M. Grätzel, Nat. Commun. 6 (2014) 242.
[12] P. Wang, S.M. Zakeeruddin, R. Humphry-Baker, J.E. Moser, M. Grätzel, Adv.

Mater. 15 (2003) 2101.
[13] S.S. Yuan, Q.W. Tang, B.B. Hu, C.Q. Ma, J.L. Duan, B.L. He, J. Mater. Chem. A 2 (2014) 2814.
[14] J. Tang, J. Hua, W. Wu, J. Li, Z. Jin, Y. Long, H. Tian, Energy Environ. Sci. 3 (2010) 1736.
[15] Q.H. Li, H.Y. Chen, L. Lin, P.J. Li, Y.C. Qin, M.J. Li, B.L. He, L. Chu, Q.W. Tang, J. Mater. Chem. A 1 (2013) 5326.
[16] N. Cai, S.J. Moon, L. Cevey-Ha, T. Moehl, R. Humphry-Baker, P. Wang, S.M. Zakeeruddin, M. Grätzel, Nano Lett. 11 (2011) 1452.
[17] X.X. Chen, Q.W. Tang, B.L. He, L. Lin, L.M. Yu, Angew. Chem. Int. Ed. 53 (2014) 10799.
[18] Q.H. Li, J.H. Wu, Q.W. Tang, Z. Lan, P.J. Li, J.M. Lin, L.Q. Fan, Electrochem. Commun. 10 (2008) 1299.
[19] Q.D. Tai, B. Chen, F. Guo, S. Xu, H. Hu, B. Sebo, X.Z. Zhao, ACS Nano 5 (2011) 3795.
[20] S.N. Yun, H. Zhang, H.H. Pu, J.H. Chen, A. Hagfeldt, T.L. Ma, Adv. Energy Mater. 3 (2013) 1407.
[21] H. Wang, Y.H. Hu, Energy Environ. Sci. 5 (2012) 8182.
[22] S.K. Swami, N. Chaturvedi, A. Kumar, R. Kapoor, V. Dutta, J. Frey, T. Moehl, M. Grätzel, S. Mathew, M.K. Nazeeruddin, J. Power Sources 275 (2015) 80.
[23] Y.Y. Duan, Q.W. Tang, J. Liu, B.L. He, L.M. Yu, Angew. Chem. Int. Ed. 53 (2014) 14569.
[24] H.Y. Cai, Q.W. Tang, B.L. He, R. Li, L.M. Yu, Nanoscale 6 (2014) 15127.
[25] W. Zhang, Y.M. Cheng, X. Yin, B. Liu, Macromol. Chem. Phys. 212 (2011) 15.
[26] F. Xu, L.T. Sun, Energy Environ. Sci. 4 (2011) 818.
[27] W. Wang, X. Pan, W. Liu, B. Zhang, H. Chen, X. Fang, J. Yao, S.Y. Dai, Chem. Commun. 50 (2014) 2618.
[28] Q. Dai, D.R. MacFarlane, P.C. Howlett, M. Forsyth, Angew. Chem. Int. Ed. 44 (2004) 313.
[29] W. Yuan, H. Zhao, H. Hu, S. Wang, G.L. Baker, ACS Appl. Mater. Interfaces 5 (2013) 4155.
[30] Q.W. Tang, L. Lin, X. Zhao, K. Huang, J.H. Wu, Langmuir 28 (2012) 3972.
[31] H. Xia, Q. Wang, Chem. Mater. 14 (2002) 2158.
[32] P. Anilkumar, M. Jayakannan, Langmuir 22 (2006) 5952.
[33] Q.W. Tang, J.H. Wu, X.M. Sun, Q.H. Li, J.M. Lin, Langmuir 25 (2009) 5253.
[34] F.L. Lu, F. Wudl, M. Nowak, A.J. Heeger, J. Am. Chem. Soc. 108 (1986) 8311.
[35] N.R. Chiou, A.J. Epstein, Adv. Mater. 17 (2005) 1679.
[36] Q.W. Tang, J.H. Wu, X.M. Sun, Q.H. Li, J.M. Lin, M.L. Huang, Chem. Commun. (2009) 2166.
[37] Z.Y. Tang, J.H. Wu, M. Zheng, J.H. Huo, Z. Lan, Nano Energy 2 (2013) 622.
[38] X.Q. Xing, D.P. Zhang, Y.D. Li, J. Power Sources 279 (2015) 205.
[39] G.T. Yue, J.H. Wu, Y.M. Xiao, M.L. Huang, J.M. Lin, J.Y. Lin, J. Mater. Chem. A 1 (2013) 1495–1501.
[40] Y.Y. Duan, Q.W. Tang, B.L. He, R. Li, L.M. Yu, Nanoscale 6 (2014) 12601.
[41] P.K. Babu, A. Lewera, J.H. Chung, R. Hunger, W. Jaegermann, N. Alonso-Vante, A. Wieckowski, E. Oldfield, J. Am. Chem. Soc. 129 (2007) 15140.
[42] Y.S. Shi, Y.H. Wang, M. Zhang, X.D. Dong, Phys. Chem. Chem. Phys. 13 (2011) 14590.
[43] Y.Q. Wang, Y.M. Sun, B. Song, J.T. Xi, Sol. Energy Mat. Sol. C 92 (2008) 660.
[44] F.F. Santiago, J. Bisquert, E. Palomares, L. Otero, D.B. Kuang, S.M. Zakeeruddin, M. Grätzel, J. Phys. Chem. C 111 (2007) 6550.

Journal of Power Sources 264 (2014) 83–91

Contents lists available at ScienceDirect

Journal of Power Sources

journal homepage: www.elsevier.com/locate/jpowsour

Full-ionic liquid gel electrolytes: Enhanced photovoltaic performances in dye-sensitized solar cells

Qinghua Li [a], Qunwei Tang [b,*], Benlin He [b], Peizhi Yang [c]

[a] Key Laboratory of Nondestructive, Ministry of Education, Nanchang Hangkong University, Nanchang 330063, Jiangxi Province, PR China
[b] Institute of Materials Science and Engineering, Ocean University of China, Qingdao 266100, Shandong Province, PR China
[c] Key Laboratory of Advanced Technique & Preparation for Renewable Energy Materials, Ministry of Education, Yunnan Normal University, Kunming 650092, PR China

HIGHLIGHTS

- Ionic liquid-imbibed gel electrolyte is synthesized to replace traditional liquid electrolyte.
- Nonvolatility of ionic liquid is expected to enhance the long-term stability of DSSCs.
- The ionic conductivity of ionic liquid-imbibed gel electrolyte is enhanced.
- The conversion efficiency of the quasi-solid-state DSSC is 7.19%.

GRAPHICAL ABSTRACT

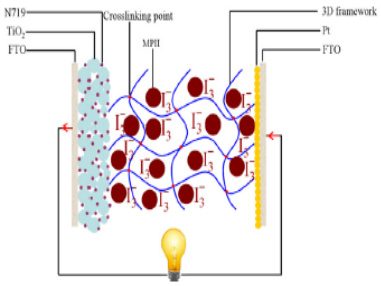

ARTICLE INFO

Article history:
Received 10 March 2014
Received in revised form
3 April 2014
Accepted 17 April 2014
Available online 28 April 2014

Keywords:
Ionic liquid
Gel electrolyte
Quasi-solid-state dye-sensitized solar cell
Three-dimensional framework
Amphiphilic hydrogel

ABSTRACT

Liquid electrolytes containing redox species have been widely used in dye-sensitized solar cells (DSSCs), whereas the volatility of organic solvents has been a tremendous obstacle for their commercial application. To assemble durable DSSCs, here we report the synthesis of full-ionic liquid electrolyte, in which 1-butyl-3-methylimidazolium nitrate is employed as solvent and 1-methyl-3-propylimidazolium iodide is iodide source. Using the imbibition performance of amphiphilic poly(acrylic acid/gelatin) [poly(AA/GR)] and poly(acrylic acid/cetyltrimethyl ammonium bromide) [poly(AA/CTAB)] matrices, full-ionic liquid electrolytes are imbibed into three-dimensional framework of poly(AA/GR) or poly(AA/CTAB) to form stable gel electrolytes. Room-temperature ionic conductivities as high as 17.82 and 18.44 mS cm^{-1} are recorded from full-ionic liquid imbibed poly(AA/GR) and poly(AA/CTAB) gel electrolytes, respectively. Promising power conversion efficiencies of 7.19% and 7.15% are determined from their DSSC devices in comparison with 6.55% and 6.12% from traditional acetonitrile-based poly(AA/GR) and poly(AA/CTAB) gel electrolytes, respectively. The new concept along with easy fabrication demonstrates the full-ionic liquid electrolytes to be good alternatives for robust gel electrolytes in quasi-solid-state DSSCs.

1. Introduction

Dye-sensitized solar cell (DSSC), an electrochemical device directly converting solar energy to electricity, has attracted growing interests because of their merits on relatively high power conversion efficiency, low fabrication cost, and environmental-friendliness [1–6]. A typical DSSC device is composed of a dye sensitized TiO_2 photoanode, a counter electrode, and redox electrolyte. The task of redox electrolyte is to regenerate excited dye molecules and to be subsequently reduced by the counter electrode. To obtain higher reaction kinetics, organic solvents such as

* Corresponding author. Tel./fax: +86 532 66781690.
E-mail address: tangqunwei@ouc.edu.cn (Q. Tang).

http://dx.doi.org/10.1016/j.jpowsour.2014.04.095
0378-7753/

acetonitrile are always employed as mediums for the transportation of iodide/triiodide (I^-/I_3^-) redox couples [7–10]. However, low ionic conductivity, insufficient penetration of the electrolyte into nanoporous structure of TiO_2 film, and volatility of organic solvents have been tremendous obstacles for the commercial application of DSSCs [11–13]. Therefore, it is a prerequisite to find an alternative solvent with nonvolatility, easy synthesis, low cost and environmental-friendly natures for I^-/I_3^- loading. By addressing these issues, room-temperature ionic liquids are preferred candidates.

Room-temperature ionic liquids, liquid state within temperature of 100 °C, are defined as ionic solvents composed of positively and negatively charged ions. They are always characterized with high glass transition temperature [14], reasonable thermal stability [15], high conductivity [16], and especially good dissolution to iodine and iodide [17]. Up to now, there are few reports on the employment of full-ionic liquid electrolyte in DSSCs, not to mention full-ionic liquid electrolyte imbibed three-dimensional (3D) amphiphilic framework-based quasi-solid-state DSSCs.

In the current work, 3D poly(acrylic acid/glycerol) [poly(AA/GR)] and poly(acrylic acid/cetyltrimethyl ammonium bromide) [poly(AA/CTAB)] polymer composites are employed as placeholders for full-ionic liquid loading to replace acetonitrile-contained iodide electrolytes [18,19]. Crosslinked poly(acrylic acid) is a typical 3D framework capable of absorbing enormous aqueous solution because of decoration with hydrophilic –COOH groups, however, modification of poly(acrylic acid) by glycerol (GR) or cetyltrimethyl ammonium bromide (CTAB) can generate amphiphilicity to poly(AA/GR) or poly(AA/CTAB). The imbibed full-ionic liquid electrolyte in 3D framework of poly(AA/GR) or poly(AA/CTAB) can not leak even during cell assembly and operation. The resultant gel electrolytes are subsequently assembled into quasi-solid-state DSSC devices, which are expected to be honored by long-term stability. The objectives of this study are the synthesis of full-ionic liquid imbibed poly(AA/GR) and poly(AA/CTAB) gel electrolytes and their characterizations as well as the photovoltaic performances of assembled DSSCs from the gel electrolytes.

2. Experimental

2.1. Materials

Unless noted otherwise, chemicals were purchased from Sigma–Aldrich and used as received.

2.2. Synthesis of 3D poly(AA/GR) matrix

Poly(AA/GR) matrix was synthesized by the procedures: 5 ml of GR and 10 g of acrylic acid (AA) were dispersed in 10 ml of deionized water. Subsequently, initiator potassium peroxydisulfate (KPS) (mass ratio of KPS to AA was 0.008) and crosslinker *N,N′*-methylene bisacrylamide (NMBA) (mass ratio of NMBA to AA was 0.0005) were added to the mixed solution. When the viscosity of the poly(AA/GR) prepolymers reached around 180 mPa s^{-1}, the reagent was poured into a petri dish and cooled to room temperature until the formation of an elastic gel. After rinsing with excess deionized water, the samples were vacuum dried at 80 °C. Finally, the sample was vacuum dried at 80 °C for more than 12 h.

2.3. Synthesis of 3D poly(AA/CTAB) matrix

Poly(AA/CTAB) matrix was synthesized by the procedures: 1 g of cetyltrimethyl ammonium bromide (CTAB) and 10 g of AA were dispersed in 10 ml of deionized water. Subsequently, initiator KPS (mass ratio of KPS to AA was 0.008) and crosslinker NMBA (mass ratio of NMBA to AA was 0.0005) were added to the mixed solution. When the viscosity of the poly(AA/CTAB) prepolymers reached around 180 mPa s^{-1}, the reagent was poured into a petri dish and cooled to room temperature until the formation of an elastic gel. After rinsing with excess deionized water, the samples were vacuum dried at 80 °C. Finally, the sample was vacuum dried at 80 °C for more than 12 h.

2.4. Synthesis of [AMIM]NO_3, [AMIM]BF_4, and MPII

The [AMIM]NO_3, [AMIM]BF_4, and 1-methyl-3-propylimidazolium iodide (MPII) were synthesized by following steps [20,21]: A mixture of 23.0 g of *N*-methyl-imidazolium and 25.3 g of allyl nitrate was vigorously agitated in a three-necked flask equipped with mechanical stirrer and thermometer. The excess allyl nitrate was removed by keeping temperature at 60–65 °C for 6–7 h, while the surplus *N*-methyl-imidazolium was extracted by vacuum drying at 80 °C for 48 h to obtain a transparently viscous liquid. 35.0 g of the as-synthesized viscous liquid, 20.0 g of silver nitrate, and 50.0 ml of methanol were mixed in another three-necked flask at 40 °C for 48 h to obtain [AMIM]NO_3. The unreacted sodium bicarbonate and methanol were removed in filtering and evaporating processes.

A mixture of 23.0 g of *N*-methyl-imidazolium and 25.3 g of allyl nitrate was vigorously agitated in a three-necked flask equipped with mechanical stirrer and thermometer. The excess allyl nitrate was removed by keeping temperature at 60–65 °C for 6–7 h, while the surplus *N*-methyl-imidazolium was extracted by vacuum drying at 80 °C for 48 h to obtain a transparently viscous liquid. 35.0 g of the as-synthesized viscous liquid, 20.0 g of $AgBF_4$, and 50.0 ml of methanol were mixed in another three-necked flask at 40 °C for 48 h to obtain [AMIM]BF_4. The unreacted sodium bicarbonate and methanol were removed in filtering and evaporating processes.

Methyl imidazole and iodopropane with a molar ratio of 1: 1.1 were mixed in a 250 ml neck boiling flask which was sealed by toluene. The mixture was deaerated by bubbling N_2 for 5 min and dark-agitated at 35 °C for 24 h. Resultant product was thoroughly rinsed with anhydrous ether and shaken for 20 min and then kept stilling for 1 h until the liquid became brownish red. After rotary evaporation at 30 °C for 3 h, final MPII can be obtained.

2.5. Fabrication of full-ionic liquid imbibed gel electrolytes

Full-ionic liquid imbibed poly(AA/GR) gel electrolyte was prepared according to the following procedures [22–25]: 0.2 g of poly(AA/GR) was immersed in an ionic liquid electrolyte solution at ambient temperature, resulting in the diffusion of full-ionic liquid electrolyte into poly(AA/GR) framework and formation of a swollen sample to reach absorption saturation. The ionic liquid electrolyte consisted of 0.5 M I_2, 0.01 M LiI in mixed organic solvent of 40 vol% MPII, 50 vol% [AMIM]NO_3, and 10 vol% *N*-methyl pyrrolidone. Ionic liquid imbibed poly(AA/CTAB) gel electrolyte was prepared according to the following procedures: 0.2 g of poly(AA/CTAB) was immersed in an IL electrolyte solution at ambient temperature, resulting in the diffusion of RTIL electrolyte into the poly(AA/CTAB) network and formation of a swollen sample to reach absorption saturation. The RTIL electrolyte consisted of 0.5 M I_2, 0.01 M LiI in mixed organic solvent of 40 vol% MPII, 50 vol% [AMIM]BF_4, and 10 vol% *N*-methyl pyrrolidone.

The ionic liquid loading could be calculated according to the following equation:

$$\text{Ionic liquid loading}\left(\text{g g}^{-1}\right) = \frac{W_t - W_d}{W_d} \quad (1)$$

where W_t (g) and W_0 (g) were the masses of full-ionic liquid imbibed gel electrolyte and pure matrix, respectively.

2.6. Assembly of quasi-solid-state DSSCs

A layer of TiO_2 nanocrystal anode film with a thickness of 10 μm and active area of 0.09 cm^2 was prepared by coating the TiO_2 colloid using a doctor blade technique, followed by sintering in air at 450 °C for 30 min. Subsequently, the TiO_2 film was soaked in a 0.3 mM N719 [cis-di(thiocyanato)-*N*,*N*′-bis(2,2′-bipyridyl-4-carboxylic acid-4-tetrabutylammonium carboxylate, purchased from Solaronix, SA, Switzerland] ethanol solution for 24 h to uptake N719 dye for the fabrication of dye-sensitized TiO_2 photoanode. The quasi-solid-state DSSC from full-ionic liquid imbibed poly(AA/GR) or poly(AA/CTAB) gel electrolyte at an imbibition equilibrium was fabricated by sandwiching a slice of gel electrolyte with a thickness of around 1 mm between dye-sensitized TiO_2 anode and a Pt counter electrode (300–400 μm in thickness, purchased from Dalian HepatChroma SolarTech Co., Ltd.).

2.7. Photovoltaic measurements

The photocurrent–voltage (*J*–*V*) curves of the assembled quasi-solid-state DSSCs were recorded on an Electrochemical Workstation (Xe Lamp Oriel Sol^{3}A™ Class AAA Solar Simulators 94023A, USA) under irradiation of a simulated solar light from a 100 W xenon arc lamp in ambient atmosphere. The incident light intensity was 100 mW cm^{-2} (AM 1.5) which was calibrated using a FZ-A type radiometer (purchased from Beijing Normal University Photoelectric Instrument Factory). Each DSSC device was measured at least five times to eliminate experimental error and a compromise *J*–*V* curve was employed.

2.8. Characterizations

The morphologies of the gel electrolytes were captured with a Zeiss Ultra plus field emission scanning electron microscopy (FESEM). To observe the internal 3D microstructure, swollen gel electrolytes were first cut into ultrathin film, followed by the loading into a chamber under freezing temperature and high vacuum to remove solvent. The ^{1}HNMR spectra were recorded on a Bruker Advance-400 spectrometer with d-chloroform as the solvent and tetramethylsilane as the internal standard. Fourier transform infrared spectrometry (FTIR) spectra were recorded on a Vertex 70 FTIR spectrometer (Bruker). The ionic conductivity of gel-electrolyte was measured by using a pocket conductivity meter (HANNA8733, Hanna Instruments). Thermogravimetric analyses (TGA) were conducted on a TA Instruments Model SDT Q600 thermogravimetric analyzer. The samples were heated at a heating rate of 10 °C min and atmospheric pressure, and under N_2 flow (90 mL min^{-1}). The weight loss as a function of temperature was recorded continuously in the range of 25–590 °C. Preliminary tests, small masses (20–25 mg) of each material, thinly distributed in the crucible. The ionic conductivity of gel-electrolyte was measured by using a pocket conductivity meter (HANNA8733, Hanna Instruments). The instrument was calibrated with 0.01 M KCl aqueous solution prior to experiments. Tafel-polarization curves of the symmetrical cells fabricated of samples were measured by CHI660D electrochemical workstation. The symmetrical dummy cells fabricated with two identical Pt electrodes (Pt electrode/gel electrolyte/Pt electrode). The electrochemical impedance spectroscopy (EIS) was carried out using a CHI660E electrochemical workstation at a constant temperature of 20 °C with an ac signal amplitude of 20 mV in the frequency range from 0.1 to 10^5 Hz at a 10 V dc bias in the dark. The porosity was analyzed by an AutoPore IV9500 mercury porosimeter (Micromeritics, USA) in a pressure range of 0.5–30,000 psia.

3. Results and discussion

3.1. Morphology observation

The cross-sectional SEM images of pure poly(AA/GR) and poly(AA/CTAB) matrices are shown in Fig. 1, which suggests well-interconnected and microporous frameworks capable of caging enormous full-ionic liquid electrolyte in the microporous structure because of high porosity [68.8% and 67.4% for microporous poly(AA/GR) and poly(AA/CTAB), respectively]. The absorbed full-ionic liquid electrolyte is expected to be sealed in the 3D frameworks [26–28]. The formation of 3D frameworks of poly(AA/GR) and poly(AA/CTAB) matrices is a typical free radical process. Complex monomers from AA/GR or AA/CTAB are formed by the hydrogen-bonding between AA (C═O) and GR (-OH) or electrostatic attraction of AA (negatively charged) and CTAB (positively charged) during the mixing process. For the polymerization, thermal cleavage of initiator KPS can initiate the complex monomers and crosslinker NMBA to generate radicals. During the complicated polymerization process, a 3D framework can be formed because of the macrobiradicals nature of NMBA [18,19,29,30]. In fact, the pore size and porosity can be controlled by adjusting synthesis conditions, such as initiator dosage, crosslinker dosage, reaction temperature, concentration of AA monomer, and mass ratio of AA to GR or mass ratio of AA to CTAB. The matrix framework with higher porosity can provide higher ionic liquid loading in per unit volume of gel electrolyte, therefore, the transfer ability of gel electrolyte toward I^-/I_3^- redox couples is further enhanced. The increased charge-transfer capacity can accelerate the recovery of excited dyes and redox reaction between $I^- \leftrightarrow I_3^-$, which is favorable to elevating photocurrent density and fill factor of DSSC device. The focus of the current work was to display the feasibility of employing amphiphilic poly(AA/GR) or poly(AA/CTAB) gel material as a placeholder to fabricate robust gel electrolyte and therefore efficient DSSC device.

3.2. Structural analysis

^{1}HNMR spectrum of [AMIM]NO_3 was provided to confirm its molecular structure. Fig. 2a gives δ values of 5.4, 6.0, and 4.8, revealing the hydrogen atom positions in (1)–(3). The hydrogen atom at position (4) can be confirmed by detecting δ value of 3.9, whereas the single peak at $\delta = 7.5$ is a coupling reflection of hydrogen atoms posited at (5) and (6), and $\delta = 8.7$ is attributed to D_2O. Till now, we can make a conclusion that the chemical structure of [AMIM]NO_3 is in the inset of Fig. 2a. The ^{1}HNMR spectrum of [AMIM]BF_4 is provided in Fig. 2b, giving δ values of 5.0, 6.2, and 5.6, revealing the hydrogen atom positions in (1)–(3). The hydrogen atom at position (4) can be confirmed by detecting δ value of 4.0, whereas the single peak at $\delta = 7.6$ is a coupling reflection of hydrogen atoms posited at (5) and (6), and $\delta = 8.8$ is attributed to D_2O. Till now, we can make a conclusion that the chemical structure of [AMIM]BF_4. Fig. 2c shows the ^{1}HNMR spectrum of MPII, giving δ values of 1.0, 2.1, and 4.3 which are attributed to the hydrogen atoms at position (1), (2), and (3) in *n*-propyl, respectively. Hydrogen atom at position (4) gives a δ of 4.1, and coupling of (5) & (6) atoms shows a single peak at $\delta = 7.7$, whereas peak at $\delta = 4.8$ is attributed to D_2O and hydrogen atom at position (7) gives a peak at $\delta = 4.8$. Fig. 2d gives the FTIR spectrum of resultant MPII, showing absorption bands at 2960, 2870, 1572, 1172, 1432, 954, and 3170 cm^{-1} which can be attributed to C–H stretching in $-CH_3$ group, C–H stretching in $-CH_2$ group, C═N stretching in imidazole

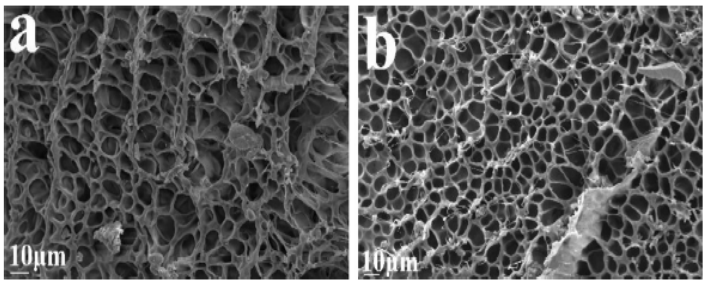

Fig. 1. SEM photographs of (a) pure poly(AA/GR) and (b) poly(AA/CTAB) matrices.

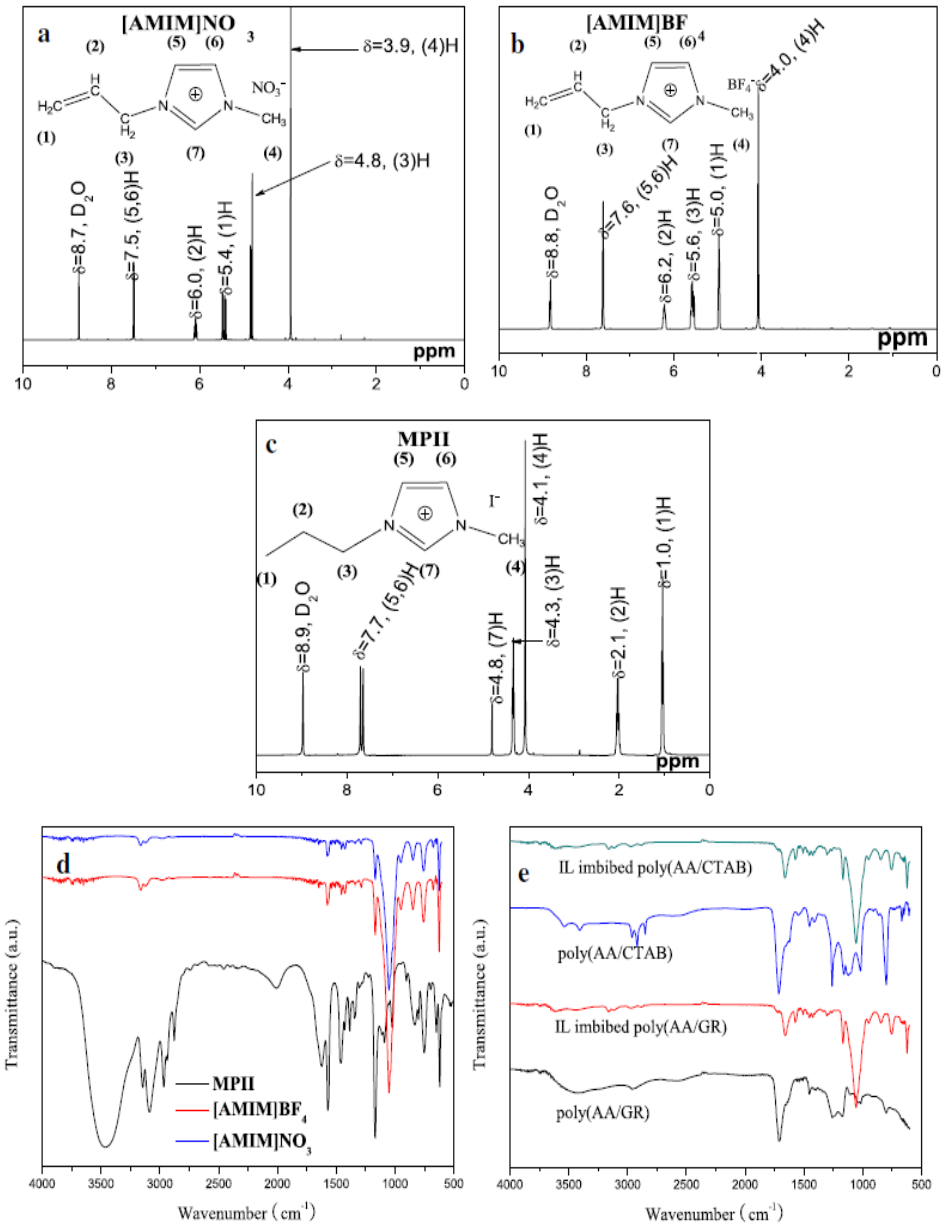

Fig. 2. ^{1}HNMR spectra of (a) [AMIM]NO_3, (b) [AMIM]BF_4, and (c) MPII, and FTIR spectra of (d) [AMIM]NO_3, [AMIM]BF_4, and MPII, and (e) pure poly(AA/GR) matrix, full-ionic liquid imbibed poly(AA/GR), pure(AA/CTAB), and full-ionic liquid imbibed poly(AA/CTAB). If not special specified, "IL" in the figure represents "full-ionic liquid".

ring, C–H bending in imidazole ring, C–H bending in side $-CH_2$ group, stretching of imidazole ring, and O–H in H_2O, respectively. By combining ^{1}HNMR and FTIR spectra, we can confirm that inset in Fig. 2c is the molecular structure of MPII. All the absorption bands of [AMIM]NO_3, [AMIM]BF_4, and MPII can be detected in IL imbibed poly(AA/GR) or poly(AA/CTAB) electrolyte (Fig. 2e), indicating that the ILs have been incorporated into the 3D framework of poly(AA/GR) or poly(AA/CTAB) gel.

3.3. Thermal analysis

The thermal analysis behaviors of pure poly(AA/GR) and pure poly(AA/CTAB) matrices are shown in Fig. 3. The main thermal degradation of matrix under nitrogen atmosphere occurs in a narrow temperature region between 350 and 450 °C. However, the imbibition of IL electrolyte into 3D framework of poly(AA/GR) or poly(AA/CTAB) results in a decreased thermal stability, giving a decomposition temperature region between 300 and 400 °C because of the poor thermal performance of room-temperature ILs. It is noteworthy to mention that the weight losses of pure poly(AA/GR) or poly(AA/CTAB) matrix and IL imbibed poly(AA/GR) or poly(AA/CTAB) electrolyte within 100 °C are nearly the same, indicating that the IL can be well-sealed in the 3D frameworks of gel matrices. The good thermal stability and good ionic liquid retention along with easy synthesis demonstrates the IL imbibed gel electrolyte to be good candidate in quasi-solid-state DSSC devices.

3.4. Ionic conductivity

The ionic liquid loading and ionic conductivity of the IL imbibed poly(AA/GR) gel electrolyte are shown in Fig. 4a. The highest ionic liquid loading of 8.03 g g^{-1} and an ionic conductivity of 17.82 mS cm^{-1} are recorded at an imbibition time of 18 days, which are higher than that from acetonitrile-contained poly(AA/GR) [23]. The measured ionic conductivity from gel electrolyte is close to 18.72 mS cm^{-1} from pure IL electrolyte, indicating that the 3D framework provides facile channels for rapid charge transfer. The increased liquid electrolyte dosage in per unit volume of gel electrolyte and ionic transfer ability are expected to have an acceleration effect on power conversion efficiency of the quasi-solid-state DSSCs. The imbibition kinetics of dense poly(AA/GR) matrix in IL electrolyte, shown in inset of Fig. 4a, is mainly due to the Flory theory from osmotic pressure across the poly(AA/GR) matrix. The loading of IL electrolyte increases with elongation of swelling time, indicating a stepwise diffusion of IL electrolyte into 3D framework of poly(AA/GR). The absorption equilibrium can be obtained at swelling time of around 17 days, and no further diffusion occurs under longer immersion time. Similar trend is also detected from IL imbibed poly(AA/CTAB) gel electrolyte (Fig. 4c), in which the highest IL electrolyte loading and ionic conductivity are 13.66 g g^{-1} and 18.44 mS cm^{-1}, respectively. In order to determine the loading of IL electrolyte by poly(AA/GR) or poly(AA/CTAB), the accumulative IL electrolyte loading over time have been fitted using the Fickian theory [24].

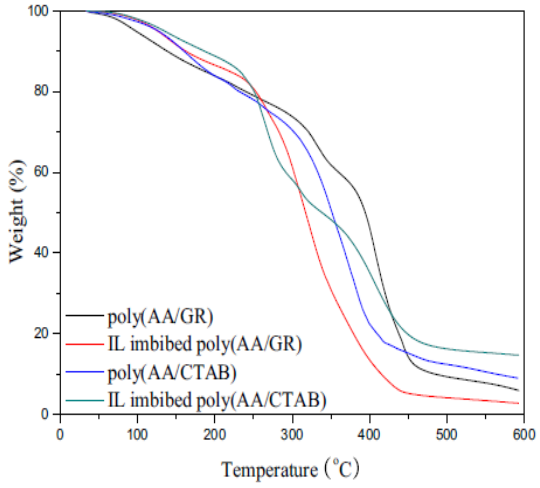

Fig. 3. TGA curves of pure poly(AA/GR), full-ionic liquid imbibed poly(AA/GR), pure poly(AA/CTAB), and full-ionic liquid imbibed poly(AA/CTAB).

$$\frac{M_t}{M_\infty} = kt^n \tag{2}$$

where M_t and M_∞ are the masses of the loaded IL electrolyte at time t and at equilibrium, respectively. k is a characteristic rate constant relating to the properties of poly(AA/GR) or poly(AA/CTAB), and n is a transport number characterizing the transport mechanism. $n \leq 0.5$ suggests a Fickian or Case I transport behavior in which the poly(AA/GR) or poly(AA/CTAB) framework relaxation is much faster than the diffusion; $n = 1$ gives a non-Fickian or Case II mode of transport where IL electrolyte uptake is controlled by diffusion process. $0.5 < n < 1$ refers to an anomalous or a Case III mode in which structural relaxation is comparable to diffusion. By plotting $\log(M_t/M_\infty)$ vs $\log(t)$, the n value are calculated as 0.60 and 0.63 for poly(AA/GR) and poly(AA/CTAB), respectively, indicating an anomalous mechanism mode in which structural relaxation is comparable to diffusion.

The conductivity–temperature (σ–T) relationships for the IL imbibed poly(AA/GR) and poly(AA/CTAB) gel electrolytes at various imbibition time are shown in Fig. 4b and d, respectively. From the figures, one can find that the conductivity increases with elevation of temperature and the $\ln(\sigma)$ versus $1/T$ plots is almost linear, which is in a good agreement with previous results [22,23,25,31].

The elevation of ionic conductivity with temperature is assigned to enhancement of ions transportation. The data can be better fitted by Arrhenius equation:

$$\sigma(T) = A\exp\left(\frac{-E_a}{k_B T}\right) \tag{3}$$

where A is a constant, E_a is the activation energy, k_B is Boltzmann's constant, and T is the absolute temperature. According to Fig. 4b and Equation (3), the E_a values for the IL imbibed poly(AA/GR) gel electrolyte are calculated as 22.06 kJ mol^{-1} (1 day), 18.36 kJ mol^{-1} (4 days), 17.18 kJ mol^{-1} (7 days), 14.44 kJ mol^{-1} (10 days), 10.21 kJ mol^{-1} (13 days), and 9.67 kJ mol^{-1} (17 days). However, the E_a for the IL imbibed poly(AA/CTAB) gel electrolyte are calculated as 21.84 kJ mol^{-1} (1 day), 19.28 kJ mol^{-1} (5 days), 16.18 kJ mol^{-1} (10 days), 13.86 kJ mol^{-1} (15 days), 10.95 kJ mol^{-1} (20 days), and 8.97 kJ mol^{-1} (22 days). Low E_a value in gel electrolyte suggests a facile ionic transport along conducting channels. It is reasonable that the conducting channels tend to be interconnecting at higher imbibition aging because of gradual diffusion and rearrangement of IL within 3D poly(AA/GR) or poly(AA/CTAB) framework. Therefore, the interconnected micropores of poly(AA/GR) or poly(AA/CTAB) framework provides superhighway for facile ion transport. There is a consensus that the ionic conductivity is determined by the thermal hopping frequency in the case of an ionic transport process involving intermolecular ion hopping, resulting in proportional relationship to $\exp(-E_a/K_bT)$ and therefore leading to an Arrhenius conductivity–temperature relationship [32]. The ion hopping

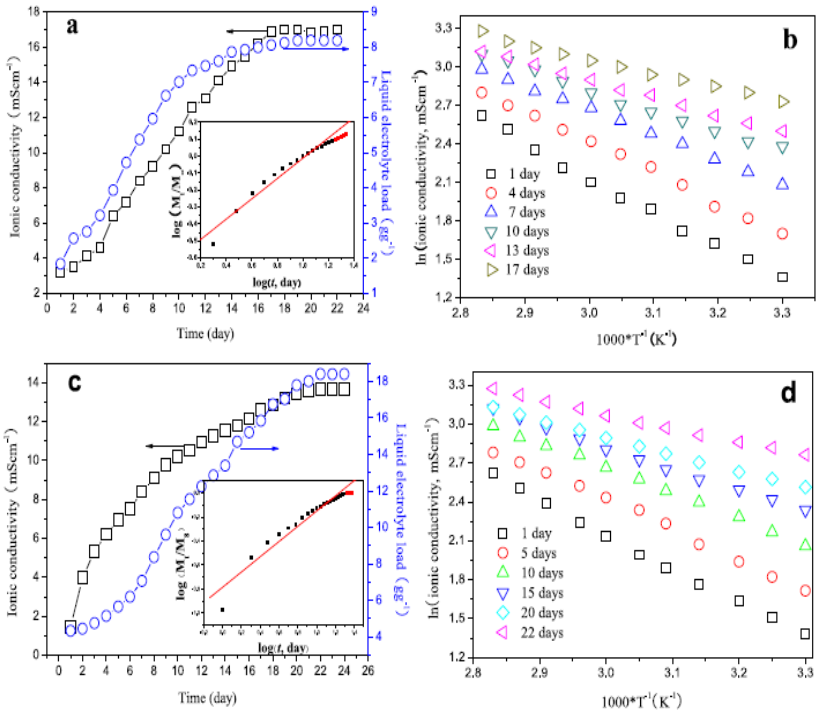

Fig. 4. Dependence of ionic liquid-based gel electrolyte loading and ionic conductivity on imbibition time: (a) poly(AA/GR) and (c) poly(AA/CTAB). The inset shows the imbibition kinetics of poly(AA/GR) or poly(AA/CTAB) toward full-ionic liquid electrolyte. Dependence of ionic conductivity on temperature at different imbibition time: (b) poly(AA/GR) and (d) poly(AA/CTAB).

kinetics and ionic conductivity are expected to be significantly enhanced at higher imbibition aging.

3.5. Electrochemical behaviors of the gel electrolytes

As a powerful tool to explore the electrochemical process, EIS has been widely employed in testing the electrocatalytic activity for the regeneration of redox species. For EIS experiments, the Pt/gel electrolyte/Pt is contained in a symmetric cell composed of a gel electrolyte sandwiched by two FTO supported Pt glass electrodes. Fig. 5a shows the Nyquist plots of Pt/gel electrolyte/Pt devices using the four electrolytes. Typically, the intercept on the real axis (high frequency) can be attributed to the series resistance (R_s) between counter electrode and the gel electrolyte. The first semicircle (middle frequency) can be assigned to the resistance capacitance networks of the electrode/electrolyte interface, including the charge transfer resistance (R_{ct}). The EIS curves are shown in Fig. 5a and the data are summarized in Table 1. In the current research, the R_{ct} values of IL imbibed poly(AA/GR) gel electrolyte and acetonitrile-contained poly(AA/GR) gel electrolyte are 7.55 and 13.57 Ω cm^2, respectively. Similarly, the R_{ct} values of IL imbibed and acetonitrile-contained poly(AA/CTAB) gel electrolytes are 9.07 and 9.31 Ω cm^2, respectively. Compared with acetonitrile-contained poly(AA/GR) and poly(AA/CTAB), the decreased R_{ct} of IL imbibed poly(AA/GR) and poly(AA/CTAB) may be the result of enhancement of ionic conductivity in the resultant IL electrolyte than that of acetonitrile-contained liquid electrolyte. Lower R_{ct} in IL imbibed poly(AA/GR) or poly(AA/CTAB) gel electrolyte reveals that the charge-transfer ability at IL imbibed gel electrolyte/Pt interface is higher than that in acetonitrile-contained gel electrolyte/Pt

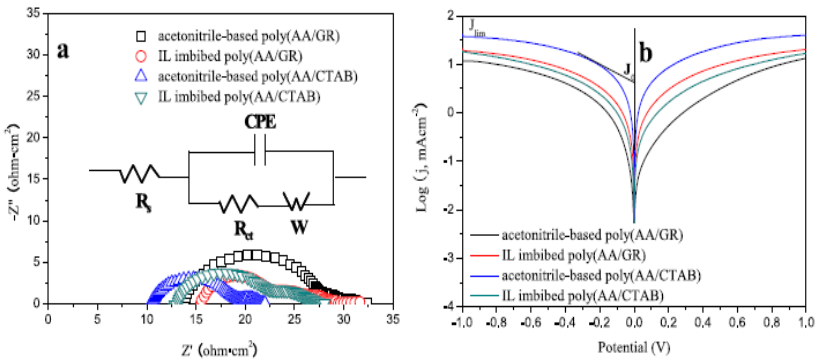

Fig. 5. (a) Nyquist plots and (b) Tafel-polarization curves of acetonitrile-contained iodide imbibed poly(AA/GR), acetonitrile-contained iodide imbibed poly(AA/CTAB), full-ionic liquid imbibed poly(AA/GR), and full-ionic liquid imbibed poly(AA/CTAB) gel electrolytes. Inset is a related equivalent circuit diagram.

Table 1
The photovoltaic performances of the quasi-solid-state DSSC based on different electrolytes.

Gel electrolytes	R_s (Ω cm^2)	R_{ct} (Ω cm^2)	V_{oc} (V)	J_{sc} (mA cm^{-2})	FF	η (%)
Acetonitrile-contained iodide imbibed poly(AA/GR)	13.84	13.57	0.708	13.60	0.68	6.55
Full-ionic liquid imbibed poly(AA/GR)	15.36	7.55	0.730	14.27	0.69	7.19
Acetonitrile-contained iodide imbibed poly(AA/CTAB)	10.73	9.31	0.751	13.58	0.60	6.12
Full-ionic liquid imbibed poly(AA/CTAB)	12.95	9.07	0.750	14.44	0.66	7.15
Full-ionic liquid	–	–	0.731	14.14	0.70	7.27

interface. The rapid transport of refluxed electrons from Pt counter electrode to gel electrolyte is expected to accelerate the reduction reaction of iodides.

Tafel-polarization measurements are used to reconfirm the electrocatalytic activity of the gel electrolytes, which is also performed with the dummy cells similar to those used in EIS measurements, as shown in Fig. 5b. A larger slope in the anodic or cathodic branch indicates a higher exchange current density (J_0) on the electrode. J_0 can be also calculated by Equation (4) [33]:

$$J_0 = \frac{RT}{nFR_{ct}} \tag{4}$$

Apparently, the calculated J_0 also follows the order of IL imbibed poly(AA/GR) or poly(AA/CTAB) gel electrolyte > acetonitrile-contained poly(AA/GR) or poly(AA/CTAB) gel electrolyte, suggesting that IL imbibed poly(AA/GR) electrolyte shows a superior electrocatalytic activity for triiodides reduction, which is consistent with the J_{sc} order. In addition, the Tafel polarization curves contain the information about limiting current density (J_{lim}), which can be expressed as:

$$J_{lim} = \frac{2neD_cN_A}{l} \tag{5}$$

The IL imbibed poly(AA/GR) or poly(AA/CTAB) electrolyte shows a high limiting diffusion current density (J_{lim}) relative to that of pure poly(AA/GR) or poly(AA/CTAB), reflecting a higher diffusion velocity for the redox couple in the electrolyte. In theory, J_0 varies inversely with R_{ct}. With the EIS results, the change tendency of J_0 for various electrodes is generally in accordance with those presented in the Tafel curve plots. J_{lim} is determined by the diffusion properties of the redox couple and the counter electrodes; At the same potential, a large J_{lim} indicates a large diffusion coefficient and a small Z_W [34,35]. The J_{lim} value of IL imbibed poly(AA/GR) or poly(AA/CTAB) gel electrolyte is higher than that of acetonitrile-contained gel electrolyte. Consequently, we can make a conclude from the electrochemical and EIS results that IL imbibed poly(AA/GR) or poly(AA/CTAB) gel electrolyte has a higher electrocatalytic activity than acetonitrile-contained gel electrolyte. The order of electrocatalytic activity well explains the order of J_{sc} [36,37].

3.6. Photovoltaic behaviors of the quasi-solid-state DSSCs

The photocurrent versus photovoltage (J–V) curves of quasi-solid-state DSSCs from various gel electrolytes are shown in Fig. 6a. As a reference, the J–V curve of the DSSC employing IL is also recorded under one sun illumination. The IL electrolyte contains: 0.5 M I_2, 0.01 M LiI, 40 vol% MPII, 50 vol% [AMIM]NO_3, and 10 vol% *N*-methyl pyrrolidone. The acetonitrile-contained liquid electrolyte contains: 0.1 M LiI, 0.01 M I_2, 20 vol% NMP and 80 vol% acetonitrile. Under a simulated solar light irradiation with intensity of 100 mW cm^{-2}, the photoelectric parameters of DSSCs such as short circuit current density (J_{sc}), open circuit voltage (V_{oc}), fill factor (FF) and energy conversion efficiency (η) are summarized in Table 1. It is evident that nearly all photoelectric parameters of the quasi-solid-state DSSC from IL imbibed poly(AA/GR) or poly(AA/CTAB) gel electrolyte are higher than that from traditional gel electrolyte. J_{sc} is dependent on the electron density on conduction band of TiO_2, whereas the photogenerated electrons are injected from excited dyes. The maximum V_{oc} is determined by the difference between the quasi Fermi energy of electrons in TiO_2 and redox potential energy of electrolyte [38]. However, the real V_{oc} of a DSSC is generally smaller than this theoretical limit, and one of the reasons is a backward reaction between electrons and redox electrolyte [39]. From the dark J–V characteristics, as shown in Fig. 6b, it is apparent that the DSSCs employing IL imbibed poly(AA/CTAB) and acetonitrile-based poly(AA/CTAB) gel electrolytes have the smallest dark current density at the same voltage. The dark current density in DSSC device is attributed to the triiodides combination with electrons on CB of TiO_2 at the TiO_2/electrolyte interface. The smaller dark current density indicates that the reduction of triiodides on the TiO_2/electrolyte interface is retarded. This is a key factor for the highest V_{oc} from IL imbibed poly(AA/CTAB) and acetonitrile-based poly(AA/CTAB) gel electrolytes based DSSCs. Interestingly, the DSSC from IL imbibed poly(AA/GR) gel electrolyte has larger dark current but lower R_{ct} than that from IL imbibed poly(AA/CTAB). Generally, a larger R_{ct} means a facile transportation of I^-/I_3^- redox species within 3D framework of matrix. However, the porosity of poly(AA/GR) (68.8%) is larger than 67.4% for poly(AA/CTAB),

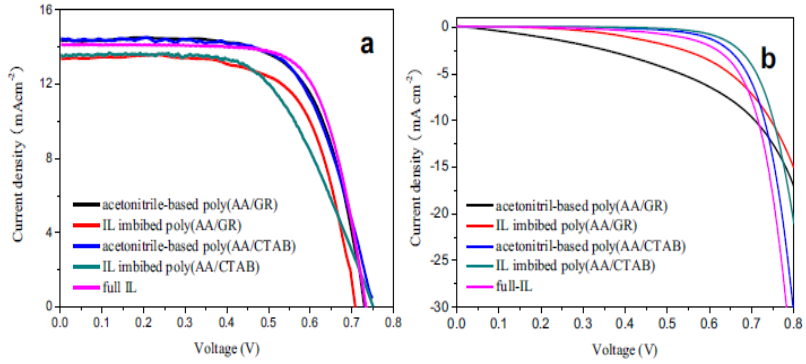

Fig. 6. Characteristic photocurrent–voltage (J–V) curves of quasi-solid-state DSSCs from acetonitrile-contained iodide imbibed poly(AA/GR), acetonitrile-contained iodide imbibed poly(AA/CTAB), full-ionic liquid imbibed poly(AA/GR), full-ionic liquid imbibed poly(AA/CTAB) gel electrolytes, and full-ionic liquid: (a) under one sun illumination; (b) in the dark.

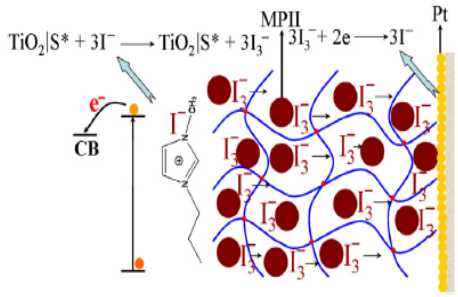

Fig. 7. Schematic illustration on the quani-solid-state DSSC from full-ionic liquid imbibed gel electrolyte.

yielding an increased contact rate of triiodides with photo-generated electrons.

It has been known that the IL imbibed poly(AA/GR) or poly(AA/CTAB) has an increased charge-transfer ability. Once the excited dyes release electrons, iodide ions participate in their regeneration and change into triiodides, as shown in Fig. 7. Therefore, the enhancement in R_{ct} can accelerate the reaction kinetics of dye recovery and therefore the electron density on conduction band of TiO_2. Moreover, the *FF* is also a parameter relating to the charge-transfer ability of electrolyte material. The DSSCs employing IL imbibed poly(AA/GR) and poly(AA/CTAB) display power conversion efficiencies of 7.19% and 7.15% from their quasi-solid-state DSSCs in comparison with 6.55% and 6.12% from traditional acetonitrile-contained poly(AA/GR) and poly(AA/CTAB) gel electrolytes, respectively. Although the efficiencies from IL imbibed poly(AA/GR) and poly(AA/CTAB) based DSSCs are lightly lower than 7.27% from IL based DSSC, the retention of IL has been significantly enhanced. To reveal the potential mechanism of conversion efficiency, it is believed as a comprehensive effect of ionic conductivity of gel electrolyte, retention of solvent, and charge-transfer ability at gel electrolyte/Pt counter electrode interface. From the results, we can conclude that all of these performances have been enhanced in IL imbibed poly(AA/GR) or poly(AA/CTAB) gel electrolyte in comparison with that of acetonitrile-contained liquid electrolyte imbibed ones.

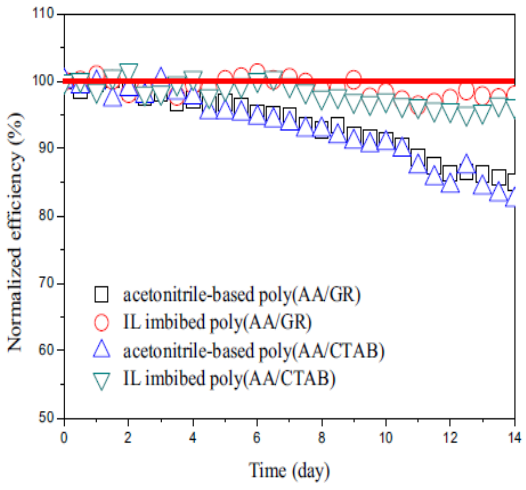

Fig. 8. Normalized power conversion efficiencies of DSSCs from acetonitrile-based liquid electrolyte-imbibed and ionic liquid-imbibed poly(AA/GR) and poly(AA/CTAB) gel electrolytes.

Fig. 8 shows the normalized power conversion efficiencies of DSSCs from IL imbibed poly(AA/GR) and poly(AA/CTAB) gel electrolytes, as a comparison, the results from acetonitrile-based liquid electrolyte-imbibed poly(AA/GR) and poly(AA/CTAB) electrolyte are also provided. After a work over 14 days, nearly 97% efficiencies are remained in the DSSCs from ionic liquid-based gel electrolytes, whereas that is only 83% for traditional acetonitrile-based ones because of the volatilization of organic solvent from 3D poly(AA/GR) or poly(AA/CTAB) framework. The volatilization of acetonitrile is expected to lose the medium for ionic transfer within gel electrolyte, therefore, the excited dye molecules can not be recovered by redox couples. Until now, we can make a conclusion that the DSSCs from IL imbibed poly(AA/GR) and poly(AA/CTAB) gel electrolytes have a reasonable durability.

4. Conclusions

In summary, iodide-containing room-temperature ILs have been successfully synthesized and imbibed into 3D frameworks of amphiphilic poly(AA/GR) and poly(AA/CTAB) matrices to form a durable gel electrolytes. Ionic conductivities of 17.82 and 18.44 mS cm^{-1} are recorded from IL imbibed poly(AA/GR) and poly(AA/CTAB), respectively. The quasi-solid-state DSSCs have promising power conversion efficiencies of 7.19% and 7.15% employing IL imbibed poly(AA/GR) and poly(AA/CTAB) gel electrolytes, respectively, which are higher than 6.55% and 6.12% of the DSSCs from acetonitrile-contained poly(AA/GR) and poly(AA/CTAB) gel electrolytes. Moreover, the DSSCs from IL imbibed poly(AA/GR) and poly(AA/CTAB) gel electrolytes have a good stability that from traditional acetonitrile-based gel electrolytes. This research opens a gateway to improve the photovoltaic performances of DSSCs and highlights competitive capacity of the quasi-solid-state DSSCs among photovoltaic devices.

Acknowledgments

The authors gratefully acknowledge the financial support of the National Natural Science Foundation of China (61366003, U1037604), The Science and Technology Project of the Education Department of Jiangxi Province, China (GJJ13474), Fundamental Research Funds for the Central Universities (201313001, 201312005), Shandong Province Outstanding Youth Scientist Foundation Plan (BS2013CL015), Doctoral Fund of Ministry of Education of China (20130132120023), Shandong Provincial Natural Science Foundation (ZR2011BQ017), and Research Project for the Application Foundation in Qingdao (13-1-4-198-jch).

References

[1] B. O'Regan, M. Grätzel, Nature 353 (1991) 737–740.
[2] U. Bach, D. Lupo, P. Comte, J.E. Moser, F. Weissortel, J. Salbeck, et al., Nature 395 (1998) 583–585.
[3] M. Grätzel, Nature 414 (2001) 338–344.
[4] Y. Hua, S. Chang, H. Wang, D. Huang, J. Zhao, T. Chen, et al., J. Power Sources 243 (2013) 253–259.
[5] J. Zhang, S. Li, H. Ding, Q. Li, B. Wang, X. Wang, H. Wang, J. Power Sources 247 (2014) 807–8012.
[6] J. Yu, J. Fan, B. Cheng, J. Power Sources 196 (2011) 7891–7898.
[7] H. Chen, Y. Chiang, C. Kung, N. Sakai, M. Ikegami, Y. Yamauchi, et al., J. Power Sources 245 (2014) 411–417.
[8] J. Chen, T. Peng, W. Shi, R. Li, J. Xia, Electrochim. Acta 107 (2013) 231–237.
[9] N. Jeon, D. Hwang, Y. Kang, S. Im, D. Kim, Electrochem. Commun. 34 (2013) 1–4.
[10] F. Matteocci, G. Mincuzzi, F. Giordano, A. Capasso, E. Artuso, C. Barolo, et al., Org. Electron. 14 (2013) 1882–1890.
[11] S. Nakade, T. Kanzaki, Y. Wada, S. Yanagida, Langmuir 21 (2005) 10803–10807.
[12] J. Freitas, A.F. Nogueira, M. Paoli, J. Mater. Chem. 19 (2009) 5279–5294.
[13] A. Nogueira, C. Longo, M. Paoli, Coord. Chem. Rev. 248 (2004) 1455–1468.

[14] J. Pitawala, M.A. Navarra, B. Scrosati, P. Jacobsson, A. Matic, J. Power Sources 245 (2014) 830–835.
[15] Q.W. Tang, Y. Li, Z.Y. Tang, J.H. Wu, J.M. Lin, M.L. Huang, J. Mater. Chem. 21 (2011) 16010–16017.
[16] Q.W. Tang, J.H. Wu, Z.Y. Tang, Y. Li, J.M. Lin, J. Mater. Chem. 22 (2012) 15836–15844.
[17] S.T. Fei, S.H.A. Lee, S.M. Pursel, J. Basham, A. Hess, C.A. Grimes, et al., J. Power Sources 196 (2011) 5223–5230.
[18] Q. Li, X. Chen, Q. Tang, H. Xu, B. He, Y. Qin, J. Mater. Chem. A 1 (2013) 8055–8060.
[19] Q. Li, Q. Tang, L. Lin, X. Chen, H. Chen, L. Chu, et al., J. Power Sources 245 (2014) 468–474.
[20] V. Jovanovski, B. Orel, I. Jerman, S.B. Hočevar, B. Ogorevc, Electrochem. Commun. 9 (2007) 2062–2066.
[21] Z. Zhang, Y. Wu, Q. Ge, S. Sun, C. Shi, Sol. Energy 84 (2010) 390–393.
[22] J. Wu, Z. Lan, J. Lin, Adv. Mater. 19 (2007) 4006–4011.
[23] Q. Li, J. Wu, Z. Tang, Y. Xiao, M. Huang, J. Lin, Electrochim. Acta 55 (2010) 2777–2781.
[24] N.W. Franson, N.A. Peppas, J. Appl. Polym. Sci. 28 (1983) 1299.
[25] J. Wu, S. Hao, Z. Lan, J. Am. Chem. Soc. 130 (2008) 11568–11569.
[26] S.S. Yuan, Q.W. Tang, B.L. He, Y. Zhao, J. Power Sources 260 (2014) 225–232.
[27] S.S. Yuan, Q.W. Tang, B.L. He, P.Z. Yang, J. Power Sources 254 (2014) 98–105.
[28] S.S. Yuan, Q.W. Tang, B.B. Hu, C.Q. Ma, J.L. Duan, B.L. He, J. Mater. Chem. A 2 (2014) 2814–2821.
[29] Z.Y. Tang, J.H. Wu, Q. Liu, M. Zheng, Q.W. Tang, Z. Lan, et al., J. Power Sources 203 (2012) 282–287.
[30] Z.Y. Tang, Q. Liu, Q.W. Tang, J.H. Wu, J.L. Wang, S.H. Chen, et al., Electrochim. Acta 58 (2011) 52–57.
[31] J. Wu, S. Hao, Z. Lan, J. Lin, M. Huang, Y. Huang, et al., Adv. Funct. Mater. 17 (2007) 2645–2652.
[32] A. Agrios, A. Hagfeldt, J. Phys. Chem. C 112 (2008) 10021–10026.
[33] B.L. He, Q.W. Tang, J.H. Luo, Q.H. Li, X.X. Chen, H.Y. Cai, J. Power Sources 256 (2014) 170–177.
[34] Y.D. Wang, M.X. Wu, X. Lin, Z.C. Shi, A. Hagfeldt, T.L. Ma, J. Mater. Chem. 22 (2012) 22155–22159.
[35] F. Gong, H. Wang, X. Xu, G. Zhou, Z. Wang, J. Am. Chem. Soc. 134 (2012) 10953–10958.
[36] J.D. Roy-Mayhew, D.J. Bozym, C. Punckt, I.A. Aksay, ACS Nano 4 (2010) 6203–6211.
[37] A. Hanch, A. Georg, Electrochim. Acta 46 (2001) 3457–3466.
[38] D. Cahen, G. Hodes, M. Grätzel, J.F. Guillemoles, I. Riess, J. Phys. Chem. B 164 (2000) 2053–2059.
[39] H.S. Jung, J.K. Lee, J. Phys. Chem. Lett. 4 (2013) 1682–1693.

INTERNATIONAL JOURNAL OF HYDROGEN ENERGY 39 (2014) 4447–4458

Available online at www.sciencedirect.com

ScienceDirect

journal homepage: www.elsevier.com/locate/he

Incorporation of H_3PO_4 into three-dimensional polyacrylamide-graft-starch hydrogel frameworks for robust high-temperature proton exchange membrane fuel cells

Qi Qin [a], Qunwei Tang [a,*], Qinghua Li [b], Benlin He [a], Haiyan Chen [a], Xin Wang [a,*], Peizhi Yang [c]

[a] Institute of Materials Science and Engineering, Ocean University of China, Qingdao 266100, Shandong Province, PR China

[b] National Defense Key Disciplines Laboratory of Light Alloy Processing Science and Technology, Nanchang Hangkong University, Nanchang 330063, PR China

[c] Key Laboratory of Advanced Technique & Preparation for Renewable Energy Materials, Ministry of Education, Yunnan Normal University, Kunming 650092, PR China

ARTICLE INFO

Article history:
Received 14 October 2013
Received in revised form
30 December 2013
Accepted 30 December 2013
Available online 28 January 2014

Keywords:
Proton exchange membrane
Fuel cell
Hydrogel material
Proton conductivity

ABSTRACT

To enhance the anhydrous proton conductivities of proton exchange membranes, we report here the incorporation of H_3PO_4 into three-dimensional (3D) framework of polyacrylamide-graft-starch (PAAm-g-starch) hydrogel materials using extraordinary absorption of hydrogels to H_3PO_4 aqueous solution. Intrinsic microporous structure can close to seal H_3PO_4 molecules in the interconnected 3D frameworks of PAAm-g-starch after suffering from dehydration. The hydrogel membranes are thoroughly characterized by morphology observation, thermal stability, swelling kinetics, proton-conducting performances as well as electrochemical behaviors. The results show that the H_3PO_4 loadings and therefore the proton conductivities of the hydrogel membranes are dramatically enhanced by employing PAAm-g-starch matrix. H_3PO_4 loading of 88.68 wt% and an anhydrous proton conductivity as high as 0.046 S cm^{-1} at 180 °C are recorded. A fuel cell using a thick membrane shows a peak power density of 517 mW cm^{-2} at 180 °C by feeding with H_2/O_2 streams. The high H_3PO_4 loading, reasonable proton conductivity in combination with simple preparation, low cost and scalable matrix demonstrates the potential use of PAAm-g-starch hydrogel membranes in high-temperature proton exchange membrane fuel cells.

1. Introduction

Proton exchange membrane fuel cell (PEMFC) is well-known an electrochemical device converting chemical energy of fuels into electricity and characterized by a high efficiency and a low environmental impact. It is believed as one of the solutions to ecology damage, environmental pollution and energy exhaustion [1–3]. Among the components of a PEMFC, proton

* *Corresponding authors*. Tel./fax: +86 532 66781690.
E-mail addresses: tangqunwei@hotmail.com (Q. Tang), wangxinhd@ouc.edu.cn (X. Wang).

0360-3199/$ – see front matter
http://dx.doi.org/10.1016/j.ijhydene.2013.12.205

exchange membrane (PEM), transferring protons from anode to cathode, is of great significance in determining the fuel cell performances [4]. The ability of generating power has a strong dependence on capacity of transferring protons. Therefore, proton conductivity is a key criterion in evaluating the superiority of a PEM. To date, the most successful low-temperature PEMs are Nafion-related membranes, in which high price has been fully reflected [5]. By addressing this issue, sulfonation of engineering polymers such as polyether ether ketone, polyimide, polysulfone, and polyphenylene sulfide et al. has been employed as low-temperature PEMs [5]. All of these membranes give drawbacks of dependence on hydration degree and environmental pollution in sulfonation treatment. In a real fuel cell, the low-temperature operation offers demerits on water management along with high cost [6]. One of the effective solutions to overcome these issues is the employment of high-temperature PEMs, in which the anhydrous proton conductors are incorporated [7,8]. At temperatures of higher than 100 °C, the electrode kinetics can be significantly enhanced, which gives a low dosage of Pt material or the utilization of non-Pt catalysts. H_3PO_4 doped polybenzimidazole (PBI) membranes are believed to be promising candidates as high-temperature PEMs. The incorporation of H_3PO_4 into linear PBI originating from the protonation of C=N in repeated imidazole rings. Therefore, the H_3PO_4 loading is commonly lower than ~60 wt% which results in a relatively lower proton conductivity. Although recent research demonstrate that phosphate species could be adsorbed on the platinum catalyst surface [9,10], leading to the loss of a cell voltage, H_3PO_4 is still widely employed as anhydrous proton conductor because of its merits on high proton conductivity, low cost, and thermal stability.

In search for robust high-temperature or intermediate temperature PEMs, crosslinked hydrogel materials are promising matrix candidates because of their superabsorbing ability to H_3PO_4 or protic ionic liquid solutions [11–15]. Hydrogels are defined as 3D polymer frameworks with a suitable crosslinking degree, in which aqueous solutions are imbibed as solvents [16]. Using their extraordinary absorption ability, hydrogel materials have been successfully applied in assembling quasi-solid-state dye-sensitized solar cells [17,18] and in fabricating conducting hydrogels [19–23]. To further elevate the absorbing capacity of hydrogel materials, the incorporation of typical matrix such as polyacrylamide with natural macromolecules has been one of the efficient approaches.

Here we report the synthesis and characterization of a new class of high-temperature PEMs consisting of anhydrous 3D PAAm-g-starch framework incorporated with H_3PO_4. The focus of the current work is on the uptake of H_3PO_4, electrical and electrochemical characterizations as well as preliminary fuel cell evaluation of resultant H_3PO_4 incorporated PAAm-g-starch membranes. Other characterizations such as mechanical strength, fuel crossover, and long-term stability are not included.

2. Experimental

2.1. Synthesis of PAAm-g-starch membranes

The PAAm-g-starch membrane was synthesized according to an aqueous solution polymerization route [11–15]. In detail, a solution mixture consisting of acrylamide monomer (10 g, AAm, analytical reagent, Sinopharm Chemical Reagent Co., Ltd) and starch (0, 0.2 and 0.35 g, analytical reagent, Sinopharm Chemical Reagent Co., Ltd) was made by agitating in deionized water (15 mL) in a water-bath at 80 °C. Under vigorous agitation, crosslinker N,N′-(methylene)bisacrylamide (0.008 g, NMBA, Sinopharm Chemical Reagent Co., Ltd) and initiator ammonium persulfate (0.0225 g, APS, Sinopharm Chemical Reagent Co., Ltd) were subsequently added to the above mixture. When the viscosity of the PAAm-g-starch reached around 180 mPa s^{-1}, the reagent was poured into a Petri dish and cooled to room temperature with the formation of an elastic transparent gel. The PAAm-g-starch membranes were then molded into φ 3 cm die. After rinsing with deionized water to remove unreacted monomers or oligomers, the membranes were dried under vacuum at 60 °C for 24 h.

2.2. Preparation of H_3PO_4 incorporated PAAm-g-starch membranes

The dried PAAm-g-starch membranes were immersed in H_3PO_4 aqueous solution with concentration varying from 1 to 9 M in a sealed bottle at room temperature for 15 days to reach absorption equilibrium. The resultant products were then rinsed and dried under vacuum at 60 °C for 2 days to drive off all water as much as possible and obtain the anhydrous H_3PO_4 incorporated PAAm-g-starch membranes. H_3PO_4 loading (wt %) was determined by measured according to the equation:

$$H_3PO_4\ \text{loading(wt\%)} = \frac{W_d - W_0}{W_d} \times 100\% \quad (1)$$

where W_d (g) was the mass of anhydrous H_3PO_4 incorporated PAAm-g-starch membrane, W_0 (g) was the mass of dried PAAm-g-starch membrane.

2.3. Electrochemical characterizations

The proton conductivity of the H_3PO_4 incorporated PAAm-g-starch membranes in either hydrous or anhydrous state were characterized with ac-impedance spectroscopy using a CHI660E Electrochemical Workstation in a frequency range of 0.01 Hz–2 MHz and an ac amplitude of 10 mV in temperature range of 25–165 °C. Double coated PELCO Tabs™ carbon conductive tapes (TED PELLA, INC, 90% of polymer acrylic adhesive and 10% of carbon black) with a thickness of 0.1 mm were used as the electrodes. The ohmic resistance associated with the membrane was determined from high frequency intersection of the spectrum with the Z′ axis, from which the proton conductivity can be calculated based on dimensional information.

Cyclic voltammetry (CV) was conducted at room temperature in 0.05 or 0.1 M H_3PO_4 aqueous solution using a three-compartment glass cell. The platinum wire with a diameter of 0.4 mm was pierced into a hydrated H_3PO_4 incorporated PAAm-g-starch hydrogel which was used as working electrode. A platinum sheet and Ag/AgCl were used as counter electrode and reference electrode, respectively. Before the measurement, the electrolyte was deoxygenated by nitrogen bubbling for 5 min. The scan rate was 50 mV s^{-1}.

INTERNATIONAL JOURNAL OF HYDROGEN ENERGY 39 (2014) 4447–4458

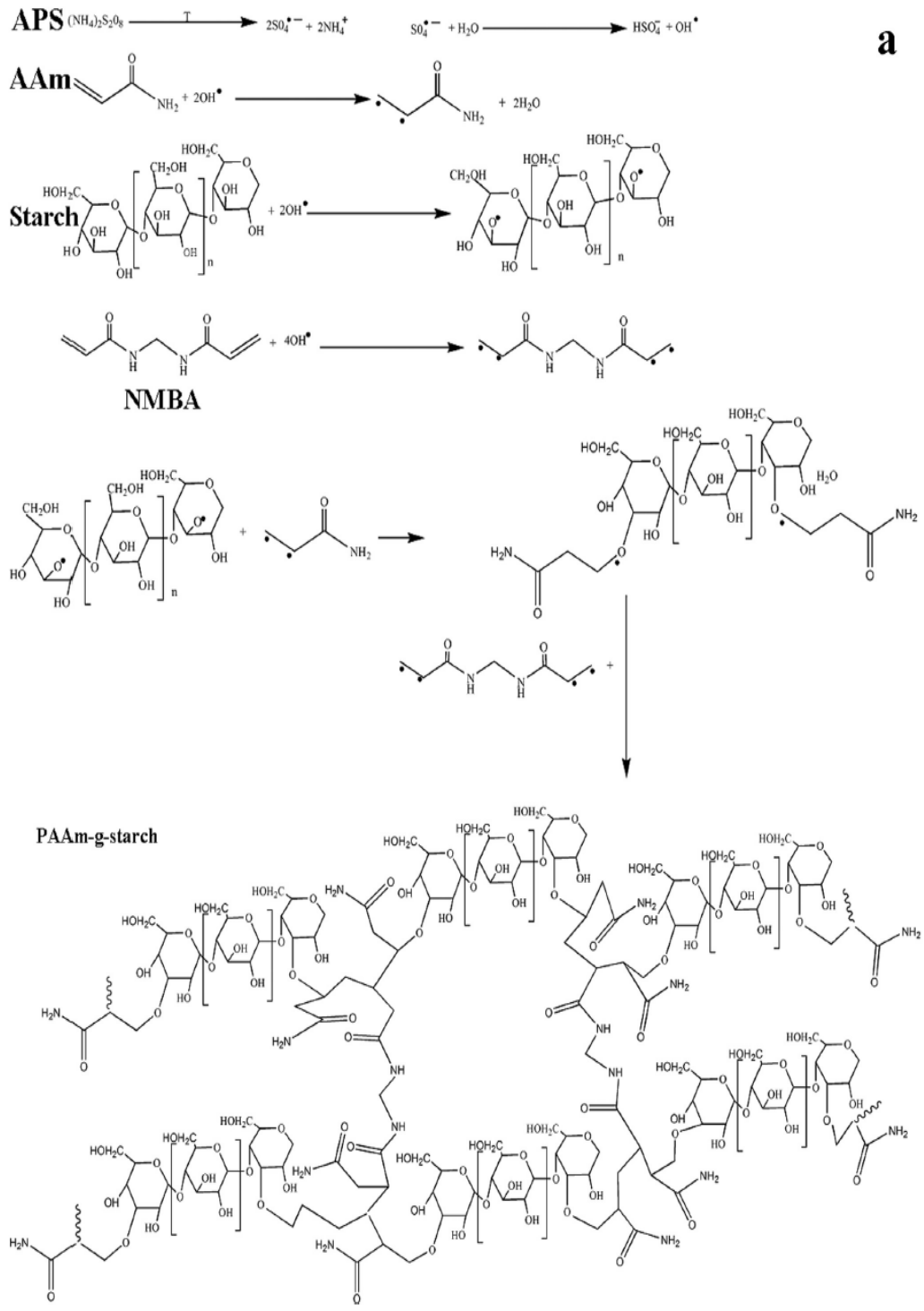

Fig. 1 – (a) Schematic of synthesis of PAAm-g-starch hydrogel matrix, (b) proposed proton transfer mechanism in H_3PO_4 incorporated PAAm-g-starch membrane under anhydrous conditions.

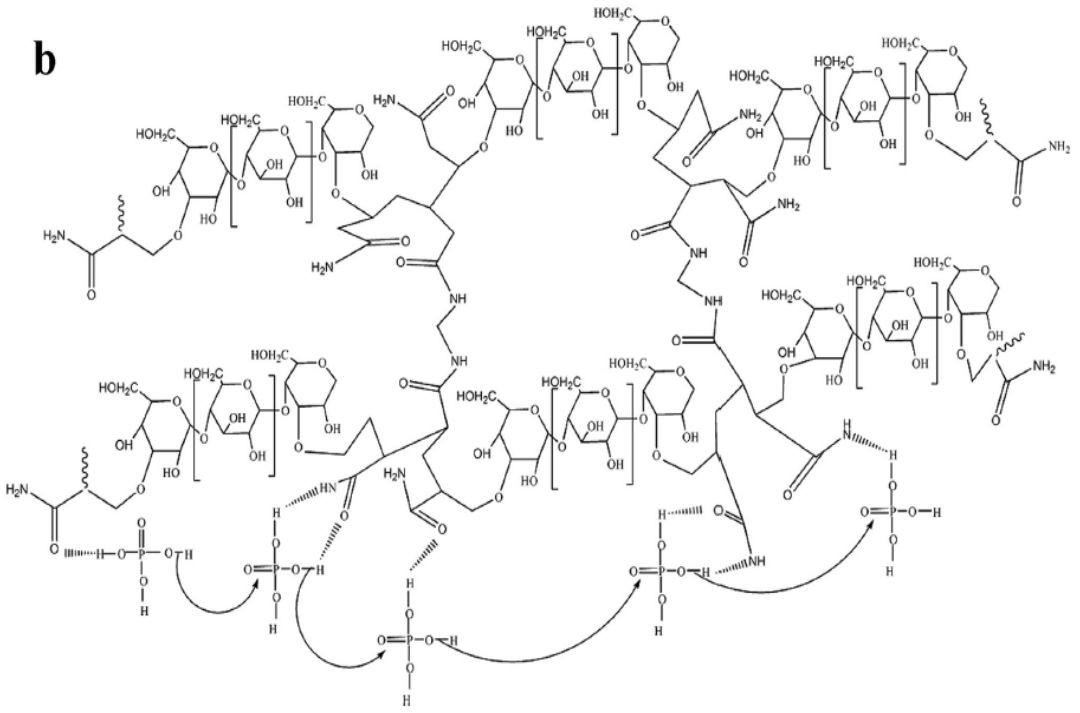

Fig. 1 – (continued).

2.4. *Membrane electrode assembly (MEA) and fuel cell tests*

The gas diffusion electrodes (GDE, acquired from BASF Fuel Cell, Inc., formerly E-Tek, Inc.) with a platinum loading of 1.0 mg cm^{-2}, were used for this study. The MEA with an active area of 10 cm^2 was fabricated by hot-pressing a PAAm-g-starch membrane between the two Kapton framed electrodes. The MEA was then assembled into a single cell fuel cell testing rig. The gas flow fields were made from graphite plates with single serpentine gas channels. Stainless steel end plates with attached heaters were used to clamp the graphite flow plates. A commercial fuel cell testing station (Fuel Cell Technology, Inc.) was used for fuel cell testing, while H_2 and pure oxygen (or air) were fed to the anode and cathode without any humidification, respectively. The instrument was controlled by home-programmed LabView Software (National Instruments, Austin, TX).

2.5. *Other characterizations*

The morphologies of the porous structures were captured with a zeiss emission scanning electron microscopy (SEM). To observe the internal 3D microstructure of the PAAm-g-starch membrane, a swollen PAAm-g-starch hydrogel was freeze dried at a freezing temperature of around −60 °C for 72 h. Fourier transform infrared spectrometry spectra (FTIR) were recorded on a Vertex 70 FTIR spectrometer (Bruker). The gas permeability was measured by the equal pressure method with a gas chromatograph (Hewlett–Packard Series II 5890), equipped with a packed-bed column and an integrator, monitoring the amounts of H_2 that permeated across the H_3PO_4 incorporated PAAm-g-starch framework membrane with H_3PO_4 loading of 88.68 wt% from one side to the other. A thick membrane was set in a cell with a gas inlet and outlet, where the temperature (25–180 °C) was controlled. H_2 was supplied at a flow rate of 30 mL min^{-1}. To evaluate the dimension stability of the membrane against the temperature, the 88.68 wt% H_3PO_4 incorporated PAAm-g-starch was molded to a disc with a diameter of 2 cm. The specimen was kept in the temperature ranging from 25 to 180 °C for 30 min and the diameters were measured at anhydrous conditions because of the potential use in high-temperature PEMFCs. The thermal gravimetric analysis-differential scanning calorimetry (TGA-DSC) tests were conducted on a TA TGA 2050 instrument. The experimental procedure consisted of heating the samples in flowing nitrogen (99.999% purity, 100 mL min^{-1}) at a heating rate of 10 °C min^{-1} from room temperature to 780 °C until all the samples were completely consumed. The tensile strength-elongation tests of the H_3PO_4 incorporated PAAm-g-starch membranes were carried out using an INSTRON Model 5583 testing machine. The test conditions were controlled as follows: the temperature was 25 °C, the size of the sample was 5 mm × 5 mm × 80 mm, the distance between two square panels was 20 mm, and the crosshead speed ws 100 mm min^{-1}. The porosity and pore size were analyzed by an AutoPore IV9500 mercury

porosimeter (Micrometritics, USA) in a pressure range of 0.5–30,000 psia.

3. Results and discussion

3.1. Synthesis and morphology of 3D PAAm-g-starch framework

The synthesis of PAAm-g-starch composite polymer is a simple process schematically illustrated in Fig. 1. The polymerization of PAAm-g-starch originated from the free radical reaction of initiator APS, AAm monomers, crosslinker NMBA, and starch. The resultant PAAm-g-starch framework is believed as a 3D structure because of the macrobiradical nature of NMBA.

The incorporation of H_3PO_4 aqueous solution into 3D PAAm-g-starch framework is primarily driven by the osmotic pressure present across the membrane [24]. Generally, the absorption of H_3PO_4 aqueous solution by PAAm-g-starch causes PAAm-g-starch framework to stretch and expand considerably in volume, the process of which can be briefly summarized by three steps: (i) the adsorption of H_2O molecules on the surface of PAAm-g-starch because of the strong hydrophilicity of $-CONH_2$, $-OH$, and $-NH_2$; (ii) Relaxation of PAAm-g-starch chains in H_3PO_4 aqueous solution; (iii) stretch of whole PAAm-g-starch macromolecule chains in H_3PO_4 aqueous solution. The swollen of PAAm-g-starch membranes in H_3PO_4 aqueous solution results in gradual decrease in osmotic pressure, and a swelling equilibrium will be obtained at equal value of expansibility and contractility of PAAm-g-starch (i.e., the osmotic pressure across the membrane is zero).

The cross-sectional SEM image of PAAm-g-starch is shown in Fig. 2, which suggests a well-interconnected and microporous framework capable of caging enormous H_3PO_4 aqueous solution into the microporous structure. The absorbed H_3PO_4 is expected to be sealed in the 3D system in a drying process. In fact, the pore size and porosity can be controlled by adjusting synthesis conditions, such as initiator dosage, crosslinker dosage, reaction temperature, concentration of AAm monomer, and mass ratio of AAm to starch. The focus of the current work is to display the feasibility of employing PAAm-g-starch hydrogel material as a H_3PO_4 supporter to fabricate robust PEMs. The porosity and pore diameter of the PAAm-g-starch membrane in our conditions are 75.1% and 12.6 μm, respectively. Such a high porosity is expected to imbibe enormous H_3PO_4 within the 3D framework. Moreover, the loading of H_3PO_4 will give an expansion in volume of anhydrous membrane, as is also shown in Fig. 2.

3.2. Molecular structure

The FTIR spectra of 79.33 and 88.68 wt% H_3PO_4 incorporated PAAm-g-starch membranes are employed to demonstrate the bonding between H_3PO_4 and matrix and indicate the difference at low and high H_3PO_4 dosages. As is shown in Fig. 3, the absorption bands at 1660, 1449, 1125, and 982 cm^{-1} in H_3PO_4 incorporated PAAm-g-starch are originated from the vibrations of C=O stretching, C–N stretching, and $-NH_2$ wagging, respectively [22]. However, band intensity at 982 cm^{-1} is

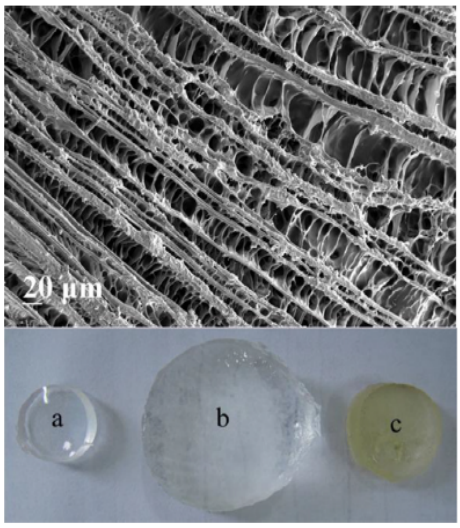

Fig. 2 – Top: cross-sectional SEM image of PAAm-g-starch membrane; Down: macroscopic morphologies of (a) anhydrous PAAm-g-strarch, and 88.68 wt% H_3PO_4 incorporated PAAm-g-starch in (b) fully hydrated and (c) dried states.

enhanced because of the strong absorption of P–O symmetric stretching in H_3PO_4 incorporated PAAm-g-starch membranes at higher H_3PO_4 loading. A peak at 886 cm^{-1} attributing to in-plane bending of PO_4^{3-} is generated because of the incorporation of H_3PO_4. The change of absorption bands suggests that H_3PO_4 molecules interact with C=O, C–N, and $-NH_2$ groups by O–H···O=C, O–H···N–C, O–H···NH_2 to form hydrogen bonds [11–15]. The formation of these hydrogen bonds plays an important role in the conductivity behavior of the membranes.

3.3. Loading of H_3PO_4

The swelling kinetics of dense PAAm-g-starch membranes in concentrated H_3PO_4 aqueous solution, shown in Fig. 4, is

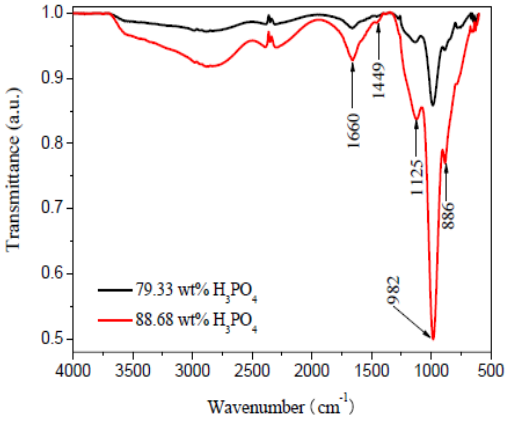

Fig. 3 – FTIR spectra of anhydrous (a) 79.33 wt% and (b) 88.68 wt% H_3PO_4 incorporated PAAm-g-starch membranes.

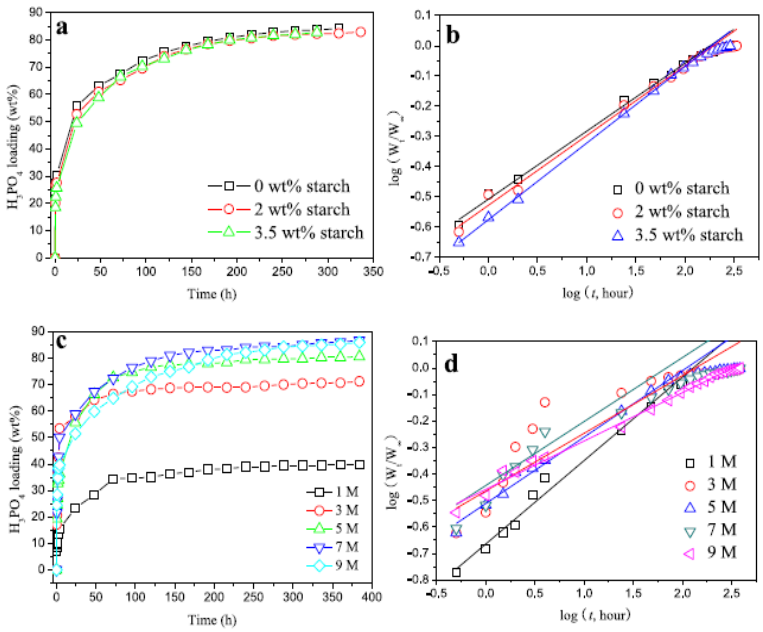

Fig. 4 – (a) Swelling kinetics of PAAm-g-starch membranes at various starch dosages in 5 M H_3PO_4 aqueous solution, and (c) and (d) swelling kinetics of PAAm-g-starch membranes with starch dosage of 2.0 wt% in various concentrations of H_3PO_4 aqueous solutions.

mainly due to the Flory theory from osmotic pressure across the membranes. The H_3PO_4 loading increases with elongation of swelling time, indicating a diffusion of H_3PO_4 solution into 3D framework of PAAm-g-starch membranes. An absorption equilibrium can be obtained at swelling time of around 10 days, and no further diffusion occurs under longer immersion time. In order to determine the nature of H_3PO_4 loading by PAAm-g-starch membranes, the accumulative H_3PO_4 loading over time have been fitted using the Fickian theory [14,25].

$$\frac{W_t}{W_\infty} = kt^n \tag{2}$$

where W_t and W_∞ are the mass of the loaded H_3PO_4 at time t and at equilibrium, respectively. k is a characteristic rate constant relating to the properties of PAAm-g-starch membranes, and n is a transport number characterizing the transport mechanism, it is dimensionless. $n \leq 0.5$ indicates a Fickian or Case I transport behavior in which the relaxation of PAAm-g-starch framework is much faster than the diffusion; $n = 1$ suggests a non-Fickian or Case II mode of transport where H_3PO_4 uptake is controlled by diffusion process. $0.5 < n < 1$ demonstrates an anomalous or a Case III mode in which structural relaxation is comparable to diffusion. By plotting $\log(W_t/W_\infty)$ vs $\log(t)$, the n values from the membranes at various starch dosages and in various H_3PO_4 solutions summarized in Table 1 are all lower than 0.5, suggesting a Fickian mechanism. The result indicates that the loading of H_3PO_4 from dilute H_3PO_4 aqueous solution is controlled by the relaxation of PAAm-g-starch framework, which is opposite to that in deionized water.

Table 1 – Absorption parameter (n) values of PAAm-g-starch matrix for H_3PO_4 absorption.

Starch/AAm ratio (g/g)	n values at various concentrations of H_3PO_4 aqueous solution (M)				
	1	3	5	7	9
0/10	–	–	0.225	–	–
0.2/10	0.315	0.241	0.231	0.218	0.182
0.35/10	–	–	0.253	–	–

Proton conductivity is a key parameter for H_3PO_4 incorporated PAAm-g-starch membranes and is highly dependent on the H_3PO_4 loading. To explore higher H_3PO_4 loading and therefore better proton conductivity, anhydrous PAAm-g-starch membranes are immersed into H_3PO_4 aqueous solution with concentrations from 0.05 to 9 M. The H_3PO_4 loading is always controlled by Flory theory [26,27]:

$$H_3PO_4 \text{ solution loading} = \frac{\left(\frac{i}{2V_u I^{1/2}}\right)^2 + \frac{1/2 - X_1}{V_1}}{V_e/V_0} \tag{3}$$

$$H_3PO_4 \text{ loading} = H_3PO_4 \text{ solution loading} \times H_3PO_4 \text{ concentration} \tag{4}$$

where i/V_u is the concentration of fixed charges referred to the anhydrous PAAm-g-starch membrane, I is ionic strength in the H_3PO_4 aqueous solution, V_e/V_0 is crosslinking density of PAAm-g-starch, and $(1/2-X_1)/V_1$ is relative to water affinity of PAAm-g-starch. After systematic variation of concentration of H_3PO_4 aqueous solution, we find that the H_3PO_4 loading increases in the target concentrations (Fig. 5a), leading to increased anhydrous proton conductivity at room temperature. The H_3PO_4 loading is 88.68 wt% from the absorption of PAAm-g-starch in H_3PO_4 aqueous solution of 8 M, and the

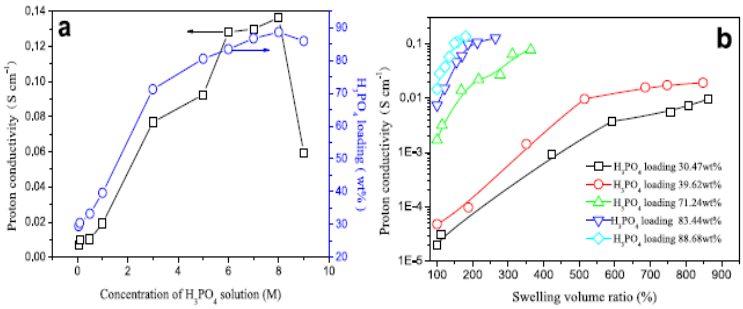

Fig. 5 – (a) Fully-hydrous proton conductivity and H_3PO_4 loading of the H_3PO_4 incorporated PAAm-g-starch membrane as a function of H_3PO_4 concentration at fully hydrated equilibrium state and room temperature. (b) Room-temperature proton conductivity of the hydrated H_3PO_4 incorporated PAAm-g-starch membranes as a function of swelling volume ratio.

room-temperature hydrous proton conductivity is as high as 0.136 S cm^{-1}.

3.4. *Thermal and mechanical performances*

In the TGA analysis (Fig. 6a), the weight loss started at about ~100 °C is attributed to water evaporation. However, the decomposition between temperatures of 120–180 °C can be attributed to the loss of PAAm-g-starch oligomers. The weight losses at 180 °C for PAAm-g-starch, and 39.62 and 88.68 wt% H_3PO_4 incorporated PAAm-g-starch are 6, 4.5, and 4 wt%, respectively, indicating a good thermal stability in high-temperature PEMs. From Fig. 6b, one can see that the glass transition temperature for three membranes is around 73.6 °C, no apparent deviation is observed. Fig. 6c shows the σ-ε plots of H_3PO_4 incorporated PAAm-g-starch membranes at room temperature. There is a good correlation between the breaking stress and breaking strain, and the maximum breaking stress and breaking strain of 88.68 wt% H_3PO_4 incorporated PAAm-g-starch membrane are 17.7 MPa and 972%, respectively, while those for pure PAAm-g-starch are 12.7 MPa and 544%, respectively. The enhancement in mechanical strength is believed to the hydrogen-bonding between H_3PO_4 molecules and PAAm-g-starch backbone.

3.5. *Proton conductivity*

There is a high dependence of proton conductivity of a PEM on water content. However, there is an universality in hydrogel materials that the volume will be elevated by the filling of aqueous solution, therefore, swelling volume ratio (defined as $V_{swollen}/V_{dry}$) can be employed to evaluate the dependence of H_3PO_4 incorporated PAAm-g-starch membranes on water content. Data on room-temperature proton conductivity from

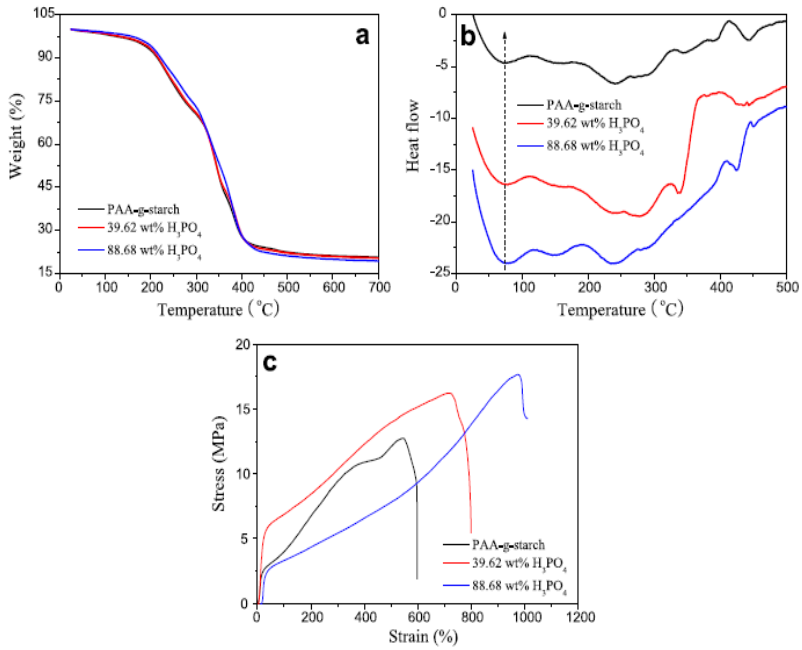

Fig. 6 – (a) TGA, (b) DSC, and (c) σ–ε curves of pure PAAm-g-starch, and 39.62 and 88.68 wt% H_3PO_4 incorporated PAAm-g-starch membranes.

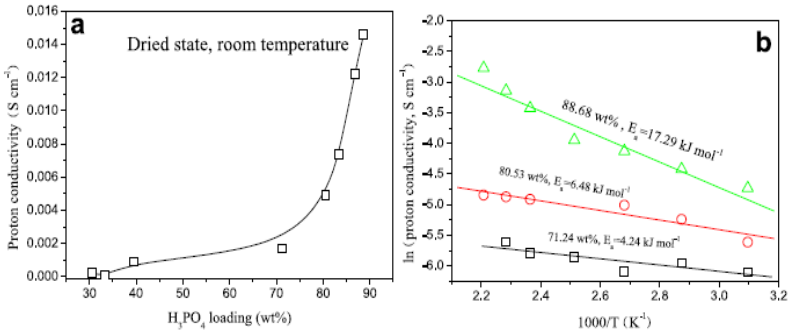

Fig. 7 – (a) Room-temperature anhydrous conductivity percolation effect of H_3PO_4 incorporated PAAm-g-starch membranes. (b) Arrhenius plots of H_3PO_4 incorporated PAAm-g-starch membranes measured in dry air.

hydrated H_3PO_4 incorporated PAAm-g-starch membranes, recorded during dehydrated process of hydrous membranes, are shown in Fig. 5b. In the initial stage, the proton conductivity is elevated by two orders of magnitude compared with that at anhydrous state. Take 39.62 wt% H_3PO_4 imbibed PAAm-g-starch membrane as an example, the anhydrous proton conductivity (proton conductivity at swelling volume ratio of 100%) is in the level of $\sim 10^{-5}$ S cm^{-1}, and it rushes up to $\sim 10^{-2}$ S cm^{-1} at swelling volume ratio of around 500%. With further increase in swelling volume ratio, the room-temperature conductivity reaches an equilibrium.

It has been pointed out that PAAm-g-starch membrane is a 3D polymer framework with extraordinary capability of absorbing H_3PO_4 aqueous solution. The imbibed H_3PO_4 molecules are believed to attach on inner-surface of microporous structure to form superhighways for proton transport. To record the formation of conducting channels, anhydrous proton conductivities are plotted as a function of H_3PO_4 loading at room temperature (Fig. 7a), giving a typical percolation effect. The turning point in proton conductivity is defined as percolation threshold. From Fig. 7a, one can see that the percolation threshold value is at ~70% H_3PO_4 loading, indicating the interconnection of conducting regions from H_3PO_4 at ~70% H_3PO_4. For example, the anhydrous conductivity is in the level of $\sim 10^{-4}$ S cm^{-1} at H_3PO_4 loading of 30.47 wt%, and it increases to 1.7×10^{-3} S cm^{-1} at a weight percentage of 71.24 wt % H_3PO_4. A maximum conductivity value of 0.0146 S cm^{-1} is achieved for the 88.68 wt% H_3PO_4 incorporated PAAm-g-starch membrane. The conductivity response of the membrane can be described by traditional percolation theory [28]:

$$\sigma = C|f - f_c|^{\beta} \quad (5)$$

where σ is proton conductivity, f is weight fraction of H_3PO_4 in PAAm-g-starch membrane, f_c is percolation threshold where the transition take places, C is a constant and β is a critical exponent (an index of system dimensionality, theoretically 1.3 and 1.94 for ideal 2D and 3D systems, respectively) [28]. We also fit the experimental data using a percolation theory, yielding $f_c = 71.8$ wt%, $\beta = 2$, and $C = 5.05 \times 10^{-5}$. The fitted percolation threshold is nearly the same to that for shown in Fig. 7a, supporting the formation of 3D interconnecting channels in H_3PO_4 incorporated PAAm-g-starch membranes.

The proton conductivity from H_3PO_4 incorporated PAAm-g-starch membranes measured under dry air from 25 to 180 °C follows an Arrhenius relationship reasonably well as shown in Fig. 7b. It is noteworthy to mention that the activation energy, E_a, increases with H_3PO_4 loading, which is opposite to that of H_3PO_4 doped PBI membranes, but consistent with our previous reports and other system on PAM/H_3PO_4 membranes [11–15]. Only at a higher H_3PO_4 loading is E_a closer to that of pure H_3PO_4 (23.05 kJ mol^{-1}). Lower E_a values in conducting composites suggest a facile proton transport along conducting channels. It is reasonable that the conducting channels tend to be interconnecting at higher H_3PO_4 loading and the conducting regions composed of H_3PO_4 are isolated at lower H_3PO_4 loading. Therefore, there is a probability that the functional groups such as $-NH_2$, O–H, C=O, and C–N in PAAm-g-starch can form hydrogen bonds with H_3PO_4 molecules and serve as pathways for proton transfer as illustrated in Fig. 1. The potential mechanism has been described in our previous report [13]. The proton conductivities of the resultant membranes at low H_3PO_4 loading are mainly the result of low concentration of protons and hydrogen bonds from H_3PO_4 and PAAm-g-starch framework. An interconnecting channel from

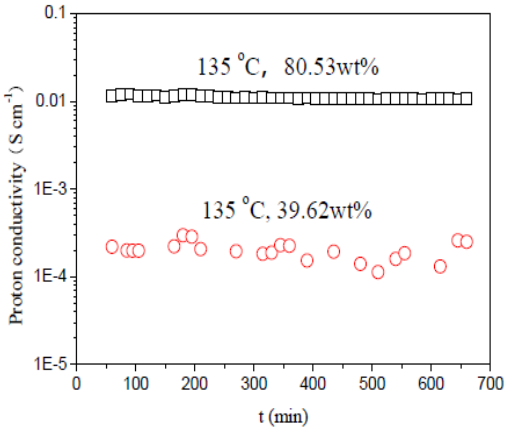

Fig. 8 – Stability of anhydrous proton conductivity for 80.53 and 39.62 wt% H_3PO_4 incorporated PAAm-g-starch membrane measured at 135 °C.

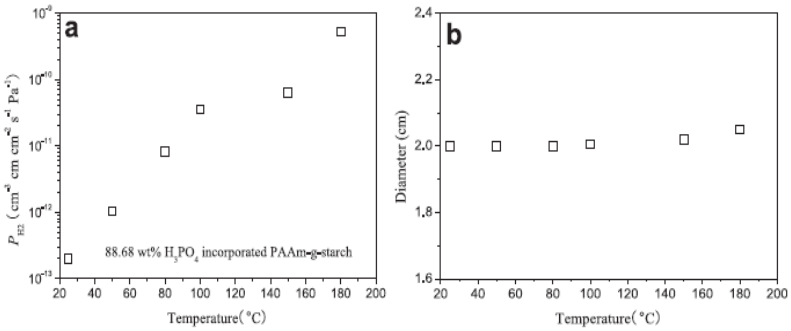

Fig. 9 – (a) H_2 permeability and (b) dimension stability as a function of temperature for 88.68 wt% H_3PO_4 incorporated PAAm-g-starch membrane.

either hydrogen-bond bridges of H_3PO_4 molecules or H_3PO_4/PAAm-g-starch or both for proton transport is formed at high H_3PO_4 loading.

The proton conductivity stabilities of anhydrous 80.53 and 39.62 wt% H_3PO_4 incorporated PAAm-g-starch membrane measured in dry air is shown in Fig. 8 for 135 °C. Over an 11 h period, no apparent decrease in proton conductivity is observed in 80.53 wt% H_3PO_4 incorporated PAAm-g-starch, suggesting that no serious H_3PO_4 leakage occurs during the operation. However, the fluctuation in 39.62 wt% H_3PO_4 incorporated PAAm-g-starch may be the results of unconnected channels for proton transfer. As has been described in Fig. 7a, the percolation threshold is around 71.8 wt% H_3PO_4, suggesting that the membrane at a H_3PO_4 loading of 39.62 wt% does not form interconnected channels within the 3D framework. 11 h-stability presented here is far from being optimized but the recoded conductivity stability along with low-cost synthesis and scalable materials promise the new membranes to be potential candidates in high-temperature PEMFCs.

3.6. *Fuel permeation and dimensional stability*

The low fuel permeability is significant to enhance the fuel cell performances. Fig. 9a shows temperature dependence of H_2 permeability in H_3PO_4 incorporated PAAm-g-starch

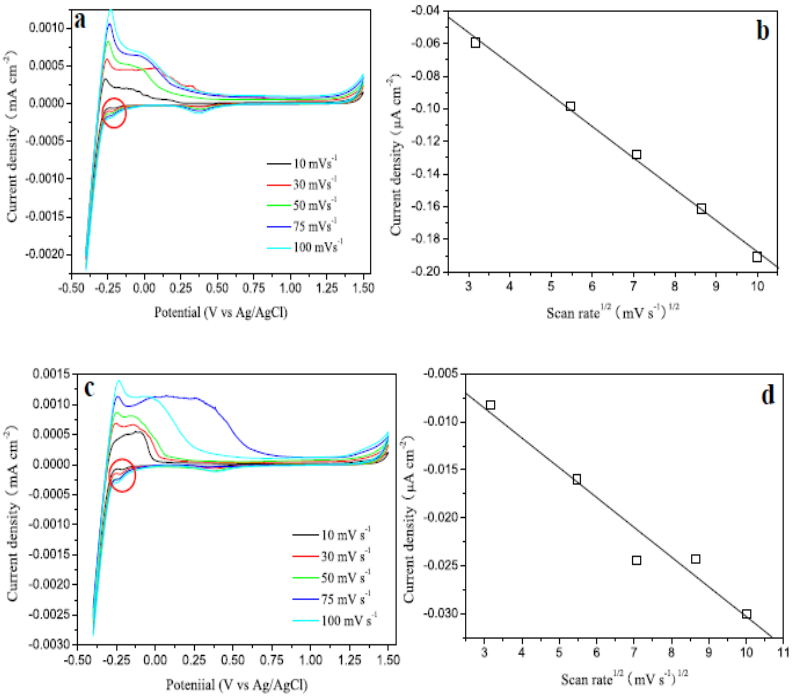

Fig. 10 – CV curves recorded in (a) 0.1 and (c) 0.05 M H_3PO_4 aqueous solution incorporated PAAm-g-starch hydrogel using Pt wire as working electrode. From inner to outer: 10, 30, 50, 75, and 100 mV s^{-1}. (b) and (d) Linear relationships of peak current density as a function of scan rate$^{1/2}$.

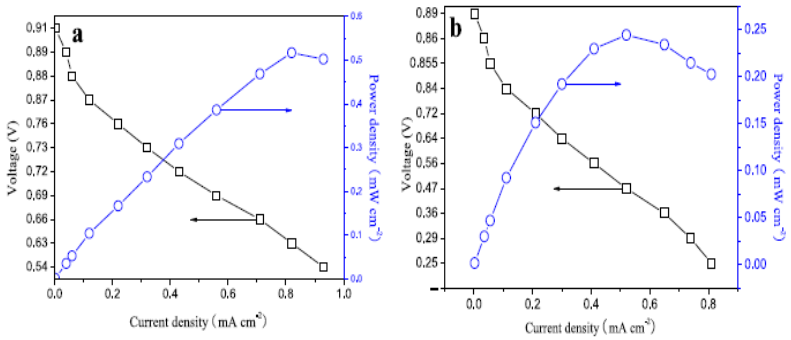

Fig. 11 – V–I and P–I characteristics of 88.68 wt% H_3PO_4 incorporated PAAm-g-starch membrane at 180 °C under anhydrous conditions: (a) Gas stream: H_2/O_2, 180 °C; gas flow rates: H_2 1.2 stoich, O_2 2 stoich. (b) Gas stream: H_2/air, 180 °C; gas flow rates: H_2 1.2 stoich, air 2 stoich.

membrane with H_3PO_4 loading of 88.68 wt%. The H_2 permeability coefficients at ~135 °C is in the order of ~10^{-11} cm^{-3} cm cm^{-2} s^{-1} Pa^{-1} compared with that of ~10^{-8} cm^{-3} cm cm^{-2} s^{-1} Pa^{-1} for Nafion 112 and PIL/sulfonated polyimide membranes [6]. H_2 permeability increases by orders of magnitude with increasing temperature. The significantly low fuel permeation is expected to enhance the fuel cell performances.

The dimension stability of the 88.68 wt% H_3PO_4 incorporated PAAm-g-starch membrane against temperatures is shown in Fig. 9b. The diameter remained unchanged at temperatures below 80 °C. Interestingly, there is a slightly increase in diameter at temperatures higher than 100 °C. The relative dimensional stability demonstrates the membrane to be potentially used in high-temperature PEMFCs.

3.7. *Electrochemical behaviors*

3D PAAm-g-starch hydrogel material not only uptakes enormous H_3PO_4 and retain in the framework, but provides interconnecting channels for proton transport. Microporous structure can be apparently observed from the SEM morphology. To determine the unobstructed transport of protons within the micropores, CV measurements are carried out by piercing a platinum wire into a hydrated H_3PO_4 incorporated PAAm-g-starch hydrogel membrane which is used as working electrode. A platinum sheet is employed as a counter electrode accompanied with an Ag/AgCl reference electrode. The electrolyte is H_3PO_4 aqueous solution with the same concentration to that for swelling of PAAm-g-starch. Fig. 10a and Fig. 10c shows the CV plots obtained from 0.05 to 0.1 M H_3PO_4 solution incorporated PAAm-g-starch membrane. A typical hydrogen desorption peak area appears at the potential range of around −0.3 to 0.3 V because of the oxidation reaction:

$$H_2 \rightarrow 2H^+ \quad (6)$$

$$2H^+ \rightarrow H_2 \quad (7)$$

In the reduction scan, all the CVs show peaks at around 0.3 V, corresponding to the reduction of surface oxides on Pt wires. The distinctive feature in this peak is that the position of peak shifted toward lower potential. A hydrogen adsorption peak is recorded in the potential region of −0.3 to −0.1 V to the reduction of protons (Equation (7)), showing the characterized curves of Pt electrode in H_3PO_4 aqueous solution. The results can be employed to detect the proton transport in hydrated H_3PO_4 incorporated PAAm-g-starch membranes. By plotting the peak current of hydrogen adsorption versus square root of scan rate as shown in Fig. 10b and d, we can quantify the intrinsic relations of proton transport in the hydrated H_3PO_4 incorporated PAAm-g-starch membranes. One can see that the membrane scanned at higher scan rate has considerable higher reduction peak current than those at lower ones. The increased peak current values suggest a large surface area and fast reaction rate, which makes the PEMs robust in transferring protons within the interconnecting channels. Furthermore, we can conclude that the proton transfer is dominated by the diffusion of counterions in the PEMs, $H_2PO_4^-$, HPO_4^{2-}, PO_4^{3-}, causing the diffusional behavior in the cyclic voltammograms [29].

To elucidate the diffusion of protons in a H_3PO_4 incorporated PAAm-g-starch membrane, Randles-Sevcik theory is employed and presented [30]:

$$J_{red} = Kn^{1.5}ACD_n^{0.5}\upsilon^{0.5} \quad (8)$$

where J_{red} is the peak current density corresponding to reduction of protons (mA cm^{-2}), K is 2.69 × 10^5, n is the number of electrons of reduction reaction, A is the electrode area (cm^2), C represents the bulk concentration of protons (mol L^{-1}), D_n is the diffusion coefficient of protons (cm^{-2} s^{-1}). Take the CV curve at a scan rate of 100 mV s^{-1} as an example, the D_n values are 4.39 × 10^{-8} and 4.56 × 10^{-7} cm^{-2} s^{-1} in 0.1 and 0.05 M H_3PO_4 aqueous solutions, respectively. The results indicate that the protons have an enhanced diffusion kinetics at the anhydrous membranes with lower H_3PO_4 concentrations.

3.8. *Fuel cell*

A PAAm-graft-chitosan membrane with a thickness of around 500 μm was eventually assembled into a fuel cell for performance evaluation. Detailed description of fuel cell assembly can be found in the Experimental Section. The *V–I* and *P–I*

characteristics measured at 180 °C with dry H_2 as the fuel and dry oxygen as the oxidant are shown in Fig. 11. A maximum power density of 517 mW cm^{-2} @ 0.82 A cm^{-2} was achieved at 180 °C from 88.68 wt% H_3PO_4 incorporated PAAm-g-starch membrane. However, the highest powder density was 24.4 mW cm^{-2} @ 0.52 A cm^{-2} by feeding with H_2/air streams. While the demonstrated performance is lower compared to H_3PO_4-doped PBI [31], the overall performance is satisfactory and comparable to other proposed PEMFCs [32], considering the fact that both membrane and electrode were not optimized. The cell ohmic resistance was approximately 103 mΩ at 180 °C using H_2/air streams, which was close to the calculated membrane resistance of 108.7 mΩ using the conductivity shown in Fig. 7b.

4. Conclusions

In summary, a new class of 3D framework of PAAm-g-starch composite polymers have been synthesized as high-temperature PEMs using their extraordinary absorption and retention to H_3PO_4. The protons transfer via the Grotthuss mechanism, migrating across hydrogen bonds present in H_3PO_4 as well as those formed between H_3PO_4 molecules and functional groups such as C=O, C–N, and $-NH_2$ in PAAm-g-starch. The H_3PO_4 is solidly caged inside the 3D framework after dehydration, mitigating the loss of H_3PO_4. A high and stable anhydrous proton conductivity of 0.046 S cm^{-1} at is obtained at 180 °C. A fuel cell using a thick membrane showed a peak power density of 517 mW cm^{-2} with O_2 and H_2 as the oxidant and fuel, respectively. The interconnecting micropores of the membranes provide good superhighways for proton transfer. These profound advantages along with low-cost synthesis, robust proton conductivity, and easy film-forming promise the new membranes to be strong candidates as high-temperature PEMs. The technology presented in this work opens a new prospect in our mind to design the high-temperature PEMs with enhanced conductivity.

Acknowledgments

The authors gratefully acknowledge Ocean University of China for providing Seed Fund to this project, and Fundamental Research Funds for the Central Universities (201313001, 201312005), Shandong Province Outstanding Youth Scientist Foundation Plan (BS2013CL015), Doctoral Fund of Ministry of Education of China (20130132120023), Shandong Provincial Natural Science Foundation (ZR2011BQ017), Research Project for the Application Foundation in Qingdao (13-1-4-198-jch), and National Natural Science Foundation of China (U1037604).

REFERENCES

[1] Steele BCH, Heinzel A. Materials for fuel-cell technologies. Nature 2001;414:345–52.
[2] Moghaddam S, Pengwang E, Jiang YB, Garcia AR, Burnett DJ, Brinker CJ, et al. An inorganic-organic proton exchange membrane for fuel cells with a controlled nanoscale pore structure. Nat Nanotechnol 2010;5:230–6.
[3] Tang QW, Wu JH, Tang ZY, Li Y, Lin JM. High-temperature proton exchange membranes from ionic liquid absorbed/doped superabsorbents. J Mater Chem 2012;22:15836–44.
[4] Higashihara T, Matsumoto K, Ueda M. Sulfonated aromatic hydrocarbon polymers as proton exchange membrane for fuel cells. Polymer 2009;50:5341–57.
[5] Zhang F, Cui ZM, Li NW, Dai L, Zhang SB. Synthesis of sulfonated poly(arylene-co-naphthalimide)s as novel polymers for proton exchange membranes. Polymer 2008;49:3272–8.
[6] Lee SY, Ogawa A, Kanno M, Nakamoto H, Yasuda T, Watanabe M. Nonhumidified intermediate temperature fuel cells using protic ionic liquids. J Am Chem Soc 2010;132:9764–73.
[7] Lin B, Cheng S, Qiu L, Yan F, Shang S, Lu J. Protic ionic liquid-based hybrid proton conducting membranes for anhydrous proton exchange membrane application. Chem Mater 2010;22:1807–13.
[8] Noto VD, Negro E, Sanchez JY, Iojoiu C. Structure-relaxation interplay of a new nanostructured membrane based on tetraethylammonium trifluoromethanesulfonate ionic liquid and neutralized nafion 117 for high-temperature fuel cells. J Am Chem Soc 2010;132:2183–95.
[9] Kaserer S, Caldwell KM, Ramaker DE, Roth C. Analyzing the influence of H_3PO_4 as catalyst poison in high temperature PEM fuel cells using in-operando X-ray absorption spectroscopy. J Phys Chem C 2013;117:6210–7.
[10] Kamat A, Herrmann M, Ternes D, Klein O, Krewer U, Scholl S. Experimental investigations into phosphoric acid adsorption on platinum catalysts in a high temperature PEM fuel cell. Fuel Cells 2011;11:511–7.
[11] Tang QW, Qian GQ, Huang K. H_3PO_4-imbibed three-dimensional polyacrylamide/polyacrylamide hydrogel as high-temperature proton exchange membrane with excellent acid retention. RSC Adv 2012;2:10238–44.
[12] Tang QW, Qian GQ, Huang K. Hydrophobic hydrogels caged H_3PO_4 as a new class of high-temperature proton exchange membranes with enhanced acid retention. RSC Adv 2013;3:3520–5.
[13] Tang QW, Huang K, Qian GQ, Benicewicz BC. Phosphoric acid-imbibed three-dimensional polyacrylamide/poly(vinyl alcohol) hydrogel as a new class of high-temperature proton exchange membrane. J Power Sources 2013;229:36–41.
[14] Tang QW, Yuan SS, Cai HY. High-temperature proton exchange membranes from microporous polyacrylamide caged phosphoric acid. J Mater Chem A 2013;1:630–6.
[15] Tang QW, Cai HY, Yuan SS, Wang X, Yuan WQ. Enhanced proton conductivity from phorophoric acid-imbibed crosslinked 3D polyacrylamide frameworks for high-temperature proton exchange membranes. Int J Hydrogen Energy 2013;38:1016–26.
[16] Lin JM, Tang QW, Hu D, Sun XM, Li QH, Wu JH. Electric field sensitivity of conducting hydrogels with interpenetrating polymer network structure. Colloids Surf A 2009;346:177–83.
[17] Li QH, Chen HY, Lin L, Li PJ, Qin YC, Li MJ, et al. Quasi-solid-state dye-sensitized solar cell from polyaniline integrated poly(hexamethylene diisocyanate tripolymer/polyethylene glycol) gel electrolyte. J Mater Chem A 2013;1:5326–32.
[18] Li QH, Chen XX, Tang QW, Xu HT, He BL, Qin YC. Imbibition of polypyrrole into three-dimensional poly(hydroxyethyl methacrylate/glycerol) gel electrolyte for robust quasi-solid-state dye-sensitized solar cells. J Mater Chem A 2013;1:8055–60.
[19] Tang QW, Lin JM, Wu JH, Zhang CJ, Hao SC. Two-steps synthesis of a poly(acrylate-aniline) conducting hydrogel

with an interpenetrated networks structure. Carbohyd Polym 2007;67:332–6.
[20] Tang QW, Wu JH, Lin JM, Li QH, Fan SJ. Two-step synthesis of polyacrylamide/polyacrylate interpenetrating network hydrogels and its swelling/deswelling properties. J Mater Sci 2008;43:5884–90.
[21] Tang QW, Wu JH, Sun H, Lin JM, Fan SJ, Hu D. Polyaniline/polyacrylamide conducting composite hydrogel with a porous structure. Carbohyd Polym 2008;74:215–9.
[22] Tang QW, Wu JH, Sun H, Fan SJ, Hu D, Lin JM. Superabsorbent conducting hydrogel from poly(acrylamide-aniline) with thermo-sensitivity and release properties. Carbohyd Polym 2008;73:473–81.
[23] Tang QW, Wu JH, Lin JM. A multifunctional hydrogel with high conductivity, pH-responsive and release properties from polyacrylate/polyaniline hybrid. Carbohyd Polym 2008;73:315–21.
[24] Enscore DJ, Hopfenberg HB, Stannett VT. Effect of particle size on the mechanism controlling n-hexane sorption in glassy polystyrene microspheres. Polymer 1997;18:793–800.
[25] Franson NW, Peppas NA. Influence of copolymer composition on non-Fickian water transport through glassy copolymers. J Appl Polym Sci 1983;28:1299–310.
[26] Flory PJ. Principles of polymer chemistry. New York: Cornel University Press; 1953.
[27] Tang QW, Sun XM, Li QH, Lin JM, Wu JH. Preparation of porous polyacrylate/poly(ethylene glycol) interpenetrating network hydrogel and simplification of Flory theory. J Mater Sci 2009;44:3712–8.
[28] Wang W, Fernando K, Lin Y, Meziani MJ, Veca LM, Cao L, et al. Metallic single-walled carbon nanotubes for conductive nanocomposites. J Am Chem Soc 2008;130:1415–9.
[29] Lv ZB, Yu JF, Wu HW, Shang J, Wang D, Hou SC, et al. Highly efficient and completely flexible fiber-shaped dye-sensitized solar cell based on TiO_2 nanotube array. Nanoscale 2012;4:1248–53.
[30] Daeneke T, Mozer AJ, Kwon TH, Duffy NW, Holmes AB, Bach U, et al. Dye regeneration and charge recombination in dye-sensitized solar cells with ferrocene derivatives as redox mediators. Energy Environ Sci 2012;5:7090–9.
[31] Zhai Y, Zhang H, Xing D, Shao Z. The stability of Pt/C catalyst in H_3PO_4/PBI PEMFC during high temperature life test. J Power Sources 2007;164:126–33.
[32] Geormezi M, Deimede V, Gourdoupi N, Triantafyllopoulos N, Neophytides S, Kallitsis JK. Novel pyridine-based poly(ether sulfones) and their study in high temperature PEM fuel cells. Macromolecules 2008;41:9051–6.

第35卷 第6期
2015年6月

光 学 学 报
ACTA OPTICA SINICA

Vol. 35, No. 6
June, 2015

非晶硅/微晶硅叠层太阳电池中间层的研究

涂 晔[1,2] 杨 雯[1,2] 杨培志[1,2] 段良飞[1,2] 张力元[1,2] 宋肇宁[3]

[1]可再生能源材料先进技术与制备教育部重点实验室,云南 昆明 650500

[2]云南师范大学 太阳能研究所, 云南 昆明 650500

[3]托莱多大学物理与天文学系莱特光伏创新与商业化中心, 俄亥俄州, 托莱多市 43606

摘要 叠层结构是提高硅基薄膜太阳电池效率和稳定性的有效方法,其中子电池的电流匹配是提高叠层电池效率的关键,而中间层技术能有效地改善子电池电流的匹配情况。介绍了非晶硅/微晶硅叠层电池的中间反射层和隧道结的结构、特性及材料种类,结合两者的理论基础提出隧穿反射层的概念,分析其工作原理并给出了薄膜材料的选择原则和范围。隧穿反射层在叠层结构中不仅起到常规中间反射层的作用,解决电池内部的陷光问题,还可优化叠层太阳电池的隧道结,解决子电池对光生载流子的有效收集问题。

关键词 材料; 叠层太阳电池; 中间层; 隧道结; 电流匹配; 隧穿反射层

中图分类号 TN302 **文献标识码** A

doi: 10.3788/AOS201535.0616003

Research on Interlayer in "a-Si:H/μc-Si:H" Tandem Solar Cells

Tu Ye[1,2] Yang Wen[1,2] Yang Peizhi[1,2] Duan Liangfei[1,2] Zhang Liyuan[1,2] Song Zhaoning[3]

[1]*Key Laboratory of Renewable Energy Advanced Materials and Manufacturing Technology, Ministry of Education, Kunming, Yunnan* 650500, *China*

[2]*Solar Energy Research Institute, Yunnan Normal University, Kunming, Yunnan* 650500, *China*

[3]*Wright Center for photovoltaics Innovation and Commercialization, Department of Physics and Astronomy, University of Toledo, Toledo, Ohio* 43606, *USA*

Abstract Tandem structure is able to improve the efficiency and stability of silicon-based thin film solar cells. The current matching of sub cells that limiting the efficiency of the tandem devices can be effectively improved by employing an interlayer. This paper introduces the structure, properties and materials of the intermediate reflector and tunnel junction in "a-Si:H/μc-Si:H" solar cells. Based on the theoretical foundation, the concept of "tunnel recombination reflector" short for the tunnel recombination junction as a light reflector is proposed and its working principle and materials selection are discussed. In the tandem devices, such interlayer not only plays the role of intermediate reflector that enhances light-trapping, but also optimizes the tunnel junction to improve charger carrier collection.

Key words materials; tandem solar cells; interlayer; tunnel junction; current matching; tunnel recombination reflector

OCIS codes 160.4760; 160.2220; 310.1620; 350.6050

1 引 言

非晶硅/微晶硅(a-Si:H/μc-Si:H)叠层电池,简称非/微叠层电池,由不同带隙的a-Si:H顶电池与μc-Si:H底电池串联而成。这种叠层结构既能拓宽电池的光谱响应范围,提高太阳光谱的利用率,又能降低不稳定的非晶硅顶电池的厚度,抑制光致衰减(SW)效应,从而改善太阳电池的整体稳定性。然而,叠层结构并不是

收稿日期: 2014-12-03; **收到修改稿日期**: 2015-02-26

基金项目: 国家自然科学基金联合基金(U1037604)

作者简介: 涂 晔(1985—),女,博士研究生,从事硅基薄膜材料及太阳电池方面的研究。E-mail:tuye0106@163.com

导师简介: 杨培志(1966—),男,研究员,博士生导师,主要从事高效太阳能利用材料及器件方面的研究。

E-mail: pzhyang@hotmail.com(通信联系人)

子电池的简单串联，其总电池的电流取决于最小的子电池电流。IMT小组[1]于1996年提出在非/微叠层电池的子电池之间插入一层中间层，目的就是为了把一部分光反射回顶电池，以提高顶电池的光吸收，从而提高其短路电流密度。Hegedus S等[2]在1995年研究了非晶硅/非晶硅叠层电池中隧道结的电流输运机制，提高了子电池对载流子的收集。因此，为了提高顶、底电池的匹配电流，研究叠层电池子电池之间的中间层技术非常关键。本文以非晶硅/微晶硅叠层电池的中间层技术为研究对象，分别研究了中间反射层和隧道结的结构、特性及材料种类，结合两者的理论基础提出了隧穿反射层的概念，分析了其工作原理，给出了隧穿反射层薄膜材料的选择原则和范围。

2 中间层

2.1 中间反射层

2.1.1 结构与特性

非/微叠层电池的顶、底电池对可见光波段的响应范围不同，顶电池约为300~700 nm，底电池约为500~1000 nm。由于非晶硅材料存在光致衰减效应，为降低效率的衰减，顶电池本征层的厚度一般较薄，但这会使顶电池的短路电流密度(J_{sc})小于微晶硅底电池的J_{sc}，进而影响叠层电池的整体J_{sc}。因此为了提高顶电池J_{sc}，可以在顶、底电池之间插入一层中间反射层(IR)，起到选择性反射层的作用，以提高500~700 nm波段可见光的反射率，进而改善顶电池对短波光的吸收利用率。图1为具有中间反射层的双结叠层电池结构图。

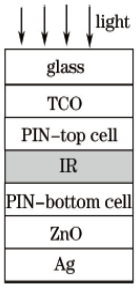

图1 具有中间反射层的双结叠层电池结构

Fig.1 Double junction tandem cells with intermediate reflector

2.1.2 材料种类

中间反射层材料主要有三类：1) 等离子体增强化学气相沉积(PECVD)法制备的硅合金薄膜，如：SiO_x、SiN_x、SiC_x、SiO_xC_y、SiO_xN_y和SiC_xN_y等，但研究较多的是N型a-SiO_x∶H和μc-SiO_x∶H；2) 物理溅射或低压力化学气相沉积(LPCVD)、金属有机化合物化学气相沉积(MOCVD)等方法制备的金属氧化物，如：ZnO、ZnO∶Al、ZnO∶Ga、SnO_2、SnO_2∶F、TiO_2∶Nb等，或者化学法结合原子层沉积制备的ZnO∶Al反蛋白石；3) 金属纳米材料，如：Au、Ag纳米颗粒。

IMT选择了ZnO作为中间反射层材料，研究了不同厚度的ZnO对叠层电池I-V特性的影响，并得出ZnO厚度应小于100 nm的结论[3]；J Krc等[4]分别对50 nm厚的ZnO和n&k_MgF_2(折射率n和消光系数k变化的MgF_2)，以及25/5/25 nm厚的ZnO/N-a-Si∶H/ZnO作为中间反射层进行了研究，其中采用ZnO时子电池的匹配电流最大；C Das等[5-8]选择的中间反射层材料是μc-SiO_x∶H，其制备工艺与叠层电池顶、底电池的制备相兼容，通过改变制备气体的比值可调控材料的光、电性能；J Üpping等[9]基于ZnO∶Al反蛋白石材料，研究了三维光子晶体作为中间反射层的应用，据称此三维材料的中间反射层效果是其他类型材料的2.25倍。Kaneka公司研发了一种在600 nm处的折射率为1.7的新材料，获得了良好的中间反射层效果，由此制备的面积为1 cm^2的叠层电池的初始效率高达15%，但具体的材料及厚度等参数未见报道。

2.2 隧道结

2.2.1 结构与特性

为了提高顶、底电池电流匹配，除了在子电池交界处插入一层中间反射层之外，还研究了子电池交界处的界面特性，并将此界面称为隧道结或隧穿复合结(TRJ)，如图2所示。在硅薄膜叠层太阳电池$P_1I_1N_1/P_2I_2N_2$

结构中，隧道结N_1/P_2特性的好坏对电池性能参数V_{oc}、I_{sc}、F_F均有重要影响，隧道结N_1/P_2相对电池内建电场E_1、E_2为反偏结，任何寄生势垒都将使电池的电流电压特性变差。而且，若子电池电流不相等，在N_1/P_2隧道结处的电子和空穴不能完全复合，则多余的载流子就会在结处积累，削减子电池的电场，进而影响硅基薄膜叠层太阳电池的性能。因此，为提高叠层太阳电池的效率，子电池之间需要采用性能良好的隧道结。

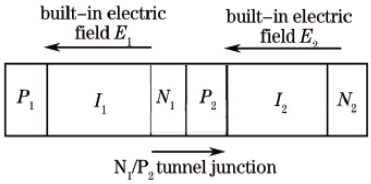

图2 PIN型硅基叠层电池的N_1/P_2隧道结结构

Fig.2 N_1/P_2 tunnel junction in PIN silicon-based tandem cells

2.2.2 材料种类

为了降低子电池相邻界面处的寄生势垒，分别对NP隧道结进行了N层、P层厚度调节，以及插入N型或P型非晶硅、非晶硅碳、微晶硅或纳米晶硅的研究。

1) N型硅薄膜及合金

对于柔性衬底上的N-I-P型非/微叠层电池，R L Stolk等[11]在N型和P型微晶硅之间的隧道结处插入5 nm厚的N型非晶硅层，以减少或阻止顶电池沉积时氢扩散对微晶硅底电池的破坏。Li G J等[12-13]提出双N层隧道结的概念，即对顶电池的N型层采用了3 nm厚的非晶硅与23 nm厚的微晶硅的组合，减少了顶电池的漏电，进而提高了叠层电池的开路电压和填充因子。Amornrat L等[14]在非晶硅氧/微晶硅(a-SiO∶H/μc-Si∶H)叠层电池隧道结处插入一层N型微晶硅氧(μc-SiO∶H)层，研究表明改良后的隧道结可提高叠层电池的填充因子(FF)。

2) P型硅薄膜及合金

N. Palit等[15]通过对隧道结处不同P层材料(分别为μc-Si:H和a-SiC:H)中的自由空穴的运动机理的研究，得出除了隧穿运动、电场作用外，扩散运动起主要作用并使光生空穴朝隧道复合结处移动的结论。提出隧道结处的P型层需具有高的自由空穴密度，以提高电池的FF。Hegedus S等[2]从*I*-*V*特性、温度、量子效率等方面研究了基于非晶硅的N/P隧道结的电流输运机制。在N型层和P型层之间插入一层P型掺硼非晶硅，并将隧道结的非晶硅层用微晶硅层取代，能降低电阻率增加载流子在结处的复合率。Lanli Chen等[16]研究了叠层电池中高质量的N-P$^+$-P(a-Si/na-Si/μc-Si)隧道结，认为隧道结处插入P$^+$-na-Si层后的缺陷态密度能达到2.7×10^{19} cm^{-3}，比插入P$^+$-a-Si层获得的复合几率高，且阻抗值低。Ping-Kuan Chang等[17]研究了非晶硅/非晶硅叠层电池的隧道结，结构为：N-P-P(μc-Si∶H/μc-Si∶H/a-SiC∶H)，通过调整顶、底电池本征层的厚度(60 nm和250 nm)，得到最优的非/非叠层电池的初始转换效率为10.29%。

3 新型隧穿反射层的提出

3.1 基于良好光学特性的中间反射层

电池的光电转换过程中还存在光的反射和透射损失，因此需要寻求好的光管理设计方案。虽然目前已提出很多方法来尽量降低这些损失，如各类陷光结构和绒面材料，以及背反射电极等，但这些技术与结构还有很大的发展空间。中间反射层是电池内部陷光的一个关键层，不仅起到承上启下的作用，还有利于抑制光致衰减。中间反射层的插入可提高硅基薄膜叠层电池界面处短波段光的反射率，在对底电池光谱响应范围影响不大的情况下，可增大非晶硅顶电池的短路电流密度，从而提高子电池的电流匹配度，进而增加电池的整体转换效率。图3为叠层电池插入中间反射层后子电池交界处的光线传输分布。

顶电池非晶硅的带隙(E_g)大于底电池微晶硅的带隙，因此从可见光光谱分布来看，顶电池主要吸收短波长光，而底电池主要吸收长波长光；同时，由于非晶硅和微晶硅的折射率相近，分别约为3.1和3.3，使子电池界面处可见光的反射率较低。基于这两点，中间反射层材料必须具有一定的折射率和厚度，即必须满足对对短波段光(500~700 nm)反射率高，对长波段光(700~1000 nm)透射率高的特性。本课题组[18]对叠层电池中间反射层的光学性能做了一定的研究，模拟计算表明中间反射层的反射率与各层折射率有着密切相关的联系；

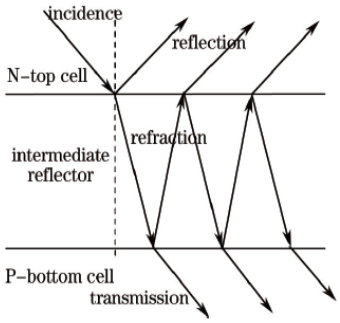

图3 叠层电池中间反射层界面处的光线传输分布

Fig.3 Light transmission distribution at the interface of intermediate reflector in tandem cells

$$R=\frac{n^2(n_t-n_b)^2\cos^2\frac{\delta}{2}+(n^2-n_tn_b)^2\sin^2\frac{\delta}{2}}{n^2(n_t+n_b)^2\cos^2\frac{\delta}{2}+(n^2+n_tn_b)^2\sin^2\frac{\delta}{2}},\tag{1}$$

式中R为中间反射层处的反射率，n、n_t、n_b分别为中间反射层、顶电池N层以及底电池P层的折射率，δ为顶电池N层与中间反射层交界处可见光的入射角。

由(1)式推导计算出$R_{max}=\left(\frac{n^2-n_tn_b}{n^2+n_tn_b}\right)^2$，理论上当$n\ll\sqrt{n_tn_b}$时，$R_{max}$能趋近于100%，但$R_{max}$过大势必会影响底电池对长波光的吸收。经计算得出中间反射层材料的折射率n约为1.59，厚度约为150/n即94.3 nm时，对波长为500~700 nm可见光的R_{max}可达到35.96%。

3.2 基于良好电学性能的隧道结

叠层电池中，隧道结是一个与子电池内建电场方向相反的PN结，在工作状态下，本征层内的光生电子和光生空穴会在内建电场的作用下分别向N层和P层移动。对于PIN型非/微叠层电池来说，非晶硅顶电池的光生电子和微晶硅底电池的光生空穴必须在隧道结处快速复合，以免电荷积累而削弱内建电场，减少顶、底电池对光生载流子的收集，进而降低电池的匹配电流。图4为叠层电池隧道结的工作原理。

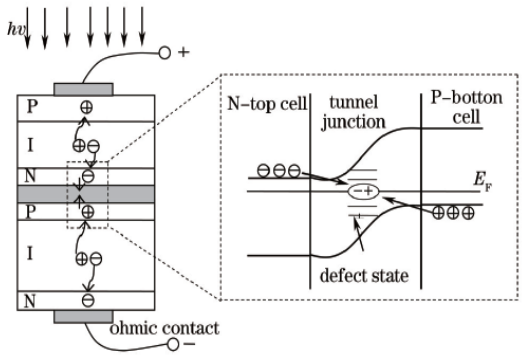

图4 隧道结的工作原理

Fig.4 Working principle of tunnel junction

由图4可知，光生电子和光生空穴分别从N层和P层隧穿到同一个缺陷态，发生隧穿复合，复合速率U_N为

$$U_N=N_tr_nn_ue^{-\frac{2}{h}\sqrt{2m(U_0-E)}d},\tag{2}$$

式中N_t为缺陷态密度，r_n为电子俘获系数，n_u为由顶电池N层向隧道结移动的光生电子数，U_0与d分别为势垒高度与宽度，E为电子动能。不同材料的N_t、U_0与d均不同，但由(2)式可知，复合速率U_N的影响因素主要来自于缺陷态密度N_t。因此，只要缺陷态密度足够高，光生载流子就会在隧道结处完全复合，不产生寄生势垒，也不会对子电池的电场产生影响。

综上所述，研究隧道结技术的重点就是如何提高结界面处的复合速率，目前行之有效方法就是在结界面处生长一层重掺杂的硅合金薄膜或高缺陷态的氧化物，例如NbO_x、TiO_x、SiO_x等。

3.3 兼具良好光学性能与电学性能的隧穿反射层

3.3.1 隧穿反射层的工作原理

目前，对叠层结构所引入的中间反射层和隧道结的研究尚是独立的，具有选择性反射作用的中间反射层是基于光学的反射与透射原理，具有较大缺陷态密度的隧道结是基于电学的隧穿复合理论，其研究成果难以大幅提高叠层太阳电池的性能。

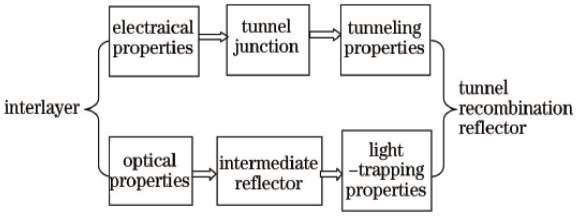

图5 隧穿反射层的提出

Fig.5 Proposing the tunnel recombination reflector

如图5所示，综合考虑叠层结构的子电池界面对整个电池的光学性能和电学性能的影响，结合中间反射层的作用与隧道结的原理，在子电池界面处制备一层既具有选择性反射作用，又具有高缺陷态密度的薄膜，称此兼具陷光性能和隧穿性能的薄膜为隧穿反射层(TRR)，以改善硅基薄膜叠层太阳电池的电流匹配度，降低光学损失与电学损失，提高电池效率和稳定性。图6为隧穿反射层的工作原理。

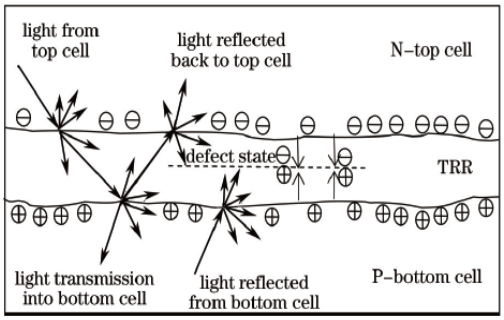

图6 隧穿反射层的工作原理

Fig.6 Working principle of tunnel recombination reflector

由图6可看出TRR兼具了中间反射层的光学优点和隧道结的电学性能，一方面起到选择性反射的作用，解决叠层电池内部的陷光问题，另一方面优化了叠层太阳电池的隧道结，解决顶、底电池内部对光生载流子的有效收集问题。隧穿反射层具有宽带隙、高电导率、低折射率、高缺陷态密度等特点，能有效地提高硅基薄膜叠层太阳电池的转换效率和稳定性。

3.3.2 隧穿反射层材料的选择原则

鉴于中间反射层的折射率须尽量靠近1.59，且具备足够高的电导率和宽带隙，同时隧道结必须具备高的缺陷态密度，因此，低折射率、高电导率、宽带隙、高缺陷态密度等要求成为隧穿反射层材料的选择原则。

1) 硅基薄膜合金

非晶硅薄膜材料可以与锗(Ge)、碳(C)和氧(O)等元素形成合金来调节其光学与电学性能。

非晶硅锗(a-SiGe:H)合金材料具有较窄的带隙，通过改变Ge含量，可实现a-SiGe∶H合金的带隙在1.1~1.7 eV之间进行调控，其带隙随锗含量增加而降低，a-SiGe∶H合金的带隙过窄不符合隧穿反射层的选择原则。非晶硅碳(a-SiC∶H)合金薄膜材料具有较宽的带隙，通过改变C含量可实现a-SiC∶H合金薄膜的带隙在1.7~2.2 eV之间变化，且a-SiC∶H合金材料缺陷态密度较高，适宜做隧道结材料，但其折射率通常在2.6以上，不符合隧穿反射层对低折射率的要求。

非晶硅氧(a-SiO∶H)合金材料也是一种宽带隙薄膜材料，通过改变O含量还可以对a-SiO∶H合金薄膜带隙进行调控。相应的SiO及SiO_2材料的折射率在1.46~1.55之间，属低折射率材料，改变O含量也可以调节SiO_x薄膜的折射率。此外，随着氧含量的增加，缺陷态会增加一个数量级(由于O为二配位，Si为四配位，配位

数的差异造成悬挂键增加)。然而,O增加也会导致光电导率下降,故须对薄膜进行金属掺杂。经金属掺杂后的a-SiO:H或SiO_x薄膜,由于其电导率大大提升,且缺陷态密度高,同时还属于宽带隙及低折射率材料,非常适宜于用作隧穿反射层。图7为硅氧薄膜掺杂后的二维(2D)网络结构。

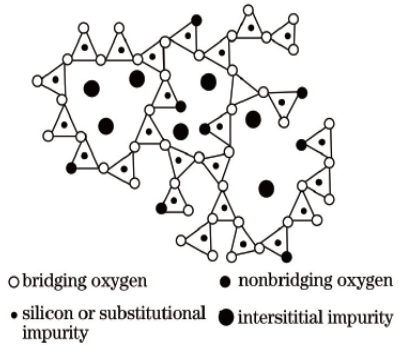

图7 掺杂后的硅氧薄膜二维网络结构

Fig.7 2D network structure of doped SiO_x thin film

由上图可知,非桥键氧原子和键不饱和的硅原子会带入悬挂键,掺杂后的间隙式杂质与替位式杂质会引入大量的缺陷。由于金属杂质铝在硅氧网络中,既可以起间隙式杂质,又可以起替位式杂质的作用,用铝掺杂较其他杂质能更有效地提高硅氧薄膜的缺陷态密度,且氧化硅与氧化铝混合物的折射率大概在1.65左右。因此,掺铝的硅氧薄膜将会是非常好的隧穿反射层材料。

2) 金属化合物

NbO_x、TiO_x等金属氧化物非常适宜做隧道结材料,因其具有高缺陷态密度,但两者的折射率过高,NbO_x的折射率大于2.3,TiO_x的折射率大于2.5,均不符合隧穿反射层对低折射率的要求;金属氧化物ZnO及AZO(ZnO:Al)因透明、导电、折射率适中(约为2.0)而成为中间反射层材料的研究热门,但由于其具有横向分流的电学特性,会对叠层电池性能造成一定的影响;其他透明导电膜(TCO)薄膜,如掺杂的SnO_2:F(FTO)、SnO_2:Sb(ATO)和In_2O_3:Sn(ITO)等,均为重掺杂材料,不仅带隙宽,而且具有高电导率,光电性质随掺杂金属的氧化状态及浓度可调,是很好的隧道结材料,但是其折射率均在2.2以上,不太符合隧穿反射层材料的选择要求;其他金属化合物,如MgF_2和LiF等材料折射率均小于1.4,CaF_2折射率在1.5左右,重金属(如:Cu、Ag、Au等)掺杂能改善其导电性,增加缺陷密度,但随掺杂浓度的增加会使带隙一定程度上变窄,折射率变大,且材料具有一定的毒性。若使用恰当,并调整好平衡掺杂浓度,MgF_2、LiF和CaF_2等金属氟化物将会是很有潜力的隧穿反射层材料。

4 结 论

通过以上总结可知,研究子电池之间的中间层技术,即研究中间反射层及隧道结对提高顶、底电池的匹配电流,提高叠层电池的整体转换效率非常关键。目前,对叠层结构的上述两方面研究尚独立进行:具有选择性反射作用的中间层是基于光学的反射与透射原理;而具有较大缺陷态密度的隧道结是基于电学的隧穿复合理论,其研究成果难以大幅提高叠层太阳电池的性能。对叠层电池的子电池交界处的中间层进行了细致的研究,主要包括以下三个方面:1) 基于光学性能的中间反射层;2) 基于电学性能的隧道结;3) 结合光学性能和电学性能的新型隧穿反射层。隧穿反射层材料的选择原则为低折射率、高电导率、宽带隙、高缺陷态密度等。在硅薄膜合金和金属化合物薄膜材料中,掺杂的硅氧薄膜与金属氟化物将有潜力成为隧穿反射层材料。

参 考 文 献

1 Fisher D, Dubail S, Selvssssan J A A, *et al*.. The "micromorph" solar cell: extending a-Si:H technology towards thin film crystalline silicon[C]. Proceedings of 25th IEEE Photovoltaic Specialists Conference, Washington DC, 1996: 1053-1056.

2 Hegedus S, Kampas F, Xi Jianping. Current transport in amorphous silicon n/p junctions and their application as "tunnel" junction in tandem solar cells[J]. Applied Physics Letters, 1995, 67(6): 813-815.

3 Domine D, Bailat J, Steinhauser J, *et al*.. Micromorph solar cell optimization using a ZnO layer as intermediate reflector[C]. Proceedings of 2006 IEEE 4th World Conference on Photovoltaic Energy Conversion, Hawaii, 2006: 1456-1468.

4 J Krc, K Brecl, F Smole, et al.. The effects of enhanced light trapping in tandem micromorph silicon solar cells[J]. Solar Energy Materials & Solar Cells, 2006, 90(18): 3339-3344.

5 C Das, A. Lambertz, J. Huepkes, *et al*.. A constructive combination of antireflection and intermediate reflector layers for a-Si/μc-Si thin film solar cells[J]. Applied Physics Letters, 2008, 92(5): 053509.

6 V Smirnov, A Lambertz, B Grootoonk, *et al*.. Microcrystalline silicon oxide (μc-SiOx∶H) alloys: a versatile material for application in thin film silicon single and tandem junction solar cells[J]. Journal of Non-crystalline Solids, 2012, 358(17): 1954-1957.

7 A. Lambertz, V. Smirnov, T. Merdzhanova, *et al*.. Microcrystalline silicon-oxygen alloys for application in silicon solar cells and modules[J]. Solar Energy Materials & Solar Cells, 2013, 119: 134-143.

8 Lisha Bai, Bofei Liu, Xiaodan Zhang, *et al*.. The trade-off light trapping between top and bottom cell in micromorph tandem solar cells with sputtering ZnO∶Al glass substrate[J]. Journal of Power Sources, 2014, 266(15): 138-144.

9 J üpping, A Bielawny, Ralf B Wehrspohn, *et al*.. Three-dimensional photonic crystal intermediate reflectors for enhanced light-trapping in tandem solar cells[J]. Advanced Materials, 2011, 23(34): 3896-3900.

10 Yamamoto K, Nakajima A, Yoshimi M, *el al*.. High efficiency thin film silicon hybrid cell and module with newly developed innovative interlayer[C]. Proceedings of 2006 IEEE 4th World Conference on Photovoltaic Energy Conversion, Hawaii, 2006: 1489-1492.

11 R L Stolk, H Li, C H M van der Werf, *et al*.. Improvement of the tunnel-recombination junction in N-I-P micromorph tandem silicon solar cells with hot-wire deposited absorber layers[C]. 19th European Photovoltaic Solar Energy Conference, Paris, 2, 2004: 1.

12 Li G J, Hou G F, Han X Y, *et al*.. The study of a new n/p tunnel recombination junction and its application in a-Si∶H/μc-Si∶H tandem solar cells[J]. Chinese Physics B, 2009, 18(4): 1674-1678.

13 Hou Guofu, Lu Peng, Han Xiaoyan, *et al*.. Improving the light-soaking stability of a-Si:H/μc-Si:H tandem solar cells[J]. Acta Phys Sin, 2012, 61(13): 138401.
侯国付, 卢 鹏, 韩晓艳, 等. 提高非晶硅/微晶硅叠层太阳电池光稳定性的研究[J]. 物理学报, 2012, 61(13): 138401.

14 Amornrat L, Songkiate K, Sorapong I, *et al*.. Advantages of N-Type hydrogenated microcrystalline silicon oxide films for micromorph silicon solar cells[J]. International Journal of Photoenergy, 2013, 2013(06): 513284.

15 N Palit, A Dasgupta, S Ray, *et al*.. Hole diffusion at the recombination junction of thin film tandem solar cells and its effect on the illuminated current-voltage characteristic[J]. Journal of Applied Physics, 2000, 88(5): 2853-2861.

16 Lanli Chen, Mingji Shi, Jiahui Yu. Good quality n(a-Si)-p^{+}(na-Si)-p(uc-Si) tunnel junction for tandem solar cells[J]. Solid State Phenomena, 2012, 181-182: 336-339.

17 Pingkuan Chang, Chunhsiung Lu, Chihhung Yeh, *et al*.. High efficiency a-Si:H/a-Si∶H solar cell with a tunnel recombination junction and a n-type μc-Si∶H layer[J].Thin Solid Films, 2012, 520(9): 3684-3687.

18 Tu Ye, Yang Wen, Yang Peizhi, *et al*.. Optical design and calculation of interlayer in thin film silicon tandem solar cells[J]. Acta Optica Sinica, 2014, 34(6): 0622006.
涂 晔, 杨 雯, 杨培志, 等. 硅基薄膜叠层太阳能电池中间层的光学设计与计算[J]. 光学学报, 2014, 34(6): 0622006.

栏目编辑: 韩 峰

文章编号:1001-9731(2015)增刊(Ⅰ)-0001-04

Sn 基Ⅷ型笼合物 $Ba_8Ga_{16}Sn_{30}$ 热电材料研究进展*

申兰先,刘祖明,邓书康,孟代仪,晒旭霞

(云南师范大学 可再生能源材料先进技术与制备教育部重点实验室,
云南省农村能源工程重点实验室,太阳能研究所,昆明 650500)

摘 要: Ⅷ型 Sn 基笼合物 $Ba_8Ga_{16}Sn_{30}$由于具有优异的热电传输特性而被认为是最具有应用前景的热电材料之一。介绍了Ⅷ型 Sn 基笼合物的晶体结构、合成方法及理论和实验方面的研究情况,并对有关研究进展进行评述,同时提出进一步研究该笼合物的一些建议。

关键词: Sn 基笼合物;Ⅷ型笼合物;热电材料;热电性能

中图分类号: TN383 文献标识码:A

DOI:10.3969/j.issn.1001-9731.2015.增刊(Ⅰ).001

1 引 言

能源短缺与环境污染已成为当前至关重要的问题,因此寻求及有效地利用化石燃料之外的清洁能源成为当今世界各国的焦点。温差发电技术是利用半导体热电材料的塞贝克(Seebeck)效应直接将热能转换为电能的技术,具有体积小、成本低、寿命长、环境友好等特点,因此被认为是最具有应用前景的清洁能源转换技术之一。热电材料的热电性能用无量纲性能指数 ZT 描述,即

$$ZT = \frac{\alpha^2 \sigma T}{\kappa}$$

其中,α、σ 和 κ 分别为材料的 Seebeck 系数、电导率和热导率,T 为绝对温度。在相同的温差下,ZT 值越大,材料及相应器件的热电转换效率就越高,因此高性能热电材料必须同时具有较高的功率因子 $P(P=\alpha^2\sigma)$和较低的热导率 κ。

自从 Slack 提出“声子玻璃-电子晶体”(PGEC)概念以来,人们就一直致力于寻找具有这种性质的热电材料。具有“笼子”状结构的笼合物正是具有这种性质的热电材料[1-8],即具有像玻璃那样低的热导率和晶体一样高的电性能。研究表明,笼合物具有较低的热导率主要是由于其结构中包含有类似于笼子的空洞,而填充原子的半径小于空洞半径,填充原子与框架原子的耦合较弱,其容易在空洞中“扰动”,这种扰动能强烈散射传热声子,从而降低其热导率,同时对载流子的输运没有显著影响。目前对笼合物的研究主要集中在 Si 基、Ge 基和 Sn 基笼合物方面,而且由于 Sn 与 Ge、Si 相比原子较重,并且 Sn 为主体原子组成的笼子尺寸较大,因而具有更低的热导率,进而 Sn 基笼合物热电材料成为研究的热点[9-12]。Sn 基笼合物具有Ⅰ型和Ⅷ型两种结构,其中Ⅷ型 Sn 基笼合物由于具有优异的热电传输特性而被认为最具有应用前景的热电材料之一。本文重点介绍 Sn 基Ⅷ型笼合物的晶体结构及其热电传输特性,对其研究进展进行评述。

2 Ⅷ型笼合物热电材料晶体结构

笼合物是一类由原子或分子组成的具有开放式、“笼子”形状框架结构,其由框架原子构成的空洞内可填充孤立原子(如碱金属或碱土金属)的化合物。根据笼合物中多面体空洞形状的不同,笼合物可分为不同的类型,其中研究较多的有Ⅰ型笼合物和Ⅷ型笼合物,一般通式为 M_xX_{46}(其中 M 为碱金属或碱土金属),当 X 为 Ge、Si、或 Sn 时则形成 Ge 基、Si 基或 Sn 基笼合物,Ⅲ族原子可以部分置换框架原子形成 $A_8^{Ⅱ}B_{16}^{Ⅲ}B_{30}^{Ⅳ}$。Ⅷ型 $Ba_8Ga_{16}Sn_{30}$笼合物属于简单立方结构,空间群为 $I\bar{4}3m$。图 1[13] 所示为Ⅷ型 Sn 基笼合物的晶体结构图,晶胞包含 8 个扭曲的十二面体,框架由第Ⅲ族元素 Ga 和第Ⅳ族元素 Sn 通过 sp^3 轨道杂化构成,Ba 原子填充在由 23 个框架原子构成的 8 个多面体空洞内,相邻的两个多面体之间由 8 个框架原子构成的多面体相连。该笼合物中填充原子只有一种占位,占据空洞中的8c 位置,热振动参数(各向异性位移参量)为 0.000459 nm^2;框架原子有 4 种占位,分别为 2a、8c、12d 和 24g,热振动参数分别为 0.00013,0.000115,0.000152和 0.000129 nm^2[14],另有文献表明,对Ⅷ-$Ba_8Ga_{16}Sn_{30}$笼合物,框架上 12d 和 8c 位置各有 8 个 Ga 原子且化合物中无 Ga—Ga 键为其最低能量构型[15]。Ⅷ-$Ba_8Ga_{16}Sn_{30}$笼合物属间接带隙材料,禁带宽度为 0.32 eV[16],价带由框架原子 Ga 和 Sn 的原子轨道构成,导带由 Ga、Sn 和填充原子 Ba 的原子轨道构成。

最近,孟等[17] 采用 Sn 自熔剂法制备的 Mg 掺杂Ⅷ型 Sn 基单晶笼合物 $Ba_8Ga_{16-x}Mg_xSn_{30}$($x=0,0.5,1.0,1.25$ 和 1.5),结果发现,随 Mg 掺杂量的增加,对应化

* 基金项目:国家自然科学基金资助项目(51262032)
收到初稿日期:2014-09-27 收到修改稿日期:2015-03-20 通讯作者:邓书康,E-mail:skdeng@126.com
作者简介:申兰先 (1978-),女,云南镇雄人,在读博士,助理研究员,主要从事新能源材料研究。

合物的熔点略有升高，晶格常数减小，掺杂样品中填充原子 Ba 的实际含量低于理想值 8.0，其在十二面体空洞中的占有率约为 0.93（Mg 的名义含量 $x=1.5$ 时），而 Mg 的实际含量也较低。可以推断 Mg 掺杂后晶格常数的减小主要是由于 Ba 的含量低于 8.0，从而致使部分空洞未被填充而导致“笼子”尺寸收缩。

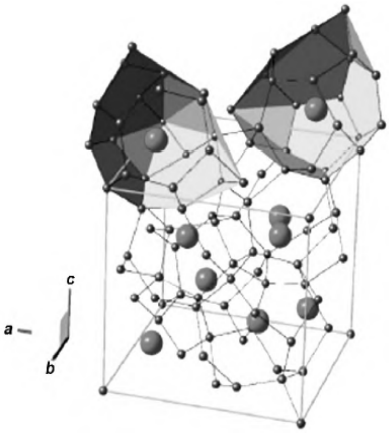

图 1 Ⅷ型笼合物 $Ba_8Ga_{16}Sn_{30}$ 的结构图

Fig 1 Structural diagram of type-Ⅷ clathrates $Ba_8Ga_{16}Sn_{30}$

3 Ⅷ型 Sn 基笼合物合成方法

目前，Ⅷ型 Sn 基笼合物仅有 $Ba_8Ga_{16}Sn_{30}$ 化合物，该化合物的电传导类型可通过框架 Ga、Sn 原子比例进行调制，微调 Ga/Sn 原子比使之偏离理想值 16/30，Ga 过量时表现为 p 型传导，Sn 过量时表现为 n 型传导[18]。因此对应的具有 p 型传导的Ⅷ型 Sn 基笼合物采用 Ga 自熔剂法，具有 n 型传导的采用 Sn 自熔剂法。2005 年，Huo 等[13]首次通过 Ga、Sn 自溶剂法分别制备了 p 型和 n 型单晶Ⅷ型 $Ba_8Ga_{16}Sn_{30}$ 化合物，2008 年，Suekuni 等[19]通过差热分析和粉末 XRD 研究了该笼合物的熔点，研究表明该化合物的熔点为（520 ± 3）℃。与 Ga、Sn 自溶剂法合成该笼合物的合成温度相当，具体合成过程为采用高纯单质元素 Ba、Ga、Sn，按化学计量比称量（Ga 过量或 Sn 过量）混合后置于石英管中真空密封，将石英管放入箱式高温炉内，经 3 h 缓慢加热到 763 K 后恒温 10 h，然后经 50 h 缓慢降温至 663 K，随后将石英管取出并采用离心分离技术将剩余熔态的 Ga 或 Sn 分离即得到单晶材料。Kuznetsov 等[20]采用直接熔融法合成了 $Ba_8Ga_{16}Sn_{30}$ 多晶化合物，具体方法为在氩气保护下，高纯单质元素按化学计量混合后置于内壁涂有石墨层的氧化铝坩埚中，然后再将坩埚放入石英管内；样品在炉内以 5 K/min 的速率缓慢加热到高于该化合物的熔点 30 ~ 100 K，在此温度恒温 2 ~ 3 h，然后取出样品于空气中冷却，为了确保样品的均匀化，把样品放入氩保护气氛的内壁涂石墨层的石英管中，在低于熔点温度 100 ~ 150 K 热处理 150 ~ 720 h。

4 Ⅷ型 Sn 基笼合物热电传输特性

4.1 Ⅷ型 Sn 基笼合物理论研究

近几年，国内外研究者对Ⅷ型 Sn 基笼合物热电材料的理论进行了大量研究，获得了一些重要的研究结果。Kono 等[16]采用密度泛函理论对Ⅷ型 $Ba_8Ga_{16}Sn_{30}$ 的电子结构计算表明，p、n 型获得高 ZT 值的适合的载流子浓度约为 $10^{20}/cm^3$，而实际合成的材料载流子浓度约为 $10^{19}/cm^3$，通过对该材料的载流子浓度进行优化，材料的 ZT 有望大于 1.0。之后该课题组[21]采用 WIEN2k 计算 Sb 掺杂Ⅷ型 $Ba_8Ga_{16}Sn_{30}$ 的电子结构和热电性能，发现掺杂后材料带隙变宽和有效质量均增大，说明 Sb 掺杂提供可调空穴浓度从而达到最优载流子浓度范围，此外掺杂的 p 型和 n 型材料的 Seebeck 系数和未掺杂的差不多，掺杂后材料的 ZT 值 > 1。Li 等[22]对该化合物的第一性原理计算表明费米能级附近能带结构较复杂，态密度的峰值出现在基本带隙中，这是填充原子 Ba 和框架原子 Sn、Ga 的成键轨道杂化所致。

据文献[14]报道，$Eu_8Ga_{16}Ge_{30}$ 笼合物具有Ⅰ型结构和Ⅷ型结构，在温度 696 ℃时，Ⅷ型结构向Ⅰ型结构发生固-固相结构转变。对于 Sn 基 $Ba_8Ga_{16}Sn_{30}$ 笼合物结构方面的研究，早在 1986 年 Eisenmann 等[23]就报道了 $Ba_8Ga_{16}Sn_{30}$ 笼合物具有两种结构。2000 年，Kuznetsov 等[20]采用直接熔融法合成多晶样品 $Ba_8Ga_{16}Sn_{30}$ 笼合物，结果表明该笼合物晶格常数与之前报道的数据相差较大，并认为其可能的原因是此笼合物存在两种结构或是化合物形成时的非均匀反应造成；另外，合成的多晶化合物与Ⅰ型笼合物相比具有较高的 Seebeck 系数（室温下为 −185 μV/K）和较低的载流子浓度（室温下为 2.2×10^{19} cm^{-3}）。最近的研究表明，对于 Sn 基单晶笼合物 $Ba_8Ga_{16}Sn_{30}$，在相同的起始原料化学计量比下，不同的反应温度可以得到不同结构的 Sn 基笼合物。在较高的温度下（900 ℃）反应得到具有Ⅰ型结构（β 相）的 $Ba_8Ga_{16}Sn_{30}$ 笼合物，在较低的温度下（490 ℃）反应得到具有Ⅷ型结构（α 相）的 $Ba_8Ga_{16}Sn_{30}$ 笼合物[19]。为了探索该笼合物两种不同结构稳定存在的温度范围，Saiga 等[24]采用 Ga、Sn 双自熔剂和 Sn 自熔剂分别制得具有 p 型和 n 型的Ⅰ型 Sn 基 $Ba_8Ga_{16}Sn_{30}$ 笼合物，并研究其高温结构稳定性，结果表明样品从 300 ~ 600 K 加热过程和从 600 ~ 300 K冷却过程中，其电阻率随温度的变化不可逆，因此其猜测样品在高温下可能存在结构转变。为了进一步证实其猜想，将样品加热到 600 K 再冷却到室温后对其进行 XRD 分析，结果发现样品衍射峰完全为典型的Ⅷ型结构衍射峰，而且这种Ⅰ型到Ⅷ的转变是不可逆的，即样品从 600 ~ 300 K 的降温过程中没有发生Ⅷ

型到Ⅰ型的转变。为了更进一步确定样品结构转变的温度,Du 等[25]对该笼合物 α↔β 结构相转变进行了详细的探索,对具有Ⅰ型结构的 Sn 基笼合物加热过程中相转变通过差热(DTA)和原位粉末 X 射线衍射(PXRD)分析,结果表明加热温度低于 466 ℃时仍为Ⅰ型结构,当温度高于 466 ℃时,Ⅰ型结构转变为Ⅷ结构,受体系热动力学支配Ⅷ结构稳定存在于 466 ~ 500 ℃之间,这与之前报道的 $Eu_8Ga_{16}Ge_{30}$ 笼合物高温是 β 相相反。此外,当温度升到 910 ℃时,降温过程中在约 570 ℃出现 $Ba(Ga/Sn)_4$ 晶核的微弱峰,且样品的最终结构是 β 相结构,与初始样品是 α 相还是 β 相无关,只与熔融状态的化学成分和温度有关。这与文献[9]的实验结果基本一致。Li 等[15]通过密度泛函理论研究了静压对Ⅷ型 $Ba_8Ga_{16}Sn_{30}$ 的结构和电子结构的影响,研究表明该化合物是稳定相,随着压强的增加稳定性变差,在体积膨胀时,Ⅷ型有向Ⅰ型转变的趋势;电子结构计算表明,该化合物是间接带隙半导体,带隙值为 0.19 eV,且带隙随着压强的增大而增大,压强对该化合物的带边结构的位置没有显著的影响。这表明压力调节能改变该笼合物的带隙和带边结构,从而可以通过压力调节来优化材料的热电性能。

4.2 Ⅷ型 Sn 基笼合物实验研究

研究表明[26],Ⅷ型 $Ba_8Ga_{16}Sn_{30}$ 化合物在 150 ~ 300 K 温度范围内表现为半导体传导特性且具有较低的热导率。Huo 等[13]通过 Sn 自溶剂方法制备了单晶Ⅷ型 $Ba_8Ga_{16}Sn_{30}$ 化合物并对其高温热电传输特性进行了研究。研究表明单晶Ⅷ型 $Ba_8Ga_{16}Sn_{30}$ 化合物表现为 n 型传导,电导率和 Seebeck 系数随温度的变化表现为典型的重掺杂半导体性质,且 Seebeck 系数随温度的增加而单调增加,由于较低的载流子浓度(室温载流子浓度为 3.7×10^{19} cm^{-3}),从而导致较高的 Seebeck 系数,在 550 K 处 Seebeck 系数高达 243 μV/K。在低温区域载流子散射以杂质电离散射机制为主,随温度的升高逐渐过渡为以声学波散射为主。在 150 K 处热导率为 1.1 W/(m·K)。Saiga 等[18]合成了 Sb 掺杂Ⅷ型 $Ba_8Ga_{16}Sn_{30}$,结果表明对 p、n 型样品掺杂后载流子浓度均增加,且 p 型样品功率因子得到改善,得出的结论与 Kono 等[16]的理论预测相符。Sb 掺杂后所制备的 n 型和 p 型 $Ba_8Ga_{16}Sn_{30}$ Ⅷ型单晶笼合物的最大 ZT 值在 $T=450$ K 附近分别为 0.90 和 0.88。为了得到更高 ZT 值的热电材料,在Ⅷ型 Sn 基笼合物中,Deng 等[27]通过 Al 掺杂,采用 Sn 自熔剂法制备了具有 n 型传导的单晶笼合物 $Ba_8Ga_{16-x}Al_xSn_{30}$,在载流子浓度变化不大的情况下,材料的电导率显著提高,在 500 K 时样品 $Ba_8Ga_{10}Al_6Sn_{30}$ 获得最大 ZT 值 1.2。用同样的方法采用 Cu 掺杂制备的具有 n 型传导的 $Ba_8Ga_{16-x}Cu_xSn_{30}$ 单晶笼合物,在 540 K 时样品 $Ba_8Ga_{15.967}Cu_{0.033}Sn_{30}$ 获得最大 ZT 值 1.35[28]。最近,孟等[29]采用 Sn 自熔剂法制备了 Ge 掺杂Ⅷ型 Sn 基单晶笼合物 $Ba_8Ga_{16-x}Ge_xSn_{30}$ $(0\leqslant x\leqslant1.0)$,通过估算样品热导率后,在 $x=0.5$ 时,样品在 500 K 附近取得最大 ZT 值 1.25。

5 结 语

综上所述,Ⅷ型 Sn 基笼合物 $Ba_8Ga_{16}Sn_{30}$ 由于具有较低热导率和优越的电传输特性即具有声子玻璃和电子晶体特性,从而在大规模中温温差发电领域具有潜在的应用前景。但Ⅷ型 Sn 基笼合物 $Ba_8Ga_{16}Sn_{30}$ 在使用温度范围内其结构和性能稳定性方面的研究仍然是空白,其次该体系对大规模温差发电而言其 ZT 值相对较低,体系的热电性能还有待于进一步优化。通过对该化合物的理论与实验结合有望提高材料的 ZT 值。具体可以从以下几个方面尝试。

(1) 采用理论计算(如密度泛函理论计算等),从理论上探讨哪种原子(单原子或双原子)作为填充原子和哪种原子对框架原子进行掺杂更有利于提高材料的热电性能,以对实际材料制备提供理论指导。

(2) 采用原子半径较小的 Sr、Yb 等掺杂制备双原子填充的 Sn 基笼合物,以此提高填充原子的热振动参数及体系混乱度,在保证较高电性能的前提下,进一步降低材料的晶格热导率,从而对材料的热电性能进行优化。

(3) 对于该体系材料的制备主要采用自熔剂法,为了获得大尺寸、高性能的热电材料,可以探索新的制备方法,如布里奇曼法和提拉法等。

另外,对该体系而言,具有 n 型传导的化合物具有较高 ZT 值,而 p 型材料的 ZT 值相对较低。因此如何进一步提高 p 型材料的 ZT 值将是又一个研究重点。

参考文献:

[1] Kahn D, Lu J P. Structural properties and vibrational modes of Si_{34} and Si_{46} clathrates [J]. Physical Review B, 1997, 56: 13898.

[2] Cahill D G, Watson S K, Pohl R O. Lower limit to the thermal conductivity of disordered crystals [J]. Physical Review B, 1992, 46: 6131.

[3] Hermann R P, Schweika W, Leupold O, et al. Neutron and nuclear inelastic neutron and nuclear inelastic scattering study of the Ba^-, Sr^-, and Eu^- filled germanium clathrates [J]. Physical Review B, 2005, 72: 174301.

[4] Mélinon P, Kéghélian P, Blase X, et al. Electronic signature of the pentagonal rings in silicon clathrate phases: comparison with cluster-assembled films [J]. Physical Review B, 1998, 58: 12590.

[5] Tournus F, Masenelli B, and Mélinon P. Guest displacement in silicon clathrates [J]. Physical Review B, 2004, 69: 035208.

[6] Fang S L, Grigorian L, Eklund P C, et al. Raman scattering from vibrational modes in Si_{46} clathrates [J]. Physical Review B, 1998, 57: 7686.

[7] Guyot Y, Grosvalet L, Champagnon B. Gruneisen parameters for silicon clathrates determined by Raman scattering [J]. Physical Review B, 1999,60:14507.

[8] Beekman M. Synthesis and transport properties of type Ⅱ clathrates [P]. NJ: 08855-1331,2005.

[9] Nolas G S, Cohn J L, Slack G A, et al. Semiconducting Ge clathrates: promising candidates for thermoelectric applications [J]. Appl Phys Lett, 1998, 73: 178-180.

[10] Saramat A, Svensson G, Palmqvist A E C, et al. Large thermoelectric figure of merit at high temperature in czochralski-grown clathrate $Ba_8Ga_{16}Ge_{30}$ [J]. J Appl Phys, 2006, 99:023708.

[11] Avila M A, Suekuni K, Umeo K, et al. $Ba_8Ga_{16}Sn_{30}$ with type-Ⅰ clathrate structure: drastic suppression of heat conduction [J]. Appl Phys Lett, 2008, 92: 041901.

[12] Volmer M, Sternemann C, Tse J S, et al. Charge transfer in silicon clathrates studied by compton scattering [J]. Phys Rev B, 2007, 76: 233104.

[13] Huo D, Sakata T, Sasakawa T, et al. Structural, transport, and thermal properties of the single-crystalline type-Ⅷ clathrate $Ba_8Ga_{16}Sn_{30}$ [J]. Physical Review B, 2005, 71:075113.

[14] Paschen S, Carrillo-Cabrera W, Bentien A, et al. Structural, transport, magnetic, and thermal properties of $Eu_8Ga_{16}Ge_{30}$ [J]. Physical Review B, 2001, 64:2144041-11.

[15] Li D C, Fang L, Deng S K, et al. Structural and electronic properties of type-Ⅰ and type-Ⅷ $Ba_8Ga_{16}Sn_{30}$ clathrates under compression [J]. Physica B, 2012, 407 : 1238-1243.

[16] Kono Y, NOhya, Taguchi T, et al. First-principles study of type-Ⅰ and type-Ⅷ $Ba_8Ga_{16}Sn_{30}$ clathrates [J]. J Appl Phys, 2010, 107:123720.

[17] Meng Daiyi, Shen Lanxian, Li Decong, et al. Structural and electrical transport properties of Mg-doped n-type Sn-based type Ⅷ single crystalline clathrate [J]. Acta Phys Sin, 2014, 63(17):177401 1-6.

[18] Saiga Y, Suekuni K, Deng S K, et al. Optimization of thermoelectric properties of type-Ⅷ clathrate $Ba_8Ga_{16}Sn_{30}$ by carrier tuning [J]. J Alloy Compd, 2010,507:1-5.

[19] Suekuni K, Avila M A, Umeo L, et al. Simultaneous structure and carrier tuning of dimorphic clathrate $Ba_8Ga_{16}Sn_{30}$ [J]. Physical Review B,2008,77: 235119 1-8.

[20] Kuznetsov V L, Kuznetsova L A, Kaliazin A E, et al. Preparation and thermoelectric properties of $A^{Ⅱ}B^{Ⅲ}B^{Ⅳ}$ clathrate compounds [J]. Journal of Applied Physics, 2000,87(11): 7871-7875.

[21] Kono Y, Akai K, Ohya N, et al. Electronic structures and thermoelectric properties of Sb-doped type-Ⅷ clathrate $Ba_8Ga_{16}Sn_{30}$ [J]. Materials Transactions, 2012,53(4) : 636-640.

[22] Li Yang, Gao J, Chen N, et al. Electronic structure and physical properties of $Ba_8Ga_{16}Sn_{30}$ clathrates with type-Ⅰ and type-Ⅷ structure [J]. Physica B,2008, 403:1140-1141.

[23] Eisenmann B, Schäfer H, Zagler R, Die verbindungen $A_8^{Ⅱ}B_{16}^{Ⅲ}B_{30}^{Ⅳ}$ ($A^{Ⅱ}$=Sr, Ba; $B^{Ⅲ}$=Al, Ga; $B^{Ⅳ}$=Si, Ge, Sn) und ihre käfigstrukturen [J]. Journal of the Less Common Metals, 1986,118(1): 43-55.

[24] Saiga Y, Suekuni K, Du B, et al. Thermoelectric properties and structural instability of type-Ⅰ clathrate $Ba_8Ga_{16}Sn_{30}$ at high temperatures [J]. Solid State Communications, 2012, 152:1902-1905.

[25] Du Baoli, Saiga Y, Kajisa K, et al. Study of α↔β transformation in the dimorphic clathrate$Ba_8Ga_{16}Sn_{30}$ [J]. Philosophical Magazine, 2012, 92(19-21): 2541-2552.

[26] Nolas G S, Cohn J L, Dyck J S, et al. Low-temperature transport properties of polycrystalline $Ba_8Ga_{16}Sn_{30}$ [J]. Journal of Materials Research, 2004,19:3556.

[27] Deng Shukang, Saiga Y, Suekuni K, et al. Enhancement of thermoelectric efficiency in type-Ⅷ clathrate $Ba_8Ga_{16}Sn_{30}$ by Al substitution for Ga [J]. J Appl Phys, 2010, 108 (7): 073705.

[28] Deng Shukang, Saiga Y, Kajisa K, et al. High thermoelectric performance of Cu substituted type-Ⅷ clathrate $Ba_8Ga_{16-x}Cu_xSn_{30}$ single crystals [J]. J Appl Phys, 2011, 109(10):103704.

[29] Meng Daiyi, Shen Lanxian, Shai Xuxia, et al. Growth and thermoelectric properties of Ge doped n-type Sn-based type-Ⅷ single crystalline clathrate [J]. Acta Phys. Sin. 2013, 62(24):247401 1-6.

The recent research developments of Sn-based type-Ⅷ clathrates $Ba_8Ga_{16}Sn_{30}$ thermoelectric materials

SHEN Lanxian, LIU Zuming, DENG Shukang, MENG Daiyi, SHAI Xuxia

(Education Ministry Key Laboratory of Renewable Energy Advanced Materials and Manufacturing Technology, Yunnan Provincial Renewable Energy Engineering Key Laboratory, Solar Energy Research Institute, Yunnan Normal University, Kunming 650500, China)

Abstract: The Sn-based type-Ⅷ clathrate $Ba_8Ga_{16}Sn_{30}$ was considered one of the most promising thermoelectric materials because of its excellent thermoelectric properties. The crystal structure, synthesis methods, theoretical and experimental research of Sn-base type-Ⅷ compound were introduced and reviewed. In addition, some approaches have been proposed for further research the compound.

Key words: **Sn-based clathrate; type-Ⅷ clathrate; thermoelectric materials; thermoelectric properties**

第36卷 第7期 太 阳 能 学 报 Vol. 36, No. 7
2015年7月 ACTA ENERGIAE SOLARIS SINICA Jul., 2015

文章编号:0254-0096(2015)07-1556-05

衬底及其温度对铝诱导非晶硅薄膜晶化的影响

段良飞[1,2], 张力元[1,2], 杨培志[1,2], 化麒麟[1,2], 邓 双[1,2], 彭柳军[1,2]

(1. 可再生能源材料先进技术与制备教育部重点实验室, 昆明 650092; 2. 云南师范大学太阳能研究所, 昆明 650092)

摘 要: 利用磁控溅射镀膜技术,采用不同温度在玻璃、单晶硅衬底上溅射α-Si/Al膜,并在N_2气氛中进行快速光热退火;利用X射线衍射(XRD)仪和拉曼散射光谱仪对薄膜样品进行表征分析。结果表明:单晶硅衬底有利于α-Si/Al膜的晶化;衬底温度从室温到200 ℃之间逐渐升高,薄膜的晶粒尺寸及晶化率增加;随着温度进一步升高,薄膜的晶粒尺寸及晶化率又降低。单晶硅衬底上200 ℃时α-Si/Al膜可直接晶化。通过计算,得出衬底参数对薄膜的晶相比、晶粒尺寸、带隙及界面体积分数的调制关系。

关键词: 衬底; 非晶硅; 铝诱导; 退火; 晶化

中图分类号: TK513.5 **文献标识码**: A

0 引 言

高效、低成本和环境友好的太阳电池一直是人们追求的目标。晶体硅太阳电池由于需要大量原料,未来成本下降的空间有限。为此,薄膜太阳电池引起了人们的关注[1]。其中,非晶硅(α-Si)薄膜太阳电池具有制造工艺简单,原材料用量少(仅为晶体硅的约1%[2]),易实现大面积生产,可在柔性衬底上制备等优点,成为未来太阳电池发展的重点之一,但非晶硅薄膜存在光致衰退(S-W)效应,使其光电转换效率低和稳定性差等,严重制约了市场空间[3]。为有效避免非晶硅薄膜的光致衰减效应,人们研究了微晶硅薄膜(μc-Si),μc-Si薄膜具有较高的载流子迁移率和较大的吸收系数,可有效降低光致衰退效应,并拓宽光谱响应范围,同时还具有非晶硅薄膜的诸多优点,得到广大研究者的青睐[4,5],因此,微晶硅薄膜成为制备高效、稳定的硅基薄膜太阳电池的基础材料[5,6]。微晶硅薄膜通常通过非晶硅晶化来获得,在常规高温退火、快速光热退火、金属诱导和激光退火等晶化方法中[7,8],快速光热退火和金属诱导晶化由于具有设备简单,退火温度低、时间短,适于大面积制备等特点,近些年来得到广泛应用[9,10]。本文采用磁控溅射镀膜技术,分别在玻璃和单晶硅衬底上采用不同温度制备非晶硅(α-Si)/铝(Al)膜,通过快速光热退火实现了薄膜的晶化,研究衬底及其温度对α-Si/Al膜晶化效果的影响。

1 实 验

1.1 薄膜的制备

实验采用JCP-450型三靶磁控溅射镀膜仪,以多晶p型Si靶(纯度99.999%、电导率0.02 Ω·cm)和纯度99.999%的Al靶为靶材,以玻璃片和单晶硅片为衬底,依次使用丙酮、无水乙醇和去离子水分别超声波清洗10 min;溅射气体使用纯度为99.99%的Ar,本底真空为6.0×10^{-4} Pa,工作气压为2.0 Pa,Ar流量为20 sccm,先溅射一层非晶硅薄膜,溅射功率为120 W,时间为3.0 h,衬底温度控制在150~250 ℃之间,再在非晶硅表面溅射一层Al膜,溅射功率为60 W,时间为30 s,衬底温度为室温。利用RTP-500型快速退火炉在N_2气氛中对α-Si/Al薄膜进行快速退火。

1.2 薄膜的性能表征

采用Bruker Apex II X射线衍射仪表征样品的晶体结构,计算微晶晶粒尺寸;采用英国RENISHAW公司的INVIA共焦显微拉曼光谱仪进行拉曼散射光谱测试,分析样品的相成分,计算晶化率。

收稿日期: 2013-05-29

基金项目: 国家自然科学基金联合基金(U1037604)

通信作者: 杨培志(1966—),男,博士、教授、博士生导师,主要从事太阳能利用材料及器件方面的研究。pzhyang@hotmail.com

2 结果与分析

2.1 微晶硅薄膜XRD分析

衬底及其温度对α-Si薄膜的生长及晶化具有重要的影响。以单晶硅Si(100)片和玻璃片作为衬底，衬底温度从室温~250 ℃逐渐变化，制备α-Si薄膜/Al膜样品，并对其进行快速退火处理，得到不同衬底及衬底温度下α-Si/Al膜的晶化效果。薄膜的制备工艺参数如表1所示。

表1 样品制备参数

Table 1 Preparation parameters of samples

样品	衬底	衬底温度/℃	退火温度/℃	退火时间/s
A	Si(100)	室温	550	300
B	Si(100)	150	550	300
C	Si(100)	200	550	300
D	Si(100)	250	550	300
E	玻璃	200	550	300
F	Si(100)	200	未退火	—

为了对比衬底对非晶硅薄膜晶化的影响，测试样品C、E的X射线衍射谱，如图1a所示。从图1a可看出200 ℃退火后样品C出现了尖锐的Si(400)衍射峰，强度高、对称性好；样品E在相同条件下退火则出现了Si(111)和Si(220)两个衍射峰，且强度低、对称性较差，其中Si(111)衍射峰强于Si(220)衍射峰。为了比较衬底温度对非晶硅薄膜晶化的影响，测试了单晶样品A、B、C、D、F的X射线衍射谱，如图1b所示。从图1b可看出，样品均出现了明显的Si(400)衍射峰，峰值强度和对称性随衬底温度从室温~200 ℃逐渐增加，200~250 ℃又逐渐降低。

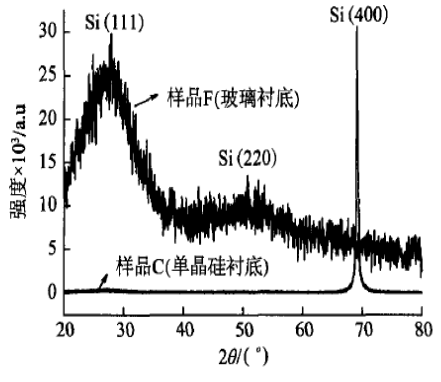

a. 不同衬底XRD图

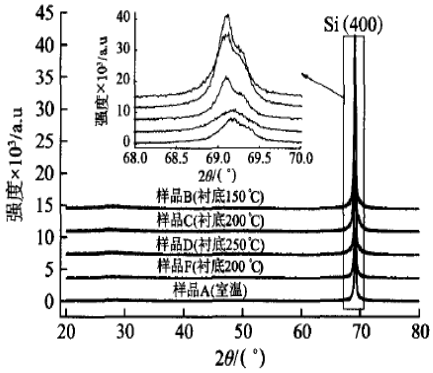

b. 不同衬底温度XRD图

图1 微晶硅薄膜的XRD谱图

Fig. 1 The XRD spectrograms of microcrystalline silicon thin films

通过计算获得样品XRD谱的半高宽w(FWHM)；采用Scherrer公式计算晶粒尺寸大小D。

$$D=K\lambda/(w\cos\theta) \quad (1)$$

式中，D——晶粒尺寸，nm；K——Scherrer常数，为0.89；λ——X射线波长，为0.154056 nm；w——积分半高宽，rad；θ——衍射角。结果如表2所示。

表2 样品晶化参数

Table 2 crystallization parameters of samples

样品	半高宽 2θ/(°)	晶粒尺寸/nm	晶化率/%	E_g/eV	f_{ab}/%
A	0.41	23.24	30.29	1.54	18.6
B	0.39	24.44	41.79	1.49	20.8
C	0.36	26.47	44.34	1.48	21.7
D	0.38	25.08	41.72	1.49	20.3
E	0.67	14.23	40.09	1.48	18.4
F	0.42	22.69	40.23	1.50	21.2

2.2 微晶硅薄膜拉曼分析

图2为样品的拉曼光谱，从图2可看出，样品E在487.00 cm^{-1}处有明显的峰，样品F的拉曼位移为489.00 cm^{-1}，相对于非晶硅的TO(transverse optical)模式480.00 cm^{-1}有一点移动($\Delta\nu$=9 cm^{-1})，说明样品出现了晶化，但其比例小，多数还是非晶成分；样品C的峰值位于492.61 cm^{-1}，表明薄膜的微晶成分比E多。

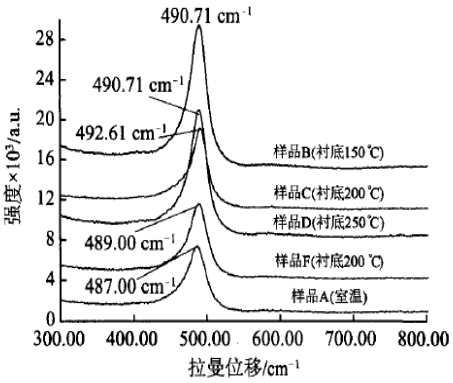

图2 不同衬底温度样品的拉曼谱

Fig. 2 Raman of different substrate temperature

从图2还可得出,拉曼谱峰值在一定衬底温度范围从室温~200 ℃,随衬底温度的升高拉曼谱峰位逐渐蓝移,而后从200~250 ℃,样品拉曼谱峰值位随衬底温度升高逐渐红移,表明薄膜均已结晶,但结晶程度不同,从室温~200 ℃结晶成分逐渐增加,200~250 ℃结晶度又逐渐降低。

α-Si/Al膜在晶化过程中,静态物质的相含量会发生改变,这种变化对薄膜的物化性质具有重要影响,在拉曼散射谱中,通过对样品拉曼谱图及拉曼谱峰值位移的分析,并利用 X_c 晶化率公式计算的α-Si/Al膜的晶化率。

$$X_c=(I_{510}+I_{520})/(I_{510}+I_{520}+I_{480}) \tag{2}$$

式中,I_{520}、I_{510} 和 I_{480} ——中心位置在位移为520、510和480 cm^{-1} 附近特征峰的曲线进行面积积分后的积分强度[11]。晶化率的计算结果如表2所示。

2.3 衬底及其温度对微晶硅薄膜的带隙、界面体积分数的影响

通常认为,微晶硅材料是由非晶、晶粒、界面等组成的混合相材料,晶相比、晶粒尺寸及界面体积分数对薄膜的光电性能具有重要的影响。对于晶硅,带隙为1.12 eV;而非晶硅的带隙为1.75 eV[12]。这里用表观带隙(E_g)来描述微晶硅材料的带隙,它是按材料的晶化率以及非晶相和晶相对带隙的贡献来计算的。如式(13)、式(14)所示[13]:

$$E_g=1.12X_c+1.75(1-X_c) \tag{3}$$

500 cm^{-1} 附近的峰由多种因素引起,由于晶粒尺寸大于2 nm,500 cm^{-1} 附近的拉曼峰主要来自界面的贡献,界面体积分数为:

$$f_{ab}\equiv I_{gb}/(I_g+I_{gb}+YI_a) \tag{4}$$

式中,I_g、I_{gb}、I_a ——晶粒、界面、非晶通过高斯拟合后的积分强度;Y 取0.9。

与XRD结果对应,可得到不同晶相比、晶粒尺寸所对应的薄膜带隙和界面体积分数的变化趋势,结果如表2所示。由表2可知,单晶硅Si(100)具有高的对称性和取向性,作为衬底时起到籽晶的作用,可作为晶种在非晶硅薄膜晶化过程中起到诱导作用。相同条件下,单晶硅衬底上可获得较大晶粒尺寸的微晶硅薄膜,因此,单晶硅衬底样品C的晶粒尺寸(26.47 nm)比相同条件玻璃衬底样品E的晶粒尺寸(14.23 nm)大,样品C的晶化率(44.34%)比E的晶化率(40.09%)高。

衬底温度提高,原子能量升高,扩散迁移速率快,在衬底表面能充分弛豫。理论指出,固体原子的扩散时一个热激活过程,扩散系数 D 和温度的关系可表示为[14]:

$$D=D_0\exp(-E_d/kT) \tag{5}$$

式中,E_d ——扩散激活能,对于Si,E_d=4.7~5.1 eV;k ——玻尔兹曼常数;$D_0=cv_0\alpha^2$,c 在一维、二维、三维的情况下分别为1/2、1/4、1/6,表示有2、4、6个扩散方向,Si中 $D_0=10^3 cm^2/s$。

由此可见扩散系数是温度(T)的函数,随温度升高扩散迁移率增加,因此加温有助于Si原子的充分弛豫,但随温度升高,迁移距离 $\alpha=(D_0/cv_0)^{1/2}$ 随温度升高间隙原子振动频率变大,扩散距离 α 变小,而且,随温度升高,空位、间隙原子浓度[14]:

$$\rho_v=\exp[-(E-TS)/kT] \tag{6}$$

式中,$E-TS$ ——缺陷形成的自由能。

缺陷浓度与温度成正比,因此,随温度升高首先原子扩散系数增加,从而增大了薄膜的结晶速率,促进其晶粒长大,所以衬底温度从室温~200 ℃,晶粒尺寸和晶化率逐渐增大、薄膜带隙逐渐降低、界面体积分数增加。然而,衬底温度超过200 ℃时,硅原子在衬底上的弛豫路径变短,缺陷态密度增加,反而抑制了薄膜的晶粒的形成和长大,因此,衬底温度在200~250 ℃范围内,晶粒尺寸和晶化率随温度升高逐渐降低、薄膜带隙增加、界面体积分数逐渐降低。

样品F为未退火样品,在衬底温度200 ℃时出现了晶化,晶粒尺寸达22.69 nm,晶化率为40.23%。说明采用单晶硅衬底,200 ℃即可实现

α-Si/Al 膜的晶化，且晶化率达到微晶硅薄膜太阳电池器件要求(晶化率高于 40%)[15]。

3 结 论

采用磁控溅射镀膜技术，在不同温度下，分别在单晶硅和玻璃片上溅射制备α-Si/Al 膜，并对其进行快速退火。结果表明：单晶硅衬底因其起到籽晶的作用，通过与 Al 膜的协同诱导作用，降低晶化率，提高薄膜的晶化率、促进晶粒尺寸长大；衬底温度的提升，有助于提高薄膜的结晶速率，促进晶粒长大，然而，衬底温度过高时，随着薄膜的悬键密度和缺陷态密度的增加，晶化率降低；α-Si/Al 膜可直接在 200 ℃的单晶硅衬底上晶化。通过对微晶硅薄膜的带隙及界面体积分数的计算，得到衬底及其温度对薄膜晶粒尺寸、晶相比、带隙及界面体积分数的调节控制关系。从这些结果中可得出，衬底及其温度对非晶硅薄膜的晶化具有重要影响，通过制备参数之间的调制，可获得不同晶粒尺寸及晶化率的微晶硅薄膜，从而获得渐变带隙微晶硅薄膜材料。

[参考文献]

[1] 林揆训，林璇英，梁厚蕴. 非晶硅薄膜的低温快速晶化及其结构分析[J]. 物理学报，2002，51(4)：863—865.

[1] Lin Kuixun, Lin Xuanying, Liang Houyun. Rapid crystallization of a-Si films at low temperatures and structure analyses of the crystallized films[J]. Acta Physica Sinica, 2002, 51(4): 863—865.

[2] 罗士雨，冯 磊，汪 洪. 非晶硅薄膜制备及其晶化特性研究[J]. 人工晶体学报，2008，37(8)：1191—1194.

[2] Luo Shiyu, Feng Lei, Wang Hong. Study on the preparation of amorphous silicon film and its crystallization property[J]. Journal of Synthetic Crystals, 2008, 37(8): 1191—1194.

[3] 陈庆东，王俊平，李 洁. VHF-PECVD沉积本征微晶硅薄膜激活能特性研究[J]. 人工晶体学报，2009，38(6)：1425—1428.

[3] Chen Qingdong, Wang Junping, Li Jie. Investigation on activation energy of intrin sic microcrystalline silicon thin films deposited by VHF-PECVD[J]. Journal of Synthetic Crystals, 2009, 38(6):1425—1428.

[4] Ling Zhipeng, Ge Jia, Mueller Thomas. Optimisation of p-doped μc-Si:H emitter layers in crystalline-amorphous silicon heterojunction solar cells[J]. Energy Procedia, 2012, 15(1): 118—128.

[5] 张晓丹，赵 颖，魏长春，等. 微晶硅材料和电池特性的相关研究[J]. 太阳能学报，2007，28(12)：1305—1309.

[5] Zhang Xiaodan, Zhao Ying, Wei Chuangchu, et al. Study of relationship between microcrystalline silicon thin film and solar cells[J]. Acta Energiae Solaris Sinica, 2007, 28(12): 1305—1309.

[6] 夏冬林，杨 晟，徐 慢. 金属铝诱导法低温制备多晶硅薄膜[J]. 感光科学与光化学，2006，24(2)：87—91.

[6] Xia Donglin, Yang Sheng, Xu Man. Preparation of polycrystalline silicon films by aluminum-induced crystallization at low temperature[J]. Photographic Science and Photochemistry, 2006, 24(2): 87—91.

[7] Kishore Ram, Hotz Chris, Naseem H A. Aluminum-induced crystallization of amorphous silicon (α-Si) at 150 ℃[J]. Electrochemical and Solid-State Letters, 2001, 4(2): 14—16.

[8] Ching Minghsu Ming Changyu. Deterioration of aluminum induced crystallization of sputtered silicon by film stress[J]. Journal of Materials Science Letters, 2003, 22(1): 1079—1081.

[9] Kishore R, Sood K N. Microstructural and analytical investigation of low temperature crystallized amorphous silicon/crystallized silicon interface using SEM and EDS[J]. Journal of Materials Science Letters, 2002, 21(1): 647—648.

[10] 杨仕娥，文黎巍，陈永生，等. 衬底温度和硼掺杂对P型氢化微晶硅薄膜结构和电学特性的影响[J]. 物理学报，2008，57(8)：5176—5180.

[10] Yang Shie, Wen Liwei, Chen Yongsheng, et al. Substrate temperature and B-doping effects on microstructure and electronic properties of p-type hydrogenated microcrystalline silicon films[J]. Acta Physica Sinica, 2008, 57(8): 5176—5180.

[11] 王 宙，曹 健. 铝诱导晶化真空蒸镀多晶硅薄膜的研究[J]. 功能材料，2012，43(5)：573—575.

[11] Wang Zhou, Cao Jian. Study on Al-induced crystallization of polycrystalline silicon thin films by vacuum evaporation[J]. Journal of Functional Materials, 2012, 43(5): 573—575.

[12] 张晓丹. 器件质量级微晶硅薄膜及高效微晶硅太阳电池的制备研究[D]. 天津：南开大学，2005，88—120.

[12] Zhang Xiaodan. Preparation and study of device grade

microcrystalline silicon thin film for solar cells and efficient microcrystalline silicon solar cells[D]. Tianjin: Nankai University, 2005, 88—120.

[13] 彭文博, 刘石勇, 肖海波, 等. 微晶硅薄膜带隙态及微结构的研究[J]. 物理学报, 2009, 58(8): 5717—5718.

[13] Peng Wenbo, Liu Shiyong, Xiao Haibo, et al. Gap states and microstructure of microcrystalline silicon thin films[J]. Acta Physica Sinica, 2009, 58(8): 5717—5718.

[14] 吴自勤, 王 兵. 薄膜生长[M]. 北京: 科学出版社, 2001, 87—181.

[14] Wu Ziqin, Wang Bing. Thin film growth[M]. Beijing: Science Press, 2001, 87—181.

[15] 俞远高, 侯国付, 王 锐, 等. 微晶硅材料及其在太阳电池中的应用[J]. 激光与光电子进展, 2006, 43(8): 48—55.

[15] Yu Yuangao, Hou Guofu, Wang Rui, et al. Microcrystalline silicon and its application in solar cells [J]. Laser & Optoelectronics Progress, 2006, 43(8): 48—55.

EFFECT OF SUBSTRATE AND ITS TEMPERATURE ON ALUMINUM INDUCED AMORPHOUS SILICON FILMS RAPID CRYSTALLIZATION

Duan Liangfei[1,2], Zhang Liyuan[1,2], Yang Peizhi[1,2], Hua Qilin[1,2], Deng Shuang[1,2], Peng Liujun[1,2]

(1. *Key Laboratory of Renewable Energy Advanced Materials and Manufacturing Technology of Ministry of Education of China, Kunming* 650092, *China*; 2. *Solar Energy Research Institute, Yunnan Normal University, Kunming* 650092, *China*)

Abstract: Amorphous silicon(α-Si)/aluminum(Al) films were prepared by magnetron sputtering based on glass and monocrystalline silicon substrate at different temperatures, and then annealed by RTA in N_2 atmosphere. X-ray diffraction (XRD) instrument and Raman scattering were used to analyse the structure and properties of μc-Si films. The results showed that monocrystalline silicon substrate and heating can improve the crystallization of α-Si/Al films; The crystalline volume fraction of μc-Si films increased with the increasing of substrate temperature from ambient to 200 ℃. And then crystalline volume fraction decreased with increasing of substrate temperature from 200 ℃ to 250 ℃. α-Si/Al films can be crystallized in the substrate of monocrystalline silicon with substrate temperatures 200 ℃. The effects of substrate parameters on crystallization rate, grain size, band gap and the volume fraction of interface were obtained by calculating.

Keywords: substrate; amorphous silicon; aluminum induced; rapid annealing; crystallization

第44卷 第1期 人 工 晶 体 学 报 Vol.44 No.1
2015年1月 JOURNAL OF SYNTHETIC CRYSTALS January,2015

铝诱导非晶硅薄膜晶化动力学研究

张力元[1,2],段良飞[1,2],杨 雯[1,2],杨培志[1,2],邓 双[1,2],涂 晔[1,2],陈小波[1,2]
(1.云南师范大学可再生能源材料先进技术与制备教育部重点实验室,昆明 650092;2.云南师范大学太阳能研究所,昆明 650092)

摘要:为探讨其晶化过程及动力学机理,本文采用磁控溅射技术制备Al/Si薄膜,并利用快速光热退火制备微晶硅。通过采用不同的衬底温度及对铝膜进行退火处理,探究其晶化动力学过程。利用拉曼散射光谱(Raman)仪和X射线衍射(XRD)仪对薄膜进行性能表征。结果表明:退火及衬底加热均能在界面形成非共融的硅铝化合物;延长退火时间能使Al/Si界面充分扩散,达到成核条件。较大的铝晶粒及其择优取向,能有效改善铝诱导晶化效果。

关键词:非晶硅薄膜;磁控溅射;铝诱导;动力学
中图分类号:O484 文献标识码:A 文章编号:1000-985X(2015)01-0085-05

Crystallization Kinetics of Aluminum-induced Amorphous Silicon Thin Films

ZHANG Li-yuan[1,2], *DUAN Liang-fei*[1,2], *YANG Wen*[1,2], *YANG Pei-zhi*[1,2],
DENG Shuang[1,2], *TU Ye*[1,2], *CHEN Xiao-bo*[1,2]
(1. Key Laboratory of Renewable Energy Advanced Materials and Manufacturing Technology, Ministry of Education, Yunnan Normal University, Kunming 650092, China; 2. Solar Energy Research Institute, Yunnan Normal University, Kunming 650092, China)

(*Received* 11 *September* 2014, *accepted* 8 *October* 2014)

Abstract: In order to investigate the kinect mechanism of Aluminum-induced crystallization of amorphous silicon, microcrystalline silicon thin films were prepared by rapid photo-thermal annealing of magnetron sputtered Al/Si thin films. The thin films prepared at various substrate temperatures and annealing time were characterized by Profile-system, Raman scattering spectroscopy (Raman) and X-ray diffraction (XRD). The results show that annealing and substrate heating lead to the formation of silicon-Aluminum composite at the Al/Si interface. Prolonged annealing time promotes the interdiffusion of Al and Si, facilitating the nucleation of microcrystalline silicon. The optimized Aluminum grain size and orientation, effectively improve the effect of Aluminum induced crystallization.

Key words: amorphous silicon thin film; magnetron sputtering; aluminum-induced; kinetic

1 引 言

随着硅基薄膜太阳电池的发展,非晶/微晶硅叠层太阳电池、微晶硅和多晶硅薄膜材料成为人们研究的热点[1,2]。微晶硅和多晶硅通常通过非晶硅晶化获得,因此非晶硅的低温晶化成为了关注的焦点,而金属诱导晶化是普遍使用并能有效降低晶化温度的方法。金属诱导晶化法是在非晶硅薄膜的上面镀一层金属膜或者在镀有金属膜的基片上镀一层非晶硅膜,然后在低温下进行退火处理,在金属的诱导下,使非晶硅低温晶化而获得多晶硅,其原理是由于金属与非晶硅界面的相互扩散,使非晶硅中的Si-Si键强度减弱,同时金属与

收稿日期:2014-09-11;修订日期:2014-10-08
基金项目:国家自然科学基金联合基金(U1037604)
作者简介:张力元(1990-),男,云南省人,硕士研究生。E-mail:zhangmiliyuan@126.com
通讯作者:杨培志,研究员,博士生导师。E-mail:pzhyang@hotmail.com

非晶硅通常有较低的共晶温度，从而使非晶硅能够在低于 600 ℃ 发生晶化。可用来诱导的金属很多，如 Al、Au、Ag 和 Ni 等，不同的金属诱导效果略有不同[3]，其中又以铝诱导晶化（AIC）效果较好。快速光热退火以其快速高效、所需设备简单、适于大面积制备等优点成为金属诱导晶化中首选的退火方法，近年来受到人们的重视。

AIC 制备微晶硅可大幅降低晶化温度。迄今为止，已有大量低温晶化的报道，个别晶化温度甚至低于 100 ℃[4]。但 AIC 制备微晶硅本身利用了 Al 的重掺杂，薄膜的用途受限，且制备时薄膜的厚度和多余铝的腐蚀去除等均是一些亟待解决的问题。对 AIC 整个过程的机理研究，对降低晶化温度，以及解决 Al 引入带来的一系列问题，具有指导意义。本文利用磁控溅射法在单晶硅 Si（100）和普通玻片上沉积了 Al 膜，经过退火处理后再在 Al 膜上沉积非晶硅（a-Si）薄膜，利用快速光热退火对 Al/Si 薄膜进行退火；研究了 AIC 的动力学机理。

2 实　　验

2.1 薄膜的制备

室温下，采用 JCP-450 三靶磁控溅射镀膜系统，以单晶 P 型硅靶（纯度 99.999%、电导率 0.02 Ω·cm）和金属 Al 靶为原料，在单晶硅 Si（100）衬底上溅射 Al/a-Si 膜。衬底依次使用无水乙醇和去离子水超声清洗 15 min，并用氮气吹干；溅射气体使用纯度为 99.99% 的 Ar，本底真空为 6.0×10^{-4} Pa，Ar 流量为 20 sccm，其中射频溅射非晶硅薄膜的功率为 100 W，衬底温度分别为室温（25 ℃）及 200 ℃；溅射铝膜的功率为 70 W，衬底温度为室温。利用 RTP-500 型快速光热退火炉在不同温度下对薄膜进行快速退火。Oliver Nasta 等[5]的研究表明结晶态 Si 最终会完全取代 Al 层，且 Al 层厚度决定了所形成微晶硅薄膜的厚度。故衬底/Al/a-Si 的结构有助于多余铝的去除，本文实验均采用此结构。

2.2 薄膜的性能表征

X 射线衍射测试采用 Bruker Apex II X 射线衍射仪；拉曼（Raman）光谱测试采用英国 RENISHAW 公司的 INVIA 共焦显微拉曼光谱仪。

3 结果与讨论

3.1 不同温度下退火

衬底为单晶硅，衬底温度为室温，铝膜溅射时间为 30 s；非晶硅薄膜的溅射时间为 1.5 h，衬底温度为 200 ℃。样品 A、B、C、D 为 Al/a-Si 膜；将样品放入退火炉中进行快速光热退火，退火时间为 5 min，其工艺参数如表 1 所示。

表 1 样品的晶化参数

Table 1 Crystallization parameters of the samples

Sample	A	B	C	D
Annealing temperature/℃	500	550	600	Non-annealed
Annealing time/min	5	5	5	

图 1 是样品 A、B、C、D 的拉曼光谱。从图中可以看出，不同退火温度下样品的拉曼特征峰值差别不大，均位于 500 ± 1 cm^{-1}，处于非晶硅的横向光学声子振动膜峰 480 cm^{-1} 和单晶硅晶粒缺陷或晶粒间界峰 510 cm^{-1} 之间[6]。说明薄膜此时还未成核结晶，而是一种介于非晶态与晶态间的非共融态，Si-Si 键由饱和键转变为非饱和 Al-Si 键。样品 D 为未退火样品，可以看出射频磁控溅射时，由于衬底温度 200 ℃，不断生长的 Si 薄膜与衬底上已溅射的 Al 膜发生作用。部分 Si 扩散到 Al 膜，形成 Al-Si 键，大大降低了成核所需能量，但温度还达不到异质成核的能量条件。通过样品 A、B、C 可看出：退火后随着温度的升高，拉曼峰的强度不断提高，即所形成的 Al-Si 化合物的浓度增加。其原因在于随着温度的升高，Si 的扩散率增加。B、C 样品的退火温度在铝硅共晶点 577 ℃ 附近，退火后并未形成晶态 Si，这是由于退火时间过短，并未达到成核所需

的结构和能量条件,即单位体积内没有形成可以稳定长大的一定数量的晶核。

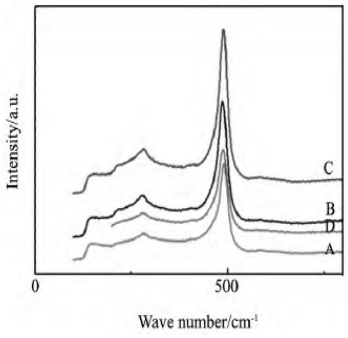

图 1　不同退火温度下铝诱导非晶硅薄膜晶化的 Raman 图谱

Fig. 1　Raman spectra of Aluminum-induced amorphous silicon thin films at different annealing temperature

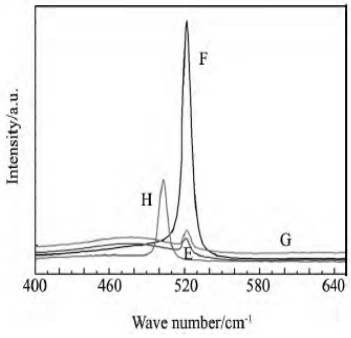

图 2　Al 处理后退火样品 Raman 图谱

Fig. 2　Raman spectra of annealing samples after Al processing

3.2　先退火处理 Al 膜,再延长 Al/a-Si 膜的退火时间

由于在衬底加热的条件下 Al 膜上溅射 a-Si 膜会发生反应,不能真实的体现出铝晶粒对非晶硅晶化的作用,因此,采用衬底温度为室温以及对铝膜先进行退火处理的方式溅射 a-Si 膜。在与 3.1 相同的实验条件下制备 Al 膜,并将其以表 2 的工艺参数退火,退火后再在室温下溅射 a-Si 膜。为与 3.1 比较,退火时间延长至 30 min,退火温度为 500 ℃。

表 2　Al 膜的退火参数

Table 2　Annealing parameters of Al films

Sample	E	F	G
Annealing temperature/℃	0	150	250
Annealing time/min	0	5	5

图 2 是样品 E、F、G、H 退火 30 min 后的拉曼光谱。从图中可以看出,E、F、G 三个样品均出现了 520 cm^{-1}峰,而中心位置在 520 cm^{-1}附近的峰代表单晶硅的横向光学声子振动膜[7],即样品均达到了不同程度的晶化。样品 H 为对照组,H 退火时间为 5 min,E 和 H 均没有对其 Al 膜进行退火处理,直接溅射 a-Si 膜后再退火,对比样品 E 和 H,可看出延长退火时间,501 cm^{-1}处非共融态 Al-Si 化合物的峰消失并形成一个低谷,继而在 480 cm^{-1}处出现非晶硅的横向光学声子振动膜峰包和 520 cm^{-1}处单晶硅的横向光学声子振动膜峰。样品 F 在 Al 膜 150 ℃退火后,其它峰均消失,但出现了很强的 520 cm^{-1}峰。利用晶化率 $X_c = (I_{510} + I_{520}) / (I_{510} + I_{520} + I_{480})$ 计算公式可算出晶化率,式中,I_{520}、I_{510}和 I_{480}是中心位置在 520 cm^{-1}、510 cm^{-1}和 480 cm^{-1}附近特征峰的曲线进行面积积分的积分强度,可以得到晶化率为 88%,其晶化效果显著。但在 Al 膜的退火温度升高后获得的样品 G,与未处理 Al 的样品 E 所得结果相差不大。

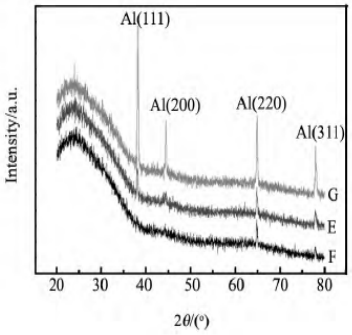

图 3　Al 膜 XRD 图谱

Fig. 3　XRD patterns of Al films

图 3 是 E、F、G 样品中 Al 膜的 XRD 图谱。样品 E 为未处理的 Al 膜,可看出通过双脉冲磁控溅射生长的 Al 膜具有四个峰,分别对应于 Al 的(111)晶面、(200)晶面、(220)晶面和(311)晶面。150 ℃退火 5 min 后(111)晶面和(200)晶面的衍射峰消失。250 ℃退火 5 min 后四个衍射峰的强度增加,且更为尖锐。利用谢乐公式:$Size = K\lambda / B\cos\theta$,式中 Size 表示晶粒尺寸(nm),$K$ 为常数,一般取 $K = 1$,λ 是 X 射线的波长($Cu\ K_\alpha$:0.154056 nm),B 是样品衍射峰的半高宽(Rad),θ 则是衍射角(Rad)。通过 Jade 5.0 全峰拟合后算出不

同样品中 Al 膜晶粒的平均尺寸分别为:E:49.0nm,F:76.2nm,G:51.9nm。可以看出较大 Al 晶粒和(220)、(311)择优取向,能有效的增强诱导晶化效果,而(111)(200)取向不利于 Al 诱导晶化。其原因可能在于(220)、(311)择优取向与所形成微晶硅取向一致起到类似籽晶层的作用,而较大的晶粒具有较宽的晶界更易形成利于形核的凹面和平面结构。

3.3 动力学分析

一般认为,铝诱导晶化的过程为:由于 Al 晶界与 Al/a-Si 界面的接触,大大降低了 Si 结晶的自由能[8],退火后 Si-Si 键断裂并通过扩散的方式渗入铝膜,与铝原子相互作用形成 Al-Si 键,在 Al/a-Si 界面附近形成非共融的硅铝化合物,Si-Si 键由饱和键转变为非饱和键,Si-Si 键的键能降低,同时形成非稳定态的硅铝化合物,且 Al-Si 键断裂所需能量较低[9]。所以 Si 首先在 Al/a-Si 界面形核,之后 Si 晶粒在 Al/a-Si 界面和衬底束缚下长大。不断长大的 Si 晶粒会形成一个 Si 的耗尽层,非晶 Si 原子由于浓度梯度的作用加之非晶态 Si 的自由能高于结晶态 Si,双重作用下非晶态 Si 定向的扩散到已形成的晶核周围并在衬底的束缚下延横向生长。根据 Si-Al 相图,Al 在晶体硅中的溶解度很低,因此多余的 Al 原子被不断长大的晶粒“排挤”,并沿 Al/a-Si 界面扩散到 a-Si 层中,横向生长的结果是形成了如图 4 所示的 a-Si/μ-Si/衬底结构。

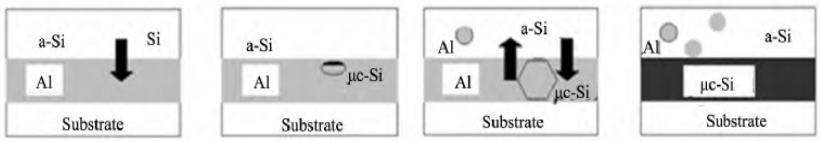

图 4 AIC 过程示意图

Fig. 4 Diagram of AIC process

实验结果验证了铝诱导非晶硅晶化的四个过程:(1)在温度的作用下原非晶硅中的 Si-Si 键断裂,并通过扩散的方式进入 Al 膜,形成非稳定态的硅铝化合物。通过拉曼图谱可看出,无论是通过退火还是溅射时衬底加温都要进行此过程,升温可加速反应的进行。(2)退火时间足够,达到异质成核条件时,便成核长大。(3)非稳定态的硅铝化合物不断的形成稳定态的晶态硅,其拉曼图谱可看出 501 cm^{-1} 处非共融态 Al-Si 化合物的峰消失形成一个低谷,出现刚形成的晶态硅峰和还未参与成核长大的非晶硅峰。(4)形成稳定的晶态硅。

实验结果还表明:Al 膜对非晶硅的晶化工艺有显著影响,通过对 Al 膜的处理观察到,大晶粒和特定取向可显著增强非晶硅的晶化效果。其原因在于,Al-Si 键的非稳定状态导致 Si 的异质成核发生在铝硅晶界处,较大的铝晶粒因其晶界较宽有利于 Si 原子异质成核。根据非均匀形核理论,形核需要三个条件:过冷、结构起伏以及能量起伏。而较宽的晶界更易形成利于形核的凹面和平面结构,同时,Al 的(220)和(311)为形核择优取向,能降低形核所需能量。

4 结 论

根据动力学理论验证了铝诱导非晶硅晶化的全过程机理。在衬底加温的 Al 膜采用磁控溅射生长非晶硅薄膜和对 Al/Si 薄膜退火均能形成非稳定态的硅铝化合物。增加退火时间能使非稳定态的硅铝化合物有效的晶化。150 ℃ Al 膜退火形成较大晶粒和(220)、(311)择优取向,能有效的增强诱导晶化效果。

参 考 文 献

[1] 蔡宏琨,陶 科,王林申. 柔性衬底非晶硅薄膜太阳电池界面处理的研究[J]. 物理学报,2009,**58**(11):7921-7924.

CaiH K, Tao K, Wang L S. Interface Treatment of Amorphous Silicon Film Solar Cells on Flexible Substrate [J]. *Acta Phys Sinica*, 2009, **58**

(11):7921-7924(in Chinese).

[2] 靳瑞敏,王玉仓,陈兰莉,等. 退火温度和时间对制备多晶硅薄膜的影响[J]. 材料导报,2010,**24**(3):89-91.
Jin R M, Wang Y C, Chen L L, et al. The Effect of Annealing Temperature and Time on Fabricating Poly-Si Thin Films [J]. *Materials Review*, 2010,**24**(3):89-91(in Chinese).

[3] 方晓玲. 非晶硅薄膜光学性质的研究及铝诱导晶化法制备多晶硅薄膜[D]. 西安:陕西师范大学硕士学位论文,2008,5.
Fang X L. The Research of Amorphous Silicon Thin Film Optical Properties and The Preparation of Aluminum Induced Crystallization Polycrystalline Silicon Thin Film [D]. Xi'an:Master's Thesis of Shaanxi Normal University,2008,5(in Chinese).

[4] 王成龙,苗树翻,范多旺. 铝诱导晶化低温制备多晶硅薄膜的机理研究[J]. 真空科学与技术学报,2013,**33**(11):1139-1143.
Wang C L, Miao S F, Fan D W. Mechanism of Low Temperature Growth of M-Induced Polycrystalline Si Film [J]. *Chinese Journal of Vacuum Science and Technology*,2013,**33**(11):1139-1143(in Chinese).

[5] Oliver N, Wenham S R. Elucidation of the Layer Exchange Mechanism in the Formation of Polycrystalline Silicon by Aluminum-induced Crystallization [J]. *Journal of Applied Physics*,2000,**88**(1):124-132.

[6] Han D X, Lorentzen J D, Weinberg-Wolf J. Raman Study of Thin Films of Amorphous-to-microcrystalline Silicon Prepared by Hot-wire Chemical Vapordeposition [J]. *J. Appl. Phys*,2003,**94**:2930-2936.

[7] Yue G Z, Lorentzen J D, Lin J. Photolu minescence and Raman Studies in Thin-film Materias: Transition from Amorphous to Microcrystalline Silicon [J]. *Applied Physics Letters*,1999,**75**(4): 492-494.

[8] Porter D A, Easterling K E. Phase Transformations in Metals and Alloys [M]. London:Chapman and Hall,1992.

·信　　息·

合肥研究院在柔性超级电容器研究中取得进展

近期,中国科学院合肥物质科学研究院固体物理研究所微纳技术与器件研究室研究员叶长辉带领的研发团队在柔性超级电容器研究方面取得新进展。相关研究成果已发表在英国皇家化学会《材料化学》杂志上(*J. Mater. Chem. A*, 2014, 2, 20916-20922;*J. Mater. Chem. A*, 2015, 3, 617-623)。

随着柔性可穿戴式及便携式功能化电子器件的发展,要求驱动其工作的供能器件不仅能提供足够的功率及能量密度,还需具有良好的柔韧性。超级电容器以其较高的功率密度、循环稳定性以及可实现快速充放电,是一种非常有应用潜力的供能器件,然而其较低的能量密度一直限制着其实际应用。因此,如何进一步提高超级电容器的能量密度并使其柔性化是目前超级电容器研究领域的热点。

聚苯胺是一种具有特殊的电学、光学性质,且经掺杂后可具有导电性的高分子化合物,其在电子工业、信息工程、国防工程等的开发和发展方面都具有多种用途。通过一系列实验,该课题组研究人员利用原位电沉积技术在柔性导电基底上均匀地制备了一层聚苯胺薄膜,并以此作为复合电极进一步制备了柔性超级电容器。这种超级电容器具有 51.7 mF·cm^{-2}最大面电容,以及 5.57 mWh·cm^{-3}最大能量密度,其并联后可以有效地驱动 LED 灯数分钟,并且展现出优异的柔韧性和循环稳定性。

此外,固体所课题组研究人员进一步将普通激光打印技术和原位电沉积技术相结合,改进了该柔性超级电容器的构型,制备了一种具有插指状构型的柔性超级电容器,具有这种插指状构型的柔性超级电容器可以有效地抑制初始放电电压的压降,并且在和柔性用电器件结合方面具有更大优势。

上述研究得到了国家重大科学研究计划、国家自然科学基金和中科院百人计划项目的资助。

(来源:中国科学院合肥物质科学研究院)

第 44 卷 第 10 期
2015 年 10 月

人 工 晶 体 学 报
JOURNAL OF SYNTHETIC CRYSTALS

Vol. 44 No. 10
October, 2015

Sn 自溶剂含量对 Al 掺杂 VIII 型 Sn 基单晶笼合物电传输特性的影响

申兰先[1]，李德聪[2]，刘虹霞[1]，刘祖明[1]，邓书康[1]

（1. 云南师范大学太阳能研究所，可再生能源材料先进技术与制备教育部重点实验室，
云南省农村能源工程重点实验室，昆明 650500；2. 云南开放大学光电工程学院，昆明 650500）

摘要：通过 Sn 自熔剂法制备了 Al 掺杂 VIII 型 Sn 基单晶笼合物 $Ba_8Ga_{10}Al_6Sn_x$（x = 40，50，60；Sn40，Sn50，Sn60），并研究 $Ba_8Ga_{10}Al_6Sn_x$ 单晶笼合物的结构和电传输特性对自熔剂 Sn 初始含量的依赖性。结果表明，Al 的实际含量随 Sn 自熔剂含量的增加而基本保持不变，说明 Sn 的起始含量对 Al 在该笼合物中固溶度的影响较小；室温下 Sn60 样品的载流子浓度较高，这可能是因 Al 在笼合物 $Ga_8Ga_{16}Sn_{30}$ 中的占位不同而导致费米能级附近能带色散关系发生变化所引起；另一方面，在 300～600 K 的温度范围内，获得较高功率因子的是 Sn 初始含量为 50 的样品，在 488 K 处获得最大值 1.82×10^{-3} W·m^{-1}·K^{-2}；获得较低功率因子的是 Sn 初始含量为 40 的样品，而功率因子较低主要是由于该样品电导率较低。

关键词：VIII 型笼合物；Sn 基笼合物；电传输特性

中图法分类号：TQ174　　文献标识码：A　　文章编号：1000-985X(2015)10-2810-05

DOI:10.16553/j.cnki.issn1000-985x.2015.10.031

Effects of Sn-flux Content on the Electric Transmission Properties of Al-doped Sn-based Type-VIII Single Crystalline Clathrate

SHEN Lan-xian[1], *LI De-cong*[2], *LIU Hong-xia*[1], *LIU Zu-ming*[1], *DENG Shu-kang*[1]

(1. Key Laboratory of Renewable Energy Advanced Materials and Manufacturing Technology, Ministry of Education, Yunnan Provincial Renewable Energy Engineering Key Lab, Solar Energy Research Institution, Yunnan Normal University, Kunming 650500, China; 2. College of Optoelectronic Engineering, Yunnan Open University, Kunming 650500, China)

(*Received* 18 *March* 2015, *accepted* 25 *July* 2015)

Abstract: The Al-doped type-VIII Sn-based single crystalline clathrate $Ba_8Ga_{10}Al_6Sn_x$ (x = 40, 50, 60; Sn40, Sn50, Sn60) were grown by Sn-flux method, and the effects of Sn starting content on the structure and electronic properties of the clathrates $Ba_8Ga_{10}Al_6Sn_x$ were investigated. The research results show that the Al actual content in the samples almost keep invariable with the increase of Sn starting content, which suggests that the effects of the starting content of Sn on the solid solubility of Al in the samples is very unconspicuous; At room temperature, Sn60 sample has higher carrier concentration, this may be due to the difference of the location and distribution of Al atomic in compound $Ga_8Ga_{16}Sn_{30}$, and which leads to differences in density of States near the Fermi. In addition, in 300-600 K Sn50 sample has higher power factor, and Sn40 samples has lower power factor due to the higher resistivity, and a maximum power

收稿日期：2015-03-18；修订日期：2015-07-25

基金项目：国家自然科学基金(51262032)

作者简介：申兰先(1978-)，女，云南省人，博士研究生，助理研究员。

通讯作者：邓书康，教授。E-mail：skdeng@126.com

factor of 1.82×10^{-3} W·m^{-1}·K^{-2} for Sn50 is obtained at about 488 K.

Key words: type-VIII clathrate; Sn-based clathrate; electronic property

1　引　　言

自从 Slack 提出“声子玻璃-电子晶体”(PGEC)概念以来,基于这种概念的材料引起热电领域研究学者们强烈的兴趣,而 Sn 基笼合物 $Ba_8Ga_{16}Sn_{30}$ 正是具有 PGEC 结构的典型代表之一[1-3],即 $Ba_8Ga_{16}Sn_{30}$ 的传热性能像玻璃,而导电性能像晶体。自 2000 年发现 Sn 基笼合物 $Ba_8Ga_{16}Sn_{30}$ 存在 I 型和 VIII 型两种结构以来,人们就不断探索如何提高该笼合物的热电转换效率,为此,大多数研究者通过框架原子部分取代、改变框架原子的比例或者通过掺杂的方式改善 Sn 基笼合物的热电性能。到目前为止,研究者们采用 Cu、Al、Sb、Ge、Mg 等元素对框架原子进行部分取代或者掺杂研究,在制备方法上,多采用 Sn 自熔剂法、Ga 自熔剂法及 Ga 和 Sn 双自熔剂法,其中通过 Sn 自熔剂法分别制得的 Cu、Al、Ge 掺杂的 $Ba_8Ga_{16}Sn_{30}$ VIII 型笼合物获得较高 ZT 值[4-11]。研究表明,Sn 自熔剂法能够获得性能较好的 n 型单晶 VIII 型笼合物 $Ba_8Ga_{16}Sn_{30}$,通过改变 Ga 和 Sn 含量比值能对其载流子类型和浓度进行调制;通过 Sn 自熔剂法,当 Sn 的起始含量为 50 而制备的 Al 掺杂 n 型传导的单晶笼合物 $Ba_8Ga_{16-x}Al_xSn_{30}$,在载流子浓度变化不大的情况下,材料的电导率显著提高,$Ba_8Ga_{10}Al_6Sn_{30}$ 在 500 K 获得最大 ZT 值 1.2[9]。迄今为止,$Ba_8Ga_{10}Al_6Sn_{30}$ 笼合物的电传输特性对自溶剂 Sn 起始量的依赖关系未见报道。为此,本文将研究 $Ba_8Ga_{10}Al_6Sn_x$ 单晶笼合物结构和电传输特性随自溶剂 Sn 初始含量的变化关系。

2　实　　验

VIII 型 Sn 基单晶笼合物 $Ba_8Ga_{10}Al_6Sn_x$ 样品制备采用 Sn 自熔剂法。采用高纯单质 Al(块状,99.999%)、Sn(块状,99.999%)、Ba(块状,99.9%)和 Ga(块状,99.999%),按 Ba: Ga: Al: Sn = 8: 10: 6: x (x = 40,50,60;Sn40,Sn50,Sn60)的原子比称量后放入石英玻璃管内,抽真空后密封,并将密封的石英管放入箱式高温炉内。样品的合成条件为:经 3 h 升温到 763 K(即升温速率为 2.57 K/min),在此温度保温 10 h,然后经 50 h(即 2 K/h 的速率)缓慢降温到 663 K,在该温度下取出装有样品的石英玻璃管采用离心法将过量 Sn 从单晶中分离。

样品的相组成采用 X 射线衍射仪(XRD,日本理学 Ul tima IV)进行表征;样品的各元素实际含量通过电子探针微观分析(EPMA,JXA-8230)获得;在真空下测试样品的电阻率 和 Seebeck 系数 α,测试的温度范围为 300 ~ 600 K;室温下样品的 Hall 系数通过直流法测得,磁场强度为 1 T。

3　结果与讨论

3.1　样品结构及含量分析

表 1 为所制备样品的各元素实际含量及室温下的电性能参数。从含量上看,各元素在单晶中的实际含量基本符合 $Ba_8Ga_{10}Al_6Sn_{30}$,尽管 Sn 的含量比理想值 30 稍多,Ga 和 Al 的含量之和比理想值 16 稍小,但框架元素总含量仍然在 46 附近。从表中还可看出,当 Sn 熔剂的初始含量增加时,Al 在样品中的实际含量基本不变,同时晶格常数变化不大,说明 Sn 起始含量对 Al 在该笼合物中固溶度无显著影响。之前研究表明[9-11],无论是 Sn 自熔剂法(Sn 过量)还是 Ga 自熔剂法(Ga 过量)所制备的 Ga 位(或 Sn 位)掺杂的 $Ba_8Ga_{16}Sn_{30}$ 单晶化合物,Ga 位和 Sn 位框架原子比基本接近 16/30(III 族原子与 IV 族原子的比例),表明过量 Ga 与过量 Sn 只是提供笼合物单晶的合成环境,而对框架原子的总量没有显著的影响。本文采用 Sn 自溶剂法合成笼合物时,保持 Ga 和 Al 的起始含量不变,改变 Sn 的起始含量,这将导致材料合成过程中体系热力学和动力学环境发生变化,以至材料的合成速率、各原子的迁移路径及所经过的亚稳中间相发生改变,因而在体系热力学及动力学共同作用下各元素成分含量由于自补偿效应最终使得(Ga + Al)/Sn 接近 16/30,总的框架原子之和接近 46。另外,在 VIII 型结构笼合物的框架上有 2a,8c,12d 和 24g 四种位置,材料合成环境的改

变可能导致框架上三种原子的占位发生了重排，而框架原子的重排会导致材料的电子结构空间拓扑性发生变化，从而会影响材料的热电性能。

图 1 所示为不同 Sn 起始含量即 Sn40、Sn50 和 Sn60 样品的断面抛光扫描电镜图，样品尺寸均为 5 mm 以上，从图上可知，扫描范围内样品均为较好单晶材料，说明 Sn 含量的变化宏观上对样品的晶体质量无明显影响。样品 Sn40、Sn50、Sn60 的粉末 XRD 图谱如图 2 所示。从图中可看出，三个样品的衍射峰与 VIII 型 Sn 基笼合物（空间群为 $I\bar{4}3m$）典型的衍射峰有微小差别，即图中 $2\theta = 32°$ 附近出现的微弱衍射峰，这是因为样品表面粘附有未完全分离的自熔剂 Sn 引起的。

表 1 Sn40（a）、Sn50（b）、Sn60（c）样品中各元素的实际含量及室温下的电性能参数

Table 1 Crystal composition and their electronic properties of the sample Sn40, Sn50 and Sn60

Sample	Crystal composition	(Ga + Al) /Sn	$n/10^{19}$ cm^{-3}	a/nm	ρ/mΩ · cm	H/cm^2 · V^{-1} · s^{-1}	R_H/cm^3 · C^{-1}	Effective mass m^* /m_0
Sn40	$Ba_{7.99}Ga_{10.20}Al_{5.66}Sn_{30.18}$	15.86/30.18	6.65	11.629	5.34	17.73	-9.39×10^{-2}	0.89
Sn50	$Ba_{8.02}Ga_{10.18}Al_{5.67}Sn_{30.18}$	15.85/30.18	5.88	11.626	3.83	27.75	-10.61×10^{-2}	0.78
Sn60	$Ba_{8.08}Ga_{10.00}Al_{5.81}Sn_{30.15}$	15.81/30.15	9.43	11.623	3.45	19.21	-6.62×10^{-2}	0.87

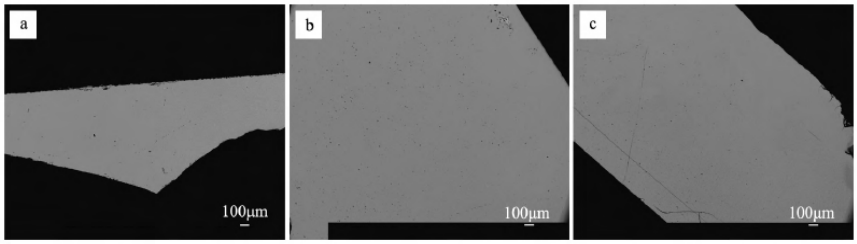

图 1 Sn40、Sn50 和 Sn60 样品的断面扫描电镜图（a）Sn = 40；（b）Sn = 50；（c）Sn = 60

Fig. 1 SEM images of cross section for the sample Sn40, Sn50 and Sn60

3.2 电传输特性

从热电材料热电性能的 ZT 表达式，即

$$ZT = \alpha^2\sigma T/\kappa$$

可知，材料 ZT 的大小取决于材料的 Seebeck 系数 α、电导率 σ 和热导率 κ，而 ZT 值越高说明材料及器件热电转换效率就越高。因此，高功率因子 P（$P = \alpha^2\sigma$）和低热导率 κ 是保证材料具有高性能的关键。本论文中，由于所制备样品尺寸不能满足测试热导率的尺寸要求，因而本文仅对其电传输特性进行研究。Seebeck 系数可用如下式表示，即

$$\alpha = \frac{\mathrm{d}V}{\mathrm{d}T} = -\frac{k}{e}\left[\frac{(2+\ln\frac{N_c}{n})n\mu_n - (2+\ln\frac{N_v}{p})p\mu_p}{n\mu_n + p\mu_p}\right]$$

p、n 型半导体的 Seebeck 系数分别表示为

$$\alpha = \frac{\mathrm{d}V}{\mathrm{d}T} = -\frac{k}{e}(2+\ln\frac{N_c}{n})$$

$$\alpha = \frac{\mathrm{d}V}{\mathrm{d}T} = \frac{k}{e}(2+\ln\frac{N_v}{p})$$

从上面的表达式可看出，p 型半导体的 Seebeck 系数为正，n 型的为负，表明 Seebeck 系数可以用来判断导电类型、热电转换效率及测量温度等。

图 3 为 Sn40、Sn50、Sn60 样品的 Seebeck 系数随温度 T 的变化关系。由图 3 观察到三个样品的 Seebeck 系数均为负值，表 1 中给出的霍尔系数也为负值，均说明所制备样品为 n 型半导体。对于 $Ba_8Ga_{16}Sn_{30}$ 化合物，其框架原子的能带结构主要由 Ga 和 Sn 通过 sp^3 轨道杂化而成，因此框架原子形成的能带结构中由于 Ga 原子的引入而存在缺少电子的轨道，这种缺少电子的轨道由填充原子捐献电子而补偿。当框架上有 16 个 Ga 原子时，

缺少的 16 个电子刚好由 8 个碱土金属填充原子提供的 16 个电子所补偿,此时对应的笼合物是一种理想状态的高补偿本征半导体。如果 III 族原子与 VI 族原子比值大于 16/30,在框架中就有缺少电子的轨道,对应的化合物是 p 型半导体;反之,如果 III 族原子与 VI 族原子比值小于 16/30,则是 n 型导电[12]。由表 1 可以看出(Ga + Al)/Sn 的值小于 16/30,所以电子是多子空穴是少子,从而表现出了 n 型导电。在测量温度范围内(300 ~ 600 K),随着温度的增加,所有样品的 Seebeck 系数绝对值均单调递增,但是当温度高于 540 K 以后 Seebeck 系数的绝对值变化较平缓,这是由于高温下本征激发开始发生,从而出现电子和空穴的双模式传导,这种混合传导模式导致 Seebeck 系数绝对值增加缓慢。从图 3 中可以看出,室温下,Sn 起始含量为 40 的 Seebeck 系数绝对值最大(其值为 252 μV/K),Sn 起始含量为 60 的 Seebeck 系数绝对值最小(其值为 207 μV/K)。研究表明[13,14],若忽略散射因子,Seebeck 系数的变化决定于材料的载流子浓度和有效质量,即 Seebeck 系数正比于材料的有效质量,反比于载流子浓度。本文测量了室温下样品的霍尔系数,根据公式 $n = -1/(qR_H)$ (q 为电子电量,R_H 为霍尔系数)和 $\mu_H = \sigma|R_H|$ 计算了样品的载流子浓度和迁移率(见表 1)进一步研究其电传输特性。从表 1 中可以看出,当 Sn 的起始含量为 60 时(即样品 Sn60)载流子浓度较高,因此其 Seebeck 系数较低。通过样品的载流子浓度和 Seebeck 系数估算的样品有效质量(其值分别为 0.89、0.78、0.87,见表 1)相差不大,说明上述样品 Seebeck 系数的变化主要由材料的载流子浓度变化所致。

图 4 所示为 Sn40、Sn50、Sn60 样品的电阻率 ρ 与温度 T 的关系。所有样品在温度 300 ~ 600 K 范围内电阻率都随温度的增加而增加,表现出典型的重掺杂半导体行为。Sn50 和 Sn60 样品的电阻率变化不大,而 Sn40 样品的电阻率显著升高,这是由于该样品的载流子浓度及其迁移率均较低所致。

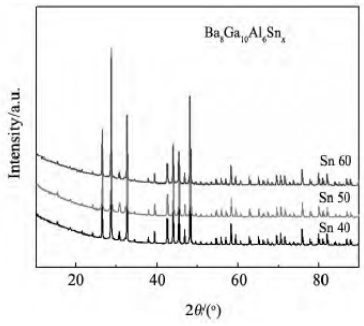

图 2　Sn40、Sn50、Sn60 样品的粉末 XRD 图谱

Fig. 2　XRD patterns for the sample Sn40, Sn50 and Sn60

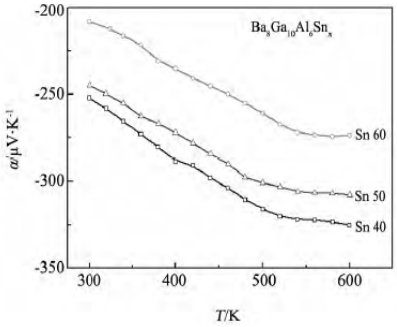

图 3　Sn40、Sn50、Sn60 样品的 Seebeck 系数与温度的关系

Fig. 3　Seebeck coefficient as a function of temperature for the sample Sn40, Sn50 and Sn60

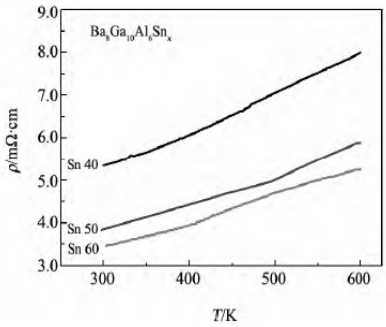

图 4　Sn40, Sn50 和 Sn60 样品的电阻率 ρ 与温度的关系

Fig. 4　Temperature dependence of electrical conductivity for the sample Sn40, Sn50 and Sn60

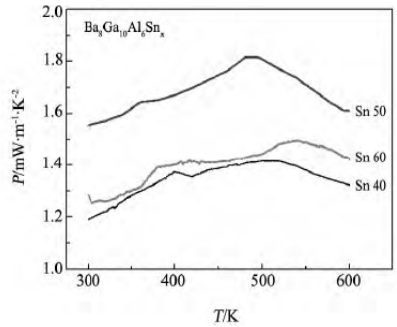

图 5　Sn40, Sn50 和 Sn60 样品的功率因子 P 与温度 T 的关系

Fig. 5　Temperature dependence of power factor for the sample Sn40, Sn50 and Sn60

另外,从表 1 可看出自溶剂 Sn 含量的改变对 Al 的实际含量影响不大(Al 的实际含量分别为 5.66、5.

67、5.81)，但室温下，与 Sn40、Sn50 相比较，Sn60 样品的载流子浓度较高，这是可能是由于 Sn 起始含量的改变引起材料合成的动力学环境和热力学环境发生变化，从而改变了笼合物框架上所有原子的重排，这种重排会导致电子结构发生变化，从而影响材料的电导率。

图 5 给出了 Sn40、Sn50、Sn60 样品的功率因子 P 与温度的关系。从图中可知，当 Sn 的起始含量为 50 时（即 Sn50）对应的样品功率因子有最大值，在 488 K 附近为 1.82×10^{-3} W·m^{-1}·K^{-2}，而 Sn40 的样品由于电阻率较高，因此其功率因子最低。

4 结 论

探索自溶剂 Sn 的起始含量的改变对 VIII 型 Sn 基单晶笼合物 $Ba_8Ga_{10}Al_6Sn_x$ ($x=40,50,60$) 的结构性质的影响，并研究单晶笼合物热电传输特性对 Sn 自熔剂起始含量的依赖关系。结果表明，对不同 Sn 起始含量的样品，Al 的实际含量基本不变，同时晶格常数变化不大，说明 Sn 起始含量对 Al 在该笼合物中固溶度无显著影响；所有样品在测试温度范围内均表现出 n 型传导特性，样品 Seebeck 系数绝对值和电阻率均随着温度的升高逐渐增大，样品表现出重掺杂半导体特性。当自溶剂 Sn 的起始含量为 60 时（Sn60）具有较高的载流子浓度，这是可能是由于 Sn 起始含量的改变引起材料合成的动力学环境和热力学环境发生变化，从而改变了笼合物框架上所有原子的重排，这种重排会导致电子结构发生变化，从而影响材料的电导率；结果表明：在 300～600 K 温度范围内，Sn 起始含量为 50 的样品具有较高的功率因子，在 488 K 处获得最大值 1.82×10^{-3} W·m^{-1}·K^{-2}，而 Sn40 样品由于较高的电阻率导致了较低的功率因子。

参 考 文 献

[1] Kahn D, Lu J P. Structural Properties and Vibrational Modes of Si_{34} and Si_{46} Clathrates [J]. *Physical Review B*, 1997, **56**: 13898.

[2] Cahill D G, Watson S K, Pohl R O. Lower Limit to The Thermal Conductivity of Disordered Crystals [J]. *Physical Review B*, 1992, **46**: 6131.

[3] Hermann R P, SchweikaW, LeupoldO, et al. Neutron and Nuclear Inelastic Neutron and Nuclear Inelastic Scattering Study of the Ba-, Sr-, and Eu-filled Germanium Clathrates [J]. *Physical Review B*, 2005, **72**: 174301.

[4] Melinon P, Keghelian P, Blase X, et al. Electronic Signature of the Pentagonal Rings in Silicon Clathrate Phases: Comparison with Cluster-assembled Films [J]. *Physical Review B*, 1998, **58**: 12590.

[5] Tournus F, Masenelli B, and Melinon P. Guest Displacement in Silicon Clathrates [J]. *Physical Review B*, 2004, **69**: 035208.

[6] Fang S L, Grigorian L, and Eklund P C, et al. Raman Scattering from Vibrational Modes in Si_{46} Clathrates [J]. *Physical Review B*, 1998, **57**: 7686.

[7] Guyot Y, Grosvalet L, Champagnon B. Gruneisen Parameters for Silicon Clathrates Determined by Raman Scattering [J]. *Physical Review B*, 1999, **60**: 14507.

[8] Beekman M. Synthesis and Transport Properties of Type II Clathrates [A]. 2005. Clemson, SC, United States: Institute of Electrical and Electronics Engineers Inc. [C]. Piscataway, NJ 08855-1331, United States.

[9] Deng S K, Saiga Y, Suekuni K, et al. Enhancement of Thermoelectric Efficiency in Type-VIII Clathrate $Ba_8Ga_{16}Sn_{30}$ by Al Substitution for Ga [J]. *J. Appl. Phys.*, 2010, **108** (7): 073705.

[10] Deng S K, Saiga Y, Kajisa K, et al. High Thermoelectric Performance of Cu Substituted type-VIII Clathrate $Ba_8Ga_{16-x}Cu_xSn_{30}$ Single Crystals [J]. *J. Appl. Phys.*, 2011, **109** (10): 103704.

[11] 孟代仪，申兰先，晒旭霞，等. Ge 掺杂 n 型 Sn 基 VIII 型单晶笼合物的制备及热电传输特性 [J]. 物理学报，2013，**62** (24)：247401 1-5.
Meng D Y, Shen L X, Shai X X, et al. Growth and Thermoelectric Properties of Ge Doped n-type Sn-based Type-VIII Single Crystalline Clathrate [J]. *Acta Physica Sinica*, 2013, **62** (24): 247401 1-5.

[12] 李德聪. Ge 基及 Sn 基笼合物的制备、结构及热电特性研究 [D]. 重庆：重庆大学博士学位论文，2012.
Li D C. The Study on Preparation, Structure and Thermoelectristics in Ge- and Sn-Based Clathrates Materials [D]. Chongqing: Doctoral Thesis of Chongqing University, 2012.

[13] Bentien A, Ph. D thesis [M]. Max-Planck-Institut f˙ur Chemishe Physik Fester Stoffe, Dresden (2004).

[14] Snyder G J. Complex Thermoelectric Materials [J]. *Nat Mater*, 2008, (7): 105-114.

第44卷 第1期 人 工 晶 体 学 报 Vol. 44 No. 1
2015年1月 JOURNAL OF SYNTHETIC CRYSTALS January, 2015

衬底温度对磁控共溅射制备的Zn(O,S)薄膜结构和光电性能的影响

彭柳军[1,2],杨 雯[1,2],陈小波[1,2],自兴发[1,2],杨培志[1,2],宋肇宁[3]

(1. 云南师范大学可再生能源材料先进技术与制备教育部重点实验室,昆明 650092;
2. 云南师范大学太阳能研究所,昆明 650092;3. 美国托莱多大学物理与天文系,托莱多 43606)

摘要:采用磁控共溅射沉积法,以氧化锌和硫化锌为靶材,在不同衬底温度下制备了Zn(O,S)薄膜。采用X射线衍射仪、原子力显微镜、紫外-可见-近红外分光光度计、霍尔测试仪和拉曼光谱测试仪对Zn(O,S)薄膜进行了结构和光电特性研究。结果表明:Zn(O,S)薄膜具有六方纤锌矿结构,属于二模混晶;在可见-近红外波段的吸收率小于5%;其为N型半导体,电学特性随衬底温度的变化而变化;衬底温度为200 ℃时制备的厚度为167 nm的Zn(O,S)薄膜的载流子浓度达到8.82×10^{19} cm^{-3},迁移率为19.3 $cm^2/V\cdot s$,表面呈金字塔结构。

关键词:Zn(O,S)薄膜;磁控共溅射;衬底温度;光电性能

中图分类号:O484 文献标识码:A 文章编号:1000-985X(2015)01-0038-05

Effect of Substrate Temperature on Structure and Photoelectric Properties of Zn(O,S) Thin Films Deposited by Magnetron Co-sputtering

PENG Liu-jun[1,2], *YANG Wen*[1,2], *CHEN Xiao-bo*[1,2], *ZI Xing-fa*[1,2], *YANG Pei-zhi*[1,2], *SONG Zhao-ning*[3]

(1. Key Laboratory of Advanced Technique and Preparation for Renewable Energy Materials, Ministry of Education, Yunnan Normal University, Kunming 650092, China; 2. Solar Energy Research Institute, Yunnan Normal University, Kunming 650092, China;
3. Department of Physics and Astronomy, University of Toledo, Toledo 43606, USA)

(*Received* 12 *September* 2014, *accepted* 27 *October* 2014)

Abstract: Zn(O,S) thin films were deposited by magnetron co-sputtering using ZnO and ZnS as targets under different substrate temperature. The structure, optical and electrical properties of films were studied by means of XRD, AFM, Raman spectrometer, UV-Vis-NIR spectrophotometer and Hall measurement system. The results show that these films are two-mode mixed crystals with a hexagonal wurtzite structure; the optical absorption of the films is lower than 5% in the range of visible to near-infrared spectral region; they are n-type semiconductors, and the electrical properties of them were obviously different with different sputtering substrate temperature; the carrier concentration and hall mobility of the film with 167 nm thickness deposited under 200 ℃ is 8.82×10^{19} cm^{-3} and 19.3 $cm^2/V\cdot s$, respectively, and the film has a pyramid shaped surface structure.

Key words: Zn(O,S) thin film; magnetron co-sputtering; substrate temperature; photoelectric property

收稿日期:2014-09-12;修订日期:2014-10-27

基金项目:国家自然科学基金(U1037604)

作者简介:彭柳军(1983-),男,江西省人,硕士研究生。E-mail: pengdinghui@foxmail.com

通讯作者:杨培志,研究员,博士生导师。E-mail:pzhyang@hotmail.com

1 引　　言

铜铟镓硒(CIGS)薄膜太阳电池由于具有转换效率高和弱光性能好等优点,近年来受到人们的极大关注。典型的 CIGS 太阳电池结构为:衬底/背电极/吸收层(CIGS)/缓冲层/窗口层/前电极。目前 CIGS 太阳电池的规模生产大都采用化学水浴法(CBD)制备硫化镉(CdS)缓冲层。然而,CdS 有毒、不环保;CBD "湿"法制备工艺与 CIGS 太阳电池的其他各层的真空"干法"制备工艺不匹配,不利于规模化流水线生产;生产过程中存在废液回收问题。此外,CdS 的禁带宽度为 2.4 eV,对波长在 300 ~ 500 nm 范围的太阳光有较强吸收,不利于吸收层对太阳光的充分利用[1]。因此,探索无镉缓冲层材料的"干法"制备成为人们的研究热点,其中磁控溅射方法由于是一种成熟的半导体薄膜制备方法而受到人们的重视[2]。目前,规模生产的 CIGS 太阳电池的窗口层通常采用磁控溅射法,吸收层大多采用共蒸发或共溅射后硒化法。因此,用磁控溅射制备缓冲层可减少 CIGS 太阳电池制备工艺种类,有利于流水线生产,从而降低 CIGS 太阳电池生产成本[1]。在无镉缓冲层材料的选择方面,从光学带隙、导带边失配以及与吸收层的结构匹配等因素综合考虑,ZnO、ZnS 和 Zn(O,S)进入人们的视野,其中 Zn(O,S)成为近来研究的热点。

国际上,日本的 Showa Shell SekiyuK. K. 旗下的 Solar Frontier[3] 采用 CBD 法沉积的 Zn(O,S)薄膜作为缓冲层的 CIGS 太阳电池的光电转换效率达到了 19.7%,Okamoto 等[5] 实验研究了采用不同的氧、硫组分配比制备 Zn(O,S)薄膜来调节半导体的电子亲和势和光学带隙;瑞典乌普萨拉大学[6] 采用原子层沉积(ALD)制备的 Zn(O,S)薄膜作为缓冲层的 CIGS 太阳电池获得了 18.5% 的光电转换效率;美国可再生能源实验室(NREL)[7] 采用反应溅射制备的 Zn(O,S)缓冲层的 CIGS 太阳电池获得了 13% 的光电转换效率,科罗拉多州立大学物理系 Shabati 教授等研究人员[8] 对 CIGS 太阳电池的 Zn(O,S)缓冲层进行了理论研究,获得了不同 O/O + S 配比的 Zn(O,S)缓冲层与 CIGS 吸收层之间的导带边失配与 CIGS 太阳电池理论效率的关系;德国柏林的亥姆霍兹国家研究中心联合会[4] 取得了突破性进展,其采用单靶溅射 ZnS 和 ZnO 的混合物陶瓷靶制备的 Zn(O,S)缓冲层的 CIGS 太阳电池获得了 18.3% 的光电转换效率。国内目前对磁控共溅射制备 Zn(O,S)薄膜的研究鲜见报道。在磁控溅射制备薄膜的过程中,衬底温度是影响薄膜性能的重要因素,而 Zn(O,S)薄膜的结构和光电性质又决定着其作为 CIGS 太阳电池缓冲层的效果。因此,有必要深入研究衬底温度对 Zn(O,S)薄膜的结构和光电性能的影响。本文采用磁控共溅射方法,在不同衬底温度下制备了 Zn(O,S)薄膜,并对其结构和光电性能进行了研究。

2 实　　验

2.1 Zn(O,S)薄膜的制备

本实验采用磁控共溅射沉积法制备 Zn(O,S)薄膜。所用 ZnS 靶和 ZnO 靶纯度均为 99.99%。衬底温度分别为:室温(25 ℃)、100 ℃、200 ℃和 300 ℃。为了制备与 CIGS 太阳电池吸收层匹配的具有理想组分比(O/O + S)的 Zn(O,S)薄膜,溅射 ZnO 靶采用的脉冲电源功率为 60 W,溅射 ZnS 靶采用的射频电源的功率为 20 W,本底压强为 0.5 Pa,工艺参考了文章《溅射气压对硼掺杂 ZnO 薄膜光电特性的影响》[9],溅射时间为 30 min。

2.2 样品的性能表征

采用 Rigaku TTR III 型 X 射线衍射仪(XRD)表征 Zn(O,S)薄膜的物相结构;采用 SPA400 型原子力显微镜(AFM)表征薄膜的表面形貌;采用英国 RENISHAW 公司 INVIA 共焦显微拉曼光谱仪表征薄膜的晶相与组分;采用 Hitachi4100 型紫外-可见光(UV-vis)分光光度计表征其光学吸收特性;采用椭圆偏振仪测试薄膜的厚度;采用 Crosstech HMS300 霍尔测试仪测试薄膜的电阻率、载流子浓度和霍尔迁移率等电学参数。

3 结果与讨论

3.1 衬底温度对薄膜结构特性的影响

图 1 为不同衬底温度下沉积的 Zn(O,S) 薄膜的 XRD 图谱。由图可见，各衬底温度下生长的 Zn(O,S) 薄膜均为多晶薄膜，具有六方纤锌矿结构(α 相)，且呈 c 轴择优取向生长，与单靶溅射的 ZnO 薄膜的相结构相同，但不同于单靶溅射的闪锌矿结构的 ZnS 薄膜。

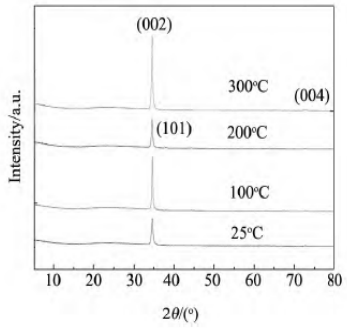

图 1 不同衬底温度下沉积的 Zn(O,S) 薄膜的 XRD 图谱

Fig. 1 XRD patterns of Zn(O,S) thin films deposited at different substrate temperatures

位于 34.62°、36.74°和 72.74°的衍射峰分别对应于(002)、(101)和(004)晶面。其中，(002)晶面衍射峰最强，表明薄膜沿(002)晶面取向生长。随着衬底温度的增加，(002)晶面衍射峰逐渐增强，衬底温度为 200 ℃时还出现了微弱的(101)晶面的衍射峰，可能与 Zn(O,S) 薄膜取向生长减弱有关。不同衬底温度下生长的薄膜都出现了微弱的(004)晶面衍射峰，且强度随衬底温度的升高而增强。通常，随着衍射峰的增强，半高宽下降，晶粒尺寸增大。

由 X 射线衍射谱峰位衍射角可计算薄膜的晶面间距，计算公式如下：

$$2d_{hkl} \cdot \sin\theta = n\lambda \tag{1}$$

式中，d_{hkl} 为晶面间距，θ 为衍射角，n 为衍射级数，λ 为 X 射线波长，采用铜靶的衍射仪取 0.15406 nm。

对于六方纤锌矿结构晶体，根据其衍射峰峰位对应的晶面指数还可计算出晶格常数，计算公式如下：

$$d_{hkl} = \frac{1}{\sqrt{\frac{4}{3}\left(\frac{h^2+hk+k^2}{a^2}\right)+\left(\frac{l}{c}\right)^2}} \tag{2}$$

根据(1)式和(2)式，可算出六方纤锌矿结构的 Zn(O,S) 的晶面间距及其晶格常数，结果由表 1 给出。表 1 中 θ 为衍射角，d 为晶面间距，a、c 为晶格常数，下标表示晶面指数，从表 1 中可见：衬底温度为 200 ℃时制备的薄膜的晶格常数最大，与太阳电池吸收层的晶格失配度最小；衬底温度为 300 ℃时制备的 Zn(O,S) 薄膜除(002)晶面的衍射峰外，还有较弱的(004)晶面衍射峰，因此，算出的晶格常数 c 有偏差，说明过高的衬底温度可能导致薄膜晶格发生畸变。

表 1 不同衬底温度下制备 Zn(O,S) 薄膜的晶格常数

Table 1 The lattice constants of Zn(O,S) thin films deposited at different substrate temperatures

T_{sub}/℃	$2\theta_{(002)}$/(°)	$d_{(002)}$/nm	c/nm	$2\theta_{(101)}$;$2\theta_{(004)}$/(°)	$d_{(101)}$; $d_{(004)}$/nm	a;c/nm
25	34.62	0.25888	0.51776	/	/	/
100	34.66	0.25859	0.51718	$36.84_{(101)}$	$0.24377_{(101)}$	0.32503
200	34.58	0.25917	0.51834	$36.74_{(101)}$	$0.24441_{(101)}$	0.32589
300	34.6	0.25903	0.51805	$72.74_{(004)}$	$0.12989_{(004)}$	0.51958

图 2 是不同衬底温度下沉积的 Zn(O,S) 薄膜的表面形貌图。可以看出：衬底温度对薄膜表面形貌影响很大。衬底温度较低时，薄膜表面颗粒较小，这主要是由于衬底表面吸附原子的扩散速率和扩散能低，随着衬底温度升高，衬底表面吸附原子获得了足够的能量扩散到平衡位置，晶粒尺寸增大，薄膜结晶质量改善。从形貌上看，不同衬底温度下生长的薄膜均较致密，可满足缓冲层材料的要求。为了更好地与吸收层结合，要求薄膜表面平坦，粗糙度小。表 2 列出了 Zn(O,S) 薄膜粗糙度的均方根值(RMS)。衬底温度为常温时沉积的薄膜表面粗糙度的均方根值 RMS 最小，最平坦；100 ℃时沉积的薄膜的表面粗糙度最大；温度继续升高界面缺陷减少，表面粗糙度下降。其中(c)图衬底温度为 200 ℃时沉积的薄膜表面呈现了金字塔结构，减反效果好，可做减反层材料[10]，同时也非常致密，能对吸收层有良好的包覆性，适合做 CIGS 太阳电池的缓冲层。

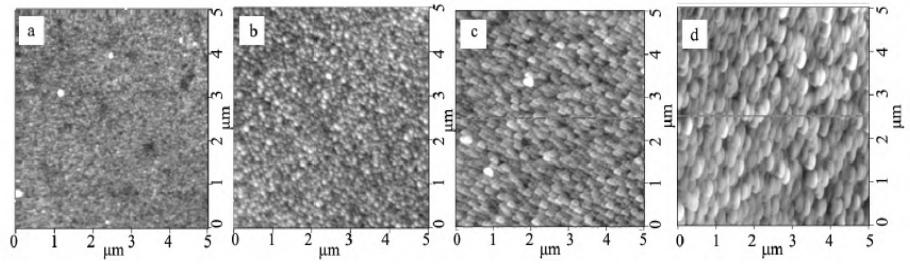

图 2　不同衬底温度下 Zn(O,S) 薄膜的 AFM 表面形貌图 (a) 常温;(b) 100 ℃;(c) 200 ℃;(d) 300 ℃

Fig. 2　AFM images of Zn(O,S) thin films deposited at different substrate temperatures

表 2　不同衬底温度下制备的 Zn(O,S) 薄膜的粗糙度

Table 2　RMS of Zn(O,S) thin films deposited at different substrate temperatures

Substrate temperature	RMS Roughness/nm
(a) 25℃	1.517
(b) 100℃	4.957
(c) 200℃	2.647
(d) 300℃	2.913

图 3 是不同衬底温度下沉积的 Zn(O,S) 薄膜的拉曼谱。从图中可以看出,衬底温度为 25 ℃下制备的 Zn(O,S) 薄膜的谱图中出现了 104 cm^{-1}、444.6 cm^{-1}、569.9 cm^{-1} 三个峰位,与纤锌矿结构的纯 ZnO 的 101 cm^{-1}、444 cm^{-1}、579 cm^{-1} 三个峰位相对应,前两个峰位有蓝移,第三个峰略有红移。随着温度的升高,拉曼频移峰位略有蓝移,可能是衬底温度升高导致的薄膜内部应力的差异所致。衬底温度为 25 ℃下制备的 Zn(O,S) 薄膜的拉曼光谱还出现了微弱的 58 cm^{-1}、281 cm^{-1}、356 cm^{-1} 三个峰[9],与纤锌矿结构的 ZnS 拉曼峰位相对应,随着衬底温度的升高,三个峰位都有蓝移,这也可能是应力差异所引起。Zn(O,S) 薄膜同时存在两套独立的光学模,且其频率分别接近于两种纯晶体的拉曼光谱频移峰,说明其为二模混晶,即属于集团模型。上述结果表明:薄膜为六方纤锌矿结构的 ZnO 和 ZnS 的混合多晶薄膜,其中由于 ZnO 所占比例较大,因此对应于 ZnO 的峰位强度远大于 ZnS 的峰位强度。图中各薄膜样品在 1121 ~ 1125 cm^{-1} 间的峰对应于 II-VI 族化合物半导体的双声子模的特征谱[10]。

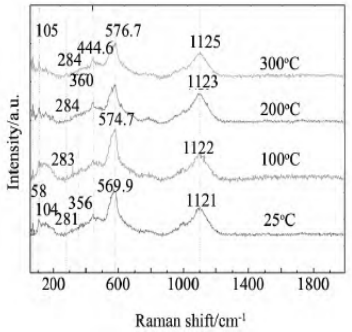

图 3　不同衬底温度下沉积的 Zn(O,S) 薄膜的拉曼谱

Fig. 3　Raman spectra of Zn(O,S) thin films deposited at different substrate temperatures

3.2　衬底温度对薄膜电学特性的影响

Zn(O,S) 薄膜通常为具有自补偿效应的 N 型半导体,衬底温度对 Zn(O,S) 薄膜的电学特性有显著影响。图 4 是 Zn(O,S) 薄膜的电阻率 ρ、载流子浓度 n 和迁移率 μ 随衬底温度变化的关系图。由图可知,薄膜的电阻率随衬底温度上升而呈先减小后增大的变化趋势,与薄膜沉积速率呈相同趋势,而霍尔迁移率的变化趋势则与此相反。

衬底温度从常温升高到 100 ℃时,溅射粒子获得足够大能量来形核、结晶,并且晶粒随之增大、晶界减少、结晶质量改善,载流子复合减少,迁移率增大;衬底温度继续升高到 200 ℃时,电阻率缓慢增大,迁移率缓慢减小,载流子浓度增加,这与其 AFM 的表面形貌特征相对应,表面平坦,载流子表面复合少,浓度大。另外随着衬底温度增加,Zn(O,S) 薄膜会逐渐偏离化学计量比,O 和 S 逸出使得计量比 Zn/(O,S) > 0.5,产生 Zn 间隙、O 空位、S 空位,由 Zn 间隙、O 空位、S 空位和 O、S 替代 Zn 位置产生的施主缺陷增加,因此 Zn(O,S) 薄膜为 N 型;当温度进一步升高到 300 ℃时,缺陷有可能增多,载流子容易在晶格畸变缺陷处被复合,载流子

浓度略有下降。载流子浓度越大，越有利于用作 CIGS 太阳电池的缓冲层，衬底温度为 200 ℃ 时制备的 Zn(O,S) 薄膜厚度为 167 nm，载流子浓度最高达到 8.82×10^{19} cm^{-3}，迁移率为 19.3 $cm^2/V\cdot s$。

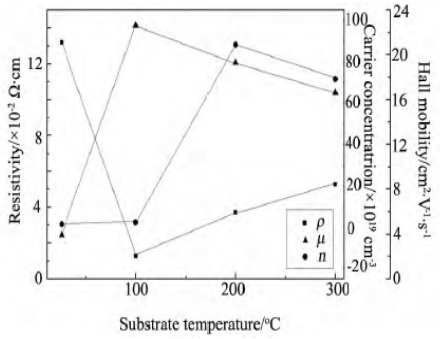

图 4 不同衬底温度下 Zn(O,S) 薄膜的电阻率 ρ、载流子浓度 n 和迁移率 μ

Fig. 4 Electrical resistivity ρ, carrier concentration n and hall mobility of Zn(O,S) thin films at different substrate temperatures

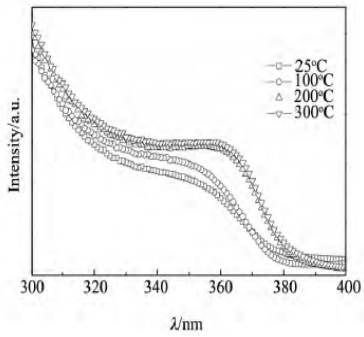

图 5 不同衬底温度下 Zn(O,S) 薄膜的吸收光谱

Fig. 5 Absorption spectra of Zn(O,S) films at different substrate temperature

3.3 衬底温度对薄膜光学特性的影响

不同衬底温度下沉积的 Zn(O,S) 薄膜的吸收光谱如图 5 所示。从图中可以看出，在可见光-近红外光范围内薄膜的吸收率均小于 5%；在紫外光范围，衬底温度为 25 ℃ 时沉积的 Zn(O,S) 薄膜的本征吸收强度最大，衬底温度升高到 100 ℃，其本征吸收率最低，吸收强度随衬底温度升高而增加，这与沉积速率变化导致的薄膜厚度的变化一致。此外，Zn(O,S) 薄膜的吸收边中间有明显的台阶，衬底温度越高，台阶越明显，这说明薄膜成分是 ZnS 和 ZnO 的混合物 Zn(O,S)，吸收边台阶处两边分别代表了 ZnO 和 ZnS 的吸收特性，与拉曼光谱一致。利用吸收率带边延长的方法可计算出 ZnO 和 ZnS 对应的光学带隙分别约为 3.18 eV 和 3.76 eV，随着温度的升高，吸收边略有红移，光学带隙略有减小，这可能与晶粒尺寸大小有关，晶粒尺寸小，量子尺寸效应明显，光学带隙变宽[10]。

4 结 论

用磁控共溅射制备的 Zn(O,S) 薄膜具有纤锌矿结构，属于二模混晶，是 N 型半导体，在可见-近红外光范围内，具有良好的透光率；衬底温度对其结构、表面形貌和光电性质均有影响。在衬底温度为 200 ℃ 时薄膜具有良好的光电特性：薄膜表面呈金字塔结构，有利于减反射；薄膜的载流子浓度最高，用作 CIGS 太阳电池缓冲层，能减小耗尽区厚度，提高结区对光生载流子的分离收集效率。这些结果可为“干法”制备优质 CIGS 太阳电池缓冲层材料提供指导。

参 考 文 献

[1] Naghavi N, Abou-Ras D, Allsop N. Buffer Layers and Transparent Conducting Oxides for Chalcopyrite Cu(In, Ga)(S, Se)$_2$ Based Thin Film Photovoltacics: Present Status and Current Developments [OL]. Prog Photovolt Res Appl, 2010.

[2] 叶志镇, 吕建国, 吕 斌, 等. 半导体薄膜技术与物理 [M]. 杭州: 浙江大学出版社, 2008: 34-63.

[3] Gifford J. Solar Frontier Achieves CIGS "Cells" at 19.7% [EB/OL]. http://www.pv-magazine.com/news/details/beitrag/solar-frontier-achieves-cigs-cells-at-197_100009746/#axzz3C31X60gb.

[4] Klenk R, Steigert A, Rissom T, et al. Junction Formation by Zn(O,S) Sputterting Yields CIGS-based Cells with Efficiencies Exceeding 18% [J]. *Progress in Photovoltaics*, 2014, **22**: 161-165.

[5] Okamoto A, Minemoto T, Takakura H. Application of Sputtered $Zn_{1-x}O_x$ Buffer Layers for Cu(In, Ga)Se_2 Solar Cells [J]. *Japanese Journal of Applied Physics*, 2011, **50**: 04DP10-1 - 04DP10-2.

[6] Zimmermann U, Ruth M, Edoff M. Cadmium-free CIGS Mini-modules with ALD-Grown Zn(O, S)-Based Buffer Layers [C]. 21st European Photovoltaic Solar Energy Conference, Germany, Dresden, 2006, **9**: 4-8.

（下转第 54 页）

Zhang Y B, Ding Y P, Gao J Q, et al. Study on the Process of Sol Gel Preparation of Continuous Mullite Fiber [J]. *Journal of Synthetic Crystals*, 2009, **38**(s): 203-206 (in Chinese).

[10] Okada K I Y, Yasohama S, Hayashi S et al. Sol-Gel Synthesis of Mullite Long Fibres from Water Solvent Systems [J]. *Journal of the European Ceramic Society*, 1998, **18**(13): 1879-1884.

[11] 付顺德, 徐建峰, 刘丽彬. 胶体粘度和纤维化工艺条件对80多晶氧化铝纤维性能的影响 [J]. 耐火材料, 2010, **44**(2): 116-118.
Fu S D, Xu J D, Liu L B. Influence of Colloidal Viscosity and Fibrosis Process Conditions on the Properties of 80 Polycrystalline Alumina Fiber [J]. *Refractory*, 2010, **44**(2): 116-118 (in Chinese).

[12] 王志明, 王 昊. Al_2O_3-SiO_2 胶体的红外吸收光谱分析 [J]. 玻璃纤维, 2000, **1**: 6-8.
Wang Z M, Wang H. Analysis of Infrared Absorption Spectra of Al_2O_3-SiO_2 Colloids [J]. *Glass Fiber*, 2000, **1**: 6-8 (in Chinese).

[13] 黄前军, 陈小军, 陈立富. 溶胶凝胶法制备多晶氧化铝纤维的研究 [J]. 厦门大学学报, 2006, **45**(3): 376-378.
Huang Q J, Chen X J, Chen L F. Study of the Sol-Gel Preparation of Polycrystalline Alumina Fibers [J]. *Journal of Xiamen University*, 2006, **45**(3): 376-378 (in Chinese).

[14] 李呈顺, 张玉军, 鹿成洪, 等. 钇铝石榴石纤维纺丝原液的制备及结构与流变性研究 [J]. 无机化学学报, 2009, **24**(4): 623-628.
Li C S, Zhang Y J, Lu C H, et al. Preparation, Structure and Rheological Behavior of Yttrium Aluminum Garnet Fiber Precursor [J]. *Chinese Journal of Inorganic Chemistry*, 2009, **24**(4): 623-628 (in Chinese).

[15] 吴其晔, 巫静安. 高分子材料流变学 [M]. 北京: 高等教育出版社, 2002: 8-10.

[16] 杨涛峰, 李瑶君, 陈大俊. 氨纶纺丝流体的流变性为 [J]. 弹性体, 2002, **12**(5): 37-39.
Yang T F, Li Y J, Chen D J. Rheological Properties of Fluid for Spandex Spinning [J]. *Elastomer*, 2002, **12**(5): 37-39 (in Chinese).

[17] 张耀明, 李巨白, 姜肇中. 玻璃纤维与矿物棉全书 [M]. 北京: 化学工业出版社, 2001: 20-24.

[18] 谢皮斯基. 纤维成形基本原理 [M]. 上海: 上海科学技术出版社, 1983: 35-38.

[19] 李呈顺, 张玉军, 张景德. 溶胶凝胶法制备多晶莫来石纤维 [J]. 无机材料学报, 2009, **24**(4): 849-852.
Li C S, Zhang Y J, Zhang J D. Polycrystalline Mullite Fiber Prepared by Sol-Gel Method [J]. *J. Inorg. Mater.* 2009, **24**(4): 849-852 (in Chinese).

[20] 史铁钧. 高分子流变学基础 [M]. 北京: 化学工业出版社, 2009: 27-30.

[21] Zhang Y B, Ding Y P, Gao J Q, et al. Millite Fibers Prepared by Sol-Gel Method Using Polyvinyl Butyral [J]. *Journal of the European Ceramic Society*, 2009, **29**: 1101-1107.

[22] Liu S, Liu J C, Du H Y, et al. Microstructure of Mullite Fiber-based Hierarchical Structures Adjusted by Al/Si Mole Ratio of the Raw Material Powders [J]. *Ceramic International*, 2014, **40**: 11405-11410.

(上接第42页)

[7] Ramanathan K, Mann J, Glynn S, et al. A Comparative Study of Zn(O,S) Buffer Layers and CIGS Solar Cells Fabricated by CBD, ALD, and Sputtering [C]. The 2012 IEEE Photovoltaic Specialists Conference, Austin, Texas, 2012, 1.

[8] Shabati S, James R. Impact of the Band Offset for n-Zn(O,S)/p-Cu(In,Ga)Se_2 Solar Cells [J]. *IEEE Journal of photovoltaics*, 2014, **4**(2): 3.

[9] 张光寅, 蓝国祥, 王玉芳. 晶格振动光谱学 [M]. 高等教育出版社, 2001.

[10] Ghosh P, Jana S, Nandy S, Chattopadhyay K. Size-dependent Optical and Dielectric Properties of Nanocrystalline ZnS Thin Films Synthesized via Rf-magnetron Sputtering Technique [J]. *Materials Research Bulletin*, 2007, **42**: 505-514.

[11] 黄焱球, 刘梅冬, 曾亦可. 氧化锌薄膜的拉曼光谱研究 [J]. 功能材料, 2002, **33**(6): 653-655.
Huang Y Q, Liu M D, Zeng Y K. Raman Spectroscopy Study of ZnO Thin Films [J]. *Journal of Functional Materials*, 2002, **33**(6): 653-655.

第44卷 第3期 人 工 晶 体 学 报 Vol. 44 No. 3
2015年3月 JOURNAL OF SYNTHETIC CRYSTALS March, 2015

化学浴沉积法制备ZnS薄膜的结构及可见-近红外光谱特性研究

刘 颖[1],缪彦美[1],郝瑞亭[1],郭 杰[1],杨海刚[2,3]

(1.云南师范大学太阳能研究所,可再生能源材料先进技术与制备教育部重点实验室,昆明 650500;
2.河南师范大学物理与电子工程学院,新乡 453007;3.华北电力大学可再生能源学院,北京 102206)

摘要:采用化学水浴法,以$ZnSO_4$、柠檬酸钠、$NH_3 \cdot H_2O$、$SC(NH_2)_2$为反应物,在玻璃衬底上制备了ZnS薄膜,采用XRD、SEM、分光光度计、台阶仪等手段研究了水浴温度、沉积时间、pH值等条件对ZnS薄膜的晶体结构、表面形貌、光学性能的影响。结果表明,ZnS薄膜经退火后出现明显特征衍射峰,为闪锌矿结构,可见光范围内平均透过率均大于80%。经过工艺优化,在水浴温度为80 ℃、沉积时间为1 h、pH=10条件下沉积的ZnS薄膜表面均匀致密,可见光范围内平均透过率为89.6%,光学带隙为3.82 eV,适合做铜铟镓硒和铜锌锡硫薄膜太阳电池的缓冲层。

关键词:ZnS薄膜;缓冲层;化学浴沉积;透过率

中图分类号:TM914.4+2 **文献标识码**:A **文章编号**:1000-985X(2015)03-0610-06

Structures and Visible-near Infrared Spectral Properties of ZnS Thin Films Prepared by Chemical Bath Deposition

LIU Ying[1], *MIAO Yan-mei*[1], *HAO Rui-ting*[1], *GUO Jie*[1], *YANG Hai-gang*[2,3]

(1. Key Laboratory of Renewable Energy Advanced Materials and Manufacturing Technology, Ministry of Education, Institute of Solar Energy, Yunnan Normal University, Kunming 650500, China; 2. College of Physics and Electronic Engineering, Henan Normal University, Xinxiang 453007, China; 3. Institute of Renewable Energy, North China Electric Power University, Beijing 102206, China)

(*Received* 30 *November* 2014, *accepted* 25 *December* 2014)

Abstract: Zinc sulfide thin films were deposited on glass substrates by chemical bath deposition, using $ZnSO_4$, sodium citrate, $NH_3 \cdot H_2O$ and $SC(NH_2)_2$ as reactants. The influence of deposition temperature, deposition time and pH value on the structures, the surface morphologies and the optical properties of ZnS thin films were studied by XRD, SEM, spectrophotometer, and step tester. The results indicate that the diffraction peak of deposited ZnS thin film clearly appears after being annealed, which presents a sphalerite structure, and the thin films have more than 80% average transmittance in visible region. After process optimization, under the condition of 80 ℃, 1 h, pH=10, the surface of ZnS film is uniform and dense, and the average transmittance is 89.6% in visible region, while the optical band gap is 3.82 eV, which is suitable for buffer layer of CIGS and CZTS thin film solar cells.

Key words: ZnS thin film; buffer layer; chemical bath deposition; transmittance

收稿日期:2014-11-30;**修订日期**:2014-12-25

基金项目:国家自然科学基金(61176127,61006085,11474248);国家国际科技合作重点项目(2011DFA62380);教育部博士点基金(20105303120002)

作者简介:刘 颖(1989-),女,山西省人,硕士研究生。E-mail:lying_km@sina.com

通讯作者:郝瑞亭,博士,副教授。E-mail:ruitinghao@semi.ac.cn

1 引　言

在铜铟镓硒(CIGS)和铜锌锡硫(CZTS)薄膜太阳电池结构中,缓冲层是十分关键的组成部分,它是连接宽带隙窗口层与窄带隙吸收层之间的过渡,起到了减少晶格失配和优化能带结构的作用。目前CIGS和CZTS薄膜太阳电池最常用的缓冲层材料为CdS[1],但重金属Cd会对环境造成污染。ZnS是Ⅱ-Ⅵ族化合物直接带隙半导体材料,具有闪锌矿和纤锌矿两种晶体结构[2],其禁带宽度为3.6~3.8 eV[3],比CdS(2.42 eV)宽,可提高太阳电池吸收层的光谱利用范围,进而提高短路电流和光电转换效率。制备ZnS薄膜的方法有许多,例如,化学水浴沉积(CBD)、金属有机化学气相沉积(MOCVD)、分子束外延、磁控溅射、电子束蒸发等[4-6]。其中,CBD的成本最低,且操作简单,适合工业化生产[7]。采用CBD法制备ZnS薄膜通常采用水合肼作为络合剂,而水合肼具有极强毒性。Jonston等[8]的研究表明,柠檬酸钠与水合肼在改善ZnS薄膜表面形貌及调节沉积速率等方面具有相似的作用。此外,国内外许多研究小组展开了对ZnS薄膜的研究,但由于反应的复杂性,系统地研究水浴温度、沉积时间、pH值对ZnS薄膜的综合影响的报道却很少。因此,本文采用柠檬酸钠作为络合剂制备ZnS薄膜,并对水浴温度、沉积时间、pH值对ZnS薄膜性能的影响进行了系统性的分析。

2 实　验

采用25.4 mm×76.2 mm×1.5 mm规格的载玻片作为衬底,在清洗剂和盐酸中浸泡30 min后,依次在丙酮、无水乙醇、去离子水中超声清洗30 min。配制反应溶液时,先将0.1 mol/L的$ZnSO_4$与一定浓度的$NH_3 \cdot H_2O$溶液混合,调节pH值至预设值,加入0.1 mol/L的柠檬酸钠作为络合剂,搅拌至白色絮状沉淀消失,最后加入0.01 mol/L的$SC(NH_2)_2$。实验所用化学试剂均为分析纯。将溶液混合均匀后放入恒温水浴锅中进行加热,当温度到达预设值时放入清洗干净的玻璃衬底,沉积一定时间后取出,用去离子水冲去表面的沉淀颗粒后烘干。实验遵循控制单一变量的原则,将各反应物浓度保持一定,分别调节沉积时间(0.5~4 h)、水浴温度(70~95 ℃)、pH值(9~11),分析以上三个变量对ZnS薄膜性能的影响,并通过工艺优化得出最佳反应条件。

采用KLATencor P-6型台阶仪对薄膜厚度进行测试;采用Rigaku ultima Ⅳ型X射线衍射仪对薄膜的晶体结构进行测试;采用Hitachi S4800型扫描电子显微镜对薄膜的表面形貌进行测试;采用Shimadzu UV-3600型紫外-可见-近红外分光光度计对薄膜的透过率进行测试。

3 结果与讨论

3.1 薄膜厚度分析

图1为不同沉积时间和水浴温度下制备的ZnS薄膜的厚度。从图中可以看出,随着沉积时间的增加,薄膜呈现形核-线性生长-饱和的生长过程:沉积初期,由于络合物的形成和分解都需要一定时间,因此衬底上主要发生的是吸附形核过程;随着沉积时间的增加,$[Zn(NH_3)_4]^{2+}$的形成速率逐渐趋于平稳,ZnS薄膜的沉积速率保持稳定,薄膜呈现线性生长;沉积时间进一步增加,溶液中的Zn^{2+}与S^{2-}逐渐减少,薄膜生长趋于饱和[9]。因此,实验中应将沉积时间控制在薄膜线性生长的时间范围内,才能得到膜厚适中、性能良好的薄膜。同时,水浴温度的升高加快了沉积速率,缩短了薄膜线性生长阶段的时间,反应在短时间内迅速达到饱和。水浴温度为80 ℃时,1~2 h范围为薄膜线性生长阶段,因此,重点对在该范围内沉积的ZnS薄膜的性能进行研究。

3.2 薄膜物相分析

图2为不同退火条件下ZnS薄膜的XRD图谱。由于单步沉积所制备的ZnS薄膜厚度均在100~200 nm左右,在测试过程中X射线全部穿透薄膜,不能检测出薄膜的衍射峰(如图2d所示),因此在利用XRD分析薄膜晶体结构时需进行多步沉积,将薄膜厚度增至微米级。此外,CBD法所制备的ZnS薄膜的结晶性较差(如图2c),需进行退火处理以提高薄膜的结晶度[10]。

在氮气氛围中300 ℃下退火2 h可以发现微弱的衍射峰(如图2b),进一步提高退火温度至400 ℃可以发现,在28.6°、47.5°、56.3°出现明显衍射峰,与PDF标准衍射卡05-0566一致,分别对应闪锌矿结构ZnS的(111)、(220)、(311)晶面(如图2a)。这说明,ZnS薄膜在300 ℃左右时开始结晶,随着退火温度的逐渐升高,薄膜的结晶性变好,衍射峰变强。

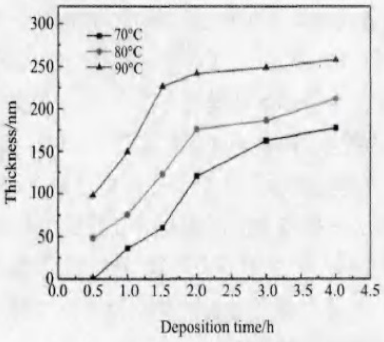

图1 不同沉积时间及水浴温度下制备的ZnS薄膜的厚度(pH=10)

Fig. 1 Thickness of ZnS thin films deposited at different time and temperatures (pH=10)

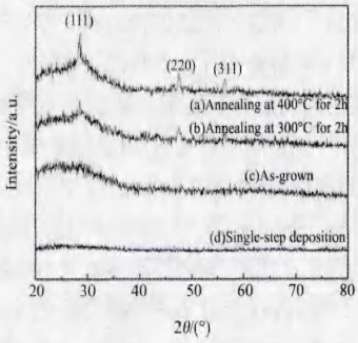

图2 不同退火条件下ZnS薄膜的XRD图谱(a)400 ℃下退火2 h;(b)300 ℃下退火2 h;(c)未退火;(d)单步沉积

Fig. 2 XRD patterns of ZnS thin films at different annealing conditions

3.3 薄膜表面形貌分析

在CBD反应中存在两种机制[11],即离子离子机制和簇簇机制。离子离子机制是指在衬底表面反应生成的沉积粒子结合形成ZnS薄膜的过程;簇簇机制是指在溶液内部形成的沉积粒子结合成ZnS并通过迁移吸附到衬底上的过程。这两种机制共同存在,相互制约。离子离子机制占主导时主要发生异质反应[12]:首先,在表面活性点上$[Zn(NH_3)_4]^{2+}+2OH^- \rightleftharpoons [Zn(OH)_2]_{ads}+4NH_3$,然后$[Zn(OH)_2]_{ads}$与$SC(NH_2)_2$结合生成复杂的络合物,最后,络合物分解生成ZnS薄膜。此时形成的薄膜颗粒较小,表面形貌致密均匀;而簇簇机制占主导时主要发生同质反应:溶液内部游离的Zn^{2+}与S^{2-}结合,即$Zn^{2+}+S^{2-} \rightleftharpoons ZnS$,生成的ZnS粒子迁移到衬底表面吸附。由于在迁移过程中,ZnS颗粒不断碰撞并聚集,导致形成的薄膜颗粒较大,表面针孔较多,附着性较差。

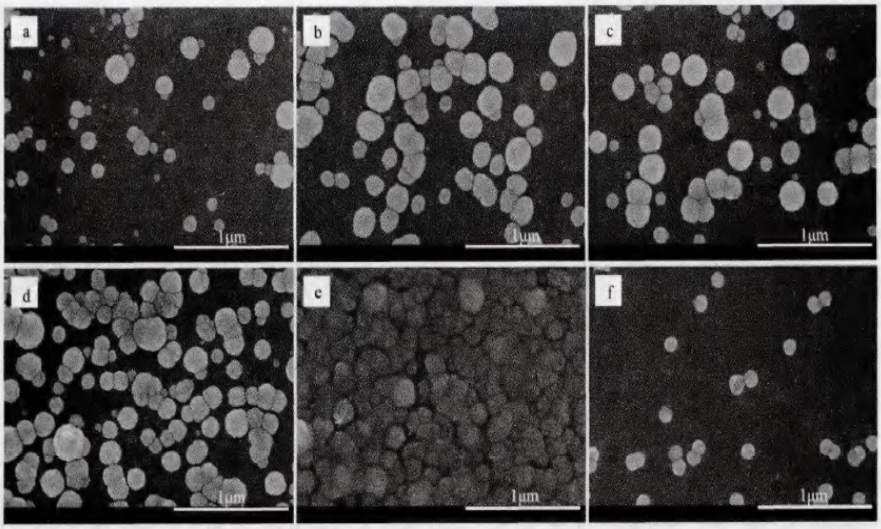

图3 不同工艺条件下ZnS薄膜的表面形貌(a)1 h、80 ℃、pH=9;(b)2 h、80 ℃、pH=9;(c)1 h、85 ℃、pH=9;(d)1 h、95 ℃、pH=9;(e)1 h、80 ℃、pH=10;(f)1 h、80 ℃、pH=11

Fig. 3 SEM images of ZnS thin films deposited at different conditions

图3是不同工艺条件下沉积的ZnS薄膜的表面形貌照片。从图中可以看出,沉积时间、水浴温度及pH值对薄膜表面形貌的影响均较为显著。由图3a、3b可以看出,随着沉积时间由1 h增至2 h,薄膜表面的大颗粒增多,从反应原理方面分析,随着沉积时间的增加,溶液中NH_3逐渐耗尽,$[Zn(NH_3)_4]^{2+}$的浓度随之减少,溶液中的Zn^{2+}将与S^{2-}发生同质反应生成ZnS颗粒,反应逐渐趋于簇簇机制,仅用肉眼便可观察出此条件下制备的ZnS薄膜表面十分粗糙且附着性较差。同样地,由图3a、3c、3d可以看出,薄膜表面的大颗粒随着水浴温度的升高也会逐渐增多,这是由于较高温度加快了沉积速率,反应很快趋于簇簇机制,使得表面大颗粒较多。值得注意的是,pH值对改善ZnS薄膜的表面形貌起着重要作用,如图3a、3e、3f所示。当pH=9时,溶液中NH_3较少,由于$Zn^{2+}+4NH_3 \rightleftharpoons [Zn(NH_3)_4]^{2+}$,此时溶液中存在大量游离的$Zn^{2+}$,仅有少部分结合成$[Zn(NH_3)_4]^{2+}$,因此溶液中主要发生同质反应$Zn^{2+}+S^{2-} \rightleftharpoons ZnS$,簇簇机制占主导地位,在此条件下沉积的ZnS薄膜表面存在许多零散分布的ZnS颗粒且附着性较差;当pH增至10时,$[Zn(NH_3)_4]^{2+}$增多,异质反应增强,离子离子机制趋于主导地位,薄膜由许多小颗粒密排而成,表面相对平整、均匀;进一步增大pH值至11,由于溶液中OH^-浓度很大,$Zn^{2+}+2OH^- \rightarrow Zn(OH)_2\downarrow$,生成的$Zn(OH)_2$沉淀吸附在薄膜表面阻碍了ZnS薄膜的沉积,因此衬底表面几乎没有连续的ZnS薄膜生成。由此可见,具有最佳表面形貌的条件为1 h、80 ℃、pH=10,下文中进一步分析了在该条件下制备的ZnS薄膜同时具有较为优异的光学性能。

3.4　薄膜光学性能分析

图4、5分别为不同水浴温度及pH值下制备的ZnS薄膜的透过率。从图中可以看出,所制备的ZnS薄膜在可见光范围内的平均透过率均在80%以上,在330 nm左右呈现明显的紫外吸收边。随着水浴温度由80 ℃升至95 ℃,ZnS薄膜的透过率逐渐降低,而pH值由9升至11,ZnS薄膜的透过率先升高后降低。产生该结果的主要原因是不同水浴温度和pH值对薄膜表面形貌及膜厚的影响较大而导致的。其中,在1 h、80 ℃、pH=10时,ZnS薄膜在可见光范围内平均透过率为89.6%,而此条件下制备的ZnS薄膜表面形貌最好,再次验证了表面形貌对薄膜透过率具有直接影响。

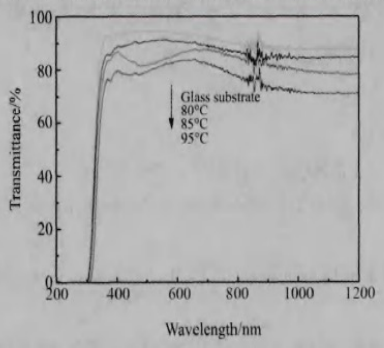

图4　不同水浴温度下制备的ZnS薄膜的透过率(1 h、pH=10)

Fig. 4　Transmission curves of ZnS thin films deposited at different temperatures (1 h, pH=10)

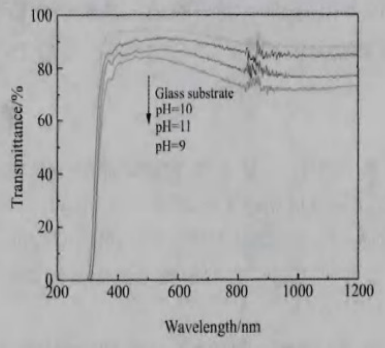

图5　不同pH值下制备的ZnS薄膜的透过率(1 h、80 ℃)

Fig. 5　Transmission curves of ZnS thin films deposited at different pH values (1 h, 80 ℃)

由于ZnS是直接带隙半导体材料,其光学带隙与吸收系数之间满足Tauc方程[13]:

$$\alpha h\nu = A(h\nu - E_g)^{1/2} \tag{1}$$

而吸收系数可以由透过率和薄膜厚度计算得出,即:

$$\alpha = -\ln T/d \tag{2}$$

其中,α为吸收系数,E_g为光学带隙,$h\nu$为光子能量,T为薄膜透过率,d为薄膜厚度,A为常数。利用(2)式并结合测得的薄膜透过率及厚度计算出α,将α带入到(1)式,画出$(\alpha h\nu)^2$-$h\nu$曲线,将曲线的线性部分延长,该延长线在横轴上的截距即为薄膜的光学带隙。如图6、7所示,沉积时间为1 h、1.5 h、2.5 h时所制备出的ZnS薄膜光学带隙分别为3.82 eV、3.79 eV、3.78 eV,水浴温度为80 ℃、85 ℃、90 ℃时所制备出的ZnS薄膜光学带隙分别为3.82 eV、3.78 eV、3.71 eV,也就是说,所制备出的ZnS薄膜的光学带隙均大于ZnS体材料

的光学带隙(3.6 eV),同时,随着沉积时间和水浴温度的升高,ZnS 薄膜的光学带隙出现明显红移。这是量子约束效应引起的[14]。当粒径减小到一定值时,费米能级附近的电子态由连续的变为准离散的能级,就会出现禁带变宽的效应。在较短的沉积时间及较低的水浴温度下,构成薄膜的 ZnS 颗粒的粒径较小,因此出现禁带变宽的现象。

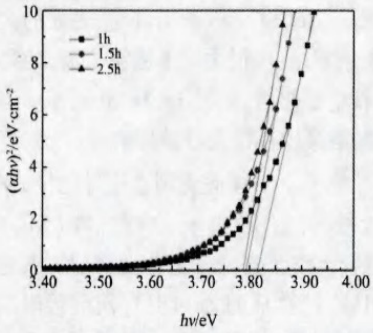

图6 不同沉积时间下制备的 ZnS 薄膜的光学带隙(80 ℃、pH = 10)

Fig. 6 Optical band gap of ZnS films deposited at different time (80 ℃, pH = 10)

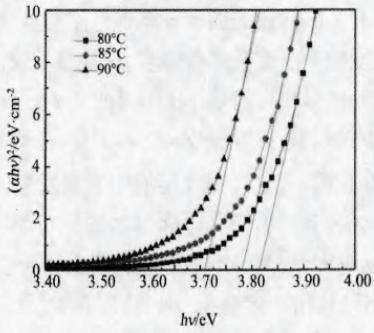

图7 不同水浴温度下制备的 ZnS 薄膜的光学带隙(1 h、pH = 10)

Fig. 7 Optical band gap of ZnS films deposited at different temperatures (1 h, pH = 10)

4 结 论

采用化学水浴法以柠檬酸钠为络合剂制备了 ZnS 薄膜,制备出的 ZnS 薄膜经退火后呈现闪锌矿结构,水浴温度、沉积时间、pH 值对 ZnS 薄膜的表面形貌、透过率及光学带隙具有显著影响。经过工艺优化,在 80 ℃、1 h、pH = 10 条件下沉积的 ZnS 薄膜表面较为平整,厚度为 75.62 nm,可见光范围内平均透过率为 89.6%,光学带隙为 3.82 eV,适合做 CIGS 和 CZTS 薄膜太阳电池的缓冲层。

参 考 文 献

[1] 焦 静,沈鸿烈,王 威,等. 化学浴法制备 CdS 薄膜及其光电性能研究[J]. 人工晶体学报,2013,**42**(7):1299-1304.
Jiao J, Shen H L, Wang W, et al. Study on Preparation and Photoelectric Properties of CdS Thin Films by Chemical Bath Deposition[J]. *Journal of Synthetic Crystals*,2013,**42**(7):1299-1304(in Chinese).

[2] Liu Q, Mao G B, Ao J P. Chemical Bath Deposited ZnS Thin Films: Preparation and Characterization[J]. *Applied Surface Science*,2008,**254**(18):5711-5714.

[3] Naghavi N, Renou G, Bockelee V, et al. Chemical Deposition Methods for Cd-free Buffer Layers in CI(G)S Solar Cells: Role of Window Layers [J]. *Thin Solid Films*,2011,**519**(21):7600-7605.

[4] 杨定宇,郑家贵,朱兴华,等. 电子束蒸发制备 CdS 多晶薄膜及性质研究[J]. 真空科学与技术学报,2009,**29**(4):427-430.
Yang D Y, Zheng J G, Zhu X H, et al. Growth and Characterization of CdS Polycrystalline Films by Electron Beam Evaporation[J]. *Chinese Journal of Vacuum Science and Technology*,2009,**29**(4):427-430(in Chinese).

[5] Islam M A, Hossain M S, Aliyu M M, et al. Comparison of Structural and Optical Properties of CdS Thin Films Grown by CSVT, CBD and Sputtering Techniques[J]. *Energy Procedia*,2013,**33**:203-213.

[6] Fang J, Holloway P H, Yu J E, et al. MOCVD Growth of Non-epitaxial and Epitaxial ZnS Thin Films[J]. *Applied Surface Science*,1993,**70-71**:701-706.

[7] 杨德仁. 太阳电池材料[M]. 北京:化学工业出版社,2006:294-300.

[8] Johnston D A, Carletto M H, Reddy K T R, et al. Chemical Bath Deposition of Zinc Sulfide Based Buffer Layers Using Low Toxicity Materials [J]. *Thin Solid Films*,2002,**403-404**:102-106.

[9] Huda Abdullah, Norhabibi Saadah, Sahbuddin Shaari. Effect of Deposition Time on ZnS Thin Films Properties by Chemical Bath Deposition (CBD) Technique[J]. *World Applied Sciences Journal*,2012,**19**(8):1087-1091.

[10] 孟 飞,张谷一,何建平,等. 化学水浴法制备 ZnS 薄膜[J]. 电源技术,2007,**31**(12):998-999.

Meng F, Zhang G Y, He J P, et al. ZnS Thin Films Prepared by Chemical Bath Deposition[J]. *Chinese Journal of Power Sources*, 2007, **31**(12): 998-999(in Chinese).

[11] Tec-Yam S, Rojas J, Rejón V, et al. High Quality Antireflective ZnS Thin Films Prepared by Chemical Bath Deposition[J]. *Materials Chemistry and Physics*, 2012, **136**: 386-393.

[12] Ortega-Borges R, Lincot D. Mechanism of Chemical Bath Deposition of Cadmium Sulfide Thin Films in the Ammonia-thiourea System[J]. *Journal of the Electrochemical Society*, 1993, **140**(12): 3464-3473.

[13] Dhere N G, Waterhouse D L, Sundaram K B, et al. Studies on Chemical Bath Deposited Cadmium Sulphide Films by Buffer Solution Technique [J]. *Journal of Materials Science*, 1995, **6**: 52-59.

[14] Peng X Y, Gu H W, Zhang T, et al. Morphological Evolution of CdS Films Prepared by Chemical Bath Deposition[J]. *Rare Met.*, 2013, **32**(4): 380-389.

(上接第 598 页)

[22] Andreas S, Philipp K, Günter H, et al. 175 fs Tm: Lu_2O_3 Laser at 2.07 μm Mode-locked Using Single-walled Carbon Nanotubes[J]. *Opt. Express*, 2012, **20**(5): 5313-5318.

[23] Lagatsky A A, Sun Z, Kulmala T S, et al. 2 μm Solid-state Laser Mode-locked by Single-layer Graphene[J]. *Appl. Phys. Lett.*, 2013, **102**: 013113.

[24] Koopmann P, Peters R, Petermann K, et al. Crystal Growth, Spectroscopy, and Highly Efficient Laser Operation of Thulium-doped Lu_2O_3 Around 2 μm[J]. *Appl. Phys B*, 2011, **102**: 19-24.

[25] Xie G Q, Tang D Y, Tan W D, et al. Subpicosecond Pulse Generation from a Nd: CLNGG Disordered Crystal Laser[J]. *Opt. Lett.*, 2009, **34**: 103-105.

[26] Gao W L, Xie G Q, Ma J, et al. Spectroscopic Characteristics and Efficient Laser Operation of Tm: CLNGG Disordered Crystal[J]. *Laser Phys. Lett.*, 2013, **10**: 055809.

[27] Ma J, Xie G Q, Gao W L, et al. Diode-pumped Mode-locked Femtosecond Tm: CLNGG Disordered Crystal Laser[J]. *Opt. Lett.*, 2012, **37**: 1376-1378.

[28] Ma J, Xie G Q, Lv P, et al. Graphene Mode-locked Femtosecond Laser at 2 μm Wavelength[J]. *Opt. Lett.*, 2012, **37**: 2085-2087.

[29] Troshin A E, Kisel V E, Yasukevich A S, et al. Spectroscopy and Laser Properties of Tm^{3+}: $KY(WO_4)_2$ Crystal[J]. *Appl. Phys. B*, 2007, **86**: 287-292.

[30] Lu Y L, Dai Y B, Yang Y, et al. Anisotropy of Thermal and Spectral Characteristics in Tm: YAP Laser Crystals[J]. *Journal of Alloys and Compounds*, 2008, **453**: 482-486.

[32] Lagatsky A A, Fusari F, Kurilchik S V, et al. Optical Spectroscopy and Efficient Continuous-wave Operation Near 2 μm for a Tm, Ho: KYW Laser Crystal[J]. *Applied Physics B*, 2009, **97**: 321-326.

[32] Sun S L, Yang F G, Cao T, et al. Infrared Spectroscopic Properties of Tm^{3+}, Ho^{3+}: $NaY(WO_4)_2$ Single Crystals[J]. *Journal of Alloys and Compounds*, 2011, **509**: 6987-6993.

[33] TsoY F, Huber G, Robert B. Spectroscopy and Diode Laser-Pumped Operation of Tm, Ho: YAG[J]. *Journal of Quantum Electronics*, 1988, **24**: 924-933.

(上接第 609 页)

[17] Fan J, Sale F. The Microstructures, Magnetic Properties and Impedance Analysis of Mn-Zn Ferrites Doped with B_2O_3[J]. *Journal of the European Ceramic Society*, 2000, **20**(16): 2743-2751.

[18] Alexandre R B, Maria L, Gregori B, et al. Effect of Mn Substitution on the Microstructure and Magnetic Properties of $Ni_{0.5-x}Zn_{0.5-x}Mn_{2x}Fe_2O_4$ Ferrite Prepared by the Citrate-nitrate Precursor Method[J]. *Materials Chemistry and Physics*, 2007, **105**: 229-233.

[19] 余　忠,兰中文,王京梅. 添加 CaO、V_2O_5 对高频 MnZn 铁氧体性能的影响[J]. 材料研究学报, 2004, **18**(2): 176-180.
Yu Z, Lan Z W, Wang J M. Influence of Cao and V_2O_5 on High Frequeney MnZn Power Ferrite[J]. *Journal of Materials Research*, 2004, **18**(2): 176-180(in Chinese).

第44卷 第2期 人 工 晶 体 学 报 Vol. 44 No. 2
2015年2月 JOURNAL OF SYNTHETIC CRYSTALS February, 2015

Ge覆盖层诱导晶化多晶Si薄膜的晶化特性研究

邓书康,董国俊,杨晓坤,刘虹霞,侯德东,李 明
(云南师范大学太阳能研究所,教育部可再生能源材料先进技术与制备重点实验室,昆明 650500)

摘要:采用电子束蒸发技术在衬底温度为180 ℃条件下生长具有Ge覆盖层的非晶Si薄膜,并于500 ℃、600 ℃、700 ℃真空退火5 h。采用Raman散射、X射线衍射(XRD)、全自动数字式显微镜等对所制备薄膜的晶化特性进行研究。结果表明,Ge覆盖层具有诱导非晶Si薄膜晶化的作用,且随着退火温度的升高a-Si薄膜晶化越显著。具有Ge覆盖层非晶薄膜经500 ℃退火5 h沿Si(400)方向开始晶化,对应晶粒尺寸约为4.9 nm。将退火温度升高到700 ℃时,非晶硅薄膜几乎全部晶化,晶化多晶Si薄膜在Si(400)方向表现出很强的择优取向特性,晶粒尺寸高达23.3 μm。与相同条件下制备的无Ge覆盖层的非晶Si薄膜相比,晶化温度降低了300 ℃。

关键词:多晶硅薄膜;电子束蒸发;非晶硅;Ge诱导晶化
中图分类号:TM914.4 **文献标识码**:A **文章编号**:1000-985X(2015)02-0420-05

Study on the Crystallization Properties of Poly-Si Films Induced Crystallization by Ge Capping Layer

DENG Shu-kang, DONG Guo-jun, YANG Xiao-kun, LIU Hong-xia, HOU De-dong, LI Ming
(Key Laboratory of Renewable Energy Advanced Materials and Manufacturing Technology, Ministry of Education, Solar Energy Research Institute, Yunnan Normal University, Kunming 650500, China)

(*Received* 9 *June* 2014, *accepted* 11 *November* 2014)

Abstract: a-Si thin films with a capping layer of Ge (a-Si/Ge films) were deposited on Si substrates at 180 ℃ by electron beam evaporation (EBE), and then annealed for 5 h at 500 ℃, 600 ℃, 700 ℃ in vacuum. The annealed films were investigated by Raman scattering, X-ray diffraction (XRD) and Automatic digital microscope. The results show that the capping Ge can induce a-Si crystallization, and as the annealing temperature increasing, the crystallization of a-Si films become more significant. The a-Si begin to crystallize with orientation of Si(400) annealed at 500 ℃ for 5 h, and the corresponding grain sizes is about 4.9 nm. When the annealing temperature increased to 700 ℃, the crystallized film has a strong preferred orientation of Si(400), the grain size is as large as 23.3 μm. The crystallization temperature decreased by 300 ℃ compared to that a-Si film without Ge capping layer.

Key words: poly-Si films; electron beam evaporation; amorphous silicon; Ge-induced crystallization

1 引 言

多晶硅薄膜具有较高的载流子迁移率和稳定的光电性能,同时其具有制作面积大、成本低廉的优点,因而被广泛运用于半导体器件及集成电路中,如太阳电池[1-3]、平板显示器(FPD)[4]、薄膜晶体管(TFT)[5,6]等。一般多晶硅薄膜的制备方法有等离子体增强化学气相沉积法(PECVD)[7]、固相结晶法(SPC)[8,9]、

收稿日期:2014-06-09;**修订日期**:2014-11-11
基金项目:国家国际科技合作专项项目(2011DFA62380);云南省自然科学基础研究项目(2010DC053)
作者简介:邓书康(1974-),男,云南省人,博士,副教授。E-mail:skdeng@126.com

金属诱导法[10-13]、激光诱导法(LC)[14]等。相比较其它方法而言,金属诱导法制备多晶 Si 薄膜的晶化温度低,晶化时间短,所制备晶粒尺寸大,薄膜均匀性好,同时采用与 Si 物理性质相似的 Ge 为金属诱导源,通过 Ge 诱导制备多晶 Si 薄膜,可以减少残留金属原子对薄膜的污染,有利于制备出高性能的半导体器件。在我们的前期工作中[15],采用电子束蒸发技术,将具有 Ge 填埋层的非晶 Si 薄膜在 400 ℃退火 5 h 实现晶化,但 Ge 填埋层的存在对后续器件的应用会产生一定的限制。针对上述特点,本文在衬底温度约为 180 ℃条件下采用电子束蒸发技术结合退火工艺,并通过后续化学腐蚀法去除 Ge 覆盖层[16],制备出具有高度择优取向的多晶硅薄膜,并对所制备的多晶硅薄膜的晶化特性进行了研究。

2　实　　验

采用电子束蒸发在 Si 衬底上制备多晶 Si 薄膜。衬底经过 2.5% 氢氧化钠溶液和无水乙醇分别超声清洗 5 min 和 10 min,去离子水冲洗和高纯氮气吹干后放入生长室,整个样品的生长在电子束蒸发设备内进行,真空度为 4.0×10^{-4} Pa,衬底温度为 180 ℃。蒸发源为高纯 Ge (块状:99.99%) 和高纯 Si(块状:99.99%),衬底为(400)取向的单晶 Si 衬底,蒸发源与衬底间距为 10 cm。首先在衬底上蒸镀 Si 薄膜 180 min,对应的高压为 8000 V,束流 0.05 A,然后在上述 Si 薄膜上蒸镀 Ge 覆盖层,蒸镀时间 60 min,对应高压为 8000 V,束流 0.1 A 。将生长态薄膜分别经 500 ℃、600 ℃、700 ℃温度下真空退火 5 h,后将 Ge 覆盖层进行剥蚀去除。同时为了便于比较,在相同的生长条件下在 Si (400) 衬底上制备了一个无 Ge 盖帽层的非晶 Si 薄膜样品,并于 500 ℃、600 ℃、700 ℃、800 ℃下进行真空退火研究。采用 Raman 散射(英国 Renishaw 公司共焦显微拉曼光谱仪),X 射线衍射(XRD,日本理学 TTRIII 型转靶多功能 X 射线衍射仪),全自动数字式显微镜对所制样品进行结构表征。

3　结果与讨论

3.1　样品的 Raman 散射分析

图 1 为生长的具有 Ge 覆盖层的 a-Ge/Si 薄膜在不同温度下真空退火 5 h 后的 Raman 图谱,入射光功率为 30 mW,从图中可以看出经 500 ℃、600 ℃退火后样品的类光学声子峰(To)出现在 295 cm^{-1}处,这是硅薄膜表面覆盖层 Ge-Ge 振动所引起的频率峰。当退火温度为 700 ℃时,样品的 Raman 峰出现在 292 cm^{-1}、392 cm^{-1}、470 cm^{-1},分别对应为 Ge-Ge、Si-Ge 和 Si-Si 的 To 峰,与 $Si_{1-x}Ge_x$ 结构中主要的三种振动模态在拉曼光谱中反映的三种频率峰(Ge-Ge ~ 300 cm^{-1},Si-Si ~ 500 cm^{-1},Si-Ge ~ 400 cm^{-1})相近。说明 700 ℃退火薄膜在 Raman 光谱穿透的深度范围内存在一定量的硅锗合金,但样品所检测到的峰位与文献[17]报道的 $Si_{1-x}Ge_x$ 特征峰相比发生了一定频移。这可能是与上述 $Si_{1-x}Ge_x$ 合金相比,700 ℃退火 5 h 的样品存在局域应力,从而使得 Si-Si 与 Ge-Ge 的振动发生频移;另一方面因原子局域受限,Si、Ge 相邻原子结合时,由于 Ge 原子质量较大,跟不上 Si-Si 原子的振动使得 Si-Si 振动模态向低频移动。对于上述薄膜表面产生硅锗合金的原因是由于在退火温度较高时,在 Si、Ge 界面处原子发生互扩散,从而在界面处形成硅锗合金。

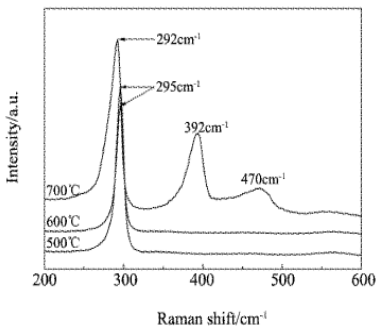

图 1　a-Ge/Si 薄膜在不同温度下真空退火的 Raman 图谱

Fig. 1　Raman spectra of a-Si/Ge films annealed at different temperatures

由于 Raman 光谱穿透深度有限,图 1 中 Raman 谱反映出的只是表层薄膜信息。为了对薄膜晶化特性进一步了解,利用化学法将 Ge 覆盖层剥蚀并进行 Raman 散射分析,以期获得 Si 薄膜的晶化特性。

图 2 不同温度退火的薄膜通过腐蚀剥脱 Ge 覆盖层后薄膜的 Raman 图谱。从图中可以看出,700 ℃退火的样品 Ge 层剥脱后在 520 cm^{-1}处出现半峰宽(FWHM)为 7 cm^{-1}的尖锐的 Si-Si 键 To 峰,未出现 Ge 及硅锗

合金的原子振动信息,说明表层覆盖的 Ge 及硅锗合金全部被腐蚀且 700 ℃退火样品中的非晶 Si 已全部晶化。700 ℃退火后样品的 Si-Si To 峰与单晶 Si 的 To 峰(FWHM = 3.5 cm^{-1})相比峰形有所展宽,说明对应薄膜原子排列相对紊乱。500 ℃、600 ℃退火样品薄膜去除 Ge 覆盖层的 Raman 光谱中也未出现 Ge 的信息,但在 480 cm^{-1}附近出现一宽阔的散射峰,表现为典型的非晶 Si 结构,但考虑到 700 ℃退火样品的晶化效果,我们推测可能在 500 ℃、600 ℃温度退火时由于 Si、Ge 界面原子存在互扩散,当把表层的 Ge 进行腐蚀剥脱后,在 Si 表面会留下一定无序态的 Si,但内部薄膜可能已经开始晶化。

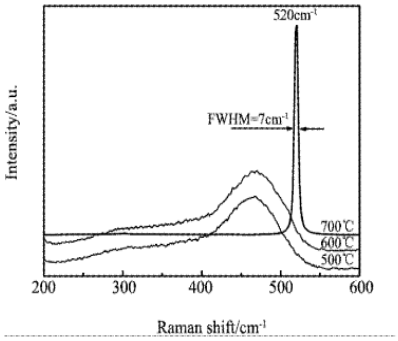

图 2 不同温度退火的薄膜剥脱 Ge 覆盖层后的 Raman 图谱

Fig. 2 Raman spectra of a-Si films after removing capping Ge annealed at different temperatures

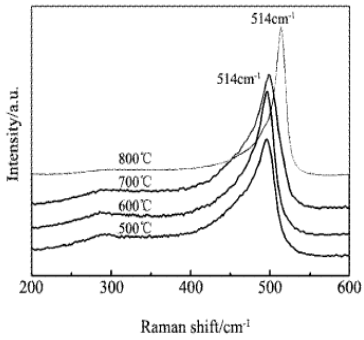

图 3 不同温度退火的非晶 Si 薄膜的 Raman 图谱

Fig. 3 Raman spectra of a-Si films annealed at different temperatures

图 3 为在相同的生长条件下 Si (400) 衬底上制备的无 Ge 覆盖的非晶 Si 薄膜样品 500 ℃、600 ℃、700 ℃、800 ℃下进行真空退火后的 Raman 光谱。从图中可见,当退火温度低于 800 ℃时,样品仍然为非晶态,而当退火温度为 800 ℃时,样品的 Raman 散射峰在 514 cm^{-1}处出现了一个较宽阔的类 To 峰,这是样品内部部分非晶 Si 晶化的结果。

3.2 样品的 XRD 分析

为了进一步证实具有 Ge 覆盖 500 ℃、600 ℃温度退火样品中非晶 Si 部分晶化的推测及 700 ℃退火样品中硅锗合金的存在,以及进一步探究薄膜的结晶特性,对未剥脱 Ge 层的不同温度下退火的薄膜进行 XRD 分析。图 4 为具有 Ge 覆盖样品经 500 ℃、600 ℃、700 ℃退火 5 h 后的 XRD 图谱及 Si、Ge 的标准衍射峰。经 500 ℃、600 ℃退火后的样品除明显出现 Ge(111),Ge(220),Ge(311)等 Ge 晶化的衍射峰外在 2θ = 69.2°附近还出现比较宽阔的 Si(400)的衍射峰。在我们前期工作中[15],在相同条件下制备的具有 Ge 填埋层的多晶 Si 薄膜在相同的衍射条件下 XRD 图谱中并未出现衬底峰,因此可以断定 Si(400)面的衍射峰并不是衬底衍射峰,而是外延非晶硅薄膜沿 Si(400)方向具有择优取向晶化的衍射峰。从其 XRD 半峰宽可以看出随着退火温度的升高晶化效果越好。通过 Sherrer 公式 $D_{hlk} = k\lambda/\beta\cos\theta$ 对其晶粒尺寸进行估算,其中,D_{hlk}为沿垂直于晶面(hlk)方向的晶粒直径,k 为 Sherrer 常数(本文取 1.05),λ 为入射 X-射线波长(CuK_α,0.15405 nm),β 为半高宽 FWHM(rad),θ 为布拉格衍射角(°),得到 500 ℃退火样、600 ℃退火样品的晶粒尺寸 D_{400}分别约为 4.9 nm、21.1 nm。与上述相同制备条件下,在 Si 衬底上直接沉积的 Si 薄膜,在退火温度高达 800 ℃退火 5 h 薄膜才部分晶化,说明通过 Ge 覆盖诱导,能显著降低非晶 Si 薄膜的晶化温度,且晶化后的多晶 Si 薄膜较强的择优取向特性。从图 3 中还可见,当退火温度为 700 ℃时,除在 2θ = 69.2°附近

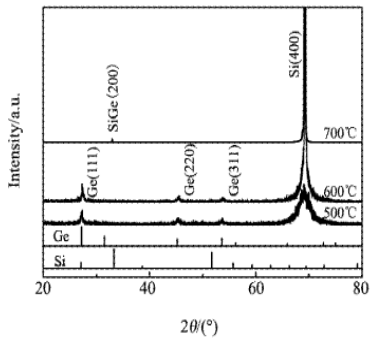

图 4 不同温度退火样品的 XRD 图谱

Fig. 4 XRD patterns of a-Si/Ge films annealed at different temperatures

出现 Si(400)尖锐的衍射峰外还出现了 SiGe(200)衍射峰,从而进一步证实 700 ℃退火样品中硅锗合金的存在。

3.3　样品的表面腐蚀分析

为了获得 700 ℃退火 5 h 多晶 Si 薄膜的晶粒大小,将其腐蚀剥脱 Ge 层后的薄膜置于混合酸溶液(HF:HNO_3:H_2O = 5:3:10)中腐蚀 5 min,通过全自动数字式显微镜观察薄膜的表面形貌,如图 5 所示,700 ℃退火后的薄膜晶粒尺寸高达 23.3 μm。

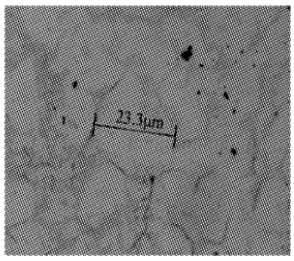

图 5　700 ℃退火样品剥脱 Ge 层后腐蚀表面图

Fig. 5　The surface corrosion picture after removing the Ge layer for sample annealed at 700 ℃

4　结　　论

采用电子束真空蒸发技术,利用 Ge 覆盖层诱导晶化法在 Si 衬底上制备了多晶 Si 薄膜。通过 Raman 散射、XRD、全自动数字式显微镜对样品进行结构表征。结果表明,Ge 有诱导多晶 Si 晶化的作用,且随着退火温度升高晶化效果越好。衬底温度约为 180 ℃下生长的具有 Ge 覆盖层的 a-Si 薄膜经 500 ℃、600 ℃退火 5 h 后在 Si(400)方向表现出一定的生长趋势,晶粒尺寸大小分别约为 4.9 nm、21.1 nm,而当 700 ℃退火 5 h 后薄膜在 Si(400)方向表现出较强生长择优取向特性,晶粒尺寸高达 23.3 μm。

参　考　文　献

[1] Paetzold U W, Zhang W D, Prompers M, et al. Thin-Film Silicon Solar Cell Development on Imprint-Textured Glass Substrates[J]. *Materials Science & Engineering B*, 2013, **178**(9): 617-622.

[2] Yang H, Wang H, Chen G, et al. A Study of Electrical Uniformity for Monolithic Polycrystalline Silicon Solar Cells[J]. *Solar Energy Materials and Solar Cells*, 2002, **1**(3): 407-412.

[3] Abass A, Maes B, Gestel D V, et al. Effects of Inhomogeneous Grain Size Distribution in Polycrystalline Silicon Solar Cells[J]. *Energy Procedia*, 2011, **10**: 55-60.

[4] Boyce J B, Lu J P, Ho J, et al. Pulsed Laser Crystallization of Amorphous Silicon for Polysilicon Flat Panel Imagers[J]. *Journal of Non-Crystalline Solids*, 2002, **299**: 731-735.

[5] Fogarassy E, Prevot B, Unamuno S, et al. Pulsed Laser Crystallization of Hydrogen-free a-Si Thin Films for High-mobility Poly – Si TFT Fabrication [J]. *Applied Physics A Solids and Surfaces*, 1993, **56**(4): 365-373.

[6] Byun C W, Son S W, Lee Y W, et al. High Performance Low Temperature Polycrystalline Si Thin-Film Transistors Fabricated by Silicide Seed-Induced Lateral Crystallization[J]. *Electronic Materials Letters*, 2012, **8**(3): 251-258.

[7] Pan Y Q. Properties of Silicon Nitride Films Deposited by Radio Frequency Plasma Enhanced Chemical Vapour Deposition[J]. *Acta Photonica Sinica*, 2007, **36**(6): 1097-1101. (in Chinese)

[8] Park C D, Kim H Y, Cho M H, et al. Solid-phase Crystallization of Hydrogenated Amorphous Silicon/hydrogenated Microcrystalline Silicon Bilayers Deposited by Plasma-enhanced Chemical Vapor Deposition[J]. *Thin Solid Films*, 2000, **359**(2): 268-274.

[9] Jin R M, Lu J X, Li R, et al. Solid-phase Crystallization of Amorphous Silicon Films by Rapid Thermal Annealing[J]. *Semiconductor Photonics and Technology*, 2005, **11**(1): 37-39.

[10] Cordon I, Carnel L, Gestel D V, et al. Development of Efficient Thin-Film Polycrystal-Line-Silicon Solar Cells Based on Aluminium-Induced Crystallization[J]. *International Photovoltaic Science & Engineering Coference*(*PVSEC*-15), 2005, **65**(1): 937-938.

[11] Zhai X L, Tan R Q, Dai S X, et al. Research Progress in Preparation of Polycrystalline Silicon Thin Films by Aluminum Induced Crystallization [J]. *Materials Review A*, 2012, **26**(11): 148-152.

[12] Kim D Y, Gowtham M, Shim M S, et al. Polycrystalline Silicon Thin Film Made by Metal-Induced Crystallization[J]. *Materials Science in Semiconductor Processing*, 2004, **7**(4): 433-437.

[13] 张良艳,林祖伦,祁康成,等. 金属 Ni 诱导非晶硅薄膜晶化研究[J]. 电子器件,2010,**33**(1):10-12.
Zhang Y L, Lin Z L, Qi K C, et al. Study on Nickel-Induced Crystallization of Amorphous Silicon Thin Films[J]. *Chinese Journal of Electron Devices*, 2010, **33**(1): 10-12. (in Chinese)

[14] 戴永兵,邹雪城,徐重阳,等. 准分子激光诱导非晶硅晶化制备多晶硅薄膜晶体管[J]. 微电子学,2000,**30**(5):343-346.
Dai Y B, Zou X C, Xu C Y, et al. Polycrystalline Silicon Thin Film Transistor Fabricated by Excimer Laser Crystallization of Amorphous Silicon [J]. *Microelectron ics*, 2000, **30**(5): 343-346. (in Chinese)

[15] Sun Q L, Deng S K, Shen L X, et al. Low Temperature Stress-Induced Re-Crystallization of Poly-Si Thin Films on c-Si Wafer with a Buried Ge Layer[J]. *Journal of Synthetic crystals*, 2013, **42**(6): 1082-1086.

[16] Lü F, Liu C X, Yang H X, et al. Properties Analysis of Alkali Etching on Ge Wafer[J]. *Semiconductor Technology*, 2007, **32**(11): 967-969.

[17] 段宝兴,杨银堂. 利用 Keating 模型计算 $Si_{(1-x)}Ge_x$ 及非晶硅的拉曼频移[J]. 物理学报,2009,**58**(10):14-18.
Duan B X, Yang Y T. Calculation of Raman Shifts of $Si_{(1-x)}Ge_x$ and Amorphous Silicon Using Keating Model[J]. *Acta Physica Sinica*, 2009, **58**(10): 14-18(in Chinese)

·信 息·

美高能所稀土纳米材料生物效应研究取得系列进展

纳米二氧化铈是最重要的一种稀土纳米材料,研究表明纳米二氧化铈具有很高的表面活性,使其不仅可用作工业催化剂,亦有望作为生物模拟酶用于生物医学领域。但与成熟的工业应用相比,其生物医学应用尚处于萌芽阶段。其中一个主要的瓶颈问题是具有生物模拟酶活性的纳米二氧化铈必须满足粒径小于 5 nm、表面有大量的 Ce(Ⅲ)等条件,而这样的纳米颗粒往往不符合生物医学应用的要求或者在生理条件下极易失活。

中国科学院高能物理研究所多学科中心环境毒理组的科研人员发现,通过与电子供体发生电子转移,可以使原本不具有模拟酶活性的纳米二氧化铈活化,获得超氧化物歧化酶(SOD)活性,且活性远远超过天然酶。利用这种方法,不同尺寸和形貌的纳米二氧化铈均可以被活化。该工作揭示了纳米二氧化铈表面化学行为与其化学形态之间的关系,为新型纳米酶的设计提供了基础,将有力推进纳米二氧化铈在生物医学领域的实际应用。相关结果已发表于《德国应用化学》(*Angew Chem Int Ed*, DOI: 10.1002/ange.201410398),并入选 Wiley-VCH 的 Hot Topics in Surfaces and Interfaces。

高能所环境毒理组在稀土元素化学与稀土元素生物效应方面有 30 余年的积淀。上世纪 80 年代起,利用中子活化分析技术陆续开展了土壤、生物样品中稀土元素的含量与化学形态、稀土元素的植物生理效应及神经毒理的研究。成功研制了性能优异的新型掺钆液体闪烁体,用于大亚湾反应堆中微子实验,解决了重大技术难题。近年来,在科技部和基金委的大力支持下,结合所"一三五"规划,研究组充分发挥同步辐射技术在化学形态分析方面的优势,将工作重点转向稀土纳米材料的环境行为与生物效应。研究了水生态系统中的纳米二氧化铈的分布与归趋(*Chemosphere*, 2012, 89: 530-535; *Nanoscale Res Lett*, 2012, 7:84)。评价了纳米二氧化铈对多种模式生物,如大肠杆菌(*Nanotoxicology*, 2012, 6: 233-240; Environ Pollut, 2015, 196: 194-200)、秀丽隐杆线虫(*Environ Sci Technol*, 2011, 45: 3725-3730)和大鼠、小鼠(*Nanotechnology*, 2010, 21: 285103; *Int J Mol Sci*, 2014, 15, 6072-6085)等的生物效应。系统研究了稀土氧化物纳米材料与植物的相互作用(*Chemosphere*, 2010, 78: 273-279; *Nanotoxicology*, 2011, 5: 743-753; *Nanotoxicology*, DOI: 10.3109/17435390.2014.921344; *Environ Sci Technol*, 2012, 46(3): 1834-1841; *RSC Adv*, 2015, 5, 4554-4560)。首次发现纳米二氧化铈的生物转化现象,确定了转化条件(*ACS Nano*, 2012, 6: 9943-9950; *Environ Pollut*, 2015, 198: 8-14),解释了纳米二氧化铈植物毒性种间差异的机制(*Nanotoxicology*, DOI:10.3109/17435390.2013.855829)。研究工作两次被英国皇家化学会期刊选为封面文章发表(*Metallomics*, 2011, 3: 816-822; *Environ Sci: Nano*, 2014, 1: 459-465)。 (来源:中国科学院高能物理研究所)

第44卷 第12期 人 工 晶 体 学 报 Vol. 44 No. 12
2015年12月 JOURNAL OF SYNTHETIC CRYSTALS December, 2015

单质靶溅射制备 CZTS 薄膜及太阳电池

蒋 志,李志山,杨敏,刘思佳,刘 涛,郝瑞亭,王书荣
(云南师范大学太阳能研究所,教育部可再生能源材料先进技术与制备重点实验室,
云南省农村能源重点工程实验室,昆明 650500)

摘要:采用单质靶磁控溅射制备 Cu_2ZnSnS_4(CZTS)薄膜,研究了薄膜的元素组分、升温速率、硫化温度对薄膜表面平整性以及晶粒尺寸的影响。通过 SEM 与 AFM 表征薄膜的表面形貌与表面粗糙度,用 EDS 检测薄膜的元素组分。所制备的样品的 Cu/(Zn + Sn)、Zn/Sn 处于最优范围。通过 XRD 及 Raman 检测薄膜的结晶情况以及薄膜中的二次相,通过上述测试分析判定 CZTS 薄膜品质良好。最终制备出以 CZTS 为吸收层的薄膜太阳电池,通过 $I \sim V$ 特性检验了 CZTS 电池性能参数,得到效率为 0.83% 的 CZTS 薄膜太阳电池,并通过改进硫化退火工艺将效率提高至 1.58%。

关键词: CZTS 薄膜,太阳电池,磁控溅射,硫化,转换效率
中图法分类号:O484.1 **文献标识码**: A **文章编号**:1000-985X(2015)12-0-

Fabrication of CZTS Thin Film and Solar Cells by Element Targets

JIANG Zhi, LI Zhi-shan, YANG Min, LIU si-jia, LIU Tao, HAO Rui-ting, WANG shu-rong
(Solar Energy Research Institute of Yunnan Normal University, Kunming 650500, China)

(*Received* 17 *June* 2015, *accepted* 24 *August* 2015)

Abstract: The process of fabricating CZTS thin film by metal elemental target magnetron sputtering is simple. But the adhesiveness and flatness is not so satisfied. The influence of component, heating ramp and sulfuring temperature on the surface flatness and grain sizes of CZTS film were studied. The ratio of Cu/(Zn + Sn) and Zn/Sn of prepared samples were at the best range. Then the crystallization and secondary phases were characterized by XRD and Raman scattering. Through the above characterization, we confirm the samples were pure CZTS phase. Finally, Then CZTS absorber based solar cells were prepared and the electronic performance of cells was measured by *I-V* testing. The CZTS solar cells with conversion efficiencies of 0.83% were obtained. Finally, the PCE of second CZTS cell is 1.58% by further improving the sulfuring and annealing process of CZTS thin film.

Key words: CZTS thin film, solar cells, magnetron sputtering, sulfuring, conversion efficiency

1 引 言

由于铜锌锡硫(CZTS)属于直接带隙半导体材料,有较高的光吸收系数($\geq 10^4$)与匹配太阳光谱的带隙(1.45 eV),最重要的是 Cu、Zn、Sn、S 元素在地壳中的含量丰富且无毒无污染,所以 CZTS 薄膜作为薄膜太阳电池的吸收层,是 CIGS、CdTe 薄膜的的理想替代材料,随着 Ga 与 In 等资源在其他半导体产业中的需求增大,因此 CZTS 薄膜太阳电池近几年来引起了很多科研机构及团体的关注与兴趣。

收稿日期:2015-06-17;**修订日期**:2015-08-24
基金项目:国家科技合作重点项目(2011DFA62380);国家自然科学基金(61176127);国家自然科学基金(61167003)
作者简介:蒋 志(1991-)男,云南省人,硕士。E-mail: 439832914@qq.com
通讯作者:王书荣,副教授。E-mail:shrw88@aliyun.com

CZTS 薄膜的制备方法大致分为两类:物理法(真空法)与化学法(非真空法)。其中物理法主要包括:磁控溅射法、真空蒸镀法、激光脉冲沉积法,化学法主要包括:电化学法、溶胶凝胶法、旋转涂布法等。在 CZTS 薄膜的材料制备方面新加坡国立大学的材料科学与工程学院采用共蒸的方式制备出 CZTSSe 薄膜[1]。西班牙的 Andrew Fairbrother, 等人采用单质金属叠层的预制层制备了 CZTS 薄膜并研究了 CZTS 薄膜在富锌条件下的生成机制[2]。韩国的 Hyesun Yoo, JunHo Kim 通过磁控溅射金属靶研究了不同沉积顺序的 CZT 预制层对 CZTS 薄膜生长的影响[3],而 Muhamad I. Amalden 研究了硫化温度对 CZTS 薄膜中二次相的影响[4]。中南大学的研究小组利用反应溅射法制备 CZTS 薄膜并研究了薄膜的相关电学与光学性质[5]。在 CZTS 薄膜太阳电池器件制作方面,IBM 采用蒸发法制备出效率为 8.4% 的 CZTS 薄膜电池,其最大短路电流密度为 23.4mA/cm^2[6],这是目前 CZTS(不含硒)薄膜电池的世界纪录,根据等电子替代的原则,将 CZTS 中的一部分或全部硫(S)用硒(Se)替代得到 CZTSSe/CZTSe,美国 NREL 用真空蒸镀 CZTSSe 制备效率为 9.15% 的薄膜电池[7],虽然开路电压只有 300 ~ 400 mV,但短路电流密度达到了 37.4mA/cm^2。日本丰田公司以磁控溅射 CZT 预制层为基础制备出效率为 7.6% 的 CZTS 薄膜电池[8],这是目前采用溅射法获得的 CZTS 电池的最高效率。其次 Stanford University、AQT Solar、国内南开大学、Solar Frontier 等都通过溅射制备 CZTSSe 薄膜的方式分别制作出转换效率为 9.3%、9.3%、8.7%、10.8% 的 CZTSSe 薄膜电池[9-11],这代表了目前 CZTSSe 薄膜电池的世界领先水平。与真空法相比,非真空法所需要的工艺与设备条件相对简单,并且操作简便、原材料便宜。IBM 的 Shafaat Ahemd 等人和日本大阪大学的 Feng Jiang 等人采用电化学沉积铜锌锡(CZT)预制层后硫化退火的两步法分别制备出效率为 7.3% 和 8.0% 的 CZTS 薄膜电池[12,13]。2009 年 IBM 实验室的 Teodor K Todorov, Kathleen B Reuter, David B Mitzi 采用一种简便的以联氨为基础溶剂的 sol-gel 结合 spin-coating 的方法,后高温退火制备 CZTSSe 吸收层,获得了效率为 9.6% 的 CZTSSe 电池[14],经过对工艺的改进与优化后 2012 年该小组的成员使用同样的方法将 CZTSSe 电池的效率提高到 11.1%[15]。到 2013 年末该小组制作的 CZTSSe 薄膜太阳电池的转换效率已高达 12.6%[16]。与非真空法相比,虽然真空法在原材料成本及成膜设备方面投资较高,但真空法仍然拥有非真空法不可比拟的优势,即工艺过程可控,工艺重现性好,薄膜均匀性高等优点,考虑到目前产业化的 CIGS 薄膜以真空法为主以及 CZTS 薄膜对 CIGS 薄膜在生产工艺上的继承,所以对真空法制备 CZTS 薄膜的充分研究可以为以后 CZTS 薄膜太阳电池的产业化打下坚实的基础。本实验采用金属单质靶磁控溅射制备 CZTS 薄膜,主要研究元素组分、硫化温度、升温速率对薄膜的影响,发现元素组分、升温速率会对薄膜的平整度造成较大影响。并通过测试相应的电池样品来研究薄膜品质对电池性能的影响。

2 实 验

采用国产高真空磁控溅射成膜系统以及高纯金属单质靶制备 CZTS 薄膜预制层。首先将钠钙玻璃(SLG)衬底放入重铬酸钾中浸泡,浸泡 30 分钟后依次用丙酮、酒精、去离子水超声清洗钠钙玻璃并用氮气吹干,将玻璃衬底片放入磁控溅射腔室的样品台,将真空度抽至 5×10^{-4} Pa,通入氩气,调至工作压强 1.5 ~ 0.3 Pa,设定基片台的旋转速率为 7 r/min。钼背电极的制备:将直流电源的功率调至 180 W 分别在 1.5 Pa、1.0 Pa、0.5 Pa、0.3 Pa 的工作压强下溅射钼靶(4N)20 min、10 min、15 min、45 min 得到多层结构的厚度为 1 μm 的钼(Mo)背电极层。铜锌锡预制层的制备:以 Sn→Cu→Zn 的顺序分层直流溅射锡靶(4N)、铜靶(4N)、锌靶(4N)得到铜锌锡(CZT)金属预制层,锡、铜、锌的溅射功率与时间见表 1,得到 Sn/Cu/Zn 结构的 CZTS 预制层(S31),将预制层放入退火炉中在 200 ~ 300 ℃,氮气保护下进行合金,随后在常压与氮气保护下对经过合金处理的预制层进行硫化,得到最终的 CZTS 薄膜。通过光学显微镜(Leica DM6000M)与电子显微镜(FEI quanta200)、原子力显微镜(NSK SPA-400)、EDS(EDAX)、XRD(Rigaku UltimaIV)、Raman(Renishaw inVia)分别对薄膜的表面形貌、表面粗糙度、元素组分、结晶、二次相进行表征,并通过以上测试数据分析 CZTS 薄膜中元素组分、硫化过程中的升温速率及时间对 CZTS 薄膜平整度、晶粒尺寸的影响。最后通过太阳光模拟器(NEWPORT)作为光源在 AM1.5 (100 mW/cm^2)的条件下利用美国 KEITHLEY 公司生产的 2400

型数字源表完成 CZTS 电池样品的 $I \sim V$ 特性测试。

表 1　S31, S85 预制层的组分元素组分

Table 1　The composition of S31 and S85 precursor

Sample(precursor)	Cu At%	Sn At%	Zn At%	Cu/(Zn + Sn)	Zn/Sn
design	30	20	50	0.43	2.50
S31	35.97	18.55	45.48	0.56	2.45
precursor	(100 W, 23 min)	(50 W, 38 min)	(50W, 6 min)		
S85	35.24	24.10	40.66	0.54	1.68
precursor	(100W, 21min)	(50W, 46min)	(50W, 5 min)		

预制层按厚度 d = 500 nm,Cu/(Zn + Sn)、Zn/Sn 的最优比例进行设计,根据相应金属的密度以及摩尔质量粗略计算出 Cu、Zn、Sn 每一层的沉积时间,由于溅射得到的金属膜层与相应的块体材料在密度上的偏差,所以需要在计算时乘上一个修正因子从而得到厚度更准确的 CZT 预制层。

3　结果和讨论

表 2 为相应预制层硫化后得到的 CZTS 薄膜,其中 S31 为初次计算硫化得到的 CZTS 薄膜,可以看出 S31 中的 Sn 含量明显偏少,Zn 含量偏多。为了得到组分更为合理的 CZTS 薄膜,将 S31 的 Sn 含量与 Zn 含量经过调整后制备出 S85 的 CZTS 薄膜样品,S85 预制层的元素组分、比例及其相应的溅射功率、时间见表 1。图 1 为 S31 与 S85 在光学显微镜下放大 5000 倍得到的表面形貌,图 1a 中的黑色圆环区域相比薄膜表面的其余部分向下凹陷,根据表 1 中的元素组分可以看出该薄膜中锡含量相对偏少,所以造成薄膜表面凹陷可能是由于 Sn 的不足造成 Cu、Zn 无法与足够的 Sn 元素形成 CZTS 晶体来填补图 1a 中所示的凹陷部分,于是在薄膜表面留下凹陷。同时由于 Cu 不能与 Zn 形成三元硫化物,所以在该区域形成了铜硫相($Cu_{2-x}S$)。从两个薄膜的 XRD(图 2)可以看出,在 S31 的主衍射峰 28.48°(112)左边以及 33.03°(200)的右边存在两个较微弱的衍射峰,经对比 ICDD 数据基本判定为 $Cu_{2-x}S$ 的衍射峰,而 S85 的衍射图谱则看不出这两个 $Cu_{2-x}S$ 衍射峰。S85 硫化得到的 CZTS 薄膜样品的表面形貌如图 1b 所示,从图中可以看出通过增加薄膜样品中的 Sn 含量使薄膜中的凹陷明显减少甚至消失。从而使硫化后的薄膜表面更平整、均匀。

表 2　S31, S85 预制层硫化后得到的 CZTS 薄膜的元素组分

Table 2　The composition of CZTS thin film from S31 and S85 precursor

Sample	Cu At%	Sn At%	Zn At%	S At%	Cu/(Zn + Sn)	Zn/Sn	S/M	Alloying temperature and time	Sulfuring temperature and time
S31 sulfuring	23.96	8.15	21.01	46.88	0.82	2.58	0.88	320 ℃,30 min	575 ℃,30 min
S85 sulfuring	22.42	10.16	18.01	49.41	0.80	1.77	0.98	320 ℃,30 min	575 ℃,30 min

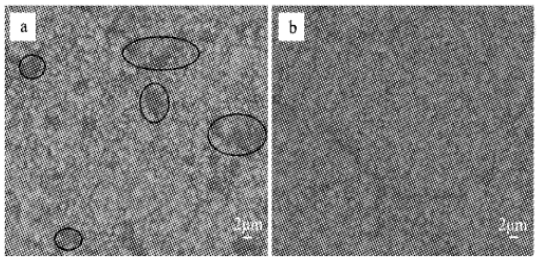

图 1　光学显微镜下样品 S31(a)与 S85(b)的表面形貌(放大 5000 倍)

Fig. 1　The morphology of S31(a) and S85(b) under 5000 magnification times by optical microscope

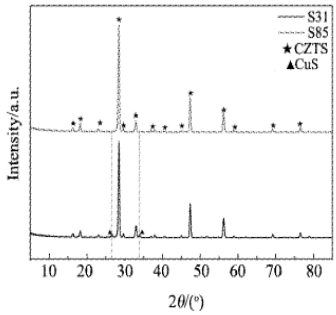

图 2　S31 与 S85 的 XRD 图谱

Fig. 2　XRD pattern of S31 and S85

除组分会影响 CZTS 薄膜表面形貌及平整度外。硫化时的升温速率对薄膜表面形貌的影响同样至关重要,图 3 中的 a(S85-1)、b(S85-2)、c(S85-3)样品在合金之后分别以 12 ℃/min、25 ℃/min、38 ℃/min 的速率

升至 575 ℃硫化 30 min 得到的 CZTS 薄膜表面 SEM(1000 倍)图,可以看出升温速率的快慢对 CZTS 薄膜的表面形貌有很大的影响,从图中可以看出,硫化时较慢的升温速率有利于薄膜的表面更平整,而升温过快导致薄膜表面平整度有所下降,这很可能是因为在慢速升温的过程中,预制层中的 Cu、Zn、Sn 各元素与 S 充分发生反应分别形成 Cu、Zn、Sn、的硫化物,各金属硫化物在经过反应生成 CZTS 薄膜,从而保证薄膜中形成不同物质的晶体时晶格常数逐渐变大,同时薄膜也逐渐膨胀,在此过程中薄膜所受的应力能够逐渐释放。相反快速升温过程不能保证预制层薄膜中的各金属在达到目标温度前已充分反应形成各自的金属硫化物,尤其在薄膜底层还存在部分的金属单质以及合金,在 580 ℃的温度下直接与 S 发生反应得到 CZTS 晶体,而 CZTS 晶体的晶格常数比 Cu、Zn、Sn 的大,所以当薄膜底层晶体从金属晶体变成 CZTS 晶体时,晶格常数瞬间变大,导致薄膜膨胀过快,造成薄膜底部的张应力无法释放,残留在薄膜底部,最终导致整个薄膜表面的平整度下降甚至薄膜从衬底脱落,而较慢的升温速率可以使薄膜中的晶格常数变化所带来的应力逐渐释放,从而降低甚至消除应力对薄膜的表面形貌造成的影响。图 4a、b 分别为 S85-1 与 S85-2 的 AFM 图,通过计算得到两个样品的粗糙度均方根(RMS)值分别为 14.2 nm 与 30.4 nm,可以看出,通过降低升温速率可以明显提高薄膜的表面平整度。

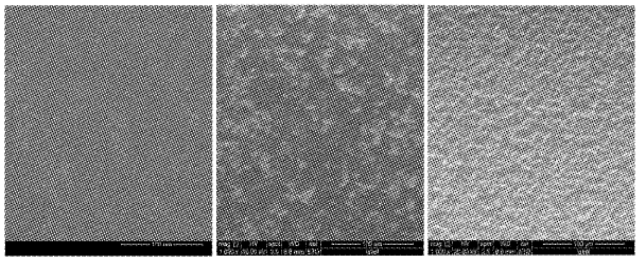

图 3 样品 S85-1(a)、S85-2(b)、S85-3(c)表面形貌图(放大 1000 倍)

Fig. 3 The morphology of S85-1(a), S85-2(b), S85-3(c) under 1000 magnification times

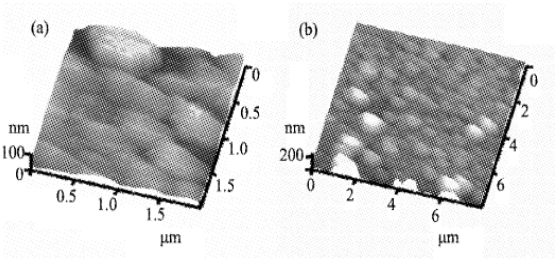

图 4 S85-1(a)与 S85-3(b)的 AFM 三维图与表面图

Fig. 4 AFM image and 3D patterns of S85-1(a), S85-3(b)

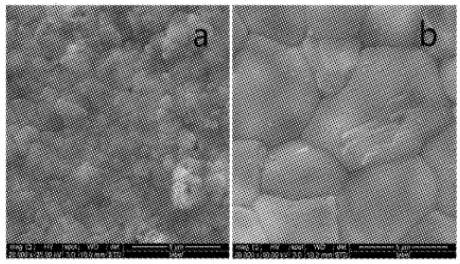

图 5 样品 S85-1(a)、S85-4(b)表面 SEM 图

Fig. 5 The morphology of S85-1(a), S85-4(b)

表 3 S85-1、S85-2、S85-3、S85-4 的相应合金及硫化条件

Table 3 The alloying and sulfuring condition of S85-1, S85-2, S85-3, S85-4

Sample	Alloying temperature and time	Sulfuring temperature and time	Heating ramp
S85-1	320 ℃, 30 min	575 ℃, 30 min	12 ℃/min
S85-2	320 ℃, 30 min	575 ℃, 30 min	25 ℃/min
S85-3	320 ℃, 30 min	575 ℃, 30 min	38 ℃/min
S85-4	320 ℃, 30 min	590 ℃, 30 min	12 ℃/min

硫化退火的温度同样是薄膜中颗粒变大的关键因素,图 5a(S85-1)和 b(S85-4)所示样品分别以 12 ℃/min 的速率升至 575 ℃和 590 ℃硫化 30 min 得到的薄膜样品的表面 SEM(20000 倍)图,从图中可以看出适当的增加硫化退火温度能明显提高薄膜的颗粒尺寸,使薄膜中的大部分颗粒尺寸达 5μm 以上,大幅度减少晶粒间界,并且提高了薄膜的表面致密度,有助减少和避免 CZTS 作为薄膜电池吸收层时的晶界复合所带来

的漏电。但是,硫化温度也不能过高,否则 CZTS 又会分解成各金属的硫化物(二次相)。图 6a 中的四条曲线分别为 S85-1、S85-2、S85-3、S85-4 四个样品的 XRD 图谱,从四个样品的衍射峰的相对强度可以看出较高的硫化温度及较慢的升温速率对薄膜的结晶情况及晶体质量有明显改善,另外从 XRD 中并未看到薄膜中含有 $Cu_{2-x}S$、SnS_{2-x}相,但是仅凭 XRD 并不能准确判断样品是否含有其它二次相(铜锡硫、硫化锌),因为 CZTS 的衍射峰与铜锡硫(CTS)、硫化锌(ZnS)的衍射峰重叠。因此对上述的四个样品进行拉曼检测得到图 6b 所示的拉曼图谱,从图 6 中同样能看出 CZTS 薄膜的三大拉曼散射主峰(286 ~ 288 cm^{-1}、336 ~ 339 cm^{-1}、368 ~ 372 cm^{-1}),与其它文献中提到的 CZTS 的拉曼散射峰一致[13-16]。并且从拉曼散射谱中并未观察到 CTS、ZnS 以及 MoS_2 的存在,当然未反映出 MoS2 可能是因为 CZTS 薄膜对 MoS_2 的拉曼散射信号产生影响。从拉曼散射峰的相对强度同样可以判断薄膜的晶体质量,所得结果与 XRD 图谱反映的情况一致。表明所制备的薄膜为 CZTS 单相多晶薄膜且为贫铜富锌结构,适合进一步制作成薄膜太阳电池器件。

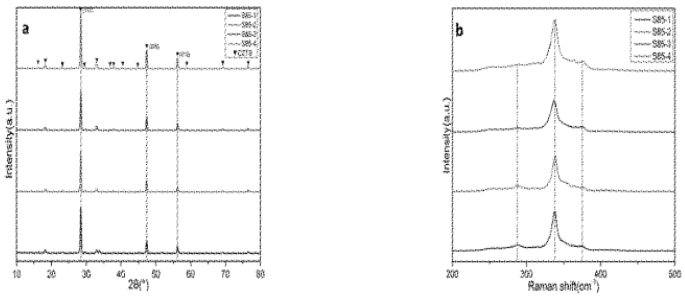

图 6　S85-1、S85-2、S85-3、S85-4 样品的 XRD(a)与 Raman(b)图

Fig6　XRD and Raman patterns of S85-1, S85-2, S85-3, S85-4

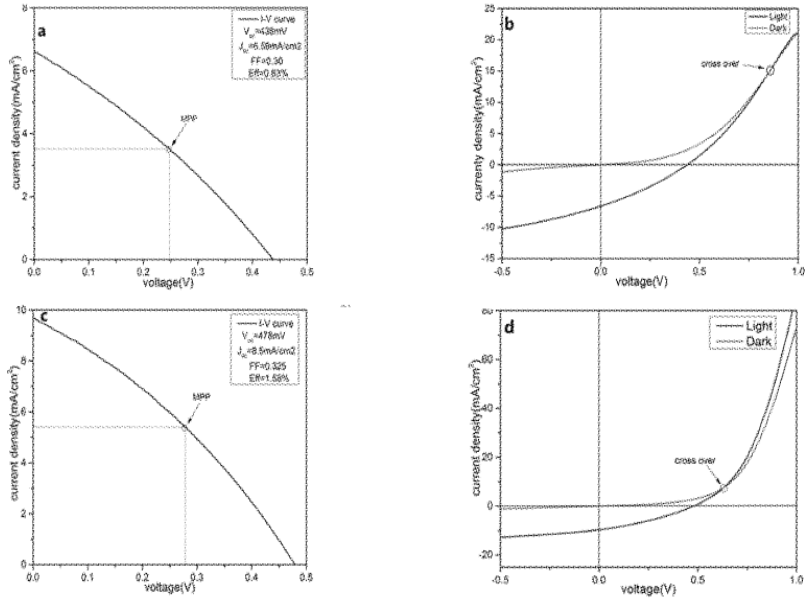

图 7　样品 C85-1(a,b)与 C85-4(c,d)的 $J \sim V$ 光照与暗特性曲线

Fig. 7　The light and dark *J-V* curve of C85-1(a, b) and C85-4(c, d)

在制备好的 CZTS 薄膜样品(S85-1,S85-4)的基础上,采用化学浴法(CBD 法)和溅射法分别制备 CdS 缓冲层与 i-ZnO/AZO 窗口层,通过真空蒸镀 Ni/Al 顶电极得到 SLG/Mo(1 μm)/CZTS(2.5 μm)/CdS(100 nm)/i-ZnO(90 nm)/AZO(600 nm)/Ni-Al 结构的 CZTS 薄膜太阳电池 C85-1 与 C85-4,总面积均为 0.2 cm^2。

采用氙灯光源在AM1.5的条件下测试C85-1与C85-4薄膜电池样品,得到两个样品的I-V特性曲线图(图7b、d),并测得C85-1与C85-4的相应参数列于表4。很明显,与目前世界上转换效率较高的CZTS薄膜电池在性能上还有很大差距,尤其是在短路电流密度与填充因子方面还有很大的提升空间,而影响短路电流密度与填充因子的主要是串联电阻,从图7b、d可以看出,由于电池样品的暗特性与光照特性曲线存在交点,说明在CZTS吸收层与Mo层以CZTS吸收层与CdS缓冲层之间存在着明显的势垒,对电子的输运造形成阻碍,增加了电池的串联电阻。另外从SEM与AFM可以看出,目前我们制备的CZTS吸收层表面平整度及均匀性还不够理想,部分区域CZTS覆盖不致密,导致最终的电池存在部分漏电,从而降低并联电阻Rsh与开路电压Voc。所以为了防止漏电,需要沉积较厚的缓冲层、窗口层将漏电通道封闭,但这样做又增大了窗口层对短波部分光谱的吸收以及电池的串联电阻,造成薄膜电池的短路电流密度和填充因子较低,其次如果吸收层与Mo电极接触不理想:即CZTS与Mo电极之间存在孔洞、间隙或者MoS2,则会引入很大的接触电阻从而增加串联电阻,降低Jsc与FF。此外,为减小吸收层的体电阻,需要保证吸收层中CZTS晶粒在纵向的生长能够贯穿整个吸收层。通过抑制硫化退火过程中硫化钼的生成,改善缓冲层与窗口层的沉积工艺,优化电极制作工艺形成较理想的金属半导体欧姆接触。进一步减少相互层之间的界面态,钝化晶界,减少体内复合与界面复合。通过以上改进步骤,有望制作出更高转换效率的CZTS薄膜电池。

表4 不同电池样品的相关参数

Table 4 The parameters of different cell samples

Sample	V_{oc}/mV	J_{sc}/mA·cm^{-2}	*FF*	Efficiency/%
C85-1	438	6.59	0.30	0.83%
C85-4	478	8.5	0.325	1.58%

4 结 论

薄膜的组分硫化过程的升温速率对薄膜的表面形貌都有较大影响,其中锡元素的缺失及升温速率过快都不利于CZTS薄膜表面形貌及晶粒的均匀性,尤其是对表面平整度的影响。此外,较慢的升温速率有利于薄膜表面平整度的提高。适当地提高硫化温度可以使薄膜中的晶粒尺寸增大,通过降低预制层硫化退火时的升温速率及提高硫化退火温度,最终制备出平整、单相、致密、晶粒优良的CZTS薄膜。并在此基础上制备出效率分别为0.83%和1.58%的CZTS薄膜太阳电池。

参 考 文 献

[1] Yin X, Huang T J, Tang C, et al. Significantly Different Mechanical Properties and Interfacial Structures of $Cu_2ZnSn(S,Se)_4$ Films Prepared from Metallic and Sulfur-contained Precursors[J]. *Solar Energy Materials and Solar Cells*, 2015, **134**: 389-394.

[2] Fairbrother A, Fontané X, Izquierdo-Roca V, et al. On the Formation Mechanisms of Zn-rich Cu_2ZnSnS_4 Films Prepared by Sulfurization of Metallic Stacks[J]. *Solar Energy Materials and Solar Cells*, 2013, **112**: 97-105.

[3] Yoo H, Kim J H. Comparative Study of Cu_2ZnSnS_4 Film Growth[J]. *Solar Energy Materials and Solar Cells*, 2011, **95**(1): 239-244.

[4] Amal M I, Kim K H. Crystallization of kesterite Cu_2ZnSnS_4 Prepared by the Sulfurization of Sputtered Cu-Zn-Sn Precursors[J]. *Thin Solid Films*, 2013, **534**: 144-148.

[5] Liu F, Li Y, Zhang K, et al. In situ Growth of Cu_2ZnSnS_4 Thin Films by Reactive Magnetron Co-sputtering[J]. *Solar Energy Materials and Solar Cells*, 2010, **94**(12): 2431-2434.

[6] Shin B, Gunawan O, Zhu Y, et al. Thin Film Solar Cell with 8.4% Power Conversion Efficiency Using an Earth-abundant Cu_2ZnSnS_4 Absorber [J]. *Progress in Photovoltaics: Research and Applications*, 2013, 21(1): 72-76.

[7] Repins I, Beall C, Vora N, et al. Co-evaporated $Cu_2ZnSnSe_4$ Films and Devices[J]. *Solar Energy Materials and Solar Cells*, 2012, **101**: 154-159.

[8] Green M A, Emery K, Hishikawa Y, et al. Solar Cell Efficiency Tables (Version 45)[J]. *Progress in Photovoltaics: Research and Applications*, 2015, **23**(1): 1-9.

[9] Chawla V, Clemens B. Effect of Composition on High Efficiency CZTSSe Devices Fabricated Using Co-sputtering of Compound Targets[C]// Photovoltaic Specialists Conference (PVSC), 2012 38th IEEE. IEEE, 2012: 002990-002992.

[10] Li J, Zhang Y, Zhao W, et al. A Temporary Barrier Effect of the Alloy Layer During Selenization: Tailoring the Thickness of $MoSe_2$ for Efficient $Cu_2ZnSnSe_4$ Solar Cells[J]. *Advanced Energy Materials*, 2015, **5**(9).

[11] Hiroi H, Sakai N, Kato T, et al. High voltage Cu_2ZnSnS_4 Submodules by Hybrid Buffer Layer[C]//Photovoltaic Specialists Conference (PVSC), 2013 IEEE 39th. IEEE, 2013: 0863-0866.

[12] Ahmed S, Reuter K B, Gunawan O, et al. A High Efficiency Electrodeposited Cu_2ZnSnS_4 Solar Cell[J]. *Advanced Energy Materials*, 2012, **2**(2): 253-259.

[13] Jiang F, Ikeda S, Harada T, et al. Pure Sulfide Cu_2ZnSnS_4 Thin Film Solar Cells Fabricated by Preheating an Electrodeposited Metallic Stack [J]. *Advanced Energy Materials*, 2014, **4**(7).

[14] Todorov T K, Reuter K B, Mitzi D B. High-Efficiency Solar Cell with Earth-Abundant Liquid-Processed Absorber[J]. *Advanced Materials*, 2010, **22**(20): E156-E159.

[15] Todorov T K, Tang J, Bag S, et al. Beyond 11% Efficiency: Characteristics of State-of-the-art $Cu_2ZnSn(S,Se)_4$ Solar Cells[J]. *Advanced Energy Materials*, 2013, **3**(1): 34-38.

[16] Wang W, Winkler M T, Gunawan O, et al. Device Characteristics of CZTSSe Thin-Film Solar Cells with 12.6% Efficiency[J]. *Advanced Energy Materials*, 2014, **4**(7).

第34卷 增刊 硅 酸 盐 通 报 Vol. 34 Supplement
2015年11月 BULLETIN OF THE CHINESE CERAMIC SOCIETY November, 2015

磁控溅射制备 CZTS 薄膜的研究

李志山,王书荣,蒋 志,杨 敏,刘 涛,郝瑞亭
(云南师范大学太阳能研究所,教育部可再生能源材料先进技术与制备重点实验室,云南省农村能源重点工程实验室,昆明 650500)

摘要:本文采用单周期和多周期磁控溅射 ZnS-SnS-Cu 制备 CZST 薄膜。通过 X 射线衍射仪(XRD)、拉曼光谱仪(Raman)、高倍光学显微镜、扫描电子显微镜(SEM)、能谱仪(EDS)和热探针对所制备的 CZTS 薄膜的晶体结构、拉曼位移、表面形貌、化学组分和导电类型进行研究分析。分析结果表明,所制备 CZTS 薄膜的粘附性和结晶质量随着溅射周期的增加得到很大的改善,所制备的 CZTS 无 $Cu_{2-x}S$ 等其它二次相,且薄膜表面光滑、晶粒均匀致密、无孔洞。所制备的 CZTS 薄膜在化学组分是贫铜富锌(Cu/Zn + Sn≈0.88,Zn/Sn≈1.09),符合高效率太阳能电池吸收层的要求。

关键词:磁控溅射; CZTS; 薄膜电池; 硫化
中图分类号: O484 **文献标识码**:A **文章编号**:1001-1625(2015)S-0127-05

Cu_2ZnSnS_4 Thin Films Prepared by Magnetron Sputtering

LI Zhi-shan, WNAG Shu-rong, JIANG Zhi, YANG Min, LIU Tao, HAO Rui-ting
(Solar Energy Research Institute, Key Laboratory of Advance Technology and Preparation for Renewable Energy Materials, Ministry of Education, Yunnan Province Key Lab of Rural Energy Engineering, Yunnan Normal University, Kunming 650500, China)

Abstract: In this work, CZTS thin films were synhesized by the sulfurization of sputtered singly-period or multi-period ZnS-SnS-Cu precursors. The morphology, crystal structure, raman shift, surface morphology, chemical composition and conduction type of CZTS thin films were characterized by X Ray Diffraction (XRD), Raman spectroscopy, high-times optic microscope, scanning electron microscopy (SEM) equipped with an energy dispersive spectrometer (EDS) and thermal probe. The results show that the adhesion and crystal quality of CZTS thin films would be greatly improved with the increase of sputtering periods, there is no $Cu_{2-x}S$ and other second phase. The surface of CZTS thin films is very smooth, the grains are uniform and compact, and no holes. The preparated CZTS thin films were copper-poor and zinc-rich in chemical composition. It meets the requirements of high efficiency solar cells absorption layer.

Key words: sputtering; CZTS; thin film solar cells; sulfurization

1 引 言

新型四元化合物 CZTS 薄膜吸收层由于其具有与目前研究应用最广泛的 CIGS 薄膜太阳电池吸收层有相似的结构,它具有锌黄锡矿结构,并且相比于 CIGS 薄膜而言。它不含有稀有元素 In 和 Ga,且不含有毒元素 Se,并且 Zn、Sn 和 S 的成本也远远低于 In 和 Ga。其禁带宽度为 1.45 eV[1] 与单结薄膜太阳电池吸收层所

基金项目:国家科技合作重点项目(2011DFA62380);国家自然科学基金(61176127,61167003)
作者简介:李志山(1990-)男,硕士. 主要从事铜锌锡硫薄膜太阳电池的研究.
通讯作者:王书荣,博士,副教授.

要求的最佳禁带宽度1.5 eV十分接近,其理论效率可达32.2%[2],其为直接带隙半导体材料,吸收系数大于10^4 cm^{-1}[3]。因此,CZTS薄膜非常适合做新型薄膜太阳电池的吸收层。

目前制备CZTS薄膜的方法有很多,但主要分为两大类,真空法和非真空法。其中真空法主要包括磁控溅、脉冲激光沉积、蒸发等;非真空法主要包括溶胶凝胶、电化学沉积、喷雾热解等。基于CZTS(包括CZTS、CZTSe和CZTSSe)的薄膜太阳电池吸收层的效率由日本的Hironori Katagiri于1996年首次用分部蒸发制备出效率为0.66%的器件[4]。Katagiri研究小组于1999年在镀Mo的钠钙玻璃上沉积CZTS薄膜将效率提升到2.63%[5]。在2003年该小组通过优化硫化工艺,将效率提高到5.45%[6]。随后在2008年该小组通过对吸收层进行去离子水侵泡去除氧化物将效率提高到6.77%[7]。2010年Todorov等用联氨做溶剂通过化学方法制备出基于CZTSSe薄膜吸收层效率为9.6%的太阳能电池[8]。一年后又把该效率提升至10.1%[9]。2012 Todorov等将其效率提升至11.1%[10]。而基于磁控溅射化合物靶制备CZT(S,Se)的文献报道相比于其他方法较少。其中2008年Katagiri等通过共溅射ZnS-SnS-Cu后硒化制备出6.77% CZTSSe薄膜电池[8]。2012年Chawl和Clemens共溅射$Cu_x(S,Se)_y$-$Zn_x(S,Se)_y$-$Sn_x(S,Se)_y$然后在高温下退火制备出9.3%的CZTSSe薄膜电池[11]。2013年日本丰田研发中心分步溅射ZnS-Sn-Cu后在H_2S气氛下硫化制备出7.6%的纯CZTS薄膜电池[12],7.6%的效率也是磁控溅射制备纯CZTS薄膜电池之最。2014年国内南开大学李建军等人分步溅射Cu-ZnS-SnS预置层后硒化方法制备出3.35%的CZTSSe薄膜电池[13],并主要研究了6种不同叠层顺序对CZTSSe薄膜性能的影响。

截止目前,基于纯的CZTS薄膜吸收层的太阳电池的效率为8.4%,由IBM用共蒸发法制备[14],为世界纪录。同时IBM用涂覆法制备的基于CZTSSe薄膜吸收层的太阳电池效率达到12.6%[15],也为世界纪录。虽然如此,基于CZTS薄膜吸收层的太阳电池效率距离32.2%的理论效率还有很大的差距,因此优化吸收层的晶体质量、改善薄膜应力提高粘附性、生长大尺寸的晶粒、优化化学组分、减少粗糙度等还有很多的工作需要做。因为以上每一个因素都会对电池的效率起着至关重要的作用。本文通过磁控溅射ZnS-SnS-Cu预置层并后硫化的方法制备CZTS薄膜,重点研究了不同溅射周期对薄膜的粘附性和晶体质量的影响,通过优化制备工艺条件,特别是溅射周期。最终研制出了符合高效率太阳能电池吸收层要求的CZST薄膜。

2 实 验

2.1 CZTS薄膜的制备

本实验用新型太阳能电池磁控溅射成膜系统制备CZTS薄膜过程如下:采用钠钙玻璃做基底,对钠钙玻璃进行丙酮 、酒精 和去离子水超声清洗后,用氮气吹干后放入溅射腔室中,本底真空为5.0×10^{-4} Pa,首先在钠钙玻璃上直流溅射1 μm的钼,工作压强为1.6~0.3 Pa渐变,功率为180 W;预置层厚度和组分理论上设计为:d=600 nm,Cu/(Zn+Sn)≈0.65,Zn/Sn≈1.4。随后根据实验测出的ZnS、SnS、Cu的溅射速率,用射频溅射ZnS-SnS-Cu制备600 nm的预置层(Cu为顶层),其中ZnS的厚度为274 nm,SnS的厚度为233 nm,Cu的厚度为93 nm。工作压强为0.3 Pa,ZnS、SnS、和Cu的溅射功率分别为50 W、50 W、100 W;溅射沉积Mo/ZnS/SnS/Cu预置层的周期分别为单周期、两周期和四周期。将制备好的预置层在快速退火炉中进行低温热处理,热处理条件为高纯N_2气氛下温度为280 ℃保温30 min;最后将热处理后的薄膜进行硫化处理,硫化条件为高纯N_2气氛下将热处理后的薄膜与硫粉放入石墨舟里在温度为580 ℃的硫化炉中保温25 min得到CZTS薄膜吸收层。

2.2 测试与表征

采用日本理学Ultima IV X射线衍射仪(XRD)、Renishaw in Via拉曼光谱仪(Raman)、莱卡高倍光学显微镜(Leica CTR6000)、配备能谱仪(EDS)的FEI Quanta 2000扫描电子显微镜(SEM)和热探针对所制备的CZTS薄膜的晶体结构、拉曼位移、化学组分和表面形貌进行和导电类型进行表征。

3 结果与讨论

图1为采用不同周期溅射制备的CZTS薄膜的表面形貌。从图1可以看出,对于单周期制备的CZTS薄

膜表面脱落比较严重(颜色亮的地方为脱落的部分),两周期制备的 CZTS 薄膜表面少量地方脱落,而四周期制备的 CZTS 薄膜表面平整,没有脱落的地方。对于薄膜脱落是由于各层间存在较大的应力,尤其是最下层 ZnS 和 Mo 层之间有较大的热应力,薄膜间粘附性差,加上各层间热膨胀系数不一,所以在高温硫化的过程中导致薄膜脱落。由图可知可以通过增加溅射周期来减小各分层的厚度,从而高温硫化时各分层之间的热应力能得到充分释放而改善薄膜的粘附性问题,考虑到溅射周期数越多将会导致制备工艺过程比较复杂,所以本文选择最佳制备周期为四周期。

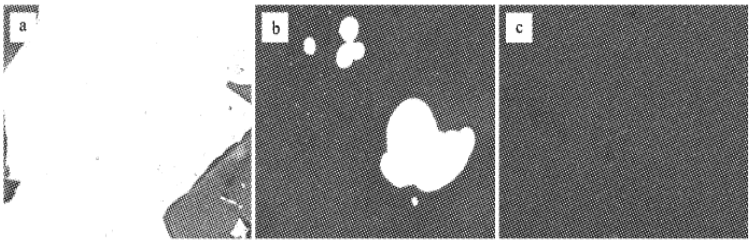

图 1　不同溅射周期制备的 CZTS 薄膜的 50 倍显微镜图像(a)单周期;(b)两周期;(c)四周期

Fig. 1　50 times microscope images of the CZTS thin films obtained at the different sputtering periods

对不同周期制备的 CZTS 薄膜的 XRD 测试结果如图 2 所示,由该图可知,不同周期所制备的 CZTS 薄膜都没有杂相,基本上为纯 CZTS 相,且在不同的 2θ 角所有的衍射峰基本一样,只是峰强不一样,其中 A 为单周期溅射,B 为两周期溅射,C 为四周期溅射,由图表明 CZTS 薄膜结晶质量和结晶度随着溅射周期的增加明显提高,这是因为随着随着溅射周期的增加,其应力得以释放,所以其结晶质量和结晶度有很明显的加强。图中 2θ 为 28.5°、47.5°、56.3°是 CZTS 三个主峰,分别对应(112)、(220)、(312)面,并且沿(112)晶向面择优取向生长,其他一些较弱的峰与锌黄锡矿结构的 CZTS 标准卡(JCPDS 26-0575)完全一致。

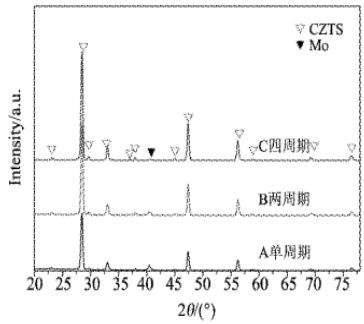

图 2　不同溅射周期制备的 CZTS 薄膜的 XRD 谱图

Fig. 2　XRD patterns of the CZTS thin films obtained at the different sputtering periods

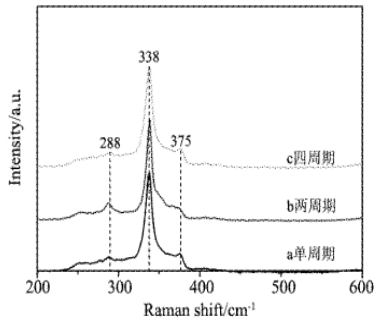

图 3　不同溅射周期制备的 CZTS 薄膜的拉曼谱图

Fig. 3　Raman spectra of the CZTS thin films obtained with different sputtering periods

由于锌黄锡矿的 CZTS 和立方 ZnS、四角 Cu_2SnS_3 等具有非常相似的晶体结构,主峰的位置也基本重合,因此单从 XRD 不能完全证明没有立方 ZnS、四角 Cu_2SnS_3 等这些二次相。因此,为了进一步分析 CZTS 薄膜是否为真正地单相,分别对不同周期溅射制备的薄膜做了激光器光源为 514 nm 的 Raman 测试。图 3 为所测得的拉曼谱,图中表明不同周期(a 单周期、b 两周期、c 四周期)所制备的 CZTS 拉曼位移基本一致,且无立方相的 ZnS(351 cm^{-1}),四角的 Cu_2SnS_3(297 cm^{-1} 和 353 cm^{-1})和六角的 $Cu_{2-x}S$(475 cm^{-1})[16] 等,这和 XRD 测试结果一样。其三个特征峰 288 cm^{-1}、338 cm^{-1} 和 375 cm^{-1} 符合标准 CZTS 薄膜的测试结果。该结果表明不同周期制备的 CZTS 薄膜为单相结构,满足制备 CZTS 薄膜太阳电池的要求。

对不同周期制备的 CZTS 薄膜的 XRD 测试结果如图 4 所示,其中 a、b、c 分别为单周期,两周期和四期所

制备的 CZTS 薄膜的 SEM 形貌图。从图中可以看出来,CZTS 薄膜表面致密性和晶粒尺寸随着溅射周期的增加得到了很大的改善,因为随着溅射周期的增加,高温硫化时薄膜间的热应力得到充分释放。两周期和四周期的 CZTS 的表面明显要好于单周期的,而对于两周期和四周期而言,晶粒尺寸没有显著的改变,但相比两周期而言,四周期的晶粒尺寸大小更加均匀,表面更加致密,孔洞明显减少。

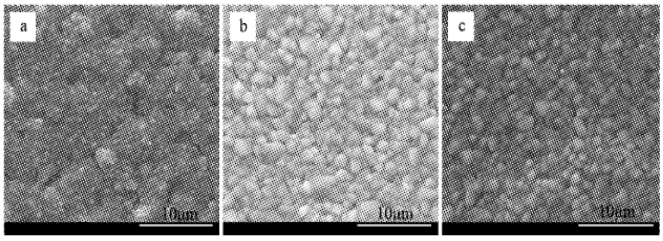

图 4 不同溅射周期制备的 CZTS 薄膜的 SEM 形貌图(a)单周期;(b)两周期;(c)四周期

Fig. 4 SEM images of the CZTS thin films obtained at the different sputtering periods

对不同周期制备的 CZTS 薄膜的 EDS 测试结果如表一所示,从表一可以看出,不同溅射周期在相同条件下硫化后制备的 CZTS 薄膜的成分基本相同,微弱的不同可能由于周期越多,元素间在硫化的过程中相互扩散越充分,严格控制好温度和时间就能避免元素的损失。从上表可以看出所制备的 CZTS 中的 Cu/(Zn + Sn) 和 Zn/Sn 的比例都在高效 CZTS 薄膜太阳电池的最佳比例范围内 Cu/(Zn + Sn) ≈0.8 ~ 0.92,Zn/Sn ≈ 1.05 ~ 1.25。最后,对所制备的 CZTS 薄膜用热探针进行检测,所有的样品都为 P 型半导体薄膜。由上面的结果可知,所制备的 CZTS 薄膜为贫铜富锌的单相结构,且导电类型为 P 型,非常适合用作高效薄膜太阳电池的吸收层。

表 1 不同溅射周期硫化后制备的 CZTS 薄膜的成分

Tab. 1 Component and atomic ratio of the CZTS thin films obtained at the different sputtering periods

周期数	Elemental composition/at%				Cu/(Zn + Sn)	Zn/Sn
	Cu	Zn	Sn	S		
单周期	22.70	12.93	11.98	52.39	0.91	1.08
两周期	22.07	12.99	12.01	52.93	0.88	1.08
四周期	21.84	13.01	11.94	53.21	0.88	1.09

4 结 论

本文采用磁控溅射单周期、两周期和四周期成功的制备 CZTS 薄膜,通过优化工艺条件最后制备出符合太阳能电池吸收层要求的贫铜富锌的 CZST 薄膜。由高倍显微镜测试分析可知,四周期所制备的 CZTS 薄膜在高温硫化后薄膜表面平整,无脱落现象;由 XRD 测试分析表明,四周期溅射制备的 CZTS 薄膜的结晶质量最好峰强最强;由 Raman 测试分析表明,所制备的薄膜为纯的 CZTS 相,无其他杂相;由 SEM 测试分析表明,四周期溅射制备的 CZTS 薄膜的表明光滑平整,空洞最少,晶粒大小最均匀;由能谱仪(EDS)和热探针测试分析表明,所制备的 CZTS 薄膜属于贫铜富锌的 P 型半导体材料。综上可知,四周期下所制备的 CZTS 薄膜在化学组分是贫铜富锌(Cu/Zn + Sn ≈0.88,Zn/Sn ≈1.09),符合高效率太阳能电池吸收层的要求。

参 考 文 献

[1] Ito K, Nakazawa T. Electrical and optical properties of stannite-type quaternary semiconductor thin films[J]. *Japanese Journal of Applied Physics*, 1988, **27**(11R): 2094.

[2] Shockley W, Queisser H J. Detailed balance limit of efficiency of p-n junction solar cells[J]. *Journal of applied physics*, 1961, **32**(3): 510-519.

[3] Jimbo K, Kimura R, Kamimura T, et al. Cu_2ZnSnS_4-type thin film solar cells using abundant materials[J]. *Thin Solid Films*, 2007, **515**(15):

5997-5999.

[4] Katagiri H, Nishimura M, Onozawa T, et al. Rare-metal free thin film solar cell[C]. Power Conversion Conference-Nagaoka 1997, Proceedings of the. IEEE, 1997, 2: 1003-1006.

[5] Katagiri H, Saitoh K, Washio T, et al. Development of thin film solar cell based on Cu_2ZnSnS_4 thin films[J]. *Solar Energy Materials and Solar Cells*, 2001, **65**(1): 141-148.

[6] Katagiri H, Jimbo K, Moriya K, et al. Solar cell without environmental pollution by using CZTS thin film[C]. Photovoltaic Energy Conversion, 2003. Proceedings of 3rd World Conference on. IEEE, 2003, 3: 2874-2879.

[7] Katagiri H, Jimbo K, Yamada S, et al. Enhanced conversion efficiencies of Cu_2ZnSnS_4-based thin film solar cells by using preferential etching technique[J]. *Applied physics express*, 2008, **1**(4): 041201.

[8] Todorov T K, Reuter K B, Mitzi D B. High-efficiency solar cell with earth-abundant liquid-processed absorber[J]. *Advanced materials*, 2010, **22**(20): E156-E159.

[9] Barkhouse D A R, Gunawan O, Gokmen T, et al. Device characteristics of a 10.1% hydrazine-processed $Cu_2ZnSn(Se,S)_4$ solar cell[J]. *Progress in Photovoltaics: Research and Applications*, 2012, **20**(1): 6-11.

[10] Todorov T K, Tang J, Bag S, et al. Beyond 11% efficiency: characteristics of state-of-the-art $Cu_2ZnSn(S, Se)_4$ solar cells[J]. *Advanced Energy Materials*, 2013, **3**(1): 34-38.

[11] Chawla V, Clemens B. Effect of composition on high efficiency CZTSSe devices fabricated using co-sputtering of compound targets[C]. Photovoltaic Specialists Conference (PVSC), 2012 38th IEEE. IEEE, 2012: 002990-002992.

[12] Fukano T, Tajima S, Ito T. Enhancement of conversion efficiency of Cu_2ZnSnS_4 thin film solar cells by improvement of sulfurization conditions[J]. *Applied Physics Express*, 2013, **6**(6): 062301.

[13] Li J, Zhang Y, Wang H, et al. On the growth process of $Cu_2ZnSn(S,Se)_4$ absorber layer formed by selenizing Cu-ZnS-SnS precursors and its photovoltaic performance[J]. *Solar Energy Materials and Solar Cells*, 2015, **132**: 363-371.

[14] Shin B, Gunawan O, Zhu Y, et al. Thin film solar cell with 8.4% power conversion efficiency using an earth-abundant Cu_2ZnSnS_4 absorber[J]. *Progress in Photovoltaics: Research and Applications*, 2013, **21**(1): 72-76.

[15] Wang W, Winkler M T, Gunawan O, et al. Device characteristics of CZTSSe thin-film solar cells with 12.6% efficiency[J]. *Advanced Energy Materials*, 2014, **4**(7): 1301465.

[16] Fernandes P A, Salomé P M P, Da C A F. Study of polycrystalline Cu_2ZnSnS_4 films by Raman scattering[J]. *Journal of Alloys and Compounds*, 2011, **509**(28): 7600-7606.

第34卷 增刊 硅 酸 盐 通 报 Vol. 34 Supplement
2015年11月 BULLETIN OF THE CHINESE CERAMIC SOCIETY November, 2015

磁控溅射金属预置层后硒化制备 $Cu_2ZnSnSe_4$ 薄膜

李志山,王书荣,蒋 志,杨 敏,刘思佳,郭任君,唐 语,郝瑞亭,杨培志
(云南师范大学太阳能研究所,教育部可再生能源材料先进技术与制备重点实验室,云南省农村能源重点工程实验室,昆明 650500)

摘要:采用磁控溅射 Zn-Cu-Sn-Cu 金属预置层并后硒化的方法在镀钼玻璃衬底上制备了 CZTSe 薄膜。利用 X 射线衍射仪(XRD)、拉曼光谱测试仪(Raman)、扫描电子显微镜(SEM)、能谱仪(EDS)和热探针对所制备 CZTSe 薄膜的晶相结构、拉曼位移、表面形貌、化学组分和导电类型进行表征分析,分析结果表明:所制备 CZTSe 薄膜结晶质量好、无二次相、晶粒均匀致密、化学组分是贫铜富锌的,且导电类型为 p 型,符合高效率太阳电池吸收层的要求。将 CZTSe 吸收层制备成有效面积为 0.35 cm^2 的 Mo/CZTSe/CdS/i-ZnO/ZnO:Al/Ni-Al 电池,其效率为 1.17%,开路电压为 419 mV,短路电流密度为 10.21 mA/cm^2,填充因子为 27%。

关键词:磁控溅射; CZTSe; 硒化; 开路电压
中图分类号:TM914 **文献标识码**:A **文章编号**:1001-1625(2015)S-0198-04

Growth of $Cu_2ZnSnSe_4$ Thin Films by Selenization of Sputtered Metallic Precursors

LI Zhi-shan, WANG Shu-rong, JIANG Zhi, YANG Min, LIU Si-jia, GUO Ren-jun, TANG Yu, HAO Rui-ting, YANG Pei-zhi
(Key Laboratory of Advance Technology and Preparation for Renewable Energy Materials, Ministry of Education, Yunnan Province Key Lab of Rural Energy Engineering, Solar Energy Research Institute, Yunnan Normal University, Kunming 650500, China)

Abstract: CZTSe thin films were fabricated on Mo-coated soda-lime glass substrates. The crystal structure, Raman shift, surface morphology, chemical composition and conduction type of CZTSe thin films were investigated by X Ray Diffraction (XRD), Raman spectroscopy (Raman), scanning electron microscopy (SEM) equipped with an energy dispersive spectrometer (EDS) and thermal probe. The results show that the preparation of CZTSe film with dense and uniform crystal grains which also demonstrates good quality of crystallization, besides there is no other second phase. The chemical composition of CZTSe was poor copper and zinc rich, and p-type conduction. The active area of 0.35 cm^2 cells was fabricated as the order of Mo/CZTSe/CdS/i-ZnO/ZnO: Al/Ni-Al, which has 1.17% efficiency, an open-circuit voltage of 419 mV, current density of 10.21 mA/cm^2 and fill factor of 27%.

Key words: magnetron sputtering; CZTSe; selenization; open-circuit voltage

1 引 言

尽管铜铟镓硒(CIGS)和碲化镉(CdTe)太阳电池仍然是化合物半导体薄膜电池吸收层的主流材料,但因 CIGS 中其组成元素铟和镓在自然界中含量少,属于稀缺元素,且价格昂贵,而 CdTe 中因其 Cd 是重金属

基金项目:国家自然科学基金(61167003,61176127)
作者简介:李志山(1990-),男,硕士研究生. 主要从事铜锌锡硫薄膜太阳电池方面的研究.
通讯作者:王书荣,博士,副教授.

元素,会对环境造成严重的威胁[1,2]。因此,基于 Cu_2-Ⅱ-Ⅳ-$Ⅵ_4$ 的四元化合物半导体:Cu_2ZnSnS_4(CZTS),$Cu_2ZnSnSe_4$(CZTSe),和 $Cu_2ZnSn(S_{1-x}Se_x)_4$[3-5],由于其组成元素在自然界中丰富且无毒,可以满足 TW 级生产,且其价格相对较低。再者其属于直接带隙 P 型半导体,有高的吸收系数($>10^4$ cm^{-1}),带隙可通过控制 S/(S+Se)的比例 0~1 来调节使其在 1.0 eV~1.5 eV 之间[6-9]。并且其太阳电池其理论效率可达 32.2 %[10],是一种有替代 CdTe 和 Cu(In,Ga)Se_2(CIGS)的新型薄膜太阳电池材料。

目前所制备的基于 CZTS、CZTSe 和 CZTSSe 的薄膜电池世界纪录分别为 8.4%[11]、11.6%[12]和 12.6%[13]。虽然如此,基于 CZTS 薄膜吸收层的太阳电池效率距离 32.2 % 的理论效率还有很大的差距。本文通过磁控溅射 Sn-Cu-Zn-Cu 金属预置层后硒化的方法制备出特性较好的 CZTSe 薄膜,能符合高效率太阳能电池吸收层要求的 CZTSe 薄膜。并将其制备成完整的电池器件,取得了 1.17% 的光电转换效率和高达 419 mV 的开路电压。

2　实　验

2.1　实验过程

预置层采用新型国产太阳能电池磁控溅射成膜系统制备,过程如下:按照 Mo/Sn/Cu/Zn/Cu 的溅射顺序。首先在清洗干净的钠钙玻璃衬底上直流溅射 1 μm 厚的钼背电极,工作压强为 1.6 Pa 线性渐变至 0.3 Pa,溅射功率为 180 W;随后用射频磁控溅射 Sn/Cu/Zn/Cu 制备金属预置层,工作压强为 0.3 Pa,功率分别为 50 W、100 W、50 W、100 W,预置层厚度设计为:$d\approx700$ nm,化学组分为:Cu/(Zn+Sn)≈0.7,Zn/Sn≈1.3。所有靶材的纯度为 99.99 %,本底真空为 5.0×10^{-4} Pa。将制备好的金属预置层在快速退火炉中进行不同温度的低温热处理,低温热处理的目的是让 Cu 、Zn 、Sn 三种金属互扩散混合均匀。最后将低温热处理后的金属薄膜预制层进行硒化处理,硒化条件为:将热处理后的预置层与固态硒粉与少量锡粉放入石墨舟里温度为 570 ℃的高纯 N_2 气氛下硒化 20 min 后自然冷却至室温得到 CZTSe 薄膜吸收层,硒化时压力维持在 3000 Pa,升温速率为 25 ℃/min,锡粉和硒粉的质量分别为 50 mg 和 600 mg。最后在 CZTSe 吸收层上用化学水浴法(CBD)沉积 50 nm 的 CdS,然后用射频磁控溅射依次沉积 50 nm 的 i-ZnO 和 400 nm 的 ZnO:Al,最后再用电子束热蒸发沉积 2 μm 的 Ni/Al 电极。

2.2　测试与表征

采用日本理学 Ultima IV X 射线衍射仪(XRD)、配备能谱仪 EDS (EDAX)的 FEI Quanta 2000 扫描电子显微镜(SEM)和热探针对所制备 CZTSe 薄膜的晶相结构、表面形貌、化学组分、进行表征分析。为了确定 CZTSe 相的纯度,对所制定的样品进行了拉曼光谱测试,最后对 CZTSe 薄膜电池的 *I-V* 特性进行表征,测试在标准测试条件下(AM1.5, 100 mW/cm^2, 300 K)进行,采用 NEWPORT 太阳光模拟器作为光源,利用美国 KEITHLEY 公司生产的 2400 数字源表完成。

3　结果与讨论

将溅射的金属预置层在 200 ℃、250 ℃、300 ℃不同温度下在高纯 N_2 气氛下热处理 30 min,将未经过低温热处理的预置层和不同温度下热处理后的预置层在高纯 N_2 气氛下 570 ℃硒化 20 min 自然冷却至室温,侧得 XRD 分别如图 1 所示,从图 1 可以看出,不同温度下热处理的预置层最后在相同条件下硒化后的结晶质量有所不同,其中最差的是未经过低温热处理的,结晶质量最好的是在 250 ℃低温热处理的,其相对衍射强度较强,且衍射主峰强半高全宽(FWHM)较窄。可见金属预置层先在适当低温热处理后高温硒化有助于改善晶体质量,有利于后续的高温硒化充分形成 CZTSe。由硒化的 XRD 图可以看出,所制备的 CZTSe 三个比较强的峰在图中 2θ 分别为 27.2°、45.1°、53.4°,与之分别对应(112)、(220)、(312)面,并且沿(112)晶向择优取向生长,其余的峰都与锌黄锡矿结构的 CZTSe 标准卡片(JCPDS 052-0868)相对应,这与很多文献报道的相一致[14-16]。同时从图中未能观察到 CuSe、Cu_2Se、SnSe 和 Sn_2Se 等二次相的衍射峰。

由于 ZnSe 和 Cu_2SnSe_3 等二次相与 CZTSe 有非常相似的晶体结构,仅从 XRD 检测很难发现薄膜中的这些二次相,为了进一步分析 CZTSe 薄膜的结构,对在低温 250 ℃热处理后高温 570 ℃硒化的的样品进行了拉

曼光谱测试,如图2所示,在扫描波长为172 cm^{-1}、195 cm^{-1}和236 cm^{-1}时,明显的观察到CZTSe的特征峰,其中位于195 cm^{-1}的拉曼峰为主峰,该拉曼光谱与许多文献报道相符合[17]。且该拉曼光谱与XRD测试结果相一致,并没有发现ZnSe(250 cm^{-1})等的拉曼特征峰存在。这说明薄膜样品不含二次相或二次相含量极少不在仪器仪器的检测范围内。

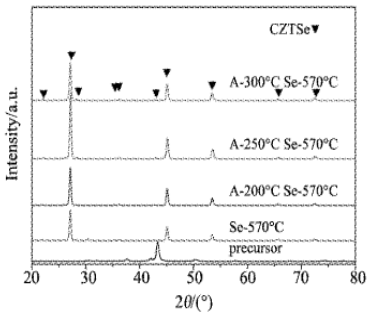

图1 预置层,预置层在不同温度下合金后硒化CZTSe薄膜的XRD图谱

Fig. 1 XRD patterns of the CZTSe films as-deposited precursor, alloyed at different temperatures after selenided

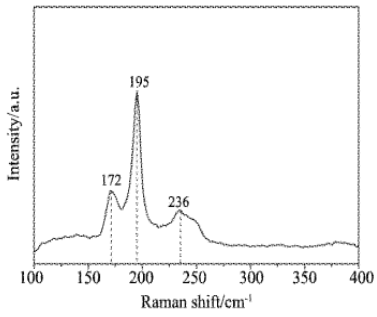

图2 250 ℃合金,570 ℃硒化的CZTSe薄膜的Raman图谱

Fig. 2 Raman spectrum of the CZTSe was alloyed at 250 ℃ and selenide at 570 ℃

图3为CZTSe薄膜先在低温250 ℃热处理后高温570 ℃硒化的SEM表面形貌图,其中a、b、c分别对应10000倍、20000倍和50000倍。从图中可以看出来,CZTSe薄膜表面致密性好,基本无空洞,晶粒大小均匀。但表面平整性不太好,晶粒比较小,大小在0.6 μm左右,这将不利于载流子的输运,因为晶界数目较多。最终将会导致电池的短路电流密度很小。

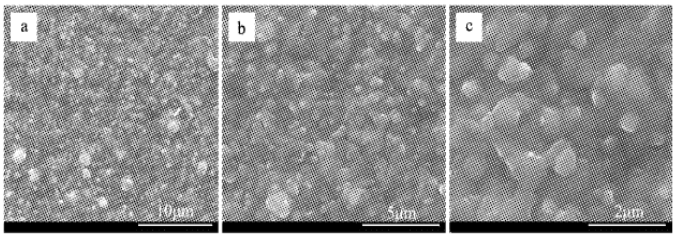

图3 250 ℃合金,570 ℃硒化的CZTSe薄膜的SEM表面形貌图

Fig. 3 SEM images of the CZTSe thin films was alloyed at 250 ℃ and selenide at 570 ℃

CZTSe薄膜的化学组分由EDS测试,表一为CZTSe薄膜先在低温250 ℃热处理后高温570 ℃硒化所测试的化学组分。从表1可以看出所制备的CZTSe在组分上偏离化学配比,属于贫铜富锌Cu/(Zn+Sn)=0.86,富锌Zn/Sn=1.15,Se/M为1.12,符合高效率太阳能电池吸收层的要求。这也和许多文献报道的一致,高效CZTSe薄膜太阳电池的最佳比例范围内Cu/(Zn+Sn)≈0.8~0.92,Zn/Sn≈1.05~1.25。

表1 250 ℃合金,570 ℃硒化的CZTSe薄膜的化学组分和原子比,其中M=Cu+Zn+Sn

Tab. 1 Component and atomic ratio of the CZTSe thin films was alloyed at 250 ℃ and selenide at 570 ℃, M=Cu+Zn+Sn

Elemental composition(at%)				Cu/(Zn+Sn)	Zn/Sn	Se/M
Cu	Zn	Sn	Se			
21.86	13.56	11.80	52.78	0.86	1.15	1.12

图4为在所制备的CZTSe薄膜上:采用化学水浴(CBD)、磁控溅射、蒸发依次沉积硫化镉(CdS)缓冲层、

氧化锌/掺铝氧化锌(ZnO/AZO)窗口层、镍/铝(Ni/Al)栅线电极得到 CZTSe 薄膜太阳电池的 *J-V* 曲线,电池的有效面积为 0.35 cm^2。由图可知,所制备 CZTSe 薄膜电池的开路电压(V_{oc})为 419 mV,短路电流密度(J_{sc})为 10.21 mA/cm^2,填充因子(*FF*)为 27%,效率为 1.17%。相比于其他文献报道的,电压比较高,而短路电流和填充因子非常低。这可能是由于在硒化过程中产生一定厚度的 $MoSe_2$,导致背电极与吸收层接触不好,其次由于表面较粗糙,在蒸发制备上电极时与窗口层接触不好等产生较大的接触电阻,最终增大了电池的串联电阻;再者可能是薄膜电池中的缺陷较多复合较严重,收集到栅极的光生载流子偏少,最终导致短路电流和填充因子较低。

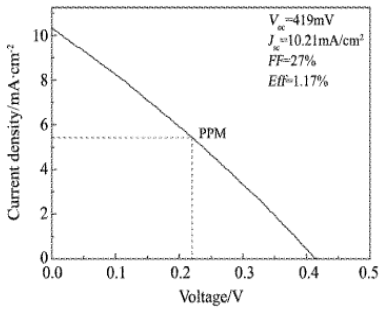

图 4　CZTSe 太阳电池的的 *J-V* 曲线

Fig. 4　*J-V* characteristics of CZTSe solar cells (AM1.5, 100 mW/cm^2)

4　结　论

采用磁控溅射在钼衬底上溅射 Sn-Cu-Zn-Cu 金属预置层后硒化的方法制备出 CZTSe 薄膜。所制备 CZTSe 薄膜结晶质量好、晶粒均匀致密、化学组分是贫铜富锌的,导电类型为 P 型,符合高效率太阳电池吸收层的要求。并且本文得出预置层最佳合金温度为 250 ℃。将最优的 CZTSe 吸收层按照 Mo/CZTSe/CdS/i-ZnO/ZnO: Al/Ni-Al 的顺序制备成太阳能电池器件,*J-V* 测试结果表明所制备的 CZTSe 薄膜电池开路电压为 419 mV,但短路电流密度和填充因子非常低,导致效率非常低。所以今后的工作重点在于如何提高短路电流和填充因子,重点是提高表面平整度,采用化学腐蚀去除可能存在的二次相,改善硒化工艺增大晶粒尺寸,优化电极的制备,以便减小串联电阻,提高短路电流密度和填充因子进一步提高 CZTSe 的效率。

参　考　文　献

[1] Green M A. Estimates of Te and In prices from direct mining of known ores[J]. *Progress in Photovoltaics: Research and Applications*, 2009, **17**(5): 347-359.

[2] Fthenakis V M, Moskowitz P D. Thin-film photovoltaic cells: health and environmental issues in their manufacture use and disposal[J]. *Progress in Photovoltaics: Research and Applications*, 1995, **3**(5): 295-306.

[3] Wang K, Gunawan O, Todorov T, et al. Thermally evaporated Cu_2ZnSnS_4 solar cells[J]. *Applied Physics Letters*, 2010, **97**(14): 3508.

[4] Guo Q, Ford G M, Yang W C, et al. Fabrication of 7.2% efficient CZTSSe solar cells using CZTS nanocrystals[J]. *Journal of the American Chemical Society*, 2010, **132**(49): 17384-17386.

[5] Barkhouse D A R, Gunawan O, Gokmen T, et al. Device characteristics of a 10.1% hydrazine-processed $Cu_2ZnSn(Se, S)_4$ solar cell[J]. *Progress in Photovoltaics: Research and Applications*, 2012, **20**(1): 6-11.

[6] Das S, Frye C, Muzykov P G, et al. Deposition and characterization of low-cost spray pyrolyzed Cu_2ZnSnS_4 (CZTS) thin-films for large-area high-efficiency heterojunction solar cells[J]. *ECS Transactions*, 2012, **45**(7): 153-161.

[7] Das S, Mandal K C. Comparison of Cu_2ZnSnS_4 thin film properties prepared by thermal evaporation of elemental metals and binary sulfide sources [C]. Photovoltaic Specialists Conference (PVSC), 2012 38th IEEE. IEEE, 2012: 002674-002678.

[8] Repins I, Beall C, Vora N, et al. Co-evaporated $Cu_2ZnSnSe_4$ films and devices[J]. *Solar Energy Materials and Solar Cells*, 2012, **101**: 154-159.

[9] Riha S C, Parkinson B A, Prieto A L. Compositionally tunable $Cu_2ZnSn(S_{1-x}Se_x)_4$ nanocrystals: probing the effect of Se-inclusion in mixed chalcogenide thin films[J]. *Journal of the American Chemical Society*, 2011, **133**(39): 15272-15275.

[10] Shockley W, Queisser H J. Detailed balance limit of efficiency of p-n junction solar cells[J]. *Journal of applied physics*, 1961, **32**(3): 510-519.

[11] Shin B, Gunawan O, Zhu Y, et al. Thin film solar cell with 8.4% power conversion efficiency using an earth-abundant Cu_2ZnSnS_4 absorber[J]. *Progress in Photovoltaics: Research and Applications*, 2013, **21**(1): 72-76.

[12] Lee Y S, Gershon T, Gunawan O, et al. $Cu_2ZnSnSe_4$ thin-film solar cells by thermal co-evaporation with 11.6% efficiency and improved minority carrier diffusion length[J]. *Advanced Energy Materials*, 2015, **5**(7): 1401372-1401376.

(下转第 206 页)

第34卷 增刊 硅 酸 盐 通 报 Vol. 34 Supplement
2015年11月 BULLETIN OF THE CHINESE CERAMIC SOCIETY November, 2015

磁控溅射法制备铜锌锡硫薄膜电池

杨 敏,王书荣,蒋 志,李志山,刘思佳,郭任君,唐 语,郝瑞亭,杨培志
(云南师范大学太阳能研究所,教育部可再生能源材料先进技术与制备重点实验室,云南省农村能源重点工程实验室,昆明 650500)

摘要:采用磁控溅射法,先在镀钼的钠钙玻璃衬底上共溅射Cu、Sn金属层后,然后在顶部溅射一层ZnS,制备出Cu_2ZnSnS_4(CZTS)薄膜的预制层。对预制层进行低温合金,然后以硫粉作为硫源在石英管中进行高温硫化,得到表面平整但晶粒较小的CZTS薄膜。通过X射线衍射仪(XRD)、扫描电镜(SEM)及能谱仪(EDS)分别对薄膜的晶体结构、表面形貌和薄膜组分进行分析表征;并用拉曼光谱表征了CZTS相的纯度。最后用所得到的CZTS薄膜制备了太阳电池,其开路电压:V_{oc}=442 mV,短路电流密度:J_{sc}=5.08 mA/cm^2,光电转换效率达到0.62% 。

关键词:铜锌锡硫(CZTS); 磁控溅射; 硫化; 薄膜太阳电池
中图分类号: TM912 **文献标识码**:A **文章编号**:1001-1625(2015)S-0222-05

Cu_2ZnSnS_4 Thin Film Solar Cells Prepared by Sulfurization of Sputtered Precursors

YANG Min, WANG Shu-rong, JIANG Zhi, LI Zhi-shan, LIU Si-jia,
GUO Ren-jun, TANG Yu, HAO Rui-ting, YANG Pei-zhi
(Yunnan Province Key Lab of Rural Energy Engineering, Solar Energy Research Institute of Yunnan Normal University, Key Laboratory of Advance Technology and Preparation for Renewable Energy Materials, Ministry of Education, Kunming 650500, China)

Abstract: The precursors of Cu_2ZnSnS_4 (CZTS) thin films were prepared on Mo-coated soda lime glasses by sulfurization of magnetron sputtered (Cu + Sn)/ZnS layers. Prior to sulfurization, the precursors were soft annealed under lower temperature. CZTS thin films with smooth surface but fine grains were obtained by high temperature annealing under sulfur vapor atmosphere. The crystal structure, surface morphology and composition of the films were characterized by X-ray diffraction (XRD), scanning electron microscope (SEM) and energy dispersive spectrometry (EDS) respectively. Meanwhile the purity of CZTS thin film phases was identified by raman spectroscopy. The conversion efficiency of the fabricated CZTS film solar cell was 0.62% with an open-circuit voltage of 442 mV, a short-circuit current density of 5.08 mA/cm^2.

Key words: Cu_2ZnSnS_4 (CZTS); magnetron sputtering; sulfurization; thin film solar cells

1 引 言

如今$CuIn_{1-x}Ga_xSe_2$(CIGS)薄膜太阳电池的光电转换效率已超过了20%[1],然而因其含有稀缺元素In和Ga,造成大规模工业化生产成本较高。Cu_2ZnSnS_4(CZTS)与CIGS的晶体结构相似[2],用地壳含量比较丰富的Zn和Sn代替了In和Ga元素,被认为是极有可能取代CIGS的薄膜太阳电池材料[3]。

基金项目:国家自然科学基金(61167003);国家自然科学基金(61176127)
作者简介:杨 敏(1992-)女,硕士研究生.主要从事铜锌锡硫薄膜太阳电池方面的研究.
通讯作者:王书荣,博士,副教授.

CZTS 是直接带隙四元化合物半导体,成分无毒且环境友好。其禁带宽度为 1.4 ~ 1.5 eV,具有较大的光吸收系数(10^4 cm^{-1})[4]。近几年国内外的许多研究机构对 CZTS(Se)薄膜及 CZTS(Se)薄膜电池展开了更深入的研究,并取得了突破性的进展。美国 IBM 用热蒸发法制备出纯的 CZTS 薄膜电池,效率达到 8.4%[5],居于目前世界领先水平。

制备 CZTS 薄膜的方法主要有磁控溅射[6]、真空蒸发[7]、喷雾热解[8]、溶胶凝胶[9]和电化学沉积[10]等。其中磁控溅射是一种可大面积生产薄膜太阳电池,容易调控实验条件并且操作方便的真空镀膜方法[11]。通常溅射法制备 CZTS 薄膜的工艺有:分步/共溅射金属单质靶形成前驱体,然后高温硫化[12-14];其次还有分步/共溅射金属化合物靶(或混合金属单质靶)制备 CZTS 前驱体,然后硫化[15-17]等。而根据南开大学报道,在高温及 S/Se 分压较高的情况下进行硫化或硒化,容易在 CZTS(Se)/Mo 的界面形成较厚的 MoS_2/$MoSe_2$ 增加了电池的串联电阻。为解决这个问题,南开大学对预制层进行了 300 ℃的低温合金处理,有效抑制了 MoS_2/$MoSe_2$ 的生成[18]。并且,在很多文献中表明,Cu、Sn 金属层毗邻,有利于提高薄膜的质量和器件的性能[19]。因此,本文采用共溅射 Cu、Sn 金属层后,在其顶部溅射一层 ZnS 制备出 CZTS 的预制层(SLG/Mo/Cu + Sn/ZnS),然后在氮气保护下以 260 ℃温度进行低温合金,最后把合金的样品放置在石墨舟中以 600 ℃高温进行硫化。得到表面平整、致密的 CZTS 薄膜。用其制备的 CZTS 薄膜太阳电池光电转换效率为 0.62%。电池效率低的原因可能是因为 CZTS 吸收层晶粒较小,晶界复合比较严重。而且硫化过程中锡的损失可能导致薄膜中形成一些二次相,增加了漏电机制。有关电池效率低的更多原因,有待在今后的研究过程中进行更完善的性能测试及探讨研究。

2　实　验

2.1　CZTS 薄膜吸收层及电池的制备

利用高真空磁控溅射成膜系统在镀 Mo(1 μm)的钠钙玻璃上制备 CZTS 薄膜的预制层。溅射顺序为 Cu、Sn 共溅射,然后溅射 ZnS,靶材的纯度都为 99.99%。用射频电源溅射三靶,溅射功率分别为:Cu-100 W,Sn-50 W,ZnS-50 W。工作气压为 0.3 Pa,靶极距约为 8 cm,基片台的转速为 8 rpm,且衬底不加温,得到预制层的总厚度约为 500 nm。将预制层放入退火炉中进行低温合金处理,合金条件为:2000 Pa 的氮气气氛下,以 30 ℃/min 的升温速率从室温升到目标温度 260 ℃,合金时间为 25 min。合金结束后,把样品放置在石墨舟中进行硫化:以硫粉(纯度为 99.99%)作为硫源,在 3000 Pa 的氮气气氛保护下,硫化温度 600 ℃,保持 30 min,样品硫化结束后,自然冷却到室温。用化学水浴法在 CZTS 吸收层上沉积 n 型 CdS 缓冲层(50 ~ 60 nm),用溅射法制备 i-ZnO(50 ~ 70 nm)和 ZnO: Al(400 nm),最后用热蒸发法蒸镀上 Ni-Al 电极,电池的有效面积为 0.25 cm^2。

2.2　CZTS 吸收层及电池的测试表征

采用日本理学 Ultima IV X 射线衍射仪(XRD)、Renishaw in Via 拉曼光谱仪(Raman)、配备能谱仪(EDS)的 FEI Quanta 2000 扫描电子显微镜(SEM)对所制备 CZTS 薄膜的晶体结构、表面形貌、相的纯度及化学组分进行表征分析。CZTS 薄膜电池的 *I-V* 特性是采用 NEWPORT 太阳光模拟器作为光源,标准测试条件下(AM1.5, 100 mW/cm^2, 300 K),利用美国 KEITHLEY 公司生产的 2400 数字源表完成。

3　结果与讨论

3.1　CZT 合金层及 CZTS 吸收层的特性表征

CZTS 薄膜预制层(Cu + Sn/ZnS)及经过 260 ℃合金后的 XRD 图谱如图 1 所示。从图中可以看出,未合金时薄膜中主要含有 Cu、ZnS、Cu_6Sn_5 和 Cu_5Zn_8,其中 Cu_6Sn_5 衍射峰较为明显,ZnS 的衍射峰较弱。经过低温合金后,Cu_6Sn_5 衍射峰减弱,ZnS 的衍射峰增强,然而最显著的变化是薄膜中有 SnS_2 和 Cu_4SnS_4 相的生成。文献中报道,CZTS 薄膜硫化温度到达 350 ℃时有三元化合物 Cu_2SnS_3 的生成,当温度到达 400 ℃时 Cu_2SnS_3 由立方晶体结构转化成四方晶体结构,硫化温度超过 450 ℃后 Cu_2SnS_3 和 ZnS 反应生成 Cu_2ZnSnS_4[20]。因此根据

CZTS 薄膜形成机制，薄膜中有 SnS_2 和 Cu_4SnS_4 的形成，更利于在之后的高温硫化中生成 Cu_2SnS_3 相，并且薄膜的体膨胀效应得到抑制，当 Cu_2SnS_3 与 ZnS 反应时薄膜的均匀性及致密性得到增强。

图 2 为 CZTS 薄膜的 SEM 图。其中图 2a 是未经过合金直接硫化的 CZTS 薄膜，图 2b 是通过 260 ℃合金 25 min 后，硫化得到的 CZTS 薄膜，二者除合金条件不同外，其余工艺条件都相同。可以看出，未合金直接硫化的 CZTS 薄膜表面较为粗糙、有大块晶体生成，可能是 Cu-S 或 Sn-S 等二次相，并且晶界明显，这会对薄膜电池的特性产生不利影响，如增加漏电机制使得开路电压下降，或是增加了电池的串联电阻等。合金之后再硫化的 CZTS 薄膜表面平整度得到很大改善。没有大块晶体的凝聚，晶粒均匀致密，不足之处就是晶粒较小导致存在大量的晶界。

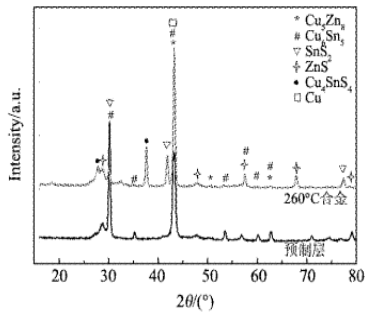

图 1 预制层及 260 ℃合金后的 XRD 图谱

Fig. 1 XRD patterns of the precursor and the sample annealed at 260 ℃

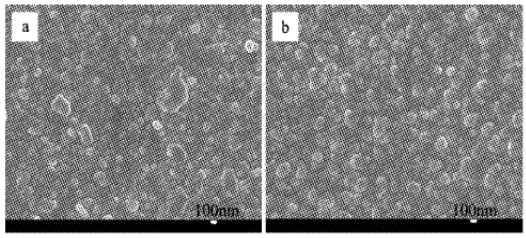

图 2 CZTS 薄膜的 SEM 图(a)未合金，直接硫化；(b)260 ℃合金后硫化

Fig. 2 SEM images of the CZTS thin films (a) sulfuring without annealing; (b) sulfuring after 260 ℃ annealing

图 3 是 CZTS(经过 260 ℃合金)的 XRD 图和 Raman 图谱，从 XRD 图中可以看出 CZTS 衍射峰强度较强，峰的位置与铜锌锡硫的 X 射线衍射标准卡(PDF #026-0575)吻合，说明薄膜结晶度良好。为进一步确认 CZTS 中是否含有其他二次相(因 ZnS 与 Cu_2SnS_3 的 XRD 衍射峰与 CZTS 主峰重合)，对其进行了拉曼测试，结果显示铜锌锡硫的拉曼峰值：251 cm^{-1}，288 cm^{-1}，338 cm^{-1}和373 cm^{-1}与其他文献[21]中提到的 CZTS 主峰(251 ~ 252 cm^{-1}，286 ~ 288 cm^{-1}，336 ~ 339 cm^{-1}，351 cm^{-1}及 368 cm^{-1})相符，但在 275 cm^{-1}的位置存在一个较弱的拉曼峰，相关文献中报道有可能是 ZnS 相[22]。

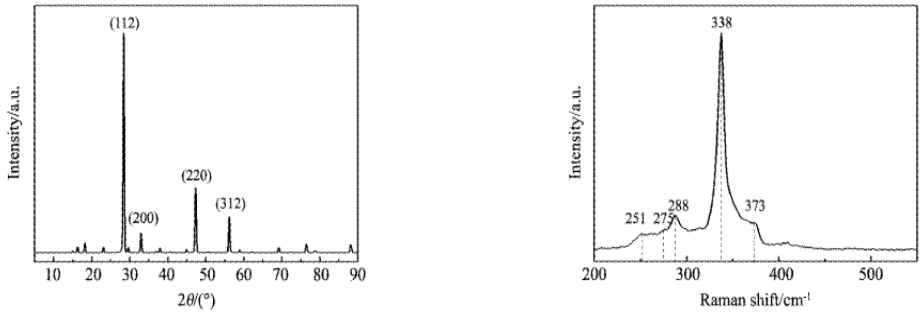

图 3 (a)CZTS 的 XRD 图谱；(b)CZTS 的拉曼图

Fig. 3 (a) XRD pattern; (b) raman analysis of CZTS

表 1 CZTS 薄膜组分及元素比例

Tab. 1 Chemical composition of CZTS thin film

Elemental composition(at%)				Cu/(Zn + Sn)	Zn/Sn	S/M
Cu	Zn	Sn	S			
23.37	13.39	10.46	52.78	0.98	1.28	1.12

为确定 CZTS 薄膜(经过 260 ℃合金)中的元素及比例,对其进行 EDS 测试,测试结果如表 1 所示。可以看出薄膜的组分偏离化学配比,并且稍微贫铜富锌。再者 Sn 的损失较多,主要是因为在高温硫化时形成不稳定、易挥发的 SnS_x[23],从而使得薄膜中 Sn 的含量减少。为抑制 Sn 的损失,可以在今后的硫化工艺中加入 SnS_2,或是采用快速升温硫化的办法,减少硫化时间,降低 SnS_x 的流失。结合拉曼图谱分析,证明所制备的 CZTS 薄膜中确实含有 ZnS 二次相。如果 CZTS 薄膜中富锌太多,会在 CZTS 晶体之间形成 ZnS 晶粒,阻碍晶体长大且得到细晶组织,这种现象被称作齐纳钉扎[24]。晶粒尺寸小会造成光生载流子在晶界处复合严重,影响太阳电池的开路电压、短路电流。并且 ZnS 作为宽带隙半导体材料,存在于 CZTS 中会增加薄膜电池的体电阻,降低电池的填充因子,对器件的光电转换效率产生了不利影响。

3.2　CZTS 薄膜电池特性

图 4 为 CZTS 薄膜电池在标准光照下的 *J-V* 特性曲线图。光电转换效率为 0.62%(电池有效面积为 0.25 cm^2),短路电流和填充因子都很小,证明电池的串联电阻大,导致这一结果的主要原因就是 CZTS 薄膜中可能大量的 ZnS 二次相,再者薄膜电池中的深能级缺陷较多、载流子复合较严重。影响 CZTS 薄膜电池效率的因素较多,器件的工作机制也较为复杂。因此要找到电池效率低的真正原因,还需要对 CZTS 薄膜电池进行更完善的性能测试分析。

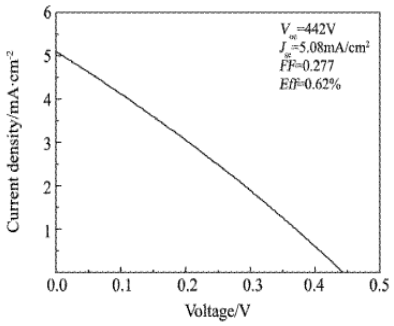

图 4　CZTS 薄膜太阳电池标准光照条件下 *J-V* 特性曲线

Fig. 4　Illuminated *J-V* characteristics (AM1.5, 100 mW/cm^2, 300 K) of CZTS film solar cell

4　结　论

采用射频磁控溅射法在镀 Mo 的钠钙玻璃上制备 CZTS 薄膜的预制层。溅射顺序为 Cu、Sn 共溅射,再溅射 ZnS。对预制层进行 260 ℃的低温合金,然后以硫粉作为硫源在 600 ℃的高温下硫化,得到表面平整但晶粒较小的 CZTS 薄膜。用所得到的 CZTS 薄膜制备太阳电池,结构为 SLG/Mo/CZTS/CdS/ZnO/ZnO:Al/Ni-Al,开路电压:V_{oc} = 442 mV,短路电流密度:J_{sc} = 5.08 mA/cm^2,其光电转换效率达到 0.62% 。通过测试分析,CZTS 薄膜中生成了 ZnS 等二次相,增加了电池的体电阻,阻碍了 CZTS 晶体的生长。晶粒尺寸小会造成光生载流子在晶界处复合,影响太阳电池的开路电压、短路电流,使得 CZTS 薄膜电池的光电转换效率降低。薄膜组分的优化及二次相的消除有待在今后的研究过程中改善。因器件的工作机制较为复杂,要找到电池光电转换效率低的真正原因,还需对其做光谱响应等更多更细致的性能测试。

参　考　文　献

[1] Martin A. Green1, Keith Emery. Solar cell efficiency tables (version 42)[J]. *Progress in Photovoltaics: Research and Applications*, 2013, **21**: 827-837.

[2] Jiang M L, Yan X Z. Cu_2ZnSnS_4 thin film solar cells: present status and future prospects[J]. *Sol Cells Res Appl Prospect*, 2013, **5**: 107-143.

[3] Yan C, Chen J. Kesterite Cu_2ZnSnS_4 solar cell from sputtered Zn/(Cu & Sn) metal stack Precursors[J]. *Journal of Alloys and Compounds*, 2014, **610**: 486-491.

[4] Hao X J, Yang K. Fabrication of Cu-Zn-Sn-S-O thin films by the electrochemical deposition method and application to heterojunction cells[J]. *International Journal of Photoenergy*, 2012, **154704**: 6.

[5] Byungha S, Oki G. Thin film solar cell with 8.4% power conversion efficiency using an earth-abundant Cu_2ZnSnS_4 absorber[J]. *Progress in photovoltaics*, 2013, **21**: 72-76.

[6] Jae-Seung S, Sang-Yul L. Electrical and optical properties of Cu_2ZnSnS_4 thin films prepared by rf magnetron sputtering process[J]. *Solar Energy Materials and Solar Cells*, 2003, **75**: 155-162.

[7] Katagiri H, Nagaoka N C. Solar cell without environmental pollution by using CZTS thin film[J]. *Photvoltaics Energy Conversion*, 2003, **3**: 2874-2879.

[8] Kamoun N, Bouzouita H. Fabrication and characterization of Cu_2ZnSnS_4 thin films deposited by spray pyrolysis technique[J]. *Thin Solid Films*, 2007, **515**(15): 5949-5952.

[9] Kunihiko T, Masatoshi O. Cu_2ZnSnS_4 thin film solar cells prepared by non-vacuum processing[J]. *Solar Energy Materials and Solar Cells*, 2009, **93**(5): 583-587.

[10] Gurav K V, Pawar S M. Electrosynthesis of CZTS films by sulfurization of CZT precursor: effect of soft annealing treatment[J]. *Applied Surface Science*, 2013, **283**: 74-80.

[11] Yeon H J, Bhaskar C M. Single elementary target-sputtered Cu_2ZnSnS_4 thin film solar cells[J]. *Solar Energy Materials and Solar Cell*, 2015, **132**: 136-141.

[12] Amin E, Pravakar P. Rajbhandari. Cu_2ZnSnS_4 solar cells fabricated by short-term sulfurization of sputtered Sn/Zn/Cu precursors under an H_2S atmosphere[J]. *Thin Solid Films*, 2015, **577**: 62-66.

[13] Andrew F, Xavier F. On the formation mechanisms of Zn-rich Cu_2ZnSnS_4 films prepared by sulfurization of metallic stacks[J]. *Solar Energy Materials and Solar Cells*, 2013, **112**: 97-105.

[14] Souhaib O, Guy B. Photoluminescence study and observation of unusual optical transitions in $Cu_2ZnSnSe_4$/CdS/ZnO solar cells[J]. *Solar Energy Materials and Solar Cells*, 2015, **134**: 340-345.

[15] Hironori K, Kazuo J. Enhanced conversion efficiencies of Cu_2ZnSnS_4-based thin film solar cells by using preferential etching technique[J]. *Applied Physics Express*, 2008, **1**: 041201.

[16] Yeon H J, Bhaskar C M. Single elementary target-sputtered $Cu_2ZnSnSe_4$ thin film solar cells[J]. *Solar Energy Materials and Solar Cells*, 2015, **132**: 136-141.

[17] Kazuo J, Ryoichi K. Cu_2ZnSnS_4-type thin film solar cells using abundant materials[J]. *Thin Solid Films*, 2007, **515**(15): 5997-5999.

[18] Li J J, Zhang Y. A temporary barrier effect of the alloy layer during selenization: tailoring the thickness of $MoSe_2$ for efficient $Cu_2ZnSnSe_4$ solar cells[J]. *Advanced Energy Materials*, 2015, **5**(9).

[19] Hyesun Y, Jun H K. Growth of Cu_2ZnSnS_4 thin films using sulfurization of stacked metallic films[J]. *Thin Solid Films*, 2010, **518**(22): 6567-6572.

[20] Muhamad I A, Kyoo H K. Crystallization of kesterite Cu_2ZnSnS_4 prepared by the sulfurization of sputtered Cu-Zn-Sn precursors[J]. *Thin Solid Films*, 2013, **534**: 144-148.

[21] Jiang F, Ikeda S. Pure sulfide Cu_2ZnSnS_4 thin film solar cells fabricated by preheating an electrodeposited metallic stack[J]. *Advanced Energy Materials*, 2014, **4**(7): 589.

[22] Fernandesa P A, Salomé P M P. Study of polycrystalline Cu_2ZnSnS_4 films by Raman scattering[J]. *Journal of Alloys and Compounds*, 2011, **509**(28): 7600-7606.

[23] Sammi K, Misol O. Effect of Sn-layer addition to precursors on characteristics of $Cu_2ZnSn(S,Se)_4$ thin-film solar cell absorber[J]. *Thin Solid Films*, 2013, **549**: 59-64.

[24] Jonathan J, Scragg, Tove E. Rapid annealing of reactively sputtered precursors for $Cu_2ZnSnSe_4$ Solar Cells[J]. *Progress in Photovoltaics: Research and Applications*, 2014, **22**(1): 10-17.

第34卷 增刊 硅 酸 盐 通 报 Vol. 34 Supplement
2015年11月 BULLETIN OF THE CHINESE CERAMIC SOCIETY November, 2015

电化学法制备 Cu_2ZnSnS_4 薄膜及其特性研究

蒋 志,王书荣,李志山,杨 敏,刘思佳,郭任君,唐 语,郝瑞亭,杨培志
(云南师范大学太阳能研究所,教育部可再生能源材料先进技术与制备重点实验室,云南省农村能源重点实验室,昆明 650500)

摘要:采用两电极的电化学沉积方在钼衬底上制备了 Cu_2ZnSnS_4(CZTS)薄膜。将 Cu、Zn、Sn 三种金属元素按一定的顺序分步沉积在钼片上得到 CZT 薄膜前驱体,把预制层放置在 S 的气氛中并在 N_2 的保护下退火硫化得到 CZTS 薄膜。通过 SEM、EDS、XRD 分析了 CZTS 薄膜的表面形貌、元素组分、结晶情况,并用拉曼光谱进一步确定了薄膜的晶体成分。最后将 CZTS 薄膜经过后步工艺制作成 CZTS 薄膜太阳电池,并通过 *I-V* 测试得到了该电池的效率及其它相应参数。

关键词:CZTS; 薄膜电池; 电化学沉积; 硫化; 效率
中图分类号: O484 **文献标识码**:A **文章编号**:1001-1625(2015)S-0303-05

Characteristics and preperation of Cu_2ZnSnS_4 Film by Electrochemical Method

JIANG Zhi, WANG Shu-rong, LI Zhi-shan, YANG Min, LIU Si-jia, GUO Ren-jun, TANG Yu, HAO Rui-ting, YANG Pei-zhi
(Yunnan Province Key Lab of Rural Energy Engineering, Solar Energy Research Institute, Key Laboratory of Advance Technology and Preparation for Renewable Energy Materials, Ministry of Education, Yunnan Normal University, Kunming 650500, China)

Abstract: The Cu_2ZnSnS_4 (CZTS) film was fabricated on Mo substrate through electrochemical method. Cu, Zn, Sn was deposited on Mo slice in a certain order to obtain the CZT precursor. The CZTS film was finally prepared by annealing the precursor under S/N_2 atmosphere. The surface morphology, elemental constitution and crystallization of CZTS film was investigated by scan electron microscopy (SEM), energy dispersive X-ray analysis (EDS) and X-ray diffraction (XRD), and the crystal composition was further confirmed by Raman spectroscopy. Finally, the CZTS cells were prepared by depositing buffer and window layer based on the CZTS films. And the efficiency of device and other parameters were tested by *I-V*.

Key words: CZTS film; thin film cell; electrochemical deposition; sulfuration; efficiency

1 引 言

随着能源的日益紧缺和人类环保意识的逐渐增强,光伏发电逐渐显示出其独特的优势。光伏发电是一种零排放的清洁能源,也是一种能够大规模应用的现实能源,因此其技术研发和商业化受到各国政府的普片重视,应用领域也更加广泛。而低成本高效薄膜太阳能电池是未来光伏电池的主流发展方向,薄膜太阳电池主要有以下优点:(1)光吸收系数高;(2)能源回收期较短;(3)便于大面积、连续和自动化生产;(4)可以制备在轻便的柔性衬底上。Cu_2ZnSnS_4(CZTS)薄膜太阳电池是一种新型薄膜太阳电池,其禁带宽度为 1.45 ~

基金项目:国家自然科学基金(61167003,61176127)
作者简介:蒋 志(1991-),男,硕士研究生. 主要从事铜锌锡硫薄膜太阳电池方面的研究.
通讯作者:王书荣,博士,副教授.

1.50 eV,与太阳电池所要求的最佳禁带宽度(1.5 eV)十分接近,其次 CZTS 为直接带隙半导体材料,具有很高的光吸收系数,因此只需 1 μm 的厚度就能做太阳电池的吸收层,加之该材料中的各元素在地壳中含量丰富,还因其成分无毒和环境友好,因而成为薄膜太阳电池吸收层的最佳候选材料之一。

目前 CZTS 薄膜的制备方法很多,分为物理法和化学法两类,物理法包括磁控溅射法,电子束蒸发法[1],真空蒸镀法等等。2006 年日本 Katagiri 运用射频与溅射一体化真空系统(inline-type vacuum apparatus),成功制备出铜锌锡硫薄膜太阳电池,其转换效率高达 6.7%[2]。IBM 公司采用真空蒸镀法制作出来的效率达到了 8.4% CZTS 薄膜电池,其最大短路电流密度为 23.4 mA/cm^2,这是目前采用物理方法获得的最高效率[3]。相比物理法,化学法对制备成本和制备条件要求较低,化学法包括溶胶溶剂法[4],旋转涂布法[5],电化学沉积法[6-10]等。Ahmed, Reuter 等采用电化学法制备出效率为 7.3% 的 CZTS 薄膜电池[11]。2012 年,IBM 将联氨法制作的 CZTSSe 薄膜太阳电池的转换效率提高到 11.1%,到 2013 年末该小组制作的 CZTSSe 薄膜太阳电池的转换效率已高达 12.6%[12],这是目前 CZTSSe 薄膜电池的最高转换效率。电化学在涂层电镀,电路板印刷方面已大规模产业化应用,所以以电化学法为基础制备 CZTS 薄膜太阳电池,在成本,工艺成熟度方面具有很大的优势。IBM 的 Shafaat Ahemd 等和日本大阪大学的 Feng 等采用电化学沉积铜锌锡(CZT)预制层后硫化退火的两步法分别制备出效率为 7.3% 和 8.0% 的 CZTS 薄膜电池[13,14]。在本文中,采用简单的二电极电化学法沉积 CZTS 预制层,最后将预制层硫化制得 CZTS 薄膜。通过 SEM、XRD、EDS 和 Raman 研究分析薄膜的表面形貌、晶体质量、化学组分和二次相等特性。最后用 *I-V* 测试表征该薄膜制备的 CZTS 薄膜太阳电池的性能。

2 实 验

实验采用简单普通的两电极系统,石墨电极作为阳极,钼片衬底(18 mm × 20 mm)作为阴极。在电化学沉积之前,先后用丙酮、酒精除去钼片和石墨电极表面有机物,最后用大量去离子水将钼片冲洗干净。使用一个输出为 5 V/25 V 的恒电压源,将石墨电极与钼片分别连接到恒压源的正极与负极,同时在电路中串联一个电阻箱。分别配制 500 mL 0.06 M 的 Cu_2SO_4 溶液和 500 mL 0.06 M 的 $SnSO_4$ 溶液,在两种溶液中分别加入 0.4 M 的 $Na_3C_6H_5O_7$ 做为络合剂,用酒石酸将溶液的 pH 值调至 4 ~ 5。最后配制 0.2 M 的 $ZnSO_4$ 溶液,并加入有机物来抑制氢离子的电解。按照 Cu→Sn→Zn 的顺序在钼片衬底上沉积金属预制层。调节电流保持在 14.5 mA 沉积 Zn 5 min,13.5 mA 沉积 Cu 5 min, 9.5 mA 的电流沉积 Sn 7 min,得到 CZTS 预制层。将预制层和硫粉放入石墨舟内,当石英退火炉温度恒定在 580 ℃时通入氮气,2 min 后把石墨舟推入退火炉进行硫化退火(20 min),退火完成后取出硫化好的 CZTS 薄膜。

用 SEM(FEI quanta200)、EDS(EDAX)、XRD(Rigaku UltimaIV)、Raman(Renishaw inVia)表征了薄膜的表面形貌、元素组分、晶体质量以及薄膜中的二次相。在太阳光模拟器(NEWPORT)作为光源在 AM1.5 (100 mW/cm^2)的条件下利用美国 KEITHLEY 公司生产的 2400 型数字源表完成 CZTS 电池样品的 *I-V* 特性测试。

3 结果与讨论

图 1 为退火后薄膜样品的 XRD 图谱,从图中可以明显的观察到 $2\theta = 28.45°$、$47.32°$、$56.13°$的三个主峰,分别对应 CZTS 的(112)、(220)、(312)三个面,其中(112)面的衍射峰强度最大,同先前的研究成果[14-16]和 CZTS 的衍射数据(JCPDS 26-0575)吻合。另外两个衍射峰($2\theta = 58.65°$、$73.72°$)属于钼片衬底,不同的是,钼的主衍射峰在 $2\theta \approx 40.5°$,造成差异的原因是本实验用的衬底并非磁控溅射镀钼,而是轧制的钼金属片,不同的处理工艺对同种材料晶体生长的择优取向有很大的影响,其实仔细观察 XRD 图谱可以看到在 $2\theta \approx 40.5°$有一个 Mo 的衍射峰,这三个衍射峰同样与 Mo 的衍射数据(JCPDS 65-7442)吻合。其次从衍射图谱中并未观测到 MoS 的衍射峰,从图中也不能观察到 Cu_xS、SnS、ZnS、Cu_2SnS_3 这些二次相的衍射峰,可能因为 Cu_xS、SnS、ZnS、Cu_2SnS_3 这些二次相与 CZTS 晶体结构相似并且有部分衍射峰重叠,所以从 XRD 图谱中不能

完全确定是否存在上述二次相[17-20]。为了进一步确认薄膜样品是否属于单相的 CZTS,对样品做了 Raman 分析,从图 2 中可以看到 CZTS 的 Raman 主峰(338 cm^{-1})以及另外的两个 Raman 峰(287 cm^{-1}、368 cm^{-1}),这与文献中所提供的数据是一致[20]。并且未观察到上述二次相的 Raman 峰,说明薄膜样品不含二次相或二次相含量极少低于仪器的检测限。

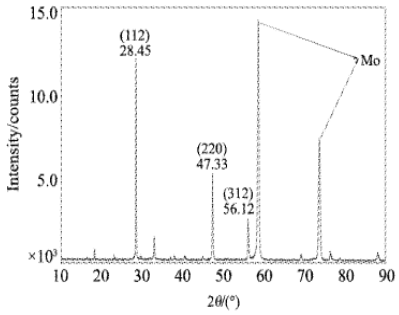

图 1　薄膜样品的图谱

Fig. 1　XRD pattern of CZTS thin film

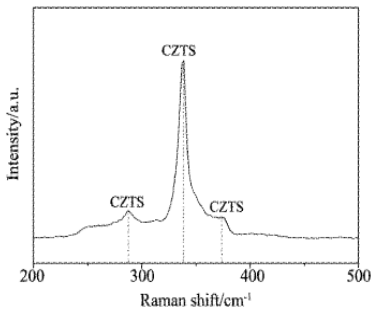

图 2　CZTS 薄膜样品的拉曼散射光谱

Fig. 2　Raman spectrum of CZTS thin film

图 3 中的两幅图片分别是同一 CZTS 薄膜在不同放大倍数下的 SEM 表面形貌,从图中可以看出薄膜表面平整度较差,晶粒大小不均,尺寸分布在 0.5 ~ 3 μm 之间。根据以前的研究报道,在富铜条件下形成的晶体较大[21],为了避免 Cu→Sn→Zn 的沉积顺序造成靠近衬底的薄膜底部出现小晶粒,所以将 Cu 沉积在底部可以消除薄膜底部出现较小的晶粒,从而避免薄膜在纵向上出现分层形成双层结构(bilayer)。如果 CZTS 薄膜出现双层结构,会增加串联电阻,不利于电子在以 CZTS 薄膜作为吸收层的电池中的输运。最终影响了薄膜电池的输出功率,所以要尽量避免小晶粒的出现。表 1 是样品的 EDS 分析结果,可以看到 Cu、Sn、Zn、S 各元素比较接近化学配比,从样品的原子比可以看出,制备的 CZTS 薄膜属于贫铜富锌型,高效率 CZTS 薄膜太阳电池中的各元素原子比一般保持在 Cu/(Zn + Sn) = 0.80 ~ 0.95,Zn/Sn = 1.05 ~ 1.30 之间[22],从 EDS 测试结果中还可以得到 Zn/Sn = 1.09,处于正常范围。此外 EDS 结果显示薄膜中含有 8.83% 的氧,这可能是由于退火使用的石墨舟在退火前其腔体内的空气未完全排净,导致薄膜被部分氧化,在结合以上的 XRD 和 Raman 分析薄膜中并没有杂相存在,所以薄膜中的氧很可能与硫形成同族替代,从而使少量的 CZTS 变成 CZT(SO)。

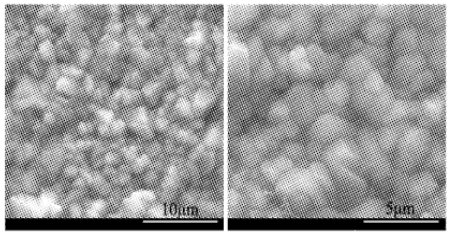

图 3　CZTS 薄膜的表面形貌图

Fig. 3　SEM images of CZTS thin film

表 1　硫化后得到的 CZTS 薄膜元素组分及比例

Tab. 1　Composition and element ratio of as-prepared CZTS thin film

Zn/Sn	Element	Cu	Zn	Sn	S	O	Cu/(Zn + Sn)
Cu	23.02	12.78	11.69	43.98	8.83	0.94	1.09

在制备好的 CZTS 薄膜的基础上,采用化学水浴(CBD)、磁控溅射、真空蒸镀分别沉积硫化镉(CdS)缓冲层、氧化锌/掺铝氧化锌(ZnO/AZO)窗口层、镍/铝(Ni/Al)栅线电极得到 CZTS 薄膜太阳电池。用氙灯光源在 AM1.5 的条件下测试制备好的 CZTS 薄膜电池样品,得到样品的 *I-V* 特性曲线(图 4),其开路电压 V_{oc} = 448 mV、短路电流密度 J_{sc} = 9.60 mA/cm^2、填充因子 *FF* = 0.3、转换效率 *Eff*(%) = 1.30%。很明显,与目前世界上较高效率的 CZTS 薄膜电池相比,在性能参数上有很大差距,尤其是在短路电流密度与填充因子方面

[4] Tanaka K, Oonuki M, Moritake N, et al. Cu_2ZnSnS_4 thin film solar cells prepared by non-vacuum processing[J]. *Solar Energy Materials and Solar Cells*, 2009, **93**(5): 583-587.

[5] Mitzi D B, Gunawan O, Todorov T K, et al. The path towards a high-performance solution-processed kesterite solar cell[J]. *Solar Energy Materials and Solar Cells*, 2011, **95**(6): 1421-1436.

[6] Jeon M, Shimizu T, Shingubara S. Cu_2ZnSnS_4 thin films and nanowires prepared by different single-step electrodeposition method in quaternary electrolyte[J]. *Materials Letters*, 2011, **65**(15): 2364-2367.

[7] Pawar B S, Pawar S M, Shin S W, et al. Effect of complexing agent on the properties of electrochemically deposited Cu_2ZnSnS_4 (CZTS) thin films [J]. *Applied Surface Science*, 2010, **257**(5): 1786-1791.

[8] Scragg J J, Dale P J, Peter L M. Towards sustainable materials for solar energy conversion: preparation and photoelectrochemical characterization of Cu_2ZnSnS_4[J]. *Electrochemistry Communications*, 2008, **10**(4): 639-642.

[9] Ennaoui A, Lux-Steiner M, Weber A, et al. Cu_2ZnSnS_4 thin film solar cells from electroplated precursors: novel low-cost perspective[J]. *Thin Solid Films*, 2009, **517**(7): 2511-2514.

[10] Katagiri H, Jimbo K, Maw W S, et al. Development of CZTS-based thin film solar cells[J]. *Thin Solid Films*, 2009, **517**(7): 2455-2460.

[11] Ahmed S, Reuter K B, Gunawan O, et al. A high efficiency electrodeposited Cu_2ZnSnS_4 solar cell[J]. *Advanced Energy Materials*, 2012, **2**(2): 253-259.

[12] Wang W, Winkler M T, Gunawan O, et al. Device characteristics of CZTSSe thin-film solar cells with 12.6% efficiency[J]. *Advanced Energy Materials*, 2014, **4**(7).

[13] Ahmed S, Reuter K B, Gunawan O, et al. A high efficiency electrodeposited Cu_2ZnSnS_4 solar cell[J]. *Advanced Energy Materials*, 2012, **2**(2): 253-259.

[14] Jiang F, Ikeda S, Harada T, et al. Pure sulfide Cu_2ZnSnS_4 thin film solar cells fabricated by preheating an electrodeposited metallic stack[J]. *Advanced Energy Materials*, 2014, **4**(7).

[15] Wang Y, Gong H. Cu_2ZnSnS_4 synthesized through a green and economic process[J]. *Journal of Alloys and Compounds*, 2011, **509**(40): 9627-9630.

[16] Chen Q, Cheng S, Zhuang S, et al. Cu_2ZnSnS_4 solar cell prepared entirely by non-vacuum processes[J]. *Thin Solid Films*, 2012, **520**(19): 6256-6261.

[17] Jeon M, Shimizu T, Shingubara S. Cu_2ZnSnS_4 thin films and nanowires prepared by different single-step electrodeposition method in quaternary electrolyte[J]. *Materials Letters*, 2011, **65**(15): 2364-2367.

[18] Schorr S, Weber A, Honkimäki V, et al. In-situ investigation of the kesterite formation from binary and ternary sulphides[J]. *Thin Solid Films*, 2009, **517**(7): 2461-2464.

[19] Weber A, Mainz R, Unold T, et al. In-situ XRD on formation reactions of Cu_2ZnSnS_4 thin films[J]. *Physica Status Solidi (c)*, 2009, **6**(5): 1245-1248.

[20] Mitzi D B, Gunawan O, Todorov T K, et al. The path towards a high-performance solution-processed kesterite solar cell[J]. *Solar Energy Materials and Solar Cells*, 2011, **95**(6): 1421-1436.

[21] Todorov T, Kita M, Carda J, et al. Cu_2ZnSnS_4 films deposited by a soft-chemistry method[J]. *Thin Solid Films*, 2009, **517**(7): 2541-2544.

[22] Hoffman R. Materials for CZTS photovoltaic devices[D]. Cornell University Chemical Engineering, 2009.

光 电 子 · 激 光
第 26 卷 第 8 期 2015 年 8 月 Journal of Optoelectronics · Laser Vol. 26 No. 8 August 2015

DOI:10.16136/j.joel.2015.08.0227

环氧树脂多模光波导的研制

刘 涛,杨 敏,蒋 志,李志山,王书荣*

(云南师范大学 太阳能研究所,教育部可再生能源材料先进技术与制备重点实验室,云南省农村能源重点工程实验室,云南 昆明 650500)

摘要:以环氧树脂为材料,用简单、低成本的非接触式光刻法制作多模光波导。通过实验,找出一种可靠有效的有机溶剂作为显影剂及其相应的显影时间;并研究了温湿度和旋涂工艺对光波导厚度的影响;以及光刻掩模版透光部分宽度、光刻掩模版与下包层之间的间距、曝光光强和曝光时间对光波导宽度的影响。扫描电子显微镜(SEM)对样品形貌分析表明,脊形光波导表面光滑且侧壁笔直,光波导芯横截面约为 50 μm×50 μm。采用 cut-back 法,测出环氧树脂多模光波导的传输损耗为 0.1 dB/cm@850 nm。考虑到光电集成过程中对光波导的高温冲击,对样品进行了热稳定性试验,获得的最高稳定温度为 210 ℃。

关键词:非接触式光刻;多模光波导;环氧树脂;光损耗;热稳定性
中图分类号:TN253 文献标识码:A 文章编号:1005-0086(2015)08-1468-05

Development of epoxy resin multimode optical waveguides

LIU Tao, YANG Min, JIANG Zhi, LI Zhi-shan, WANG Shu-rong*

(Key Laboratory of Advance Technology and Preparation for Renewable Energy Materials, Ministry of Education of China, Yunnan Province Key Laboratory of Rural Energy Engineering, Solar Energy Research Institute, Yunnan Normal University, Kunming 650500, China)

Abstract: The multimode optical waveguides are fabricated using epoxy resin materials, and the non-contact lithography is adopted as a simple and cost-effective process. A kind of reliable and efficient developer and corresponding developing time are found by a lot of experiments, and The effects of temperature and humidity, and spin-coating process on the waveguides thickness were studied; the effect of transparent portion width of lithography mask, the spacing between lower cladding layer and lithography mask, exposure intensity and time on the width of the optical waveguides are also studied. The morphology of the samples is observed by scanning electron microscopy (SEM), and the fabricated ridge optical waveguides with cross sectional size of approximately 50 μm×50 μm have smooth surfaces and vertical sidewalls. The transmission loss of epoxy resin multimode optical waveguides at wavelength of 850 nm is measured to be 0.1 dB/cm by cut-back method. Taking account of the high temperature shock on optical waveguide during optoelectronic integrated process, the thermal stability of the fabricated optical waveguides is tested and the attainable highest thermal stability temperature is 210 ℃.

Key words: non-contact lithography; multimode optical waveguide; epoxy resin; optical loss; thermal stability

1 引 言

光波导可以分为无机[1]和有机[2]光波导,当然也有研究者用无机和有机材料混合制作光波导热光开关[3,4]。有机聚合物光波导作为一种短距离光信号传输通道,集成于印刷电路板(PCB)中制成光 PCB (OPCB)并得到应用[5~7]。目前制作低损耗光波导的材料大致分为两类:一类是热塑

* E-mail:shrw88@aliyun.com
收稿日期:2015-04-10 修订日期:2015-06-28
基金项目:国家自然科学基金(61167003)资助项目

性聚合物,如聚甲基丙烯酸甲酯(PMMA)、丙烯酸酯(Acrylate)及其衍生物、聚碳酸酯和全氟环丁烷等[8],用这类材料制作光波导传输损耗较低,其中以 PMMA 制作的直光波导最低传输损耗为 0.027 dB/cm@850 nm[9];但用这类材料制作光波导最大的缺点是热稳定性能差,它们的玻璃转化温度 T_g 通常小于 100 ℃[10],制约了其在 OPCB 中的应用,因为在制作 OPCB 的过程中要经历温度为 160 ℃、时间大于 1 h 的高温压制过程[11]。另一类光波导材料是可高温硬化的聚合物,如聚酰亚胺(Polyimide)及其氟化物[12]、聚硅氧烷(Polysiloxane)及其衍生物、环氧树脂(Epoxy resin)[13]和负光刻胶 SU-8(Negative photoresist SU-8)[14]等,用这类材料制作的多模光波导传输损耗通常小于 0.36 dB/cm@850 nm,而且 T_g 通常大于 200 ℃,显然这种类型的光波导适合高温下压制成 OPCB 实现光互连。紫外光固化环氧树脂(UV-cured epoxy resin)[15]具有高的热稳定性(T_g 为 200 ℃左右)、低光传输损耗(0.13 dB/cm@850 nm)以及折射率可控范围大(1.48～1.60)等优点,适合用于光波导的制作。

光波导制作工艺,目前有:光刻法,包括 Photo-lithography process[16]、photo-bleaching process-[17]和反应离子蚀刻(RIE)工艺[18];模版复制法,包括热模压(Hot embossing)工艺[8]、软光刻(Soft lithography)工艺[19];其它方法,包括激光烧蚀、紫外光直写[20]、双光子直写[21]、电子束直写[22]和微针孔直写[23]等。其中对于紫外光可固化有机聚合物光波导材料,较之其它工艺,采用 Photo-lithography process 制作光波导的综合性能优良,且适用于工业化生产,是一种实用性强的工艺。理论上,以环氧树脂为材料,采用光刻法制作光波导不能像负光刻胶 SU-8 那样进行接触曝光[10],只能采用近距离曝光(非接触曝光);加之,较难找到一种有效的有机溶剂做显影剂。本文通过实验找出一种有效的有机溶剂做显影剂,并采用非接触式光刻法成功研制了环氧树脂多模光波导,且获得了较低的光传输损耗,为环氧树脂多模光波导大规模应用于光互连中奠定基础。

2　制作光波导

实验所用光固化环氧树脂材料由日本 NTT 公司购买。用于制作包层的环氧树脂,其折射率为 1.50±0.005,而用于制作芯层的环氧树脂,其折射率为 1.52±0.005。

2.1　制作光波导下包层

取少量低折射率环氧树脂涂敷于清洗后干燥的 FR4 基片(10 cm×10 cm)上,将涂敷后并在高真空中除去气泡的样品置于匀胶机的承片台上。根据环境温度及所需下包层厚度设计匀胶机旋涂工艺,因为膜厚与温度、转速、旋转时间成反比[15],因此可以通过调整这些参数对膜的均匀性及膜厚进行控制。采用旋涂法得到下包层厚约为 25 μm 的环氧树脂薄膜的实验工艺为:在室内环境温度为 22 ℃、湿度为 45%RH 条件下,先低转速 510～530 r/min 旋转 18 s,然后高转速 1810～1820 r/min 旋转 100 秒。光刻机自动调平后,将下包层匀胶后的基片放于光刻机承片台上,设定曝光时间并进行曝光。为保证下包层固化充分完全,可以长时间曝光,也可以曝光后用 hotplate 或者鼓风恒温干燥箱在 80℃左右进行时间为 15 min 左右的热烘烤以便进一步固化下波导层。制作下包层的曝光光强为 15 mW/cm^2、曝光时间为 10 min。

2.2　制作光波导芯层

取少量高折射率环氧树脂涂敷于下包层上,先以制作下包层类似的旋涂工艺,制备出具有一定厚度的均匀芯层环氧树脂薄膜;再采用非接触式光刻法制作光波导芯层。由于波导宽度主要取决于光刻掩模版透光部分宽度、光刻掩模版与下包层之间的间距、曝光光强及曝光时间,所以在光刻掩模版与芯层薄膜之间存在间隙的前提下,通过综合考虑这些参数,可以制备出具有理想宽度的光波导。光刻后,首先,在 85～90 ℃下进行时间为 1 min 左右的前烘烤;其次,将经前烘烤后的样品放于显影溶剂中显影,将显影后的样品放于无水酒精中清洗 30 s 并取出样品用 N_2 吹干;最后,在显微镜下观察光波导表面是否光滑,波导宽度和波导厚度是否为预期值,并以观察到的实验结果对制作工艺进行调整。若显影后形成的光波导达到预期要求,则可以通过紫外曝光进一步硬化显影后形成的脊形光波导。实验中,通过控制旋涂工艺控制芯层厚度,通过控制光刻工艺控制光波导芯层宽度,再经过合理的显影工艺,进而制作出具有理想几何结构、表面光滑且侧壁笔直的脊形光波导芯。实验中,制备的脊形光波导芯长为 8.5 cm。

在光波导芯层的制作过程中,分别尝试使用醋酸异丙酯、四氢呋喃、无水酒精、丙酮、无水酒精与丙酮的混合溶液作为显影溶剂;将相同工艺条件下制作并经前烘烤后的样品放于以上有机溶剂中进行显影,通过大量实验最后发现,以无水酒精与丙酮按体积比为 1∶2 进行混合作为显影溶剂,显影时间 120～180 s,能够有效溶解未被紫外光固化的环氧树脂,且显影后脊形光波导芯层表面光滑。从而证实,无水酒精与丙酮按体积比为 1∶2 进行混合,可以作为

一种有效可靠的显影溶剂。

2.3　上包层制作

以制作下包层相似的工艺制作上包层，但需要根据温度设置合适的转速、旋转时间以确保显影后的光波导被上包层全覆盖。也可以重复多次旋涂—曝光过程制作上包层。实验中，上包层的旋涂工艺为：环境温度为 24.4 ℃、湿度为 39%条件下，首先以低速挡转速 510～530 r/min，旋转 2 次，每次 9 s；然后，以低速挡转速 510～530 r/min，时间 6 s，高速挡转速 1 000～1 100 r/min 左右，时间 6 s，低速—高速连续旋转 5 次；最后，以曝光光强为 15 mW/cm^2、曝光时间为 18 min 为条件进行曝光固化，制成均匀平整厚为 81 μm 的上包层环氧树脂薄膜。

3　实验结果和讨论

在扫描电子显微镜(SEM)下观察脊形光波导芯层，如图 1 所示。从图可以看出，光波导芯层的表面光滑且侧壁笔直，拥有较笔直的侧壁和表面光滑的光波导有望获得较小的光传输损耗。

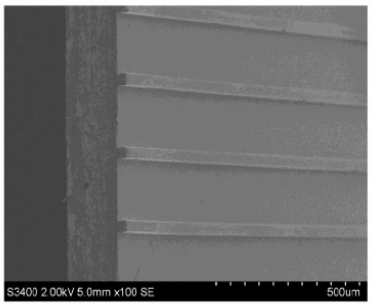

图 1　脊形光波导 SEM 表面形貌图

Fig. 1　SEM image of the ridge optical waveguide

图 2 为以白光从光波导一端入射在显微镜下观察光波导另一端的横截面图。从图可以看出，光波导芯层约为 50 μm×50 μm，其所对应样品的芯层制作工艺为：温度为 23.6 ℃、湿度为 40%条件下，首先以转速为 510～530 r/min，旋转时间为 9 s，进行 2 次低速旋转；然后，以低转速510 r/min，旋转时间为 9 s，高转速 1 810～1 820 r/min，旋转时间为 10 s，进行 2 次低速—高速连续旋涂，每次旋涂停止除去膜层中的气泡再进行下次旋涂；再以光刻掩模版与下包层之间的间距为 300 μm、光刻掩模版透光部分宽为 40 μm、曝光光强为 15 mW/cm^2 和曝光时间为 90 s 作为非接触式光刻条件进行光刻；光刻后，以烘烤温度为 90 ℃、烘烤时间为 3 min 进行前烘烤；前烘烤完成后，进行 2 min 的显影，显影后放于无水酒精中清洗 30 s，取出吹干；最后对脊形光波导以曝光光强为 15 mW/cm^2、曝光时间为 6 min 进行紫外曝光，进一步光固化光波导。

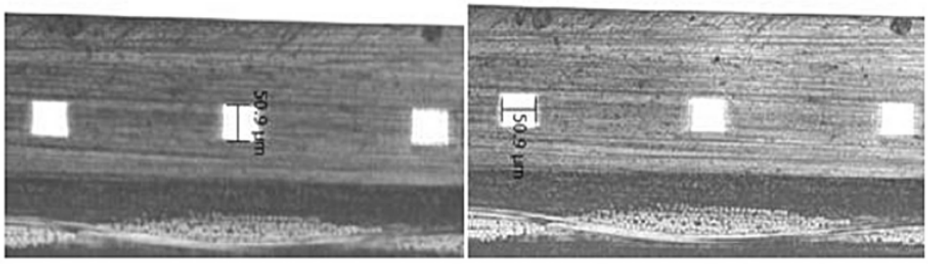

(a)　　(b)

图 2　光波导横截面图

Fig. 2　Cross section photographs of the fabricated channel waveguide

使用 cut-back 法，测量样品的光传输损耗。以垂直腔表面发射激光器(VCSEL)作为光源，通过 GI50/125 μm 的多模光纤(MMF)将波长为 850 nm 的光耦合进入光波导，用光功率计测量 MMF 输出的光功率和经过多模光波导传输后输出的光功率，可以得到插入损耗。为使光纤与光波导之间的耦合损耗最低，需要对光波导端面进行处理。其步骤为：用 1 000、2 000、3 000、5 000 和 7 000 目的砂纸依次对光波导阵列横截面进行研磨，更换不同目数的砂纸进行研磨前，需要用沾有无水酒精的棉签对端面进行擦洗；然后用镜面抛光布对光波导阵列端面进行抛光处理，直到光波导端面平整光滑。从图 3 可以看出，光波导长度和插入损耗成线性关系，直线的斜率 0.10 dB/cm 即为光传输损耗。

热稳定性测试：在空气气氛下，将样品置于热烘烤箱中，在温度分别为 100、150、200、210、220、230

和 240 ℃下热烘烤 1 h。每次烘烤后,测出光波导的插入损耗。从图 4 可以看出,样品的插入损耗在 210 ℃以下无明显变化,表明样品可以经受光电集成过程中的高温冲击。

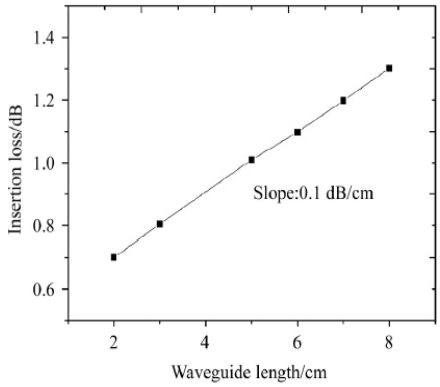

图 3　插入损耗与波导长度的关系

Fig. 3　Insertion loss as a function of waveguide length

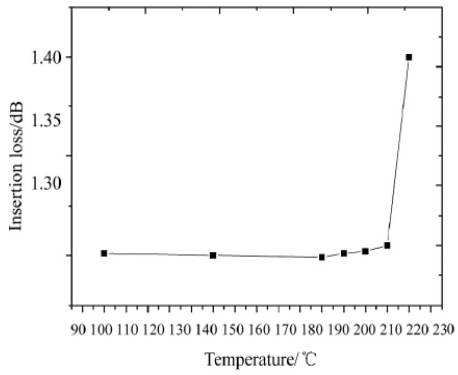

图 4　不同温度下空气中热烘烤 1 h 之后的插入损耗变化图

Fig. 4　Insertion loss of optical waveguide as a function of baking temperature for 1 h under an atmosphere of air

4　结　论

以紫外光固化环氧树脂为材料,用非接触式光刻法成功制作环氧树脂多模光波导;通过实验,找到了一种有效的有机显影剂—无水酒精与丙酮按体积比为 1∶2 的混合溶液。样品的 SEM 图及横截面图显示,脊形光波导芯表面光滑且侧壁笔直,光波导芯层约为 50.0 μm×50.0 μm。以 VCSEL 作为光源,使用 cut-back 法测出样品的光传输损耗为 0.1 dB/cm@850 nm。热稳定性实验中,获得样品最高热稳定温度为 210 ℃,证实了样品能经受光电集成过程中的热焊接高温冲击。本文研制的样品有望在光互连中大规模应用。

参考文献:

[1] HONG Jian-xun. Researches on the transmission properties of the silicon slot optical waveguides and the transmission loss measurement[J]. Journal of Optoelectronics · Laser, 2013, **24**(7): 1286-1290.
洪建勋. Si 基槽型光波导的传输特性分析和传输损耗的测量[J]. 光电子 · 激光, 2013, **24**(7): 1286-1290.

[2] LI Kang, PANG Fu-fei, WU Jin-hua, et al. Fabrication and performance teting of the low-loss interconnect polymer optical waveguide[J]. Journal of Optoelectronics · Laser, 2013, **24**(4): 716-719.
李康, 庞拂飞, 吴金华, 等. 低损聚合物互连光波导的制备及性能测试[J]. 光电子 · 激光, 2013, **24**(4): 716-719.

[3] ZHAO Shi-min, CONG Long-yuan, HAN Chao, et al. Study of hybrid SiO_2/polymer Y branch waveguide thermo-optic switches[J]. Journal of Optoelectronics · Laser, 2013, **24**(2): 253-257.
赵世民, 丛隆元, 韩超, 等. SiO_2/聚合物 Y 分支波导型热光开关研究[J]. 光电子 · 激光, 2013, **24**(2): 253-257.

[4] LIANG Lei, QV Lu-cheng, ZHANG Li-jun, et al. Fabrication and measurement of a polymer/SiO_2 hybrid waveguide 2×2 thermo-optic switch[J]. Journal of Optoelectronics · Laser, 2014, **25**(4): 642-647.
梁磊, 曲禄成, 张立钧, 等. 聚合物/SiO_2 混合波导 2×2 热光开关的制备与测试[J]. 光电子 · 激光, 2014, **25**(4): 642-647.

[5] Taubenblatt A M. Optical interconnects for high-performance computing[J]. Journal of Lightwave Technology, 2012, **30**(4): 448-458.

[6] Tan M R T, Mclaren M, Jouppi N P. Optical interconnects for high-performance computing systems[J]. IEEE Micro, 2013, **33**(1): 14-21.

[7] Benner A. Optical interconnect opportunities in supercomputers and high end computing[A]. Proc. of Optical Fiber Communication Conference and Exposition (OFC/NFOEC), and the National Fiber Optic Engineers Conference [C]. 2012, 1-60.

[8] Lee B T, Kwon M S, Yoon J B, et al. Fabrication of polymeric large-core waveguides for optical interconnects using a rubber molding process[J]. IEEE Photonics Technology Letter, 2000, **12**(1): 62-64.

[9] Kakaaki Ishigure, Yosuke Nitta. On-board fabrication of multi-channel polymer optical waveguide with graded-index cores by soft-lithography[J]. Proceedings of 60th Electronic Components and Technology Conference

(ECTC), Las Vegas, NV, USA, June 2010, 275-281.

[10] Kim J S, Ki J J. Fabrication of multimode pwaveguide and micromirrors using deep X-rany lithography [J]. IEEE Photonics Technology letter, 2004, **16**(3): 798-800.

[11] Lehmacher S, Neyer A. Integrations of polymer optical waveguides into printed circuit boards [J]. Electronic Letter, 2000, **36**(12): 1052-1053.

[12] Ando A. Optical properties of fluoridated polyimides and their applications to optical components and waveguide circuits[J]. Journal of Photopolymer Science and Technology, 2004, **17**(2): 219-232.

[13] Hikita M, Yoshimura R, Usui M, et al. Polymeric optical waveguides for optical interconnections [J]. Thin solid films, 1998, **331**(1): 303-308.

[14] Yang B, Yang L, Hu R, et al. Fabrication and characterization of small optical ridge waveguides based on SU-8 polymer [J]. Journal of Lightwave Technology, 2009, **27**(18): 4091-4095.

[15] Watanabe T, Hikita M, Amano M, et al. Vertically stacked coupler and serially grafted waveguide: Hybrid waveguide structures formed using an electro-optic polymer[J]. Journal of Applied Physics, 1998, **83**(2): 639-649.

[16] Roger Dangel, Folkert Horst, Daniel Jubin, et al. Development of versatile polymer waveguide flex technology for use in optical interconnects [J]. Journal of Lightwave Technology, 2013, **31**(24): 3915-3926.

[17] Kim S, Geary K, Fetterman H R, et al. Photo-bleaching induced electro-optic polymer modulators with dual driving electrodes operating at 1.55 μm wavelength [J]. Electronics Letters, 2003, **39**(18): 1321-1322.

[18] Koji Enbutsu, Makoto Hikita, Ryoko Yoshimura, et al. Multimode polymeric optical waveguides with high thermal stability using UV cured epoxy resins[J]. Jpn. J. Applied Physics B, 1998, **37**(6): 3662-3664.

[19] NI Wei. The research of short distance optical interconnection based on soft lithography[D]. Zhejiang: Zhejiang university, 2009.
倪玮. 基于软光刻的短距离光互连研究[D]. 浙江：浙江大学, 2009.

[20] Dellmann L, Berger C, Beyeler R, et al. 120 Gb/s optical card-to-card interconnect link demonstrator with embedded waveguides[J]. Proceedings of 57th Electronic Components and Technology Conference(ECTC), 2007, 1288-1293.

[21] Ishihara J, Komatsu K, Sugihar O, et al. Fabrication of three-dimensional calixarene polymer waveguides using two-photon-assisted polymerization [J]. Applied Physics Letters, 2007, **90**(3): 033511.

[22] Maruo Y Y, Sasaki S, Tamamura T. Channel-optical-waveguide fabrication based on electron-beam irradiation of polyimides[J]. Applied Opt., 1995, **34**: 1047-1052.

[23] Soma K, Ishigure T. Fabrication of a graded-index circular-core polymer parallel optical waveguide using a micro-dispenser for a high-density optical printed circuit board[J]. IEEE Journal of Selected Topics in Quantum Electronics, 2013, **19**(2): 3600310.

作者简介：
王书荣 (1968－)，博士，副教授，主要从事半导体材料和半导体光电子器件研究.

第45卷 第6期 激光与红外 Vol.45,No.6
2015年6月 LASER & INFRARED June,2015

文章编号:1001-5078(2015)06-0599-06

·综述与评论·

有机聚合物光波导制作工艺综述

刘 涛,李志山,蒋 志,杨 敏,王书荣
(云南师范大学 太阳能研究所,教育部可再生能源材料先进技术与制备重点实验室,
云南省农村能源重点工程实验室,云南 昆明 650500)

摘 要:有机聚合物光波导光互连已成为实现短距离计算通信设计目标的最佳解决方法。短距离光互连是未来互连方向,综合性能优良的聚合物多模光波导是光互连中的重要组成部分。有机聚合物光波导的制作工艺对光波导的性能具有重要影响,故此对有机聚合物光波导的制作工艺进行了综述,并提出了一些未来的研发方向。

关键词:聚合物光波导;光波导制作工艺;光损耗
中图分类号:TN929.1 **文献标识码**:A **DOI**:10.3969/j.issn.1001-5078.2015.06.001

Fabrication process of organic polymer optical waveguide

LIU Tao,LI Zhi-shan,JIANG Zhi,YANG Min,WANG Shu-rong
(Solar Energy Research Institute,Key Laboratory of Advance Technology and Preparation for Renewable Energy Materials,Ministry of Education,Yunnan Province Key Lab of Rural Energy Engineering,
Yunnan Normal University,Kunming 650500,China)

Abstract:The organic polymer optical waveguide interconnects become the best solution to realize short distance computation and communication design. Short distance optical interconnection is the direction of future interconnects,and excellent comprehensive performance of polymer multimode optical waveguide is an important component in optical interconnection. The fabrication process of organic polymer optical waveguide has important influence on the performance of optical waveguide,therefore the fabrication process of organic polymer optical waveguide is summarized,and puts forward some own ideas.

Key words:polymer optical waveguide;polymer optical waveguide fabrication process;optical loss

1 引 言

信息时代下,人们对数据传输性能的要求越来越高。在长距离有线通信领域,光纤通信技术能够满足这种高性能需求,然而在短距离信息传输方面,因成本要求,目前仍然以电互连为主。但电互连存在固有的电磁干扰、高损耗和低带宽等缺点,限制了数据传输性能的进一步提升。光波导作为光信号通道,其较之电信通道具有高带宽、抗电磁干扰、低损耗、低能耗、低串扰、小物理尺寸等优点,使光互连成为解决高速电信号互连瓶颈的一个有效方法[1-2],早已成为关注和研究的焦点。

基金项目:国家自然科学基金资助项目(No.61167003)资助。
作者简介:刘 涛(1988-),男,硕士研究生,主要从事光波导器件的研究。
通信作者:王书荣,博士,副教授,主要从事半导体材料和半导体光电子器件研究。E-mail:shrw88@aliyun.com
收稿日期:2014-09-12;**修订日期**:2014-11-04

目前认为光电印刷电路板(OPCB)之间的互连采用光纤带比较好,而在 OPCB 内各模块之间的互联采用嵌入式光波导互连很有前途,且光波导是芯片间光互连的必然选择[3-5]。虽然传统的有机聚合物光波导在通信波长(1.31 μm 和 1.55 μm)传输损耗高、温度稳定性差,但其光学特性、热学特性、柔韧性可以通过热处理及合成过程进行改进[6-7];且新型有机聚合物作为一类光波导材料通常有大的透明窗口、柔韧性好、通信波段损耗低、易于加工等优点[8],其优越的综合性能使其成为加工制作光通信元件的首选材料。随着聚合物光通信的蓬勃发展,其在光通信领域的应用前景日益显著;将 OPCB 集成于超级计算机中,可使其计算速度提高 1000 倍以上[2,9]。加之,高带宽聚合物多模光波导能否在光互连中大规模应用,主要取决于其损耗特性、热特性和成本,而光波导制作工艺对光波导性能和成本有重大影响,因此本文着重对目前光波导的光损耗特性和各种制作工艺进行较全面的综述,同时也指出未来聚合物多模光波导的研发方向。

2 有机聚合物光波导的性能和应用要求

有机聚合物光波导的性能主要是光损耗特性和热特性,而光波导的光损耗主要取决于散射损耗;其中散射损耗包括表面散射损耗和体散射损耗。光波导芯层表面会有一定的粗糙度,这会引起一定程度的表面散射损耗。体散射损耗主要是由材料中各种杂质,以及成型光波导中的结构缺陷、裂纹、折射率不均匀等各种缺陷引起;为了最小化体散射损耗,光波导材料必须为高纯材料,尽量减少波导中的缺陷并保证芯层表面光滑,且制作过程中必须在严格清洁的超净室完成[10]。因此,有机聚合物光波导制作工艺对光波导的光损耗性能有重要影响。有机聚合物光波导的热特性主要是热稳定性、热老化特性,及光损耗和波导折射率与温度的变化关系,有机聚合物光波导制作工艺对光波导的热特性也有决定性的意义。

聚合物多模光波导光互连的应用需要满足如下基本要求[11]:①在通信波长 850 nm、1310 nm、1550 nm等附近的传输损耗低;②有较高的光电非线性系数与热稳定性(T_d > 250 ℃,能经受集成光电装置时的热焊接过程),较低的介电常数与热损耗系数;③其制作工艺简单、与电子加工技术相兼容、重复性好、成本低,且所制备的光波导散射损耗小、尺寸稳定、柔韧性好;④芯层比包层的折射率至少大 0.8%,各层之间粘附性好,且具有匹配的热膨胀系数;⑤光波导各接触层之间不相溶,后续层的固化温度应该小于前一层的玻璃态转化温度 T_g,即下包层固化温度 > 芯层固化温度 > 上包层固化温。

3 有机聚合物光波导制作工艺

3.1 光刻法

(1)平板影印(Photolithography)技术,一般的平板影印工序[12]如图 1 所示,其中烘干是为了增加胶膜的耐磨性及层间的粘附性;曝光是为了让胶膜充分吸收光能发生光化学反应,其关键控制参数是曝光时间、曝光波长及曝光量:$E = It$(其中,I 为光强,t 为曝光时间)。对于以紫外光固化材料作为芯层及包层材料,并用平板影印技术加工制作光波导,其制作工序可以省略热固化过程[13]。这种技术成熟、工艺简单且与 PCB 加工工艺兼容性高、可实现大面积生产,其缺点在于需要严格控制侧蚀,制作符合尺寸要求的光波导,材料需为光敏材料[14]。

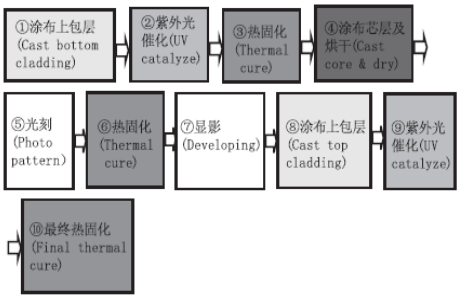

图 1 一般的平板影印工序

对于光致抗蚀剂(Photoresist),若曝光部分发生交联反应,经过显影后,曝光部分保留下来而未曝光部分被除掉,称其为负性光致抗蚀剂,反之则称为正性光致抗蚀剂。选择光致抗蚀剂时不但要考虑其是否满足作为光波导材料的基本要求,还要考虑其涂布的均匀性、对光源的灵敏度、图形的分辨率以及对蚀刻工艺的耐腐蚀性等因素[15]。若以正性光致抗蚀剂作为光波导芯层材料,则在使用过程中芯层可能会因为缓慢曝光而折射率发生改变进而失去传输光信号的能力,故通常选择负性光致抗蚀剂作为光波导材料。

(2)光漂白(Photo-bleaching)技术,光漂白技术

制作聚合物光波导的工序如图2所示。

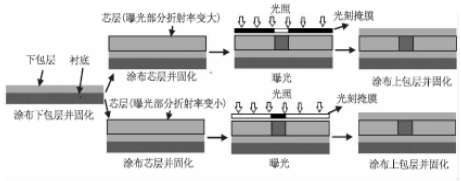

图2 不同芯层材料(上/下面为曝光部分折射率变大/小)的光波导光漂白工序

其原理是利用某些聚合物材料所特有的光敏性,在光照下曝光部分发生光化学反应,通过控制曝光时间和曝光光强,控制曝光部分薄膜的折射率,最终在曝光部分与未曝光部分形成折射率差,同时避免了其他制备方法中物理作用、化学作用对器件的损伤[16]。这种技术的优点在于工艺简单、效率高、折射率易控、对器件损伤小,缺点在于要求材料为特殊光敏材料[17]。此外光漂白技术可以制作低散射损耗、低串扰的渐变折射率圆芯光波导[18]。

(3)反应离子蚀刻(RIE)技术,对于不同的材料以反应离子蚀刻工序制作光波导,其工序不尽相同;以紫外固化环氧树脂(UV Cured Epoxy Resins)为材料制作光波导为例[19],工序如图3所示。

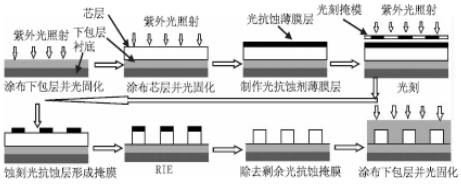

图3 反应离子蚀刻工序(以紫外固化环氧树脂为材料制作光波导为例)

而对于以聚硅氧烷为包层材料,以氘化聚硅氧烷为芯层材料制作光波导时,其固化过程为热固化过程[20]。反应离子蚀刻技术属于干法刻蚀技术,是利用高能量等离子体轰击及化学反应来达到蚀刻的一项技术[6]。因为蚀刻过程中,工艺参量对被蚀刻元件的质量有决定性影响,这些工艺参量主要包括:射频功率、腔室压强、反应时的抽速、反应气体与辅助气体的混合比等。这些参量之间既独立可调又相互影响,因而蚀刻工艺有相当大的灵活性。这一技术的优点在于工艺成熟、与传统集成电路工艺相兼容、无材料限制、对器件损伤小;缺点在于工艺复杂、加工效率低、侧壁粗糙度大、造价较高。

3.2 模板复制法

(1)加热模压(Hot Embossing)技术,其制作工序如图4所示。

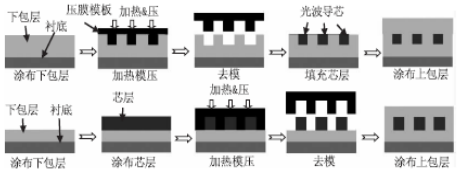

图4 两种加热模压制造光波导过程

(上面为凹槽填充法;下面为脊形覆盖法)

用此方法制作光波导,首先需根据所需制作光波导的几何结构及间距,设计制作满足需求且表面光滑的高精度压膜模板。该方法工艺简单成本较低,可实现大面积生产[21-22],但其对模板要求高,且加热模压过程中会对膜层产生损伤致使传输损耗较大。对于凹槽填充法,若填充的芯层材料过多(对于脊形覆盖法,若加热模压过程不充分),光波导之间下包层上有芯层薄膜残留,将会增加信道间串扰。根据压膜模板材料的不同,加热模压工艺分为金属模压工艺和橡胶模压工艺[22]。

(2)软光刻(Soft Lithography)技术,其特点是用弹性模代替加热模压中使用的硬模,其优点在于软光刻灵活性更高、不受材料限制、可以在非平面内制作光波导,并能用于制作三维结构,折射率渐变圆芯光波导,且没有光散射、衍射带来的精度限制[23],其缺点在于对原始母板及柔性印模的高精度要求。软光刻过程中控制弹性模的形变量是获得高质量光波导的关键。用此工艺制作光波导前,首先要根据需求制作原始母板,然后以原始母板用再铸模法制作柔性印模[24]。用于制作柔性印模的材料有聚氨酯(Polyurethanes)、聚酰亚胺(Polyimides)和Novolac树脂等,但是相对而言聚二甲基硅氧烷(Poly-dimethyl-siloxane,PDMS)的综合性能高,是软刻蚀技术中最常用的印模材料。最后以柔性印模制作光波导,主要有再铸模法、微传递成模、毛细管成模、溶剂辅助成模四种不同的方法[18]。

3.3 其他方法

除以上介绍的聚合物光波导加工工艺外,还有多种其他加工工艺,如表1所示。

表 1 部分聚合物光波导加工方法对比

聚合物光波导加工方法	主要优点	主要缺点
激光烧蚀	工艺简单,加工精度高,易于制作柔性化光波导,速度快,无污染,成本低	波导边沿粗糙度大,有烧蚀残留
紫外光直写[25]	工艺简单,较为成熟,可实现大尺寸加工	制作周期长,设备昂贵,侧蚀需要严格控制,光敏材料
双光子直写[26]	工艺简单,材料内部直接成型	制作周期长,设备昂贵,波导形貌不易控制,材料难得
电子束直写[27]	工艺简单,材料上直接成型	设备昂贵,粗糙度难控制,可加工面积有限
质子束直写	工艺简单,材料上直接成型	设备昂贵,可加工面积有限,波导成型结构受界面效应影响
空间选择极化	工艺简单	材料的特性要求较高,控制折射率较难
微针孔直写[28]	工艺简单,大面积生产,渐变折射率圆芯光波导	不能制作交叉结构的光波导,波导成型结构受界面效应影响

4 不同材料及光波导加工工艺传输损耗对比

表 2 光波导传输损耗比较

光波导制作机构	波导成型工艺	光波导芯材料	传输损耗 dB/cm(波长 μm)
NTT	Photolithography	SU-8	0.07(0.68),0.08(0.83),0.50(1.31),4.72(1.55)
	RIE	SU-8	0.24(0.68),0.13(0.83),0.68(1.31),4.76(1.55)
	RIE	Halogenated Acrylate	0.02(0.83),0.07(1.31),1.7(1.55)
	RIE	Deuterated Polysiloxane	0.17(1.31),0.43(1.55)
Micro-resist Tech.	Photolithography	Polysiloxane	0.1(0.85),0.26(1.30)
Dow Corning	Photolithography	Polysiloxane	0.04(0.85)
Rohm & Haas	Photolithography	Polysiloxane	0.03(0.85)
State Key Lab. of Modern Opt. Instrum. ,Zhejiang Univ.	Photolithography	SU-8	0.019(0.6328),0.036(0.83),0.077(1.31),0.125(1.55)
Technical Univ. of Dortmund	Soft Photolithography	Poly-dimethyl-siloxane	0.035(0.85)
Allied Signal	Photo-exposure & Wet Etch,RIE, Laser Ablation	Acrylate	0.02(0.84),0.2(1.30),0.5(1.55)
		Halogenated crylate	<0.01(0.84),0.03(1.30),0.07(1.55)
		UV Acrylate	0.02(0.84),0.03(1.30);0.05(1.55)
	Laser Ablation,RIE	Halogenated Acrylate	0.01(0.84),0.06(1.30)
IBM and Dow Corning	Spin Coating and UV Photolithography	WG-1010	0.031(0.85)
	Draw-down Coating and UV-Laser Direct Writing	WG-1010	0.046-0.050(0.85)
Asahi Glass Co. Ltd.	UV Photolithography	Perfluorinated Poly (butenyl vinyl ether)	0.047(1.31),0.049(1.55),0.070(1.65)
Faculty of Science and Technology, Keio Univ.	Mosquito Method	UV curable silicone resins	0.033-0.045(0.85)
	Soft-lithography	PMMA	0.027(0.85)

从表2可以看出,一般来说,相同条件下较之其他工艺,平板影印工艺制作的光波导的损耗较低;对于聚硅氧烷光敏化材料,采用平板影印工艺制作的多模光波导,在850 m通信窗口,其最低损耗为0.03 B/cm,这是目前得到的较好结果。尽管采用软光刻法制作的PMMA多模光波导,在850 m通信窗口,其传输损耗最低为0.027 dB/cm,但是以PMMA材料制作的光波导热稳定特性较差;采用激光直写或激光烧蚀法制作的聚合物多模光波导,虽然也可获得较低的光损耗,但制作成本较高;SU-8光波导材料虽然廉价,但光传输损耗较大;丙烯酸酯类光波导的传输损耗低,但热稳定性差。

5 结 语

综上所述,虽然国内外对有机聚合物光波导光通信的相关研究已取得一定的成果,但仍然需要从材料、加工工艺、光耦合技术、光互连技术、集成光学等相关方面进行研发。就加工工艺而言,目前存在多种优缺点不尽相同的聚合物光波导制作工艺,结合我们对聚合物光波导的研制经历,认为对于紫外光可固化聚合物光波导材料,较之其他工艺,平板影印工艺制作的光波导的综合性能优良,且适用于工业化生产,是一种实用性强的工艺。对于这种工艺,重点研究曝光光强及烘烤温度对光波导特性的影响。再者,未来研发的方向主要是研制新型低成本紫外光敏化聚合物材料,且要求该材料的光传输特性和热稳定性较好,只有达到此结果,才能早日实现低成本低损耗聚合物多模光波导短距离光互连的目标。

参考文献:

[1] CHO I K, YOON K B, AHN S H. Experimental demonstration of 10 Gbit/s transmission with an optical backplane system using optical slots[J]. Opt. Lett., 2005, 30(13): 1635-1637.

[2] TAUBENBLATT A M. Optical interconnects for high-performance computing[J]. Journal of Lightwave Technology, 2012, 30(4): 448-458.

[3] 行松健一. 光开关与光互连[M]. 崔敦杰, 译. 北京: 科学出版社, 2002: 87-93.

[4] ZHANG Yimo. Optics inter-connected networks techniques[M]. Beijing: Publishing House of electronics Industry, 2006: 134-145. (in Chinese)

张以谟. 光互连网络技术[M]. 北京: 电子工业出版社, 2006: 134-145.

[5] WITTMANN B, JOHNCK M, NEYER A, et al. POF-Based Interconnects for Intracomputer Applications[J]. IEEE Journal of Selected Topics in Quantum Electronics, 1999, 5(5): 1243-1248.

[6] JAE-WOOK K, JAE-PIL K, WON-YOUNG L, et al. Low-loss fluorinated poly(arylene ether sulfide) waveguides with high thermal stability[J]. Journal of Lightwave Technology, 2001, 19(6): 872-875.

[7] Eldada L, Shacklette L W. Advances in polymer integrated optics[J]. IEEE Journal of Selected Topics in Quantum Electronics, 2000, 6(1): 54-68.

[8] KIM J S, KANG J W, KIM J J. Simple and low cost fabrication of thermally stable polymeric multimode waveguides using a UV-curable epoxy[J]. Jpn. J. Applied Phys., 2003, 42(3): 1277-1279.

[9] Tan M R T, Mclaren M, Jouppi N P. Optical Interconnects for high-performance computing systems[J]. IEEE Micro, 2013, 33(1): 14-21.

[10] Kinoshita R, Moriya K, Choki K, et al. Polymer optical waveguides with gI and W-Shaped cores for high bandwidth density On-Board interconnects[J]. Journal of Lightwave Technology, 2013, 31(24): 4004-4015.

[11] 张金星. 基于光波导互连的EOPCB的研究[D]. 武汉: 华中科技大学, 2011.

[12] Roger Dangel, Folkert Horst, Daniel Jubin, et al. Development of versatile polymer waveguide flex technology for use in optical interconnects[J]. Journal of Lightwave Technology, 2013, 31(24): 3915-3926.

[13] Joon-Sung Kim, Jang-Joo Kim. Stacked polymeric multimode waveguide arrays for two-dimensional optical Interconnects[J]. Journal of Lightwave Technology, 2004, 22(4): 840-844.

[14] Houbertz R, Domann G, Cronauer C, et al. Inorganic-organic hybrid materials for application in optical devices[J]. Thin Solid Films, 2003, 442(1-2): 194-200.

[15] Streppel U, Dannberg P, Achter C W, et al. New Wafer-scale fabrication method for stacked optical waveguide interconnects and 3d micro-optic structures using photo-responsive(inorganic-organic hybrid) polymers[J]. Optical Materials, 2003, 21(1-3): 475-483.

[16] Hong MA, Alex K Y Jen, Larry R Dalton. Polymer-based optical waveguides: materials processing and devices[J]. 2002, 14(19): 1339-1365.

[17] Mederer F, JÄGer R, Unold H J, et al. 3-Gb data transmission with GaAs VCSEL over PCB integrated polymer waveguides[J]. IEEE Photonics Technology Letters,

2001,13(9):1032 – 1034.

[18] 刘伟庭. 柔性微图形复制技术的研究[D]. 杭州:浙江大学,2003.

[19] Koji Enbutsu, Makoto Hiklta, Ryoko Yoshimura, et al. Multimode polymeric optical waveguides with high thermal stability using UV cured epoxy resins[J]. Jpn. J. Applied Physics,1998,37(6B):3662 – 3664.

[20] Usui M, Hikita M, Watanabe T, et al. Low-loss passive polymer optical waveguides with high environmental stability[J]. J. Lightwave Technology, 1996, 14(10): 2338 – 2343.

[21] Joon-Sung Kim, Jae-Wook Kang, Jang-Joo Kim. Simple and low cost fabrication of thermally stable polymeric multimode waveguides using a UV-curable epoxy[J]. Jpn. J. Applied physics,2003,42(3):1277 – 1279.

[22] Byung-Tak Lee, Min-Suk K, Jun-Bo Yoon, et al. Fabrication of polymeric large-core waveguides for optical interconnects using a rubber molding process[J]. IEEE Photonics Technology Letters,2000,12(1):62 – 64.

[23] 倪玮. 基于软光刻的短距离光互连研究[D]. 杭州:浙江大学,2009.

[24] Guomin Jiang, Baig S, Wang M R. Flexible polymer waveguides with integrated mirrors fabricated by soft lithography for optical interconnection[J]. Journal of Lightwave Technology,2013,31(11):1835 – 1841.

[25] Griese E. A high-performance hybrid electrical-optical interconnection technology for high-speed electronic systems [J]. IEEE Transactions on Advanced Packaging,2001,24(3):375 – 383.

[26] Ishihara Jiro, Komatsu K, Sugihara K, et al. Fabrication of three-dimensional calixarene polymer waveguides using two-photon-assisted polymerization[J]. Applied Physics Letters,2007,90(3):033511 – 033511 – 3.

[27] Maruo Y Y, Sasaki S, Tamamura T. Channel-optical-waveguide fabrication based on electron-beam irradiation of polyimides [J]. Applied Opt., 1995, 34(6): 1047 – 1052.

[28] Soma K, Ishigure T. Fabrication of a graded-index circular-core polymer parallel optical waveguide using a microdispenser for a high-density optical printed circuit board [J]. IEEE Journal of Selected Topics in Quantum Electronics,2013,19(2):3600310 – 3600310 – 10.

云南师范大学学报(自然科学版)
2015 年 7 月 35 卷 4 期(Vol. 35 No. 4)

Journal of Yunnan Normal University
DOI:10.7699/j.ynnu.ns-2015-045

全玻璃真空太阳集热管空晒性能的数值模拟分析*

刘佰红， 高文峰， 刘滔， 林文贤， 邢秀兰， 胡小芳
(云南师范大学 太阳能研究所,教育部可再生能源材料先进技术与制备重点实验室,云南 昆明 650092)

摘 要： 利用 FLUENT 对 Ø58×1 800 mm 全玻璃真空管在不同发射率、真空度下空晒热性能进行数值模拟与分析,并通过空晒实验来验证模拟结果的正确性.数值分析结果表明:发射率越低,真空管的热损失越小,真空管的热性能越好.真空管空晒热性能随真空夹层压强的增加而减小,真空管空晒性能变化主要位于 10^{-1}～10 Pa 范围,当压强小于 10^{-1} Pa 或大于 10 Pa 时,由真空夹层间气体的导热损失引起的真空管热性能变化已不明显,为了保证良好的真空管热性能,真空夹层的真空度应当维持在 10^{-2} Pa 的数量级.

关键词： 发射率;真空度;热损系数;空晒性能参数

中图分类号： TK513 **文献标志码：** A **文章编号：** 1007-9793(2015)04-0005-06

1 引 言

真空管具有结构简单、价格便宜、安装和运输方便、保温性能好、光热转换效率高等优点[1],因而在我国有着广泛的应用市场.

目前真空管性能的研究主要集中在理论分析与实验结合的方面,殷志强等人[2]从能量方程式推导出真空太阳能集热管的光一热性能参数,分析了真空管热性能的影响因素,提出了真空管空晒热性能评价标准,并做相应的实验进行验证.Ma[3]通过实验分析了空晒性能参数、闷晒太阳辐照量和平均热损系数三个参数对真空管热性能的影响,得出涂层发射比是影响真空管空晒性能参数和平均热损系数的主要因数,增大涂层吸收比可以提高真空管的闷晒性能.Badar 等人[4]通过实验测量和数学模型相结合的方式分析了真空夹层内残余气体对真空管热量损失的影响,但热损测量值比理论值高.吴家庆等人[5]通过对全玻璃真空集热管的真空获得与真空寿命的研究表明:从良好的绝热效果和投资成本综合考虑,真空度选择在 10^{-4}～10^{-5} 托(1.33×10^{-2} Pa～1.33×10^{-3} Pa)为宜.Gui 等人[6]研究了选择性吸收涂层发射率的影响,结果表明:真空管夹层间的压强在不大于 5×10^{-2} Pa 时,由真空夹层间空气的导热引起的损失可以忽略.杨静芸等人[7]利用 FLUENT 对三腔式全玻璃真空管与常规全玻璃真空管在闷晒状态下管内流体的流动状态及性能进行数值模拟与分析,结果表明三腔式全玻璃真空管相较于常规全玻璃真空管具有启动速度快、温升高、管内流体流速大等特点.

本文采用数值模拟方法对 Ø58×1 800 mm 全玻璃真空管空晒状态下的热性能、管内工质的温度分布及变化情况进行模拟分析.探讨真空管高温状态下热损失机理及影响因数,为优化真空管的生产工艺和技术提供依据.

2 全玻璃真空太阳集热管热性能的影响因素分析

真空管在不同的辐射强度及环境温度下其空

* 收稿日期:2015-06-10
基金项目:国家自然科学基金资助项目(51266016,51469035).
作者简介:刘佰红(1989-),男,河南信阳人,硕士研究生,主要从事太阳能热利用及计算流体力学方面研究.
通信作者:高文峰(1970-),男,副教授,主要从事太阳能热利用及计算流体力学方面研究.E-mail:413900096@qq.com.

晒温度存在很大的差异,殷志强等人[2]通过大量的测试实验,分析得出了评价真空管空晒性能的参数

$$Y=\frac{(T_g-T_a)}{G}=\frac{A_c(\tau\alpha)}{A_aU_l} \tag{1}$$

式中:A_c 为真空管的有效采光面积(m^2);A_a 为内管的表面积(m^2);τ 为罩玻璃管透射比(AM1.5);α 为吸收涂层的吸收比(AM1.5);G 为太阳辐照度(W/m^2);U_l 为热损系数($W/m^2\cdot K$);T_a 为环境温度(K);T_g 为加热工质平均温度(K).从式(1)中可以看出,热损系数对真空管空晒性能参数起着决定性作用.真空管的热损主要有三个部分构成:不锈钢卡子和管口玻璃传导热损;吸收涂层的发射热损;真空夹层气体的导热.因此热损系数

$$U_l=\frac{k_g}{A_c}+\frac{2K}{d_2\ln\frac{d_2}{d_1}}+\varepsilon_T(T_g^{\,2}+T_a^{\,2})(T_g+T_a) \tag{2}$$

式中:k_g 为真空管内不锈钢卡子和开口端玻璃传导损失$k_g\approx0.003\ 2\ W/K$[2];K 为真空管夹层气体的导热系数($W/(m\cdot K)$);ε_T 为内管温度为 T 时吸收涂层的半球发射比.

3 数值模型及边界条件

选择市场常见的普通全玻璃真空管作为分析案例,真空管的外管管径为 58 mm,管长为 1 800 mm,内管管径为 47 mm,玻璃管壁厚为 1.7 mm,容积 3.26 L.根据全玻璃真空管的几何尺寸,利用 ICEM 构建网格模型.

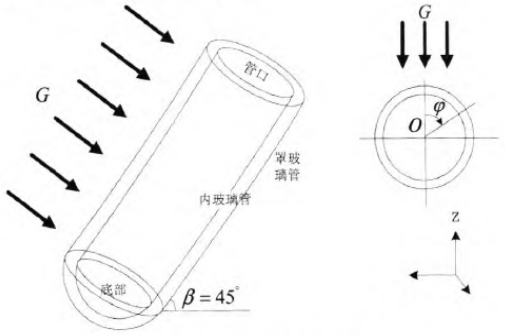

图 1 全玻璃真空管空晒示意图

Fig. 1 Schematic diagram of stagnation of the all-glass evacuated tubes

将 ICEM 生成的网格模型,导入 Fluent 中求解计算,根据实际辐射情况,建立辐射模型边界条件,真空管南北向放置,倾角 45°,地点设置为昆明(E102°N25°),模拟时间为 2014 年 11 月 21 日 13 时,其模型示意图如图 1 所示.为便于研究,需要对模型做以下几方面的假设:

1)采用 Boussinesq 假设,并假设在空晒条件下真空管内的空气随温度的热膨胀系数为 1/273K;

2)真空管底部卡子无热传导损失;

3)忽略能量方程中的黏性耗散热;

4)涂层的吸收率和发射率不随温度的变化而改变;

5)真空管玻璃的物性参数均不随温度的变化而改变.

在不影响计算结果精度的前提下,为了减少 FLUENT 求解计算时间,需要进行网格独立性验证.分别计算了 3 种不同网格数下真空管空晒最高温度,结果见表 1.对三种网格数下的计算结果进行对比可以得出,当网格数为 174 477 时,继续增加网格数量,空晒最高温度几乎不变,因此选择 174 477 的网格数进行求解计算.

表 1 三种网格数网格独立性验证

Table 1 The grid-independent examination for three grid systems

网格数	82 503	174 477	382 721
空晒最高温度/K	559.452	559.523	559.531

4 实验验证

为了验证模拟结果的正确性,根据 GB/T17049—2005[8]的方法及步骤进行了真空管空晒测试,分别选取 5 根透过率与吸收率相近的真空管,对应的发射比为 0.028、0.031、0.041、0.06、0.082,测试期间太阳辐照度 900~1 000 W/m^2,环境温度 15~20 ℃,记录真空管内温度变化.利用 FLUENT 对发射比分别为 0.04、0.06、0.08、0.1、0.12 的真空管进行空晒数值模拟,并与测试结果进行对比.

图 2 为模拟与测试的空晒性能参数 Y-ε 的曲线,由图 2 可以看出,2 条曲线变化趋势一致,真空管的空晒性能参数随发射率的升高呈现出降低

的趋势，相同发射率下实验测得的真空管空晒性能参数比模拟结果平均低 50 K·m²·(kW)⁻¹，这是由于真空管的涂层吸收比随温度的升高变化不大，而涂层发射比随空晒温度升高却迅速增大，史月艳等人[9]测量不同温度下 AlN-Al 真空管的发射比，结果表明 300 ℃下真空管的发射比比 80 ℃下真空管的发射比增加了 57.1%. 所以发射比在 0.041、0.06、0.082 时实验所测的空晒性能参数 Y 应近似等于发射比在 0.06、0.09、0.12时模拟所得的空晒性能参数，从图中可以看出当模拟发射比比实验发射比大 50%时，模拟与实验所得的空晒性能参数几乎相等. 总体看来，模拟结果与实验测试结果吻合较好，所以通过模拟求解计算，用于分析真空管的热性能是合理的.

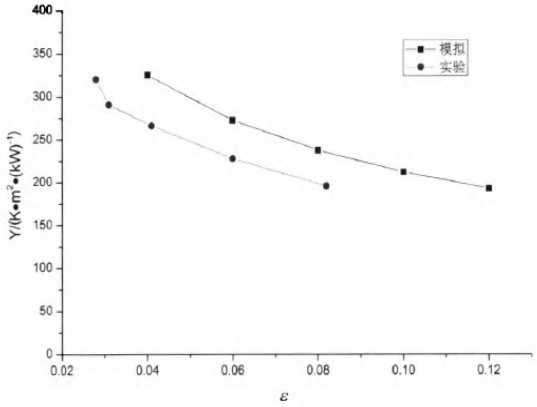

图 2　空晒性能参数的数值模拟结果与实验对比

Fig. 2　The stagnation parameter comparison curve of numerical simulation result and test result

5　模拟结果与分析

5.1　发射率对真空管热性能的影响分析

1)不同发生率下真空管空晒温度对比

初始辐照 G＝988 W/m²，环境温度为 300 K，τ=0.92，α=0.92，忽略真空部分的导热损失，分别将涂层的发射率设定为 0.04、0.06、0.08、0.1、0.12，对真空管进行 120min 的辐射模拟求解计算，每隔 10min 取一次数据，将统计的结果进行整理分析得出不同发射率下，真空管内空晒温度随空晒时间的变化关系，如图 3 所示. 从图中可以看出，不同发射率下真空管空晒温度曲线变化趋势相同，初始阶段，温度迅速升高，随着空晒时间的增长，温度升高的速率逐渐趋缓并达到相应的平衡状态，温度不再升高. 发射率在 0.04、0.06、0.08、0.1、0.12 下分别对应的空晒温度为 610 K、560 K、520 K、480 K，即发射率越低其空晒温度越高.

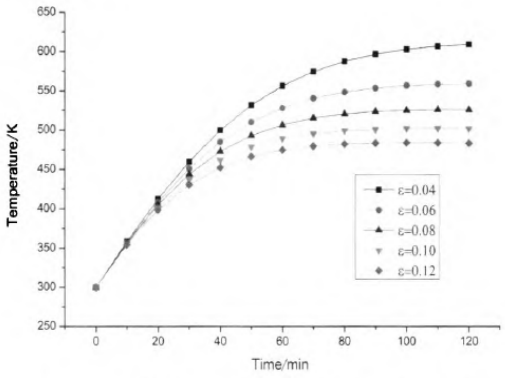

图 3　不同发射率下真空管空晒温度随时间的变化

Fig. 3　Stagnation temperature change along the time of all-glass evacuated tube with different emittance

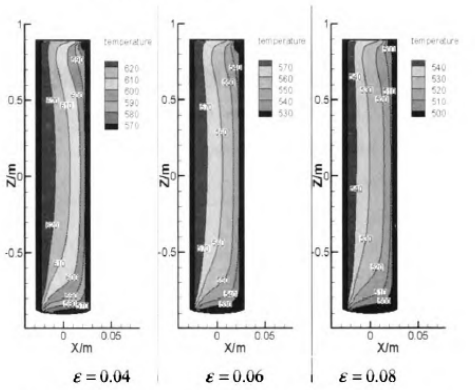

图 4　不同发射率下真空管轴向截面的等温图

Fig. 4　Isothermal diagram of axial section of the all-glass evacuated tubes under different emissivity

当真空管空晒温度不再升高时，截取真空管轴向截面，如图 4 所示，发射率分别为 0.04、0.06、0.08 时真空管内部温度的等温线图. 从图中可以看出发射率低的真空管内部的整体温度明显高于发射率高的真空管内部的整体温度. 图中等温度曲线显示，真空管中部温度变化较为均匀，加热壁面(左边为太阳辐射面)附近工质温度较高，向右温度逐渐降低. 底部和顶部温度变化较大，且两端平均温度相对中部平均温度较低，这是由于真空管空晒情况下，由管口导热引起的损失较大，所以靠近管口的工质温度较低，而底部则是

在密度差引起的热浮力作用下,使得管底部工质的温度低于中部工质温度.

2)发射率对真空管热损系数的影响

图 5 为辐射强度 988 W/m^2,环境温度为 300 K,真空管的热损系数随空晒温度的变化关系,从图中可以看出真空管的热损系数随温度的升高逐渐增大,发射率越高,其曲线斜率越大,热损系数随温度的变化越明显.

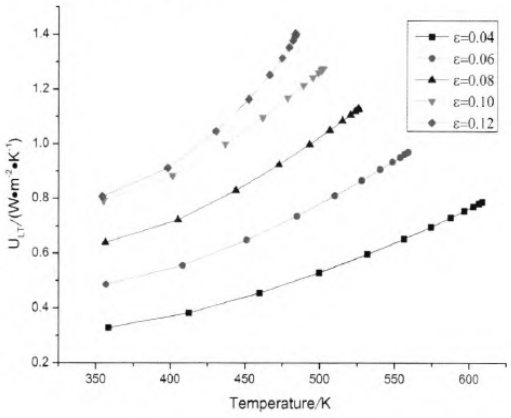

图 5 真空管的热损系数随空晒温度的变化关系

Fig. 5 The correlations between heat loss coefficient and air drying temperature

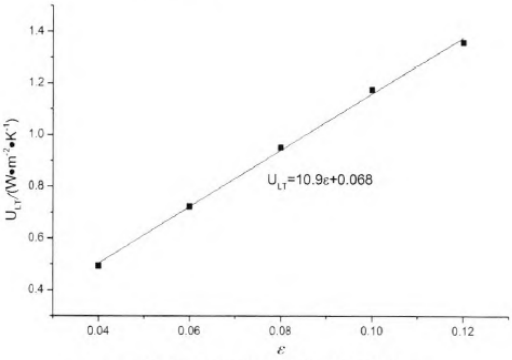

图 6 热损系数随发射率的变化关系

Fig. 6 The correlations between heat loss coefficient and emissivity

图 6 为 G=988 W/m^2,环境温度为 300 K,真空管空晒温度为 480 ℃时,发射率与热损系数的关系,从图 6 中可以得出真空管的热损系数随发射率的增加几乎成线性正比例增加,其线性回归公式

$$U_{LT}^{*}=10.9\varepsilon+0.068 \qquad (3)$$

式(3)中,U_{LT}^{*}:热损系数(拟合值),W/(m^2 · K);发射率从 0.04 增加到 0.12,真空管的热损系数由 0.5 W/(m^2 · K)增加到 1.4 W/(m^2 · K).

3)发射率对空晒性能参数的影响

如图 7 所示,真空管的空晒性能参数随涂层发射率的增加而减小,发射率为 0.04 时真空管的热性能参数为 Y=325 K · m^2 · (kW)$^{-1}$,当发射率增加到 0.12 时真空管的热性能参数 Y=193 K · m^2 · (kW)$^{-1}$,真空管的 Y 减少了 132 K · m^2 · (kW)$^{-1}$,其拟合公式

$$Y^{*}=350e^{-16.5\varepsilon}+150 \qquad (4)$$

式(4)中,Y* 为空晒性能参数(拟合值),K · m^2 · (kW)$^{-1}$.

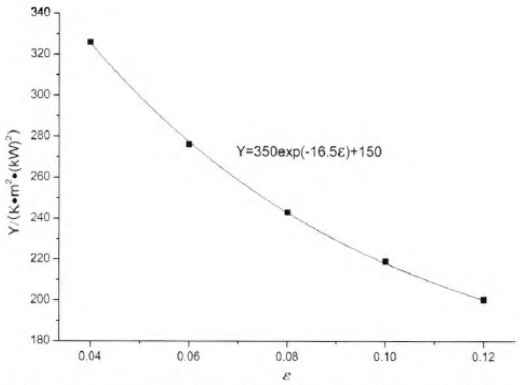

图 7 真空管空晒性能参数 Y 与涂层发射率的关系

Fig. 7 The correlations between the stagnation parameter Y of all-glass evacuated tube and emittance

5.2 真空度对真空管空晒性能的影响

1)真空度对空晒温度的影响

为了探究真空夹层的真空度对真空管空晒性能的影响,分别选取了 10^{-3} Pa、10^{-2} Pa、10^{-1} Pa、1.0 Pa、10 Pa、10^{2} Pa、10^{3} Pa 的真空压强进行模拟求解,辐照 G=988 W/m^2,环境温度为 300 K,$\varepsilon=0.06$,$\alpha=0.92$,$\tau=0.92$,对真空管进行 120 min 的辐射模拟求解计算,分析模拟结果,得到真空管内空晒温度随时间的变化关系,如图 8 所示.从图 8 中可以看出,真空管内的空晒温度开始一段时间内温度迅速升高,随着空晒时间的增长,温度升高速率逐渐趋缓,最后达到相应的平衡状态,温度不再升高.真空管夹层间的压强越大,空晒最高温度越低,达到平衡状态所用时间就越短.

当真空管空晒温度不再升高时,截取真空管轴向截面,得到压强分别为 1.0×10^{-3}、1.0 Pa、1.0×10^{5} Pa 时真空管内部温度等温线图,如图 9 所示.图中真空管的左侧为太阳辐射壁面,所以左侧温度较高,右侧温度较低;压强低的真空管内部

的整体温度明显高于压强高的真空管内部的整体温度；真空管中部温度变化较为均匀，顶部和底部温度变化较大，且平均温度相对中部温度较低. 这是由于真空管在空晒情况下，管内温度较高，由管口导热引起的损失较大，所以靠近管口的工质温度较低，而底部则是在密度差引起的热浮力作用下，使得真空管低部工质的温度低于中部工质温度.

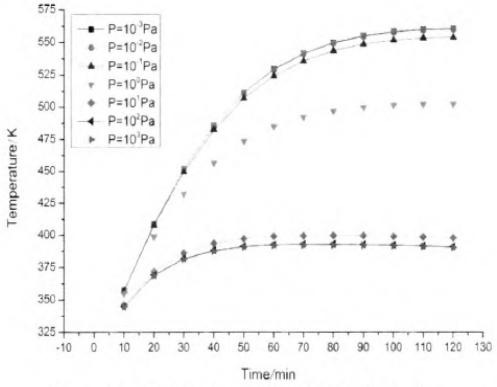

图 8　真空管空晒温度随时间的变化的关系

Fig. 8　The variation of air drying temperature in radiation time

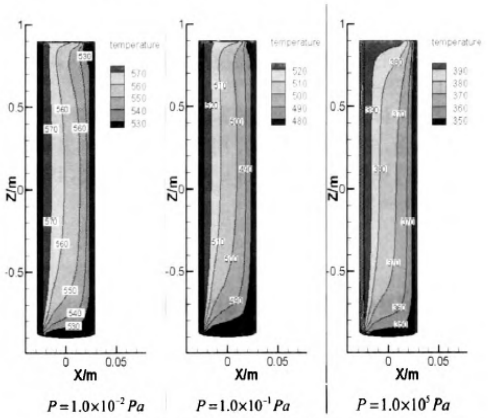

图 9　不同真空度下真空管轴向截面的等温图

Fig. 9　Isothermal diagram of axial section of the all-glass evacuated tubes in different vacuum degrees

2）真空度对热损系数的影响

图 10 表示不同真空度下真空管的热损系数随空晒温度的变化关系，不同曲线分别对应着不同的真空度，真空管的热损系数随温度的升高逐渐的增大，压强位于 10^{-3} Pa、10^{-2} Pa、10^{-1} Pa 时，热损系数随温度变化的曲线几乎重合，空晒温度 560 K 下的热损系数 1.0 W/(m² · K)比空晒温度 355 K 下的热损系数 0.5 W/(m² · K)增加了一倍. 然而当压强高于 1.0 Pa 时，其热损系数将不随温度的增加而增加.

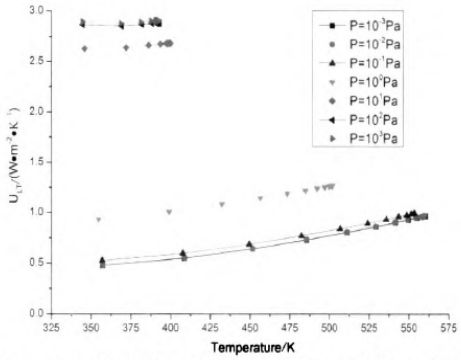

图 10　不同真空度下热损系数随空晒温度的变化关系

Fig. 10　The correlations between heat loss coefficient and air drying temperature under different vacuum degrees

如图 11 为空晒温度 390 K 时真空管的热损系数随真空度的变化关系，从图中曲线可以看出压强为 10^{-1}～10 Pa 是热损系数变化最为明显的区域，当压强从 10^{-1} Pa 升高到 10 Pa 时，热损系数从 0.5 W/(m² · K)增大到 2.7 W/(m² · K). 当压强小于 10^{-1} Pa 或大于 10^{2} Pa 时，热损系数的变化很小.

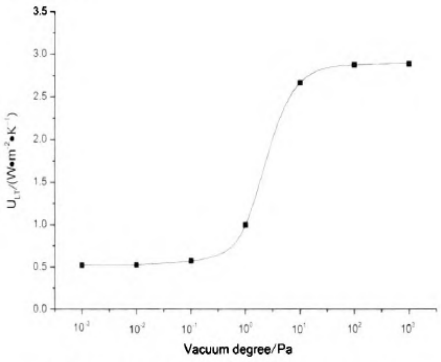

图 11　热损系数随真空度的变化关系

Fig. 11　The correlations between heat loss coefficient and air drying temperature under different vacuum degrees

3）真空度对空晒性能的影响

图 12 为真空管空晒性能参数随真空度的变化关系，真空管的空晒性能参数随压强的升高而降低，从图 12 中可以看出空晒性能参数随压强的变化主要位于 10^{-1}～10 Pa 的范围，其空晒性能参数从 264 K · m² · (kW)$^{-1}$下降到 102 K · m² · (kW)$^{-1}$，当压强小于 10^{-1} Pa 或大于 10 Pa 时热损系数变化很小. 所以为了保证良好的真空管热性能，通常需要将真空管夹层间的压强维持在 10^{-2} Pa 的数量级.

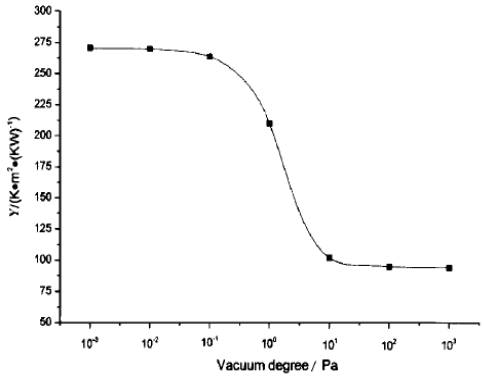

图12 真空管空晒性能参数与真空度的关系

Fig. 12 The correlations between Stagnation parameter and vacuum degree

6 结 论

通过对全玻璃真空管的空晒性能及其影响因素模拟分析,得出以下结论:

1)影响真空管空晒性能的主要参数为发射率和真空度.

2)真空管的热损系数随发射率的增加而增大,且同一发射率下其热损系数随真空管空晒温度的升高而增大,发射率升高真空管的空晒性能参数下降.

3)真空管空晒性能变化主要位于 10^{-1}～10 Pa 范围,当压强小于 10^{-1} Pa 或大于 10 Pa 由真空夹层间气体导热损失引起空晒性能的变化很小,所以为了保证良好的真空管热性能,通常需要将真空管夹层间的真空度维持在 10^{-2} Pa 的数量级.

4)涂层发射率越低,由辐射引起的热损失就越小,真空管的热性能越好.

参 考 文 献:

[1] YIN ZHIQIANG. Development of solar thermal systems in China[J]. Solar Energy Materials & Solar Cells, 2005, 86: 427-442.

[2] 殷志强,唐轩. 全玻璃真空太阳集热管光—热性能[J]. 太阳能学报,2001,22(1):1-5.

[3] MA FANGFANG, GAO WENFENG, LIU TAO, et al. An experimental study on the impacts of key parameters of all-glass evacuated tubes on the thermal performances of all-glass evacuated tube solar water heaters[J]. J. Renewable Sustainable Energy, 2013, 5(2): 347-355.

[4] ABDUL WAHEED BADAR, REINER BUCHHOLZ, FELIX ZIEGLER. Experimental and theoretical evaluation of the overall heat loss coefficient of vacuum tubes of a solar collector[J]. Solar Energy, 2011, 85(7): 1447-1456.

[5] 吴家庆,陶祖岩,王凤春,等. 玻璃真空集热管的真空获得与真空寿命[J]. 清华大学学报,1982,22(2):142-148.

[7] GUI YUZONG, XUE ZUQING, ZHOU XIAOWEN, et al. Determination of emittance of selective absorbing surfaces[J]. Solar Energy, 1998, 64(4-6): 241-243.

[8] 杨静芸,高文峰,刘滔,等. 三腔式全玻璃真空管闷晒性能的数值模拟及实验验证[J]. 太阳能,2014,12(12):55-60.

[9] GB/T 17049-2005,全玻璃真空太阳集热管[S].

[10] 殷志强,史月艳,林子为. 用于全玻璃真空集热管的黑镍选择性吸收涂层[J]. 清华大学学报,1982,22(4):49-58.

Numerical Simulation and Analysis on Stagnation Performance of All-glass Evacuated Collector Tubes

LIU Bai-hong, GAO Wen-feng, LIU Tao, LIN Wen-xian, XING Xiu-lan, HU Xiao-fang

(Solar Energy Research Institute, Key Laboratory of Advanced Technique & Preparation for Renewable Energy Materials of the Ministry of Education of China, Yunnan Normal University, Kunming 650092, China)

Abstract: In this paper, FLUENT has been used to simulate and analyze the stagnation performance of all-glass evacuated tubes, which size is Ø58×1 800mm, with different emittance and vacuum degree. In addition, the accuracy of numerical simulation also being verified through test. The numerical simulation results show that the lower is the emittance, the smaller is the heat loss and the better is the thermal performance of all-glass vacuumed tubes. What's more, the stagnation performance of all-glass evacuated tube decreases with the increase of the air pressure in the vacuum jacket. The stagnation change of all-glass evacuated tube mainly in the range of 10^{-1}～10 Pa. When the air pressure is lower than10^{-1} Pa or greater than 10 Pa, the thermal performance change caused by heat conduction loss of air in the vacuum jacket is not obvious. Therefore the vacuum degree of air jacket should maintain in the order of 10^{-2} Pa in order to guarantee good thermal performance of all-glass evacuated tube.

Keywords: Emittance; Vacuum degree; Heat loss coefficient; Stagnation parameter

云南师范大学学报(自然科学版)
2015 年 7 月 35 卷 4 期(Vol. 35 No. 4)

Journal of Yunnan Normal University
DOI:10.7699/j.ynnu.ns-2015-046

一种分仓真空管太阳能热水器运行特性实验研究*

邢秀兰， 高文峰， 刘滔， 林文贤， 刘佰红， 胡小芳
(云南师范大学 太阳能研究所,教育部可再生能源材料先进技术与制备重点实验室,云南 昆明 650092)

摘 要： 对一种分仓真空管太阳能热水器在晴天和多云天两种典型天气条件下进行了实验测试与分析,并与常规真空管太阳能热水器测试对比.结果显示无论是在晴天还是在多云天气下,分仓真空管太阳能热水器三个仓在当天运行条件下温度分层都比常规真空管太阳能热水器的明显,顶部和中部水温相差不大,但与底部水温相差较大.每个仓底部存在冷水区,但高温仓内的较明显.夜间温降期间,低温仓温度分层最严重,高温仓底部水温有明显的先升温后平缓的趋势.

关键词： 分仓真空管太阳能热水器;日有用得热量;平均热损因数;热性能
中图分类号： TK515 **文献标志码：** A **文章编号：** 1007-9793(2015)04-0011-08

1 引 言

真空管太阳能热水器以其良好的集热和保温性能,近年来受到国内外众多学者的关注和研究.影响真空管太阳能热水器热性能的因素很多,Jaisankar 等[1]详细论述了太阳能热水器的优势和提高其效率的各种方法和计算;李仁飞等[2]发现真空管太阳能热水器中真空管内部水温总体比水箱内水温高,且在真空管管口的上壁面出现温度最大值,在水箱底部存在一个冷水区,主要依靠水箱内从顶部到底部的温差导热传热而被加热;杨育芹等[3]发现管间距对真空管太阳能热水器的日有用得热量有很大的影响,理论上管间距越小,日有用得热量越大,但实际情况却完全相反,管间距越小,管与管之间的遮光越厉害,系统实际的日得热量越小,性能越差;谌学先等[4]发现家用太阳热水器的水量配比越大,其平均日效率越高.

本文所研究的对象为一种分仓真空管太阳能热水器(以下简称分仓热水器),即在太阳能贮热水箱中用两个不等高的隔板将热水器水箱分为相连的三个仓,用水时冷水始终从低温仓的下部进入,再进入中温仓,最后进入高温仓,减少用水时的冷热水的掺混,最大限度地利用了水箱中的热水.而在加热期间高温仓和中温仓中的水首先被加热.为了得到分仓热水器实际运行的热性能,将参照国家标准 GB/T 18708－2002[5]对分仓热水器在晴天和多云天两种典型天气条件下进行实验测试[6],并与常规热水器对比,分析这种分仓热水器的实际运行特性及与常规真空管太阳能热水器的差别,为这种新产品的优化设计及改进提供参考.

2 实验装置、测试方法以及热性能评价指标

2.1 实验装置

实验装置采用的是一套自然循环式的分仓热水器,其主要组成部分包括集热器、水箱和支架.该热水器所用真空管规格为 Ø58×1 800 mm,管数为 20 管,正南放置,倾角为 48°,采光面积为 2.64 m^2,水箱水量[7]为 210.3 L,其结构原理图如图 1.在贮热水箱中,用两块不等高的隔板将分仓热水器分为三个仓,在使用时,由于冷水从第一仓右下方进水口进入水箱,热水从第三仓左上方出来,因此由右到左分别给三个仓命名为低温仓、中温仓和高温仓.分仓热水器贮热水箱不与真空管直接相通,在水箱下部布置一加热仓,真空管直插入加热仓,加热仓上部设有四个高度不等的循环口,与贮热水箱相通.

这种结构的设计目的有二,其一是在加热循环期间,加热仓中的水首先被真空管加热,冷水从低温仓低部进入加热仓,热水大部分进入高温仓,

* **收稿日期:** 2015-06-10
基金项目: 国家自然科学基金资助项目(51266016,51469035).
作者简介: 邢秀兰(1990-),女,广东潮州人,硕士研究生,主要从事太阳能热利用及计算流体力学方面研究.
通信作者: 高文峰(1970-),男,副教授,主要从事太阳能热利用及计算流体力学方面研究. E-mail:413900096@qq.com.

一部分进入中温仓,使高温仓中的水首先被加热,然后再到中温仓,最后再加热低温仓;当用水时,冷水始终从低温仓的下部进入底层,把热水逐渐从低温仓顶进中温仓,最后进入高温仓,这样极大地减少用水时的冷热水的掺混,最大限度地利用了水箱中的热水.

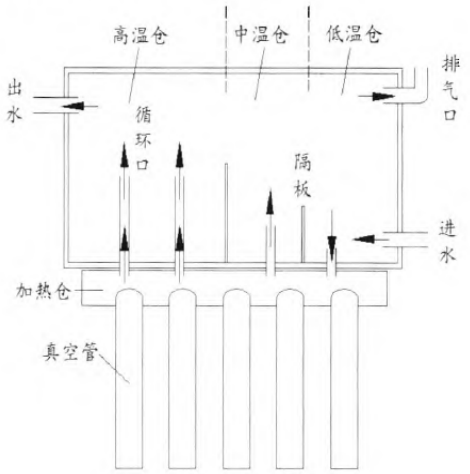

图 1 分仓热水器结构原理图

Fig. 1 Schematic diagram of the trichotomous solar water heater

2.2 实验测试方法

为了对分仓热水器白天温升以及夜晚温降情况进行实验测量,在高温仓、中温仓、低温仓三个仓内按高度等分安装上、中、下三个温度传感器.总辐射表与集热器采光面平行安装,环境温度由置于实验环境中的铂电阻温度传感器测得,风速由风速测量仪测得[8].试验在昆明的十二月份和一月份进行,试验的工作时间选择为每天太阳辐照较强的时段 9∶00－17∶00 内进行.为了得出分仓热水器运行性能,选取一套水量配比与之接近的常规真空管太阳能热水器进行对比试验.同样在常规太阳能热水器贮热水箱内按照体积等分布置上、中、下三个温度传感器监测其温度变化.

2.3 热性能评价指标

日有用得热量是判断家用太阳热水系统性能好坏的重要指标[9-11].通过对日有用得热量的测量可以评价太阳热水器在运行中转换了多少太阳辐照量为有用的热量[12];平均热损系数也是判断家用太阳热水系统热性能好坏的重要参数,反映了在无日照等条件下,热水器整体的保温性能.根据中华人民共和国国家标准《家用太阳热水系统热性能试验方法》(GB/T 18708－2002)所述的试验方法,规定家用太阳热水器的试验期间单位轮廓采光面积的日有用得热量 q 表达式为[5]

$$q=\frac{c_{pw}\rho_w V_s(T_e-T_b)}{10^6 A_c} \tag{1}$$

换算成太阳辐照量为 17MJ/(m² · d)时的日有用得热量 q_{17}:

$$q_{17}=17\frac{q}{H} \tag{2}$$

式中,c_{pw}为水的比热容,J/(kg · ℃);ρ_w 为水的密度,kg/m³;V_s 为贮热水箱中的流体容积,m³;T_e 为集热实验结束时贮热水箱内的水温,℃;T_b 为集热实验开始时贮热水箱内的水温,℃;A_c 为集热器轮廓采光面积,m²;H 为集热器采光面的日太阳辐照量,MJ/m².

平均热损系数 U_{SL}表达式为

$$U_{SL}=\frac{\rho_w c_{pw}}{\Delta\tau}\ln\left[\frac{T_i-T_{as\langle av\rangle}}{T_f-T_{as\langle av\rangle}}\right] \tag{3}$$

式中 $\Delta\tau$ 为降温时间,s;T_i 为热损实验中贮热水箱内的初始水温,℃;T_f 为热损实验中贮热水箱内的最终水温,℃;$T_{as(av)}$为热损实验中贮热水箱附近的平均空气温度,℃.

3 实验结果及分析

3.1 日有用得热量实验

3.1.1 晴天的运行特性

对分仓热水器进行多次实验测试,选取其中一个晴天条件下的数据进行分析.图 2 所示为选取的实验测试期间(2015 年 1 月 4 日 9:05－17:05)分仓热水器低温仓、中温仓、高温仓和常规热水器在晴天集热试验中的温升图.测试期间,太阳辐射强度变化为 57～1 142 W/m²,累计辐照量为 23.315 MJ/m²,环境温度为 12.2～24.7 ℃,平均值为 19.5 ℃.由图 2 可得:随着累计太阳辐照量的增大,分仓热水器三个仓和常规热水器的水温都在不断升高,常规热水器三条温升曲线基本重合.分仓热水器三个仓内顶部水温最高,中部水温次之,底部温度最低,顶部与中部水温相差较小,与底层水温相差较大,三个仓内总体温度分层明

显. 中温仓的顶部水温曲线与中部水温曲线间距是三个仓中最小的，底部水温曲线在早上 10 点之前处于缓慢升温，10 点之后才逐渐升温明显，温度与顶部、中部水温相差较大；高温仓的顶部水温曲线与中部水温曲线间距是三个仓中最大的，底部水温曲线在早上 11 点之前温度变化不大，11 点之后才逐渐有升温趋势，温度与顶部、中部水温相差是三个仓中最大的，仓内温度分层最明显. 随着累计太阳辐照量的增大，常规热水器贮热水箱内温度分层不明显，相比之下，分仓热水器无论是低温仓，中温仓还是高温仓，仓内温度分层都很明显，顶部与中部水温相差比较少，与底部温度相差最多，尤其是高温仓，温度分层最明显，底部温度与顶部温度最大温差可达 20 ℃；三个仓温度都偏低，最高温度只能到 46.7 ℃，与常规热水器底部终温相差 14.5 ℃.

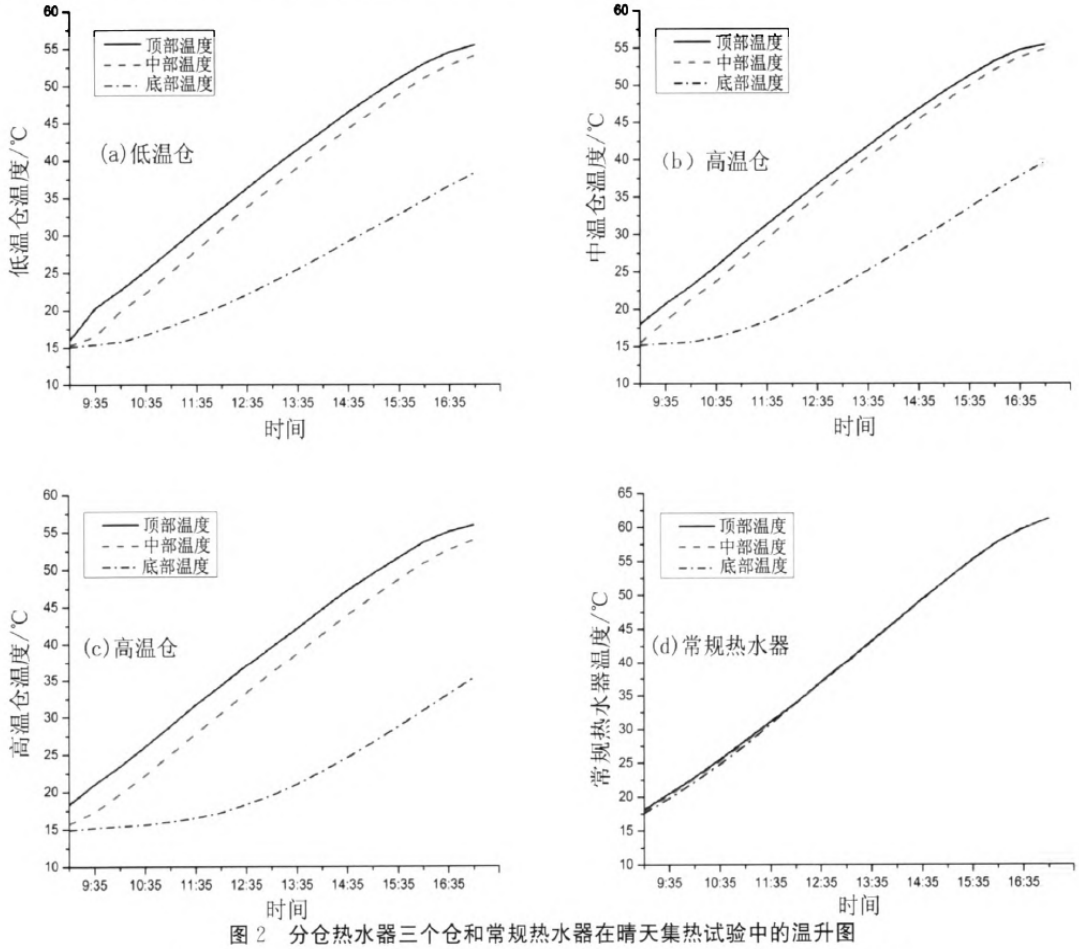

图 2　分仓热水器三个仓和常规热水器在晴天集热试验中的温升图

Fig. 2　The temperature curve in the trichotomous solar water heater and the regular solar water heater under the sunny weather condition

对比分仓热水器三个仓同样高度位置的水温温度变化，分仓热水器三个仓的顶部、中部和底部温度对比图如图 3 所示. 图 3(a)为三个仓顶部温度对比图，图中三条温升曲线基本重合；图 3(b)为三个仓中部温度对比图，其中中温仓的中部温度最高，低温仓和高温仓的温度曲线基本重合，三条温度曲线呈升温趋势；图 3(c)为三个仓底部温度对比图，在早上 10 点之前三条温度曲线重合，平缓升高，10 点之后，低温仓和中温仓的底部温度开始升温明显，其中低温仓底部温度最高，中温仓底部温度次之，下午两点后低温仓和中温仓底部温度曲线再一次相交，中温仓底部温度升温速度快于低温仓的，但两者温度相差不大，这期间高温仓底部温度曲线明显升温，但温度一直最低. 低温仓底部温度比高温仓的平均高 3.0 ℃.

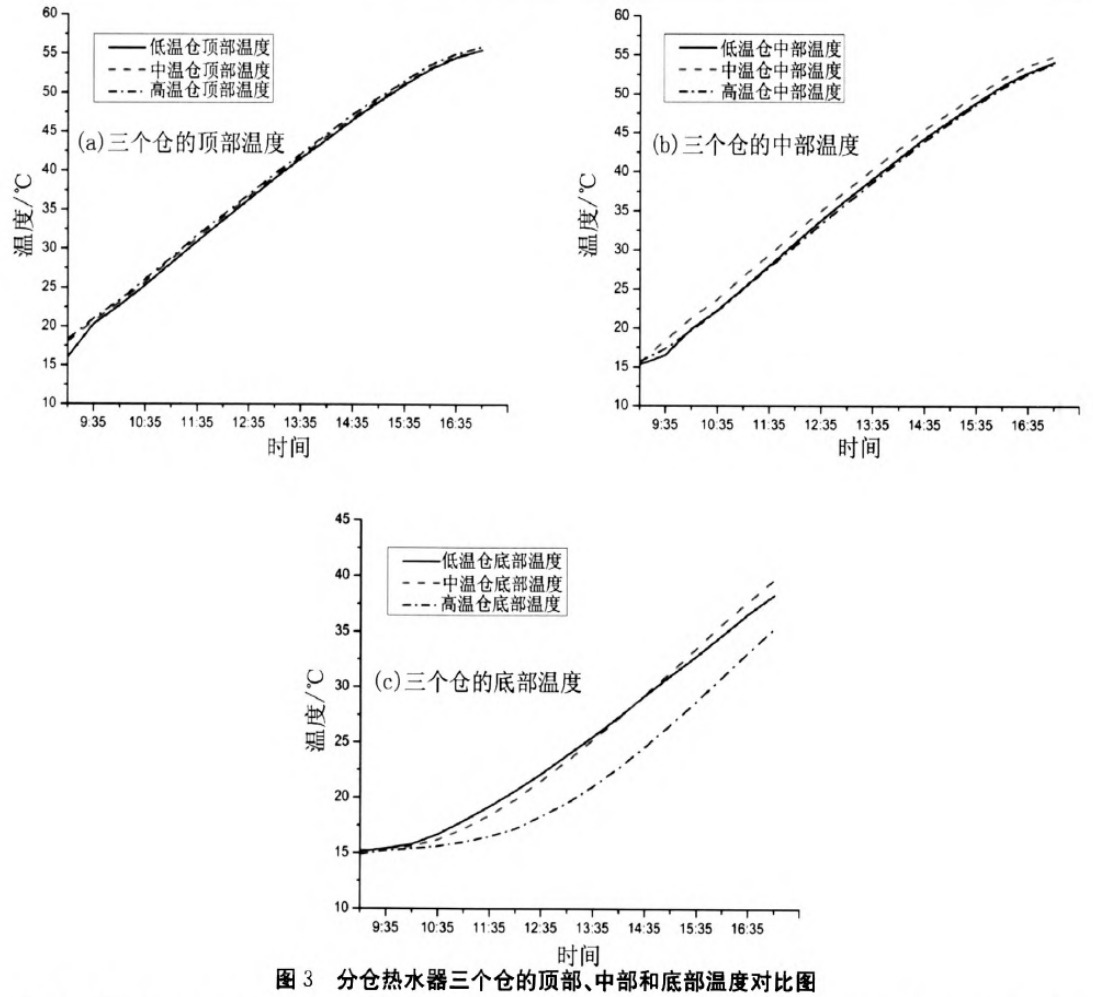

图3 分仓热水器三个仓的顶部、中部和底部温度对比图

Fig. 3 Temperature comparison diagram of top, middle and bottom in the trichotomous solar water heater

3.1.2 多云天气下的运行特性

经过对分仓热水器进行多次实验测试[13]，选取其中一天多云天气下的数据进行分析. 图4所示为分仓热水器低温仓、中温仓、高温仓在选取的实验测试期间(2014年12月31日9：05－17：05)的温度变化图. 测试期间，平均太阳辐照为377 W/m^2，累计辐照量为10.870 MJ/m^2，环境平均温度为11.2 ℃. 由图4可知，随着累计太阳辐照量的增大，分仓热水器三个仓和常规热水器的水温都在不断升高，但由于多云天气下辐照度波动比较大，温度曲线没有晴天天气下的平滑. 分仓热水器顶部水温最高，其温度曲线波动幅度最大，中部水温次之，曲线波动幅度较小，且与顶部的温差相差比较小，底部水温曲线呈平缓上升趋势，波动较小但与顶部、中部的水温相差较大. 中温仓顶部水温曲线与中部水温曲线间距是三个仓中最小的，底部水温曲线在早上11点之前升温比较慢，11点之后才明显升温，曲线较平滑，但与顶部、中部水温相差较大；高温仓的顶部水温曲线与中部水温曲线的间距是三个仓中最大的，底部水温曲线在中午12点之前温度变化不大，12点之后才逐渐有明显升温趋势，温度与顶部、中部水温相差很大，是三个仓中相差最大的；常规热水器顶部和中部两条温度曲线基本重合，底部温度曲线稍低，三条温度曲线都不平滑. 多云天气下，常规热水器水箱内有温度分层现象，但不严重，只是底部水温偏低1 ℃左右，顶部和中部温度曲线基本重合，相比之下，分仓热水器更为明显，顶部和中部温度曲线波动幅度大，温差最高可达到10 ℃，温度分层最明显的依旧是高温仓.

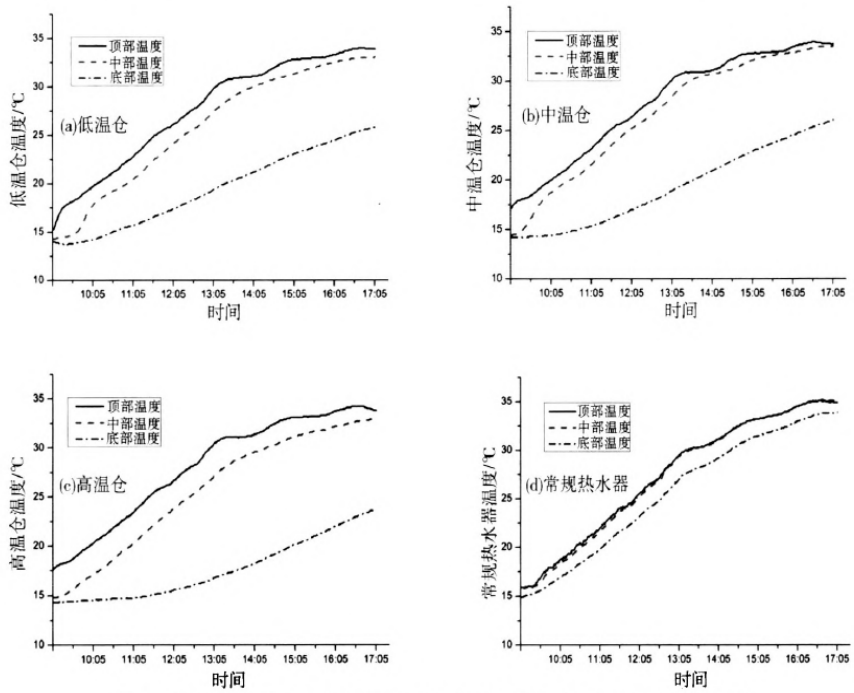

图 4　分仓热水器三个仓以及常规热水器在阴天集热试验中的温升图

Fig. 4　The temperature curve in the trichotomous solar water heater and the regular solar water heater under the cloudy weather condition

对比分仓热水器三个仓内的底部水温，如图 5 所示，三个仓内底部水温曲线平缓上升，刚开始高温仓的底部温度高于中温仓的和低温仓的，低温仓的底部温度最低；10∶30 时三个仓的底部温度一样；之后，低温仓底部温度变为最高，而高温仓的最低. 总的来说，低温仓和中温仓的底部温度相差无几，而与高温仓的温差较明显，高温仓底部温度比低温仓底部温度平均低 1.8 ℃，比中温仓平均低 1.6 ℃.

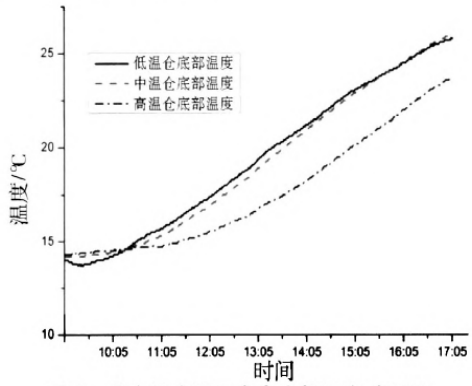

图 5　分仓热水器三个仓底部温度对比图

Fig. 5　Temperature comparison diagram in the bottom in the trichotomous solar water heater

3.1.3　不同天气下日有用得热量分析

将晴天天气下集热实验测得的分仓热水器三个仓数据取平均值，按照公式(1)、(2)计算，T_b＝16.0 ℃，T_e＝49.2 ℃，H＝24.315 MJ/m^2，得出日有用得热量 q＝11.07 MJ，换算成太阳辐照量为 17 MJ 时的日有用得热量 q_{17}＝8.07 MJ. 而常规热水器 T_b＝17.9 ℃，T_e＝61.2 ℃，H＝23.436 MJ/m^2，得出日有用得热量 q＝11.36 MJ，换算成太阳辐照量为 17 MJ 时的日有用得热量 q_{17}＝8.26 MJ. 分仓热水器晴天天气下的集热实验所

得的日有用得热量符合国家标准 GB/T 18708－2002 规定的合格标准,但其日有用得热量值比常规热水器的稍小.

同样,将多云天气下集热实验测得的分仓热水器三个仓数据取平均值,按照公式(1)、(2)计算,分仓热水器的 T_b＝15.1 ℃,T_e＝30.8 ℃,H＝10.870 MJ/m^2,得出日有用得热量 q＝5.24 MJ,换算成太阳辐照量为 17 MJ 时的日有用得热量 q_{17}＝8.19 MJ,常规热水器的 T_b＝15.6 ℃,T_e＝34.6 ℃,H＝10.368 MJ/m^2,得出日有用得热量 q＝4.98 MJ,换算成太阳辐照量为 17 MJ 时的日有用得热量 q_{17}＝8.16 MJ. 多云天气下,分仓热水器当天的日有用得热量大于常规热水器的,而由于多云天气下累计辐照量 10.870 MJ/m^2 没有达到国家标准 GB/T 18708－2002 规定的累计辐照量 17 MJ 以上,以上数据仅供参考.

3.2 平均热损系数实验

选取测试期间(2015 年 1 月 4 日 20∶00 到 1 月 5 日 04∶00)环境温度 12.8～17.9 ℃、环境平均温度为 15.0 ℃时的数据进行平均热损系数分析. 测试期间,分仓热水器三个仓和常规热水器的夜晚温降图如图 6 所示. 分仓热水器三个仓的顶部水温最高,中部水温次之,底部温度最低,温度分层明显,顶部与中部水温相差较小,与底部温度相差较大. 低温仓顶部、中部以及底部三条温度曲线呈下降趋势,其曲线间距是三个仓中最大的,即温度分层是三个仓中最明显的;中温仓顶部温度曲线和中部温度曲线的间距是三个仓中最小的,底部温度与顶部、中部水温相差较大,但其温度曲线有先升温后降温的趋势,降温幅度不大;高温仓顶部、中部以及底部三条温度曲线间距是三个仓中最小的,顶部和中部温度曲线呈降温趋势,底部温度有明显先升温后平缓的趋势;常规热水器三条温度曲线都呈降温趋势,其中中部水温最高,顶部水温次之,底部温度最低,并且底部温降最大. 与常规热水器相比,分仓热水器三个仓内温度分层更明显.

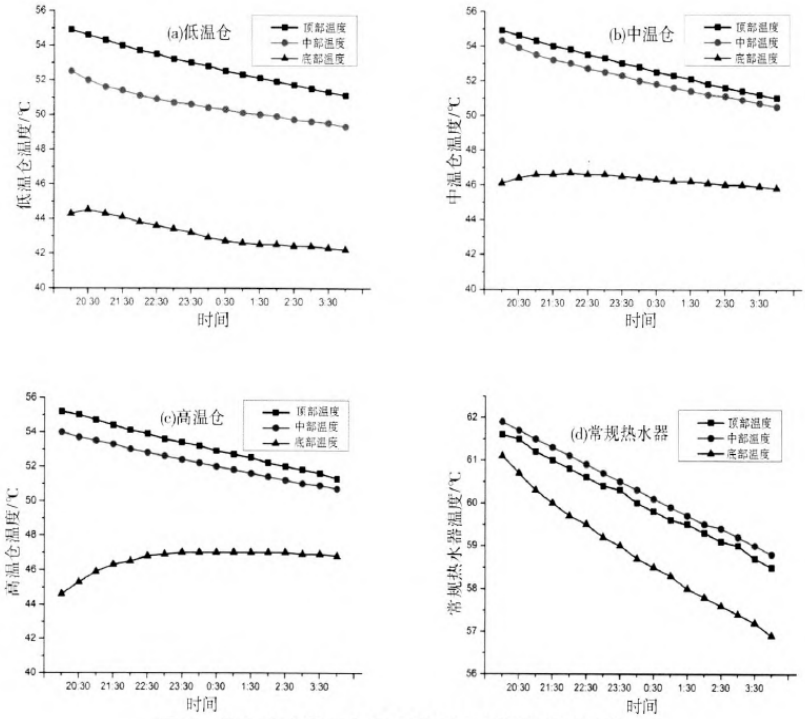

图 6 分仓热水器三个仓和常规热水器的夜晚温降图

Fig. 6 The temperature curve in the trichotomous solar water heater and the regular solar water heater during the nighttime cooling period

经过八个小时的降温测试，分仓热水器三个仓顶部、中部和底部的温降数据如表 1 所示. 由表 1 知三个仓顶部和中部水温温降相差在 1 ℃以内，底部温降相差比较大，低温仓底部水温温降为 2.1 ℃，中温仓底部水温温降为 0.3 ℃，而高温仓底部水温反倒升高了 2.2 ℃. 为了更好地了解，现作出三个仓的底部温度对比图，如图 7 所示. 图 7 中，低温仓底部温度曲线呈单纯降温趋势，中温仓底部温度曲线一直保持平缓降温趋势，而高温仓底部温度曲线有明显的先升温后平缓的趋势. 实验开始，中温仓的底部温度高于高温仓的底部温度，随着高温仓底部水温的升高，22：30 后，两条曲线相交，高温仓底部温度高于中温仓的底部温度. 这与常规热水器水箱内温度在夜晚单纯降低不同.

表 1　分仓热水器在夜间的温降结果

Table 1　The temperature data of the trichotomous solar water heater during the nighttime cooling period

项目	低温仓温度/℃			中温仓温度/℃			高温仓温度/℃		
	顶部	中部	底部	顶部	中部	底部	顶部	中部	底部
t_i	54.9	52.5	44.3	54.9	54.3	46.1	55.2	54	44.6
t_f	51.1	49.3	42.2	51	50.5	45.8	51.3	50.7	46.8
Δt	3.8	3.2	2.1	3.9	3.8	0.3	3.9	3.3	−2.2

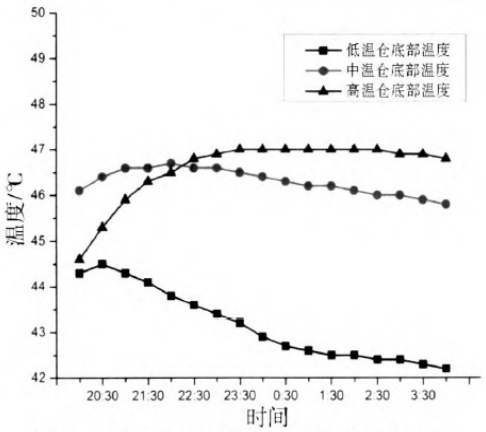

图 7　分仓热水器三个仓的底部温度对比图

Fig. 7　Temperature comparison diagram of the bottom in the trichotomous solar water heater

将分仓热水器的数据按照公式(3)计算，T_i = 51.2 ℃，T_f = 48.7 ℃，$T_{as(av)}$ = 15.0 ℃得出分仓热水器的平均热损系数 U_{SL} = 10.4；常规热水器的 T_i = 61.5 ℃，T_f = 58.1 ℃，$T_{as(av)}$ = 15.0 ℃，按照公式(3)得出平均热损因数 U_{SL} = 11.0，与常规热水器相比差别不大.

4　结　论

通过对分仓热水器在晴天和多云两种典型天气条件进行了当天热性能测试以及在夜晚的平均热损因数试验，并与常规热水器进行对比分析，可得出以下结论：

(1)无论是在在晴天还是在多云天气下，分仓真空管太阳能热水器三个仓在当天运行条件下温度分层都比常规真空管太阳能热水器明显，顶部和中部水温相差不大，但与底部水温相差较大. 每个仓底部存在冷水区，但高温仓内的较明显. 多云天气下，由于辐照度波动较大，仓内升温曲线不平滑.

(2)分仓热水器在经历夜晚降温时，低温仓温度分层最严重；与常规热水器的中部水温最高相比，分仓热水器三个仓都是顶部温度最高，并且相比常规热水器水温在夜晚呈单纯降温趋势，分仓热水器高温仓底部水温有明显的先升温然后平缓的趋势，温度升高了 2.2 ℃.

(3)在晴天及多云天气条件下,参照 GB/T 18708－2002 的试验及计算方法,分仓热水器与常规热水器的日有用得热量及平均热损因数差别不大,但分仓热水器最大的缺陷是在当天运行条件下仓内温度分层较重,这种分仓热水器设计上还应进行优化改进.

参 考 文 献:

[1] JAISANKAR S. A comprehensive review on solar water heaters[J]. Renewable and Sustainable Energy Reviews,2011,15(6):3045-3050.

[2] 李仁飞,高文峰,刘滔,等. 倾角对全玻璃真空管热水器温度场和流场的影响分析[J]. 太阳能,2014(11):25-29.

[3] 杨育芹,唐润生. 管间距对真空管家用太阳能热水器热性能的影响[J]. 云南师范大学学报:自然科学版,2014,34(1):36-40.

[4] 谌学先,高文峰. 家用太阳热水器水量配比与平均日效率关系[J]. 云南师范大学学报:自然科学版,2000,20(2):24-28.

[5] GB/T 18708－2002,家用太阳热水系统热性能试验方法[S]. 2002.

[6] 李元哲,董仁杰. 关于太阳热水器热性能评价的若干问题[J]. 太阳能,1999 (1):4-5.

[7] 管祚尧,王建伟. "日有用得热量"测试探讨[J]. 太阳能,2004 (6):41-42.

[8] 刘雪平,高文峰,许玲,等. 平板型立式水箱太阳热水器两种得热量测试方法对比研究[J]. 云南师范大学学报:自然科学版,2011,31(4):36-40.

[9] 宋爱国. 关于太阳热水器热性能评价指标[J]. 江西能源,2002 (2):43-44.

[10] GB/T 19141－2003,家用太阳热水系统技术条件[S]. 2003.

[11] 马迎昌,周玲,马光柏. 对日有用得热量试验条件的实验研究[J]. 太阳能,2011 (14):46-48+51.

[12] 李仁飞,高文峰,刘滔,等. 累计太阳辐照量对真空管太阳能热水器日得热量的影响[J]. 云南师范大学学报:自然科学版,2014,34(1):31-35.

[13] 黄祝连,张昕宇,邓昱,等. 环境温度对太阳能热水器日有用得热量测试的影响[J]. 建筑科学,2011,(S2):136-138.

Experimental Study on the Operating Characteristic of a Trichotomous Vacuum Tube Solar Water Heater

XING Xiu-lan, GAO Wen-feng, LIU Tao, LIN Wen-xian, LIU Bai-hong, HU Xiao-fang

(Solar Energy Research Institute, Key Laboratory of Advanced Technique & Preparation for Renewable Energy Materials of the Ministry of Education of China, Yunnan Normal University, Kunming 650092, China)

Abstract: In this paper, an experimental study has been carried out to examine the operating characteristic of a trichotomous vacuum tube water heater, which has three separate water tanks, under typical sunny and cloudy weather condition, which is also compared to that of a regular solar water heater. The results show that the temperature stratification of in the trichotomous solar water heater is stronger than that in the regular solar water heater, no matter it was under the sunny or cloudy weather conditions. In the trichotomous vacuum solar water heater, the temperature difference between the top and the middle is small, but there is a large temperature difference between the top and the bottom. In each water tank, there is a cold water zone in the bottom region, which is particularly evident in the high temperature water tank. During the nighttime cooling period, the temperature stratification in the low temperature water tank in the trichotomous solar water heater is the strongest, while in the bottom region of the high temperature water tank, the water temperature has the trend to rise initially but gradually become stable subsequently.

Keywords: Trichotomous vacuum tube solar water heater; Daily useful heat gain; Average storage tank heat loss coefficient; Thermal performance

第34卷 增刊 硅 酸 盐 通 报 Vol. 34 Supplement
2015年11月 BULLETIN OF THE CHINESE CERAMIC SOCIETY November, 2015

I型和VIII型Sr填充Si基、Ge基、Sn基笼合物电子结构的第一性原理研究

程 峰,王劲松,刘虹霞,申兰先,邓书康
(云南师范大学,可再生能源材料先进技术与制备教育部重点实验室,太阳能研究所,昆明 650500)

摘要:第一性原理是根据原子核和电子互相作用的原理及其基本运动规律,运用量子力学原理,从具体要求出发,经过一些近似处理后直接求解薛定谔方程的算法。本文采用第一性计算原理计算I-型和VIII-型Sr填充Si基、Ge基、Sn基笼合物的结构和性质,研究不同基团对笼合物结构与电传输特性的影响。结果表明:$Sr_8Ga_{16}Si_{30}$、$Sr_8Ga_{16}Ge_{30}$、$Sr_8Ga_{16}Sn_{30}$都是间接带隙半导体,$Sr_8Ga_{16}Sn_{30}$的带隙最小且体模量最大,$Sr_8Ga_{16}Sn_{30}$带边结构的不对称性说明$Sr_8Ga_{16}Sn_{30}$的热电性能性能可能优于$Sr_8Ga_{16}Si_{30}$、$Sr_8Ga_{16}Ge_{30}$,而引起材料结构性质差别主要为框架原子Sn、Ge、Si原子电子分布作用的结果。

关键词:第一性原理; 笼合物; 电子分布
中图分类号: **文献标识码**:A **文章编号**:1001-1625(2015)S-0335-05

First Principle Calculation of Structural and Electronical Properties for Type I and Type VIII Sr-filled Si-Ge-Sn-based Clathrates

CHENG Feng, WANG Jin-song, LIU Hong-xia, SHEN Lan-xian, DENG Shu-kang
(Solar Energy Research Institute, Education Ministry Key Laboratory of Renewable Energy Advanced Materials and Manufacturing Technology, Yunnan Normal University, Kunming 650500, China)

Abstract: First principle is an algorithm of using the principle of quantum mechanics to solve the schrodinger equation, which is according to the principle and the basic motion of interaction between atomic nucleus and electron. In this work, the structural and electronic properties of Type-I and Type-VIII Sr-filled Si-Ge-Sn-based clathrates have been investigated by fist principle calculation, and the effect of different atomic groups on the clathrate structure and electrical transport properties have been researched. The results suggested that $Sr_8Ga_{16}Si_{30}$, $Sr_8Ga_{16}Ge_{30}$ and $Sr_8Ga_{16}Sn_{30}$ are all belongs to indirect-gap semiconductors materials, and $Sr_8Ga_{16}Sn_{30}$ shows the smallest band gap and possesses the largest bulk modulus among them. The worse symmetry of band edge structure for $Sr_8Ga_{16}Sn_{30}$ indicated the higher performance than $Sr_8Ga_{16}Si_{30}$ and $Sr_8Ga_{16}Ge_{30}$ and the main reason for the differences between $Sr_8Ga_{16}Si_{30}$, $Sr_8Ga_{16}Ge_{30}$ and $Sr_8Ga_{16}Sn_{30}$ can be attributed to the different electronic distribution of Sn, Ge and Si atomic.

Key words: first principle; clathrates; electronic distribution

1 引 言

随着能源的紧缺,新能源的利用变为现代能源发展的重点。高效热电材料作为一种环境友好型新能源

基金项目:国家自然科学青年基金(51262032)
作者简介:程 峰(1988-),男,硕士研究生. 主要从事新能源材料方面的研究.

材料受到了人们的关注。热电材料的热电性能用无量纲性能指数 ZT 表示[1]，即 $ZT = \alpha^2\sigma T/\kappa$，其中 α 为材料的 Seebeck 系数，σ 为材料的电导率，κ 为材料的热导率。ZT 值越大，对应器件转换效率越高，因此人们希望通过提高热电材料的 ZT 值来提高热电器件的转换效率。近年来，具有复杂晶体结构的化合物如填充式笼合物[2-4]等由于具有较低的热导率和优越的电传输特性而成为研究的重点。

I 型和 VIII 型笼合物具有电子晶体-声子玻璃的热电传输特性[5]，是具有较高 ZT 值的热电材料之一[6-8]。I 型笼合物为简单立方结构，空间群为 $Pm\bar{3}n$，单位原包中包含有 6 个十四面体和 2 个十二面体，框架原子有 3 个晶体学位置，分别为 $6c$、$16i$ 和 $24k$，填充原子占据 $2a$ 和 $6d$ 2 个晶体学位置[9]。VIII 型笼合物也属于简单立立方结构，空间结构为 $I\bar{4}3m$，结构中只存在一种多面体[10]。框架原子存在 $2a$，$8c$，$12d$，和 $24g$ 4 个晶体学位置，填充原子只存在于 $8c$ 位置。目前研究的 I 型和 VIII 型笼合物主要为 Si 基、Ge 基、Sn 基笼合物。

在 I 型和 VIII 型 Si 基、Ge 基、Sn 基笼合物中，Sn 基笼合物由于其极低的晶格热导率 κ_L（室温 κ_L 低达 0.55 $Wm^{-1}K^2$）使其表现出良好热电性能，其中 Cu 掺杂 n 型 VIII 型单晶笼合物 $Ba_8Ga_{16}Sn_{30}$，500 K 时 ZT 值能达到 1.35[11]，Ge 掺杂 n 型 VIII 型单晶笼合物 $Ba_8Ga_{16}Sn_{30}$ 的在 500 K 时 ZT 值达到 1.25[12]。研究表明，该类化合物优越的电性能主要决定于框架原子的 sp^3 杂化，而较低的晶格热导率主要由于填充原子在多面体空洞内的“扰动”，这种扰动能对传热声子产生有效的散射，从而使其具有较低的晶格热导率，而且晶格热导率随填充原子半径的增加逐渐降低[13]。在 Sn 基笼合物的研究方面，目前主要集中在对 Ba 填充的 VIII 型 $Ba_8Ga_{16}Sn_{30}$ 的框架原子进行掺杂，通过提高材料的电传输特性对材料的热电性能进行优化。由于 Sr 与 Ba 相比半径较小，在不改变框架原子结构的条件下，与 $Ba_8Ga_6Sn_{30}$ 相比，Sr 填充 $Sr_8Ga_{16}Sn_{30}$ 笼合物由于具有更低的晶格热导率其热电性能理应更优越，但迄今为止尚未见 Sr 填充 Sn 基笼合物的报导。为了探究 Sr 填充 $Sr_8Ga_{16}Sn_{30}$ 笼合物热电材料的制备，本文基于第一性原理，分别对具有 I 型和 VIII 型结构的 Sr 填充 Si 基、Ge 基、Sn 基笼合物的电子结构、能带结构、态密度等进行计算和分析，探究不同原子基团对笼合物电子结构的影响，获得 Sn 基笼合物与 Ge 基、Si 基笼合物在电子结构上的区别，从而对该材料的热电传输特性进行预测，同时对后期材料的制备提供理论依据。

2 计算方法与理论模型

本计算基于密度泛函理论的第一性原理，电子与离子实的交互作用使用超软赝势[14]，电子的交互关联能采用广义梯度（GGA-PW91）近似处理[15,16]。在计算中取平面截断波能为 300 eV，第一布里渊区计算采用 4×4×4 进行分割选取，能量收敛精度为 10^{-6} eV/atom。在优化过程中我们采用了 BFGS 算法，先保持晶胞形状不变弛豫原子坐标，然后固定原子坐标计算平衡晶格常数，在能量最小的平衡状态计算结构性质、能带、态密度等。

为了获得在能量上支持的计算模型，我们对不同的 Ga 在 I 型 $Sr_8Ga_{16}Sn_{30}$ 中分布状况及不同 Ga-Ga 键数目对应的结构与最低能量结构的能量差 E（eV）进行计算。以 $Sr_8Ga_{16}Sn_{30}$ 为例，I 型笼合物中 Ga 存在框架上 $6c$、$16i$ 和 $24k$ 三种位置，计算表明当结构中包含有最少的 Ga-Ga 键和 $16i$ 位置上有较少的 Ga 时结构较稳定，通常认为 Ga-Ga 键由于存在静电排斥作用在能量上不受支持，并且 Ga 优先占据 $6c$ 位置，其次占据 $24k$ 位置。

VIII 型笼合物的填充原子只占据一个位置，即 $8c$ 位置，而框架原子有 $2a$，$8c$，$12d$ 和 $24g$ 四种位置。实验证明[21]Sn 优先占据 $2a$ 位置，因此在 VIII 型笼合物中 Ga 的位置分布在 $8c$，$12d$ 和 $24g$ 位置上。本工作中通过对结构进行优化，得到 VIII 型 $Sr_8Ga_{16}Sn_{30}$ 中框架上 $8c$ 位置和 $12d$ 位置上分别占据 8 个 Ga 原子时能量最低，说明这种结构越稳定，在实际过程中优先生成这种结构。

在上述优化结果的基础上，对 Si 基、Ge 基、Sn 基笼合物的晶格常数、能带结构和单点能进行计算。表 1 和表 2 分别为 I 型和 VIII 型 Si 基、Ge 基、Sn 基笼合物晶格常数、禁带宽度与单点能的对比。相比较于 Si 基和 Ge 基笼合物，Sn 基笼合物的 Sn 原子较重，组成笼子尺寸较大，所以晶格常数较大[17]，而研究表明，笼合物较低的晶格热导率主要源于填充原子在“空洞”内振动而对低频声子产生有效散射，而笼合物笼子尺寸越大，填充原子对传热声子的散射越强，导致晶格热导率越低[18,19]，说明在理论上 Sn 基笼合物较 Si 基和 Ge 基笼合物相比具有更低的晶格热导率。

表 1　I 型笼合物 $Sr_8Ga_{16}Si_{30}$、$Sr_8Ga_{16}Ge_{30}$、$Sr_8Ga_{16}Sn_{30}$ 晶格常数、单点能和禁带宽度

Tab. 1　Lattice constant, energy and band gap of type I clathrates $Sr_8Ga_{16}Si_{30}$, $Sr_8Ga_{16}Ge_{30}$, $Sr_8Ga_{16}Sn_{30}$

样品	晶格常数/nm	E_0/eV · atom^{-1}	E_g/eV
I-$Sr_8Ga_{16}Si_{30}$	1.065	−42763	0.351
I-$Sr_8Ga_{16}Ge_{30}$	1.093	−42767	0.365
I-$Sr_8Ga_{16}Sn_{30}$	1.192	−42413	0.003

表 2　VIII 型笼合物 $Sr_8Ga_{16}Si_{30}$、$Sr_8Ga_{16}Ge_{30}$、$Sr_8Ga_{16}Sn_{30}$ 晶格常数、能量和禁带宽度

Tab. 2　Lattice constant, energy and band gap of type VIII clathrates $Sr_8Ga_{16}Si_{30}$, $Sr_8Ga_{16}Ge_{30}$, $Sr_8Ga_{16}Sn_{30}$

样品	晶格常数/nm	E_0/eV · atom^{-1}	E_g/eV
VIII-$Sr_8Ga_{16}Si_{30}$	1.064	−42766	0.173
VIII-$Sr_8Ga_{16}Ge_{30}$	1.102	−42769	0.072
VIII-$Sr_8Ga_{16}Sn_{30}$	1.175	−42411	0.009

3　结果与讨论

笼合物的带隙变化对热电材料的性能有重要影响[20],图 1 为 Sr 填充 I 型和 VIII 型 Si 基、Ge 基、Sn 基笼合物的能带结构图。从图中可以看出 I 型和 VIII 型笼合物都为间接带隙半导体。结合表 I 可知具有 I 型结构的 Si 基和 Ge 基笼合物的带隙相近且远大于 Sn 基笼合物,而具有 VIII 型结构的笼合物随着框架原子外层电子数的增加带隙出现减小的趋势。对比图 2a、b,可以看出 I 型结构的 $Sr_8Ga_{16}Si_{30}$、$Sr_8Ga_{16}Ge_{30}$ 带隙高于 VIII 型结构的对应值,而 I 型和 VIII 型 $Sr_8Ga_{16}Sn_{30}$ 带隙都趋近于零,说明 $Sr_8Ga_{16}Sn_{30}$ 中的电子更容易被激发而进入导带,本征激发温度会较低,从而会导致材料最大 *ZT* 值出现的温度将较低。

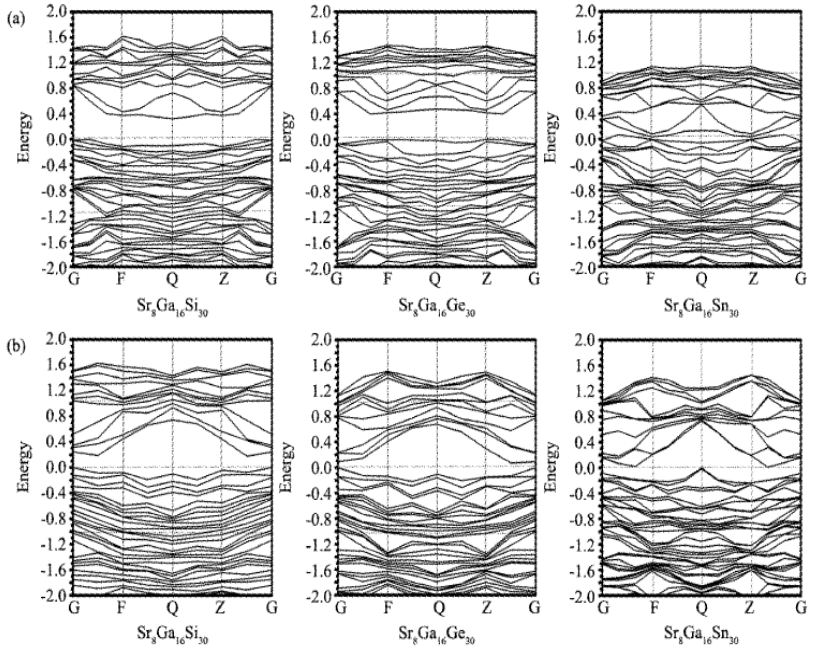

图 1　(a)I 型 $Sr_8Ga_{16}Si_{30}$、$Sr_8Ga_{16}Ge_{30}$、$Sr_8Ga_{16}Sn_{30}$ 能带结构;(b)VIII 型 $Sr_8Ga_{16}Si_{30}$、$Sr_8Ga_{16}Ge_{30}$、$Sr_8Ga_{16}Sn_{30}$ 能带结构

Fig. 1　(a) Band structure of type I clathrates $Sr_8Ga_{16}Si_{30}$、$Sr_8Ga_{16}Ge_{30}$、$Sr_8Ga_{16}Sn_{30}$;
(b) band structure of type VIII clathrates $Sr_8Ga_{16}Si_{30}$、$Sr_8Ga_{16}Ge_{30}$、$Sr_8Ga_{16}Sn_{30}$

热电材料的 Seebeck 系数和电导率都与费米能级附近的电子结构密切相关。较高的 Seebeck 系数需要

有高局域化的态密度,而较高色散度才能保证电子具有较高迁移率[21],因此高性能热电材料其能带带边结构应具有较大不对称性[22]。由图 2 可以看出对于 Si 基、Ge 基、Sn 基笼合物,I 型价带顶色散较小,VIII 型价带顶色散较大且随着 Si 基、Ge 基、Sn 基逐渐增大,即 VIII 型空穴具有较小的有效质量和较高的载流子迁移率,但 I 型较 VIII 型具有更高的局域化态密度,同时对比 $Sr_8Ga_{16}Si_{30}$、$Sr_8Ga_{16}Ge_{30}$、$Sr_8Ga_{16}Sn_{30}$可以看出 I 型和 VIII 型 Sn 基笼合物的带边结构的对称性最弱,说明 $Sr_8Ga_{16}Sn_{30}$可能具有较优越的热电性能。

为了进一步了解三种化合物的电子分布,我们同时计算了 I 型和 VIII 型 $Sr_8Ga_{16}Si_{30}$、$Sr_8Ga_{16}Ge_{30}$、$Sr_8Ga_{16}Sn_{30}$的电子总态密度如图 2 所示。图 2 表明对于 I 型和 VIII 型结构,$Sr_8Ga_{16}Si_{30}$、$Sr_8Ga_{16}Ge_{30}$、$Sr_8Ga_{16}Sn_{30}$的价带顶都处于相同的能级水平,而 $Sr_8Ga_{16}Sn_{30}$导带底明显低于 $Sr_8Ga_{16}Si_{30}$和 $Sr_8Ga_{16}Ge_{30}$,因此表现出更低的带隙。

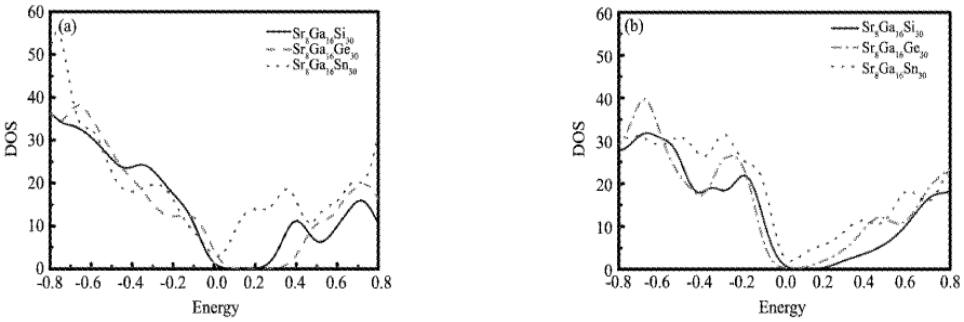

图 2 (a)I 型 $Sr_8Ga_{16}Si_{30}$、$Sr_8Ga_{16}Ge_{30}$、$Sr_8Ga_{16}Sn_{30}$电子态密度;(b)VIII 型 $Sr_8Ga_{16}Si_{30}$、$Sr_8Ga_{16}Ge_{30}$、$Sr_8Ga_{16}Sn_{30}$电子态密度

Fig. 2 (a)TDOS of type I clathrates $Sr_8Ga_{16}Si_{30}$、$Sr_8Ga_{16}Ge_{30}$、$Sr_8Ga_{16}Sn_{30}$;
(b)TDOS of type VIII clathrates $Sr_8Ga_{16}Si_{30}$、$Sr_8Ga_{16}Ge_{30}$、$Sr_8Ga_{16}Sn_{30}$

进一步分析各组成原子电子分波态密度发现 Sr 原子与 Ga 原子在各种化合物中作用相近,故本文不做详细分析。而 Si、Ge、Sn 原子的电子分波态密度对化合物影响较大。图 3 为 I 型和 VIII 型 Si、Ge、Sn 原子在各化合物中的电子分波态密度,通过与图 3 对比可以看出 I 型结构和 VIII 型结构中 Si、Ge、Sn 原子的电子分波态密度与对应的 $Sr_8Ga_{16}Si_{30}$、$Sr_8Ga_{16}Ge_{30}$、$Sr_8Ga_{16}Sn_{30}$的总态密度趋于一致,说明 $Sr_8Ga_{16}Si_{30}$、$Sr_8Ga_{16}Ge_{30}$、$Sr_8Ga_{16}Sn_{30}$的电子结构主要受 Si、Ge、Sn 电子分布影响。

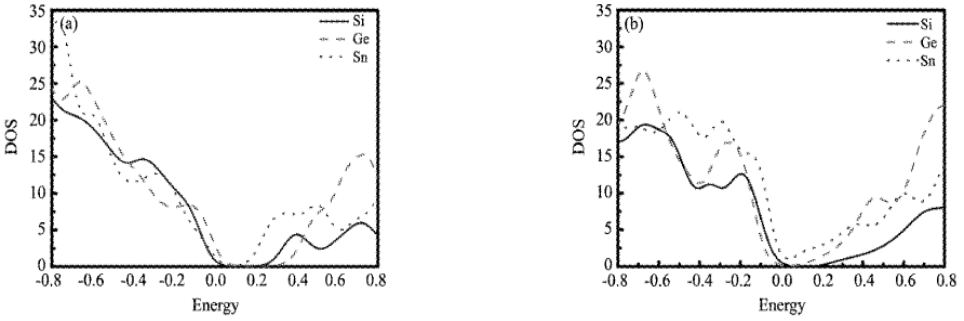

图 3 (a)I 型 Si、Ge、Sn 电子分波态密度;(b)VIII 型 Si、Ge、Sn 电子分波态密度

Fig. 3 (a)DOS of Si、Ge、Sn in type I clathrates Si、Ge、Sn;(b)DOS of Si、Ge、Sn in type VIII clathrates Si、Ge、Sn

与此同时通过分析 Si、Ge、Sn 原子各层电子的分波态密度如图 5,可以看出 Si、Ge、Sn 原子的 p 层电子对价带顶的贡献较大,I 型 Si 基笼合物的导带底受到 Si 原子 s、p、d 各电子层的综合作用,而 VIII 型 Si 基笼合物以及 I 型和 VIII 型 Ge 基、Sn 基笼合物的导带底主要受对应基团原子的 s、p 层电子影响。

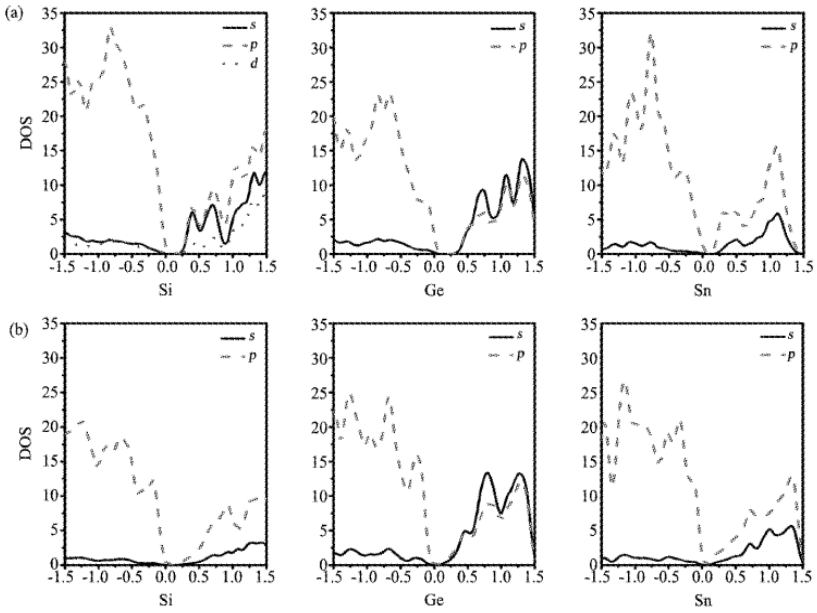

图 4　(a) I 型 Si、Ge、Sn 各层电子分波态密度;(b) VIII 型 Si、Ge、Sn 各层电子分波态密度

Fig. 4　(a) PDOS of Si、Ge、Sn in type I clathrates; (b) PDOS of Si、Ge、Sn in type VIII clathrates

4　结　论

本文基于第一性原理分别计算了 I 型和 VIII 型 Sr 填充笼合物 $Sr_8Ga_{16}Si_{30}$、$Sr_8Ga_{16}Ge_{30}$、$Sr_8Ga_{16}Sn_{30}$ 电子结构和性质。结果表明 I 型和 VIII 型笼合物都是间接带隙半导体,VIII 型笼合物较 I 型具有较高的载流子迁移率,而 I 型具有较高的局域化态密度,且随着 Si 基、Ge 基、Sn 基的变化 I 型和 VIII 型笼合物晶格常数都逐渐增加,禁带宽度趋于减小;相对于 I 型和 VIII 型 Si 基、Ge 基笼合物,Sn 基笼合物笼子尺寸较大,从而晶格热导率将更低,且空穴有效质量较小,能带带边结构不对称性较强,热电性能较好;造成 I 型和 VIII 型 Si 基、Ge 基、Sn 基笼合物结构和性质不同的原因主要为对应的 Si、Ge、Sn 原子的电子分布不同。

参　考　文　献

[1] Ioffe A F. Semiconductor thermoelements and thermoelectric cooling[M]. Abram Fedorovich, 1957.

[2] Okamoto N L, Kishida K, Tanaka K, et al. Crystal structure and thermoelectric properties of type-I clathrate compounds in the Ba-Ga-Ge system [J]. *Journal of applied physics*, 2006, **100**(7): 073504.

[3] Shao G. Prediction of structural stabilities of transition-metal disilicide alloys by the density functional theory[J]. *Acta materialia*, 2005, **53**(13): 3729-3736.

[4] Zhang J X, Qiu L Y, Zhu K J, et al. Thermosensitive micelles self-assembled by novel n-isopropylacrylamide oligomer grafted polyphosphazene[J]. *Macromolecular rapid communications*, 2004, **25**(17): 1563-1567.

[5] Slack G A, Rowe D M. CRC handbook of thermoelectrics[J]. *CRC, Boca Raton, FL*, 1995: 407440.

[6] Chen Y, Du B, Kajisa K, et al. Effects of in substitution for ga on the thermoelectric properties of type-VIII clathrate $Ba_8Ga_{16}Sn_{30}$ single crystals [J]. *Journal of Electronic Materials*, 2014, **43**(6): 1916-1921.

[7] Deng S, Saiga Y, Kajisa K, et al. High thermoelectric performance of Cu substituted type-VIII clathrate $Ba_8Ga_{16-x}Cu_xSn_{30}$ single crystals[J]. *Journal of Applied Physics*, 2011, **109**(10): 103704.

[8] Huo D, Sakata T, Sasakawa T, et al. Structural, transport, and thermal properties of the single-crystalline type-VIII clathrate $Ba_8Ga_{16}Sn_{30}$[J]. *Physical Review B*, 2005, **71**(7): 075113.

[9] Nolas G S, Cohn J L, Slack G A, et al. Semiconducting Ge clathrates: promising candidates for thermoelectric applications[J]. *Applied Physics Letters*, 1998, **73**(2): 178-180.

(下转第 343 页)